Abstract
Optomechanics with Superfluid Helium
Anna Dmitriyevna Kashkanova
2017

The field of optomechanics studies the interaction between electromagnetic and mechanical degrees of freedom via radiation pressure. This interaction is usually enhanced when both electromagnetic and mechanical degrees of freedom are normal modes of resonators, with the canonical optomechanical system being a cavity in which one mirror is mounted on a spring (thereby constituting a mechanical element). The majority of mechanical elements used in optomechanics to date are solid objects (mirrors, membranes, nanowires, etc); however fluids can also be used to form the mechanical element.

In this thesis, I describe the use of density waves in superfluid helium as a mechanical element in an optomechanical system. The reasons for using superfluid helium are the following: superfluid helium has high thermal conductivity, allowing it to be easily thermalized to cryogenic temperatures; it has negligible optical loss at IR wavelengths, which means it does not diminish the optical finesse of the cavity; finally its acoustic loss vanishes at low temperatures, allowing it to have a high mechanical quality factor.

In this system, we drive a normal mode of the density waves by modulating the optical intensity incident on the cavity. We also observe the mode's undriven thermal motion and from that extract its phonon number. The optomechanical effects of optical spring and optical damping were observed, as were signatures of the mechanical mode's quantum motion. These quantum signatures were the asymmetry between the Stokes and anti-Stokes sidebands, which arise from a combination of the mode's zero-point motion and the quantum backaction of the optical readout. We found agreement between these measurements and theoretical predictions (to within 20%) over a large range of mode temperatures.

Optomechanics with Superfluid Helium

A Dissertation
Presented to the Faculty of the Graduate School
of
Yale University
in Candidacy for the Degree of
Doctor of Philosophy

by
Anna Dmitriyevna Kashkanova

Dissertation Director: Jack Harris
December 2017

Acknowledgements

There are many people to whom I am grateful for their help, guidance and support in the last 6 years. I will not be able to thank everybody, but I will at least try to thank the people without whom writing this dissertation would be impossible, or at least very difficult and sad.

My PhD adviser, Prof. Jack Harris took me on as a graduate student, providing me an opportunity to work on a very interesting project. He taught me how to approach a new experiment and guided me every step of the way, from building the very first iteration of the experiment to writing papers. I can't thank you enough, Jack, for being a fantastic mentor, for your counsel and support and for assembling the lab of great people that I was lucky to work with. It is my also pleasure to thank the other members of my thesis committee, Prof. Steve Girvin, Prof. Peter Rakich and Prof. David Moore. Thank you for lending your time and experience, and for your comments and questions! I also would like to thank Prof. Pierre-Frainçois Cohadon for reading my thesis.

I would like to acknowledge the postdocs and graduate students with whom I have worked during various phases of this experiment. Lily Childress was the first person with whom I worked in Harris lab. Working with you, Lily, and learning from you was a great experience! Thank you for your patience in explaining things (often multiple times) and for always finding interesting questions I could tackle! I owe my gratitude to Nathan Flowers-Jacobs for his mentorship and all the help with building and designing the first helium device. Thank you for teaching me to be careful and thorough in planning and conducting experiments. Special thanks to Alexey Shkarin, who has been by my side for the last 3.5 years and with whom we built and conducted experiments, analyzed data, and learned as much as we could about superfluid optomechanics. The experiments described in this dissertation owe a lot to Alexey's knowledge of microwave engineering and his ingenuity in writing code which tremendously simplified and streamlined data collection process. I also want to acknowledge Charles Brown, who worked with us and contributed greatly to the experiment before moving on to a different project in our lab, as well as Kale Johnson, with whom we got to work together. Lucy Yu and Sean Frazier took over the project after me. It has been a pleasure to work with both of you and I am really excited to see what you will do with the helium filled cavity! Jeremy Berroir, our overlap was short, but it really made me wish you were staying here for more than just a few months to continue with our experiment.

It is my pleasure to extend my gratitude to all people with whom I discussed the issues with the experiment, who have helped and advised me along the way. Scott Hoch and Woody Underwood introduced me to the basics of optomechanics and experimental setups. Dave Mason and Anthony Lollo have been with me from day 1 to day 2200 of graduate school. Your support meant so much to me, whether it was helping me in preventing a dewar from exploding at midnight, looking over my posters and presentations, worrying together about interviews, jobs, postdocs, thesis... And also simply eating lunch with me for 6 years. I owe my gratitude to Donghun Lee who directed the setup of the dilution refrigerator and was happy to answer any questions that I had about it. I am grateful to Glen Harris, who brought a lot of knowledge about superfluid helium into our lab and with whom we had multiple fruitful discussions. I had a really wonderful time working with you, learning from you, and teaching you. I am really excited for the superfluid helium droplet project and wish you the best of luck with it.

I would like to thank Dustin Ngo and Ivana Petkovic, who always gave very useful advice, whether it was cryogenics, coding, organizing things or navigating postdoc interviews. And finally thanks to the rest of the Harris Lab with whom I did not work directly, but who definitely contributed to creating a friendly and positive atmosphere: Jack Sankey, Luyao Jiang and Manuel Castellanos-Beltran.

It is my pleasure to acknowledge Prof. Jakob Reichel and the members of his lab in Paris for helping me with machining the fibers used in the experiment. The Reichel lab was so friendly and accepting! Special thanks to Konstantin Ott and Sebastien Garcia for all the help during months leading up to my visit and while I was there. I learned a lot from you guys!

I would like to extend my gratitude to Prof. Hong Tang, Prof. Dave DeMille, Prof. Daniel McKinsey and Prof. Rob Schoelkopf for letting us borrow the equipment that was instrumental in getting the experiment to work. I am also thankful to Prof. Steve Girvin for meeting with us and giving us feedback about the project at various stages.

I am extremely thankful to the administration of the physics department, particularly to Sandy Tranquilly and Daphne Klemme for the tremendous amounts of help throughout the years.

I would also like to recognize support from the Yale Machine Shop. Thank you Vinnie, Dave and Craig for helping me build the experiments, for teaching me how to use a mill and a lathe and for all of the advice you have given me over the years.

I have made some of the best friends in New Haven and can not describe how lucky I feel. Thank you to Angela, Arina, Barry, Ben, Chris, Corey, Evan, Georgia, Hannah, Iva, Jed, Kirsty, Lynn, Ryan, Ruby, Shannon for your friendships, get-togethers, celebrations, barbecues, dinners, board games, hiking, climbing, skiing, road trips, airplane flights, help with moving multiple times! You guys are the best and this whole experience was so much better because you were here! Even though most of us have left or will soon be leaving New Haven, I hope that we will continue meeting and getting together through the years.

I would like to thank my Michigan family: Ralph, Linda, Kristi, Mandy, Markus and many more. Thank you for welcoming me into your home, for accepting me as one of your own and for your support throughout the last 14 years. I am incredibly lucky that back in 2003 you invited a girl from Uzbekistan to come and stay with you for a year.

I want to thank my family for their support. My mom encouraged me to go abroad to pursue my education, taught me the importance of thinking for myself, always inspiring me to push harder and do my best. She visited me here, when I missed her too much, got to know my friends, despite not speaking much English, and traveled with me. My father has been a great dad to me and my brother, as we were growing up. He supported us and encouraged us to pursue our dreams. My brother Oleg is someone that I can always depend on. He is loyal, caring and smart. He asks the best questions and it has always been very fun (and challenging) to explain my work to him. Finally, I would like to thank my husband Alexey. Thank you Alexey for your never-ending love, support and encouragement, for being organized and helping me plan things. Thank you for not letting me get too stressed and for helping me reach my goals. I am lucky to have married you and am excited for what is ahead of us. I love you.

Contents

List of Figures

List of Tables

List of symbols

Symbol	Description	Units
α	ratio of promptly reflected power to incident power	1
α	ratio of photons absorbed by the mirror to all photons lost in the cavity	1
α_{abs}	absorption coefficient, gives the fraction of light absorbed	1
$\alpha_{m,n}$	n^{th} zero of the derivative of J_m	1
α_{Raman}	light amplitude attenuation coefficient due to Raman scattering	m^{-1}
$\alpha_{\mathrm{Brillouin}}$	light amplitude attenuation coefficient due to Brillouin scattering	m^{-1}
α_{Total}	light amplitude attenuation coefficient due to Rayleigh+Brillouin scattering	m^{-1}
α_{3pp}	sound amplitude attenuation coefficient coefficient due to the 3 phonon process	m^{-1}
α_{hd}	sound amplitude attenuation coefficient coefficient in hydrodynamic regime	m^{-1}
α_{M}	molecular polarizability	$\mathrm{C\,m^2V^{-1}}$
α_{GM}	coefficient of the GM parameter temperature dependence $A_{\mathrm{GM}} = \alpha_{\mathrm{GM}} T^3$	$\mathrm{m\,s^2kg^{-1}K^{-3}}$
β	proportionality constant in $f_{\mathrm{app}} = \beta T^{18}$	$\mathrm{W^3m^{-5}K^{-18}}$
Γ_{ext}	rate of state transfer	s^{-1}
γ	mechanical linewidth (loss rate)	s^{-1}
γ_{ext}	mechanical linewidth due to external loss	s^{-1}
γ_{int}	mechanical linewidth due to internal loss	s^{-1}
γ_{opt}	shift in mechanical linewidth due to optical drive	s^{-1}
γ_{eff}	effective mechanical linewidth	s^{-1}
γ_{OMIT}	effective mechanical linewidth extracted from OMIT/A measurements	s^{-1}
γ_{TM}	effective mechanical linewidth extracted from thermal motion measurements	s^{-1}
γ_{mode}	total mechanical linewidth of the acoustic mode calculated from the thermal model for the second generation device	s^{-1}
$\gamma_{\mathrm{mode,int}}$	internal mechanical linewidth of the acoustic mode calculated from the thermal model for the second generation device	s^{-1}
γ_3	the coefficient for the cubic term in the phonon dispersion	$\mathrm{s^2kg^{-2}m^{-2}}$
Δ	detuning of the laser from the cavity	s^{-1}
$\Delta_{\mathrm{cav,LO}}$	detuning of the cavity from the LO	s^{-1}
$\Delta_{\mathrm{OMIT,LO}}$	effective detuning of the OMIT/A feature from the LO	s^{-1}
$\Delta_{\mathrm{LO,cav}}$	detuning of the LO from the cavity	s^{-1}
$\Delta_{\mathrm{beam,cav}}$	detuning of a beam from the cavity	s^{-1}
Δ_{TM}	effective detuning of the thermal motion Lorenzian from the center of the frequency band in which the measurement is conducted	s^{-1}
Δ_x	change in detuning of the laser from the cavity due to mirror displacement x	s^{-1}
Δ_{eff}	effective (measured) detuning of the laser from the cavity	s^{-1}
δ	phase	rad

ϵ	dielectric constant	1
ϵ	input coupling efficiency ($\kappa_{\mathrm{ext}}/\kappa$ assuming a single sided cavity)	1
ϵ	strain	1
ϵ_0	permittivity of free space	$\mathrm{C\ V^{-1}m^{-1}}$
ϵ_0	amplitude of strain associated with the acoustic mode's ZPF	1
ζ	input coupling efficiency ($\kappa_{\mathrm{ext}}/\kappa$ assuming any cavity)	1
η_δ	stochastic variable, defined so that $\langle \eta_\delta(t)\eta_\delta(t+\tau)\rangle = \delta(\tau)$	$\mathrm{s^{-1/2}}$
η	stochastic variable, defined as $\eta(t) = \sqrt{\frac{k_{\mathrm{B}}T}{\hbar\omega_{\mathrm{m}}}}\eta_\delta(t)$	$\mathrm{s^{-1/2}}$
$\hat{\eta}$	thermal noise operator	$\mathrm{s^{-1/2}}$
η	critical radius r_{crit}, assuming $n_{\mathrm{eff}} = 1$	m
η_{He}	first viscosity coefficient of helium	$\mathrm{kg\ m^{-1}s^{-1}}$
η_{film}	proportionality constant if $d_{\mathrm{film}} = \eta_{\mathrm{film}}h^{-1/3}$	$\mathrm{m^{4/3}}$
$\theta^{(q,n,m)}$	phase	rad
θ	angular coordinate in cylindrical coordinate system	rad
θ	divergence angle from a Gaussian mode	rad
θ_{c}	contact angle	rad
$\theta_{\mathrm{c,He}}$	superfluid helium contact angle	rad
κ	optical cavity linewidth (total loss rate)	$\mathrm{s^{-1}}$
κ_1	loss rate through the input mirror	$\mathrm{s^{-1}}$
κ_2	loss rate through the back mirror	$\mathrm{s^{-1}}$
κ_{ext}	external loss rate of a cavity	$\mathrm{s^{-1}}$
κ_{int}	internal loss rate of a cavity	$\mathrm{s^{-1}}$
κ_{Raman}	lower bound on optical linewidth due to Raman scattering	$\mathrm{s^{-1}}$
$\kappa_{\mathrm{Brillouin}}$	lower bound on optical linewidth due to Brillouin scattering	$\mathrm{s^{-1}}$
κ_{Total}	lower bound on optical linewidth due to Rayleigh and Brillouin scattering	$\mathrm{s^{-1}}$
κ_{th}	relaxation rate of helium temperature inside the cavity	$\mathrm{s^{-1}}$
κ_{sec}	the optical linewidth measured in seconds as the cavity length is swept	s
$\kappa_{\mathrm{ext,sec}}$	the input coupling measured in seconds as the cavity length is swept	s
κ_{S}	adiabatic compressibility	$\mathrm{m\ s^2kg^{-1}}$
κ_{T}	isothermal compressibility	$\mathrm{m\ s^2kg^{-1}}$
λ	wavelength	m
λ_{rad}	radiation wavelength	m
λ_{th}	thermal phonon wavelength	m
λ_{opt}	optical wavelength	m
λ_{ac}	acoustic wavelength	m
$\lambda_{\mathrm{opt,layer}}$	optical wavelength inside a particular DBR layer	m
$\lambda_{\mathrm{ac,layer}}$	acoustic wavelength inside a particular DBR layer	m
μ_{He}	viscosity of normal component of Helium II	$\mathrm{kg\ m^{-1}s^{-1}}$
ν	proportionality constant in $\mu_{\mathrm{He}} = \nu T^{-5} + 1.4\times10^6$ Pa s	$\mathrm{Pa\ s\ K^{-5}}$
ξ_δ	stochastic variable, defined so that $\langle \xi_\delta(t)\xi_\delta(t+\tau)\rangle = \delta(\tau)$	$\mathrm{s^{-1/2}}$
ξ_{He}	second viscosity coefficient of Helium	$\mathrm{m^{-1}s^{-1}kg}$
$\hat{\xi}_{\mathrm{int}}$	internal optical noise operator	$\mathrm{s^{-1/2}}$

$\hat{\xi}_{\mathrm{ext}}$	external optical noise operator	$\mathrm{s}^{-1/2}$
ξ	constant of proportionality in $k_{\mathrm{He}} = \xi T^3$	$\mathrm{W\ m^{-1} K^{-4}}$
ξ_{th}	constant of proportionality in $\tau_{\mathrm{th}} = \xi_{\mathrm{th}} T^{-5}$	$\mathrm{s\ K^5}$
ρ	mass density	$\mathrm{kg\ m^{-3}}$
ρ_{mat}	mass density of some material	$\mathrm{kg\ m^{-3}}$
ρ_{He}	mass density of helium II, $\rho_{\mathrm{He}} = 145$	$\mathrm{kg\ m^{-3}}$
ρ_{n}	mass density of the normal fluid component of helium II	$\mathrm{kg\ m^{-3}}$
ρ_{s}	mass density of the superfluid component of helium II	$\mathrm{kg\ m^{-3}}$
ρ_{e}	density fluctuations in time	$\mathrm{kg\ m^{-3}}$
ρ_{rad}	radiation density	$\mathrm{J\ m^{-3} Hz^{-1}}$
Σ	optomechanical self-energy	s^{-1}
σ_x	uncertainty in the position of an object	m
$\sigma_{x,\mathrm{meas}}$	uncertainty in the position of an object due to measurement	m
$\sigma_{x,\mathrm{RPSN}}$	uncertainty in the position of an object due to RPSN	m
σ_p	uncertainty in the momentum of an object	$\mathrm{kg\ m\ s^{-1}}$
σ_v	uncertainty in the velocity of an object	$\mathrm{m\ s^{-1}}$
σ_n	uncertainty in the number of photons	1
σ_P	uncertainty in power	W
σ	surface tension	$\mathrm{J\ m^{-2}}$
σ_{He}	surface tension of helium	$\mathrm{J\ m^{-2}}$
σ	transmitted optical power relative to the incident optical power	1
$\sigma_{\mathrm{dev}\to\mathrm{EDFA}}$	power incident on the EDFA relative to the power leaving the device	1
$\sigma_{\mathrm{dev}\to\mathrm{top}}$	power incident on the 99:1 beam splitter on the top of the fridge, relative to the power leaving the device	1
$\sigma_{\mathrm{top}\to\mathrm{EDFA}}$	power incident on the EDFA, relative to the power leaving the 99:1 beam splitter on the top of the fridge	1
τ	time interval	s
τ_{th}	thermal phonon lifetime	s
ϕ_{G}	Guoy phase shift	rad
ϕ_{mat}	acoustic loss angle for a material	rad
ϕ_{B}	phase of the background in the OMIT/A measurements	rad
ϕ_{L}	phase of the Lorentzian in the OMIT/A measurements	rad
χ_{xx}	mechanical susceptibility	$\mathrm{s^2 kg^{-1}}$
χ_{bb}	mechanical susceptibility	s
$\chi_{bb,\mathrm{eff}}$	effective mechanical susceptibility (including optical spring and damping)	s
χ_{aa}	cavity susceptibility	s
χ	proportionality coefficient in $Q_{\mathrm{ac,int}} = \chi / T^4$	K^4
Ψ	relative phase of the OMIT/A feature	rad
ψ	general solution to a wave equation	1
Ω	detuning of the probe beam from the control beam	s^{-1}
ω	frequency	s^{-1}
ω_{ac}	frequency on the sound wave	s^{-1}
ω_{cav}	cavity resonance frequency	s^{-1}
ω_{L}	laser frequency	s^{-1}

ω_{m}	mechanical resonance frequency	s^{-1}
$\Delta\omega_{\mathrm{m,opt}}$	shift in mechanical resonance frequency due to optical drive	s^{-1}
$\omega_{\mathrm{m,eff}}$	effective (measured) frequency of a mechanical oscillator	s^{-1}
ω_{rad}	radiation frequency	s^{-1}
ω_{FSR}	free spectral range of the cavity	s^{-1}
ω_{th}	thermal phonon frequency	s^{-1}
ω_{LO}	local oscillator frequency	s^{-1}
ω_{beam}	frequency of a beam	s^{-1}
$\omega_{\mathrm{Control(U,L)}}$	microwave tone frequency generating an upper/lower control beam	s^{-1}
ω_{Lock}	microwave tone frequency generating a lock beam	s^{-1}
ω_{Probe}	microwave tone frequency generating a probe beam	s^{-1}
ω_{VCO}	frequency of a VCO	s^{-1}
$\omega_{\mathrm{m,OMIT}}$	frequency of a mechanical oscillator extracted from the OMIT/A measurements	s^{-1}
ω_{mode}	frequency of the mechanical mode calculated from the thermal model for the second generation device	s^{-1}
$\tilde{\omega}$	complex frequency of the mechanical mode	s^{-1}
A	area	m^2
A_{s}	area	m^2
A	amplitude of an incident beam	$\mathrm{V\ m}^{-1}$
A_{B}	amplitude of the background during OMIT/A measurements	1
A_{L}	amplitude of the Lorentzian during OMIT/A measurements	1
A_{rel}	relative amplitude of the Lorentzian to the background during OMIT/A measurements	1
$A_{\mathrm{OMIT/A}}$	amplitude of the OMIT/A feature	1
$A_{\mathrm{blue(red)}}$	amplitude of the OMIT/A feature at $\Omega = \pm\omega_{\mathrm{m}}$	1
A_{GM}	Gorter-Mellink parameter	$\mathrm{s}^2\mathrm{m\ kg}^{-1}$
a	normalized phase modulation amplitude	1
a	stored energy amplitude	1
a_{i}	incident field amplitude	$\mathrm{s}^{-1/2}$
a_{t}	transmitted field amplitude	$\mathrm{s}^{-1/2}$
a_{r}	reflected field amplitude	$\mathrm{s}^{-1/2}$
$\hat{a}_{\mathrm{i}}$	light incident on the cavity (including any external optical noise)	$\mathrm{s}^{-1/2}$
$\hat{a}, \hat{a}^\dagger$	quantum ladder operators for the optical mode	$\mathrm{s}^{-1/2}$
$a_{\mathrm{blue(red)}}$	complex amplitude of the OMIT/A features	$s^{-1/2}$
$a'_{\mathrm{blue(red)}}$	relative complex amplitude of the OMIT/A features	1
a_{abs}	mirror absorption coefficient	1
a_{LO}	local oscillator amplitude	$\mathrm{s}^{-1/2}$
a_{p}	probe beam amplitude	$\mathrm{s}^{-1/2}$
a	coefficient determining how much the circulating photons contribute to the heating of helium in the cavity	K^4
$\vec{B}$	magnetic field	T
B	background noise during thermal motion measurements	$\mathrm{V}^2\ \mathrm{Hz}^{-1}$
b, b^*	classical analogs of ladder operators for the mechanical mode	1
$\hat{b}, \hat{b}^\dagger$	quantum ladder operators for the mechanical mode	1
b	coefficient determining how much the incident power contribute to the heating of helium in the cavity	$\mathrm{K}^4\mathrm{W}^{-1}$
b_v	proportionality coefficient in $\delta v_{\mathrm{He}} = b_v T^4$	$\mathrm{m\ s}^{-1}\mathrm{K}^{-4}$
b_ω	proportionality coefficient in $\delta\omega_{\mathrm{mode}} = b_\omega T^4$	$\mathrm{s}^{-1}\mathrm{K}^{-4}$
b_γ	proportionality coefficient in $\delta\gamma_{\mathrm{mode}} = b_\gamma T^4$	$\mathrm{s}^{-1}\mathrm{K}^{-4}$

C	multi-photon optomechanical cooperativity	1
C_0	single-photon optomechanical cooperativity	1
C_{th}	multi-photon optomechanical thermal cooperativity	1
C	specific heat capacity per unit mass	$\mathrm{J\,kg^{-1}K^{-1}}$
C	specific heat capacity per unit volume	$\mathrm{J\,m^{-3}K{-}1}$
C_{ii}	photocurrent autocorrelator	A^2
c	speed of light in vacuum, $c = 3 \times 10^8$	$\mathrm{m\,s^{-1}}$
c_{He}	speed of light in helium	$\mathrm{m\,s^{-1}}$
c_{mat}	speed of light in some material	$\mathrm{m\,s^{-1}}$
D_{tube}	channel diameter	m
d_{film}	thickness of helium Rollin film	m
d_{thin}	thickness of helium Rollin film at its thinnest point	m
d_{fiber}	fiber diameter	m
$d_{\mathrm{opt(ac),layer}}$	thickness of an optical (acoustic)layer in a DBR	m
$d_{\mathrm{sb,s}}$	separation of the sidebands from the carrier in the time domains	s
$\vec{E}$	electric field	$\mathrm{Vm^{-1}}$
E	an arbitrary component of an electric field, amplitude of a laser beam	$\mathrm{Vm^{-1}}$
E_0	amplitude of a laser beam, amplitude of a carrier	$\mathrm{Vm^{-1}}$
E_1	amplitude of a sideband	$\mathrm{Vm^{-1}}$
$E^{(\mathrm{circ})}$	amplitude of the circulating field	$\mathrm{Vm^{-1}}$
$E^{(\mathrm{circ,energy})}$	amplitude of the circulating field, corresponding to energy stored in a cavity	$\mathrm{Vm^{-1}s^{1/2}}$
E	energy	J
E_0	energy stored in a zero point fluctuation	J
e	electron charge $e = 1.6 \times 10^{-19}$	C
$\mathcal{F}_{\mathrm{ac}}$	cavity acoustic finesse	1
$\mathcal{F}_{\mathrm{ac,ext}}$	upper limit on cavity acoustic finesse imposed by external cavity loss	1
$\mathcal{F}_{\mathrm{ac,loss}}$	upper limit on cavity acoustic finesse imposed by acoustic loss inside the mirrors	1
$\mathcal{F}_{\mathrm{opt}}$	cavity optical finesse	1
F	force	N
F_{RP}	radiation pressure force	N
F_{RPSN}	radiation pressure shot noise force	N
F_{th}	thermal force	N
F_{sn}	force resulting from friction between normal fluid and superfluid component force	N
F	free energy	J
F_{cav}	function describing cavity response	arb
F_{OMIT}	function describing OMIT/A response	arb
F_{TM}	function describing thermal motion measurement response	$\mathrm{V^2Hz^{-1}}$
f_{diff}	fraction of phonons undergoing diffusive scattering	1
f_{spec}	fraction of phonons undergoing specular scattering	1
f_0	fraction of phonons reflected from the material	1
G_{th}	strength of the thermal force	$\mathrm{N\sqrt{s}}$
G_{RPSN}	strength of the RPSN force	$\mathrm{N\sqrt{s}}$
G_{PD}	photodetector gain	A
G	a complex number describing optomechanical coupling defined as $G = 1 + ig_{0,\mathrm{pt}}/g_0$	1
g_0	single photon radiation pressure (or electrostrictive) coupling	$\mathrm{s^{-1}}$

$g_{0,\mathrm{pt}}$	single photon photothermal coupling	s^{-1}
g_{T}	coupling rate to the temperature fluctuations	$\mathrm{s}^{-1}\mathrm{K}^{-1}$
g_{ta}	single photon heating rate	$\mathrm{s}^{-1}\mathrm{K}$
g_{tot}	total single photon optomechanical coupling (including photothermal coupling)	s^{-1}
$g_{0,\mathrm{max}}$	maximum single photon radiation pressure (or electrostrictive) coupling, achieved when the electric field has a node at the helium/mirror boundary	s^{-1}
g	multiphoton radiation pressure (or electrostrictive) coupling	s^{-1}
g	resonator g-parameters	1
$\hat{\mathcal{H}}$	Hamiltonian	J
$\hat{\mathcal{H}}_{\mathrm{int}}$	interaction Hamiltonian	J
$\hat{\mathcal{H}}_{\mathrm{int,bs}}$	beam-splitter Hamiltonian	J
$\hat{\mathcal{H}}_{\mathrm{int,pdc}}$	parametric down-conversion Hamiltonian	J
H_n	hermite polynomial of order n	1
h	height	m
h^*	height of capillary rise in a tube	m
h	Planck's constant, $h = 6.62 \times 10^{-34}$	J s
$\hbar$	reduced Planck's constant, $\hbar = h/2\pi$	J s
I	light intensity (power per unit area) $I = P/A$	$\mathrm{W\ m}^{-2}$
I	area under the Lorentzian during the thermal motion measurements	V^2
J_m	m^{th} Bessel function of the first kind	1
K	bulk modulus	Pa
K_{He}	bulk modulus of Helium II $K_{\mathrm{He}} = 8.2 \times 10^6$	Pa
k	wavenumber	m^{-1}
k	coefficient describing thermal conductivity of the fiber $k_{\mathrm{fiber}} \propto T^k$	1
$k^{(q,n,m)}$	wavenumber for the light confined in a cavity	m^{-1}
$k_{\mathrm{mod}}^{(q,n,m)}$	wavenumber for the light confined in a cavity, modified to account for the penetration of the electric field into the DBR	m^{-1}
k_{B}	Boltzmann's constant, $k_{\mathrm{B}} = 1.38 \times 10^{-23}$	$\mathrm{J\ K}^{-1}$
k_{He}	Helium heat conductivity	$\mathrm{W\ m}^{-1}\mathrm{K}^{-1}$
L	length	m
L_{cav}	cavity length	m
L_{opt}	optical cavity length	m
$L_{\mathrm{empty,opt}}$	empty optical cavity length	m
$L_{\mathrm{full,opt}}$	full optical cavity length	m
L_{mech}	mechanical cavity length (mirror separation)	m
L_{p}	penetration depth of the optical mode into the DBR	m
L	function describing complex Lorentzian on a real background	1
$L_{\mathrm{rr,bb}}$	function describing the ratio of area under the Lorentzian to the background for the theory describing thermal motion measurements (without including noise and attenuation)	s^{-1}
M	molecular mass	kg
m_{m}	mass of the mechanical resonator	kg
m	azimuthal mode number	1
N	number of absorbers on a DBR	1

N	added noise (in the units of shot noise)	1
N_{EDFA}	added noise by the EDFA (in the units of shot noise)	1
N_m	Bessel function of the second kind	1
n	number of photons	1
n_{signal}	number of photons in a signal beam	1
n_{mat}	refractive index of some material	1
n_{He}	refractive index of liquid heliuml $n_{\mathrm{He}} = 1.028$	1
n_{opt}	average occupation number for the optical mode	1
n_{m}	average occupation number for the mechanical mode	1
$n_{\mathrm{r,b}}$	occupation number for the mechanical mode extracted from the red/blue sideband	1
n_{th}	average thermal occupation number for the bath	1
n_{circ}	circulating photon number	1
n_{eff}	number of photons absorbed by a single absorber on a mirror during one cavity lifetime	1
$n_{\mathrm{circ,beam}}$	circulating photon number due to a particular beam	1
n_{mode}	average thermal occupation number for the bath calculated from the thermal model for the second generation device	1
P	power	W
P_{st}	stochastic variable, defined as $P_{\mathrm{st}}(t) = P(t) - \langle P \rangle$	W
P_{inc}	incident power	W
P_{ref}	reflected power	W
P_{circ}	circulating power	W
P_{total}	total power landing on a cavity	W
P_{fiber}	power reflected from a fiber mirror	W
P_{rr}	power reflected from a retro-reflector	W
P_{mir}	power absorbed by a single fiber mirror	W
P_{π}	the microwave power that would induce a phase change of π when sent to a phase modulator	W
$P_{\pi,\mathrm{dBm}}$	the microwave power that would induce a phase change of π when sent to a phase modulator	dBm
P_{dBm}	the microwave power sent to a phase modulator	dBm
$P_{\mathrm{rel,beam}}$	the power in a given beam relative to total power	1
$P_{\mathrm{act,beam}}$	the actual power in a given beam	W
p	pressure	Pa
p	momentum	m/s
p_{th}	thermal phonon momentum	m/s
p	normalized acoustic mode profile	1
Q	heat	J
$\dot{Q}$	heat flux	W
$\dot{Q}_1$	heat flux from a single absorber	W
Q_{m}	mechanical quality factor	1
Q_{ac}	acoustic quality factor	1
$Q_{\mathrm{ac,int}}$	limit on the acoustic quality factor by the internal cavity losses	1
$Q_{\mathrm{ac,ext}}$	limit on the acoustic quality factor by the external cavity losses	1
$Q_{\mathrm{ac,loss}}$	limit on the acoustic quality factor by loss inside the DBR stack	1
q_{opt}	number of optical half-wavelengths in the cavity, longitudinal mode number for the optical mode	1
q_{mech}	number of acoustic half-wavelengths in the cavity, longitudinal mode number for the acoustic mode	1
$\dot{q}$	heat flux per unit area	W m^{-2}

$\dot{q}_{\mathrm{crit},(1,2)}$	critical heat flux per unit area	$\mathrm{W\ m^{-2}}$
R	radius	m
R	radius of curvature	m
R_{tube}	radius of a tube	m
R_{fiber}	radius of a fiber	m
$R_{\mathrm{fer,in}}$	inner radius of a ferrule	m
$R_{\mathrm{fer,out}}$	outer radius of a ferrule	m
$R_{(\mathrm{opt,ac})}$	optical or acoustic power reflectivity	1
r	axial or radial distance	m
$r_{(\mathrm{opt,ac})}$	optical or acoustic amplitude reflectivity	1
r_{opt}	radius of an optical mode on the fiber face	m
S_{FF}	power spectral density of a force	$\mathrm{N^2Hz^{-1}}$
S_{FF}^{th}	power spectral density of a thermal force	$\mathrm{N^2Hz^{-1}}$
S_{aa}^{RPSN}	power spectral density of a field amplitude in the cavity	$\mathrm{Hz^{-1}}$
$S_{a_{\mathrm{i}}a_{\mathrm{i}}}^{\mathrm{RPSN}}$	power spectral density of a field incident on the cavity	$\mathrm{Hz^{-1}}$
S_{PP}^{RPSN}	power spectral density of shot noise power	$\mathrm{W^2Hz^{-1}}$
S_{FF}^{RPSN}	power spectral density of shot noise force on the oscillator	$\mathrm{N^2Hz^{-1}}$
$S_{\delta\hat{a}^\dagger\delta\hat{a}}$	power spectral density of photons leaving the cavity	$\mathrm{Hz^{-1}}$
$S_{\delta\hat{b}^\dagger\delta\hat{b}}$	power spectral density of phonons in the mechanical oscillator	$\mathrm{Hz^{-1}}$
S_{ii}	power spectral density of photocurrent	$\mathrm{A^2Hz^{-1}}$
S_{xx}	power spectral density of position	$\mathrm{m^2Hz^{-1}}$
s	entropy	$\mathrm{J\ K^{-1}kg^{-1}}$
s	displacement	m
$T_{(\mathrm{opt,ac})}$	optical or acoustic power transmission	1
T	temperature	K
T_λ	temperature at a λ-point of helium, $T_\lambda = 2.17$	K
T_{GS}	temperature at which the n_{th} for a mechanical oscillator is ≈ 1	K
T_{MC}	mixing chamber temperature	K
T_{dev}	device/bath temperature	K
t	time	s
$t_{(\mathrm{opt,ac})}$	optical or acoustic amplitude transmission	1
U	stored energy	J
U	acoustic mode profile	1
u	transverse profile of a propagating beam	1
u_{Gr}	Grüneisen constant	1
u	velocity	$\mathrm{m/s}$
V	volume	$\mathrm{m^3}$
V_{film}	volume of the rollin film covering the device and the sintered silver heat exchanger	$\mathrm{m^3}$
V	voltage	V
V_{DC}	DC voltage	V
V_{RF}	RF voltage	V
V_π	voltage that induces change in phase of ϕ when sent to the phase modulator	V
V_{rel}	voltage sent to the phase modulator relative to V_π	V
v	velocity	$\mathrm{m\ s^{-1}}$
v_{He}	sound velocity in helium II, $v_{\mathrm{He}} = 238.3$	$\mathrm{m\ s^{-1}}$

v_{crit}	critical superfluid film velocity	$\mathrm{m\,s^{-1}}$
v_{n}	velocity of the normal fluid component of helium II	$\mathrm{m\,s^{-1}}$
$v_{\mathrm{n,crit}}$	critical velocity of the normal fluid component of helium II	$\mathrm{m\,s^{-1}}$
v_{s}	velocity of the superfluid component of helium II	$\mathrm{m\,s^{-1}}$
$v_{\mathrm{s,crit}}$	critical velocity of the superfluid component of helium II	$\mathrm{m\,s^{-1}}$
w	beam radius	m
w_0	beam radius at the waist	m
w_f	beam radius in the fiber	m
w_m	beam radius at the cavity mirror	m
x	position	m
x_0	offset of optical mode from the ferrule axis	m
x_{ZPF}	zero-point fluctuation of the mechanical oscillator	m
$\hat{x}$	position operator	m
Z	acoustic impedance	$\mathrm{Pa\,s\,m^{-1}}$
Z_{He}	acoustic impedance of helium II, $Z_{\mathrm{He}} = 3.4 \times 10^4$	$\mathrm{Pa\,s\,m^{-1}}$
z	position	m
z_R	Rayleigh length	m

Chapter 1

Introduction

"Everything the light touches is our kingdom."
— Mufasa, *The Lion King*

The main goal of my graduate research was to develop a new kind of optomechanical system, consisting of a fiber Fabry-Perot cavity filled with superfluid helium. In this text, I will describe the work that I and my coworkers did to achieve that goal, from theoretical descriptions, to building the device, measuring the optomechanical effects and analyzing collected data. I will also talk about possibilities for future experiments and measurements. The results reported in this thesis add to the existing research in the field of optomechanics, represent one of the few cases of optomechanics with fluid as a mechanical element as well as the first demonstration of quantum optomechanical effects in a fluid.

Optomechanics studies coupling between electromagnetic and mechanical degrees of freedom. The coupling is often maximized when both the electromagnetic and mechanical degrees of freedom are normal modes of resonators. The standard realization is an optical cavity with an end-mirror on a spring, known as the canonical optomechanical system. The optomechanical coupling arises because light pushes on the oscillator via radiation pressure, and the position of the oscillator changes the resonant frequency of the cavity. There are a number of excellent articles [1, 2, 3] as well as textbooks [4, 5] reviewing the field of cavity optomechanics.

The interest in optomechanics stems from multiple directions. First, optomechanics was studied in the context of gravitational wave detection. Due to the quantum nature of light, individual photons reflect off the mirror at stochastic times. The fluctuating radiation pressure results in fluctuations of the mirror position. That radiation pressure shot noise (RPSN) is a fundamental noise source that could eventually limit the sensivity of interferometric gravitational wave detectors, such as LIGO [6]. Work is being conducted to mitigate the effects of RPSN in LIGO, however any observation of RPSN is an observation of a quantum mechanical effect in a macroscopic object, which is interesting in itself. This brings me to the next goal of optomechanics: quantum mechanics with large objects. It has been known for some time that elementary particles (such as photons and electrons) and even larger particles (such as molecules) behave according to laws of quantum mechanics - it is impossible to precisely measure their position and momentum, they can be in multiple states at the same time, and they can exhibit interference. However, people, cats and even ants seem to obey the laws of classical mechanics. Using optomechanical systems it was shown that relatively large mechanical objects can exhibit quantum behavior as well. The modes of mechanical resonators have been cooled into the quantum ground state in a number of experiments [7, 8, 9], RPSN has been observed at cryogenic and room temperatures [10, 11, 12], the modes of a mechanical oscillator have been entangled with microwave [13] and optical [14] fields, mechanical oscillators have been used to produce squeezed light [15]. It is intriguing to consider the influence of mass on the quantum behavior of the system, which would pave a road to studying gravitational decoherence mechanisms and eventually uniting the theory of gravity with quantum mechanics. This, however, is a very long-term goal. More tangible reasons to be interested in optomechanics come from the fact that optomechanical systems are very similar to standard systems used in quantum optics, such as atom-cavity QED. However, optomechanical systems are generally simpler, more robust and can easily be designed to be compatible with telecom wavelength light. This could enable mechanical oscillators to be used for

coherent quantum conversion between optical and microwave domains, and as quantum memory elements. Yet another reason is that mechanical motion can be coupled to anything, therefore mechanical elements in the quantum regime can be used to interface other quantum systems, such as NV-centers [16] or superconducting cubits [17].

There are a variety of implementations of optomechanical systems. There are cavities with actual movable end-mirrors, like the ones in the canonical system [18, 19]. A quest to separate the optical and mechanical degrees of freedom, lead our group to pioneer membrane-in-the-middle systems [20]. In those systems a thin dielectric membrane, positioned inside of a fixed cavity, serves as a mechanical oscillator. The membrane position in the cavity increases the effective cavity length. The magnitude of the increase is periodic in the membrane position. This idea has been very successful with systems used in our group [21, 22, 23, 9, 24] and in other groups [13, 24, 25]. Optomechanical crystals (a patterned dielectric material confining both optical and mechanical modes) is another extremely successful implementation [26]. Another optomechanical system is microtoroids or microspheres, in which whispering gallery optical modes couple to either a breathing mode of microtoroid/microsphere [27] or to a mode of an external beam brought into the evanescent field [28]. There are electromechanical circuits, which consist of an LC circuit in which one of the plates of the capacitor is movable [29]. Those devices are interesting because they are compatible with superconducting qubits and could be used for storing quantum information.

Optomechanical systems benefit from large optomechanical coupling (defined as the shift of the cavity resonance frequency due to zero-point-fluctuations (ZPF) of the mechanical oscillator), high optical finesse (which increases the lifetime of light in the cavity and therefore increases number of interactions each photon undergoes with the mechanical element), and high mechanical quality factor (which enhances the response of the oscillator at the mechanical resonance frequency). Additionally, good power handling and easy thermalization to low temperatures are desired, as quantum effects usually become more pronounced at cryogenic temperatures. These consideration lead us to build a superfluid helium filled Fabry-Perot cavity. Below 2.2 K Helium-4 enters a special state called Helium II, which is considered to be composed of two components: a normal component and a superfluid component. At very low temperatures (< 500 mK), the superfluid component dominates, comprising $> 99.9\%$ of total amount of helium. The superfluid component has vanishing viscosity and so can flow without loss. The density waves, which were studied in this experiment have low acoustic loss which scales as T^4 and is very small at the base temperature of a dilution refrigerator. Helium II has very low absorption and scattering of optical and near-IR photons, meaning it would not have any detrimental effect on cavity finesse. It has high thermal conductivity - which means that it can be thermalized to the temperature of the dilution refrigerator. Finally, as a fluid, it can conformally fill the cavity, so there is no need to align the mechanical element to the optical field. All of the device parameters (coupling, optical finesse and mechanical quality factor) can be calculated *a priori*. The optomechanical coupling arises because density fluctuations of helium modify the helium's index of refraction. That changes the effective cavity length, in the same way a change in mirror position does.

Superfluid helium has been extensively studied since the middle of the 20th century. Of particular relevance to the work described here are the measurements of its refractive index (dielectric constant), density, light scattering properties, sound velocity and attenuation, and thermal conductivity. The dielectric constant of helium was calculated by measuring the resonant frequencies of the lowest TE mode for an empty and filled microwave cavity in an experiment conducted in 1950 [30]. While the device used in the experiment was very similar to some of the devices employed in superfluid optomechanics nowadays [31, 32], measuring optomechanical interactions was not the goal of that experiment, and no experiments studying optomechanics with superfluid helium were conducted until the second decade of 21st century.

Therefore, as I was starting my work on the project, optomechanics with superfluid helium was still an unexplored field, which flourished in the last few years [31, 32, 33, 34, 35, 36, 37, 38, 39, 40, 41, 42, 43, 44]. There has been considerable progress: the mechanical quality factor of superfluid helium was demonstrated to be above 10^8 [32], the motion of superfluid helium modes was cooled and heated [34], superfluid helium was used for thermalize a mechanical element [45] and finally we observed quantum effects such as asymmetry and correlations of Stokes and Anti-Stokes sidebands generated by the motion of a superfluid helium density wave. There are still things left to explore, such as extending the studies of quantum effects to non-Gaussian optomechanics, probing ripplon modes (surface waves), and looking into possibilities of optomechanical coupling to vortices.

My goal with this thesis is to provide a thorough description of the experiments that I did during my graduate career as well

as a description of future goals. I hope these descriptions will be of use to students continuing the experiment. Another goal is to introduce the subject of optomechanics at a level accessible to a first-year graduate student. All derivations are provided in detail, especially things that I found particularly confusing. Finally I want to provide a concise, but useful description of the phenomena of superfluid helium, which was instrumental in our understanding of the system.

The structure of the thesis is as follows:

- **Chapter 2.** The purpose of this chapter is to introduce quantum optomechanics starting from very basic principles. I start with a historical introduction to radiation pressure and radiation pressure shot noise (RPSN). I discuss the influence of RPSN on the position measurements of a test mass and show that using a Fabry-Perot cavity improves the measurement uncertainty for a given input power. The classical equations of motion for an electromagnetic field inside a Fabry-Perot cavity are derived, starting from continuity of electric and magnetic fields at the interfaces. The equation of motion for the mechanical oscillator is derived as well. The forces acting on the mechanical oscillator are calculated. The quantum equations of motion are derived from the Hamiltonian. Finally the current state of the field of optomechanics is reviewed with the idea of convincing the reader that optomechanical cooperativity is an important figure of merit and that superfluid helium can potentially be used to achieve high optomechanical cooperativity.
- **Chapter 3.** In this chapter, I introduce superfluid helium and either postulate or derive some of the formulas that describe its properties. I review the literature in which superfluid helium was studied and give expressions for the sound attenuation, sound velocity and thermal conductivity of helium, that I will make us of the in following chapters
- **Chapter 4.** Here I discuss optomechanics with superfluid helium. I describe the mode shapes for optical and acoustic modes in a superfluid helium filled fiber cavity, discuss the mechanism of optomechanical coupling, single photon cooperativities as well as various other figures of merit. I discuss whether other materials can be used in place of superfluid helium. Finally I review the work of other groups on optomechanics with superfluid helium.
- **Chapter 5.** In this chapter I provide extensive theoretical derivations of the effects, such as dynamical back-action, measuring Brownian motion and sideband asymmetry with two control beams, and optomechanically induced transparency and amplification. I briefly discuss what effect the inclusion of photothermal coupling would have on the results.
- **Chapter 6.** Here I discuss the process of building the experiment. I talk about building and characterizing Fabry-Perot cavities. I discuss the technical details of the devices that we built. I talk about setting up the experimental gas handling system used to deliver helium to the experiment. Finally I discuss the measurement setup, calibrations that we performed and the way we take measurements and analyze the data.
- **Chapter 7.** In this chapter I discuss the first generation device including its mechanical quality factor, optomechanical coupling, temperature, which depends on both the mixing chamber temperature and the power incident on the device, and the maximum multiphoton and thermal cooperativity that can be achieved. I discuss our measurements of Brownian motion and the extracted phonon number. Finally I talk about other modes that we observed in the device (besides the paraxial mode) and discuss the way me measured and understood their frequencies and optomechanical coupling.
- **Chapter 8.** Here I discuss the second generation device. First I discuss the changes that we made, which allowed us to improve the mechanical quality factor and the power handling of the device. Then I talk about the device parameters that we achieved. I discuss the temperature of helium inside the device in detail, as well as the maximum multiphoton and thermal cooperativity. I discuss our measurements of Brownian motion and the asymmetry of the Stokes and anti-Stokes sidebands.
- **Chapter 9.** In this chapter I discuss future directions, such as non-Gaussian optomechanics, optomechanics with macroscopic cavities, and coupling to ripplon modes in half-filled cavities. I will focus on the ripplon modes, deriving the conditions for being able to partially fill a fiber Fabry-Perot cavity, mode frequencies and optomechanical coupling to the modes.

Chapter 2

Optomechanics

2.1 Radiation pressure

Sitting outside on a sunny day with a book you notice that the pages get warm in the sunlight. That is because the electromagnetic waves that sunlight is composed of carry energy. When paper absorbs that energy its temperature is increased. What you don't notice is that rays coming from the Sun are also exerting force on your book, ever so slightly pushing it away from you. That is because electromagnetic waves also carry momentum. The momentum can be transferred to a surface when light is reflected or absorbed by it, exerting a force on the surface [46]:

$$|F_{\mathrm{RP}}| = \frac{P(2-\alpha_{\mathrm{abs}})}{c} \tag{2.1}$$

Here P is the power in the incident light, c is the speed of light, and α_{abs} is the fraction of the light that is absorbed by the surface. Qualitatively, this can be understood in the following manner:

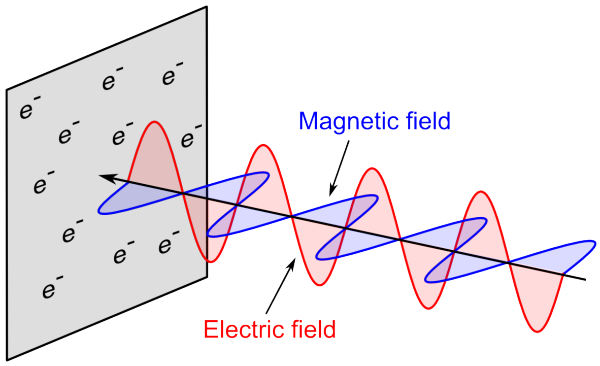

Figure 2.1: Qualitative explanation of radiation pressure

Assume some material with electromagnetic wave incident on it, as shown in figure 2.1. The electric field exerts force on the electrons $\vec{F} = -e\vec{E}$ causing them to move, therefore creating a current. The magnetic field exerts a force on the current $\vec{F} = -e\vec{v} \times \vec{B}$, pushing the material in the direction of wave propagation. However, in order for this simple model to give non-zero force, it is necessary to include some dissipation - there needs to be some resistance to the motion of the electrons [47]. This dissipation arises naturally from the absorption and from radiation of electromagnetic waves by the moving electrons.

The reason you never notice radiation pressure in everyday life is that it is very small, the radiation pressure of sunlight is ten orders of magnitude smaller than atmospheric pressure. Because of the small magnitude of radiation pressure, it was quite hard to measure. In the 18th century there was a series of attempts to measure radiation pressure without any conclusive results. One of the most famous is Crookes radiometer which was conceived in 1874 [48]. It consists of a glass bulb, inside of which there are vanes, free to rotate around a spindle. One side of the vanes is black (absorptive), the other is reflective. As light shines on the bulb, more momentum should be transferred to the reflective side, causing the radiometer to rotate. However, it was shown that radiation pressure was not, in fact, responsible for rotation. First, lowering the gas pressure inside the bulb, caused the rotation to stop. Second, the vanes were rotating in the wrong direction - with reflective side forward. After a few unsuccessful attempts, the behavior of the radiometer was explained by Osborne Reynolds, using the effect of "thermal transpiration" [49]. Thermal traspiration is a flow of a gas through porous plates, caused by the temperature difference of the plates. The gas flows from the colder side to the hotter side, which leads to higher pressure on the hotter side. The material that the vanes of the Crookes radiometer are made of does not have to be porous, as the gas molecules can move over the edges of the vanes from the light to the dark side, causing a pressure difference which rotates the vanes.

Despite failing to measure radiation pressure, Crookes radiometers are very popular as curiosity toys, as the vanes rotate under the influence of light only, without need for batteries. Figure 2.2 shows a photo of a beautiful display of radiometers found in a store in Munich, Germany.

Figure 2.2: Display of Crookes radiometers in a souvenir store in Munich

Radiation pressure was finally observed in 1900 by a Russian physicist Peter Lebedev [50] and in 1901 by American physicists Nichols and Hull, who observed the deflection of a torsion balance under illumination by a lamp [51, 52].

Despite the small magnitude of radiation pressure, it has proven to be quite useful. The Japanese space agency (JAXA) launched IKAROS (Interplanetary Kite-craft Accelerated by Radiation Of the Sun) in 2010. It is a light (2 kg), large (14 m $\times$ 14 m) solar sail, which was used to measure the force due to radiation pressure of the Sun. Another good example is optical tweezers, first built by Arthur Ashkin in 1970, which allowed for trapping of micron-sized dielectric particles, due to the change of momentum of light as it refracts inside of the particle [53]. Since then, the optical tweezer has become a very common tool in biology labs. An optical tweezer can be used to manipulate objects such as microscopic dielectric [54] and metal [55] beads, cells [56], lipid vesicles [57], RNA [58] and DNA [59].

Both of these examples can be explained using classical understanding of radiation pressure; however, the story does not end there. In 1901, German physicist Max Planck was trying to explain the experimentally obtained blackbody radiation spectrum, which classical theory was failing to explain. He was able to do it successfully by assuming that the oscillators composing the black body absorb and emit energy in discrete bundles (quanta). From this assumption he derived his

famous expression for the radiation energy density, which matched the data perfectly [60]:

$$\rho_{\rm rad}(\omega_{\rm rad}) = \frac{\omega_{\rm rad}^2}{\pi^2 c^3} \frac{\hbar\omega_{\rm rad}}{e^{\hbar\omega_{\rm rad}/k_{\rm B}T} - 1} \tag{2.2}$$

Here $\omega_{\rm rad}$ is the radiation frequency, T is the temperature of the black body, $\hbar$ is the Planck's constant and $k_{\rm B}$ is the Boltzmann constant.

In 1905 Albert Einstein wrote a paper on the photoelectric effect, where he stated that not only must oscillators emit and absorb energy in quanta, energy also travels in quanta, which we now call photons [61]. The radiation pressure force is described nicely in terms of photons. Consider a ray of light hitting the mirror. Each photon in the ray carries momentum $p = \frac{h}{\lambda_{\rm rad}}$, where h is the Planck's constant and $\lambda_{\rm rad}$ is the wavelength of light. When the photon hits the mirror it reflects with an equal and opposite momentum, so the change of its momentum is: $\Delta p = \frac{2h}{\lambda_{\rm rad}}$. That same momentum is transferred to the mirror. The force exerted on the mirror can be written as:

$$|F_{\rm RP}| = \frac{\Delta p}{\Delta t} = \frac{2\hbar\omega_{\rm rad}}{c\Delta t} = \frac{2E}{c\Delta t} = \frac{2P}{c} \tag{2.3}$$

This is consistent with the classical description, assuming $\alpha_{\rm abs} = 0$.

2.1.1 Radiation pressure shot noise

Einstein continued thinking about radiation for quite a few years, and in his 1909 paper [62] he performed a thought experiment, in which he considered a very reflective mirror with surface area A and mass m in a black box kept at temperature T. The black box emits radiation, which hits the mirror and exerts force on either front or back. If the force fluctuates, the mirror position and velocity will fluctuate as well. For simplicity he assumed that mirror reflects all radiation in a frequency range $\omega_{\rm rad} + d\omega_{\rm rad}$ and is transparent to all radiation at other frequencies. He used Planck's formula to show that the variance of the mirror velocity during some small time interval τ is given by:

$$\overline{\sigma_v^2} = \frac{\tau}{2\pi c m^2} \left[\frac{c^3 \rho_{\rm rad}(\omega_{\rm rad})^2}{4\omega_{\rm rad}} + \rho_{\rm rad}(\omega_{\rm rad})\hbar\omega_{\rm rad} \right] d\omega_{\rm rad} A \tag{2.4}$$

This expression consists of two terms, the first term is classical (it does not have $\hbar$) arising due to fluctuating interference of random waves in the box, the second term is quantum (it has $\hbar$), consistent with the assumption that radiation consists of independently moving, not too extended complexes of energy $\hbar\omega_{\rm rad}$, which arrive at the mirror at times uncorrelated with one another. This, to the best of my knowledge, is the first postulation of radiation pressure shot noise (RPSN).

In modern quantum mechanics, the fluctuations of the energy density of the radiation can be written in terms of photon creation/annihilation operators as:

$$\begin{aligned} \sigma_n^2 &= \langle n^2 \rangle - \langle n \rangle^2 \\ &= \langle \hat{a}^\dagger \hat{a} \hat{a}^\dagger \hat{a} \rangle - \langle \hat{a}^\dagger \hat{a} \rangle^2 \\ &= \langle \hat{a}^\dagger (\hat{a}^\dagger \hat{a} + 1) \hat{a} \rangle - \langle \hat{a}^\dagger \hat{a} \rangle^2 \\ &= (\langle \hat{a}^\dagger \hat{a}^\dagger \hat{a} \hat{a} \rangle - \langle \hat{a}^\dagger \hat{a} \rangle^2) + \langle \hat{a}^\dagger \hat{a} \rangle \end{aligned} \tag{2.5}$$

The first term is "wave-like" and can be viewed as Gaussian fluctuations of classical waves. The second term is "particle-like" and arises from the non-commutativity of the field amplitudes $\hat{a}$ and $\hat{a}^\dagger$ and represents the additional noise from the energy arriving in discrete quanta.

The interest in RPSN was renewed in the late 1970s, at the time when interferometric gravitational detectors were being developed. It was shown that RPSN was one of the factors limiting the detection sensitivity of mirror position [63], [6][1].

[1] Both of these papers actually address particularly the question of whether RPSN limits the sensitivity of interferometric gravitational wave detectors. The fact that RPSN would limit the sensitivity of a single mirror position detection was already well established. In the words of Carlton Caves: the "lively but unpublished controversy" was in whether a perfect beam splitter would split the fluctuations equally or not. If the fluctuations were split equally, the correlated fluctuations would not affect one's measurement of differential displacement; if they were not split equally, they would affect the measurement. The controversy was resolved with the conclusion that the RPSN does in fact limit the sensitivity of interferometric gravitational wave detectors.

To show how, we need to first talk about how position detection can be performed.

2.2 Position measurement of an object

In order to measure the distance to an object, one can use a ruler and achieve millimeter precision. However, this level of precision is often not sufficient, or using a ruler could be inconvenient (e.g. in case of measuring large distances). A fairly standard way to measure large distances is a laser rangefinder (LIDAR). A pulse of light is bounced off the object and the delay between sending the pulse and receiving it back is recorded. The range of measurements is on the order of km (or more under special conditions), with precision down to a few cm, limited by the sensitivity of the receiver as well as rise and fall time of the pulse. LIDARs have a wide range of applications: they are used to create topographical maps, for atmospheric studies and by policemen to detect the speeding cars. Different wavelengths of light can be used to target different objects. LIDAR was used to accurately measure the distance to the moon and the dynamics of the earth-moon system. That was done using retroreflectors installed on the moon during the Apollo missions [64]. Currently LIDAR technology is being considered for use in autonomous vehicles [65].

A precise measurement of the position fluctuations (with precision of less than one wavelength of light) could be done using a setup shown in figure 2.3. The displacement of the mirror by distance x leads to light traveling extra distance $2x$, which shifts the phase of the light by $2kx$ where $k = \frac{2\pi}{\lambda}$ is the wave-number, and λ is the wavelength of light. The phase of light landing on the photodetector will therefore depend on the mirror position. However, standard photodetectors can only measure intensity, so phase fluctuations need to be transformed into intensity fluctuations.

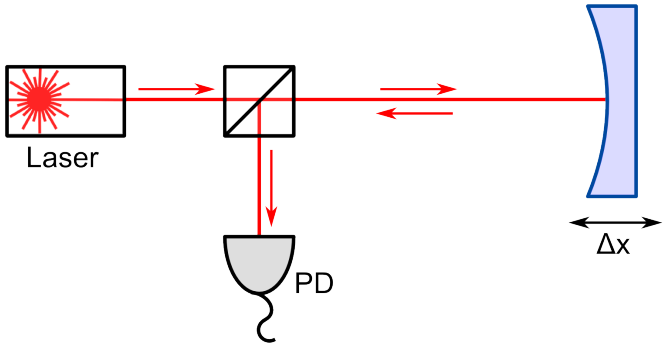

Figure 2.3: Measurement of the position of the mirror. The phase of light landing on the photodiode depends on the mirror position, but the amplitude is constant.

A historical way to transform the phase fluctuations into the intensity fluctuations is an interferometer, an example of which is shown in figure 2.4. An interferometer consists of a coherent light source incident on a beam-splitter, which splits the light into two arms (usually called the reference arm and the measurement arm) each with a mirror; the reflected light is then combined using the same beam-splitter and sent to a detector. The variation of the mirror position in the measurement arm will directly translate into variation of intensity of the detected light. Consider such an interferometer, with the length of the arms tuned so that the light interferes destructively. The time averaged intensity of the detected light, when one of the mirrors is displaced by x is given by:

$$\begin{aligned} \langle P \rangle &\propto \langle [E\sin(kL - \omega_{\mathrm{L}} t) + E\sin(k(L+2x) - \omega_{\mathrm{L}} t + \pi)]^2 \rangle \\ &= \langle 4E^2 \cos^2(k(L+x) - \omega_{\mathrm{L}} t)\sin^2(kx) \rangle \\ &= 2E^2 \sin^2(kx) \approx 2E^2 k^2 x^2 \end{aligned} \tag{2.6}$$

Here L is the distance from the beam-splitter to one of the mirrors and ω_{L} is the angular frequency of the laser. In this case power varies as position squared. A linear position measurement can be done if the length of the arms is tuned so that the light in the arms arrives at the beam splitter $\pi/2$ out of phase. This would result in the time averaged power:

$$\langle P \rangle \propto E^2 + 2E^2 kx \tag{2.7}$$

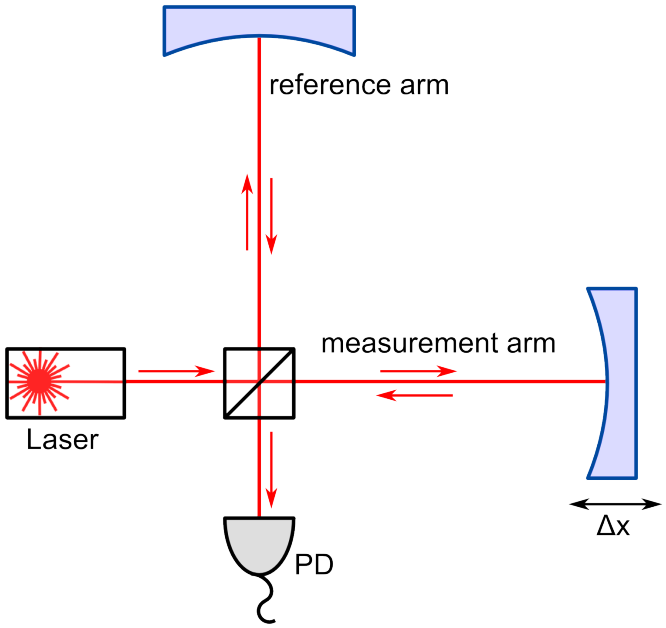

Figure 2.4: An example of interferometric measurement. The interference between the light in the reference arm and light in the measurement arm converts phase fluctuations into intensity fluctuations.

A famous example of an interferometer is the one built by Michelson and Morley [66] to measure the relative velocity of Earth and luminiferous aether - the substance in which electromagnetic waves were thought to propagate. Through their experiment Michelson and Morley concluded that aether was at rest relative to the Earth's surface, which in time lead to rejection of the idea of aether altogether.

Another example of a laser interferometry measurement is the Laser Interferometer Gravitational-Wave Observatory (LIGO), in which the interferometer arms are 4 km long. Both arms are measurement arms, because both mirrors can be affected by the gravitational wave. LIGO is designed to measure a distance change of $1/10,000^{\text{th}}$ of the width of a proton. In 2016 LIGO observed gravitational waves from a binary black hole merger [67].

Another way to transform phase fluctuations into intensity fluctuations is by using homodyne detection - adding a strong beam with amplitude $E_0 \gg E$ which is phase-locked to be $\pi/2$ out of phase with the measurement beam. That beam does not interact with the mirror and is added just before the photodetector, as shown in figure 2.5.

The power detected on the photodetector is in this case:

$$\langle P \rangle \propto \frac{E_0^2}{2} + 2E_0 Ekx \tag{2.8}$$

We will use this situation as an example to demonstrate why RPSN puts a limit on detection sensitivity.

The first term in the expression for the detected power gives the shot noise background. The number of photons landing on the photodetector in time interval τ is:

$$n = \frac{E_0^2}{2} \frac{\tau}{\hbar\omega_{\text{L}}} \tag{2.9}$$

The photon arrival times are random and uncorrelated with each other, therefore the process is Poissonian. The uncertainty

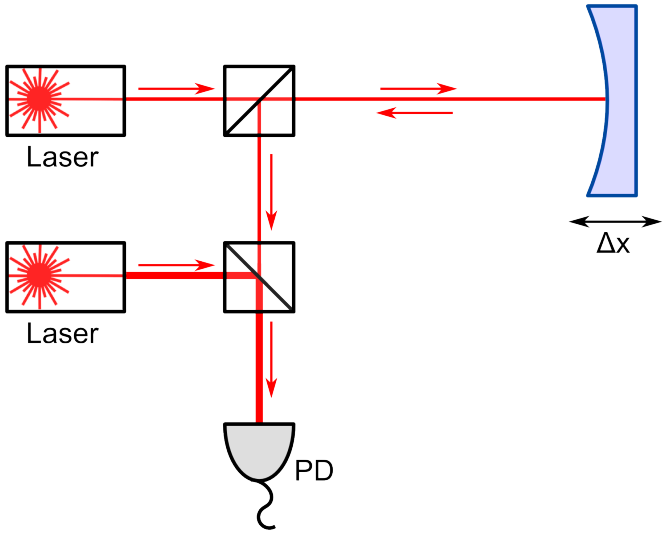

Figure 2.5: An example of homodyne measurement. The lasers need to maintain constant phase difference. It is also possible to construct the same measurement by using a single laser instead of two lasers. In that case an unequal beam-splitter and a couple of mirrors will be necessary.

in the photon number is $\sigma_n = \sqrt{n}$. The change in the number of photons due to displacement x is:

$$\Delta n = 2E_0 Ekx\frac{\tau}{\hbar\omega_{\mathrm{L}}} \tag{2.10}$$

Solving this expression we find that position is given by:

$$x = \frac{\Delta n\hbar\omega_{\mathrm{L}}}{2E_0 Ek\tau} \tag{2.11}$$

Since the uncertainty associated with the change in the number of photons is equal to the uncertainty associated with the total number of photons landing on the photodetector, the uncertainty in position is given as:

$$\sigma_{x,\mathrm{meas}} = \frac{\sigma_N\hbar\omega_{\mathrm{L}}}{2E_0 Ek} = \frac{1}{2\sqrt{2}k}\frac{1}{\sqrt{n_{\mathrm{signal}}}} \tag{2.12}$$

Where we used $E = \sqrt{\frac{n_{\mathrm{signal}}\hbar\omega_{\mathrm{L}}}{\tau}}$. Therefore the measurement uncertainty $\sigma_{x,\mathrm{meas}}$ decreases as more photons are sent on the mirror.

On the other hand, the photons push on the mirror, introducing uncertainty given as:

$$\sigma_{x,\mathrm{RPSN}} = \sigma_p\frac{\tau}{m_{\mathrm{m}}} = 2\hbar k\sqrt{n_{\mathrm{signal}}}\frac{\tau}{m_{\mathrm{m}}} \tag{2.13}$$

Here σ_p is the uncertainty in momentum, equal to momentum change per photon times the uncertainty in the photon number, and m_{m} is the mass of the mirror. Assuming $\sigma_{x\mathrm{RPSN}}$ and $\sigma_{x,\mathrm{meas}}$ are uncorrelated, the total uncertainty in the position measurement is the quadratic sum of the independent contributions: $\sigma_x = \sqrt{\sigma^2_{x,\mathrm{RPSN}} + \sigma^2_{x,\mathrm{meas}}}$. The total uncertainty is minimized for the photon number

$$n_{\mathrm{signal}} = \frac{m_{\mathrm{m}}}{2\sqrt{2}k^2\tau\hbar} \tag{2.14}$$

For this photon number, the uncertainty in the position detection is:

$$\sigma_x = \frac{1}{2^{1/4}}\sqrt{\frac{\hbar\tau}{m_{\mathrm{m}}}} \tag{2.15}$$

The minimum uncertainty in position can also be calculated from the Heisenberg Uncertainty principle $\sigma_x \sigma_p \geq \frac{\hbar}{2}$ as follows. Assume that at time $t = 0$, the minimum uncertainty product is :

$$\sigma_x(0)\sigma_p(0) = \frac{\hbar}{2} \tag{2.16}$$

The uncertainty of the position at time τ is given by

$$\sigma_x(\tau) = \sigma_x(0) + \frac{\sigma_p(0)\tau}{m_{\mathrm{m}}} = \sigma_x(0) + \frac{\hbar\tau}{2m_{\mathrm{m}}\sigma_x(0)} \tag{2.17}$$

This expression is minimized for

$$\sigma_x(0) = \frac{1}{2^{1/2}}\sqrt{\frac{\hbar\tau}{m_{\mathrm{m}}}} \tag{2.18}$$

Which is $1/2^{1/4}$ smaller than the uncertainty in the position detection found in equation 2.15.

The measurement can be improved by adding another mirror and forming an optical resonator (Fabry-Perot cavity) as shown in figure 2.6. This way each photon interacts with the movable mirror multiple times, increasing the phase change per photon by a factor equal to number of reflections off the back mirror.

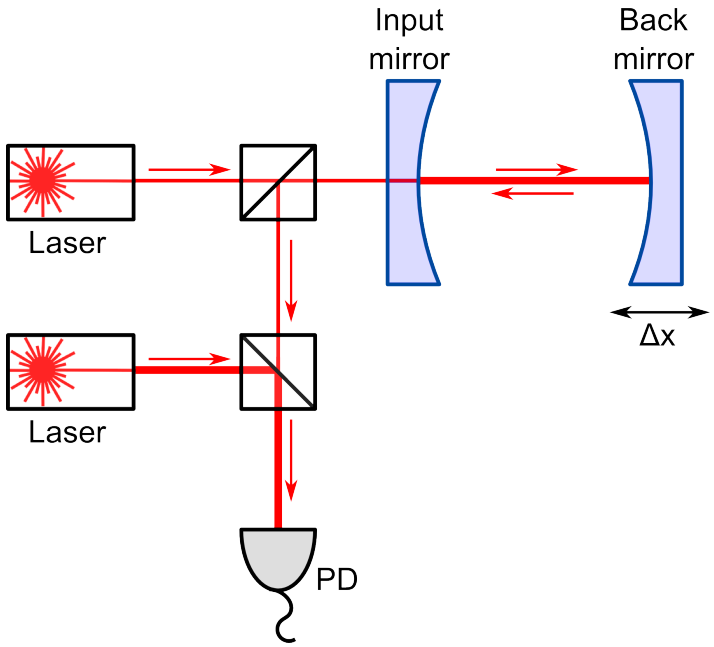

Figure 2.6: A Fabry Perot cavity consists of two mirrors facing each other. Light is coupled through an input mirror. The light reflected off and transmitted through the cavity can be recorded.

Figure 2.7 shows the change in the phase of the reflected light vs. the change is the mirror position for a single mirror (blue) and a Fabry-Perot cavity (red). In a Fabry-Perot cavity, the change in phase by 2π occurs over distance $\approx \lambda/\mathcal{F}$.

It is worthwhile to note that a Fabry-Perot cavity can be used to extract the position of the mirror without using an additional strong laser. It is possible to consider a Fabry-Perot cavity as an interferometer in which the light inside the cavity interferes with itself constructively or destructively, depending on the distance between the mirrors. The Fabry Perot cavity is the workhorse of our experiment so we will describe it in more detail.

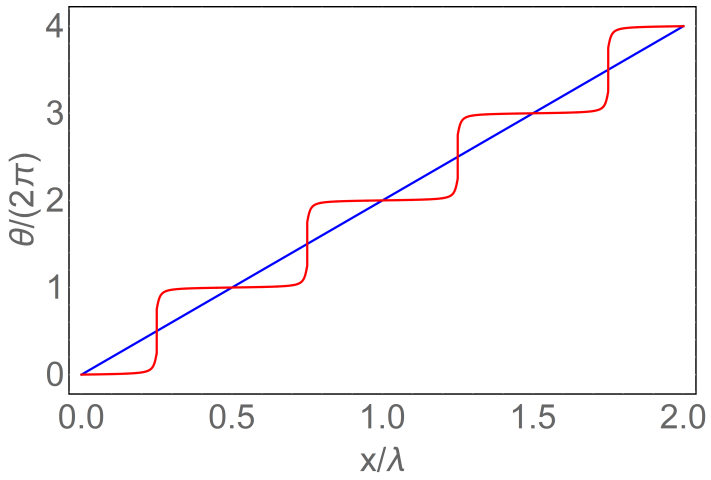

Figure 2.7: The change in the phase of the reflected light vs. the change is the mirror position for a single mirror (blue) and a Fabry-Perot cavity (red), vs. mirror displacement in the units of wavelength.

2.3 Fabry-Perot resonator

A Fabry-Perot resonator consists of two mirrors facing one another, separated by some distance L_{cav}. Similarly to standing waves on a string, the cavity can accommodate the standing waves of light, which satisfy the following relation:

$$2L_{\mathrm{cav}} = \lambda q_{\mathrm{opt}} \tag{2.19}$$

where λ is the wavelength of light, and q_{opt} is a positive integer, indicating how many half-wavelength of light are in the cavity. Using the relation between wavelength and frequency, we get the expression for the frequency of cavity modes:

$$\omega_{\mathrm{cav}} = 2\pi \frac{c}{2L_{\mathrm{cav}}} q_{\mathrm{opt}} \tag{2.20}$$

The free spectral range (FSR) is the frequency separation of different cavity modes:

$$\omega_{\mathrm{FSR}} = 2\pi \frac{c}{2L_{\mathrm{cav}}} \tag{2.21}$$

We start by assuming lossless mirrors, and an ideal cavity (no scattering or absorption). Since the mirrors transmit some of the light, the intensity of light in the cavity decays. We call the decay rate (cavity linewidth) κ. We can use it to define the cavity finesse, which is the average number of round-trips a photon makes before it leaves the cavity:

$$\mathcal{F}_{\mathrm{opt}} = \frac{\omega_{\mathrm{FSR}}}{\kappa} \tag{2.22}$$

The fields inside and outside the cavity are calculated in Appendix A.1 to be:

$$a = \frac{a_{\mathrm{i}}\sqrt{\kappa_1}}{\frac{\kappa}{2} - i\Delta} \tag{2.23}$$

$$a_{\mathrm{t}} = (-1)^{q_{\mathrm{opt}}} \frac{a_{\mathrm{i}}\sqrt{\kappa_1\kappa_2}}{\frac{\kappa}{2} - i\Delta} \tag{2.24}$$

$$a_{\mathrm{r}} = a_{\mathrm{i}} - \frac{a_{\mathrm{i}}\kappa_1}{\frac{\kappa}{2} - i\Delta} \tag{2.25}$$

Here a_{i} is the amplitude of the incident laser, κ_1 and κ_2 are loss rates through the first and second mirror and Δ is detuning of the driving laser from the cavity. Note that a has different units from a_{i}, a_{t} and a_{r}. That is because a is the

field amplitude corresponding to the *energy* stored in the cavity, while the other quantities describe the amplitude of the beam, which corresponds to the *power* in each beam.

In what follows we will work in the high finesse approximation: $\kappa \ll \Delta\omega_{\mathrm{FSR}}$, meaning that the cavity modes are spaced far enough, that the drive laser is always addressing a single cavity mode.

Equation 2.23 is a steady-state solution for laser drive at frequency ω. This is also a Fourier component of the intracavity field $a[\omega]$. Replacing $\Delta = \omega - \omega_{\mathrm{cav}}$ and rewriting equation 2.23, we arrive at:

$$-i\omega a[\omega] = a[\omega]\left(-\frac{\kappa}{2} - i\omega_{\mathrm{cav}}\right) + a_{\mathrm{i}}[\omega]\sqrt{\kappa_1} \tag{2.26}$$

Going into the time domain, and using the fact that the inverse Fourier transform of $-i\omega a[\omega]$ is $\dot{a}$, we arrive at the time-domain equation for the intracavity field.

$$\dot{a}(t) = a(t)\left(-\frac{\kappa}{2} - i\omega_{\mathrm{cav}}\right) + a_{\mathrm{i}}(t)\sqrt{\kappa_1} \tag{2.27}$$

2.3.1 Fabry-Perot resonator with one movable mirror

If one of the mirrors is moveable, the detuning of laser from the cavity changes due to the mirror motion. Displacement of the mirror by a distance x shifts the cavity resonance frequency by:

$$\Delta_x(t) = -\frac{\omega_{\mathrm{cav}}}{L_{\mathrm{cav}}}x(t) \tag{2.28}$$

This makes the total detuning:

$$\Delta_{\mathrm{eff}} = \Delta - \frac{\omega_{\mathrm{cav}}}{L_{\mathrm{cav}}}x(t) \tag{2.29}$$

Meaning that the circulating energy amplitude is:

$$a = \frac{a_{\mathrm{i}}\sqrt{\kappa_1}}{\frac{\kappa}{2} - i\Delta + i\frac{\omega_{\mathrm{cav}}}{L_{\mathrm{cav}}}x(t)} \tag{2.30}$$

The equation of motion in this case is:

$$\dot{a}(t) = a(t)\left(-\frac{\kappa}{2} - i\left(\omega_{\mathrm{cav}} + \frac{\omega_{\mathrm{cav}}}{L_{\mathrm{cav}}}x(t)\right)\right) + a_{\mathrm{i}}(t)\sqrt{\kappa_1} \tag{2.31}$$

The movable mirror can, in principle be a free mass. However, first it is impossible to have a completely free mass, short of building the experiment in the outer space. Second, a free mass has the largest response at DC, which is usually inconvenient to measure. It is much more convenient to consider the mirror as a simple harmonic oscillator. The response is maximized at the mechanical resonance frequency, which can be adjusted. Reducing the damping, which is a technical task, increases the magnitude of the response. Therefore we will consider the mirror to be a simple harmonic oscillator and will describe it in the next section.

2.4 Mechanical oscillator

2.4.1 Equations of motion of the mechanical oscillator

The differential equation describing the position of the mechanical oscillator is:

$$\ddot{x}(t) + \gamma\dot{x}(t) + \omega_{\mathrm{m}}^2 x(t) = F(t)/m_{\mathrm{m}} \tag{2.32}$$

Here γ is the mechanical linewidth, $\omega_{\rm m}$ is the mechanical resonance frequency, $m_{\rm m}$ is the mass and $F(t)$ is the driving force. We can rewrite the equation in terms of position and momentum, since $p(t) = m_{\rm m}\dot{x}(t)$, as two coupled first order differential equations:

$$\dot{x}(t) = \frac{p(t)}{m_{\rm m}} \tag{2.33}$$

$$\dot{p}(t) = -\gamma p(t) - m\omega_{\rm m}^2 x(t) + F(t) \tag{2.34}$$

The analog of the ladder operator in classical mechanics is:

$$b(t) = \sqrt{\frac{m_{\rm m}\omega_{\rm m}}{2\hbar}}\left(x(t) + \frac{i}{m_{\rm m}\omega_{\rm m}}p(t)\right) \tag{2.35}$$

The time derivative is:

$$\begin{aligned}
\dot{b}(t) &= \sqrt{\frac{m_{\rm m}\omega_{\rm m}}{2\hbar}}\left(\dot{x}(t) + \frac{i}{m_{\rm m}\omega_{\rm m}}\dot{p}(t)\right) && (2.36)\\
&= \sqrt{\frac{m_{\rm m}\omega_{\rm m}}{2\hbar}}\left(\frac{p(t)}{m} + \frac{i}{m_{\rm m}\omega_{\rm m}}\left(-\gamma p(t) - m_{\rm m}\omega_{\rm m}^2 x(t) + F(t)\right)\right) && (2.37)\\
&= -i\omega_{\rm m} b(t) + \sqrt{\frac{m_{\rm m}\omega_{\rm m}}{2\hbar}}\left(-\frac{i\gamma}{m_{\rm m}\omega_{\rm m}}p(t) + \frac{i}{m_{\rm m}\omega_{\rm m}}F(t)\right) && (2.38)\\
&= -i\omega_{\rm m} b(t) + (b^*(t) - b(t))\frac{\gamma}{2} + \frac{i}{\sqrt{2\hbar m_{\rm m}\omega_{\rm m}}}F(t) && (2.39)
\end{aligned}$$

In the high mechanical quality factor regime ($\omega_{\rm m} \gg \gamma$), the b^* term is off-resonant, resulting in the following equation for $b(t)$.

$$\dot{b}(t) = -i\omega_{\rm m} b(t) - \frac{\gamma}{2}b(t) + \frac{i}{\sqrt{2\hbar m_{\rm m}\omega_{\rm m}}}F(t) \tag{2.40}$$

2.4.2 Solution to equation of motion for x in the Fourier domain

In the Fourier domain, equation of motion for the position of the mechanical oscillator is given by:

$$-\omega^2 x[\omega] + i\omega\gamma x[\omega] + \omega_{\rm m}^2 x[\omega] = F[\omega]/m_{\rm m} \tag{2.41}$$

so:

$$x[\omega] = \frac{F[\omega]}{m_{\rm m}((\omega_{\rm m}^2 - \omega^2) + i\omega\gamma)} = F[\omega]\chi_{xx}[\omega] \tag{2.42}$$

Here $\chi_{xx}[\omega]$ is the mechanical susceptibility. The power spectral density is defined as:

$$S_{xx}[\omega] \equiv |x[\omega]|^2 \tag{2.43}$$

Therefore:

$$S_{xx}[\omega] = |F[\omega]|^2|\chi_{xx}[\omega]|^2 = \frac{S_{FF}[\omega]}{m_{\rm m}^2((\omega_{\rm m}^2 - \omega^2)^2 + \omega^2\gamma^2)} \tag{2.44}$$

2.4.3 Forces acting on a mechanical oscillator

The force $F(t)$ is a sum of thermal force, static radiation pressure, and radiation pressure shot noise. Let's consider them separately.

- **Thermal force**

  The thermal force is a stochastic force acting on the oscillator. We assume its power spectral density to be flat on the scale of γ: $S_{FF}^{\rm th}[\omega] = S_{FF}^{\rm th}$.

  The variance of a quantity is obtained by integrating its power spectral density over frequency. Since we can set the zero so that $\langle x \rangle = 0$, we find that:

$$\langle x^2 \rangle = \int_{-\infty}^{\infty} \frac{1}{2\pi} S_{xx}[\omega] d\omega = \frac{S_{FF}^{\rm th}}{2\pi m_{\rm m}^2} \int_{-\infty}^{\infty} \frac{1}{(\omega_{\rm m}^2 - \omega^2)^2 + \omega^2 \gamma^2} d\omega = \frac{S_{FF}^{\rm th}}{2 m_{\rm m}^2 \omega_{\rm m}^2 \gamma} \tag{2.45}$$

  But, from the equipartition theorem:

$$\frac{1}{2} m_{\rm m} \omega_{\rm m}^2 \langle x^2 \rangle = \frac{1}{2} k_{\rm B} T \tag{2.46}$$

  Combining, we find the power spectral density of the thermal drive:

$$S_{FF}^{\rm th} = 2 k_{\rm B} T \gamma m_{\rm m} \tag{2.47}$$

  Since the force is stochastic, we can write is as:

$$F_{\rm th} = -i G_{\rm th} \eta_\delta(t) \tag{2.48}$$

  Here $G_{\rm th}$ is the strength of the force and $\langle \eta_\delta(t)^* \eta_\delta(t+\tau) \rangle = \delta(\tau)$. The $F_{\rm th}$ and $G_{\rm th}$ are real, while $\eta_\delta(t)$ is complex, defined so that the resulting expression is similar to the expression used in the full quantum treatment. From the Wiener-Khinchin theorem, we can now write:

$$S_{FF}^{\rm th} = \int_{-\infty}^{+\infty} \langle F_{\rm th}(t) F_{\rm th}(0) \rangle e^{i\omega t} dt = G_{\rm th}^2 \tag{2.49}$$

  Therefore the thermal force is written as:

$$F_{\rm th} = -i \sqrt{2 k_{\rm B} T m_{\rm m} \gamma} \eta_\delta(t) \tag{2.50}$$

  It is convenient to define $\eta(t) = \sqrt{\frac{k_{\rm B} T}{\hbar \omega_{\rm m}}} \eta_\delta(t)$. With this definition:

$$F_{\rm th} = -i \sqrt{2 m_{\rm m} \gamma \hbar \omega_{\rm m}} \eta(t) \tag{2.51}$$

  The thermal force is completely independent of the parameters of the optical cavity.

- **Radiation pressure force.**

  If a beam of light is incident of the oscillator, the oscillator experiences radiation pressure force. The radiation pressure force is given by:

$$F_{\rm RP} = \frac{2 \langle P(t) \rangle}{c} = \frac{2 \hbar \omega_{\rm L} \langle |a_{\rm i}(t)|^2 \rangle}{c} \tag{2.52}$$

  If the mechanical oscillator is inside of an optical cavity, the radiation pressure force is given by:

$$F_{\rm RP} = \frac{2 \hbar \omega_{\rm cav} \langle |a(t)|^2 \rangle}{c} \times \frac{c}{2 L_{\rm cav}} = \frac{\hbar \omega_{\rm cav} \langle |a(t)|^2 \rangle}{L_{\rm cav}} \tag{2.53}$$

  Here we divided by the roundtrip time, because $|a(t)|^2$ gives the energy stored in the cavity.

- **Radiation pressure shot noise (RPSN)** Due to the quantum nature of light, the oscillator experiences radiation pressure shot noise. If an oscillator is illuminated with a beam of light of power P and frequency $\omega_{\rm L}$, the average number of photons hitting the oscillator in time τ is:

$$\langle n \rangle = \frac{\langle P \rangle}{\hbar \omega_{\rm L}} \tau \tag{2.54}$$

The standard deviation for a Poisson variable is:

$$\sigma_n(\tau) = \sqrt{\langle n \rangle} \tag{2.55}$$

From here we find the standard deviation of the power:

$$\sigma_P(\tau) = \sqrt{\frac{\langle P \rangle \hbar \omega_{\mathrm{L}}}{\tau}} \tag{2.56}$$

We will introduce a new stochastic variable $P_{\mathrm{st}}(t)$ with zero ensemble average $\langle P_{\mathrm{st}} \rangle = 0$:

$$P_{\mathrm{st}}(t) = P(t) - \langle P \rangle \tag{2.57}$$

Since we are measuring for time τ, the measured $\bar{P}_{\mathrm{st}}(\tau)$ is given by:

$$\bar{P}_{\mathrm{st}}(\tau) = \frac{1}{\tau} \int_0^\tau P_{\mathrm{st}}(t) dt \tag{2.58}$$

The standard deviation $\sigma_{\bar{P}_{\mathrm{st}}}(\tau) = \sigma_P(\tau)$. Since the ensemble average of P_{st} is zero, the variance $\sigma^2_{\bar{P}_{\mathrm{st}}}(\tau) = \langle \bar{P}_{\mathrm{st}}(\tau)^2 \rangle$. We calculate it below:

$$\begin{aligned} \sigma^2_{\mathrm{P}}(\tau) = \sigma^2_{\bar{P}_{\mathrm{st}}}(\tau) = \langle \bar{P}_{\mathrm{st}}(\tau)^2 \rangle &= \frac{1}{\tau^2} \int_0^\tau \int_0^\tau dt_1 dt_2 \langle P_{\mathrm{st}}(t_1) P_{\mathrm{st}}(t_2) \rangle \\ &= \frac{1}{\tau^2} \tau \int_{-\infty}^{\infty} dt \langle P_{\mathrm{st}}(t) P_{\mathrm{st}}(0) \rangle \\ &= \frac{1}{\tau} S^{\mathrm{RPSN}}_{PP}[0] \end{aligned} \tag{2.59}$$

Since shot noise is a Poisson process consisting of uncorrelated events, the power spectral density of the fluctuations is white, so $S^{\mathrm{RPSN}}_{PP}[\omega] = S^{\mathrm{RPSN}}_{PP}[0] = S^{\mathrm{RPSN}}_{PP}$. Combining with equation 2.56, we find that:

$$S^{\mathrm{RPSN}}_{PP} = \langle P \rangle \hbar \omega_{\mathrm{L}} = \langle |a_{\mathrm{i}}|^2 \rangle \hbar^2 \omega_{\mathrm{L}}^2 \tag{2.60}$$

For the light reflecting off an oscillator, the PSD of the force on the oscillator is then given by:

$$S^{\mathrm{RPSN}}_{FF} = \left(\frac{2}{c} \right)^2 S^{\mathrm{RPSN}}_{PP} = \frac{4 \langle |a_{\mathrm{i}}|^2 \rangle \hbar^2 \omega_{\mathrm{L}}^2}{c^2} \tag{2.61}$$

We write this stochastic force as:

$$F_{\mathrm{RPSN}} = G_{\mathrm{RPSN}} \xi_\delta(t) \tag{2.62}$$

Here G_{th} is the strength of the force and $\langle \xi_\delta(t) \xi_\delta(t+\tau) \rangle = \delta(\tau)$. From the Wiener-Khinchin theorem we can write:

$$S^{\mathrm{RPSN}}_{FF} = \int_{-\infty}^{+\infty} \langle F_{\mathrm{RPSN}}(t) F_{\mathrm{RPSN}}(0) \rangle e^{i\omega t} dt = G^2_{\mathrm{RPSN}} \tag{2.63}$$

And from here we find the force on the oscillator as a function of time.

$$F_{\mathrm{RPSN}}(t) = \frac{2\hbar\omega_{\mathrm{L}}}{c} \sqrt{\langle |a_{\mathrm{i}}|^2 \rangle} \xi_\delta(t) \tag{2.64}$$

Now let's consider an oscillator inside a Fabry-Perot cavity. For simplicity assume that cavity is single-sided, so $\kappa_1 = \kappa$. The circulating power in this cavity is given by:

$$\langle P_{\mathrm{circ}} \rangle = \langle E_{\mathrm{circ}} \rangle \frac{c}{2L_{\mathrm{cav}}} = \langle n_{\mathrm{circ}} \rangle \hbar \omega_{\mathrm{L}} \frac{c}{2L} \tag{2.65}$$

Where $\langle n_{\rm circ}\rangle = \langle |a|^2\rangle$ is the ensemble average of the photon number inside the cavity. It is a Poisson variable and its standard deviation is: $\sigma_{n_{\rm circ}}(\tau) = \sqrt{\langle n_{\rm circ}\rangle}$. The standard deviation of circulating power is:

$$\sigma_{P_{\rm circ}} = \sqrt{\langle n_{\rm circ}\rangle}\hbar\omega_{\rm L}\frac{c}{2L_{\rm cav}} \tag{2.66}$$

We can obtain variance by integrating the PSD:

$$\sigma^2_{P_{\rm circ}} = \int_{-\infty}^{\infty}\frac{1}{2\pi}S_{PP}^{\rm RPSN}[\omega]d\omega \tag{2.67}$$

We do not know the exact shape of $S_{PP}^{\rm RPSN}$, but for small fluctuations in power: $S_{PP}^{\rm RPSN} \propto S_{aa}^{\rm RPSN}$.

Considering equation 2.23, we can write:

$$S_{aa}^{\rm RPSN} = S_{a_{\rm i}a_{\rm i}}^{\rm RPSN}\frac{\kappa}{\left(\frac{\kappa}{2}\right)^2 + (\omega-\omega_{\rm cav})^2} \tag{2.68}$$

Therefore:

$$S_{PP}^{\rm RPSN} = S\frac{\kappa}{\left(\frac{\kappa}{2}\right)^2 + (\omega-\omega_{\rm cav})^2} \tag{2.69}$$

Where S is a constant. Using this expression for $S_{PP}^{\rm RPSN}$, we find that:$\int_{-\infty}^{\infty}\frac{1}{2\pi}S_{PP}^{\rm RPSN}d\omega = S$. Therefore $S = \langle N_{\rm circ}\rangle\left(\hbar\omega_{\rm L}\frac{c}{2L_{\rm cav}}\right)^2$. And finally:

$$S_{PP}^{\rm RPSN}[\omega] = \langle |a|^2\rangle\left(\hbar\omega_{\rm L}\frac{c}{2L_{\rm cav}}\right)^2\frac{\kappa}{\left(\frac{\kappa}{2}\right)^2 + (\omega-\omega_{\rm cav})^2} \tag{2.70}$$

The PSD of the force on the oscillator is given by:

$$\begin{aligned} S_{FF}^{\rm RPSN}[\omega] &= \left(\frac{2}{c}\right)^2\langle |a|^2\rangle\left(\hbar\omega_{\rm L}\frac{c}{2L_{\rm cav}}\right)^2\frac{\kappa}{\left(\frac{\kappa}{2}\right)^2 + (\omega-\omega_{\rm cav})^2} &(2.71)\\ &= \langle |a|^2\rangle\left(\frac{\hbar\omega_{\rm L}}{L_{\rm cav}}\right)^2\frac{\kappa}{\left(\frac{\kappa}{2}\right)^2 + (\omega-\omega_{\rm cav})^2} &(2.72)\end{aligned}$$

Therefore we write the force on the oscillator as:

$$F_{\rm RPSN} = \frac{\hbar\omega_{\rm L}}{L_{\rm cav}}\sqrt{\kappa}\sqrt{|\chi_{aa}|^2}\sqrt{\langle |a|^2\rangle}\xi_\delta(t) \tag{2.73}$$

Where χ_{aa} is cavity susceptibility, here defined as:

$$\chi_{aa}[\omega] = \frac{1}{\kappa/2 - i(\omega-\omega_{\rm cav})} \tag{2.74}$$

In the classical regime $F_{\rm th} \gg F_{\rm RPSN}$, so we will neglect the force due to radiation pressure shot noise. The classical equation for the motion of a mechanical oscillator inside a Fabry-Perot cavity is then:

$$\dot{b}(t) = -i\omega_{\rm m}b(t) - \frac{\gamma}{2}b(t) + \frac{i}{\sqrt{2\hbar m_{\rm m}\omega_{\rm m}}}(F_{\rm th}(t) + F_{\rm RP}(t)) \tag{2.75}$$

$$\dot{b}(t) = -i\omega_{\rm m}b(t) - \frac{\gamma}{2}b(t) + \frac{i}{\sqrt{2\hbar m_{\rm m}\omega_{\rm m}}}\left(\sqrt{2m_{\rm m}\gamma\hbar\omega_{\rm m}}\eta(t) + \frac{\hbar\omega_{\rm cav}\langle |a(t)|^2\rangle}{L_{\rm cav}}\right) \tag{2.76}$$

We simplify the expression and arrive at:

$$\dot{b}(t) = -i\left(\omega_{\rm m}b(t) - \sqrt{\frac{\hbar}{2m_{\rm m}\omega_{\rm m}}}\frac{\omega_{\rm cav}}{L_{\rm cav}}\langle |a(t)|^2\rangle\right) - \frac{\gamma}{2}b(t) + \sqrt{\gamma}\eta(t) \tag{2.77}$$

2.5 Classical equations of motion

Finally, we can write the classical equations of motion for the oscillator (equations 2.31 and 2.77), where we rewrote x in terms of b and b^*:

$$\dot{a}(t) = -i\left(\omega_{\rm cav}a(t) + \sqrt{\frac{\hbar}{2m_{\rm m}\omega_{\rm m}}}\frac{\omega_{\rm cav}}{L_{\rm cav}}(b(t)+b^*(t))a(t)\right) - \frac{\kappa}{2}a(t) + \sqrt{\kappa_1}a_{\rm i}(t) \tag{2.78}$$

$$\dot{b}(t) = -i\left(\omega_{\rm m}b(t) - \sqrt{\frac{\hbar}{2m_{\rm m}\omega_{\rm m}}}\frac{\omega_{\rm cav}}{L_{\rm cav}}\langle|a(t)|^2\rangle\right) - \frac{\gamma}{2}b(t) + \sqrt{\gamma}\eta(t) \tag{2.79}$$

Those equations describe the motion of the oscillator in the classical regime: $F_{\rm th} \gg F_{\rm RPSN}$. Note that optical and mechanical mode influence each other with the same prefactor, we call this prefactor g_0: the single photon optomechanical coupling:

$$g_0 = \sqrt{\frac{\hbar}{2m_{\rm m}\omega_{\rm m}}}\frac{\omega_{\rm cav}}{L_{\rm cav}} \tag{2.80}$$

With this substitution, equations become:

$$\dot{a}(t) = -i\left(\omega_{\rm cav}a(t) + g_0(b(t)+b^*(t))a(t)\right) - \frac{\kappa}{2}a(t) + \sqrt{\kappa_1}a_{\rm i}(t) \tag{2.81}$$

$$\dot{b}(t) = -i\left(\omega_{\rm m}b(t) - g_0\langle|a(t)|^2\rangle\right) - \frac{\gamma}{2}b(t) + \sqrt{\gamma}\eta(t) \tag{2.82}$$

If we were to try and include the force due to radiation pressure shot noise, we would find that the force acting on b would be:

$$F_{\rm RPSN} = g_0\sqrt{\langle|a|^2\rangle}\sqrt{\kappa}\sqrt{|\chi_{aa}|^2}\xi_\delta(t) \tag{2.83}$$

This expression gives the correct amplitude of the radiation pressure, but the phase is incorrect, as we will find in section 5.1 by applying the full quantum mechanical treatment.

2.6 Quantum equations of motion

The Hamiltonian for an optical cavity with resonance frequency $\omega_{\rm cav}$ and a mechanical oscillator with resonance frequency $\omega_{\rm m}$ is given by:

$$\hat{\mathcal{H}} = \hbar\omega_{\rm cav}(\hat{x})\hat{a}^\dagger\hat{a} + \hbar\omega_{\rm m}\hat{b}^\dagger\hat{b} \tag{2.84}$$

In this equation $\hat{a}^\dagger$ and $\hat{a}$ are cavity photon creation and annihilation operators, and $\hat{b}^\dagger$ and $\hat{b}$ are phonon creation and annihilation operators. The optical frequency of the cavity, however depends on the displacement of the movable mirror. Taylor expanding to first order:

$$\omega_{\rm cav}(\hat{x}) = \omega_{\rm cav}(x_0) + \hat{x}\frac{d\omega_{\rm cav}(x_0)}{dx} = \omega_{\rm cav}(x_0) + (\hat{b}+\hat{b}^\dagger)g_0 \tag{2.85}$$

Here we rewrote $\hat{x}$ in terms of raising and lowering operators. The optomechanical single photon coupling g_0 which gives the change in frequency due to zero-point fluctuation is defined as:

$$g_0 = \frac{d\omega_{\rm cav}(x_0)}{dx}x_{\rm ZPF} \tag{2.86}$$

and x_{ZPF} is the magnitude of zero-point fluctuation:

$$x_{\mathrm{ZPF}} = \sqrt{\frac{\hbar}{2m_{\mathrm{m}}\omega_{\mathrm{m}}}} \tag{2.87}$$

where m_{m} is the effective mode mass. With these changes the Hamiltonian becomes:

$$\hat{\mathcal{H}} = \hbar\omega_{\mathrm{cav}}(x_0)\hat{a}^\dagger\hat{a} + \hbar\omega_{\mathrm{m}}\hat{b}^\dagger\hat{b} + \hbar g_0(\hat{b}+\hat{b}^\dagger)\hat{a}^\dagger\hat{a} \tag{2.88}$$

In the canonical optomechanical system, the optomechanical coupling arises because the change in mirror position changes the cavity length, and at the same time the light field in the cavity can change the mirror position. In general, the optomechanical coupling can arise from different processes: radiation pressure, electrostriction, thermal expansion.

Radiation pressure was described in the beginning of this thesis, and it arises because the photons scattering from the material exert force on it, which is proportional to the intensity of the electric field. The electrostrictive coupling arises, because of the material polarizability. The electric field polarizes the atoms or molecules of the material, aligning them with the direction of the electric field. The polarized atoms or molecules move under the influence of the electric field gradient. The electroctrictive force is proportional to the product of the electric field and its gradient. The thermal expansion arises because the photons can get absorbed into the material and heat it up, leading to the expansion and the change in the cavity's length.

The radiation pressure and electrostriction are unitary (can be described by a Hamiltonian and are not associated with the loss of information). Radiation pressure and electrostriction are always bi-directional - the same coefficient g_0 describes how the position of the mechanical element changes the detuning of the cavity and how the change in the cavity's photon number exerts a force of the mechanical element. The thermal processes are non-unitary, therefore are of less interest for the studies of quantum mechanics.

The Heisenberg equations of motion are:

$$\dot{\hat{a}} = \frac{i}{\hbar}[\hat{\mathcal{H}},\hat{a}] \qquad \text{and} \qquad \dot{\hat{b}} = \frac{i}{\hbar}[\hat{\mathcal{H}},\hat{b}] \tag{2.89}$$

Expanding we get:

$$\dot{\hat{a}} = \frac{i}{\hbar}(\hbar\omega_{\mathrm{cav}}[\hat{a}^\dagger\hat{a},\hat{a}] + \hbar g_0(\hat{b}+\hat{b}^\dagger)[\hat{a}^\dagger\hat{a},\hat{a}]) \tag{2.90}$$

and:

$$\dot{\hat{b}} = \frac{i}{\hbar}(\hbar\omega_{\mathrm{m}}[\hat{b}^\dagger\hat{b},\hat{b}] + \hbar g_0[\hat{b}^\dagger,\hat{b}]\hat{a}^\dagger\hat{a}) \tag{2.91}$$

Using commutation relations

$$[\hat{a}^\dagger,\hat{a}] = -1 \qquad \text{and} \qquad [\hat{a}^\dagger\hat{a},\hat{a}] = -\hat{a} \tag{2.92}$$

We get the following:

$$\dot{\hat{a}} = -i(\omega_{\mathrm{cav}}\hat{a} + g_0(\hat{b}+\hat{b}^\dagger)\hat{a}) \tag{2.93}$$

$$\dot{\hat{b}} = -i(\omega_{\mathrm{m}}\hat{b} + g_0\hat{a}^\dagger\hat{a}) \tag{2.94}$$

Those equations look similar to the classical equations that we derived above. Now we add optical and thermal noises as well as the damping of the optical and mechanical modes. The form of these extra terms is the same as what we calculated classically.

$$\dot{\hat{a}} = -i(\omega_{\mathrm{cav}}\hat{a} + g_0(\hat{b}+\hat{b}^\dagger)\hat{a}) - \frac{\kappa}{2}\hat{a} + \sqrt{\kappa_{\mathrm{ext}}}\hat{a}_{\mathrm{i}} + \sqrt{\kappa_{\mathrm{int}}}\hat{\xi}_{\mathrm{int}} \tag{2.95}$$

$$\dot{\hat{b}} = -i(\omega_{\mathrm{m}}\hat{b} + g_0\hat{a}^\dagger\hat{a}) - \frac{\gamma}{2}\hat{b} + \sqrt{\gamma}\hat{\eta} \tag{2.96}$$

Here κ and γ are the damping rates for the cavity field and the acoustic mode correspondingly and $\kappa = \kappa_{\rm int} + \kappa_{\rm ext}$, where $\kappa_{\rm int}$ is the internal loss in the cavity, while $\kappa_{\rm ext}$ is the external loss of the cavity (through the mirrors); $\hat{\xi}_{\rm int}$ is the internal optical noise operator; and $\hat{a}_{\rm i}$ is the light incident on the cavity (which includes external optical noise); $\hat{\eta}$ is the thermal noise operator.

For the sake of clarity, I need to point out that previously, I used κ_1 and κ_2 as loss rates through the input and the back mirrors. I assumed a lossless cavity in which $\kappa = \kappa_1 + \kappa_2$. Now I am using $\kappa_{\rm ext}$ to indicate the external loss rate in the cavity. In the cavities used in our experiments the highest loss rate is through the input mirror ($\kappa_{\rm ext} \approx \kappa_1$). The internal loss rate $\kappa_{\rm int}$ includes any other loss in the cavity (e.g., absorption or scattering losses).

The system described by these equations of motion is the canonical optomechanical system.

2.6.1 Linearized Hamiltonian

The interaction term in the Hamiltonian is given by:

$$\hat{\mathcal{H}}_{\rm int} = -\hbar g_0 (\hat{b} + \hat{b}^\dagger)\hat{a}^\dagger \hat{a} \tag{2.97}$$

For small variations of optical field, we write $\hat{a} = \bar{a} + \delta\hat{a}$:

$$\hat{\mathcal{H}}_{\rm int} = -\hbar g_0 (\hat{b} + \hat{b}^\dagger)(\bar{a}^* + \delta\hat{a}^\dagger)(\bar{a} + \delta\hat{a}) \tag{2.98}$$

This gives, upon expansion and neglecting the second order terms:

$$\hat{\mathcal{H}}_{\rm int} = -\hbar g \bar{a}(\hat{b} + \hat{b}^\dagger) - \hbar g(\hat{b}\delta\hat{a}^\dagger + \hat{b}^\dagger\delta\hat{a} + \hat{b}^\dagger\delta\hat{a}^\dagger + \hat{b}\delta\hat{a}). \tag{2.99}$$

Here $g = g_0\bar{a}$. The first term corresponds to static displacement of the mechanical oscillator under the influence of the optical field. The remainder of the Hamiltonian can be split into two terms. The beam-splitter Hamiltonian:

$$\hat{\mathcal{H}}_{\rm int,bs} = -\hbar g(\hat{b}\delta\hat{a}^\dagger + \hat{b}^\dagger\delta\hat{a}), \tag{2.100}$$

and the parametric down conversion Hamiltonian:

$$\hat{\mathcal{H}}_{\rm int,pdc} = -\hbar g(\hat{b}^\dagger\delta\hat{a}^\dagger + \hat{b}\delta\hat{a}). \tag{2.101}$$

2.7 Review of optomechanics

As said in the introduction there are a number of great reviews of optomechanics [1, 2, 3, 4, 5] . Therefore I will not attempt to provide a comprehensive review but rather focus on convincing the reader that the optomechanical cooperativity, given by

$$C = \frac{4g}{\kappa\gamma} \tag{2.102}$$

is perhaps the most important figure of merit in Gaussian optomechanics. Here $g = g_0 n_{\rm circ}$ is the multiphoton optomechanical coupling.

For simplicity in the discussion below, I will assume that the cavity is single-sided: $\kappa_{\rm ext} = \kappa$. I will focus more on optomechanical effects relevant to our system, and will briefly mention the ones which are less relevant.

2.7.1 Dynamical back-action

The number of circulating photons in a Fabry-Perot cavity, and therefore the radiation pressure force on the mirror depends on the mirror position. Because of that, it changes the mirror's mechanical susceptibility, resulting in modifications to both mechanical resonance frequency ("optical spring": $\Delta\omega_{\mathrm{m,opt}}$) and linewidth ("optical damping": γ_{opt}). The magnitude and sign of these effects depend on the detuning and power of the drive beam. This effect is not present when the cavity is driven exactly on resonance. When the drive beam is detuned by $+\omega_{\mathrm{m}}$ from the cavity operating in the resolved sideband regime ($\omega_{\mathrm{m}} \gg \kappa$), the change in mechanical linewidth is $\gamma_{\mathrm{opt}} \approx -\frac{4g^2}{\kappa} = -C\gamma$, corresponding to the narrowing of linewidth or optical heating of the mechanical mode. On the other hand, when the drive beam is detuned by $-\omega_{\mathrm{m}}$, the change in mechanical linewidth is $\gamma_{\mathrm{opt}} \approx \frac{4g^2}{\kappa} = C\gamma$, which corresponds to broadening of linewidth or optical cooling (damping) the mechanical mode. A rigorous derivation of this effect is given in section 5.1.

The effect was first observed by the Soviet physicist Braginsky [68]. He used a microwave waveguide with one of the walls replaced by a metallic plate suspended by a quartz fiber, thus forming a pendulum. The resonant frequency of the pendulum was 3 Hz. A laser incident on the plate from the other side was used to measure its motion and observed the change in damping and spring constant of the resonator depending on the detuning of the microwave field from the cavity resonance.

The dynamical back-action is a simple way to extract optomechanical coupling, since the magnitude of the optical spring and damping are directly proportional to g_0^2 and easily measurable parameters.

2.7.2 Optomechanically induced transparency/amplification

Optomechanically induced transparency/amplification is another extremely useful effect. It can be employed for characterization of the mechanical oscillator and to extract the optomechanical coupling. The following is a short explanation of this effect.

If a single "probe" beam is swept over the cavity resonance, the cavity response Lorentzian will be observed. If two beams are sent on the resonator: a strong drive "control" beam at a frequency ω_{c} and a weaker "probe" beam at a frequency ω_{p}, the beams create intensity beating inside of the cavity. If the difference in frequencies between the control and probe beam is equal to the mechanical resonance frequency $|\omega_{\mathrm{c}} - \omega_{\mathrm{p}}| \approx \omega_{\mathrm{m}} \pm \gamma$, the mechanical resonator is driven. The motion of the resonator scatters light from the beams into sidebands ω_{m} away. One sideband of the control beam has the same frequency as the probe beam. That sideband and the probe beam can interfere constructively or destructively.

So if the probe beam is swept over the cavity in the presence of another beam, then, in addition to cavity Lorentzian, a sharp feature of width $\gamma + \gamma_{\mathrm{opt}}$ will be observed, either as a dip in the cavity Lorentzian response (optomechanically induced transparency) or a peak (optomechanically induced amplification). The relative amplitude of the feature is given by:

$$A_{\mathrm{OMIT/A}} = \frac{4g^2}{\kappa(\gamma + \gamma_{\mathrm{opt}})} \tag{2.103}$$

Using the expression for γ_{opt} given in section 2.7.1 we find that in the resolved sideband regime, for the control beam detuned by $-\omega_{\mathrm{m}}$:

$$A_{\mathrm{OMIT}} = \left|\frac{C}{1+C}\right| \tag{2.104}$$

And for the control beam detuned by $+\omega_{\mathrm{m}}$:

$$A_{\mathrm{OMIA}} = \left|\frac{C}{1-C}\right| \tag{2.105}$$

Both features become larger with increasing cooperativity. When the drive laser is on the blue side and $C \to 1$, the overall damping rate approaches zero and for $C > 1$ becomes negative In this situation, any fluctuation of the oscillator grows exponentially in time. Optomechanically induced transparency was first observed in [69], and has since been observed in multiple systems. A rigorous derivation of this effect in given in section 5.5.

2.7.3 Optomechanical cooling and heating and the mechanical occupation number

When light interacts with the mechanical oscillator, it acquires sidebands, separated from the drive laser by the mechanical frequency $\pm\omega_{\mathrm{m}}$. One way to understand those sidebands is considering how motion of the mechanical oscillator modulates the phase of light.

A complimentary way to understand sidebands is to consider a quantum picture of photons and phonons, which we will do now. Assume a single drive beam incident on an optomechanical system near cavity resonance.

Whenever a photon is scattered from the optical drive into the lower sideband, a photon of lower energy is created. The leftover energy creates a phonon in the mechanical resonator, thus increasing its mean phonon number. The operator corresponding to this case is $\hat{a}^\dagger\hat{b}^\dagger$.

On the other hand, when a photon is scattered from the optical drive into an upper sideband, a photon of higher energy is created. This energy is extracted from mechanical resonator, thus lowering its mean phonon number. The operator corresponding to this case is $\hat{a}^\dagger\hat{b}$.

Note that we always remove a photon from the drive field, but since the drive is usually very strong, the average photon number in the drive field can be assumed to be approximately constant.

If the drive beam is detuned from the cavity resonance, one of the processes gets enhanced while the other is suppressed, due to the cavity density of states, resulting in either adding phonons to the mechanical mode (heating) or removing phonons (cooling).

So, when the drive beam is detuned by $-\omega_{\mathrm{m}}$, the phonon number is:

$$n_{\mathrm{m}} = \frac{n_{\mathrm{th}} + C\left(\frac{\kappa}{4\omega_{\mathrm{m}}}\right)^2}{1+C} \tag{2.106}$$

Where n_{th} is the thermal occupation of the mechanical oscillator given by:

$$n_{\mathrm{th}} = \frac{1}{e^{\frac{\hbar\omega_{\mathrm{m}}}{k_{\mathrm{B}}T}} - 1} \approx \frac{k_{\mathrm{B}}T}{\hbar\omega_{\mathrm{m}}} - \frac{1}{2} \tag{2.107}$$

This approximation is valid for $\frac{k_{\mathrm{B}}T}{\hbar\omega_{\mathrm{m}}} > 2$.

So in order to be able to cool the oscillator to the ground state ($n_{\mathrm{m}} < 1$), the system needs to be in the resolved sideband regime. Additionally, large cooperativities and low n_{th} are desirable. Multiple groups have cooled oscillators to quantum ground state. The first resonator to reach the quantum ground state was built in Cleland and Martinis group [7]. The resonator was a piezoelectric cantilever with resonance frequency of 6 GHz, so it was in the quantum ground state ($n_{\mathrm{m}} < 0.07$) at the base temperature of the dilution refrigerator. No optomechanical cooling was necessary. Quantum ground state was next reached by Painter group [8], in which a 3.68 GHz mode of optomechanical crystal was cooled optomechanically from $n_{\mathrm{m}} \approx 120$ to $n_{\mathrm{m}} = 0.85 \pm 0.08$. More recently quantum ground state was achieved in our group at Yale [9]. A membrane with resonant frequency of 705 kHz was cooled from $n_{\mathrm{m}} \approx 10,000$ to $n_{\mathrm{m}} = 0.84 \pm 0.22$.

When the drive beam is detuned by $+\omega_{\mathrm{m}}$, the phonon number is:

$$n_{\mathrm{m}} = \frac{n_{\mathrm{th}} + C}{1 - C} \tag{2.108}$$

For cooperativity larger than 1, spontaneous oscillations occur and the oscillator is unstable. This effect has been observed experimentally in multiple systems, such as [70, 71].

The derivation of the average phonon occupation number is given in section 5.4.1.

2.7.4 Observation of asymmetry between the Stokes and anti-Stokes sidebands.

One way to measure the average occupation number of an oscillator is to consider the asymmetry between the Stokes and anti-Stokes sidebands. When the drive beam is tuned near cavity resonance, two sidebands will be present at $\pm\omega_{\rm m}$. Lower sideband corresponds to $\hat{a}^\dagger\hat{b}^\dagger$, which, acting on the state $|0,n_{\rm m}\rangle$ gives $\hat{a}^\dagger\hat{b}^\dagger|0,n_{\rm m}\rangle = \sqrt{n_{\rm m}+1}|1,n_{\rm m}+1\rangle$ while the upper sideband corresponds to $\hat{a}^\dagger\hat{b}$ and gives $\hat{a}^\dagger\hat{b}|0,n_{\rm m}\rangle = \sqrt{n_{\rm m}}|1,n_{\rm m}-1\rangle$

By Fermi's golden rule, the rate at which photons are scattered into the lower sideband is: $|\langle 1,n_{\rm m}+1|a^\dagger b^\dagger|0,n_{\rm m}\rangle|^2 = n_{\rm m}+1$ and the rate at which photons are scattered into the upper sideband is: $|\langle 1,n_{\rm m}-1|a^\dagger b^\dagger|0,n_{\rm m}\rangle|^2 = n_{\rm m}$. Since the rates are different, the size of the sidebands will be different as well.

A complimentary way to understand sideband asymmetry is to separate the power spectral density of the escaping light into four components, and look at their correlations. The first component is vacuum noise. Vacuum noise correlates with itself and results in the noise floor (equivalent to shot noise). Thermal motion of the oscillator produces sidebands on the control beam with area proportional to $n_{\rm m}$. Zero point motion of the oscillator increases the area in a way which is equivalent to increasing $n_{\rm m}$ by $1/2$. The beating between the vacuum noise and the drive beam drives the mechanical oscillator increasing the mean phonon number $n_{\rm m}$ by a quantity proportional to the optomechanical cooperativity whose exact magnitude depends on the detuning of the driving beam from the cavity. Finally the vacuum noise correlates with the response to the vacuum noise, resulting in increase of the sideband area by $1/2$ for the red sideband of the upper drive beam and decrease of the area by $1/2$ for the blue sideband of the lower control beam. All the contributions add resulting in the difference between the area of the red sideband and the blue sideband equivalent to one photon.

The height of the red sideband, is proportional to $C(n_{\rm m}+1)$, while the height of blue sideband is proportional to $Cn_{\rm m}$. The difference in height is proportional to C, therefore increasing cooperativity renders sideband asymmetry more easily observable. The expressions giving the Stokes and anti-Stokes sidebands are derived more formally in section 5.4.

2.7.5 Observation of radiation pressure shot noise

As described before, the quantum fluctuations of light in the cavity create a random force on the oscillator, known as RPSN, which changes the position of the oscillator. RPSN is usually small compared with thermal motion of the oscillator, so observing it was for a long time an outstanding challenge.

The power spectral density of RPSN force acting on an oscillator was derived in section 2.4.3 as:

$$S_{FF}^{\rm RPSN}[\omega] = \langle|a|^2\rangle\left(\frac{\hbar\omega_{\rm L}}{L_{\rm cav}}\right)^2\frac{\kappa}{\left(\frac{\kappa}{2}\right)^2+(\omega-\omega_{\rm cav})^2} \tag{2.109}$$

Near cavity resonance it is:

$$S_{FF}^{\rm RPSN}[\omega] = \langle|a|^2\rangle\left(\frac{2\hbar\omega_{\rm L}}{L_{\rm cav}}\right)^2\frac{1}{\kappa} \tag{2.110}$$

The thermal force power spectral density was shown to be:

$$S_{FF}^{\rm th} = 2k_{\rm B}T\gamma m_{\rm m} \tag{2.111}$$

In order for the shot noise to dominate over the thermal force:

$$\langle|a|^2\rangle\left(\frac{2\hbar\omega_{\rm L}}{L_{\rm cav}}\right)^2\frac{1}{\kappa} > 2k_{\rm B}T\gamma m_{\rm m} \tag{2.112}$$

This equation is simplified to:

$$\frac{4\langle|a|^2\rangle}{\kappa\gamma}\frac{\hbar}{2m_{\rm m}\omega_{\rm m}}\frac{\omega_{\rm L}^2}{L_{\rm cav}^2} > \frac{k_{\rm B}T}{\hbar\omega_{\rm m}} \tag{2.113}$$

Using the definition of g_0 given in 2.80, and defining multiphoton coupling $g = g_0\langle|a|^2\rangle$, we find:

$$\frac{4g^2}{\kappa\gamma} > \frac{k_{\rm B}T}{\hbar\omega_{\rm m}} \tag{2.114}$$

Therefore the condition for the force due to RPSN to overcome thermal force is:

$$C > n_{\rm th} \tag{2.115}$$

Correlation measurements can be performed to observe RPSN, even when the condition above is not satisfied. Using correlation measurements, RPSN was observed at room temperature in [11]. We have observed RPSN in our system [43, 12].

2.7.6 Other effects

Here I give some examples of other optomechanical effects that have been observed or used in optomechanical systems and which benefit from large optomechanical cooperativity.

2.7.6.1 Frequency conversion

The ideas of OMIT/A can be applied to quantum coherent frequency conversion. If two optical cavities of different frequencies are coupled to the same mechanical resonator, the resonator can be driven by the "control" and "probe" field of one cavity and add sidebands onto the "control" field of the other cavity. The transmission efficiency in the resolved sideband regime is given by:

$$|t|^2 = \frac{4C_{\rm I}C_{\rm II}}{(1 + C_{\rm II} + C_{\rm II})^2} \tag{2.116}$$

Where $C_{\rm (I,II)}$ are cooperativities of the "cavity 1 - oscillator" and "cavity 2 - oscillator" systems. The maximum transmission is achieved when $C_{\rm I} = C_{\rm II}$. In addition to being efficient, an ideal frequency converter should not add any noise. Any residual motion of the mechanical oscillator will add noise during the conversion process, so scattering rates need to overwhelm thermal decoherence rates ($C > n_{\rm th}$). The added noise is characterized by the effective number of noise photons added to the input signal and is given by:

$$n^{\rm add}_{\rm (I,II)} = \frac{n_{\rm th}}{C_{\rm (I,II)}} \tag{2.117}$$

Thus, the transmission efficiency is maximized and noise is minimized in the regime of high cooperativity.

The conversion between microwave and optical signals with 10% efficiency was achieved in [13]. Coherent frequency conversion between two microwave fields with 95% efficiency was achieved in [72].

2.7.6.2 State transfer and entanglement

Mechanical oscillators can be used for storing quantum information encoded in optical fields. For the drive beam detuned from the cavity by $-\omega_{\rm m}$, the interaction Hamiltonian takes the form of a beam-splitter:

$$\hat{\mathcal{H}}_{\rm int,bs} = \hbar g(\delta\hat{a}^\dagger\hat{b} + \delta\hat{a}\hat{b}^\dagger) \tag{2.118}$$

The rate of state transfer in the resolved sideband limit is given by:

$$\Gamma_{\rm ext} = \frac{4g^2}{\kappa} \tag{2.119}$$

If this transfer rate is higher than mechanical decoherence rate $n_{\rm th}\gamma$, the system is in the quantum regime. Assuming $\kappa_{\rm ext} = \kappa$, the condition for the system to be in the quantum regime is $C > n_{\rm th}$. Coherent state transfer between microwave fields and a mechanical oscillator was demonstrated in [73]. For the drive beam detuned from the cavity by $+\omega_{\rm m}$, the interaction Hamiltonian takes the form:

$$\hat{\mathcal{H}}_{\rm int,pdc} = \hbar g(\delta\hat{a}^\dagger\hat{b}^\dagger + \delta\hat{a}\hat{b}) \tag{2.120}$$

Entanglement is created as long as $C > n_{\rm th}$. This was demonstrated between microwave fields and mechanical oscillator in [74]. More recently, state transfer between an optical field and a mechanical oscillator was demonstrated in [14].

2.7.7 Optomechanical cooperativity as a figure of merit

From the descriptions of these effects, it is clear that in order to operate in quantum regime optomechanical cooperativity large compared to the bath phonon number is desired, that is:

$$C > n_{\rm th} \tag{2.121}$$

It is convenient to define thermal cooperativity:

$$C_{\rm th} = \frac{4g_0^2 n_{\rm circ}}{\kappa\gamma n_{\rm th}} \tag{2.122}$$

and aim to maximize it. The desire the maximize the thermal cooperativity lead us to consider superfluid helium for the use as mechanical oscillator. Particularly, we filled a Fabry-Perot cavity with superfluid helium and coupled its optical modes to its acoustic modes.

To maximize thermal cooperativity, the following is important:

- High optomechanical coupling g_0 - a fluid can fill an optical cavity, resulting in nearly perfect overlap of the optical and mechanical modes throughout the cavity
- Ability to handle high circulating photon number $n_{\rm circ}$ - superfluid helium has a large bandgap (19 eV) and no impurities (as they are all frozen to the walls of the container). That leads to very low optical absorption
- Small cavity linewidth κ - since superfluid helium does not absorb light, it will not have any adverse effects on cavity linewidth
- Small mechanical linewidth γ - since superfluid helium has no viscosity and no impurities, it has low mechanical loss
- Small bath phonon number $n_{\rm th}$ - superfluid helium has high thermal conductivity and the mode is in immediate contact with the bath, which can be thermalized to cryogenic temperatures

With this in mind, we conclude that a cavity filled with superfluid helium could make a perfect optomechanical system.

2.8 Summary

In this chapter we introduced optomechanics, derived the optomechanical equations of motion in both classical and quantum regimes. We discussed several optomechanical effects which all pointed to using optomechanical cooperativity as an important figure of merit describing the system. We concluded with stating that superfluid helium could make a perfect mechanical oscillator by stating several favorable properties of superfluid helium. In the next chapter, we will elaborate on those properties and calculate the parameters which would be useful for the data analysis later.

Chapter 3

Superfluid helium

As concluded in the previous chapter, superfluid helium could make a perfect optomechanical system, so this chapter will be about superfluid helium. I will start by discussing the history of its discovery and early observation of its properties. I will talk about the interaction of helium with surfaces (Rollin film), which will be important when we discuss how we fill our devices with helium. I will then discuss the interaction of helium with light waves - the measurement of dielectric constant, which is important for determining whether the device is filled with helium, the scattering and absorption of light in helium. I will show that absorption and scattering of light will not limit the optical cavity finesse. I will then talk about the interaction of helium with the sound waves, particularly about sound attenuation and velocity, which becomes important for understanding the properties of the mechanical mode. Finally I will talk about the thermal conductivity of helium, which is necessary to understand, in order to explain the temperature of the helium in the device.

3.1 Brief history of superfluid helium

In 1868, a French astronomer, Pierre-Jules-Cesar Janssen, noticed a yellow 588 nm line in the Sun's spectrum while studying a total solar eclipse. Previously this spectral line has never been observed on Earth. In the same year, Norman Lockyer observed the same line and together with a chemist Edward Frankland gave it the name "helium" using the Greek word for Sun - "Helios". The papers from Janssen and Lockyer reached the French Academy on the same day, so they are both credited with discovery [75].

Twenty seven years later, in 1895, Helium was first discovered on Earth by British scientist Sir William Ramsay, who isolated it, along with other noble gases from the atmosphere. Ramsay was awarded the Nobel Prize in Chemistry for his discovery in 1904.

Helium was liquefied for the first time in 1905 by the Dutch physicist Heike Kamerlingh Onnes in his "cold factory" in Leiden by cooling it below its boiling point of 4.2 K. He was awarded the Nobel prize in 1913 [76].

In 1938 Soviet physicist Pyotr Kapitsa published a paper on his experiments measuring abnormally low viscosity of helium below 2.2 K [77]. In that paper he wrote that "helium below the λ-point enters a special state which might be called a superfluid". The name "lambda point" comes from the plot of specific heat vs. temperature, which has a shape of Greek letter λ. In the same year Allen and Misener published a paper confirming Kapitsa's discovery [78]. Kapitsa was awarded a Nobel Prize for his contributions to low temperature physics in 1978.

In 1938, Fritz London suggested that superfluid helium could be an instance of Bose-Einstein condensate [79]. In 1939, his brother, Heinz London extended the idea of a partly-condensed gas, by proposing a "two-fluid" model of helium, in which superfluid helium is considered to consist of two fluids: a "normal" component and "superfluid" component. [80]

Lev Landau expanded the two-fluid picture of helium [81, 82] by explaining the presence of "normal fluid" in terms of elementary excitations (phonons - long wavelength density excitations and rotons - short wavelength density excitations),

which are present in helium at temperatures above absolute zero. The number of excitations increases with temperature. When the mean free path of the excitations is limited by the collisions with the walls, it is reasonable to treat the excitations as a gas. However, at high enough temperature the mean free path is limited by collisions between the excitations themselves, at which point it is necessary to treat them as a fluid.

Helium was extensively studied in the middle of 20th century. There are multiple fantastic summaries of theoretical and experimental findings [83, 84, 85]. Experimental physicists were trying to measure the fascinating properties of superfluid helium, while theoretical physicists wanted to understand those properties in terms of known atom-atom interactions.

Helium has two isotopes: Helium-3 and Helium-4. All the work described here was done with Helium-4, which is a boson and therefore can enter a superfluid phase, as explained originally by the London brothers. Helium-3, however, is a fermion, so it can only become superfluid at much lower temperatures, when atoms form into pairs, similar to Cooper pairs. Helium-3 becomes superfluid at 2.5 mK.

Here I will focus on the properties of helium which are most relevant to our experiments. I will not attempt to repeat the derivations of phenomenological and microscopic theory of helium, but will rather just use the results.

3.2 Helium interaction with surfaces (Rollin film)

In 1936 Rollin suggested that the observed high evaporation rate of superfluid helium from vessels was due to a thin surface layer of superfluid formed on the walls of the container [86]. The thin film "creeps" to the regions of higher temperature, where it evaporates [87].

A similar transport occurs between two regions of higher and lower gravity: the liquid level in two impenetrable beakers, partially submerged in superfluid Helium will in time equalize. The flow rate was found to be independent of the gravitational potential difference and only a function of the minimum periphery of connecting surface [86].

The film thickness d_{film} can by found by balancing Van der Waals attraction against gravity [88] with a typical value:

$$d_{\mathrm{film}} = \eta_{\mathrm{film}} h^{-1/3}. \tag{3.1}$$

Here $\eta_{\mathrm{film}} = 6.5 \times 10^{-9}$ m$^{4/3}$ and h is the height above the bulk helium level. The maximum volume flow rate of helium though a tube is:

$$\dot{V} = 2\pi R_{\mathrm{tube}} d_{\mathrm{thin}} v_{\mathrm{crit}} \tag{3.2}$$

Here, R_{tube} is the inner radius of the tube, d_{thin} is the film thickness at its thinnest point, and $v_{\mathrm{crit}} \simeq 30$ cm/s is the critical superfluid film velocity [88] - the maximum velocity at which the film can flow without destroying superfluidity.

3.3 Helium interaction with light waves

Due to its low refractive index superfluid helium usually looks very transparent. The propagation of light through helium has been studied since 1928 [30].

3.3.1 Dielectric constant of helium

The dielectric constant of liquid helium was first measured in 1928 by Wolfke and Keesom [89]. They measured the dielectric constant from 2 K to 4.2 K. The dielectric constant at 2 K was measured to be 1.0555. The dielectric constant of helium is low, because of its low density and polarizability.

In 1950 Grebenkemper and Hagen [30] measured the dielectric constant of liquid helium by using the shift of frequency of a resonant cavity over temperatures from 1.6 K to 4.2 K. They found dielectric constant at 1.6 K to be 1.057 (which corresponds to refractive index of 1.028). The values of dielectric constant over a wide range of temperatures is given in [90].

3.3.2 Absorption of light in helium

Helium II does not exhibit linear absorption visible of infrared light, due to its large bandgap (19.9 eV), and the lack of chemical impurities which freeze to the walls of the container.

3.3.3 Scattering of light in helium

Helium II, can however, scatter light. There are a few mechanisms by which scattering can occur.

- **Raman scattering** - discovered by an Indian physicist Sir Chandrasekhara Venkata Raman. This is inelastic (frequency-changing) scattering of light by scatterers - usually resulting in changes of internal states of scatterers. In superfluid helium, the light undergoes Raman scattering resulting in creation of rotons. The scattering rates were was measured by Greytak and Yan [91] (using light with wavelength $\lambda = 514$ nm) down to temperature of 1.16 K. They observed light amplitude attenuation coefficient of $\alpha_{\mathrm{Raman}} = 4\pi \times 6 \times 10^{-12}$ cm^{-1}. This attenuation puts a lower bound on the linewidth of any optical mode of a cavity filled with superfluid helium:

$$\kappa_{\mathrm{Raman}}/2\pi(1.2\mathrm{K}) = 2c_{\mathrm{He}}\alpha_{\mathrm{Raman}} = 4.4 \text{ Hz} \tag{3.3}$$

- **Rayleigh scattering** - named after Lord Rayleigh - elastic (non-frequency-changing) scattering of light off particles much smaller than the wavelength of radiation. In the literature [92] Rayleigh scattering is used to refer to scattering, in which the internal state of the scatterer is unchanged, but frequency could be changed - so it includes Brillouin scattering off phonons (discussed below).

  Using the expression in [92], the attenuation coefficient due to light scattering from the thermal fluctuation of a material is:

$$\alpha_{\mathrm{Total}} = \frac{\omega_{\mathrm{L}}^4}{6\pi c^4}\left[k_{\mathrm{B}}T\rho^2\kappa_{\mathrm{T}}\left(\frac{\partial\epsilon}{\partial\rho}\right)_T^2 + \frac{k_B T^2}{\rho C_{\mathrm{V}}}\left(\frac{\partial\epsilon}{\partial T}\right)^2\right] \tag{3.4}$$

  here ω_{L} is the light frequency, T and ρ are the temperature and density of the medium, ϵ is dielectric constant, κ_{T} is the isothermal compressibility and C_{V} is the constant volume heat capacity.

  In [93], the authors consider specifically the situation of liquid helium. For liquid helium, the isothermal compressibility $\kappa_{\mathrm{T}} = 2.08 \times 10^{-7}$ m $\cdot$ s^2/kg [93]. The second term in equation 3.4 is orders of magnitude smaller than the first term, so is neglected. The value of $\left(\frac{\partial\epsilon}{\partial\rho}\right)_T$ is estimated using Clausius-Mossotti relation:

$$\frac{\epsilon - 1}{\epsilon + 2} = \frac{\rho\alpha_{\mathrm{M}}}{3M\epsilon_0} \tag{3.5}$$

  here α_{M} is the molecular polarizability and M is the molecular mass.

  From this expression, they arrive at:

$$\left(\frac{\partial\epsilon}{\partial\rho}\right)_T = \frac{(\epsilon-1)(\epsilon+2)}{3\rho} \tag{3.6}$$

  giving the attenuation coefficient of:

$$\alpha_{\mathrm{Total}} = \frac{(2\pi)^3}{27\lambda^4}k_{\mathrm{B}}T\kappa_{\mathrm{T}}(\epsilon-1)^2(\epsilon+2)^2 \tag{3.7}$$

For the highest temperature of superfluid (2.2 K), assuming $\lambda = 1550$ nm, the lower bound on the optical linewidth is:

$$\kappa_{\mathrm{Total}}(2.2\mathrm{K}) = 2c_{\mathrm{He}}\alpha_{\mathrm{Total}} = 180\ \mathrm{Hz} \tag{3.8}$$

- **Brillouin scattering** - is named after French Physicist Leon Brillouin. It refers to the interaction of light and sound waves (phonons) inside a medium. The attenuation of light due to Brillouin scattering is given by the Landau-Placzek relationship [94]:

$$\frac{\alpha_{\mathrm{Brillouin}}}{\alpha_{\mathrm{Total}}} = \frac{\kappa_S}{\kappa_{\mathrm{T}}} = 0.96 \tag{3.9}$$

  Here $\kappa_{\mathrm{S}} \approx 1.99 \times 10^{-7}\ \mathrm{m \cdot s^2/kg}$ is adiabatic compressibility, which is the inverse of a bulk modulus. The Brillouin scattering therefore dominates the scattering of light in liquid helium, with only 4% of the scattered light being unchanged in frequency.

In conclusion, the lower bound on the linewidth of an optical mode in a cavity filled with superfluid helium due to scattering of light in helium is less than 1 kHz. It is completely unobservable in the cavities that we use, which have linewidths larger than 20 MHz.

3.4 Helium interaction with sound waves

The sound waves (first sound)[1] in helium were studied theoretically [95, 96, 97, 98, 99] and in multiple experiments [100, 101, 102, 103, 104, 105, 106] in the 1960s and 1970s.

One of the most comprehensive experimental studies was by Abraham et al. [104], in which the authors measured the sound velocity and attenuation for modes of various frequencies between 12 MHz and 208 MHz and for temperatures between 0.1 and 2 K.

In the appendix of their paper [104], Abraham gives formulas for attenuation and sound velocity from Khalatnikov's theory. I believe that formulas given for attenuation in [104] are off by a factor of 2. The factor of 2 is necessary for the expressions to agree with theoretical expressions for amplitude attenuation given in [107, 104, 96] for $T < 0.6$ K.

3.4.1 Attenuation of sound

For $T < 0.6$ K the main intrinsic loss mechanism for density waves (i.e., first sound) in superfluid helium is the three phonon process [96]. It can be described by an amplitude attenuation coefficient $\alpha_{3\mathrm{pp}}$

$$\alpha_{3\mathrm{pp}}(\omega_{\mathrm{ac}}) = \frac{\pi^2(u_{\mathrm{Gr}}+1)^2 k_B^4}{30\rho_{\mathrm{He}}\hbar^3 v_{\mathrm{He}}^6}\omega_{\mathrm{ac}}T^4\left(\arctan(\omega_{\mathrm{ac}}\tau_{\mathrm{th}}) - \arctan\left(\frac{3}{2}\gamma_3\bar{p}_{\mathrm{th}}^2\omega_{\mathrm{ac}}\tau_{\mathrm{th}}\right)\right) \tag{3.10}$$

Here ω_{ac} is the wave frequency, T is the temperature, $\rho_{\mathrm{He}} = 145$ kg/m^3 and $v_{\mathrm{He}} = 238$ m/s are the helium density and sound velocity, $u_{\mathrm{Gr}} = 2.84$ is the Grüneisen constant [97], $\tau_{\mathrm{th}} = \xi_{\mathrm{th}}T^{-5}$ is the thermal phonon lifetime, where $\xi_{\mathrm{th}} = 1.11 \times 10^{-7}$ s·K^5 [108] and $\bar{p}_{\mathrm{th}} = 3k_BT/v_{He}$ is the average thermal phonon momentum. Finally, γ_3 is the coefficient for the cubic term in the phonon dispersion, which is expressed as $\gamma_3 = -\frac{1}{6v_{He}}\frac{d^3\epsilon}{dp^3}$, where ϵ and p are phonon energy and momentum respectively. It has been measured to be $\gamma_3 = -8 \times 10^{47}$ kg^{-2}m^{-2}s^2 [97].

For 0.6 K$< T < 1$ K, both phonons and rotons are present and the problem becomes more complicated, however the theory by Khalatnikov [95, 104] gives an expression for attenuation for the whole range (0 K$< T < 2$ K)

[1] In addition to first sound (the pressure/density waves), second sound (heat transfer by wave-like motion) and third sound (the waves propagating in the Rollin film) have been observed in Helium II. Despite the name, second and third sounds have nothing to do with pressure/density waves and will not be discussed here

For $T > 1$ K, the collisions between quasi-particles are frequent, and equilibrium is established in time $1/\omega_{\rm ac}$, where $\omega_{\rm ac}$ is the sound frequency. This is called the hydrodynamic regime and the attenuation is given by [104]:

$$\alpha_{\rm hd}(\omega_{\rm ac}) = \frac{\omega_{\rm ac}^2}{2\rho_{\rm He} v_{\rm He}^3}\left(\frac{4}{3}\eta_{\rm He} + \xi_{\rm He}\right) \tag{3.11}$$

Here η and ξ are first and second viscosity coefficients calculated by Khalatnikov [95].

The following expression converts the amplitude attenuation into a lower bound on the linewidth of any acoustic mode in a cavity filled with helium:

$$\gamma = 2 v_{\rm He} \alpha \tag{3.12}$$

The plot of linewidth vs. temperature for 30 MHz mode (the frequency for which most complete data set is available in [104]) is shown in figure 3.1. Here the blue points represent the data, the dashed gray line is the Khalatnikov theory and the thin red line is the attenuation for 0 K $< T <$ 0.6 K given by equation 3.10. The data agrees with the theory reasonably well below 1.5 K, so we can use the theory to calculate the upper bound on the acoustic mode linewidth at any frequency.

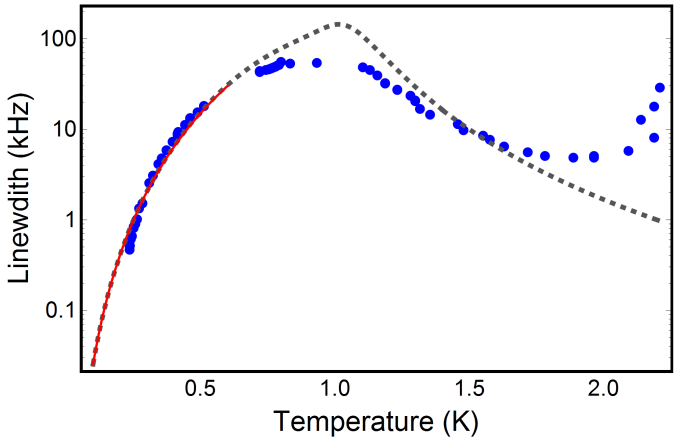

Figure 3.1: The lower limit on a mechanical linewidth of a mode in helium vs. temperature. Blue dots: data for 30 MHz mode from [104]. Gray dashed line - Khalatnikov theory described in [104]. Red line- theory given by equation 3.10.

In order to obtain a lower bound on the mode linewidth for $T > 1.5$ K, we use the approach outlined in [109]: since attenuation in the high temperature limit is proportional to the square of the frequency [104], we can use the measured attenuation at 30 MHz [104] and convert it to attenuation at any frequency.

3.4.2 Velocity of sound

For $T < 0.6$ K the change in velocity of sound is given by Maris [96] as

$$\Delta v(\omega_{\rm ac}) = \frac{\pi^2 (u_{\rm Gr}+1)^2 k_B^4}{60 \rho_{\rm He} \hbar^3 v_{\rm He}^4} T^4 \ln \frac{1 + (\omega_{\rm ac}\tau_{\rm th})^2}{1 + \left(\frac{3}{2}\gamma_3 \bar{p}_{\rm th}^2 \omega_{\rm ac}\tau_{\rm th}\right)^2} \tag{3.13}$$

The Khalatnikov theory described in [104] gives the change in sound velocity for 0 K $< T <$ 2.2 K.

The most complete data set is given in [104] for the 12 MHz mode. Additionally [109] gives data at high temperatures for 750 MHz mode. Figure 3.2 shows the data for the 12 MHz mode and the 750 MHz mode and the theory for 12 MHz mode. Here the blue points represent the 12 MHz data, green dots represent 750 MHz data, the dashed gray line is the Khalatnikov theory and the thin red line is the change in sound velocity for 12 MHz and 0 K $< T <$ 0.6 K, given by equation 3.13.

The theory and data agree in the intermediate temperature range, but disagree for low temperatures and high temperatures. However, at high temperatures, the data for 12 MHz and 750 MHz agree, so it could be reasonable to use this data to describe the sound velocity change for any frequency 12 MHz $< \omega_{ac}/2\pi <$ 750 MHz.

At low temperature 0 K $< T <$ 0.6 the data does not agree with either theory, so together with [104] we can conclude that the theory is inadequate. It is possible to fit the data with $\Delta v = b_v T^4$, shown with the thin blue line in figure 3.2, where $b_v = 0.75$ m/s·K^4.

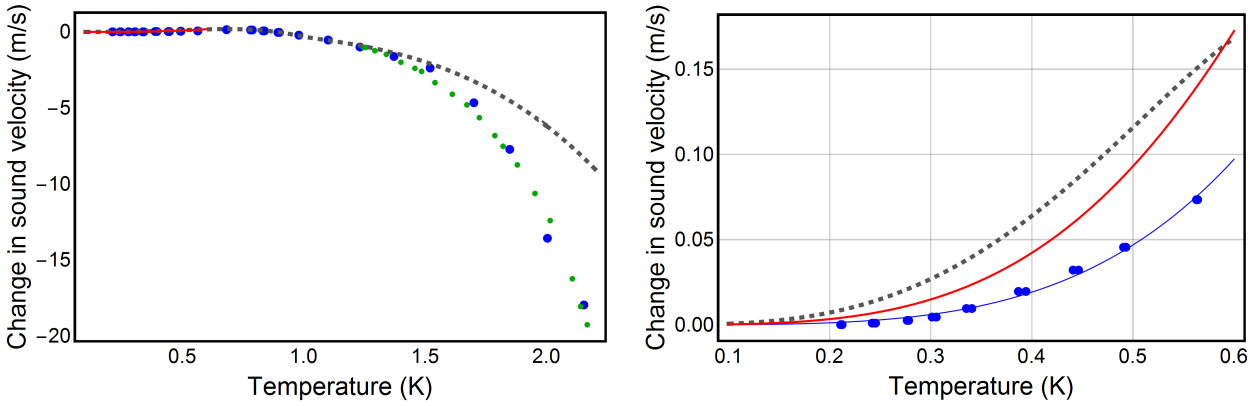

Figure 3.2: The change in sound velocity vs. temperature. Blue dots: data for 12 MHz mode from [104]. Green dots: data for 750 MHz mode from [109]. Gray dashed line- Khalatnikov theory for 12 MHz sound wave described in [104]. Red line - theory given by equation 3.10 for 12 MHz sound wave. Thin blue line: $b_v T^4$. Left: 0 K $< T <$ 2.2 K. Right: 0 K $< T <$ 0.6 K.

3.4.3 Density

Although it is not immediately obvious how density influences the interaction of helium with the sound waves, we will later see that it becomes important when we consider the propagation of acoustic waves in helium with an inhomogeneous temperature profile. Here we will show a plot of change in density (from $\rho_{He}(T = 0) = 145.14$) kg/m^3, using the values from [90].

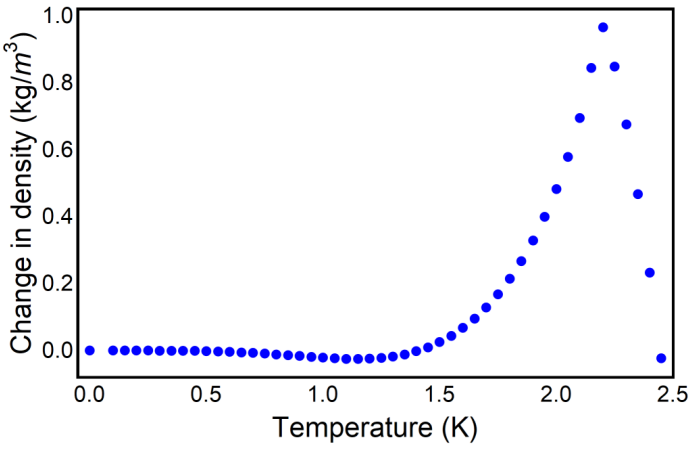

Figure 3.3: The change in density vs. temperature.

3.5 Thermal transport in liquid helium

Heat in Helium II is carried by excitations, such as phonons and rotons. At low temperatures $T \leq 0.6$ K only a small number of phonons are present, and no rotons. The phonons propagate ballistically, and their mean free path is limited by collisions with the walls of the container. As the temperature is increased, the collisions between phonons and rotons become more frequent until at ≈ 1 K, the quasi-particles form a "fluid".

The heat conductivity of helium depends on the size of the channel, on the heat flux and on the helium temperature [110, 111]. There are three main regimes for heat transport in a helium II channel:

1. **Ballistic regime.** Valid when the phonon mean free path is comparable to or larger than the radius of the channel.
2. **Landau regime.** Laminar flow. Valid when the phonon mean free path is short compared with the radius of the channel and the heat flux is low.
3. **Gorter-Mellink regime.** Turbulent flow. Valid when the phonon mean free path is short compared with the radius of the channel and the heat flux is high.

3.5.1 Heat conductivity in the Ballistic regime

The expression relating heat flow to temperature gradient in the ballistic regime is [88]:

$$\frac{\dot{Q}}{A} = -k_{\mathrm{He}}(T)\frac{dT}{dr} \tag{3.14}$$

Here A is the area over which the heat is distributed and $k(T)$ is the helium thermal conductivity through the channel, described by the following equation [111]:

$$k_{\mathrm{He}} = \frac{1}{3}C v_{\mathrm{He}} D_{\mathrm{tube}} \frac{2 - f_{\mathrm{diff}}}{f_{\mathrm{diff}}} \tag{3.15}$$

Here C is the specific heat per unit volume, D_{tube} is the channel diameter, and f_{diff} is the fraction of phonons undergoing diffusive scattering from the channel walls. For $T < 0.6$ K, the specific heat per unit volume is given by:

$$C = \frac{2\pi^2 k_{\mathrm{B}}^4}{15\hbar^3 v_{\mathrm{He}}^3} T^3 \tag{3.16}$$

We can now express conductivity as:

$$k_{\mathrm{He}}(T) = \zeta D_{\mathrm{tube}} \frac{2 - f_{\mathrm{diff}}}{f_{\mathrm{diff}}} T^3 = \xi T^3 \tag{3.17}$$

WHere $\zeta = 2.3 \times 10^5$ W$/(\mathrm{m}^2 \cdot \mathrm{K}^4)$. We approximate f by considering the fraction of the phonons reflected specularly [112]:

$$f_{\mathrm{spec}} = f_0 e^{-\frac{4\pi\sigma^2}{\lambda_{\mathrm{th}}^2}} \tag{3.18}$$

Here σ is the surface roughness of the channel. The constant f_0 is the phonon reflectivity in the absence of roughness, which can be calculated from the impedance mismatch. The most likely thermal phonon frequency is found from $\hbar\omega_{\mathrm{th}} = k_{\mathrm{B}}T$. From here we find $\lambda_{\mathrm{th}} = 2\pi v_{\mathrm{He}}/\omega_{\mathrm{th}}$. The value of f_{diff} is calculated as $f_{\mathrm{diff}} = (1 - f_{\mathrm{spec}})f_0$.

3.5.2 Heat conductivity in two-fluid regime

The total helium density is the sum of the superfluid and normal fluid densities: $\rho_{\mathrm{He}} = \rho_{\mathrm{s}} + \rho_{\mathrm{n}}$. The heat is carried by the normal fluid component. Assuming the net mass flow is zero, the heat flux density is proportional to v_{n}, the velocity of the normal fluid component:

$$\dot{q} = s\rho_{\mathrm{He}} T v_{\mathrm{n}} \tag{3.19}$$

Here s is the entropy and T is the temperature of helium. Additionally, there is no net mass flow in Helium II:

$$\rho_{\mathrm{s}} v_{\mathrm{s}} + \rho_{\mathrm{n}} v_{\mathrm{n}} = 0 \tag{3.20}$$

The hydrodynamic equations for the two components of Helium II, neglecting the terms related to the compressibility of bulk fluid are given in [83] as:

$$\rho_{\mathrm{n}} \frac{dv_{\mathrm{n}}}{dt} = -\frac{\rho_{\mathrm{n}}}{\rho_{\mathrm{He}}} \nabla p - \rho_{\mathrm{s}} s \nabla T + \mu_{\mathrm{He}} \nabla^2 v_{\mathrm{n}} + F_{\mathrm{sn}} \tag{3.21}$$

$$\rho_{\mathrm{s}} \frac{dv_{\mathrm{s}}}{dt} = -\frac{\rho_{\mathrm{s}}}{\rho_{\mathrm{He}}} \nabla p + \rho_{\mathrm{s}} s \nabla T - F_{\mathrm{sn}} \tag{3.22}$$

Here p is the pressure, μ_{He} is the normal fluid viscosity, F_{sn} is the friction between superfluid and normal fluid components (mutual friction). Gorter and Mellink showed that the mutual friction is given by [113]:

$$F_{\mathrm{sn}} = A_{\mathrm{GM}} \rho_{\mathrm{s}} \rho_{\mathrm{n}} |v_{\mathrm{s}} - v_{\mathrm{n}}|^3 \tag{3.23}$$

The A_{GM} is called “Gorter-Mellink" parameter. Measurements of A_{GM} have given different results [83], however there is general agreement that $A_{\mathrm{GM}} \propto T^3$. Using the approximate average of the data given in [83] we take $A_{\mathrm{GM}} = \alpha_{\mathrm{GM}} T^3$ with $\alpha_{\mathrm{GM}} \approx 200$ m·s/(kg·K^3).

In the steady state we can set the acceleration terms on the left hand side of equations 3.21 and 3.22 to zero.

3.5.2.1 Heat conductivity in the Landau regime

In the Landau regime the thermal flux is small, so the velocities v_{s} and v_{n} are small too. In this case, the mutual friction term is approximately zero and from equation 3.22 we get:

$$\nabla p = \rho_{\mathrm{He}} s \nabla T \tag{3.24}$$

Summing equations 3.21 and 3.22 results in the Poiseuille equation, which gives the pressure gradient due to viscous flow:

$$\nabla p = \mu_{\mathrm{He}} \nabla^2 v_{\mathrm{n}} \tag{3.25}$$

We will solve the Poiseuille equation for the simplest case of flow along a cylindrical pipe. We need to make a few assumptions: the radial and angular components of velocity are zero: $v_{\mathrm{n,r}} = v_{\mathrm{n},\theta} = 0$; the flow is axis-symmetric: $\frac{\partial p}{\partial \theta} = \frac{\partial v_{\mathrm{n,z}}}{\partial \theta} = 0$ and the flow is constant everywhere along the pipe: $\frac{\partial v_{\mathrm{n,z}}}{\partial z} = 0$. Under those assumptions we have a single equation:

$$\frac{\partial p}{\partial z} = \mu_{\mathrm{He}} \frac{1}{r} \frac{\partial}{\partial r} \left(r \frac{\partial v_{\mathrm{n,z}}}{\partial r} \right) \tag{3.26}$$

Applying the no-slip boundary condition ($v_{\mathrm{n,z}}(r = D_{\mathrm{tube}}/2) = 0$), we find the solution to this equation:

$$v_{\mathrm{n,z}} = \frac{\partial p}{\partial z} \frac{r^2 - (D_{\mathrm{tube}}/2)^2}{4\mu_{\mathrm{He}}} \tag{3.27}$$

The average velocity is found by integrating $v_{\mathrm{n,z}}$ over the cross-section of the pipe :

$$\langle v_{\mathrm{n,z}} \rangle = \frac{1}{\pi (D_{\mathrm{tube}}/2)^2} \int_0^{D_{\mathrm{tube}}/2} v_{\mathrm{n,z}} \cdot 2\pi r dr = -\frac{\partial p}{\partial z} \frac{(D_{\mathrm{tube}}/2)^2}{8\mu_{\mathrm{He}}} \tag{3.28}$$

Therefore:

$$\frac{\partial p}{\partial z} = \nabla p = -\frac{32\mu_{\mathrm{He}}\langle v_{\mathrm{n,z}}\rangle}{D_{\mathrm{tube}}^2} \tag{3.29}$$

Combining equations 3.29 and 3.24, we get the following equation:

$$\rho_{\mathrm{He}} s \nabla T = -\frac{32\mu_{\mathrm{He}}\langle v_{\mathrm{n}}\rangle}{D_{\mathrm{tube}}^2} \tag{3.30}$$

Using equation 3.19, we rewrite the product $v_{\mathrm{n}} = \frac{\dot{q}}{s\rho_{\mathrm{He}}T}$, arriving at:

$$\frac{\dot{Q}}{A} = -\frac{D_{\mathrm{tube}}^2 s^2 \rho_{\mathrm{He}}^2 T}{32\mu_{\mathrm{He}}} \nabla T \tag{3.31}$$

where $\dot{Q} = \dot{q}A$ is the total heat flux.

3.5.2.2 Heat conductivity in the Gorter-Mellink regime

In the Gorter-Mellink regime, the thermal flux is large and equations are dominated by the mutual friction term. The resulting equation is:

$$s\nabla T = A_{\mathrm{GM}}\rho_{\mathrm{n}}|v_{\mathrm{s}} - v_{\mathrm{n}}|^3 \tag{3.32}$$

Using equations 3.20 to rewrite v_{s} in terms of v_{n}, as well as equation 3.19, we get the following:

$$s\nabla T = A_{\mathrm{GM}}\rho_{\mathrm{n}} \left| \left(\frac{\rho_{\mathrm{n}}}{\rho_{\mathrm{s}}} + 1 \right) \frac{\dot{q}}{s\rho_{\mathrm{He}}T} \right|^3 \tag{3.33}$$

With a little algebra we can write:

$$\left(\frac{\dot{Q}}{A}\right)^3 = \frac{s^4\rho_{\mathrm{s}}^3 T^3}{A_{\mathrm{GM}}\rho_{\mathrm{n}}} \nabla T \tag{3.34}$$

3.5.2.3 Critical flux of the Gorter-Mellink regime

To determine whether the heat conductivity is in the Landau or the Gorter-Mellink regime, it is necessary to find whether the flux is above or below some critical flux. The critical flux is related to a critical velocity of the normal fluid $v_{\mathrm{n,crit}}$:

$$\dot{q}_{\mathrm{crit}} = s\rho_{\mathrm{He}} T v_{\mathrm{n,crit}} \tag{3.35}$$

The entropy $s(T)$ can be extracted from the values for the specific heat $C(T)$, using

$$s(T) = \int_0^T \frac{C(T')}{T'} dT' \tag{3.36}$$

The specific heat can be approximated by the following empirical expressions [114]:

$$\begin{aligned} C(T) &= \zeta_1 T^3 \quad \text{for} \quad T < 0.6\ \mathrm{K} \\ C(T) &= \zeta_2 T^{6.7} \quad \text{for} \quad 0.6 < T < 1.1\ \mathrm{K} \\ C(T) &= \zeta_3 T^{5.6} \quad \text{for} \quad 1.1 < T < 2.17\ \mathrm{K} \end{aligned} \tag{3.37}$$

Where $\zeta_1 = 20.4\ \mathrm{J/(kg \cdot K^4)}$, $\zeta_2 = 108\ \mathrm{J/(kg \cdot K^{7.7})}$, and $\zeta_3 = 117\ \mathrm{J/(kg \cdot K^{6.6})}$. The critical velocity $v_{\mathrm{n,crit}}$ can be found in two different ways, which correspond to two different origins of turbulence in helium II.

- The critical velocity that is necessary to create vortex lines in the superfluid was measured experimentally in small channels with diameter D_{tube} [114]:

$$v_{\text{s,crit}} \simeq \frac{\beta}{D_{\text{tube}}^{1/4}} \tag{3.38}$$

where $\beta = 0.03$ m$^{5/4}$/s.

Since the net mass transport is zero, absolute value of the critical velocity is:

$$v_{\text{n,crit}} = \frac{\rho_{\text{s}}}{\rho_{\text{n}}} v_{\text{s,crit}} \tag{3.39}$$

This corresponds to the critical flux:

$$\dot{q}_{\text{crit},1} = s\rho_{\text{He}} T \frac{\rho_{\text{s}}}{\rho_{\text{n}}} v_{\text{s,crit}} \tag{3.40}$$

To find the normal fluid density, we use the fact that superfluid has no entropy, so helium II entropy is written in terms of the normal component [114]:

$$\rho_{\text{He}} s = \rho_{\text{n}} s_{\text{n}} \tag{3.41}$$

The entropy of the normal fluid component $s_n = s(T_\lambda)$, and therefore the normal fluid density is:

$$\rho_{\text{n}}(T) = \frac{s(T)}{s(T_\lambda)} \rho_{\text{He}} \tag{3.42}$$

The superfluid density is: $\rho_{\text{s}}(T) = \rho_{\text{He}} - \rho_{\text{n}}(T)$. Figure 3.4 shows the density of normal fluid (blue) and superfluid (red) as a function of temperature. The dashed black line shows the total density of helium II.

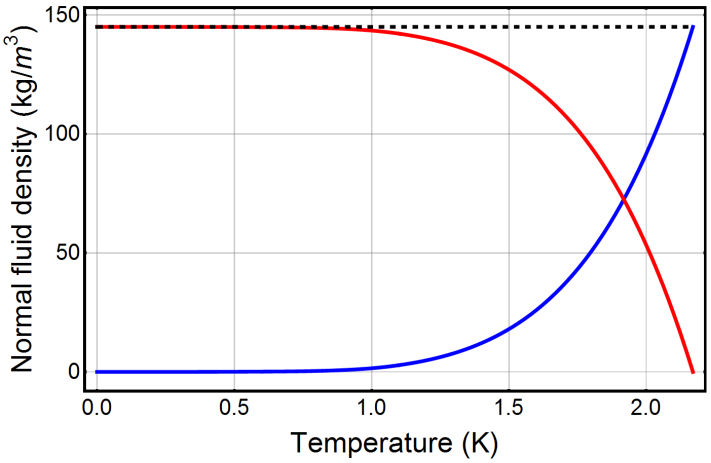

Figure 3.4: The density of normal fluid (blue) and superfluid (red) as a function of temperature. The dashed black line shows the total density of helium II.

- The turbulence in the normal component can be described in terms of the classical fluid dynamics models. In classical fluids the transition to turbulence is defined using the critical Reynolds number, which is

$$\text{Re} = \frac{\rho_{\text{He}} v_{\text{crit}} d}{\mu_{\text{He}}} \approx 1200 \tag{3.43}$$

From here we can find the critical velocity of the normal component and therefore the critical flux:

$$\dot{q}_{\text{crit},2} = \frac{1200 s T \mu_{\text{He}}}{d} \tag{3.44}$$

In practice, we evaluate Eq. 3.44 using the empirical expression for the helium viscosity (valid for $T < 1.8\text{K}$)[114]

$$\mu_{\text{He}} \approx \upsilon T^{-5} + 1.4 \times 10^{-6}\ \text{Pa} \cdot \text{s} \tag{3.45}$$

where $\upsilon = 1.4 \times 10^{-6}\ \text{Pa} \cdot \text{s/K}^5$.

The critical heat fluxes $\dot{q}_{\text{crit},(1,2)}$ are plotted vs. temperature in figure 3.5.

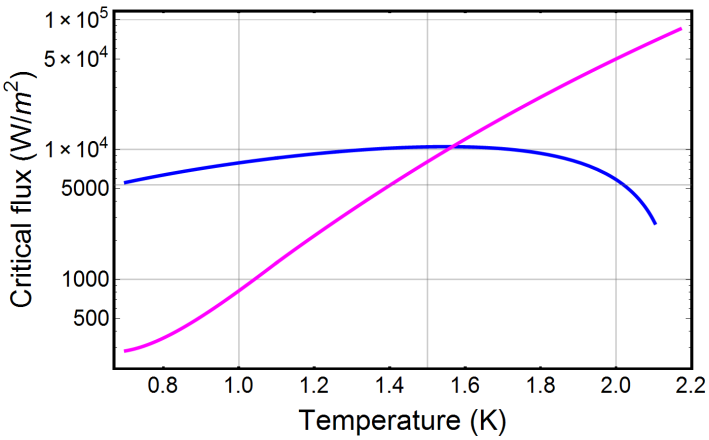

Figure 3.5: Critical flux as a function of temperature. Blue line shows the critical flux set by the superfluid turbulence and magenta line shows the critical flux set by normal fluid turbulence.

3.6 Summary

In this chapter we saw that superfluid helium does indeed have low optical absorption and small values of sound attenuation at low temperatures. We described the temperature dependence of the sound velocity, and discussed the thermal conductivity of helium in a few different regimes. The expressions derived in this chapter will be used in the data analysis for both devices. Now that we talked about optomechanics and superfluid helium separately, we will discuss the optomechanical coupling to the acoustic modes of superfluid helium in the next chapter.

Chapter 4

Optomechanics with Superfluid helium

Despite the useful properties of superfluid helium (described in the previous chapters) it had never been incorporated into an optomechanical system up until very recently. Our group, along with a few other groups, decided to use superfluid helium as an optomechanical element to make use of its unique properties. I will describe our approach in this chapter. The methods used by other groups are described in the end of the chapter in section 4.5.

To couple light to helium we use a Fabry-Perot cavity which, as described in section 2.3, accommodates a number of optical modes. We fill the space between the mirrors with superfluid helium. As soon as the cavity is filled, the helium is populated by a number of thermally excited acoustic modes (density fluctuations of helium). The optomechanical coupling arises because the effective cavity length depends on the density of helium that the optical mode overlaps with. Overlap with regions of higher helium density (higher index of refraction) increases the effective cavity length and overlap with the regions of lower helium density (lower index of refraction) decreases the effective cavity length. This renders the system similar to the canonical optomechanical system, and it is described by the same Hamiltonian.

For the discussion of the optomechanical coupling, it is useful to describe the geometry of the device. We build the device using optical fibers. The faces of the fibers have indentations on them and are coated with mirror coating. The way that we fabricate fibers and build the cavities is described in sections 6.1.1, 6.1.2 and 6.1.3.

The fibers are aligned using a ferrule - a glass cylinder with a fiber-sized bore through the center. The fibers can be aligned using one ferrule or two ferrules, as shown in figure 4.1 (a) and (b). The optical mode of the cavity is confined by the curvature of the mirrors to the small region near the axis of the cavity (figure 4.1 (c)). The paraxial acoustic mode to which the optical mode couples, has a shape similar to that of the optical mode (figure 4.1 (d)). In the case of both fibers aligned in one ferrule, there is also a "radial" mode, confined to the cylinder of helium, defined by the fiber faces and the ferrule walls (figure 4.1 (e)).

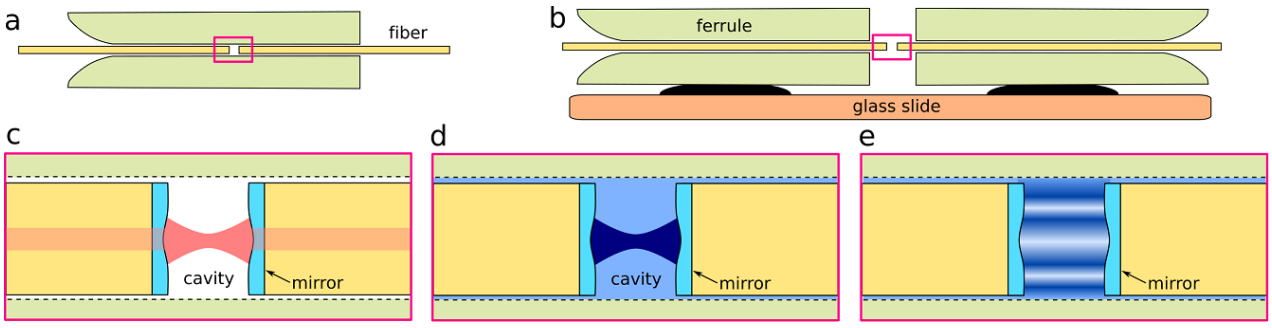

Figure 4.1: Schematics of the device. a) Two fibers aligned in one ferrule. b) Two fibers aligned using two ferrules aligned to one another c) The paraxial optical mode d) The paraxial acoustic mode e) The radial acoustic mode.

In this chapter I will derive the expressions describing the paraxial optical, paraxial acoustic and radial acoustic modes.

I will explain in detail how optomechanical coupling between optical mode and both types of acoustic modes arises and calculate the values of the single-photon optomechanical coupling g_0. Then I will focus on the paraxial acoustic mode, and will discuss the single-photon optomechanical cooperativity that can be achieved in our device. I will explain how optomechanical coupling and cooperativity change with different material parameters and discuss the possibility of using materials other than superfluid helium. Finally I will discuss the work on superfluid optomechanics performed in other groups.

4.1 Optical and acoustic mode profiles in a Fabry-Perot cavity

In this section I will derive the optical and acoustic mode profiles in a Fabry-Perot cavity. I will start by deriving a wave equation in the paraxial approximation. I will present the solutions of the wave equation and then demonstrate how this can be extended to solutions giving the electric field and acoustic mode profile inside a Fabry-Perot cavity.

4.1.1 Wave equation in the paraxial approximation

The generic form of a scalar wave equation is:

$$\nabla^2\psi(\vec{r},t) = \frac{1}{v^2}\frac{\partial^2\psi(\vec{r},t)}{\partial t^2} \tag{4.1}$$

The solution to this wave equation is a wave propagating at velocity v.

Assuming we can write the function ψ as a product of a time-independent and a time-dependent part oscillating at ω: $\psi(\vec{r},t) = \psi(\vec{r})Re[e^{i\omega t}]$, we arrive at the Helmholtz equation for the time-independent part of ψ.

$$\nabla^2\psi(\vec{r}) + k^2\psi(\vec{r}) = 0 \tag{4.2}$$

Where $k = \omega/v$ is the wave-number. Consider a wave propagating in the z-direction. For such a wave the primary spatial dependence of $\psi(\vec{r})$ will be described by e^{-ikz}. Additionally there will be some transverse variation in the x and y directions as well as variation of this profile in the z-direction. This allows us to write:

$$\psi(\vec{r}) = u(\vec{r})e^{-ikz} \tag{4.3}$$

where u describes the transverse profile of the beam. Plugging this back into the Helmholtz equation and simplifying, we get:

$$\nabla^2 u(\vec{r}) - 2ik\frac{\partial u}{\partial z} = 0 \tag{4.4}$$

The paraxial approximation consists of recognizing that the variation of the transverse mode profile $u(\vec{r})$ in the z direction is slow compared to the optical wavelength and the transverse variations, so the term $\frac{\partial^2 u}{\partial z^2}$ from the Laplacian can be dropped, leaving us with the following equation:

$$\nabla_T^2 u(\vec{r}) - 2ik\frac{\partial u}{\partial z} = 0 \tag{4.5}$$

Here ∇_T^2 is a Laplacian operating on the transverse coordinates. This looks like the free-particle Schrödinger equation in two spatial dimensions with z playing the role of time In appendix B.1 we show that the solution to this equation is:

$$u^{(m,n)}(\vec{r}) \propto \frac{w_0}{w(z)}H_n\left(\frac{\sqrt{2}x}{w(z)}\right)H_m\left(\frac{\sqrt{2}y}{w(z)}\right) \tag{4.6}$$

$$\times \exp\left(-\frac{r^2}{w(z)^2}\right)\exp\left(-i\left[\frac{kr^2}{2R(z)} - \phi_{\mathrm{G}}^{(n,m)}(z)\right]\right) \tag{4.7}$$

Here w_0 is the beam radius at the waist, defined in equation B.30; $w(z)$ is the beam radius at point z, defined in equation B.12, z is measured from the beam waist; n and m are integers specifying the transverse wave numbers; H_n and H_m are the Hermite polynomials of order n and m; r is the distance from the cavity axis; $R(z)$ is the radius of curvature of the beam at point z, defined in equation B.11; $\phi_{\mathrm{G}}^{(n,m)}(z) = (1+n+m)\arctan\left(\frac{z\lambda}{\pi w_0^2}\right)$ is the Guoy phase shift.

Therefore:

$$\psi^{(m,n)}(\vec{r}) \propto \frac{w_0}{w(z)} H_n\left(\frac{\sqrt{2}x}{w(z)}\right) H_m\left(\frac{\sqrt{2}y}{w(z)}\right) \tag{4.8}$$

$$\times \exp\left(-\frac{r^2}{w(z)^2}\right) \exp\left(-i\left[kz + \frac{kr^2}{2R(z)} - \phi_{\mathrm{G}}^{(n,m)}(z)\right]\right) \tag{4.9}$$

The solution of a wave equation for a TEM_{00} mode inside a Fabry-Perot cavity is derived in appendix B.2:

$$\psi^{(q,0,0)}(\vec{r}) \propto \frac{w_0}{w(z)} e^{-\frac{r^2}{w(z)^2}} \sin\left(k^{(q,0,0)}z + \frac{k^{(q,0,0)}r^2}{2R(z)} - \phi_{\mathrm{G}}^{(0,0)}(z) + \theta^{(q,0,0)}\right) \tag{4.10}$$

Here $k^{(q,0,0)} = \pi q_{\mathrm{opt}}/L_{\mathrm{cav}} - \arccos(\sqrt{\pm g_1 g_2}/L_{\mathrm{cav}})$ is the wavenumber, where q_{opt} is longitudinal mode number; g_1 and g_2 are resonator g-parameters defined in equation B.19; $\theta^{(q,0,0)}$, in a phase defined in equation B.28, which is there to ensure that the mode has nodes at the mirrors. If the mode has antinodes at the mirrors the equation is the same, with the exception that $\sin$ is replaced with $\cos$.

4.1.2 Optical mode profile

The wave equation for the electric field is derived from Maxwell's equations in vacuum and charge-free space:

$$\nabla^2 \vec{E}(\vec{r},t) = \frac{1}{c^2}\frac{\partial^2 \vec{E}}{\partial t^2} \tag{4.11}$$

This equation must hold for any component of the electric and magnetic field. For concreteness, assume a wave propagating in the z direction. For such wave $E_z = B_z = 0$ (electromagnetic waves are transverse). The polarization of the wave can be chosen so that either E_x or E_y is non-zero. Therefore solving equation for one component (e.g. E_x), which we will call E will give us the information we need about the field:

$$\nabla^2 E(\vec{r},t) = \frac{1}{c^2}\frac{\partial^2 E(\vec{r},t)}{\partial t^2} \tag{4.12}$$

This quation is solved, as described in section 4.1.1, and the result for TEM_{00} mode inside a Fabry-Perot cavity is:

$$E^{(q,0,0)}(\vec{r}) = E_0 \frac{w_0}{w(z)} e^{-\frac{r^2}{w(z)^2}} \sin\left(k^{(q,0,0)}z + \frac{k^{(q,0,0)}r^2}{2R(z)} - \phi_{\mathrm{G}}^{(0,0)}(z) + \theta^{(q,0,0)}\right) \tag{4.13}$$

The confinement of the optical mode is provided by the curved mirror surfaces and is due to the high reflectivity of the mirrors. The optical modes has nodes at the cavity mirrors.

An example of the solution in a typical cavity used in an experiment is shown in figure 4.2. Note that the mode is confined to the small volume in the center of the cavity.

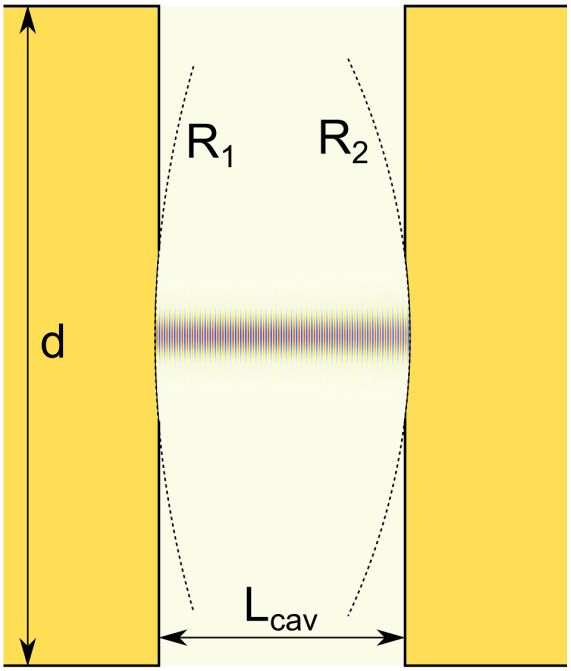

Figure 4.2: The plot of the TEM_{00} mode of the electric field inside of a cavity Fabry Perot cavity. Plot to scale. The optical wavelength is 1550 nm. The fiber diameter is $d = 200$ μm. The cavity length $L_{\text{cav}} = 80$ μm, the mirrors radii of curvature are $R_1 = 300$ μm and $R_2 = 200$ μm.

4.1.3 Acoustic mode profile

The wave equation for the acoustic mode in a homogenous medium is given in [115]:

$$\nabla^2 p_{\text{e}}(\vec{r}, t) = \frac{1}{v_{\text{He}}^2} \frac{\partial^2 p_{\text{e}}(\vec{r}, t)}{\partial t^2} \tag{4.14}$$

Here v_{He} is the speed of sound in helium and p_{e} is the pressure fluctuations in helium. There are a few solutions which describe the acoustic modes to which an optical mode would couple.

4.1.3.1 Paraxial mode

One of the solutions to the wave equation in a Fabry-Perot cavity, in a paraxial approximation, described in section 4.1.1 is a Gaussian mode, which has a very similar form to the solution found for the electric field.

$$p_{\text{e}}^{(q,0,0)}(\vec{r}) = p_{\text{e},0} \frac{w_0}{w(z)} e^{-\frac{r^2}{w(z)^2}} \cos\left(k^{(q,0,0)} z + \frac{k^{(q,0,0)} r^2}{2R(z)} - \phi_{\text{G}}^{(0,0)}(z) + \theta^{(q,0,0)} \right) \tag{4.15}$$

Here $\sin$ was replaced by $\cos$ since pressure must have antinodes at the mirror surface (velocity must be zero at the surface, assuming the glass is infinitely stiff). The confinement in this case is provided by the curved mirror surfaces and is due to the impedance mismatch between glass and helium.

It is useful to relate pressure fluctuations to density fluctuations.

We start by assuming that pressure is some function of density: $p = f(\rho)$. If we assume a liquid is at rest, with density ρ_0 we can write $p_0 = f(\rho_0)$. Now consider a small position and time dependent variation in density $\rho_e(x, t)$. The pressure can be written as:

$$p(x, t) = p_0 + p_e(x, t) = f(\rho_0 + \rho_e(x, t)) = f(\rho_0) + \rho_e(x, t) f'(\rho_0) \tag{4.16}$$

where a Taylor expansion to first order in ρ_e was performed. From equation 4.16:

$$p_e(x,t) = v^2 \rho_e(x,t) \tag{4.17}$$

where $v^2 = \left(\frac{dp}{d\rho}\right)_0$ is the definition of the sound velocity. Therefore density fluctuations are directly proportional to pressure fluctuations and we can write the density fluctuations of the paraxial mode as:

$$\rho_e^{(q,0,0)}(\vec{r}) = \rho_{e,0} \frac{w_0}{w(z)} e^{-\frac{r^2}{w(z)^2}} \cos\left(k^{(q,0,0)} z + \frac{k^{(q,0,0)} r^2}{2R(z)} - \phi_{\mathrm{G}}^{(0,0)}(z) + \theta^{(q,0,0)}\right) \tag{4.18}$$

As we will see later, the optical mode would only couple to the paraxial mode which satisfies the condition $q_{\mathrm{mech}} = 2q_{\mathrm{opt}}$, were q_{mech} and q_{opt} are the longitudinal mode number for the acoustic and optical modes correspondingly. In the next section, we will consider the modes that do not satisfy this condition.

4.1.3.2 Radial modes

The radial modes are lower frequency modes which are confined by the fiber faces and the sides of the ferrule. In this case, the optical mode will only couple to the modes with no z-dependence (because otherwise the overlap integral in the equation describing optomechanical coupling (equation 4.48) is zero), so equation 4.14 can be written in cylindrical coordinates as:

$$\frac{1}{r}\frac{\partial}{\partial r}\left(r\frac{\partial p_{\mathrm{e}}}{\partial r}\right) + \frac{1}{r^2}\frac{\partial^2 p_{\mathrm{e}}}{\partial \theta^2} = \frac{1}{v_{\mathrm{He}}^2}\frac{\partial^2 p_{\mathrm{e}}}{\partial t^2} \tag{4.19}$$

The solution to the above equation in terms of Bessel functions is found by separation of variables to be:

$$p_{\mathrm{e}}^{(m,k)}(r,\theta,t) = [A_m J_m(kr) + B_m N_m(kr)]\cos(m\theta + \delta_m) e^{ikvt} \tag{4.20}$$

Since density fluctuations are proportional to the pressure fluctuations, the same solution can be written for the density fluctuations, with A_m and B_m redefined:

$$\rho_{\mathrm{e}}^{(m,k)}(r,\theta,t) = [A_m J_m(kr) + B_m N_m(kr)]\cos(m\theta + \delta_m) e^{ikvt} \tag{4.21}$$

Here $J_m(x)$ and $N_m(x)$ are m^{th} Bessel functions of the first and second kind correspondingly, A_m, B_m and δ_m are independent constants. In order to keep the solution from diverging at $r = 0$, B_m must be zero. In order to satisfy the condition of normal velocity component being zero at the sides of the cylinder ($r = R$), the following condition needs to be satisfied:

$$\left.\frac{\partial \rho_{\mathrm{e}}}{\partial r}\right|_{r=R} = 0 \rightarrow \left.\frac{dJ_m(kr)}{dr}\right|_{r=R} = 0 \tag{4.22}$$

Here $R = R_{\mathrm{fer,in}}$, the inner radius of the ferrule. This equation is satisfied when $kR = \alpha_{mn}$, where α_{mn} is the n^{th} zero of the derivative of J_m, so:

$$\rho_{\mathrm{e}}^{(mn)}(r,\theta,t) = A_m J_m\left(\frac{\alpha_{mn} r}{R}\right)\cos(m\theta + \delta) e^{i\omega_{mn} t} \tag{4.23}$$

where the angular frequency is:

$$\omega_{mn} = k v_{\mathrm{He}} = \frac{v_{\mathrm{He}} \alpha_{mn}}{R} \tag{4.24}$$

The time independent part of the solution is:

$$\rho_e^{(m,n)}(r,\theta) = A_m J_m\left(\frac{\alpha_{mn} r}{R}\right)\cos(m\theta) \tag{4.25}$$

where the phase δ was dropped, because it is physically irrelevant. The radius of the cylinder R is the inner radius of the ferrule.

4.2 Optomechanical coupling

The optomechanical coupling arises because the optical mode's frequency changes with the local changes in refractive index. We can calculate the frequency change due to the change in refractive index using perturbation theory. The wave equation describing the optical field in helium, assuming spatial variation in c_{He}, the speed of light in helium, defined as $c_{\mathrm{He}} = c/n_{\mathrm{He}}$, is given by:

$$\nabla^2 E(\vec{r},t) = \frac{1}{c_{\mathrm{He}}^2(\vec{r})}\frac{\partial^2 E(\vec{r},t)}{\partial t^2} \tag{4.26}$$

Assuming the solution $E(\vec{r},t) = U(\vec{r})e^{i\omega t}$, we get the following equation:

$$\nabla^2 U(\vec{r}) + \frac{\omega^2 n_{\mathrm{He}}^2(\vec{r})}{c^2}\, U(\vec{r}) = 0 \tag{4.27}$$

We will now apply perturbation theory to this equation. First we will assume the following perturbations:

$$n_{\mathrm{He}}(\vec{r}) = \bar{n}_{\mathrm{He}} + \delta n_{\mathrm{He}}(\vec{r}) \tag{4.28}$$
$$U(\vec{r}) = \bar{U}(\vec{r}) + \delta U(\vec{r}) \tag{4.29}$$
$$\omega = \bar{\omega} + \delta\omega \tag{4.30}$$

The perturbation in the powers of perturbed quantities present in equation 4.27 are:

$$n_{\mathrm{He}}^2(\vec{r}) = \bar{n}_{\mathrm{He}}^2 + 2\bar{n}_{\mathrm{He}}\delta n_{\mathrm{He}}(\vec{r}) \tag{4.31}$$
$$\omega^2 = \bar{\omega}^2 + 2\bar{\omega}\delta\omega \tag{4.32}$$

Therefore equation 4.27 becomes:

$$\nabla^2(\bar{U}(\vec{r}) + \delta U(\vec{r})) + \frac{1}{c^2}(\bar{\omega}^2 + 2\bar{\omega}\delta\omega)(\bar{n}_{\mathrm{He}}^2 + 2\bar{n}_{\mathrm{He}}\delta n_{\mathrm{He}}(\vec{r}))(\bar{U}(\vec{r}) + \delta U(\vec{r})) = 0 \tag{4.33}$$

Using the fact that $\bar{U}$ solves the unperturbed wave equation and expanding and getting rid of non-linear terms, we convert equation 4.33 to:

$$\nabla^2\delta U(\vec{r}) + \frac{2\bar{\omega}\delta\omega\bar{n}_{\mathrm{He}}^2\bar{U}(\vec{r})}{c^2} + \frac{2\bar{\omega}^2\bar{n}_{\mathrm{He}}\delta n_{\mathrm{He}}(\vec{r})\bar{U}(\vec{r})}{c^2} + \frac{\bar{\omega}^2\bar{n}_{\mathrm{He}}^2\delta U(\vec{r})}{c^2} = 0 \tag{4.34}$$

We multiply equation 4.36 by $\bar{U}(\vec{r})$ and integrate over the cavity volume:

$$\int_V (\nabla^2\delta U(\vec{r}))\bar{U}(\vec{r})d^3\vec{r} + \int_V \frac{2\bar{\omega}\delta\omega\bar{n}_{\mathrm{He}}^2\bar{U}(\vec{r})^2}{c^2}d^3\vec{r} + \tag{4.35}$$
$$\int_V \frac{2\bar{\omega}^2\bar{n}_{\mathrm{He}}\delta n_{\mathrm{He}}(\vec{r})\bar{U}(\vec{r})^2}{c^2}d^3\vec{r} + \int_V \frac{\bar{\omega}^2\bar{n}_{\mathrm{He}}^2\delta U(\vec{r})\bar{U}(\vec{r})}{c^2}d^3\vec{r} = 0 \tag{4.36}$$

The first integral can be integrated by parts twice, and since the boundaries are such that either both $\bar{U}(\vec{r})$ and $\delta U(\vec{r})$ or both $\nabla\bar{U}(\vec{r})$ and $\nabla\delta U(\vec{r})$ go to zero at the boundaries, the integration gives:

$$\int_V (\nabla^2\delta U(\vec{r}))\bar{U}(\vec{r})d^3\vec{r} = \int_V \delta U(\vec{r})(\nabla^2\bar{U}(\vec{r}))d^3\vec{r} \tag{4.37}$$

This allows us to cancel the first and the last integral in equation 4.36 because $\bar{U}(\vec{r})$ solves the unperturbed wave equation. This leaves:

$$\delta\omega = -\bar{\omega}\frac{\int_V \delta n_{\mathrm{He}}(\vec{r})\bar{U}(\vec{r})^2 d^3\vec{r}}{\int_V \bar{n}_{\mathrm{He}}\bar{U}(\vec{r})^2 d^3\vec{r}} \tag{4.38}$$

We note that $U^2 = I$ (the light intensity); $\bar{\omega} = \omega_{\mathrm{cav}}$ (the unperturbed cavity resonance frequency). We would like to calculate the value of the single photon coupling g_0, which is the shift in cavity resonance frequency due to the zero-point

fluctuations of the oscillator. Therefore we assume $\delta\omega = g_0$, and δn_{He} is the zero-point fluctuation in helium refractive index. The minus sign gives the direction of the cavity frequency shift and can be dropped. Therefore equation 4.39 now becomes:

$$g_0 = \omega_{\mathrm{cav}} \frac{\int_V \delta n_{\mathrm{He}}(\vec{r}) I(\vec{r}) d^3\vec{r}}{\int_V \bar{n}_{\mathrm{He}} I(\vec{r}) d^3\vec{r}} \tag{4.39}$$

This equation gives g_0 in terms of changes in the refractive index corresponding to the acoustic mode; however, it is more convenient to describe it in terms of the dimensionless mode profile, which can be related to the change in density. Changes in the material density change the index of refraction locally as seen from the Clausius-Mossotti relation [106]:

$$\frac{n^2 - 1}{n^2 + 2} = \frac{\rho \alpha_{\mathrm{M}}}{3M\epsilon_0} \tag{4.40}$$

The refractive index of helium is $n_{\mathrm{He}} = 1.028$, so the left side of equation is approximately $2(n_{\mathrm{He}} - 1)/3$. Hence $\rho_{\mathrm{He}} \propto (n_{\mathrm{He}} - 1)$, and therefore:

$$\frac{\delta\rho_{\mathrm{He}}}{\rho_{\mathrm{He}}} = \frac{\delta n_{\mathrm{He}}}{n_{\mathrm{He}} - 1} \tag{4.41}$$

With this change, the optomechanical coupling is:

$$g_0 = \omega_{\mathrm{cav}}(n_{\mathrm{He}} - 1) \frac{\int_V I(\vec{r}) \frac{\delta\rho_{\mathrm{He}}(\vec{r})}{\rho_{\mathrm{He}}} d^3\vec{r}}{\int_V I(\vec{r}) n_{\mathrm{He}} d^3\vec{r}} \tag{4.42}$$

The relative change in density for a liquid is equivalent to the strain $\epsilon(\vec{r})$. Therefore we can express relative change in density as:

$$\frac{\delta\rho_{\mathrm{He}}(\vec{r})}{\rho_{\mathrm{He}}} \equiv \epsilon(\vec{r}) \equiv \epsilon_0 p_{\mathrm{n}}(\vec{r}) \tag{4.43}$$

where ϵ_0 is a constant that represents the amplitude of the strain field associated with the acoustic mode's zero point fluctuation, and $p_{\mathrm{n}}(\vec{r})$ is a normalized mode profile. This leads to the following expression for g_0:

$$g_0 = \omega_{\mathrm{cav}}(n_{\mathrm{He}} - 1)\epsilon_0 \frac{\int_V I(\vec{r}) p_{\mathrm{n}}(\vec{r}) d^3\vec{r}}{\int_V I(\vec{r}) n_{\mathrm{He}} d^3\vec{r}} \tag{4.44}$$

In equation 4.48 the values for all quantities except for ϵ_0 are known. To find the value of ϵ_0, we write the energy stored in the fluctuations of the mode in terms of the elastic potential energy:

$$E_0 = \int_V \frac{1}{2} K_{\mathrm{He}} \epsilon(\vec{r})^2 d^3\vec{r} = \frac{1}{2} v_{\mathrm{He}}^2 \rho_{\mathrm{He}} \epsilon_0^2 \int_V p_{\mathrm{n}}(\vec{r})^2 d^3\vec{r} \tag{4.45}$$

Here, $K_{\mathrm{He}} = v_{\mathrm{He}}^2 \rho_{\mathrm{He}}$ is the bulk modulus of Helium II.

We then equate E_0 to the mean potential energy stored in the zero point fluctuations, which is $1/2$ of total zero-point energy:

$$E_0 = \frac{\hbar\omega_{\mathrm{m}}}{4} \tag{4.46}$$

Combining equations 4.45 and 4.46, we solve for the normalization constant ϵ_0:

$$\epsilon_0 = \sqrt{\frac{\hbar\omega_{\mathrm{m}}}{2 v_{\mathrm{He}}^2 \rho_{\mathrm{He}} \int_V p_{\mathrm{n}}(\vec{r})^2 d^3\vec{r}}} \tag{4.47}$$

Using equation 4.47, the electrostrictive single-phonon coupling can be calculated from equation 4.48, given the optical and acoustic mode profiles.

4.2.1 Optomechanical coupling to paraxial acoustic mode

In this section I calculate the optomechanical coupling between a TEM_{00} mode of light and a TEM_{00} acoustic mode of helium. If the boundaries for the optical and acoustic modes are the same (optical mode has nodes at the mirror/helium interfaces, and acoustic mode has antinodes at the mirror/helium interfaces), then optical with longitudinal mode number q_{opt} will only couple to the mechanical mode with longitudinal mode number $q_{\mathrm{mech}} = 2q_{opt}$ (the overlap integral in the numerator of equation 4.48 is zero otherwise).

The optomechanical coupling depends on the cavity length and on the radius of the mirrors. In figure 4.3 I plot the coupling (g_0) multiplied by the longitudinal mode number (q_{opt}) vs. the ratio of mirror radius of curvature (ROC) to cavity length. I plot it for four different values of q_{opt}. The wavelength is assumed to be $\lambda = 1550$ nm in vacuum. The coupling for the symmetric cavity is maximized when $R_1 = R_2 \simeq 0.87L$, representing an optimal value balancing the mode volume and the mode overlap.

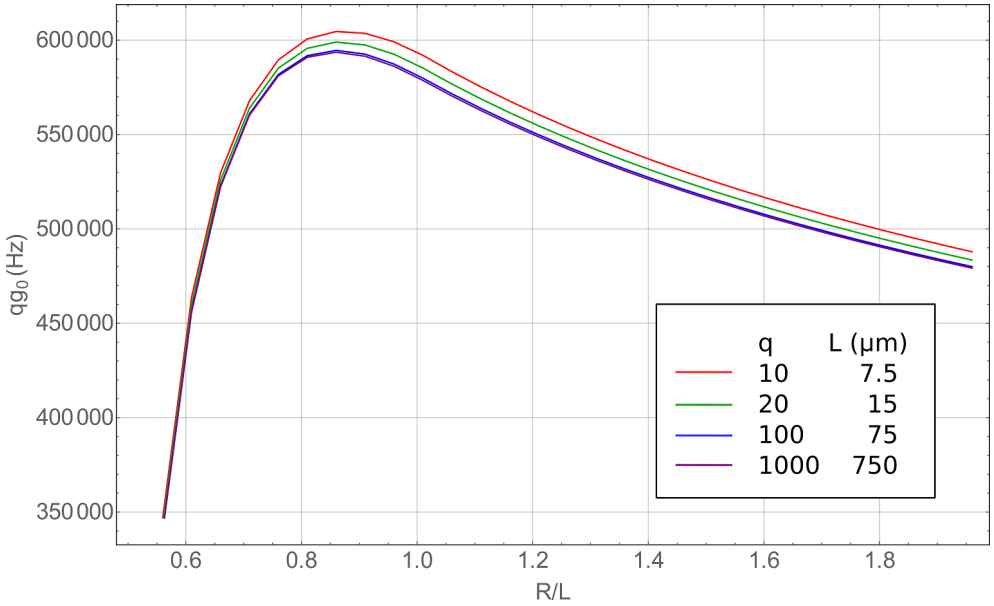

Figure 4.3: Coupling of the TEM_{00} light mode to TEM_{00} acoustic mode scaled by the longitudinal mode number for various cavity lengths and mirror ROCs.

From this plot it is also clear that g_0 is approximately inversely proportional to q_{opt} and therefore to cavity length L_{cav}, provided that ratio R/L_{cav} stays constant. This is understood in a simple manner. Consider, the equation describing g_0 in the case of an optical mode coupled to the acoustic mode in helium, where we drop all numerical constants. The fraction containing the two integrals will evaluate to a constant, independent of cavity length, for constant R/L_{cav}, therefore:

$$g_0 \propto \omega_{\mathrm{cav}} \sqrt{\frac{\omega_{\mathrm{m}}}{\int_V p_{\mathrm{n}}(\vec{r})^2 d^3\vec{r}}} \tag{4.48}$$

Note that ω_{cav} and ω_{m} only depend on laser wavelength and can be kept roughly constant as the cavity length is changed. The integral of the acoustic mode profile over the cavity volume is proportional to the volume of the mode $V_{\mathrm{mode}} \approx L_{\mathrm{cav}} w_0^2 \approx L_{\mathrm{cav}}^2$. Therefore $g_0 \propto 1/L_{\mathrm{cav}}$.

For comparison, in a canonical optomechanical system or in the membrane in the middle system, the optomechanical coupling is given by the following expression, as shown in section 2.6

$$g_0 = \frac{d\omega_{\mathrm{cav}}}{dx} x_{\mathrm{ZPF}} = \frac{d\omega_{\mathrm{cav}}}{dx} \sqrt{\frac{\hbar}{2m_{\mathrm{m}}\omega_{\mathrm{m}}}} \tag{4.49}$$

Here x is the displacement of the mirror. As the cavity length changes, the x_{ZPF} stays the same, while $d\omega_{\mathrm{cav}}/dx \propto 1/L_{\mathrm{cav}}$. This leads to the same dependence: $g_0 \propto 1/L_{\mathrm{cav}}$, however for a different reason.

In figure 4.4, I plot g_0 vs. cavity length assuming the parameters for the mirrors that we used in building our two devices. For the first device (red): $R_1 = 409$ μm, $R_2 = 282$ μm; for the second device (blue): $R_1 = 497$ μm, $R_2 = 325$ μm. The dots mark the actual cavity length in each device. In the first device the mirror separation $L_{\rm mech} \simeq 84$ μm; in the second device $L_{\rm mech} \simeq 68$ μm. The expected coupling rates are $g_0/2\pi \approx 3.6$ kHz and $g_0/2\pi \approx 4.1$ kHz.

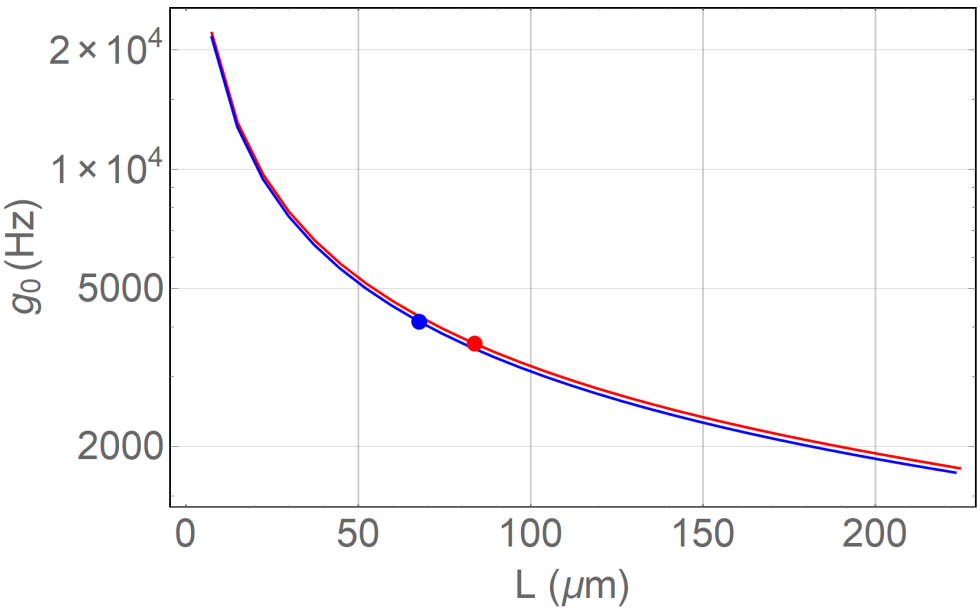

Figure 4.4: Theoretically predicted optomechanical coupling to paraxial acoustic mode in our devices. Red: optomechanical coupling in a cavity made of mirrors that compose the second device. Blue: optomechanical coupling in a cavity made of mirrors that compose the second device. Dots: optomechanical coupling in the first and second devices.

4.2.1.1 Different boundary conditions for the optical and acoustic modes

The mirrors that we used are silica fibers with the Distributed Bragg Reflectors (DBR) consisting of alternating quarter-wavelength layers of silica and tantala deposited on top. When the optical and acoustic modes are bounded by the DBR, the optical mode is weakly confined by the mirror/helium interface (small index of refraction mismatch) and leaks into the stack. The acoustic mode, on the other hand is strongly confined by the mirror/helium interface (large acoustic impedance mismatch). This leads to slightly different boundary conditions for the modes, as schematically shown in figure 4.5.

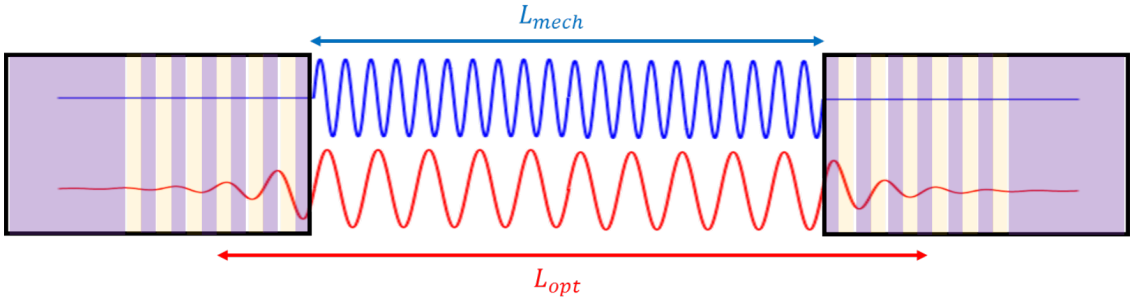

Figure 4.5: Schematic representation of an optical and acoustic mode. The optical mode penetrates into the mirror stack, while the acoustic mode is better confined within the helium. That leads to difference in effective lengths. Additionally, the optical mode will not necessarily have a node at the mirror/helium boundary but will rather have some phase ϕ, which can in principle be determined from the parameters of the mirror stack.

If the electric field has a non-zero phase at the boundary, the expression for it is modified:

$$E^{(q,0,0)}(\vec{r}) = E_0 \frac{w_0}{w(z)} e^{-\frac{r^2}{w(z)^2}} \sin\left(k_{\text{mod}}^{(q,0,0)} z + \frac{k_{\text{mod}}^{(q,0,0)} r^2}{2R(z)} - \phi_{\text{G}}^{(0,0)}(z) + \theta_{\text{mod}}^{(q,0,0)} + \phi\right) \tag{4.50}$$

where:

$$k_{\text{mod}}^{(q,0,0)} = \frac{\pi q_{\text{opt}}}{L_{\text{opt}}} - \frac{\arctan(z_1/z_R)}{L_{\text{opt}}} + \frac{\arctan(z_2/z_R)}{L_{\text{opt}}} - \frac{\phi}{L_{\text{opt}}} \tag{4.51}$$

where z_1, z_2, and z_R are defined in section B.2. The definition for θ is the same as in section B.2, but in terms of $k_{\text{mod}}^{(q,0,0)}$.

We can calculate the optomechanical coupling of the optical mode with longitudinal mode number q_{opt} to the acoustic modes with longitudinal mode number $2q_{\text{opt}}$, $2q_{\text{opt}}+1$ and $2q_{\text{opt}}-1$: $g_0(q_{\text{opt}}, 2q_{\text{opt}}, \phi)$, $g_0(q_{\text{opt}}, 2q_{\text{opt}}-1, \phi)$ and $g_0(q_{\text{opt}}, 2q_{\text{opt}}+1, \phi)$. The maximum optomechanical coupling is $g_{0,\text{max}} = g_0(q_{\text{opt}}, 2q_{\text{opt}}, 0)$. The ratios $g_0(q_{\text{opt}}, 2q_{\text{opt}}, \phi)/g_{0,\text{max}}$, $g_0(q_{\text{opt}}, 2q_{\text{opt}}+1, \phi)/g_{0,\text{max}}$ and $g_0(q_{\text{opt}}, 2q_{\text{opt}}-1, \phi)/g_{0,\text{max}}$ are shown in figure 4.6 with a blue line, dashed orange line and dashed green line correspondingly.

From the figure we see that the coupling calculated at $\phi = 0$ gives an upper bound on the optomechanical coupling $g_{0,\text{max}}$. In order to calculate the lower bound we consider the fact that we never observe coupling to the modes with the longitudinal mode number $\neq 2q_{\text{opt}}$. We can be sure (as I will show in section 8.2) that if the optomechanical coupling to the mode with longitudinal number $2q_{\text{opt}} \pm 1$ was at least 30 % of the optomechanical coupling to the mode with longitudinal mode number $2q_{\text{opt}}$, it would be observable. The black vertical lines in figure 4.6, show the value of ϕ at which the optomechanical coupling to the mode with longitudinal number $2q_{\text{opt}} \pm 1$ is 30 % of the longitudinal coupling to the mode $2q_{\text{opt}}$. That allows us to put a lower bound on the optomechanical coupling as $g_0 \geq 0.9 g_{0,\text{max}}$, where $g_{0,\text{max}}$ is the value of optomechanical coupling caclaulted for $\phi = 0$. Note that this analysis only works for $L_{\text{cav}} \gg \lambda$.

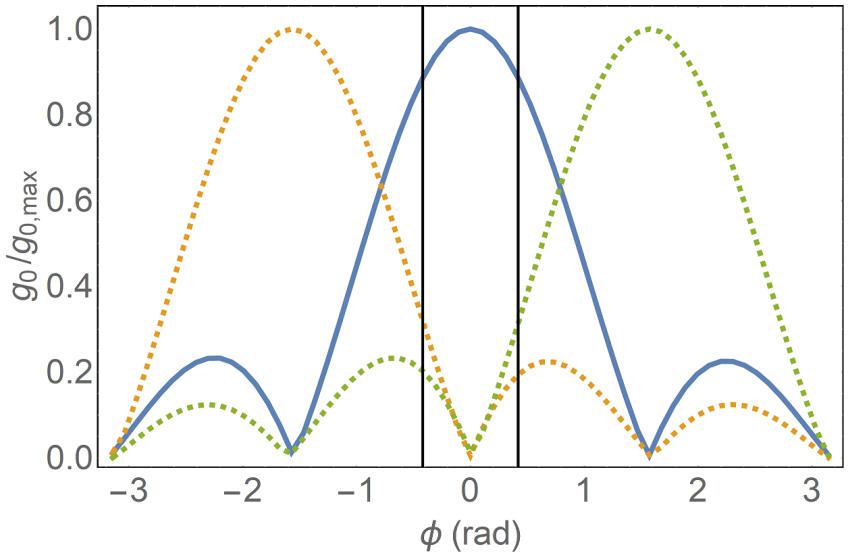

Figure 4.6: Coupling to the acoustic modes with $q_{\text{mech}} \neq 2q_{\text{opt}}$. The ratio $g_0(q_{\text{opt}}, 2q_{\text{opt}}, \phi)/g_0(q_{\text{opt}}, 2q_{\text{opt}}, 0)$ (solid blue line), $g_0(q_{\text{opt}}, 2q_{\text{opt}}+1, \phi)/g_0(q_{\text{opt}}, 2q_{\text{opt}}, 0)$ (dashed orange line) and $g_0(q_{\text{opt}}, 2q_{\text{opt}}-1, \phi)/g_0(q_{\text{opt}}, 2q_{\text{opt}}, 0)$ (dashed green line) plotted vs. the phase of the electric field at the mirror/helium boudary (ϕ)

Therefore in the first generation device the expected optomechanical coupling is 3.2 kHz$< g_0/2\pi <$ 3.6 kHz and in the second generation device 3.7 kHz$< g_0/2\pi <$ 4.1 kHz

4.2.2 Optomechanical coupling to radial acoustic mode

The coupling to a radial mode can be calculated in the similar manner. As seen from figure 4.2, the width of the mode is approximately constant throughout the cavity. In fact, for $R_1 = R_2 > 3L$, the maximum mode width is at most only

$1.2w_0$. This allows us to write a simpler expression for the optical intensity:

$$I(r,z) \propto \sin(kz)^2 e^{-\frac{2r^2}{w_0^2}} \tag{4.52}$$

While the paraxial modes are automatically aligned to each other (since they are both bounded by the fiber indentations), the radial acoustic mode is not necessarily aligned to the TEM_{00} optical mode, since the indentations on the fiber faces are not always centered on the fibers, and the fibers are possibly not centered in the ferrule. The optical mode (confined by the indentations) can be slightly offset from the center of the radial acoustic mode (confined by the inner walls of the ferrule). Assuming the existence of such an offset x_0, the optical intensity profile can be modeled in the following manner:

$$I(x,y,z) \propto \sin(kz)^2 e^{-\frac{2((x-x_0)^2+y^2)}{w_0^2}} \tag{4.53}$$

Using this expression for intensity and equation 4.25 for the acoustic mode profile we can calculate the coupling for the radial modes. We also use equation 4.24 to calculate the frequencies of the modes. We take $R_{\text{fer,in}} = 67\mu\text{m}$ (the inner radius of the ferrule used in the first generation device). The coupling to both $m = 0$ and $m = 1$ modes is shown in figure 4.7. It is clear that misalignment between the optical and acoustic modes leads to coupling to $m = 1$ mode, which would be zero in case of perfectly aligned modes. As we will see in section 7.8.4, the optomechanical coupling to these

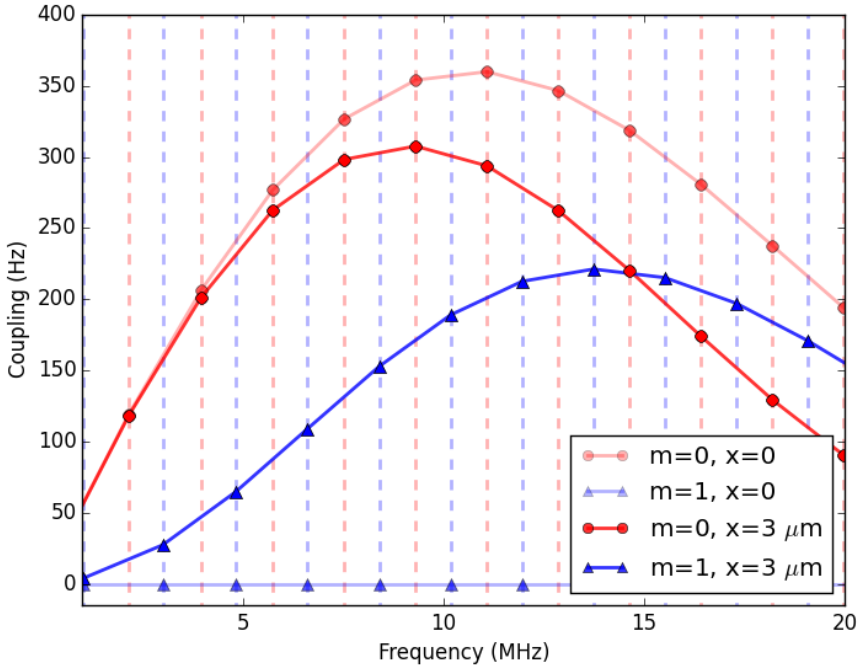

Figure 4.7: Coupling to acoustic radial modes with radial mode number $m = 0, 1$ and the offset between optical and acoustic modes $x_0 = 0, 3$ μm. The presence of the offset results in coupling to modes with $m = 1$.

modes is predominantly photothermal, which makes using them to study quantum effects challenging. Additionally, the mechanical quality factor of these modes is rather low, so for now we will focus on the paraxial modes only.

4.3 Optomechanical cooperativity

As explained in section 2.7.7, the optomechanical cooperativity C is an important figure of merit in optomechanics. While C is of interest, it is partially determined by the maximum number of photons that can be stored within the cavity.

Since this number is typically limited by thermal constraints or optical nonlinearities, it is also useful to quantify device performance by defining the power-independent quantity C_0 (single photon cooperativity) as:

$$C_0 = \frac{g_0^2}{\kappa\gamma} \tag{4.54}$$

We have shown previously, that $g_0 \propto 1/L_{\rm cav}$. The optical and mechanical linewidths are given by:

$$\kappa = \frac{c_{\rm He}}{2L_{\rm cav}} \frac{1-\sqrt{R_{\rm opt,1}R_{\rm opt,1}}}{\pi\sqrt{R_{\rm opt,2}R_{\rm opt,2}}} \approx \frac{c_{\rm He}}{2L_{\rm cav}} \frac{T_{\rm opt,1}+T_{\rm opt,2}}{2} \propto 1/L_{\rm cav} \tag{4.55}$$

$$\gamma = \frac{v_{\rm He}}{2L_{\rm cav}} \frac{1-\sqrt{R_{\rm ac,1}R_{\rm ac,2}}}{\pi\sqrt{R_{\rm ac,1}R_{\rm ac,2}}} \approx \frac{v_{\rm He}}{2L_{\rm cav}} \frac{T_{\rm ac,1}+T_{\rm ac,2}}{2} \propto 1/L_{\rm cav} \tag{4.56}$$

Here $R_{\rm (opt,ac),(1,2)}$ is the power (optical, acoustic) reflectivity of the (1st, 2nd) mirror. Since all quantities scale inversely with $L_{\rm cav}$, the single photon cooperativity is independent of length, provided $R/L_{\rm cav}$ is constant. The value of single photon cooperativity in the best case scenario ($R = 0.87L_{\rm cav}$) for the mirrors used in the experiments ($T_{\rm opt,1} \approx 100$ ppm, $T_{\rm opt,1} \approx 10$ ppm, $T_{\rm ac,1} \approx T_{\rm ac,2} \approx 10,000$ ppm) is $C_0 = 8.2 \times 10^{-4}$. The single photon cooperativity can be improved by using mirrors with higher optical and acoustic reflectivity.

Multiphoton cooperativity $C = n_{\rm circ}C_0$, and thermal cooperativity $C_{\rm th} = C/n_{\rm th}$ both depend on the power handling of the device. I will calculate the expected multiphoton and thermal cooperativities for the case of the two devices presented in this thesis in sections describing these devices.

4.4 Using materials other than superfluid helium

The optomechanical coupling described here is not particular to superfluid helium, or even to liquids in general. Consider a cavity filled with a solid material (for example glass). Since the acoustic wavelength is defined only by the optical wavelength and the acoustic mode shape is defined by the cavity parameters and the wavelength, the acoustic mode shape in any isotropic homogeneous material will be similar to the optical mode shape (barring some difference due to the presence of transverse waves in most solids). The single-photon coupling is proportional to a simple quantity:

$$g_0 \propto \frac{(n_{\rm mat}^2+2)(n_{\rm mat}^2-1)}{n_{\rm mat}\sqrt{n_{\rm mat}v_{\rm mat}\rho_{\rm mat}}} \equiv g_{\rm mat} \tag{4.57}$$

Here we did not assume that $n_{\rm mat}$ is close to 1, because for some of the materials that we consider, it isn't. In table 4.1 I show the value of $g_{\rm mat}$.

Material	n	v**(m/s)**	ρ **(kg/m^3)**	$g_{\rm mat}$ **(s$^{1/2}$m/kg$^{1/2}$)**
He II	1.028[90]	238[90]	145[90]	9×10^{-4}
Water	1.33	1500	1000	15×10^{-4}
SiO_2	1.444[116]	5,900 [117]	2,200[117]	7×10^{-4}
MgF_2	1.29 [118]	7,100 [119]	3,180[120]	3.5×10^{-4}
Diamond	2.388[121]	19,000[122]	3,520[122]	12×10^{-4}
TeO_2	2.33[123]	4,052[123]	6,040[123]	18×10^{-4}

Table 4.1: Material properties of various materials as well as their optomechanical properties.

The optomechanical coupling is expected to be approximately the same for all materials that we considered. For high optomechanical cooperativity small mechanical and optical linewidths are desirable as well. Some of the materials, like silicon dioxide and magnesium fluoride are used in optics, due to their low optical absorption, and therefore large

optical quality factors $Q_{\rm opt}$. Some materials, like tellurium dioxide and silicon dioxide (quartz) were shown to have large mechanical quality factors $Q_{\rm m}$ [123].

In conclusion, with careful selection other materials can be used in place of helium, as long as their optical and acoustic attenuations are low.

4.5 Other work on superfluid helium optomechanics

In this section I will describe other work on superfluid helium optomechanics.

Superfluid helium was explored as a mechanical resonator by Keith Schwab's group in 2014 [31]. The authors coupled the acoustic motion of superfluid helium to the $\rm TE_{011}$ mode of a cylindrical superconducting microwave resonator. The authors reached remarkable mechanical quality factors ($Q_{\rm m} = 1.4 \times 10^7$), limited by the three phonon process. The modes that they explored had frequencies between 6 and 12 kHz. The single photon optomechanical coupling was quite low at $g_0/2\pi = 4.2 \times 10^{-8}$ Hz for the 8 kHz mode. This precluded observation of the thermal motion of the acoustic mode, or the microwave field's influence on the acoustic modes.

The authors modified their system and in 2016 published a paper in which they improved the quality factors by an order of magnitude to $Q_{\rm m} = 1.4 \times 10^8$ limited by dissipation due to ^{3}He impurities. The improvements were achieved by adding sintered silver heat exchangers to the helium fill line to better thermalize the helium to the temperature of the dilution refrigerator and by improving the cooling power of the dilution refrigerator [32].

The authors state that reaching quality factors $Q_{\rm m} > 10^{10}$ should be possible in their system by improving thermalization even further, reducing clamping losses, and using helium with lower ^{3}He content. The optomechanical coupling would still be small; however, the authors suggest some interesting applications for their system, such as high frequency gravitational wave detection [39]. The single photon cooperativity is $C_0 \approx 3.3 \times 10^{-13}$. The maximum multiphoton cooperativity achieved in the device seems to be $C \approx 1 \times 10^{-4}$ and the maximum thermal cooperativity is $C_{\rm th} \approx 1 \times 10^{-9}$.

Another superfluid optomechanical system was built in Warwick Bowen's group in 2016 [34]. In this system, the authors coupled the motion of a thin film of superfluid helium to the optical whispering gallery mode (WGM) of a silica microtoroid. The modes' frequencies varied between 10 kHz and 5 MHz. The authors demostrated the mechanical quality factor $Q_{\rm m} = 5,000$. The optomechanical interaction was used to monitor the thermal motion of the superfluid, and to heat and to cool the 500 kHz modes. They achieved multiphoton cooperativity (assuming photothermal coupling in place of g_0 of $C \approx 10^{-1}$, the thermal cooperativity was $C_{\rm th} \approx 10^{-5}$ [124]. However the interaction was predominantly photothermal and hence non-unitary in origin. Using non-unitary interactions is challenging for studying quantum optomechanical effects [3]. Curiously the third sound modes of a superfluid thin film covering WGM resonator were first observed in 2010 in the group of Tobias Kippenberg. In their publication describing the modes [125], the authors suggested that those modes could be used for the study of quantum fluid physics, however, to the best of my knowledge they did not continue with that direction of work.

Another superfluid helium system was built in John Davis' group [35]. While not strictly an optomechanical system (there is no optical or microwave cavity), it was built to demonstrate superfluid's utility as a mechanical oscillator. The helium in this experiment was confined inside a parallel plate capacitor, which was used to study the dielectric properties of the fluid via capacitance measurements. The device was similar to one used by the same group previously [126] to study the first sound velocity in a confined geometry. The authors measured the 4 kHz Helmholtz mode and obtained quality factors $Q_{\rm m} \approx 200$ at 1.6 K. After cooling the device to 16 mK, the observed quality factor improved to $Q_{\rm m} \approx 9 \times 10^5$ for the 3 kHz Helmholtz mode, limited by the internal dissipation of the substrate materials [40]. The authors state that quality factor for 10^8 could be reached through the choice of substrate material and improving the design of the resonator.

In comparison with the work the Schwab's and Davis' groups, our device reached relatively low quality factor $Q_{\rm m} = 100,000$. However, due to relatively large values of electrostrictive optomechanical coupling and low photothermal coupling our device was the first to demonstrate optomechanical effects arising from a unitary interaction, and the first to demonstrate quantum optomechanical effects.

4.6 Summary

In this chapter we discussed optomechanics with superfluid helium. We derived the expression for the optomechanical coupling of the paraxial optical mode to the paraxial and radial acoustic modes. We showed that optomechanical cooperativity when the paraxial mode is addressed is roughly independent of cavity length. Finally we discussed the use of materials other than helium, and the work of other groups on superfluid helium optomechanics.

Chapter 5

Measurements theory

In this chapter the optomechanical theory is derived rigorously, focusing on the effects important in our system.

5.1 Optomechanical back-action

In this section I derive optomechanical back action (also known as optical spring/optical damping). This is an effect of the mechanical resonator changing its linewidth and frequency in response to a presence of a driving laser. The magnitude and sign of the change depends on the strength of a driving laser and its detuning from the cavity resonance. We start with equations of motion, which we derived in section 2.6:

$$\dot{\hat{a}} = -i(\omega_{\rm cav}\hat{a} + g_0(\hat{b}+\hat{b}^\dagger)\hat{a}) - \frac{\kappa}{2}\hat{a} + \sqrt{\kappa_{\rm ext}}\hat{a}_{\rm i} + \sqrt{\kappa_{\rm int}}\hat{\xi}_{\rm int} \tag{5.1}$$

and:

$$\dot{\hat{b}} = -i(\omega_{\rm m}\hat{b} + g_0\hat{a}^\dagger\hat{a}) - \frac{\gamma}{2}\hat{b} + \sqrt{\gamma}\hat{\eta} \tag{5.2}$$

In the frame rotating at $\omega_{\rm cav}$,

$$\hat{a} = \hat{a}'e^{-i\omega_{\rm cav}t} \tag{5.3}$$

$$\dot{\hat{a}} = \dot{\hat{a}}'e^{-i\omega_{\rm cav}t} + \hat{a}'e^{-i\omega_{\rm cav}t}(-i\omega_{\rm cav}) \tag{5.4}$$

Redefining $\hat{a}$, $\hat{a}_{\rm i}$, $\hat{\xi}_{\rm int}$ to be rotating at $\omega_{\rm cav}$, and writing the laser drive as $\hat{a}_{\rm i} = \hat{a}_{\rm i}e^{-i\Delta t}$, where $\Delta = \omega_{\rm L} - \omega_{\rm cav}$ is the detuning of the driving beam from the cavity

$$\dot{\hat{a}} = -ig_0(\hat{b}+\hat{b}^\dagger)\hat{a} - \frac{\kappa}{2}\hat{a} + \sqrt{\kappa_{\rm ext}}\hat{a}_{\rm i}e^{-i\Delta t} + \sqrt{\kappa_{\rm int}}\hat{\xi}_{\rm int} \tag{5.5}$$

The solution for the steady state intracavity amplitude is $\hat{a}(t) = \bar{a}e^{-i\Delta t}$, where:

$$\bar{a} = \frac{\sqrt{\kappa_{\rm ext}}\bar{a}_{\rm i}}{-i\bar{\Delta} + \frac{\kappa}{2}} \tag{5.6}$$

The zeroth order solution for the mechanical mode is:

$$\bar{b} = \frac{-ig_0|\bar{a}|^2}{i\omega_{\rm m} + \frac{\gamma}{2}} \tag{5.7}$$

where an effective detuning is defined: $\bar{\Delta} = \Delta - g_0(\bar{b}+\bar{b}^*)$.

Now we linearize equations around the mean optical amplitude $\bar{a}e^{-i\Delta t}$, mean acoustic amplitude $\bar{b}$ and average laser drive $\bar{a}_i$, by assuming $\hat{a}(t) = \bar{a}e^{-i\Delta t} + \delta\hat{a}(t)$, $\hat{b}(t) = \bar{b} + \delta\hat{b}(t)$ and $\hat{a}_{\mathrm{i}} = \bar{a}_{\mathrm{i}}e^{-i\Delta t} + \hat{\xi}_{\mathrm{ext}}(t)$. Plugging those assumptions into equations 5.5 and 5.2 and making use of equations 5.6 and 5.7 we have:

$$\delta\dot{\hat{a}}(t) = -ig_0(\delta\hat{b}(t) + \delta\hat{b}^\dagger(t))\bar{a}e^{-i\Delta t} - \frac{\kappa}{2}\delta\hat{a}(t) + \sqrt{\kappa_{\mathrm{ext}}}\hat{\xi}_{\mathrm{ext}}(t) + \sqrt{\kappa_{\mathrm{int}}}\hat{\xi}_{\mathrm{int}}(t) \tag{5.8}$$

$$\delta\dot{\hat{b}}(t) = -i\omega_{\mathrm{m}}\delta\hat{b}(t) - ig_0(\bar{a}^*e^{i\Delta t}\delta\hat{a}(t) + \bar{a}e^{-i\Delta t}\delta\hat{a}^\dagger(t)) - \frac{\gamma}{2}\delta\hat{b}(t) + \sqrt{\gamma}\hat{\eta}(t) \tag{5.9}$$

The Fourier transform of equation 5.8 is

$$-i\omega\delta\hat{a}[\omega] = -ig_0(\delta\hat{b}[\omega-\Delta] + \delta\hat{b}^\dagger[\omega-\Delta])\bar{a} - \frac{\kappa}{2}\delta\hat{a}[\omega] + \sqrt{\kappa_{\mathrm{ext}}}\hat{\xi}_{\mathrm{ext}}[\omega] + \sqrt{\kappa_{\mathrm{int}}}\hat{\xi}_{\mathrm{int}}[\omega] \tag{5.10}$$

By defining the cavity susceptibility

$$\chi_{aa}[\omega] = \frac{1}{-i\omega + \frac{\kappa}{2}} \tag{5.11}$$

and multiphoton coupling

$$g = g_0\bar{a} \tag{5.12}$$

we can rewrite equation 5.10 and its complex conjugate as

$$\delta\hat{a}[\omega] = \chi_{aa}[\omega]\left(-ig(\delta\hat{b}[\omega-\Delta] + \delta\hat{b}^\dagger[\omega-\Delta]) + \sqrt{\kappa_{\mathrm{ext}}}\hat{\xi}_{\mathrm{ext}}[\omega] + \sqrt{\kappa_{\mathrm{int}}}\hat{\xi}_{\mathrm{int}}[\omega]\right) \tag{5.13}$$

$$\delta\hat{a}^\dagger[\omega] = \chi^*_{\mathrm{cav}}[-\omega]\left(ig^*(\delta\hat{b}[\omega+\Delta] + \delta\hat{b}^\dagger[\omega+\Delta]) + \sqrt{\kappa_{\mathrm{ext}}}\hat{\xi}^\dagger_{\mathrm{ext}}[\omega] + \sqrt{\kappa_{\mathrm{int}}}\hat{\xi}^\dagger_{\mathrm{int}}[\omega]\right) \tag{5.14}$$

Here the complex conjugate of $\chi_{aa}[\omega]$ is $\chi^*_{\mathrm{cav}}[-\omega]$, because we applied complex conjugation to equation 5.8 before performing the Fourier transform. Additionally, in this case $\chi^*_{\mathrm{cav}}[-\omega] = \chi_{aa}[\omega]$. We can introduce a combined vacuum noise operator:

$$\hat{\xi} = \frac{\sqrt{\kappa_{ext}}\hat{\xi}_{\mathrm{ext}} + \sqrt{\kappa_{int}}\hat{\xi}_{\mathrm{int}}}{\sqrt{\kappa}} \tag{5.15}$$

This allows us to rewrite equations as:

$$\delta\hat{a}[\omega] = \chi_{aa}[\omega]\left(-ig(\delta\hat{b}[\omega-\Delta] + \delta\hat{b}^\dagger[\omega-\Delta]) + \sqrt{\kappa}\hat{\xi}[\omega]\right) \tag{5.16}$$

$$\delta\hat{a}^\dagger[\omega] = \chi^*_{\mathrm{cav}}[-\omega]\left(ig^*(\delta\hat{b}[\omega+\Delta] + \delta\hat{b}^\dagger[\omega+\Delta]) + \sqrt{\kappa}\hat{\xi}^\dagger[\omega]+\right) \tag{5.17}$$

We take the Fourier transform of equation 5.9

$$-i\omega\delta\hat{b}[\omega] = -i\omega_{\mathrm{m}}\delta\hat{b}[\omega] - i(g^*\delta\hat{a}[\omega+\Delta] + g\delta\hat{a}^\dagger[\omega-\Delta]) - \frac{\gamma}{2}\delta\hat{b}[\omega] + \sqrt{\gamma}\hat{\eta}[\omega] \tag{5.18}$$

combining terms with $\delta\hat{b}[\omega]$:

$$\left(-i(\omega-\omega_{\mathrm{m}}) + \frac{\gamma}{2}\right)\delta\hat{b}[\omega] = -i(g^*\delta\hat{a}[\omega+\Delta] + g\delta\hat{a}^\dagger[\omega-\Delta]) + \sqrt{\gamma}\hat{\eta}[\omega] \tag{5.19}$$

Equation for $g^*\delta\hat{a}[\omega+\Delta]$ is:

$$g^*\delta\hat{a}[\omega+\Delta] = \chi_{aa}[\omega+\Delta]\left(-i\left|g\right|^2(\delta\hat{b}[\omega] + \delta\hat{b}^\dagger[\omega]) + \sqrt{\kappa}\hat{\xi}[\omega+\Delta]g^*\right) \tag{5.20}$$

Similarly:

$$g\delta\hat{a}^\dagger[\omega-\Delta] = \chi_{aa}[\omega-\Delta]\left(i\left|g\right|^2(\delta\hat{b}[\omega] + \delta\hat{b}^\dagger[\omega]) + \sqrt{\kappa}\hat{\xi}^\dagger[\omega-\Delta]g\right) \tag{5.21}$$

Combining those equations:

$$\begin{aligned} g^*\delta\hat{a}[\omega+\Delta] + g\delta\hat{a}^\dagger[\omega-\Delta] = i\left|g\right|^2(\delta\hat{b}[\omega]+\delta\hat{b}^\dagger[\omega])(\chi_{aa}[\omega-\Delta]-\chi_{aa}[\omega+\Delta])+ \\ \sqrt{\kappa}(\chi_{aa}[\omega-\Delta]\hat{\xi}^\dagger[\omega-\Delta]g+\chi_{aa}[\omega+\Delta]\hat{\xi}[\omega+\Delta]g^*) \end{aligned} \tag{5.22}$$

Since $\gamma \ll \omega_{\mathrm{m}}$, we can neglect the counter-rotating term $\delta\hat{b}^\dagger[\omega]$, which is peaked around $-\omega_{\mathrm{m}}$. We can define the self energy of the optomechanical system:

$$\Sigma[\omega] = i\left|g\right|^2(\chi_{aa}[\omega-\Delta]-\chi_{aa}[\omega+\Delta]) \tag{5.23}$$

And the radiation pressure force:

$$\hat{F}_{\mathrm{RPSN}}[\omega] = \sqrt{\kappa}(\chi_{aa}[\omega-\Delta]\xi^\dagger[\omega-\Delta]g+\chi_{aa}[\omega+\Delta]\xi[\omega+\Delta]g^*) \tag{5.24}$$

In addition we can define the vacuum fluctuation of the intracavity field as:

$$\delta\hat{a}_\xi[\omega] = \chi_{aa}[\omega]\sqrt{\kappa}\hat{\xi}[\omega] \tag{5.25}$$

Which simplifies the expression for radiation pressure force even further:

$$\hat{F}_{\mathrm{RPSN}}[\omega] = \delta\hat{a}_\xi^\dagger[\omega-\Delta]g+\delta\hat{a}_\xi[\omega+\Delta]g^* \tag{5.26}$$

Using those definitions we can rewrite equation 5.19 as:

$$\left(-i(\omega-\omega_{\mathrm{m}})+\frac{\gamma}{2}\right)\delta\hat{b}[\omega] = -i(\Sigma[\omega]\delta\hat{b}[\omega]+\hat{F}_{\mathrm{RPSN}}[\omega])+\sqrt{\gamma}\hat{\eta}[\omega] \tag{5.27}$$

Solving for $\delta\hat{b}[\omega]$:

$$\delta\hat{b}[\omega] = \frac{-i\hat{F}_{\mathrm{RPSN}}[\omega]+\sqrt{\gamma}\hat{\eta}[\omega]}{-i(\omega-\omega_{\mathrm{m}})+\frac{\gamma}{2}+i\Sigma[\omega]} = \chi_{bb,\mathrm{eff}}[\omega](-i\hat{F}_{\mathrm{RPSN}}[\omega]+\sqrt{\gamma}\hat{\eta}[\omega]) \tag{5.28}$$

and its complex conjugate:

$$\delta\hat{b}^\dagger[\omega] = \chi^*_{bb,\mathrm{eff}}[-\omega](i\hat{F}_{\mathrm{RPSN}}[\omega]+\sqrt{\gamma}\hat{\eta}^\dagger[\omega]) \tag{5.29}$$

Here the effective mechanical susceptibility is given as:

$$\chi_{bb,\mathrm{eff}}[\omega] = \frac{1}{-i(\omega-\omega_{\mathrm{m}})+\frac{\gamma}{2}+i\Sigma[\omega]} \tag{5.30}$$

From this equation we see that the mechanical resonator is being driven by radiation pressure shot noise and the thermal noise. We can also see that the frequency and linewidth of the resonator are shifted by an amount proportional to intracavity power and dependent on cavity susceptibility.

In this notation the optical spring $\Delta\omega_{\mathrm{m,opt}}$ and optical damping γ_{opt} are correspondingly

$$\Delta\omega_{\mathrm{m,opt}} = \mathrm{Re}[\Sigma[\omega]] \tag{5.31}$$

$$\gamma_{\mathrm{opt}} = -2\mathrm{Im}[\Sigma[\omega]] \tag{5.32}$$

5.2 Optomechanical back-action when two control beams are used

It is easy to extend the treatment of the previous section to the case of two control beams. We assume that there are two control beams: one upper, detuned from the cavity by Δ_u and one lower, detuned from the cavity by Δ_l. That would mean that the drive is now written as

$$\hat{a}_{\rm i} = \hat{a}_{\rm i,l} e^{-i\Delta_l t} + \hat{a}_{\rm i,u} e^{-i\Delta_u t} \tag{5.33}$$

The solution for the steady state intracavity amplitude is

$$\hat{a}(t) = \bar{a}_l e^{-i\Delta_l t} + \bar{a}_u e^{-i\Delta_u t} \tag{5.34}$$

where:

$$\bar{a}_l = \frac{\sqrt{\kappa_{\rm ext}}\bar{a}_{\rm i,l}}{-i\bar{\Delta}_l + \frac{\kappa}{2}} \tag{5.35}$$

$$\bar{a}_u = \frac{\sqrt{\kappa_{\rm ext}}\bar{a}_{\rm i,u}}{-i\bar{\Delta}_u + \frac{\kappa}{2}} \tag{5.36}$$

Where $\bar{\Delta}$ is the effective detuning, defined in section 5.1. Following the same treatment as in section 5.1, it is easy to show that in case of two control beams:

$$\delta\hat{a}[\omega] \quad = \quad \chi_{aa}[\omega]\left(-ig_0\left(\bar{a}_l(\delta\hat{b}[\omega-\Delta_l] + \delta\hat{b}^\dagger[\omega-\Delta_l]) + \bar{a}_u(\delta\hat{b}[\omega-\Delta_u] + \delta\hat{b}^\dagger[\omega-\Delta_u])\right) + \sqrt{\kappa}\hat{\xi}[\omega]\right) \tag{5.37}$$

$$\delta\hat{b}[\omega] = \chi_{bb,\rm eff}[\omega](-i\hat{F}_{\rm RPSN}[\omega] + \sqrt{\gamma}\hat{\eta}[\omega]) \tag{5.38}$$

Where:

$$\Sigma[\omega] = ig_0^2\left(|\bar{a}_l|^2(\chi_{aa}[\omega-\Delta_l] - \chi_{aa}[\omega+\Delta_l]) + |\bar{a}_u|^2(\chi_{aa}[\omega-\Delta_u] - \chi_{aa}[\omega+\Delta_u])\right) \tag{5.39}$$

And the radiation pressure force:

$$\hat{F}_{\rm RPSN}[\omega] = g_0\left(\delta\hat{a}_\xi^\dagger[\omega-\Delta_l]\bar{a}_l + \delta\hat{a}_\xi[\omega+\Delta_l]\bar{a}_l^* + \delta\hat{a}_\xi^\dagger[\omega-\Delta_u]\bar{a}_u + \delta\hat{a}_\xi[\omega+\Delta_u]\bar{a}_u^*\right) \tag{5.40}$$

Since we are only measuring intracavity field near optical resonance $\omega \approx 0$, we can neglect two of the four sidebands: the red sideband of the lower control beam, corresponding to $\delta\hat{b}^\dagger[\omega-\Delta_l]$ and the blue sideband of the upper control beam, corresponding to $\delta\hat{b}[\omega-\Delta_u]$. The optical field is then:

$$\delta\hat{a}[\omega] = \chi_{aa}[\omega]\left(-ig_0\left(\bar{a}_l\delta\hat{b}[\omega-\Delta_l] + \bar{a}_u\delta\hat{b}^\dagger[\omega-\Delta_u]\right) + \sqrt{\kappa}\hat{\xi}[\omega]\right) \tag{5.41}$$

and

$$\delta\hat{a}^\dagger[\omega] = \chi_{aa}^*[-\omega]\left(ig_0\left(\bar{a}_l^*\delta\hat{b}^\dagger[\omega+\Delta_l] + \bar{a}_u^*\delta\hat{b}[\omega+\Delta_u]\right) + \sqrt{\kappa}\hat{\xi}^\dagger[\omega]\right) \tag{5.42}$$

5.3 Heterodyne detection

Consider heterodyne detection of the outgoing field $\delta\hat{a}_{\rm out}$ with an optical local oscillator at frequency $-\omega_{\rm LO}$, where $\omega_{\rm LO} > 0$. Ignoring the reflection of the control beams, the field incident on the photodiode after combining with the local oscillator is $\hat{a}_{\rm det} = a_{\rm LO}e^{i\omega_{\rm LO}t} + \delta\hat{a}_{\rm out}$. From standard photodetection theory [127], the autocorrelation of the photocurrent with a photodetector gain $G_{\rm PD}$ is given by:

$$\begin{aligned} C_{ii}(t,\tau) =& \langle i(t+\tau/2)i(t-\tau/2)\rangle \\ =& G_{\rm PD}^2\langle :\hat{a}_{\rm det}^\dagger(t+\tau/2)\hat{a}_{\rm det}(t+\tau/2)\hat{a}_{\rm det}^\dagger(t-\tau/2)\hat{a}_{\rm det}(t-\tau/2):\rangle \\ &+G_{\rm PD}^2\langle\hat{a}_{\rm det}^\dagger(t)\hat{a}_{\rm det}(t)\rangle\delta(\tau) \end{aligned} \tag{5.43}$$

Here :: denotes normal and time ordering of the operators. Substituting the expression for $\hat{a}_{\rm det}$, and expanding to second order in $\delta\hat{a}$, we get:

$$\begin{aligned} C_{ii}(t,\tau) \approx& G_{\rm PD}^2|a_{\rm LO}|^4 \\ &+G_{\rm PD}^2|a_{\rm LO}|^2\left(\langle\delta\hat{a}_{\rm out}^\dagger(t+\tau/2)\delta\hat{a}_{\rm out}(t+\tau/2)\rangle + \langle\delta\hat{a}_{\rm out}^\dagger(t-\tau/2)\delta\hat{a}_{\rm out}(t-\tau/2)\rangle\right) \\ &+G_{\rm PD}^2|a_{\rm LO}|^2\left(e^{i\omega_{\rm LO}\tau}\langle\delta\hat{a}_{\rm out}^\dagger(t+\tau/2)\delta\hat{a}_{\rm out}(t-\tau/2)\rangle + e^{-i\omega_{\rm LO}\tau}\langle\delta\hat{a}_{\rm out}^\dagger(t-\tau/2)\delta\hat{a}_{\rm out}(t+\tau/2)\rangle\right) \\ &+G_{\rm PD}^2(a_{\rm LO})^2e^{2i\omega_{\rm LO}t}\langle :\delta\hat{a}_{\rm out}^\dagger(t+\tau/2)\delta\hat{a}_{\rm out}^\dagger(t-\tau/2):\rangle \\ &+G_{\rm PD}^2(a_{\rm LO}^*)^2e^{-2i\omega_{\rm LO}t}\langle :\delta\hat{a}_{\rm out}(t+\tau/2)\delta\hat{a}_{\rm out}(t-\tau/2):\rangle \\ &+G_{\rm PD}^2|a_{\rm LO}|^2\delta(\tau) \end{aligned} \tag{5.44}$$

Here the first two lines give the DC component of the correlator which is not relevant to the spectrum of mechanical motion. The next line is important, when considering the autocorrelation spectrum. The next two lines are important for the sideband cross-correlation spectrum, described in [12, 128]. The last line is detector shot noise.

Consider the power spectral density of the photocurrent:

$$\begin{aligned} S_{ii}[\omega] =& \int_{-\infty}^{\infty}\overline{C_{ii}(t,\tau)}e^{i\omega\tau}d\tau \\ =& G_{\rm PD}^2|a_{\rm LO}|^2\left(\int_{-\infty}^{\infty}\overline{\langle\delta\hat{a}_{\rm out}^\dagger(t+\tau/2)\delta\hat{a}_{\rm out}(t-\tau/2)\rangle}e^{i(\omega+\omega_{\rm LO})\tau}d\tau\right. \\ &\left.+\int_{-\infty}^{\infty}\overline{\langle\delta\hat{a}_{\rm out}^\dagger(t-\tau/2)\delta\hat{a}_{\rm out}(t+\tau/2)\rangle}e^{i(\omega-\omega_{\rm LO})\tau}d\tau + 1\right) \end{aligned} \tag{5.45}$$

Here the "bar" implies a time average over all t. Note that terms in the 1st, 4th and 5th lines in $C_{ii}(t,\tau)$ average to 0. Using the definition of power spectral density, we rewrite it as:

$$S_{ii}[\omega] = G_{\rm PD}^2|a_{\rm LO}|^2\left(S_{\delta\hat{a}^\dagger\delta\hat{a}}[\omega+\omega_{\rm LO}] + S_{\delta\hat{a}^\dagger\delta\hat{a}}[-\omega+\omega_{\rm LO}] + 1\right) \tag{5.46}$$

After mixing with the local oscillator, the frequencies of the sidebands are: $\omega_{\rm LO}+\omega_{\rm r}$ and $\omega_{\rm LO}+\omega_{\rm b}$, where $\omega_{\rm r}$ and $\omega_{\rm b}$ are the separation of the blue and red sidebands from the cavity. The Fourier transfrom of the current is:

$$i_{\rm r,b}[\delta\omega] = \omega_{\rm LO} + \omega_{\rm r,b} + \delta\omega \tag{5.47}$$

Here $\delta\omega$ is the frequency shift from the maximum of the sideband.

With this we can define the power spectral density of the red sideband as:

$$\begin{aligned} S_{ii}^{(rr)}[\delta\omega] &= \langle i_r[\delta\omega](i_r[\delta\omega])^*\rangle = S_{ii}[\omega_{\mathrm{LO}}+\omega_{\mathrm{r}}+\delta\omega] \\ &= G_{\mathrm{PD}}^2|a_{\mathrm{LO}}|^2\left(S_{\delta\hat{a}^\dagger\delta\hat{a}}[\omega_{\mathrm{LO}}+\omega_{\mathrm{r}}+\omega_{\mathrm{LO}}+\delta\omega]+S_{\delta\hat{a}^\dagger\delta\hat{a}}[-\omega_{\mathrm{LO}}-\omega_{\mathrm{r}}+\omega_{\mathrm{LO}}+\delta\omega]+1\right) \\ &= G_{\mathrm{PD}}^2|a_{\mathrm{LO}}|^2\left(S_{\delta\hat{a}^\dagger\delta\hat{a}}[2\omega_{\mathrm{LO}}+\omega_{\mathrm{r}}+\delta\omega]+S_{\delta\hat{a}^\dagger\delta\hat{a}}[-\omega_{\mathrm{r}}+\delta\omega]+1\right) \end{aligned} \tag{5.48}$$

The second term corresponds to the spectrum near cavity resonance, while the first term describes the spectrum $2\omega_{\mathrm{LO}}$ away from the cavity resonance, which is heavily filtered. Therefore the expression for the power spectral density simplifies to:

$$S_{ii}^{(rr)}[\delta\omega] = G_{\mathrm{PD}}^2|a_{\mathrm{LO}}|^2\left(S_{\delta\hat{a}^\dagger\delta\hat{a}}[-\omega_{\mathrm{r}}+\delta\omega]+1\right) \tag{5.49}$$

Similarly for the blue sideband, the power spectral density is:

$$S_{ii}^{(bb)}[\delta\omega] = G_{\mathrm{PD}}^2|a_{\mathrm{LO}}|^2\left(S_{\delta\hat{a}^\dagger\delta\hat{a}}[-\omega_{\mathrm{b}}+\delta\omega]+1\right) \tag{5.50}$$

5.4 Brownian motion and correlators

For the following discussion it is important to define correlation relations for the noise operators:

$$\begin{aligned} \langle\hat{\xi}(t)\hat{\xi}(t')\rangle &= 0 & \langle\hat{\xi}[\omega]\hat{\xi}[-\omega]\rangle &= 0 \\ \langle\hat{\xi}^\dagger(t)\hat{\xi}^\dagger(t')\rangle &= 0 & \langle\hat{\xi}^\dagger[\omega]\hat{\xi}^\dagger[-\omega]\rangle &= 0 \\ \langle\hat{\xi}^\dagger(t)\hat{\xi}(t')\rangle &= 0 & \langle\hat{\xi}^\dagger[\omega]\hat{\xi}[-\omega]\rangle &= 0 \\ \langle\hat{\xi}(t)\hat{\xi}^\dagger(t')\rangle &= \delta(t-t') & \langle\hat{\xi}[\omega]\hat{\xi}^\dagger[-\omega]\rangle &= 1 \\ \langle\hat{\eta}(t)\hat{\eta}(t')\rangle &= 0 & \langle\hat{\eta}[\omega]\hat{\eta}[-\omega]\rangle &= 0 \\ \langle\hat{\eta}^\dagger(t)\hat{\eta}^\dagger(t')\rangle &= 0 & \langle\hat{\eta}^\dagger[\omega]\hat{\eta}^\dagger[-\omega]\rangle &= 0 \\ \langle\hat{\eta}^\dagger(t)\hat{\eta}(t')\rangle &= n_{\mathrm{th}}\delta(t-t') & \langle\hat{\eta}^\dagger[\omega]\hat{\eta}[-\omega]\rangle &= n_{\mathrm{th}} \\ \langle\hat{\eta}(t)\hat{\eta}^\dagger(t')\rangle &= (n_{\mathrm{th}}+1)\delta(t-t') & \langle\hat{\eta}[\omega]\hat{\eta}^\dagger[-\omega]\rangle &= n_{\mathrm{th}}+1 \end{aligned} \tag{5.51}$$

And the following definition of the Fourier transform is used:

$$\hat{x}[\omega] = \lim_{T\to\infty}\frac{1}{\sqrt{T}}\int_{-T/2}^{T/2}\hat{x}(t)e^{i\omega t}dt \tag{5.52}$$

The outgoing field from the cavity is calculated using input/output relations [**?**] :

$$\delta\hat{a}_{\mathrm{out}} = \xi_{\mathrm{ext}} - \sqrt{\kappa_{\mathrm{ext}}}\delta\hat{a}, \tag{5.53}$$

where the first term represents the prompt reflection of the incoming signal and the second term represents the signal radiated by the cavity.

The power spectral density of the light leaving the cavity is:

$$S_{\delta\hat{a}^\dagger\delta\hat{a}}[\omega] = \langle\delta\hat{a}^\dagger[\omega]_{\mathrm{out}}\delta\hat{a}[-\omega]_{\mathrm{out}}\rangle \tag{5.54}$$

$$= \kappa_{\mathrm{ext}}|\chi_{aa}[-\omega]|^2 g_0^2(|\bar{a}_l|^2 S_{\delta\hat{b}^\dagger\delta\hat{b}}[\omega+\Delta_l] + |\bar{a}_u|^2 S_{\delta\hat{b}\delta\hat{b}^\dagger}[\omega+\Delta_u] \tag{5.55}$$

Here we omit the terms $\bar{a}_l^*\bar{a}_u\langle\delta\hat{b}^\dagger[\omega+\Delta_l]\delta\hat{b}^\dagger[-\omega-\Delta_u]\rangle$ and $\bar{a}_u^*\bar{a}_l\langle\delta\hat{b}[\omega+\Delta_u]\delta\hat{b}[-\omega-\Delta_l]\rangle$, as they will be small as long as the separation of the sidebands is large: $|\Delta_u-\Delta_l-2\omega_{\mathrm{m}}| \gg \gamma$. Additionally all terms invoving $\hat{\xi}$ are zero due to normal ordering. Now let's consider the correlators of the mechanical motion:

$$S_{\delta\hat{b}^\dagger\delta\hat{b}}[\omega] = \langle\delta\hat{b}^\dagger[\omega]\delta\hat{b}[-\omega]\rangle = |\chi_{bb,\mathrm{eff}}[-\omega]|^2(S_{\hat{F}\hat{F}}^{\mathrm{RPSN}}[\omega] + S_{\hat{F}^\dagger\hat{F}}^{\mathrm{th}}[\omega]) \tag{5.56}$$

$$S_{\delta\hat{b}\delta\hat{b}^\dagger}[\omega] = \langle \delta\hat{b}[\omega]\delta\hat{b}^\dagger[-\omega]\rangle = |\chi_{bb,\mathrm{eff}}[\omega]|^2 (S^{\mathrm{RPSN}}_{\hat{F}\hat{F}}[\omega] + S^{\mathrm{th}}_{\hat{F}\hat{F}^\dagger}[\omega]) \tag{5.57}$$

Here $S^{\mathrm{RPSN}}_{\hat{F}\hat{F}}[\omega] = \langle \hat{F}_{\mathrm{RPSN}}[\omega]\hat{F}_{\mathrm{RPSN}}[-\omega]\rangle$; $S^{\mathrm{th}}_{\hat{F}^\dagger\hat{F}}[\omega] = \gamma\langle\hat{\eta}^\dagger[\omega]\hat{\eta}[-\omega]\rangle$ and $S^{\mathrm{th}}_{\hat{F}\hat{F}^\dagger}[\omega] = \gamma\langle\hat{\eta}[\omega]\hat{\eta}^\dagger[-\omega]\rangle$. The PSD for radiation pressure has 16 terms; however due to normal ordering only four are non-zero. Out of those four, two are very small and can be neglected, leaving:

$$S^{\mathrm{RPSN}}_{\hat{F}\hat{F}}[\omega] = \langle \hat{F}_{\mathrm{RPSN}}[\omega]\hat{F}_{\mathrm{RPSN}}[-\omega]\rangle = g_0^2\kappa \left(|\bar{a}_l|^2|\chi_{aa}[\omega+\Delta_l]|^2 + |\bar{a}_u|^2|\chi_{aa}[\omega+\Delta_u]|^2\right) \tag{5.58}$$

The power spectral densities of the thermal force evaluate to:

$$S^{\mathrm{th}}_{\hat{F}^\dagger\hat{F}}[\omega] = \gamma\langle\hat{\eta}^\dagger[\omega]\hat{\eta}[-\omega]\rangle) = \gamma n_{\mathrm{th}} \qquad S^{\mathrm{th}}_{\hat{F}\hat{F}^\dagger}[\omega] = \gamma\langle\hat{\eta}[\omega]\hat{\eta}^\dagger[-\omega]\rangle) = \gamma(n_{\mathrm{th}}+1) \tag{5.59}$$

So now the correlators of the mechanical motion are:

$$S_{\delta\hat{b}^\dagger\delta\hat{b}}[\omega] = |\chi_{bb,\mathrm{eff}}[-\omega]|^2 \left(g_0^2\kappa \left(|\bar{a}_l|^2|\chi_{aa}[\omega+\Delta_l]|^2 + |\bar{a}_u|^2|\chi_{aa}[\omega+\Delta_u]|^2\right) + \gamma n_{\mathrm{th}}\right) \tag{5.60}$$

$$S_{\delta\hat{b}\delta\hat{b}^\dagger}[\omega] = |\chi_{bb,\mathrm{eff}}[\omega]|^2 \left(g_0^2\kappa \left(|\bar{a}_l|^2|\chi_{aa}[\omega+\Delta_l]|^2 + |\bar{a}_u|^2|\chi_{aa}[\omega+\Delta_u]|^2\right) + \gamma(n_{\mathrm{th}}+1)\right) \tag{5.61}$$

Since the mechanical susceptibility is a much narrower function of ω than the cavity susceptibility, we can use the fact that the mechanical susceptibility is peaked around $\omega_{\mathrm{m,eff}} = \omega_{\mathrm{m}} + \mathrm{Re}[\Sigma[\omega]]$ to rewrite the correlators as:

$$S_{\delta\hat{b}^\dagger\delta\hat{b}}[\omega] = |\chi_{bb,\mathrm{eff}}[-\omega]|^2 \left(g_0^2\kappa \left(|\bar{a}_l|^2|\chi_{aa}[-\omega_{\mathrm{m,eff}}+\Delta_l]|^2 + |\bar{a}_u|^2|\chi_{aa}[-\omega_{\mathrm{m,eff}}+\Delta_u]|^2\right) + \gamma n_{\mathrm{th}}\right) \tag{5.62}$$

$$S_{\delta\hat{b}\delta\hat{b}^\dagger}[\omega] = |\chi_{bb,\mathrm{eff}}[\omega]|^2 \left(g_0^2\kappa \left(|\bar{a}_l|^2|\chi_{aa}[\omega_{\mathrm{m,eff}}+\Delta_l]|^2 + |\bar{a}_u|^2|\chi_{aa}[\omega_{\mathrm{m,eff}}+\Delta_u]|^2\right) + \gamma(n_{\mathrm{th}}+1)\right) \tag{5.63}$$

The occupation of the mechanical mode is given by the integral of its power spectral density:

$$\begin{aligned} n_{\mathrm{m}} &= \int_{-\infty}^{\infty} S_{\delta\hat{b}^\dagger\delta\hat{b}}[\omega]\frac{d\omega}{2\pi} \\ &= \frac{1}{\gamma_{\mathrm{eff}}}\left(g_0^2\kappa \left(|\bar{a}_l|^2|\chi_{aa}[-\omega_{\mathrm{m,eff}}+\Delta_l]|^2 + |\bar{a}_u|^2|\chi_{aa}[-\omega_{\mathrm{m,eff}}+\Delta_u]|^2\right) + \gamma n_{\mathrm{th}}\right) \end{aligned} \tag{5.64}$$

The first term in the equation gives the heating (driving) of the mechanical mode by the beating between the control beam and RPSN, the second term is proportional to the thermal phonon number. Using this expression for n_{m}, we can rewrite the correlators $S_{\delta\hat{b}^\dagger\delta\hat{b}}[\omega]$ and $S_{\delta\hat{b}\delta\hat{b}^\dagger}[\omega]$ as:

$$S_{\delta\hat{b}^\dagger\delta\hat{b}}[\omega] = |\chi_{bb,\mathrm{eff}}[-\omega]|^2 n_{\mathrm{m}}\gamma_{\mathrm{eff}} = \frac{n_{\mathrm{m}}\gamma_{\mathrm{eff}}}{\gamma_{\mathrm{eff}}^2/4 + (\omega+\omega_{\mathrm{m,eff}})^2} \tag{5.65}$$

$$S_{\delta\hat{b}\delta\hat{b}^\dagger}[\omega] = |\chi_{bb,\mathrm{eff}}[\omega]|^2 (n_{\mathrm{m}}+1)\gamma_{\mathrm{eff}} = \frac{(n_{\mathrm{m}}+1)\gamma_{\mathrm{eff}}}{\gamma_{\mathrm{eff}}^2/4 + (\omega-\omega_{\mathrm{m,eff}})^2} \tag{5.66}$$

Where we used:

$$\begin{aligned} &S^{\mathrm{th}}_{\hat{F}\hat{F}^\dagger}[\omega] - S^{\mathrm{th}}_{\hat{F}^\dagger\hat{F}}[-\omega] = \gamma \\ &S^{\mathrm{RPSN}}_{\hat{F}\hat{F}}[\omega] - S^{\mathrm{RPSN}}_{\hat{F}\hat{F}}[-\omega] \\ &= g_0^2\kappa \left(|\bar{a}_l|^2\left(|\chi_{aa}[\omega+\Delta_l]|^2 - |\chi_{aa}[-\omega+\Delta_l]|^2\right)\right. \\ &\left. + |\bar{a}_u|^2\left(|\chi_{aa}[\omega+\Delta_u]|^2 - |\chi_{aa}[-\omega+\Delta_u]|^2\right)\right) \\ &= -2\mathrm{Im}\Sigma[\omega] = \gamma_{\mathrm{opt}} \end{aligned} \tag{5.67}$$

The power spectral density of the outgoing light then is:

$$\begin{aligned} S_{\delta\hat{a}^\dagger\delta\hat{a}}[\omega] =& \langle \delta\hat{a}^\dagger[\omega]_{\text{out}} \delta\hat{a}[-\omega]_{\text{out}} \rangle \\ =& \kappa_{\text{ext}} |\chi_{aa}[-\omega]|^2 g_0^2 (|\bar{a}_l|^2 S_{\delta\hat{b}^\dagger\delta\hat{b}}[\omega + \Delta_l] + |\bar{a}_u|^2 S_{\delta\hat{b}\delta\hat{b}^\dagger}[\omega + \Delta_u]) \\ =& \kappa_{\text{ext}} |\chi_{aa}[-\omega]|^2 g_0^2 (|\bar{a}_l|^2 \frac{n_{\text{m}}\gamma_{\text{eff}}}{\gamma_{\text{eff}}^2/4 + (\omega + \Delta_l + \omega_{\text{m,eff}})^2} \\ &+ |\bar{a}_u|^2 \frac{(n_{\text{m}}+1)\gamma_{\text{eff}}}{\gamma_{\text{eff}}^2/4 + (\omega + \Delta_u - \omega_{\text{m,eff}})^2}) \\ =& \kappa_{\text{ext}} |\chi_{aa}[-\omega]|^2 g_0^2 (|\bar{a}_l|^2 \frac{n_{\text{m}}\gamma_{\text{eff}}}{\gamma_{\text{eff}}^2/4 + (\omega + \omega_b)^2} \\ &+ |\bar{a}_u|^2 \frac{(n_{\text{m}}+1)\gamma_{\text{eff}}}{\gamma_{\text{eff}}^2/4 + (\omega + \omega_r)^2}) \end{aligned} \tag{5.68}$$

The shot noise of the light leaving the cavity gives the background equal to 1. From here we can get the photocurrent of the individual sidebands as:

$$S_{ii}^{(rr)}[\delta\omega] \propto \left(\kappa_{\text{ext}} |\chi_{aa}[\omega_r]|^2 g_0^2 |\bar{a}_u|^2 \frac{(n_{\text{m}}+1)\gamma_{\text{eff}}}{\gamma_{\text{eff}}^2/4 + \delta\omega^2} + 1 \right) \tag{5.69}$$

$$S_{ii}^{(bb)}[\delta\omega] \propto \left(\kappa_{\text{ext}} |\chi_{aa}[\omega_b]|^2 g_0^2 |\bar{a}_l|^2 \frac{n_{\text{m}}\gamma_{\text{eff}}}{\gamma_{\text{eff}}^2/4 + \delta\omega^2} + 1 \right) \tag{5.70}$$

Thus the PSDs of both sidebands consist of a Lorentzian peak plus a constant background.

5.4.1 Phonon number in the oscillator

In this section I will calculate the average mechanical occupation number for a few separate cases:

- A single drive beam on cavity resonance. In this case, the equation 5.64 takes the following form:

$$\begin{aligned} n_{\text{m}} &= \frac{1}{\gamma_{\text{eff}}} \left(g_0^2 \kappa \left(|\bar{a}|^2 |\chi_{aa}[-\omega_{\text{m,eff}}]|^2 \right) + \gamma n_{\text{th}} \right) \\ &= \frac{1}{\gamma_{\text{eff}}} \left(g_0^2 \kappa \left(|\bar{a}|^2 \frac{1}{\kappa^2/4 + \omega_{\text{m,eff}}^2} \right) + \gamma n_{\text{th}} \right) \end{aligned} \tag{5.71}$$

  In our work, we are generally interested in the resolved sideband regime, in which $\omega_{\text{m,eff}}^2 \gg \kappa^2/4$. Additionally for a resonant drive $\gamma_{\text{opt}} = 0$, so

$$n_{\text{m}} = g^2 \frac{\kappa}{\gamma \omega_{\text{m,eff}}^2} + n_{\text{th}} = C \left(\frac{\kappa}{2\omega_{\text{m,eff}}} \right)^2 + n_{\text{th}} \tag{5.72}$$

  Here $g^2 = g_0^2 |\bar{a}|^2$ and g is multiphoton coupling strength.

- A single drive beam is detuned by $\Delta = -\omega_{\text{m,eff}}$. In this case equation 5.64 takes the following form:

$$\begin{aligned} n_{\text{m}} &= \frac{1}{\gamma_{\text{eff}}} \left(g_0^2 \kappa \left(|\bar{a}|^2 |\chi_{aa}[-\omega_{\text{m,eff}} + \Delta]|^2 \right) + \gamma n_{\text{th}} \right) \\ &= \frac{1}{\gamma_{\text{eff}}} \left(g_0^2 \kappa \left(|\bar{a}|^2 \frac{1}{\kappa^2/4 + 4\omega_{\text{m,eff}}^2} \right) + \gamma n_{\text{th}} \right) \end{aligned} \tag{5.73}$$

In the resolved sideband regime:

$$n_{\rm m} = \frac{g^2 \frac{\kappa}{4\omega_{\rm m,eff}^2} + \gamma n_{\rm th}}{\gamma + \gamma_{\rm opt}} \tag{5.74}$$

Using the fact that $\gamma_{\rm opt} = 4g^2/\kappa$ for a drive detuned by $-\omega_{\rm m}$, we arrive at the final expression:

$$n_{\rm m} = \frac{n_{\rm th} + C\left(\frac{\kappa}{4\omega_{\rm m,eff}}\right)^2}{1+C} \tag{5.75}$$

This gives the phonon number in a mechanical oscillator, when only one ("cooling") beam is on.

- A single drive beam is detuned by $\Delta = \omega_{\rm m,eff}$. In this case the expression takes the following form:

$$\begin{aligned} n_{\rm m} &= \frac{1}{\gamma_{\rm eff}}\left(g_0^2\kappa\left(|\bar{a}|^2|\chi_{aa}[-\omega_{\rm m,eff}+\Delta]|^2\right) + \gamma n_{\rm th}\right) \\ &= \frac{1}{\gamma_{\rm eff}}\left(g_0^2\kappa\left(|\bar{a}|^2\frac{1}{\kappa^2/4}\right) + \gamma n_{\rm th}\right) \\ &= \frac{\gamma n_{\rm th} + 4g^2/\kappa}{\gamma + \gamma_{\rm opt}} \end{aligned} \tag{5.76}$$

Using the fact that $\gamma_{\rm opt} = -4g^2/\kappa$ for a drive detuned by $\omega_{\rm m}$, we arrive at the final expression:

$$n_{\rm m} = \frac{n_{\rm th} + C}{1-C} \tag{5.77}$$

This gives the phonon number in a mechanical oscillator, when only the "heating" beam is on.

- Two drive beams are present, detuned by $\pm\omega_{\rm m,eff}$. The mechanical occupation number then is given by:

$$n_{\rm m} = \frac{n_{\rm th} + C_{\rm u} + C_{\rm l}\left(\frac{\kappa}{4\omega_{\rm m,eff}}\right)^2}{1 - C_{\rm u} + C_{\rm l}} \tag{5.78}$$

Here $C_{\rm u,l}$ are the cooperativities due to upper and lower beams. In almost all measurements, the power of the control beams was adjusted so that $C_{\rm u} \approx C_{\rm l}$. Additionally, the cooperativites were low enough, so that the heating of the mode by the beating between the control beam and RPSN was adding at most $1/4$ phonon.

5.5 Optomechanically induced transparency/amplification

Here I will derive the effects of optomechanically induced transparency and amplification.

5.5.1 One probe beam

When a coherent drive is applied to the mechanical mode, the noise terms become irrelevant (as the noise is generally much smaller than the drive, and incoherent), so in the equations above $\hat{\eta}[\omega] = \hat{\xi}_{\rm int}[\omega] = 0$. In the OMIT measurement scheme a strong control beam is used together with a weaker probe beam. The incident laser field was represented with $\hat{a}_{\rm i}e^{i\Delta t} = (\bar{a}_{\rm i} + \hat{\xi}_{\rm ext}(t))e^{i\Delta t}$. The term $\hat{\xi}_{\rm ext}$ was representing laser noise incident on the input mirror of the cavity. In the OMIT/A scheme $\hat{\xi}_{\rm ext}$ can represent a probe beam that is detuned from the control beam by Ω, where Ω can be either positive or negative. In the frame rotating at $\omega_{\rm cav}$, the expression for $\hat{\xi}_{\rm ext}(t)$ is

$$\hat{\xi}_{\rm ext}(t) = a_{\rm p}e^{-i(\Delta+\Omega)t} \tag{5.79}$$

Taking the Fourier transform and assuming a_{p} to be real

$$\hat{\xi}_{\mathrm{ext}}[\omega] = \sqrt{2\pi} a_{\mathrm{p}} \delta(\omega - (\Delta + \Omega)) \tag{5.80}$$

$$\hat{\xi}^{\dagger}_{\mathrm{ext}}[\omega] = \sqrt{2\pi} a_{\mathrm{p}} \delta(\omega + (\Delta + \Omega)) \tag{5.81}$$

Putting this back into equation 5.28

$$\delta\hat{b}[\omega] = \frac{-i\sqrt{\kappa_{\mathrm{ext}}}(\chi_{aa}[\omega - \Delta]\hat{\xi}^{\dagger}_{\mathrm{ext}}[\omega - \Delta]g + \chi_{aa}[\omega + \Delta]\hat{\xi}_{\mathrm{ext}}[\omega + \Delta]g^*)}{-i(\omega - \omega_{\mathrm{m}}) + \frac{\gamma}{2} + i\Sigma[\omega]} \tag{5.82}$$

we get the following:

$$\delta\hat{b}[\omega] = \frac{-i\sqrt{\kappa_{\mathrm{ext}}}\sqrt{2\pi}(\chi_{aa}[\omega - \Delta]a_{\mathrm{p}}\delta(\omega + \Omega)g + \chi_{aa}[\omega + \Delta]a_{\mathrm{p}}\delta(\omega - \Omega)g^*)}{-i(\omega - \omega_{\mathrm{m}}) + \frac{\gamma}{2} + i\Sigma[\omega]} \tag{5.83}$$

In the time domain:

$$\delta\hat{b}(t) = b_{-}[\Omega]a_{\mathrm{p}}e^{i\Omega t} + b_{+}[\Omega]a_{\mathrm{p}}e^{-i\Omega t} \tag{5.84}$$

where

$$b_{-}[\Omega] = \frac{-i\sqrt{\kappa_{\mathrm{ext}}}\chi_{aa}[-\Omega - \Delta]g}{-i(-\Omega - \omega_{\mathrm{m}}) + \frac{\gamma}{2} + i\Sigma[-\Omega]} \tag{5.85}$$

and

$$b_{+}[\Omega] = \frac{-i\sqrt{\kappa_{\mathrm{ext}}}\chi_{aa}[\Omega + \Delta]g^*}{-i(\Omega - \omega_{\mathrm{m}}) + \frac{\gamma}{2} + i\Sigma[\Omega]} \tag{5.86}$$

We are generally interested in the case of the control beam having an either positive or negative detuning from the cavity Δ and the probe beam detuned from the control beam by $\Omega \simeq \pm\omega_{\mathrm{m}}$. If Δ and Ω have the same sign, then $b_{+}[\Omega]$ and $b_{-}[\Omega]$ are both small, as they both describe the sideband of the control beam which is not on resonance. If $\Delta > 0$ and $\Omega < 0$ then b_{+} is on resonance (measuring the red sideband of the upper control beam), if $\Delta < 0$ and $\Omega > 0$, then b_{-} is on resonance (measuring the blue sideband of the lower control beam).

The optical amplitude (without accounting for intracavity optical noise) is given by equation 5.13 as:

$$\delta\hat{a}[\omega] = \chi_{aa}[\omega]\left(-ig(\delta\hat{b}[\omega - \Delta] + \delta\hat{b}^{\dagger}[\omega - \Delta]) + \sqrt{\kappa_{\mathrm{ext}}}\hat{\xi}_{\mathrm{ext}}[\omega]\right) \tag{5.87}$$

The expression for $\delta\hat{b}[\omega - \Delta]$ in the time domain is:

$$b_{-}[\Omega]a_{\mathrm{p}}e^{-i(\Delta - \Omega)t} + b_{+}[\Omega]a_{\mathrm{p}}e^{-i(\Delta + \Omega)t} \tag{5.88}$$

its complex conjugate is:

$$b^*_{-}[\Omega]a_{\mathrm{p}}e^{-i(\Delta + \Omega)t} + b^*_{+}[\Omega]a_{\mathrm{p}}e^{-i(\Delta - \Omega)t} \tag{5.89}$$

We can now express the cavity mode amplitude as

$$\delta\hat{a}(t) = a_{+}[\Omega]e^{-i(\Delta - \Omega)t} + a_{-}[\Omega]e^{-i(\Delta + \Omega)t} \tag{5.90}$$

where

$$a_{+}[\Omega] = \chi_{aa}[\Delta - \Omega]\left(-ig(b_{-}[\Omega] + b^*_{+}[\Omega])\right)a_{\mathrm{p}} \tag{5.91}$$

and

$$a_{-}[\Omega] = \chi_{aa}[\Delta + \Omega]\left(-ig(b^*_{-}[\Omega] + b_{+}[\Omega]) + \sqrt{\kappa_{\mathrm{ext}}}\right)a_{\mathrm{p}} \tag{5.92}$$

Only a_- gives the amplitude of the signal at the probe beam frequency, which is what we measure. Depending on whether we measure the blue sideband of the control beam or the red sideband, we measure either $a_{-,\mathrm{blue}}$ or $a_{-,\mathrm{red}}$. To cancel the effects of fluctuations of the power in the probe beam, we normalize $a_{-,\mathrm{blue}}$ or $a_{-,\mathrm{red}}$ relative to the background.

$$a'_{\mathrm{red}}[\Omega] = \frac{a_{-,\mathrm{red}}[\Omega]}{a_{-,\mathrm{red}}[\infty]} = \frac{-igb^*_-[\Omega]}{\sqrt{\kappa_{\mathrm{ext}}}} + 1 \tag{5.93}$$

$$a'_{\mathrm{blue}}[\Omega] = \frac{a_{-,\mathrm{blue}}[\Omega]}{a_{-,\mathrm{blue}}[\infty]} = \frac{-igb_+[\Omega]}{\sqrt{\kappa_{\mathrm{ext}}}} + 1 \tag{5.94}$$

The functions $\left|a_{(\mathrm{blue/red})}[\Omega]\right|$ and $\psi_{(\mathrm{blue/red})}[\Omega]$ are the magnitude and phase of $a'_{(\mathrm{blue/red})}[\Omega]$. We can also define values $A_{(\mathrm{blue/red})}$ and $\Psi_{(\mathrm{blue/red})}$ as follows:

$$A_{\mathrm{red}} = \mathrm{abs}\left[\frac{-igb^*_-[-\omega_{\mathrm{m}}]}{\sqrt{\kappa_{\mathrm{ext}}}}\right] \qquad \Psi_{\mathrm{red}} = \arg\left[\frac{-igb^*_-[-\omega_{\mathrm{m}}]}{\sqrt{\kappa_{\mathrm{ext}}}}\right] \tag{5.95}$$

$$A_{\mathrm{blue}} = \mathrm{abs}\left[\frac{-igb_+[\omega_{\mathrm{m}}]}{\sqrt{\kappa_{\mathrm{ext}}}}\right] \qquad \Psi_{\mathrm{blue}} = \arg\left[\frac{-igb_+[\omega_{\mathrm{m}}]}{\sqrt{\kappa_{\mathrm{ext}}}}\right] \tag{5.96}$$

Where $b^*_+[-\omega_{\mathrm{m}}]$ is the complex amplitude of the acoustic oscillator, when the the probe beam is detuned by $-\omega_{\mathrm{m}}$ from the control beam and $b_-[\omega_{\mathrm{m}}]$ is the complex amplitude of the acoustic oscillator, when the the probe beam is detuned by ω_{m} from the control beam.

We can rewrite the amplitude of the beams as:

$$A_{\mathrm{red}} = \mathrm{abs}\left[2\left|g\right|^2 \chi_{aa}[\Delta - \omega_{\mathrm{m}}]/\gamma_{\mathrm{eff}}\right] \tag{5.97}$$

$$A_{\mathrm{blue}} = \mathrm{abs}\left[-2\left|g\right|^2 \chi_{aa}[\Delta + \omega_{\mathrm{m}}]/\gamma_{\mathrm{eff}}\right] \tag{5.98}$$

5.5.2 Two probe beams

Some of the measurements (the low frequency modes) were done using two probe beams. Here we will briefly derive the expressions for the OMIT amplitude and phase in that case. In the frame rotating at ω_{cav}, the expression for $\hat{\xi}_{\mathrm{ext}}(t)$ is

$$\hat{\xi}_{\mathrm{ext}}(t) = a_{\mathrm{p}}(e^{-i(\Delta+\Omega)t} + e^{-i(\Delta-\Omega)t}) \tag{5.99}$$

Here we implicitly require that Ω is positive. Taking the Fourier transform and assuming a_{p} to be real

$$\hat{\xi}_{\mathrm{ext}}[\omega] = \sqrt{2\pi}a_{\mathrm{p}}(\delta(\omega - (\Delta + \Omega)) + \delta(\omega - (\Delta - \Omega))) \tag{5.100}$$

$$\hat{\xi}^\dagger_{\mathrm{ext}}[\omega] = \sqrt{2\pi}a_{\mathrm{p}}(\delta(\omega + (\Delta + \Omega)) + \delta(\omega + (\Delta - \Omega))) \tag{5.101}$$

Now:

$$\delta\hat{b}[\omega] = \frac{-i\sqrt{\kappa_{\mathrm{ext}}}\sqrt{2\pi}(\delta(\omega+\Omega) + \delta(\omega-\Omega))(\chi_{aa}[\omega - \Delta]a_{\mathrm{p}}g + \chi_{aa}[\omega + \Delta]a_{\mathrm{p}}g^*)}{-i(\omega - \omega_{\mathrm{m}}) + \frac{\gamma}{2} + i\Sigma[\omega]} \tag{5.102}$$

The equation in the time domain is the same, except that now

$$b_-[\Omega] = \frac{-i\sqrt{\kappa_{\mathrm{ext}}}(\chi_{aa}[-\Omega - \Delta]g + \chi_{aa}[-\Omega + \Delta]g^*)}{-i(-\Omega - \omega_{\mathrm{m}}) + \frac{\gamma}{2} + i\Sigma[-\Omega]} \tag{5.103}$$

and

$$b_+[\Omega] = \frac{-i\sqrt{\kappa_{\mathrm{ext}}}(\chi_{aa}[\Omega - \Delta]g + \chi_{aa}[\Omega + \Delta]g^*)}{-i(\Omega - \omega_{\mathrm{m}}) + \frac{\gamma}{2} + i\Sigma[\Omega]} \tag{5.104}$$

Since we required Ω to be positive, b_- is small and can be neglected. The rest of the derivation follows similarly, except that now we can measure both the upper and lower probe beams, so:

$$a_+[\Omega] = \chi_{aa}[\Delta - \Omega](-igb_+^*[\Omega] + \sqrt{\kappa_{\rm ext}})a_{\rm p} \tag{5.105}$$

and

$$a_-[\Omega] = \chi_{aa}[\Delta + \Omega]\left(-igb_+[\Omega] + \sqrt{\kappa_{\rm ext}}\right)a_{\rm p} \tag{5.106}$$

Where a_+ gives the amplitude of the lower probe beam and a_- gives the amplitude of the upper probe beam.

5.6 Photothermal coupling

Just as optical power fluctuations influence the mechanical mode via radiation pressure (or electrostriction) as described in section 2.6, the temperature fluctuations, arising due to photons heating parts of the device, can also have an effect on the mechanical mode, via photothermal coupling. There are at least two different photothermal coupling mechanisms, that can arise in our system.

First photothermal coupling can arise from the thermal expansion of the fiber mirrors due to laser heating. This expansion moves the glass/helium boundary, and this motion drives the acoustic mode.

Photothermal coupling could also arise from helium counterflow [38, 129], particularly in the geometry where a cavity is formed inside of a single ferrule. The devices, presented in this thesis, generally operate at temperatures where the two-fluid model is not valid. However, we note that thermal phonons radiated from the hot mirror will result in a net transport of helium, which must be balanced by the flow of superfluid towards the hot spot. This can lead to optomechanical coupling in the following way: scattering may prevent the thermal phonons from traveling efficiently through the thin sheath between the ferrule and the fiber, while the superfluid component travels easily through this sheath. This can create a temporary imbalance in which more helium is accumulated close to the hot mirrors, thereby driving the acoustic mode.

The photothermal force is not symmetric. The equation of motion for optical field $\delta\hat{a}$ (equation 5.5) is not influenced by the inclusion of the photothermal process, because the action of the acoustic mode on the intracavity light is only via changes in the helium density, which are fully parameterized by $\hat{b}$.

In the absence of vacuum noise (e.g. during motion of a driven response), the temperature fluctuations can be accounted by including an extra term in equation for the acoustic oscillator.

$$\dot{\hat{b}} = -i(\omega_{\rm m}\hat{b} + g_0\hat{a}^\dagger\hat{a} + g_{\rm T}\delta T) - \frac{\gamma}{2}\hat{b} + \sqrt{\gamma}\hat{\eta} \tag{5.107}$$

The last term in equation 5.107 describes the driving of the acoustic mode by changes in the helium temperature δT. The acoustic mode is coupled to the temperature fluctuations with the coupling rate g_T which has units of Hz/K. Furthermore, we assume that δT undergoes simple relaxation towards an equilibrium value set by the intracavity photon number $\hat{a}^\dagger\hat{a}$.

$$\delta\dot{T} = g_{\rm ta}\hat{a}^\dagger\hat{a} - \kappa_{\rm th}\delta T \tag{5.108}$$

In this equation $g_{\rm ta}$ is the single photon heating rate in units of K/s, and $\kappa_{\rm th}$ is the relaxation rate of the temperature of the helium inside the cavity. The $\hat{a}^\dagger\hat{a}$ gives the intracavity photon number:

$$\hat{a}^\dagger\hat{a} = |\bar{a}|^2 + (\bar{a}^*\delta\hat{a}(t) + \bar{a}\delta\hat{a}^\dagger(t)) \tag{5.109}$$

Ignoring the constant shift in temperature due to the mean photon number, we can take a Fourier transform of equation 5.108:

$$-i\omega\delta T[\omega] = g_{\rm ta}(\bar{a}^*\delta\hat{a}[\omega] + \bar{a}\delta\hat{a}^\dagger[\omega]) - \kappa_{\rm th}\delta T[\omega] \tag{5.110}$$

$$\delta T[\omega] = \frac{g_{\mathrm{ta}}}{\kappa_{\mathrm{th}}} \frac{\bar{a}^* \delta\hat{a}[\omega] + \bar{a}\delta\hat{a}^\dagger[\omega]}{1 - i\omega/\kappa_{\mathrm{th}}} \tag{5.111}$$

Since we are only interested in the response in the small band around ω_{m}, we can substitute $\omega = \omega_{\mathrm{m}}$ and transform back into time domain

$$\delta T(t) = \frac{g_{\mathrm{ta}}}{\kappa_{\mathrm{th}}} \frac{\bar{a}^* \delta\hat{a}(t) + \bar{a}\delta\hat{a}^\dagger(t)}{1 - i\omega_{\mathrm{m}}/\kappa_{\mathrm{th}}} \tag{5.112}$$

Plugging this back into equation 5.107 gives

$$\dot{\hat{b}} = -i\left(\omega_{\mathrm{m}}\hat{b} + g_0|\bar{a}|^2 + \left(g_0 + g_T \frac{g_{\mathrm{ta}}}{\kappa_{\mathrm{th}}} \frac{1}{1 - i\omega_{\mathrm{m}}/\kappa_{\mathrm{th}}}\right)(\bar{a}^*\delta\hat{a} + \bar{a}\delta\hat{a}^\dagger)\right) - \frac{\gamma}{2}\hat{b} \tag{5.113}$$

After simplifying, we have:

$$\dot{\hat{b}} = -i\left(\omega_{\mathrm{m}}\hat{b} + g_0|\bar{a}|^2 + \left(g_0 + i\frac{g_T g_{\mathrm{ta}}}{\omega_{\mathrm{m}} + i\kappa_{\mathrm{th}}}\right)(\bar{a}^*\delta\hat{a} + \bar{a}\delta\hat{a}^\dagger)\right) - \frac{\gamma}{2}\hat{b} \tag{5.114}$$

We now define

$$g_{0,\mathrm{pt}} = \frac{g_T g_{\mathrm{ta}}}{\omega_{\mathrm{m}} + i\kappa_{\mathrm{th}}} \tag{5.115}$$

The total coupling is $g_{\mathrm{tot}} = g_0(1 + ig_{0,\mathrm{pt}}/g_0) = g_0 G$, where G is defined as

$$G = 1 + i\frac{g_{0,\mathrm{pt}}}{g_0} \tag{5.116}$$

If we assume that the thermal relaxation rate κ_{th} is much smaller than the mechanical frequency ω_{m}, the photothermal force contributes a purely imaginary component of the total optomechanical coupling.

With the inclusion of photothermal force, equation 5.107 becomes:

$$\dot{\hat{b}} = -i(\omega_{\mathrm{m}}\hat{b} + g_0|\bar{a}|^2 + g_0 G(\bar{a}^*\delta\hat{a} + \bar{a}\delta\hat{a}^\dagger)) - \frac{\gamma}{2}\hat{b} + \sqrt{\gamma}\hat{\eta} \tag{5.117}$$

The linearized equation for $\delta\hat{b}$ is:

$$\delta\dot{\hat{b}}(t) = -i\omega_{\mathrm{m}}\delta\hat{b}(t) - ig_0 G(\bar{a}^*\delta\hat{a} + \bar{a}\delta\hat{a}^\dagger)) - \frac{\gamma}{2}\delta\hat{b}(t) \tag{5.118}$$

The rest of the derivation follows as before with the following results:

$$\Sigma[\omega] = iG\,|g|^2\,(\chi_{aa}[\omega - \Delta] - \chi_{aa}[\omega + \Delta]) \tag{5.119}$$

$$b_+[\Omega] = \frac{-i\sqrt{\kappa_{\mathrm{ext}}}\chi_{aa}[-\Omega - \Delta]gG}{-i(-\Omega - \omega_{\mathrm{m}}) + \frac{\gamma}{2} + i\Sigma[-\Omega]} \tag{5.120}$$

$$b_-[\Omega] = \frac{-i\sqrt{\kappa_{\mathrm{ext}}}\chi_{aa}[\Omega + \Delta]g^*G}{-i(\Omega - \omega_{\mathrm{m}}) + \frac{\gamma}{2} + i\Sigma[\Omega]} \tag{5.121}$$

And finally the OMIT/A amplitudes:

$$A_{\mathrm{red}} = \mathrm{abs}\left[2\,|g|^2\,G^*\chi_{aa}[\Delta - \omega_{\mathrm{m}}]/\gamma_{\mathrm{eff}}\right] \tag{5.122}$$

$$\Psi_{\mathrm{red}} = \arg\left[2\left|g\right|^2 G^* \chi_{aa}[\Delta - \omega_{\mathrm{m}}]/\gamma_{\mathrm{eff}}\right] \tag{5.123}$$

$$A_{\mathrm{blue}} = \mathrm{abs}\left[-2\left|g\right|^2 G \chi_{aa}[\Delta + \omega_{\mathrm{m}}]/\gamma_{\mathrm{eff}}\right] \tag{5.124}$$

$$\Psi_{\mathrm{blue}} = \mathrm{abs}\left[-2\left|g\right|^2 G \chi_{aa}[\Delta + \omega_{\mathrm{m}}]/\gamma_{\mathrm{eff}}\right] \tag{5.125}$$

The full treatment of the photothermal coupling for the thermal motion measurements requires introduction of an optical loss channel and corresponding vacuum noise for the photothermal force. Including this vaccuum noise means that mechanical oscillator is driven by an additional force, increasing its phonon occupation number n_{m}. However, we assume that this force is very small [12, 128]. Therefore the photothermal coupling does not have a significant effect on the Brownian motion measurements with the changes arising only due to the change in optomechanical self-energy, which is described above.

5.7 Summary

In this section we provided rigorous theoretical derivations of all effects which we made use of in our experiments. In the next chapters, the results obtained in this chapter will be used to fit the data and extract parameters, such as linewidth and frequency of the mechanical mode, optomechanical electrostrictive and photothermal coupling, mechanical occupation number of the mode and the thermal occupation number of the bath.

Chapter 6

Building the experiment

Previous chapters discussed the motivation for using superfluid helium filled Fabry-Perot cavity as an optomechanical systems, as well as the theory relevant to our experiments. This chapter describes how we actually built the experiment.

The main part of the experiment is the fiber cavity, therefore, I will first describe how the fiber Fabry-Perot cavities are built and characterized. Then I will discuss the assembly of the devices that were used in the experiments, as well as discuss our work on improving the device design. The experiment is performed in a dilution refrigerator, so I will talk about changes that we made to the commercial dilution refrigerator, such as adding optical fibers and helium delivery system which allowed us to fill the device with helium. Finally, I will discuss the measurement setup, the calibrations that we performed and the way data is taken and analyzed.

6.1 Building a fiber Fabry-Perot cavity

As described previously, we use fiber Fabry-Perot cavities in our experiments. In this section I will explain how we build these cavities.

6.1.1 Preparing fibers

We start with a spool of fiber[1]. The fiber can be 125 μm or 200 μm in diameter. The fiber is copper coated and has an inner carbon coating. In principle, other kinds of fiber can be used, however copper coating (not plastic) is generally desired by the mirror coating companies [116]. The fiber is cut to ≈ 30 cm pieces and the ends (≈ 10 cm) are etched in an aqueous solution of ferric chloride. The fibers are then cleaned by wiping them with acetone, then isopropanol, and cleaved, using a fiber cleaver[2]. The carbon coating is removed from the end (≈ 2 mm), by applying multiple short electric discharges in the fiber splicer[3,4] The fiber splicer is used to check the cleave angle as well. Only cleave angles below 1° are accepted. The fibers are loaded into a holder designed by Jakob Reichel's group, which uses finger springs to hold 42 fibers each. It is important that all fibers are protruding from the holder by the same amount, since the mirror coating properties depend on where exactly the fibers are located relative to the depositor (a variation of ± 1 mm results in the coating thickness variation of ± 1 %). The holder is loaded in a plastic box to protect it from dust.

The holder with 42 fibers is loaded into the CO_2 laser ablation setup in the Jakob Reichel's lab in Paris. A detailed description of the setup and the ablation process is found elsewhere [130, 131, 132, 133]. Each fiber is centered and

[1] IVGfiber; Cu1300 and Cu1300/200

[2] Newport FK11

[3] Ericsson FSU 995 FA

[4] We use the standard splicing program "NORMAL SM+SM", but stop the program after the first cleaning discharge.

inspected using an optical profilometer to extract the cleave angle. The fiber is then moved to the position of the CO_2 laser and cleaned with a weak long pulse ($P \approx 100$ mW, $t = 70 - 100$ ms). The strong short pulse ($P = 0.7 - 2.3$ W, $t = 20 - 40$ ms) is then applied to the fiber. Afterwards the fiber is returned to the profilometer for imaging. The shape of the indentation is determined by the duration of the pulse and the proximity of the fiber to the beam waist. The fiber can be shot multiple times. It was found that the core of the fiber that was used melts slower than the cladding, which results in the fiber profile having a flatness in the center. That flatness can be mediated by shooting a short pulse with the fiber close to the beam waist. The size of the indentation is determined by fitting it to a 2D Gaussian and extracting the full-width half maximum (FWHM). The ROC is determined by fitting a region near the center of the indentation (within the radius of 10-20 μm) to a parabola.

Generally, in order to build a long cavity the FWHM should be maximized (that prevents scattering of the light from the cavity mode). The ROC should be chosen to maximize the input coupling efficiency for a given cavity length. In order to maximize the input coupling, the mode field diameter in the fiber should match the mode field diameter of the cavity mode at the input mirror [130]. Figure 6.1 shows a plot of the input coupling efficiency for a symmetric cavity ($R_1 = R_2$) and asymmetric cavity ($R_1 = \infty$, R_2 varies) versus cavity length and mirror ROC. It is calculated using the following equation [130] (assuming single sided cavity $\kappa_{\text{ext}} = \kappa$):

$$\epsilon = \frac{4}{\left(\frac{w_\text{f}}{w_\text{m}} + \frac{w_\text{m}}{w_\text{f}}\right)^2 + \left(\frac{\pi n_\text{f} w_\text{f} w_\text{m}}{\lambda R}\right)^2} \tag{6.1}$$

Here w_f is the mode field radius of the fiber (for the IVG fibers that we use $w_\text{f} = 4.5\mu$m), w_m is the radius of the cavity mode at the mirrors (given by equation B.32), $n_\text{f} = 1.46$ is the fiber index of refraction and R is the mirror radius of curvature. From figure 6.1 it is clear that in order to be able to build cavities of varying length, a large range of fiber ROCs

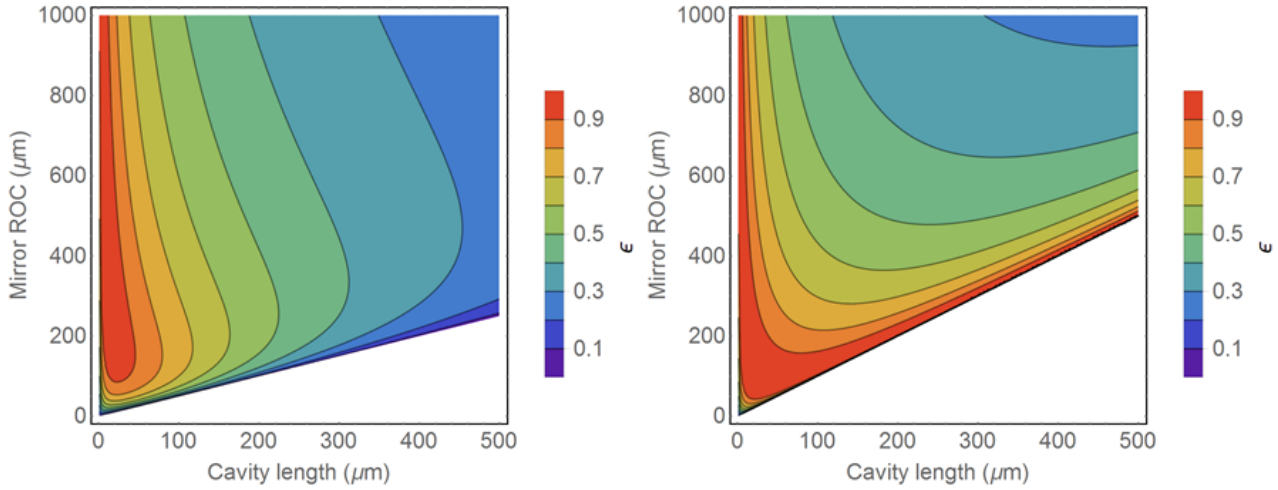

Figure 6.1: Input coupling efficiency ϵ for a symmetric cavity ($R_1 = R_2$) and for a cavity with $R_1 = \infty$ μm (only R_2 varies). White area signifies the region in which the cavity is unstable.

would be useful. However, as it is difficult to build a cavity longer than ≈ 400 μm, (a limitation imposed by the size of the indentations), it doesn't seem beneficial to have fibers with ROCs much larger than 500 μm. On the other hand having fibers with extremely small ROCs (< 100 μm) is not very useful either, as they can only be used for building very short cavities.

Figure 6.2 shows the values of the FWHM of the indentation (obtained by fitting the indentation profile to a Gaussian), as well as a value of ROC (obtained by fitting the center of the indentation profile to a parabola) for the fibers that we have made. The majority of the fibers have ROC between 100 and 600 μm. Additionally, the 200 μm fibers have much larger FWHM of the indentation. This decreases the losses for longer cavities, which makes them preferable for use in the experiments.

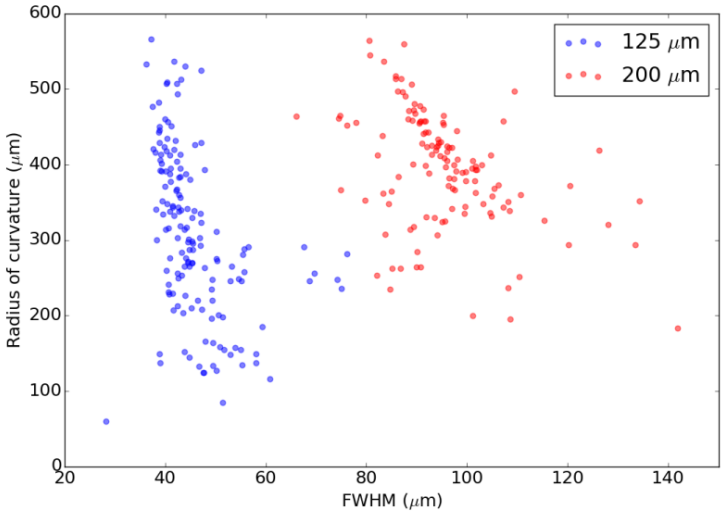

Figure 6.2: ROC of the indentations vs. FWHM of the indentations for both 125 and 200 μm diameter fibers.

6.1.2 Mirror coating

Once the fibers have indentations on them, they are loaded into specially designed substrate blanks. The substrate blanks are provided by the mirror coating company. The mirror coating company can deposit alternating layers of silica (SiO_2) and tantala (Ta_2O_5) in order to form a Distributed Bragg Reflector (DBR) with a given value of optical power transmittance $T_{\rm opt}$. The transmittance of the mirrors determines the finesse of the cavity built using these mirrors. A cavity made of two lossless mirrors with optical power transmittances $T_{1,\rm opt}$ and $T_{1,\rm opt}$ has finesse [131]

$$\mathcal{F}_{\rm opt} = \frac{2\pi}{T_{1,\rm opt} + T_{2,\rm opt}} \tag{6.2}$$

Below I will describe how transmittance can be calculated given the thicknesses of the alternating layers. Here I follow the treatment in [134]. In Figure 6.3 a schematic representation of a DBR is shown. Here the amplitude of the incident field is $E_{\rm i} = 1$, the amplitudes of reflected and transmitted fields are $E_{\rm r}$ and $E^{(\rm t)}$ correspondingly and the amplitude of the fields propagating forward and backward in the $j^{\rm th}$ layer are $E_j^{(\rm f)}$ and $E_j^{(\rm b)}$ correspondingly. The index of refraction of the material from which the wave is incident is n_i and the index of refraction of the material into which the wave is transmitted is n_t. The index of refraction of the $j^{\rm th}$ layer is n_j and the thickness of the $j^{\rm th}$ layer is d_j. The x-axis is pointing to the right.

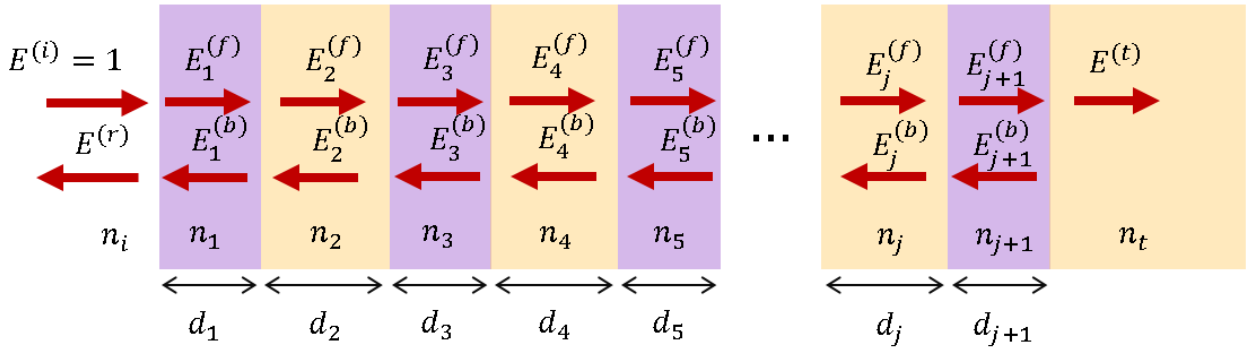

Figure 6.3: DBR structure showing the electric field in each layer. Color indicates different materials.

Assume a plane wave approaches the DBR at normal incidence. The parallel components of electric and magnetic fields must be continuous at each interface, which results in the following boundary conditions

$$E_j(x,t) = E_{j+1}(x,t) \tag{6.3}$$
$$\frac{dE_j(x,t)}{dx} = \frac{dE_{j+1}(x,t)}{dx} \tag{6.4}$$

At the first interface:

$$1 + E_\mathrm{r} = E_1^{(\mathrm{f})} + E_1^{(\mathrm{b})} \tag{6.5}$$
$$n_i\left(1 - E_\mathrm{r}\right) = n_1\left(E_1^{(\mathrm{f})} - E_1^{(\mathrm{b})}\right) \tag{6.6}$$

At the interface between the j^{th} and $(j+1)^{\mathrm{th}}$ layer:

$$E_j^{(\mathrm{f})}e^{ikn_jd_j} + E_j^{(\mathrm{b})}e^{-ikn_jd_j} = E_{j+1}^{(\mathrm{f})} + E_{j+1}^{(\mathrm{b})} \tag{6.7}$$
$$n_j\left(E_j^{(\mathrm{f})}e^{ikn_jd_j} - E_j^{(\mathrm{b})}e^{-ikn_jd_j}\right) = n_{j+1}\left(E_{j+1}^{(\mathrm{f})} - E_{j+1}^{(\mathrm{b})}\right) \tag{6.8}$$

Assuming the total number of layers is p, applying boundary conditions to the last interface yields

$$E_p^{(\mathrm{f})}e^{ikn_pd_p} + E_p^{(\mathrm{b})}e^{-ikn_pd_p} = E^{(\mathrm{t})} \tag{6.9}$$
$$n_p\left(E_p^{(\mathrm{f})}e^{ikn_pd_p} - E_p^{(\mathrm{b})}e^{-ikn_pd_p}\right) = n_tE^{(\mathrm{t})} \tag{6.10}$$

Equations 6.5-6.10 can be expressed in matrix form

$$\begin{bmatrix} 1 & 1 \\ n_i & -n_i \end{bmatrix}\begin{bmatrix} 1 \\ E_\mathrm{r} \end{bmatrix} = \begin{bmatrix} 1 & 1 \\ n_1 & -n_1 \end{bmatrix}\begin{bmatrix} E_1^{(\mathrm{f})} \\ E_1^{(\mathrm{b})} \end{bmatrix} \tag{6.11}$$

$$\begin{bmatrix} e^{ikn_jd_j} & e^{-ikn_jd_j} \\ n_je^{ikn_jd_j} & -n_je^{-ikn_jd_j} \end{bmatrix}\begin{bmatrix} E_j^{(\mathrm{f})} \\ E_j^{(\mathrm{b})} \end{bmatrix} = \begin{bmatrix} 1 & 1 \\ n_{j+1} & -n_{j+1} \end{bmatrix}\begin{bmatrix} E_{j+1}^{(\mathrm{f})} \\ E_{j+1}^{(\mathrm{b})} \end{bmatrix} \tag{6.12}$$

$$\begin{bmatrix} e^{ikn_pd_p} & e^{-ikn_pd_p} \\ n_pe^{ikn_pd_p} & -n_pe^{-ikn_pd_p} \end{bmatrix}\begin{bmatrix} E_p^{(\mathrm{f})} \\ E_p^{(\mathrm{b})} \end{bmatrix} = \begin{bmatrix} 1 & 0 \\ n_t & 0 \end{bmatrix}\begin{bmatrix} E^{(\mathrm{t})} \\ 0 \end{bmatrix} \tag{6.13}$$

Upon rearranging and combining equations 6.11-6.13 we arrive at

$$\begin{bmatrix} 1 \\ E_\mathrm{r} \end{bmatrix} = \begin{bmatrix} 1 & 1 \\ n_i & -n_i \end{bmatrix}^{-1}\prod_{j=1}^{p} M_j \begin{bmatrix} 1 & 0 \\ n_t & 0 \end{bmatrix}\begin{bmatrix} E^{(\mathrm{t})} \\ 0 \end{bmatrix} \tag{6.14}$$

where M_j is defined as

$$M_j = \begin{bmatrix} 1 & 1 \\ n_j & -n_j \end{bmatrix}\begin{bmatrix} e^{ikn_jd_j} & e^{-ikn_jd_j} \\ n_je^{ikn_jd_j} & -n_je^{-ikn_jd_j} \end{bmatrix}^{-1} \tag{6.15}$$

We define:

$$A = \begin{bmatrix} a_{11} & a_{12} \\ a_{21} & a_{22} \end{bmatrix} = \begin{bmatrix} 1 & 1 \\ n_i & -n_i \end{bmatrix}^{-1}\prod_{j=1}^{p} M_j \begin{bmatrix} 1 & 0 \\ n_t & 0 \end{bmatrix} \tag{6.16}$$

and now we have

$$\begin{bmatrix} 1 \\ E_\mathrm{r} \end{bmatrix} = A\begin{bmatrix} E^{(\mathrm{t})} \\ 0 \end{bmatrix} \tag{6.17}$$

from which we find

$$r_{\mathrm{opt}} = E_\mathrm{r} = a_{21}/a_{11} \tag{6.18}$$

$$T_{\text{opt}} = 1 - r_{\text{opt}}^2 \tag{6.19}$$

To conclude, finding the transmittivity of the DBR involves calculating the matrix A, which is straightforward, provided we know the indexes of refraction n_{i} and n_{t}, and the structure of the DBR, which is fully described by n and d of the alternating DBR layers.

The mirrors are made for a specific wavelength. They will, however, reflect light of other wavelengths in a relatively narrow band. In our experiments, we use 1550 nm light, therefore we design the stack so that it reflects 1550 nm light best. That is achieved by choosing the thickness of the layers, so that they will fit exactly one quarter wavelength of 1550 nm light. The index of refraction of silica at 1550 nm is 1.444 [135]. The index of refraction of tantala at 1550 nm is 2.0856 [136]. That gives us the desired layer thicknesses of both materials: $d_{\text{SiO}_2} = 268$ nm and $d_{\text{Ta}_2\text{O}_5} = 186$ nm. The mirrors that we use consist of either 15 or 18 layer pairs. Assume a mirror that can be described as:

$$\text{Substrate} \times (186\text{ nm } \text{Ta}_2\text{O}_5 \times 268\text{ nm } \text{SiO}_2)^{15} \times 186\text{ nm } \text{Ta}_2\text{O}_5 \tag{6.20}$$

We can calculate the finesse for a cavity made out of two such mirrors for different wavelengths (blue line). Note the that there is a region of high finesse around 1550 nm, and there is another region around 516 nm. The second region is where the thickness of the layers is $3\lambda/4$.

However the index of refraction of the materials changes with wavelength [135, 136] (dispersion), which leads to slightly different curve for the finesse vs. wavelength (red line). Note that the maximum of the lower wavelength region is displaced to 532 nm (which is the wavelength of commercially available green lasers). We observed that a high finesse ($\mathcal{F}_{\text{opt}} = 35,000$) cavity can be built with our mirrors for the 532 nm laser.

Finally, as described above, variation in ± 1 mm in fiber positioning can lead to variations of ± 1 % in layer thickness. The effect of this variation is shown with light red area.

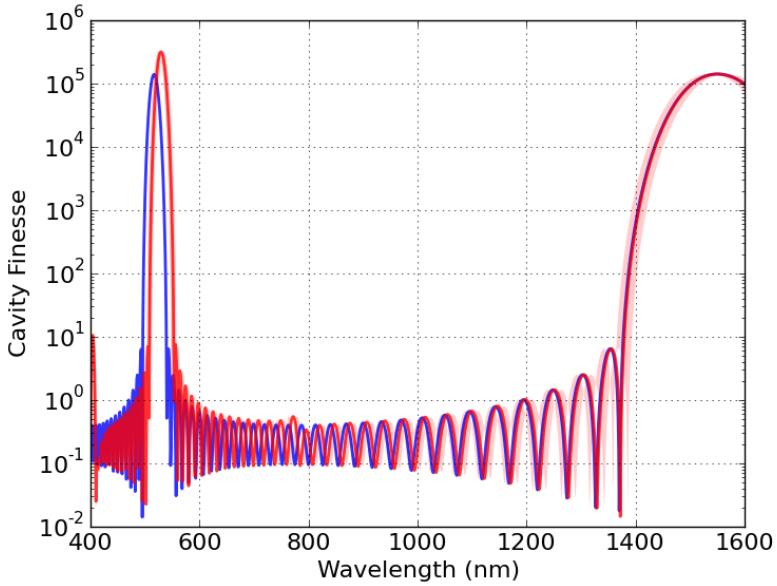

Figure 6.4: Cavity optical finesse vs. wavelength without dispersion (blue), with dispersion (red) and including ± 1 % variation in layer thickness (light red)

The values of the refractive index can vary within a few percent from one coating run to the other. The mirror coating companies adjust for it by varying the thickness of the last layer that is deposited.

After coating, the mirrors need to be annealed at for 5 hours at 300°C. Annealing reduces the absorption of the mirror coatings. It is important to avoid temperatures above 400°C, as that can have detrimental effect on the coatings [116].

Ninety percent of the effect is reached with the first minutes of the annealing [116]. Since it is undesirable to put the whole fiber into an annealing oven (the copper coating becomes brittle when heated to 300 C°), we use a small annealing setup, similar to the one used in Jakob Reichel's group, shown in figure 6.5. A 0.02 in. diameter high resistivity nickel chromium wire is wound around a glass cylinder[5]. Another glass cylinder is positioned outside to keep heat from dissipating outwards. A current supply is used to heat up the wire. A current of 3 A is enough to heat up a straight piece of wire to 300 °C [137]. Since the wire is coiled, lower current of $\approx$ 2 A is enough. The temperature inside the inner cylinder is measured using a thermocouple[6].

Figure 6.6 shows the transmission of a witness piece (glass piece that was coated alongside with our fiber and was used to monitor optical transmission) before and after annealing, as measured by LaserOptik.

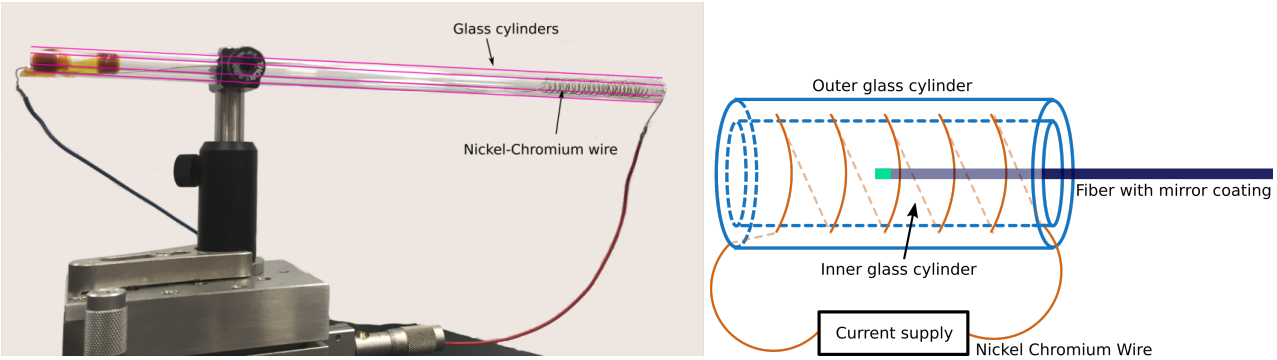

Figure 6.5: Left: A photograph of the fiber annealing setup used in the experiment. Right: Schematic diagram of the fiber annealing setup used in the experiment.

Since annealing reduces mirror absorption, it decreases internal cavity loss, increasing the finesse and the ratio of input coupling to total loss in the cavity $\kappa_{\text{ext}}/\kappa$. Figure 6.7 shows the cavity finesse and the ratio of the input coupling to total cavity loss vs. cavity length before and after annealing. It is clear that both the cavity finesse and the input coupling improve by $\approx 25\%$ of the original value.

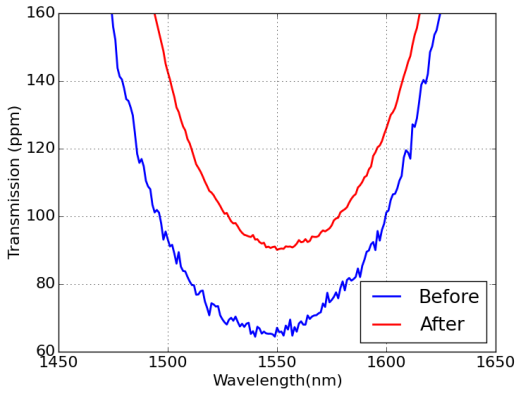

Figure 6.6: Transmission of a witness piece before (blue line) and after (red line) annealing

6.1.3 Building a cavity

After the fibers are coated, we use them to build a cavity. The coated fibers are stored in Plexiglas boxes shown in figure 6.8 to protect them from dust. Inside the boxes, the fibers are attached to aluminum blocks with double-sided

[5] McMaster 8880K78
[6] McMaster 3857K211

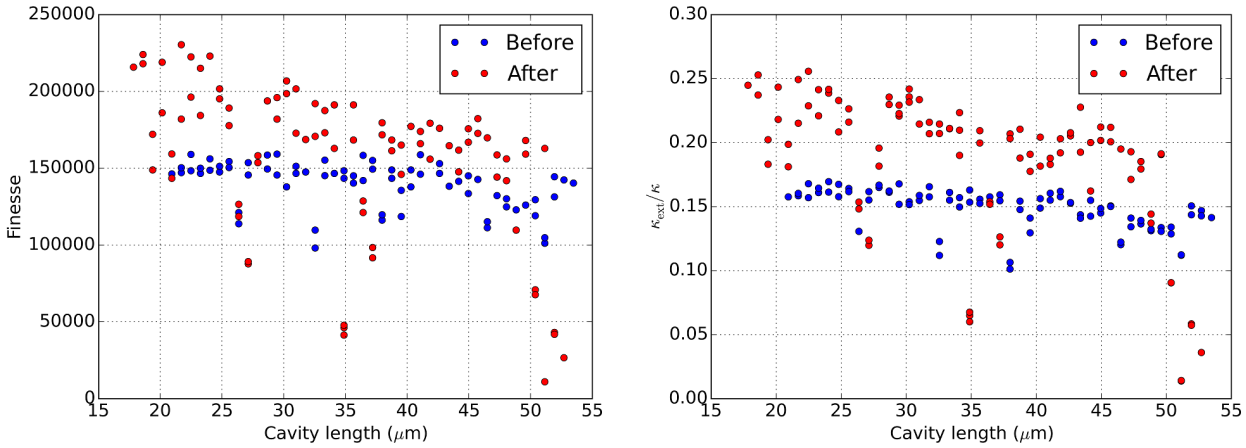

Figure 6.7: Left: Cavity finesse vs. cavity length before and after annealing. Right: Ratio of the input coupling to total cavity loss vs. cavity length before and after annealing.

tape. Care is taken to make sure the mirrored ends do not touch anything. A fiber is taken out of the box and ≈ 5 cm of copper is etched off its end (the one without mirror coating). That end is cleaved. The fiber is then spliced to a fiber pigtail[7,8].

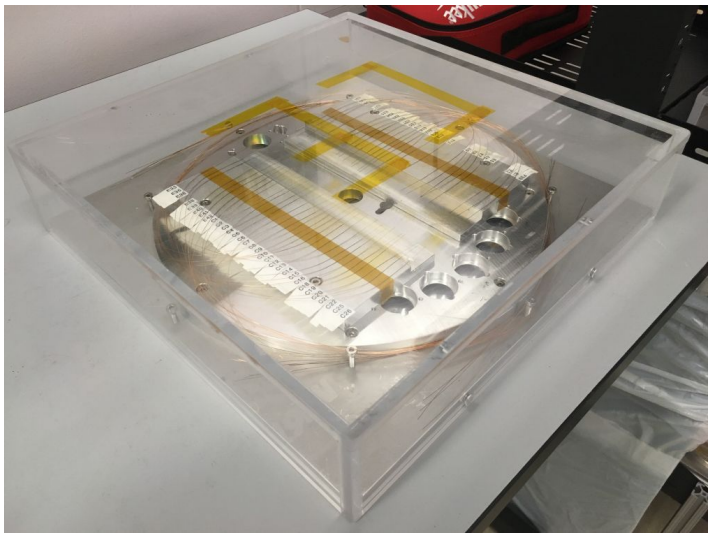

Figure 6.8: Boxes in which fibers are stored. Inside the box, there are two aluminum blocks to which we attached pieces of double sided tape. The fibers are attached to the tape.

The fiber faces are then cleaned. In order to clean a fiber face, we use lens tissue[9]. A fiber is mounted on a translation stage with a microscope camera[10] pointing at the fiber face. The lens tissue is sprayed with isopropanol and is then gently dragged across the fiber face. It could be helpful to rotate the fiber as well. Sometimes, if the fiber is particularly difficult to clean, it is helpful to drag a dry tissue over the fiber face. The fibers of the tissue can get inside the indentation and break up pieces of dust. Figure 6.9 shows an example of a fiber before and after cleaning.

[7] Fibertronics SP-12FCASM3

[8] If the fiber diameter is 125 μm, the standard splicing program "NORMAL SM+SM" is used. If the fiber is diameter 200 μm, a custom program "NORMAL 125+200" is used

[9] Thorlabs MC-5

[10] Digital USB Microscope Video Camera, purchased on Amazon.com

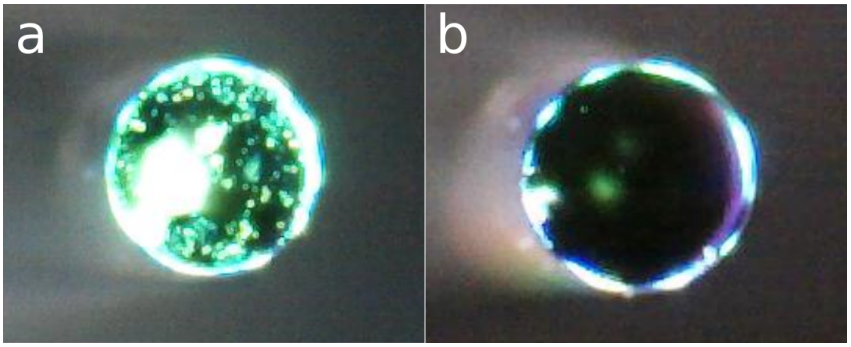

Figure 6.9: A fiber before it was cleaned (a) and after it was cleaned (b). The green spots close to the center in (b) are the highlight from a flashlight

Once both fibers are clean, we point them at one another. We use translation stages[11] with mounted pitch & yaw stages[12] and fiber rotators[13] to hold the fibers in place and align them. The piezos in the translation stages allow us to change the cavity length. When the fibers are aligned in free space, there are 12 degrees of freedom (x, y, z translation, tip/tilt of the fibers, and rotation for both fibers), however only 6 are important (everything can be achieved with one fiber fixed in place). We use two microscope cameras located at 90° angles to check the alignment. Additionally we estimate the length of the cavity using the video feed from one of the cameras. An oscilloscope can be used to monitor the transmission of the cavity, or, combined with a circulator, reflection (which is what we usually do, as that allows us to extract input coupling).

The initial characterization is almost always performed in free space. However, ultimately we need the cavities to stay aligned at cryogenic temperatures, so we use ferrules[14,15] (as shown in figure 4.1 (b)). That results in reducing the degrees of freedom down to 4 (z-translation and rotation of for both fibers), however only 3 are important (z-translation for one fiber and rotation for both fibers). Note that if the ferrule ID were exactly the same as fiber OD only two degrees of freedom would suffice (z-translation and rotation for one fiber). It is also possible for the mirror coated fiber to have slightly larger diameter than the ferrule. In that case, we need to sand the fiber.

In order to sand the fiber, first we cut off a piece of fiber ≈ 20 cm long. Then we etch all copper off the fiber in ferric chloride (mirror should never be in the ferric chloride). Once all the copper is etched off (usually ≈ 15 minutes), we clean the fiber with acetone and isopropanol and cleave it to have a piece about 10 cm long (it is necessary to do the cleaving before the sanding, because fibers become very brittle after sanding). We then sand the mirror coating off. To do that we place the fiber between two sheets of fine sand paper[16] and roll the fiber between the pieces, applying minimal pressure with a finger. This is done under a microscope. Once the fiber coating is sanded, the fiber is spliced to a new pigtail and the fiber sides and face are cleaned again.

Once the fibers are clean, they are inserted in the ferrule. The cavity can be made inside a single ferrule, or between two ferrules. It is generally simpler to optimize the cavity (linewidth and input coupling) when it is short and then increase the cavity length, while adjusting the rotation of the fibers to keep it optimized.

6.2 Characterizing a cavity

Once the cavity is built we need to extract its length, linewidth, finesse and input coupling. During this step, the cavity length is swept using translation stage piezos over some interval (2-40 μm).

[11] Thorlabs MAX302
[12] Thorlabs APY002
[13] Thorlabs HFR007
[14] Vitrocom, custom, $ID = 132 \pm 8$ μm; $L = 9$ mm; $OD = 3$ mm; used in the first generation device for 125 μm fibers
[15] Polymicro, Custom $ID = 205 \pm 3$ μm; $L = 10$ mm; $OD = 1.8$ mm; used in the second generation device for 200 μm fibers
[16] Thorlabs LF6D

6.2.1 Extracting cavity length

We can extract cavity length using a few different methods:

1. Looking at the cavity using a camera, since we know the fiber diameter, we can estimate the cavity length. This method is quick but is not very precise: the length depends on the angle at which the camera is pointing at the cavity; the diameter of the fiber after sanding is often unknown; fibers have indentations, which are impossible to see looking from the side. Additionally, this method does not work once the fiber is inside the ferrule.
2. Touching the fibers to one another, then using micrometers on the Nanomax stages. This method also does not account for the indentations.
3. Using two lasers of different wavelengths. This allows us to find the cavity length exactly, limited only by how well we know the laser wavelength [17]. The cavity of length L_{cav} accommodates q_n half-wavelengths (λ_1) and $q_n + q_m$ half-wavelengths (λ_2), where q_n is a positive integer and q_m is an integer.

   $$\lambda_1 q_n = 2L_{\text{cav}} \qquad \lambda_2(q_n + q_m) = 2L_{\text{cav}} \tag{6.21}$$

   Since we have approximate knowledge of L_{cav}, acquired using the first or second method, we can solve those equations for q_n and q_m, giving us the exact knowledge of L_{cav}.
4. Finally, we can use a widely tunable laser and find a few cavity resonances, while keeping cavity length constant. The knowledge of the wavelengths of these resonances allows us to extract the cavity length very precisely. This, however, is very time consuming and we only use this method after the fibers have been glued in place. This technique will be described later.
5. Some combination of these methods, for example using two lasers of different wavelengths to extract the cavity length at a particular point and using translation stages to change the cavity length from that point

6.2.2 Measuring prompt reflection

If the indentation is centered with the fiber core, then, when the laser is tuned far off resonance, all of the incident light is reflected back into the fiber core as shown in figure 6.10(a). However, the indentation is often slightly off-centered which leads to scattering of the incident light, as shown in figure 6.10(b).

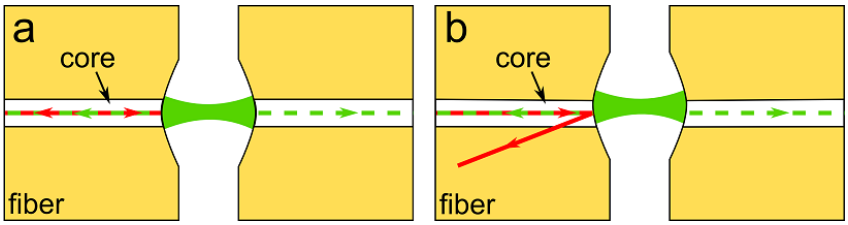

Figure 6.10: Prompt reflection from the cavity. Red line is the incident light. Green shown the mode of the cavity and the light leaking out of the cavity. (a) the indentation is aligned with the fiber core, so the promptly reflected light gets back into the fiber mode. (b) the indentation is not aligned with the fiber core, so some of the promptly reflected light get scattered.

In order to extract input coupling correctly, it is necessary to know what fraction of the light reflected from the cavity gets back into the fiber mode. We measure this as follows:

1. Assume that the fiber splices are lossless. We have measured transmission through a good splice and found that it was $\approx 99\%$.

[17] When using tunable lasers, make sure to first tune them to output the same wavelength and check if the cavity resonances of the both lasers overlap as the cavity length is swept.

2. Send light into the mirrored fiber using a circulator, and connect the other port of the circulator to a power-meter[18]. Adjust the fiber connection between the circulator and the mirrored fiber until the measured power is maximized. Record the power P_{fiber}.

3. Repeat the same step, but replace the mirrored fiber with a retroreflector[19]. Record the power P_{rr}

4. The ratio $\alpha = P_{\text{fiber}}/P_{\text{rr}}$ gives the fraction of the light reflected from the cavity that gets into the fiber mode.

Figure 6.11 shows the cavity reflection for the same input coupling and different values of $P_{\text{fiber}}/P_{\text{rr}}$ varying from 0 (purple) to 1 (red). This figure clarifies that imprecise knowledge of the prompt reflection can lead to wrong estimate for the input coupling.

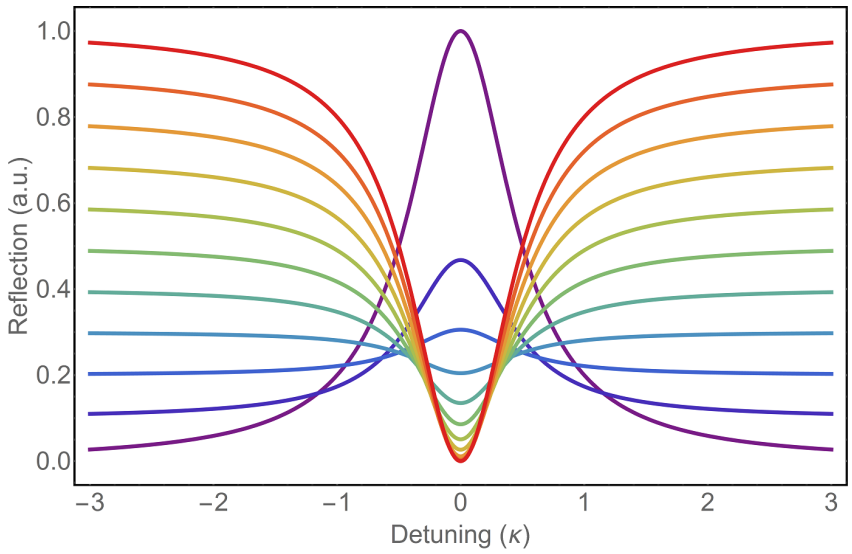

Figure 6.11: Cavity reflection for different values of $P_{\text{fiber}}/P_{\text{rr}}$ from 0 (purple) to 1 (red) in the intervals of 0.1. Input coupling is kept constant with $\kappa_{\text{ext}}/\kappa = 0.5$

6.2.3 Extracting cavity linewidth

We can find cavity linewidth in two different ways:

1. Using laser with sidebands, which is done during initial characterization.

2. Locking the laser to the cavity and using a network analyzer - this is performed during actual measurements and will be described later.

A simple scheme to extract linewidth using phase modulation is shown in figure 6.12. A laser is incident on a modulator (amplitude, phase or IQ modulator), which is driven by a microwave tone from a voltage controlled oscillator (VCO)[20] to add frequency sidebands. The frequency of the microwave tone should be larger than the cavity linewidth, or it is difficult to fit the sidebands reliably. The laser with sidebands is incident on a cavity and reflects from it, acquiring a phase. We use a circulator to separate incident and reflected beams. The reflected laser is then sent to a photodetector[21], signal from which is sent to an oscilloscope. Additionally we use a signal generator to generate a saw tooth wave with frequency

[18] Thorlabs PM100D

[19] Thorlabs P5-SMF28ER-P01-1

[20] we usually use $\omega_{\text{VCO}} \approx 1$ GHz

[21] There is a variety of photodetectors that can be used. Some examples include Thorlabs PDA10CF, Thorlabs PDA10CS, Thorlabs DET01CFC. Some photodetectors produce voltage, as they already have built-in resistors or transimpedance amplifiers, the output of those detectors can be immediately plugged into the oscilloscope. Some detectors produce current. The output of those detectors need to be sent through a 50 Ohm resistance before oscilloscope.

between 0.1 Hz and 10 Hz, which we send through an amplifier to the piezos in the translation stages in order to change the cavity length.

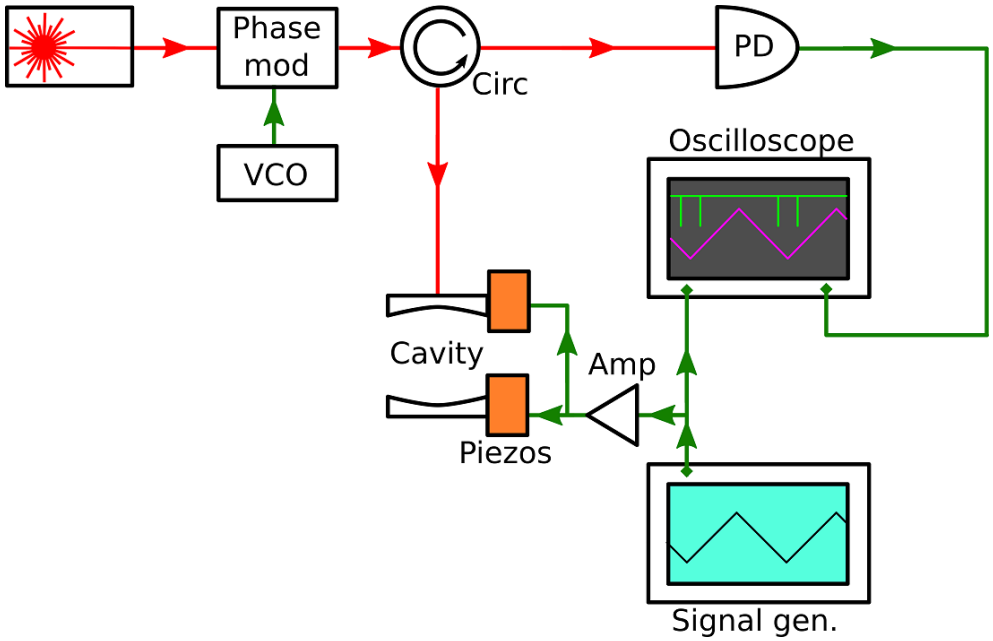

Figure 6.12: A simple sideband modulation scheme, see text for description.

Now consider the different kinds of modulation:

- **Phase modulation.** The laser generates a beam $A\cos(\omega_{\mathrm{L}}t)$. After the phase modulator the beam is: $A\cos(\omega_{\mathrm{L}}t + a\cos(\omega_{\mathrm{VCO}}t))$. Note that $\omega_{\mathrm{L}} \gg \omega_{\mathrm{VCO}}$. Assuming the phase modulation is small, we write to first order:

$$E_{\mathrm{inc}} = A\cos(\omega_{\mathrm{L}}t + a\cos(\omega_{\mathrm{VCO}}t)) \tag{6.22}$$
$$\simeq A\left(\cos(\omega_{\mathrm{L}}t) - a\sin(\omega_{\mathrm{L}}t)\cos(\omega_{\mathrm{VCO}}t)\right) \tag{6.23}$$
$$= A\left(\cos(\omega_{\mathrm{L}}t) - \frac{a}{2}\sin((\omega_{\mathrm{L}} + \omega_{\mathrm{VCO}})t) - \frac{a}{2}\sin((\omega_{\mathrm{L}} - \omega_{\mathrm{VCO}})t)\right) \tag{6.24}$$

  This gives us a carrier and two sidebands.

- **Amplitude modulation.** The laser generates a beam $A\cos(\omega_{\mathrm{L}}t)$. After the amplitude modulator the beam is: $A(1 + b\cos(\omega_{\mathrm{VCO}}t))\cos(\omega_{\mathrm{L}}t)$. This gives us the following incident field

$$E_{\mathrm{inc}} = A(1 + b\cos(\omega_{\mathrm{VCO}}t))\cos(\omega_{\mathrm{L}}t) \tag{6.25}$$
$$= A\left(\cos(\omega_{\mathrm{L}}t) + \frac{b}{2}\cos((\omega_{\mathrm{L}} + \omega_{\mathrm{VCO}})t) + \frac{b}{2}\cos((\omega_{\mathrm{L}} - \omega_{\mathrm{VCO}})t)\right) \tag{6.26}$$

- **General case**. The amplitude and phase can be modulated simultaneously. In this case, the incident field can be written as:

$$E_{\mathrm{inc}} = \mathrm{Re}\left[Ae^{i\omega_{\mathrm{L}}t} + Be^{i(\omega_{\mathrm{L}}+\omega_{\mathrm{VCO}})t} + Ce^{i(\omega_{\mathrm{L}}-\omega_{\mathrm{VCO}})t}\right] \tag{6.27}$$

  Here A, B and C are complex and carry the information about the relative phase of the beams. We will continue working with this general case.

The amplitude and phase of each reflected beam is given by:

$$L(E,t) = E\left(\sqrt{\alpha} - \frac{\kappa_{\mathrm{ext}}}{\kappa/2 + it}\right) \tag{6.28}$$

Here κ and $\kappa_{\rm ext}$, represent cavity linewidth and input coupling. The quantity $\alpha = P_{\rm fiber}/P_{\rm rr}$ gives the ratio of promptly reflected power to incident power. Therefore:

$$E_{\rm ref} = {\rm Re}\left[L(A,t)e^{i\omega_{\rm L}t} + L(B,t+d_{\rm sb})e^{i(\omega_{\rm L}+\omega_{\rm VCO})t} + L(C,t-d_{\rm sb})e^{i(\omega_{\rm L}-\omega_{\rm VCO})t}\right] \tag{6.29}$$

The photodetector[22] measures intensity of the field, and converts it to current which is directly proportional to voltage, so:

$$V(t) \propto E_{\rm ref}^2 \propto V_{\rm DC} + V_{\rm RF} \tag{6.30}$$

Where:

$$V_{\rm DC}(t) \propto \frac{|L(A,t)|^2}{2} + \frac{|L(B,t+d_{\rm sb})|^2}{2} + \frac{|L(C,t-d_{\rm sb})|^2}{2} \tag{6.31}$$

and

$$\begin{aligned} V_{\rm RF}(t) \propto\ & (L(A,t)L^*(C,t-d_{\rm sb}) + L^*(A,t)L(B,t+d_{\rm sb}))e^{i\omega_{\rm VCO}t} \\ & + (L^*(A,t)L(C,t-d_{\rm sb}) + L(A,t)L^*(B,t+d_{\rm sb}))e^{-i\omega_{\rm VCO}t} \\ & + (L^*(B,t+d_{\rm sb})L(C,t-d_{\rm sb}))e^{-2i\omega_{\rm VCO}t} \\ & + (L(B,t+d_{\rm sb})L^*(C,t-d_{\rm sb}))e^{2i\omega_{\rm VCO}t} \end{aligned} \tag{6.32}$$

Here we neglected all terms oscillating at $\omega_{\rm L}$ or faster, because they are filtered by the photodetector. In the scheme described above we send $V(t)$ into the oscilloscope. The bandwidth of oscillosope is lower than $\omega_{\rm VCO}$, so we only observe $V_{\rm DC}(t)$ on the oscilloscope. We use equation 6.31 to fit the trace acquired on the oscilloscope. The values of $\kappa_{\rm sec}$, $\kappa_{\rm ext,sec}$, A, B, C and $d_{\rm sb}$ are the fit parameters.

We find the cavity linewidth in Hz as $\kappa = \kappa_{\rm sec}\omega_{\rm VCO}/d_{\rm sb}$. The input coupling efficiency is calculated as $\zeta = \kappa_{\rm ext,sec}/\kappa_{\rm sec}$. The input coupling efficiency for a general cavity is related to the input coupling efficiency, calculated in equation 6.1 as:

$$\zeta = \frac{T_{1,\rm opt}}{T_{1,\rm opt} + T_{2,\rm opt}}\epsilon \tag{6.33}$$

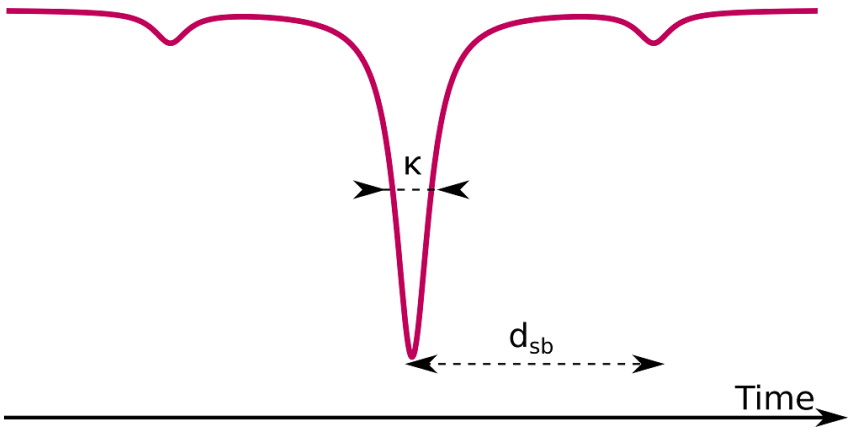

Figure 6.13: A carrier with two phase sidebands reflected from the cavity.

[22]The photodetector usually has dark voltage - the voltage it outputs when there is no light incident. The measured voltage is a sum of dark voltage and signal voltage, so the dark voltage needs to be subtracted from the measured voltage

6.2.4 Extracting cavity finesse

The cavity finesse can be extracted in two ways:

1. Once the length (L_{cav}) and the linewidth (κ) are known, cavity finesse can be found as:

$$\mathcal{F}_{\mathrm{opt}} = \frac{\omega_{\mathrm{FSR}}}{\kappa} = \frac{2\pi c}{2L_{\mathrm{cav}}\kappa} \tag{6.34}$$

2. The cavity length can be swept over a distance covering multiple resonances. The trace is centered on the oscilloscope so that two resonances are visible. The data is saved with large resolution (typically 1.25 mil. samples). The resonances are fit to find κ_{sec} and the distance between the resonances gives $\omega_{\mathrm{FSR,sec}}$. The finesse is found as:

$$\mathcal{F}_{\mathrm{opt}} = \frac{\omega_{\mathrm{FSR,sec}}}{\kappa_{\mathrm{sec}}} \tag{6.35}$$

   This method does not require sidebands on the laser, or knowledge of the cavity length. However, we found it to be unreliable, as the piezos in the translation stages do not necessarily have a linear response to the applied voltage.

6.2.5 Extracting input coupling (heterodyne detection scheme)

The scheme described above allows us to extract the cavity linewidth. The input coupling, however, can not be easily extracted. That is because the DC reflection of the cavity with $\frac{\kappa_{\mathrm{ext}}}{\kappa} = 0.5 + p$ is the same as reflection of the cavity with $\frac{\kappa_{\mathrm{ext}}}{\kappa} = 0.5 - p$, where p is any real number between 0 and 0.5. The phase response, however is very different. Since the phase can not be measured directly, we employ a heterodyne measurement scheme to extract it. The scheme is shown in figure 6.14. The optical setup is the same as in a simple DC detection scheme. The microwave setup has a few extra components. The signal from the VCO is now split using a coupler, with part of the signal going to the phase modulator and part going to the 90° splitter. The signal from the 90° splitter goes into two mixers, where it is mixed with the high frequency ($\geq \omega_{\mathrm{VCO}}$) component of the signal coming from the photodetector, which was separated from the DC signal using a bias tee. The signal from the mixers then travels into the oscilloscope where it can be measured.

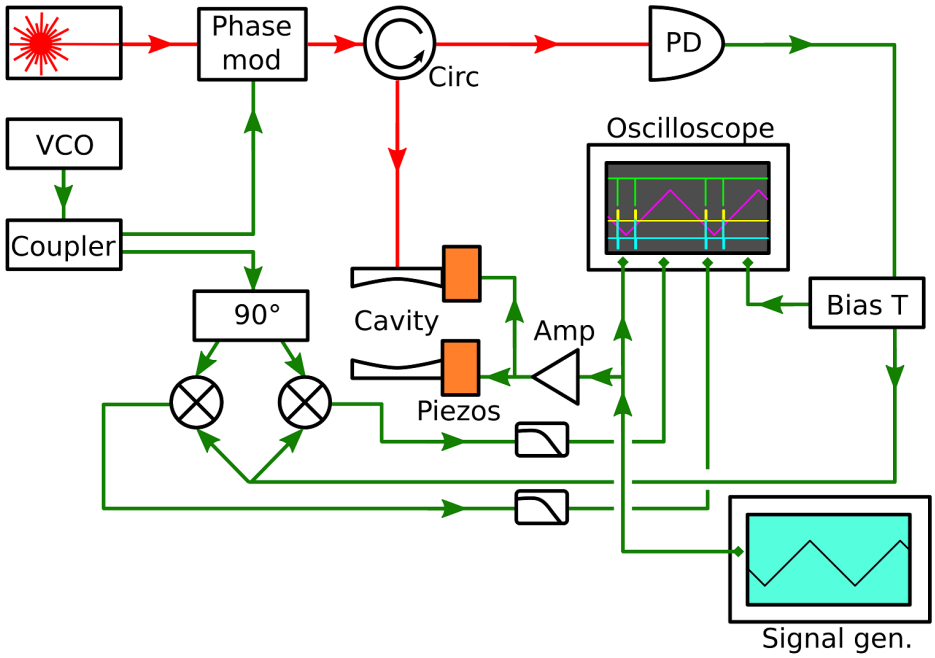

Figure 6.14: Heterodyne detection scheme. See text for description.

In this scheme, in addition to measuring V_{DC}, we can also measure V_{RF}. As seen from figure 6.14, V_{RF} is split and sent to the mixers, where it is mixed with $\cos(\omega_{\mathrm{VCO}}t)$ and $\sin(\omega_{\mathrm{VCO}}t)$. The outputs of the mixers is sent through the low pass filters into to oscilloscope. All terms oscillating faster than ω_{VCO} are filtered, leaving only:

$$V_1 \propto \mathrm{Re}\left[L(A,t)L^*(C,t-d_{\mathrm{sb}}) + L^*(A,t)L(B,t+d_{\mathrm{sb}})\right] \tag{6.36}$$

$$V_2 \propto \mathrm{Im}\left[L(A,t)L^*(C,t-d_{\mathrm{sb}}) + L^*(A,t)L(B,t+d_{\mathrm{sb}})\right] \tag{6.37}$$

Figure 6.15 shows V_{DC}, V_1 and V_2 for two different situations: phase modulation and single-sideband modulation, with the sideband π out of phase from the carrier. Different colors show different values of $\kappa_{\mathrm{ext}}/\kappa$ - red: $\kappa_{\mathrm{ext}}/\kappa = 0.6$, blue: $\kappa_{\mathrm{ext}}/\kappa = 0.4$. From the figure it is obvious that it is impossible distinguish between the two using only V_{DC}. The difference is noticeable in the V_1 and V_2. It becomes even more clear when V_1 and V_2 are plotted against each other, as in figure 6.16.

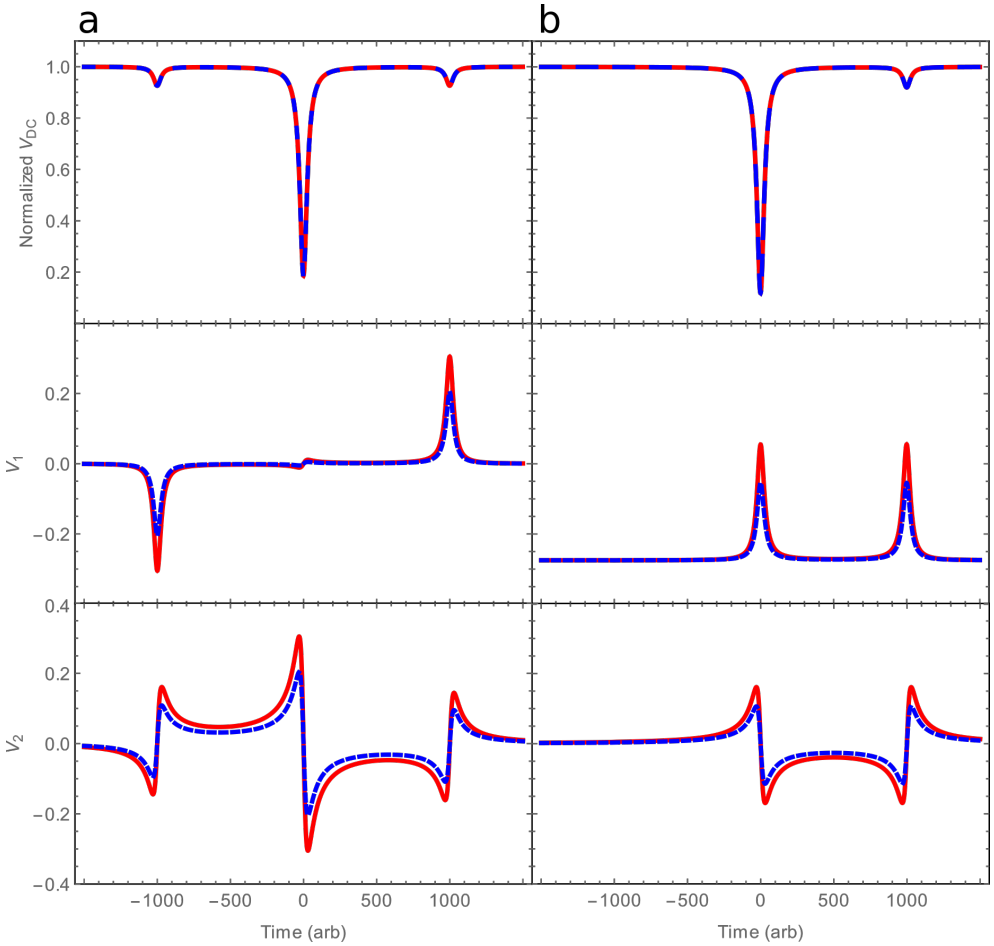

Figure 6.15: The plots of V_{DC}, V_1 and V_2 vs time. Red: $\kappa_{\mathrm{ext}}/\kappa = 0.6$, Blue: $\kappa_{\mathrm{ext}}/\kappa = 0.4$. The linewidth $\kappa = 60$ in time units and the sideband separation from the carrier is 1000 in time units. a) Phase modulation: $A = 1$, $B = 0.3$, $C = 0.3e^{i\pi}$. b) Single sideband modulation $A = 1$, $B = 0$, $C = 0.3e^{i\pi}$

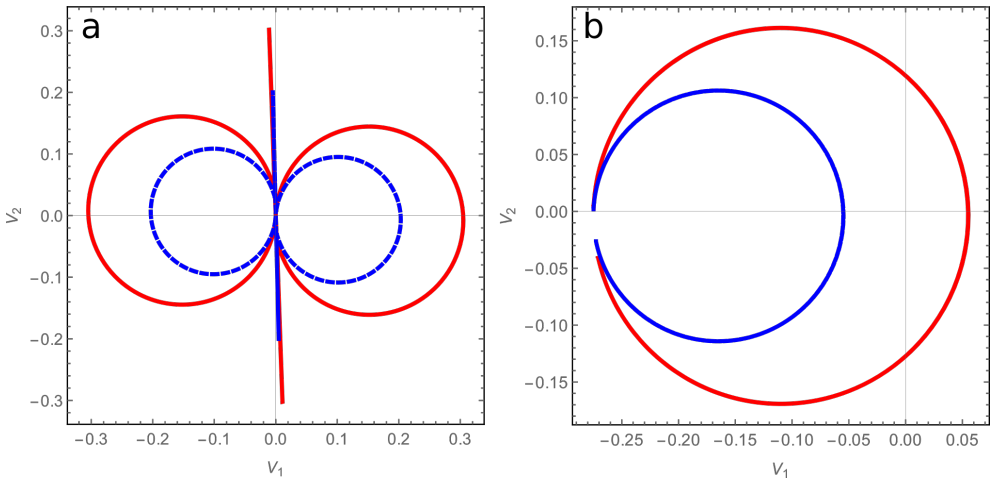

Figure 6.16: The plots of V_2 vs V_1. Red: $\kappa_{\text{ext}}/\kappa = 0.6$, Blue: $\kappa_{\text{ext}}/\kappa = 0.4$. The linewidth $\kappa = 60$ in time units and the sideband separation from the carrier is 1000 in time units. a) Phase modulation: $A = 1$, $B = 0.3$, $C = 0.3e^{i\pi}$. b) Single sideband modulation $A = 1$, $B = 0$, $C = 0.3e^{i\pi}$

6.3 Assembling the device

All data described in this thesis was taken with two devices. The assembly of these devices is described here. The first generation device included a piezo to change the length of the cavities and had the cavities formed inside a ferrule. The second generation device did not have a piezo, as we had obtained a tunable laser. In addition, the cavities in the second generation device were formed between two aligned ferrules to improve the thermal link to the mixing chamber.

After the first two devices, we tried to build a third one, to accommodate long Fabry-Perot cavities. I will briefly describe our efforts in that direction, focusing on what we learned from each attempt.

6.3.1 First generation device

The device, shown in figures 6.17 and 6.18 was designed by Nathan Flowers-Jacobs. The bottom part of the device cell is made out of brass. It has a hollowed out pocket, shown in figure 6.17(b), an indium groove, designed for 0.03" indium wire, 3 holes for the fibers on each side and 2 holes for the piezo leads on one side. The bottom part of the cell was cleaned by placing it subsequently into glass beakers filled with acetone and isopropanol, which were placed into an ultrasonic cleaner[23]. The holes for the fibers and piezo leads were cleaned particularly carefully using a scrap piece of fiber and dragging it through the holes multiple times, wiping it off with isopropanol each time, as well as spraying them with isopropanol and blowing compressed CO_2 through them[24].

Three ferrules[25] were cleaned and epoxied in the pocket, using Stycast 2850FT[26]. In order to epoxy them, we first put a small amount of epoxy on the bottom of the pocket, then carefully placed the ferrule on top of the epoxy, then threaded a piece of stripped and cleaned scrap fiber through the holes in the cell bottom and through the ferrule. That ensured that the ferrule was aligned to the holes. A shear piezo[27] was epoxied in the pocket. A small brass plate was epoxied to the top of the piezo. Stycast 2850FT was used for both epoxy joints. The wires serving as piezo leads were stripped partially, as shown in the inset of figure 6.17(b). The length of the stripped area was shorter than the depth of the piezo lead hole. That was done to ensure helium-tight seal between brass of the cell bottom and copper of the wire and no electrical contact.

[23] Bransonic B200
[24] McMaster 8431K13
[25] Vitrocom, $ID = 132 \pm 8\ \mu m$, $L = 9$ mm; $OD = 3$ mm
[26] Stycast 2850FT: black resin loaded with metal powder to match the thermal expansion coefficient of metals, high viscosity
[27] PI (Physik Instrumente) P-141.05

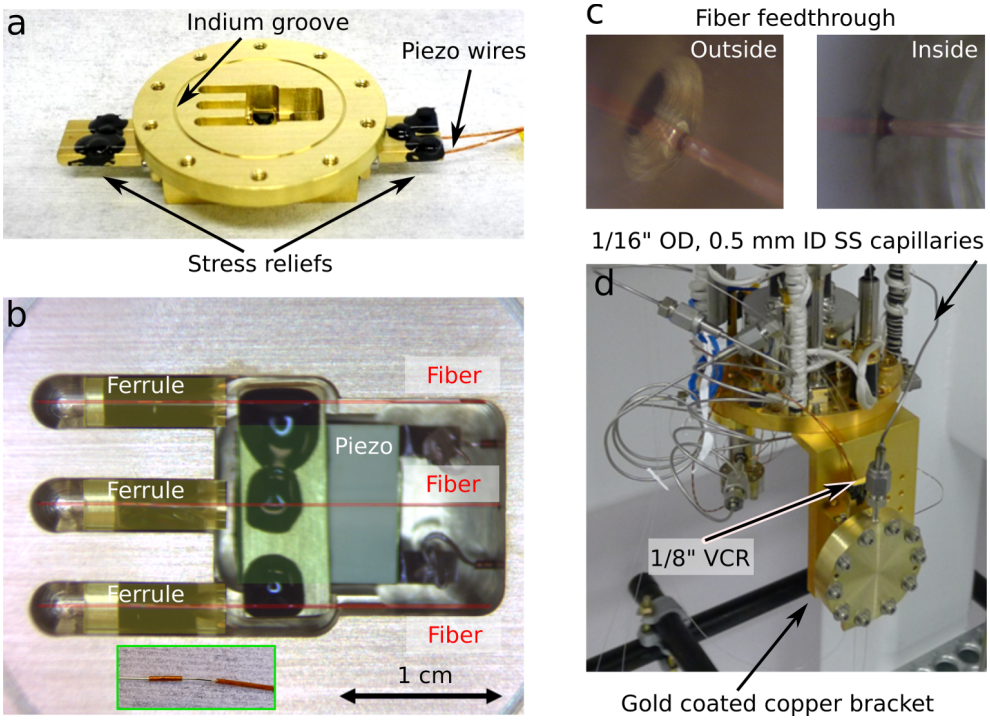

Figure 6.17: The photographs of the first generation device. (a) The cell bottom with the stress reliefs attached. (b) The pocket in the cell bottom. (c) The fiber feedthroughs epoxied with Stycast 1266. The view from the outside of the cell and from the inside the cell. (d) The device mounted on the mixing chamber of the dilution refrigerator. The device was attached to a gold-plated copper bracket.

Once the ferrules and the piezo were epoxied, we built the cavities. We used translation stages to control the fibers and insert them into the fiber holes. It was helpful to send red light into the fiber to make inserting it into the ferrule easier. Even though the cell bottom has been cleaned, it was preferable that fiber faces did not touch the sides of the holes.

The cavities were formed to be longer than the desired cavity length to account for thermal contraction. Since a piezo was involved, the thermal contraction could not be easily calculated. Instead one of the cavities was built and then cooled to 77 K. The 1310 nm light (for which the cavity has low finesse) was incident on the cavity throughout the cool-down. Recording the reflection for 1310 nm light vs. temperature, we were able to count the number of free spectral ranges that the cavity shifted through, thus estimating the cavity length change and then building the other two cavities accordingly. The thermal contraction of the cavities in this device from 300 K to 0 K was 52 μm.

In order to epoxy the fibers, we first confirmed that the part that would be epoxied into a hole was stripped down to glass (for plastic coated fibers which were used in the first generation device, that meant removing plastic by dissolving it in acetone).

We used Stycast 1266[28] to epoxy the fibers into the fiber holes, as it is slightly less viscous, than Stycast 2850FT. Later, we found that using Stycast 2850FT works just as well. We sent the mirrored fibers through the holes, formed the cavities and then put some epoxy on the outside (as shown in figure 6.17(c)). After about 10-15 minutes of waiting, the epoxy was pulled through the hole by the capillary action and formed a meniscus on the inside. The fibers on the side of the piezo were first epoxied to the brass plate, which could be moved to change the cavity length. The cavities were assembled and epoxied one by one.

The fibers can be easily broken, especially since the plastic coating had to be removed from the part of the fiber that is glued into the hole. To prevent fibers from breaking, we needed to epoxy them to something on the outside of the device, so that the fiber leaving that epoxy joint had the plastic coating on it. Therefore we designed the stress reliefs - the brass

[28] Stycast 1266: transparent resin with large thermal expansion coefficient, low viscosity

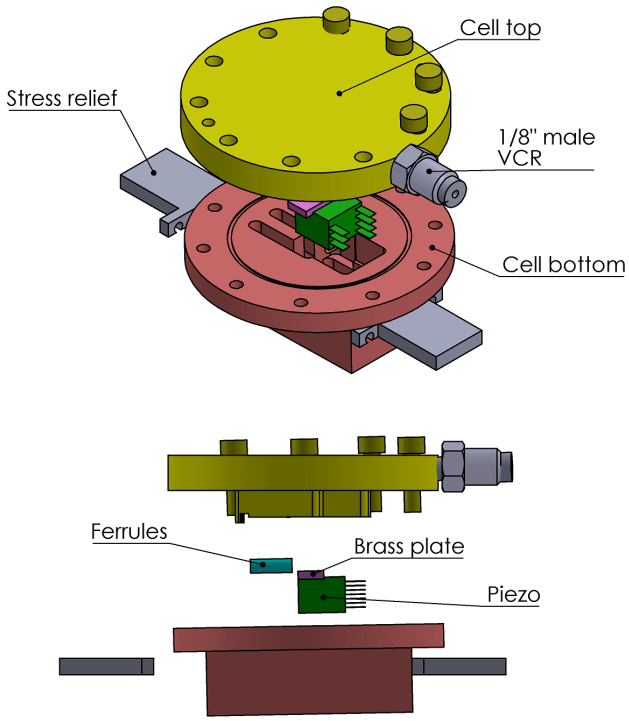

Figure 6.18: The assembly of the first generation device. The ferrules and the piezo were epoxied into the cell pocket. A brass plate was epoxied to the piezo. The cavities were assembled one by one. After all cavities were assembled and epoxied, the stress reliefs were attached. The cell top was attached with an indium seal.

plates which attach to the side of the device immediately under the fiber holes. The stress reliefs were cleaned using acetone and isopropanol. They were attached to the cell after all the cavities were epoxied. The translation stages were used to control the position of the stress reliefs as they were attached. The fibers were then epoxied to the reliefs, as shown in figure 6.19.

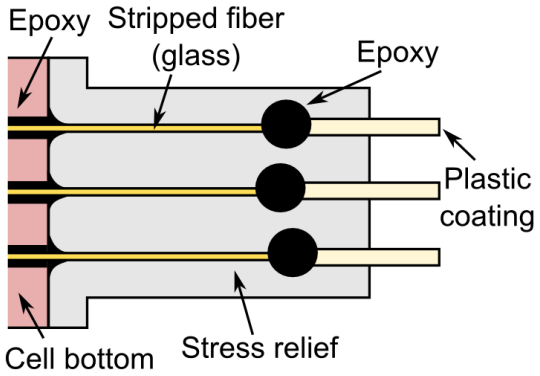

Figure 6.19: The fibers glued to the stress relief. It is necessary that the glue joint is made where so that the fiber leaving the glue joint on the size opposite of the device has plastic coating.

The cell top is machined out of brass as well. A 1/8" VCR is silver soldered to the top as shown in 6.17 (d). The cell top was attached to the cell bottom with an indium seal[29].

The device was then mounted on a gold plated copper bracket (it was not designed for this device, but was a bracket that

[29]When making indium seal, after cutting a piece of indium and cleaning it multiple times with acetone and isopropanol, smear a small amount of vacuum grease (we use Dow Corning 976V) along the indium wire - that will make removing it much easier in the future

we already had), which we attached to the mixing chamber of the dilution refrigerator.

The assembly of the device is shown in figure 6.18. The machine drawings of the cell bottom, cell top, brass plate and stress reliefs are shown in Appendix C.1.

6.3.2 Second generation device

The design of the second generation device is similar to the first generation device, but without a piezo. Stycast 2850 was used for all epoxy joints.

The cell bottom is made out of copper[30] and gold plated to improve thermal conductivity. There are three deep grooves going through the cell bottom, as shown in figure 6.20 (a), and three holes for the fibers on each side. The fiber holes are larger than than in the previous cell. The cell bottom was cleaned in the same way as in the first generation device.

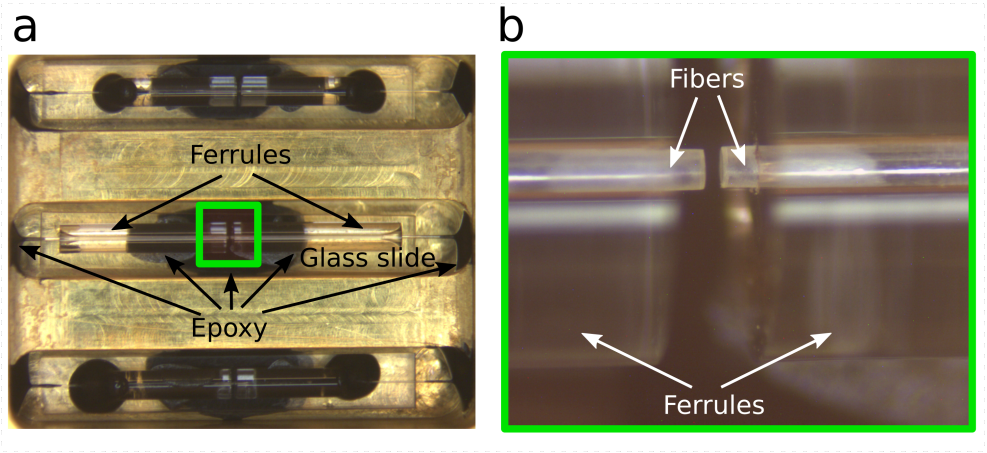

Figure 6.20: The photographs of the second generation device. (a) The grooves in the cell bottom with the glass slide and ferrules epoxied inside. (b) The cavity formed between two ferrules.

The ferrules[31] were epoxied to glass slides[32]. A small amount of epoxy was dropped on the glass slide in two places. A scrap piece of fiber[33] was threaded through the ferrules with the funnels facing away from one another. The two ferrules were then positioned on top of the glass slide with ≈0.5 mm distance between the flat ferrule faces.

After the epoxy is dry, the glass slides were epoxied inside of the grooves as shown in figure 6.20 (a). In order to epoxy the glass slides, a small amount of epoxy was dropped into the middle of the groove and the glass slide was carefully lowered on top of the epoxy. Then a piece of scrap fiber was threaded through both fiber holes and the ferrules that were epoxied to the glass slide. The epoxy was then allowed to dry.

The cavities were formed between the ferrules, as shown in figure 6.20 (b). Making cavities between the ferrules, as opposed to inside a single ferrule improved thermal contact between the device and mixing chamber.

The thermal contraction of the cavities was calculated as follows. The size of the pocket (distance between the inside walls to which the fibers were glued) was 28 mm, the distance betwee the outside walls to which the fibers were glued was 46 mum. Using the data for copper from [88] the expected thermal contraction of the cavity should be between 90 and 120 μm. The fibers would contract as well, making the thermal contraction of the cavity smaller. The thermal contraction of the fibers is estimated from [88] to be between 17 and 27 μm. Therefore the total thermal contraction was estimated to be between 73 μm and 93 μm. The cavity was built to be 90 μm longer than the desired length. The thermal contraction was measured to be 94 μm.

[30] All copper that we used was oxygen-free high thermal conductivity (OFHC) copper

[31] Polymicro, Custom $ID = 205 \pm 3$ μm; $L = 10$ mm; $OD = 1.8$ mm

[32] Howard Glass, SB-500502, Schott borofloat glass cut into 0.90" length, 0.13" width, 0.088" thickness.

[33] It is important to use the scrap fiber **without** carbon coating. Additionally carbon coating needs to be removed for all vacuum tight epoxy joints

The epoxy procedure for the cavities was similar to the first-generation device. Two of the cavities (top and bottom in figure 6.20) additionally had the fibers epoxied directly to the ferrules, which allowed to minimize thermal contraction. Since the fiber holes were larger, the epoxy was not pulled through the fiber holes through the fiber hole by the capillary action, and we added some epoxy inside of the cell, as can be seen on the left and right side of figure 6.20(a).

The stress-reliefs are made out of brass and are longer than in the previous device to accommodate longer fibers.

The cell top is made out of copper and gold plated as well. It is attached to the cell bottom using an indium seal.

The assembly of the device is shown in figure 6.21.

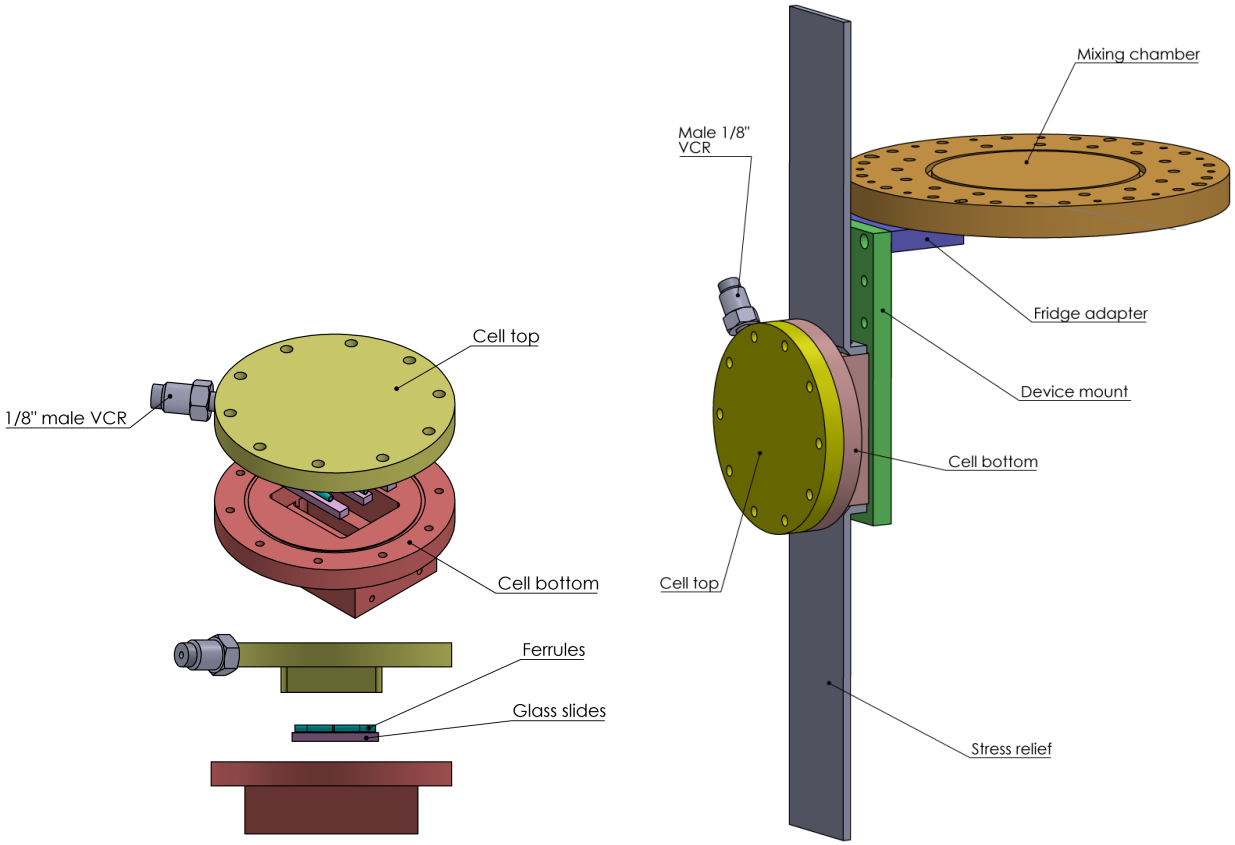

Figure 6.21: Right: The assembly of the second generation device. The ferrules were epoxied to glass slides. The glass slides were epoxied to the bottom part of the cell. After the cavities were assembled and epoxied, the stress reliefs were attached (not shown)). The top of the cell was attached with the same indium seal as in the previous device. Left: The device mounted on the mixing chamber of the dilution refrigerator.

Additionally, we designed an appropriate mount and adapter to attach the device to the mixing chamber of the dilution fridge. The mount and adapter are made of copper and gold plated. The mounting of the device to the mixing chamber is shown in figure 6.21.

The machine drawings of the cell bottom, cell top, stress reliefs, device mount and fridge adapter are shown in Appendix C.2.

6.3.3 Third generation device

The third generation device was built to be able to partially fill a cavity with liquid helium. It can be shown (see Chapter 9) that the cavity needs to be at least 260 μm long in order to be able to partially fill it (due to surface tension of liquid

helium).

A few design improvements have been made. First, since copper was not ideal for drilling narrow holes, the cell bottom was made out of brass. Gluing fibers into narrow holes means that epoxy is more likely to wick through to the inside of the puck, ensuring a better seal. However, since the brass has lower thermal conductivity than copper, in order to maximize thermal conductivity, a new top was machined out of copper and gold plated. The top was machined so that it could attach to the device mount, instead of the bottom piece, as shown in figure 6.22.

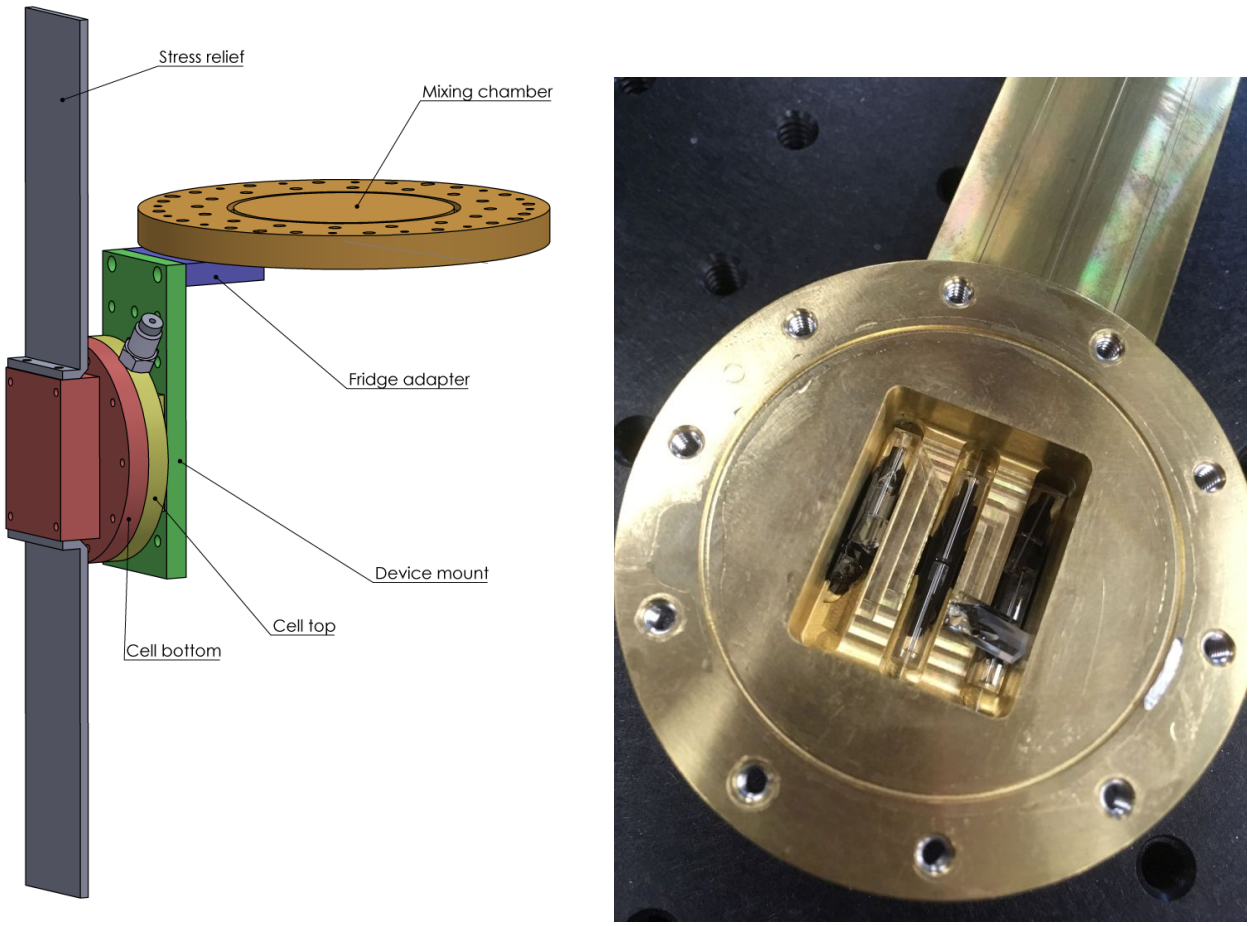

Figure 6.22: Left: The third generation device mounted on the mixing chamber of the dilution refrigerator. The device is now attached using the cell top. Right: The broken glass slides of the third generation device.

The machine drawings of the new cell top are shown in Appendix C.3. The cell bottom and stress reliefs design was the same as in the second generation device. The mount and adapter were reused from the second generation device.

Unfortunately, two cavities broke due to thermal contraction, as shown on the right of image 6.22 and one possibly got misaligned during the cool-down. The cavities broke because there was too much epoxy under the glass slide. The glass slide was effectively anchored to the brass cell in multiple points. Since the brass contracted more than the glass, the slide was broken.

6.3.4 Fourth generation device

In the previous device, we found that building long cavities between two ferrules epoxied to a glass slide was not optimal, since thermal contraction of epoxy could lead to misalignment of the ferrules and therefore the cavity fibers. We ordered

long ferrules[34] and had holes drilled into them[35] as shown in figure 6.23.

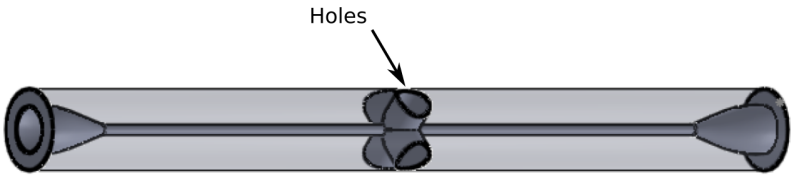

Figure 6.23: The ferrule that is used in the fourth and fifth generation device.

Additionally we addressed the issue of thermal contraction which broke the glass slides by making the cell bottom out of Invar and adding two new indentations around the center, as shown in figure 6.24 to prevent epoxy from leaving the central island and spreading on the glass slide.

The assembly of the cavities was similar to the previous device: the long ferrules were first epoxied to the glass slides. The glass slides were epoxied inside the grooves.

The stress reliefs were modified as well, as shown in figure 6.24. This was done to make attaching them easier (previously, the attachment points were very close to the fiber epoxy joints). The new stress reliefs were machined out of Invar as well.

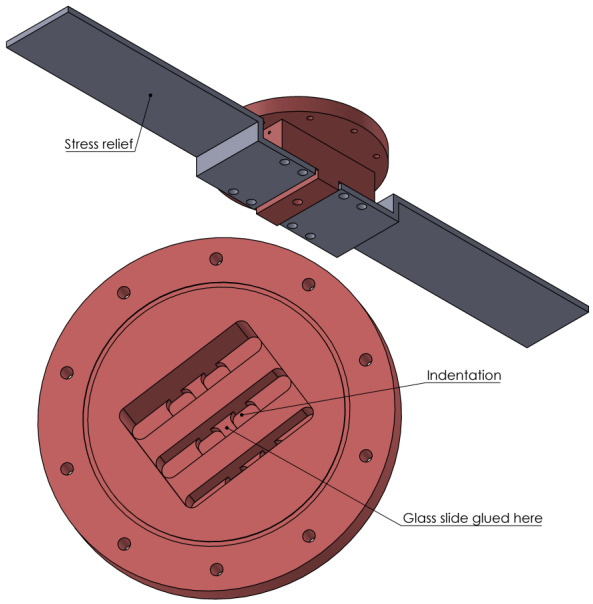

Figure 6.24: The assembly of the fourth generation device

The machine drawings of the new cell bottom and stress reliefs are shown in Appendix C.4. The cell top, the device mount and the fridge adapter were reused from the previous device.

Unfortunately, due to large differential thermal contraction between invar and Stycast 2850FT, leaks in the fiber epoxy joints opened up at 77 K. We tried warming up the device and fixing the leaks using vacuum grease, as suggested by [138]. While vacuum grease fixed the leaks at room temperature, the leaks opened up again upon the successive cool-down to 77 K.

[34] Polymicro TQN2053000, $ID = 205 \pm 3\ \mu m$, $L = 20.0 \pm 0.5$ mm; $OD = 3000 \pm 30\ \mu$m

[35] Optek Systems drilled the holes

6.3.5 Fifth generation device

This is the device that is currently being built. The device is still made out of Invar, to avoid thermal contraction. However, we have found that large differential thermal contraction of Invar and Stycast 2850 results in leaks, so we had to redesign the way fibers were epoxied into the cell bottom. Instead of simply gluing fibers into a drilled hole as we did previously (shown on the left of figure 6.25), we now drill a larger hole. Into this hole we silver solder a long thin-walled stainless steel tube[36]. We choose the length of the tube to be ≈ 5 cm. We bend the tube slightly ($\approx 10°$). The bending is necessary, so that when the tube contracts the fiber buckles in a predictable manner.

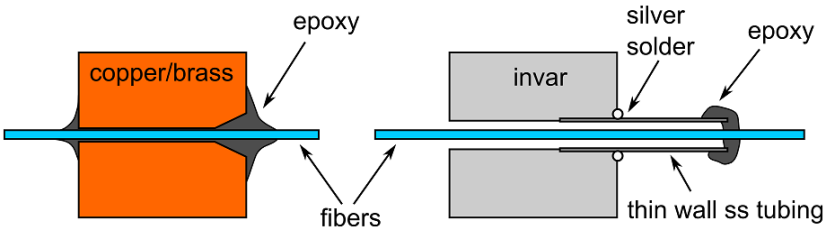

Figure 6.25: Left: the fiber feedthrough used in all prior devices devices. Right: the proposed feedthrough for the fifth generation device.

Since the fibers are epoxied to the tubes, we need to anchor them inside of the cell as well. That lead us to making small anchor points as shown in figure 6.26

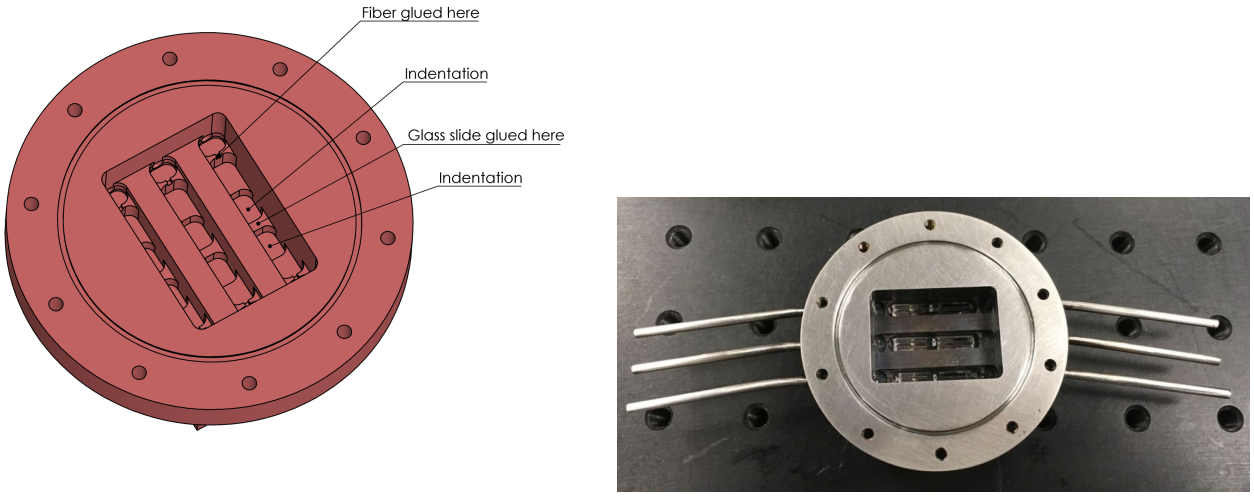

Figure 6.26: The modifications done to the fifth generation device. Right: Fiber anchors are added. Left: The tubes are silver soldered to the device

The stress reliefs were also modified to be wider, to accommodate for the bend in the tubes.

The machine drawings of the new cell bottom and stress reliefs are shown in Appendix C.5. The cell top, device mount and fridge adapter are re-used from the previous device.

[36] McMaster 5560K29, 0.095" OD, 0.005" wall thickness

6.4 Dilution refrigerator

The dilution refrigerator[37] is built by Janis Research Company. We have done two modifications to it:

1. Added plumbing for helium
2. Added fiber feedthroughs

In this section I will describe those modifications.

6.4.1 Experimentall Gas Handling System (expGHS)

The experimental gas handling system is used to prepare helium that will later fill the device. The schematics of expGHS is shown in figure 6.30.

The helium regulator[38] is a single stage high purity gas regulator, with an outlet gauge of up to 2 bar. The valves immediately next to the helium regulator are Swagelok bellow-sealed valves[39].

The panels[40] (shown in figure 6.27 and in figure 6.30 using gray squares outlined with black dashed lines) were designed by Lilian Childress and manufactured by Applied Energy Systems. The cold trap was made in Yale machine shop by bending 1/4" stainless steel tube as shown in figure 6.29 and inserting it into a 25 liter storage nitrogen dewar[41]. The pressure gauges were purchased from MKS[42]. They are a combination Pirani and piezo gauge, which allows them to have large sensitivity range.

The relief volume (2 L) is stainless steel cylinder with KF25 fitting soldered to the top of it. It is shown in figure 6.28. It was manufactured at Yale machine shop.

6.4.2 Helium plumbing inside the fridge

The helium plumbing of the dilution refrigerator is shown in figure 6.31. The ceramic break[43] is used to electrically isolate the fridge from the expGHS. The valve, shown below the break, is usually open, though sometimes we close it during leak checking. The vacuum feedthrough[44] is used to deliver helium into the IVC. The tubing used inside the IVC is thick (1/8" OD, 2.5 mm ID) stainless steel tubing from room temperature down to 4 K and thin (1/16" OD, 0.5 mm ID) stainless steel tubing past 4 K. The two capillaries are connected using a reducing adapter[45]. The reason for using two different size capillaries is that impurities will freeze at 4 K, and it is preferable that they freeze is a larger tube to prevent clogging of thinner tubing. On the other hand, the thermal link between different stages of the dilution refrigerator need to be minimized, which is why the thinner tubing is used. The tubing is thermalized at all stages of the fridge by wrapping it around copper heat sinks, as shown in figure 6.32. At the mixing chamber of the fridge the capillary is attached to a sintered-silver heat exchanger (see Appendix C.6 for machine drawings). The helium goes through the heat exchanger, comes out on the other side and goes through a 1/8" VCR female cross, which is used to be able to attach multiple devices. After the cross, the helium goes into the device.

[37] Janis DR500
[38] McMaster 7951A14
[39] Swagelok SS-4H2
[40] Applied Energy Systems, custom made
[41] International Cryogenics IC-35DX
[42] MKS 974 and MKS 910
[43] Kurt J. Lesker CFT06C0311
[44] LDS NW25xVCRM25-ST
[45] Swagelok SS-2-VCR-7-4VCRF

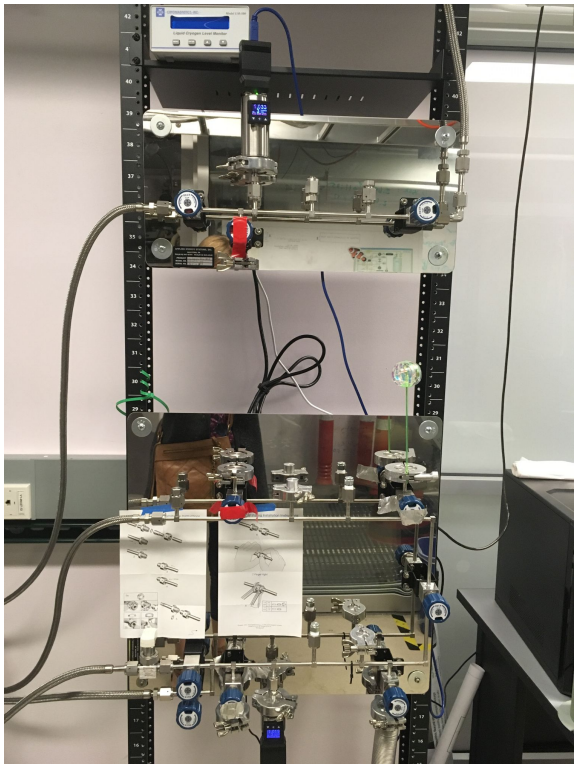

Figure 6.27: The experimental gas handling system photograph. The panels designed by the AES panels.

Figure 6.28: Helium pressure relief volume.

Figure 6.29: Nitrogen cold trap.

6.4.3 Filling the device

Helium is delivered from the ultra-high-purity (UHP) helium gas bottle in doses. When filling device we usually follow the steps below:

1. Fill the large volume (shown in green) at ≈ 1000 mbar, using the bottom pressure gauge to measure the pressure
2. Open the valve to allow helium into the giant volume (shown in purple).
3. Let helium sit in the giant volume for ≈ 1 minute. This is to ensure the impurities freeze in the nitrogen cold trap.
4. Let helium into the fridge, wait for ≈ 3 minutes.
5. Repeat steps 1-4 until the device is full, or we have to leave the system unattended.
6. Open the valve leading to the relief volume, so that in the event of unexpected helium boil-off, the helium pressure does not rise above 1 atm.

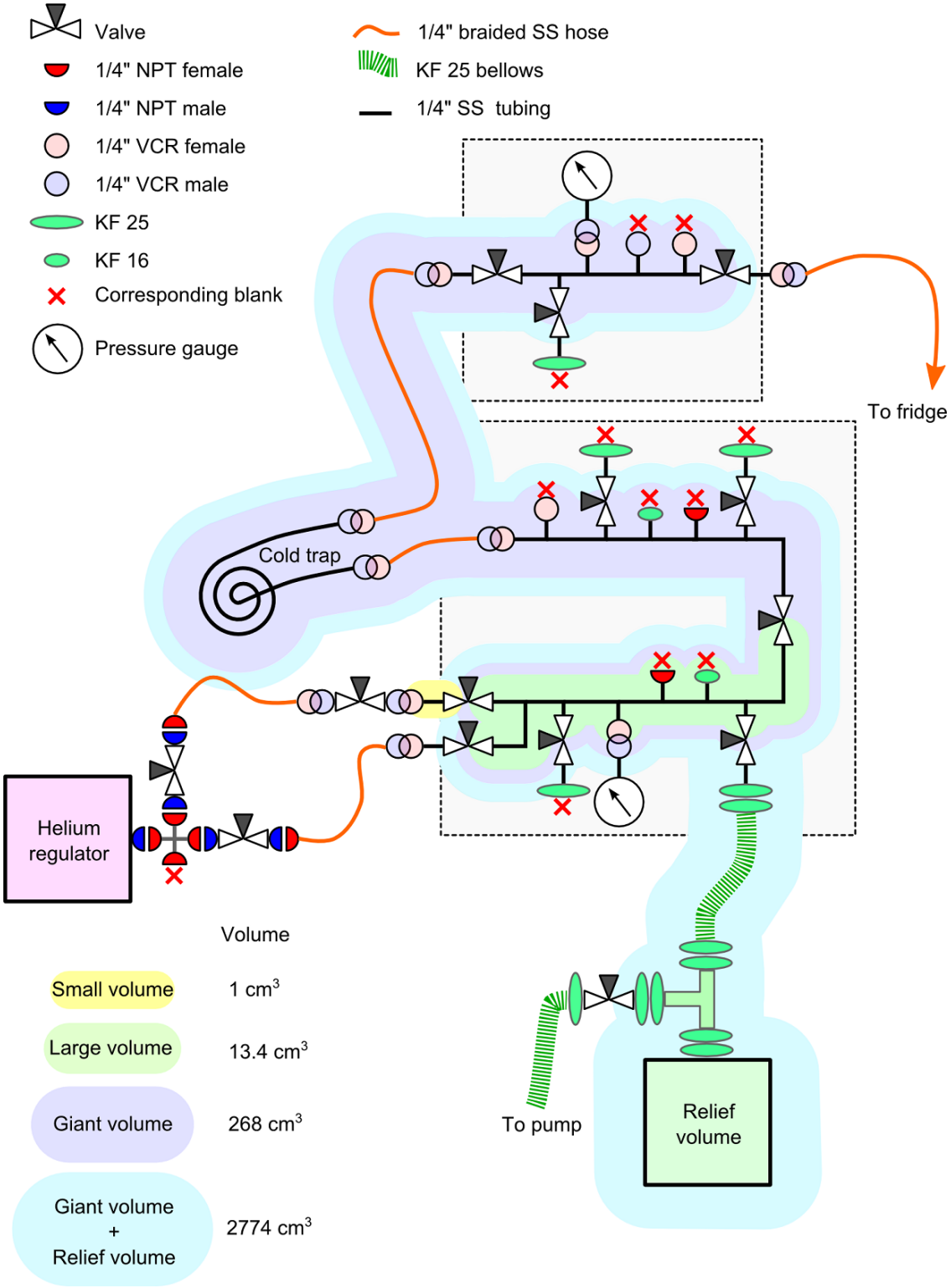

Figure 6.30: The experimental gas handling system schematics. Different colors indicate different volumes of helium.

It could also be possible to measure out the helium beforehand and let it all in at once, however that is more likely to result in impurities clogging the insides of the capillaries.

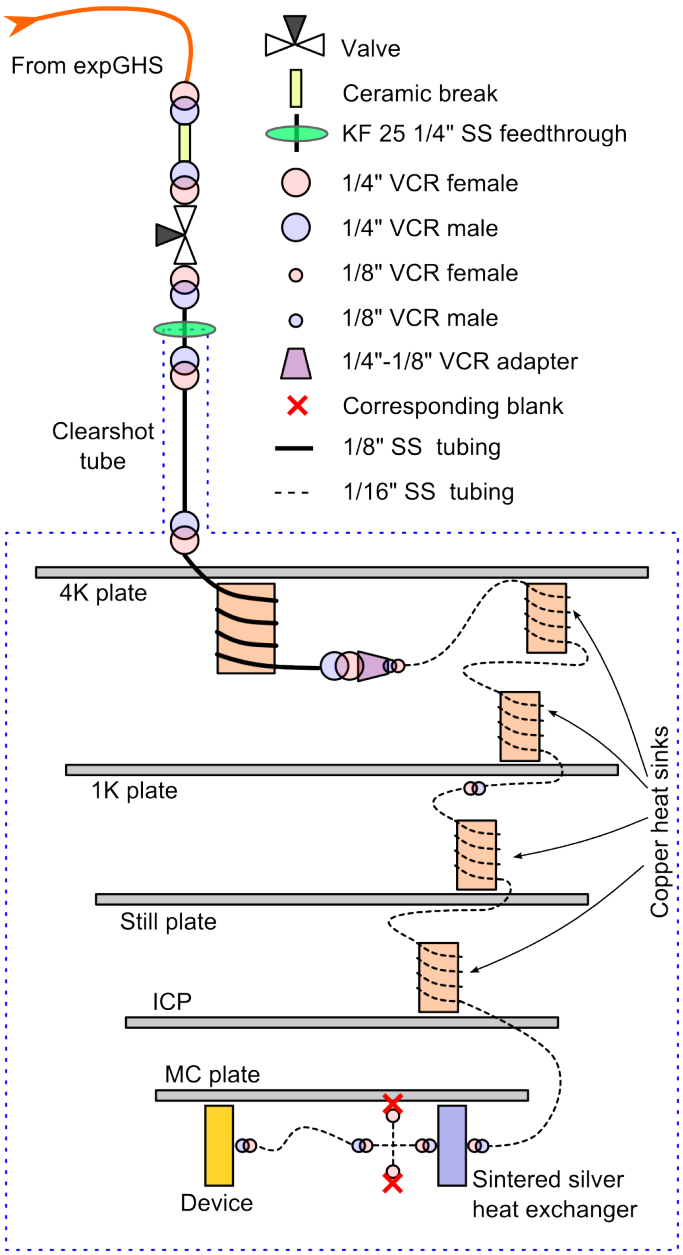

Figure 6.31: Helium plumbing of the dilution refrigerator.

6.4.4 Leak checking the plumbing and the device

Once the device is mounted on the MC and connected to the helium plumbing the system is checked for leaks. There are two ways a leak check can be performed. A leak detector[46] is used in both situations.

- Use the leak detector to pump on the expGHS, blow small amounts of helium on the device and the VCR connectors. This allows one to detect large leaks, however the small leaks may go undetected due to variations of the leak detector background.
- After the inner vacuum chamber (IVC) of the dilution refrigerator is attached, the leak detector is pumping on the IVC until the background is constant and $\leq 1 \times 10^{-9}$ Torr $\cdot$ l/s. Then a controlled amount of helium (usually

[46] Pfeiffer QualyTest

a large volume) is added to the expGHS and travels down to the device. If the leak rate stays constant for $\approx$ 20 minutes, there are no leaks. This is the way the device is tested for leaks at 77 K as well.

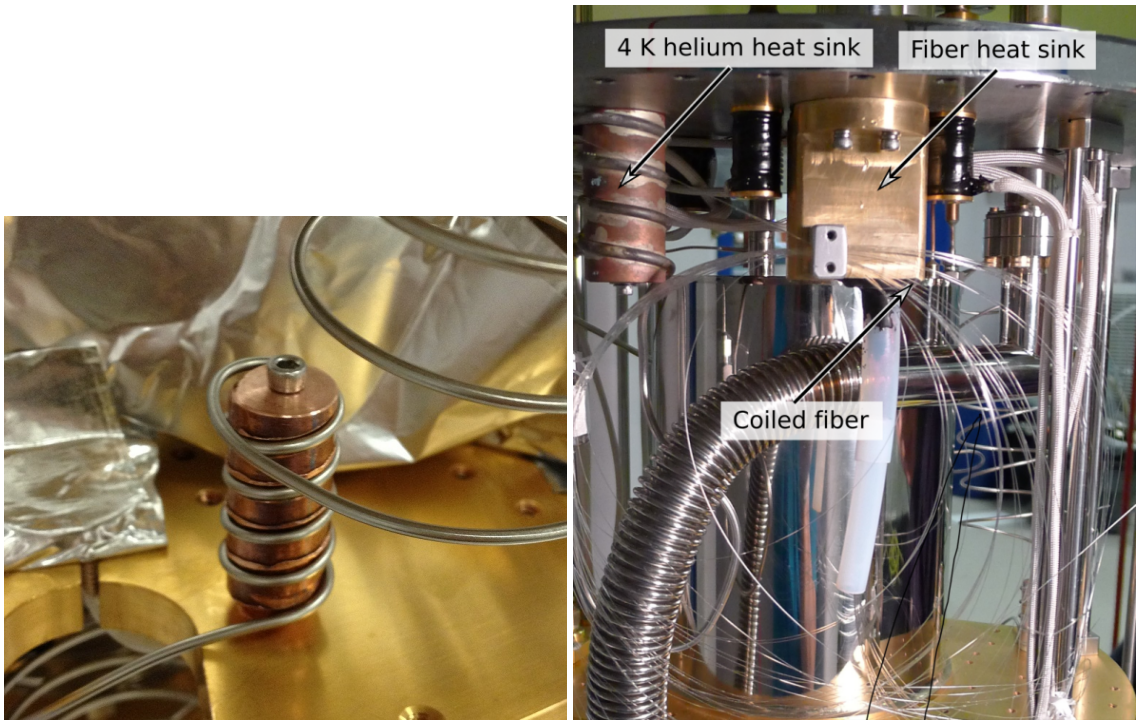

Figure 6.32: Left: Copper heat sink used to thermalize helium to the stages of the dilution refrigerator. Right:Fiber heat sink and helium heat sink at 4 K

6.4.5 Fibers in the dilution refrigerator

The room temperature fiber feedthrough is a plate with an array of 12 holes each 0.014 in diameter. A section of a fiber is stripped of plastic coating and epoxied into the hole using Stycast 2850FT epoxy. The plate design is shown in Appendix C.7. It was designed by Nathan Flowers-Jacobs. A large plastic tube is glued to both sides of the plate and filled with epoxy to prevent the fibers from breaking.

The fibers are heat-sunk at 4 K to reduce the heat load on the mixing chamber. The heatsink is a piece of brass with a large hole drilled through the middle and a couple of screw holes to attach it to the 4K plate. To heatsink the fibers we send them through the hole in the brass piece, without removing their plastic coating, and then fill the hole with Stycast 2850FT. The photo is shown in figure 6.32 (right). The machine drawing is shown in Appendix C.8.

After the device is mounted, the fibers are spliced to the device fibers. The fiber has a lot of slack between the fiber heatsink and the device, so that thermal contraction of parts of the dilution refrigerator would not damage the fiber.

6.5 Measurement setup

The purpose of this section is to describe the experimental setup used in the experiment. The measurement setup evolved over time, so in this section I will only describe the latest iteration of the setup, which was used to measure the second generation device. I will use the values for the mechanical frequency from the second generation device as well. A schematic of the setup (not including filters, amplifiers and attenuators) is shown in figure 6.33. A more detailed description of the measurement setup can be found in [128].

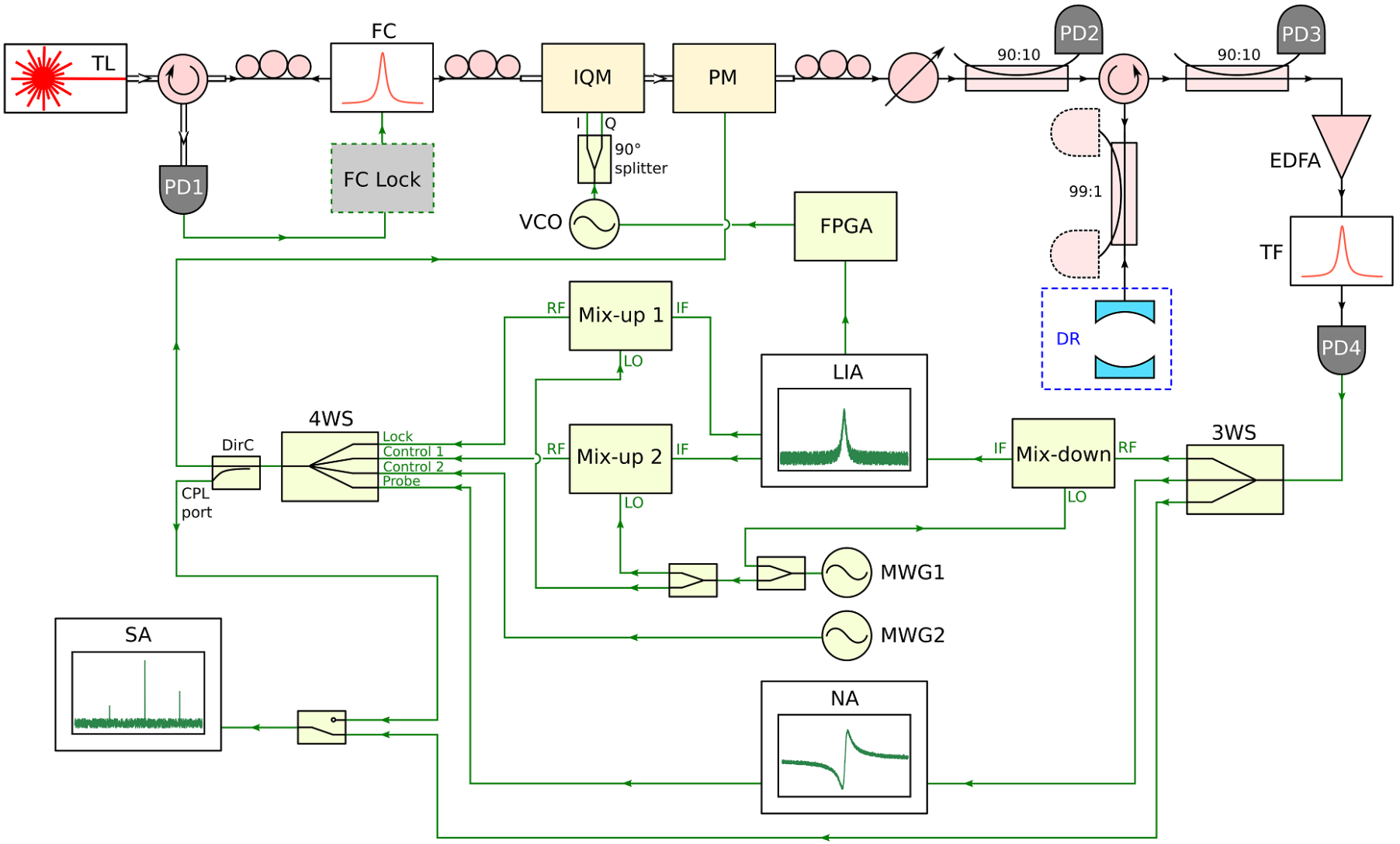

Figure 6.33: Measurement setup. SM fiber: black line. PM fiber: double black lines. Electrical path: green lines. TL: tunable laser. FC: filter cavity. FC Lock: locking circuit for the filter cavity. IQM: IQ-modulator. PM: phase modulator. PD: photodiode. EDFA: erbium doped fiber amplifier. TF: tunable filter. DR: dilution refrigerator. 3WS: three-way splitter. NA: network analyzer. LIA: lock-in amplifier. SA: spectrum analyzer. MWG: microwave generator. FPGA: field programmable gate array. VCO: voltage controlled oscillator. 4WS: four-way splitter. DirC: directional coupler.

6.5.1 Optical setup

Light is produced by a tunable laser (TL)[47] and passes through a circulator and a filter cavity (FC)[48]. The reflection from the FC is used to lock it to the frequency of the TL. Light transmitted through the FC passes through an IQ-modulator (IQM)[49] operating in the single sideband suppressed carrier mode. The IQM serves as a frequency shifter to lock the laser to the experimental cavity. The exact locking procedure is described in [128]. The tone generated by the IQM is used as a local oscillator (LO) for the heterodyne detection.

After the IQM, the frequency-shifted light passes through a phase modulator (PM)[50]. The PM is driven by up to four different tones, originating from four microwave sources described in section 6.5.2.1. Each of these tones produces sidebands on the LO. The beams incident on the cavity during different measurements are shown in figure 6.34. The relative power in all the sidebands as a function of the microwave signals driving the phase modulator was calibrated as described in section 6.5.3.

The light then goes through a variable attenuator. A 90:10 splitter sends 90% of light to the experimental cavity via a circulator; the remaining 10% is monitored using a photodiode (PD2) to record the incident power. The power incident on the cavity and reflected from the cavity is calibrated using a 99:1 splitter immediately before the dilution refrigerator (DR)[51], as described in section 6.5.3.1. The light reflected from the cavity passes through the circulator and another 90:10 splitter, which sends 10% of the power onto a PD3 and 90% towards an Erbium Doped Fiber Amplifier (EDFA)[52], which amplifies the optical signal by a factor of 20-50 and adds ≈ 4 dB noise. The noise figure of the EDFA was calibrated as described in section 6.5.3.5.

The light leaving the EDFA goes through a broadband tunable filter (TF)[53], which is used to suppress the amplified spontaneous emission (ASE) noise from the EDFA. The filtered light then lands on a photodiode (PD4)[54].

6.5.2 Microwave setup

It is convenient to separate the microwave setup into the generation part and the detection part.

6.5.2.1 Generation

Up to 4 microwave are tones used to drive the phase modulators:

- The Lock beam is used to lock the laser to the experimental cavity. The beam is generated using a lock-in amplifier (LIA)[55]. A tone at 200 MHz from the LIA is sent to a mix-up circuit. There it is mixed with a tone from a microwave generator (MWG1)[56] at 1,900 MHz. The mixed-up tone at $\omega_{\mathrm{Lock}} = 2,100$ GHz is sent to the four-way splitter (4WS) where it is combined with other tones and then sent to the phase modulator. The large ω_{Lock} is desirable because the LO should be far detuned from the cavity. That minimizes optical heating of the device by the LO.
- The upper Control (U) signal is used to generate one of the control beams. It is generated by the LIA at $\omega_{\mathrm{Lock}} + \omega_{\mathrm{m}} + \Delta_{\mathrm{Lock,cav}} + \omega_{\epsilon} - \omega_{\mathrm{MWG1}} = 2\pi \times 529.343$ MHz, where $\omega_{\mathrm{m}}/2\pi = 319.243$ MHz is the frequency of the acoustic mode, $\Delta_{\mathrm{Lock,cav}}/2\pi = 10$ MHz is the detuning of the Lock beam from the cavity resonance, $\omega_{\epsilon}/2\pi = 100$ kHz is

[47] Pure Photonics PPCL200
[48] MicronOptics FFP-TF, $\kappa/2\pi = 30$ MHz, $\omega_{\mathrm{FSR}}/2\pi = 15$ GHz
[49] EOspace QPSK modulator IQ-0DKS-25-PFA-PFA-LV-UL
[50] EOSpace phase modulator PM-0KS-10-PFA-PFAP-UL
[51] Janis DR500
[52] Nuphoton EDFA-CW-LNF-RS-10-40-FCA
[53] OzOptics TF100, 0.5 nm bandwidth
[54] Thorlabs DET08CFC
[55] Zurich Instruments UHF
[56] Vaunix Lab Brick LMS-232D

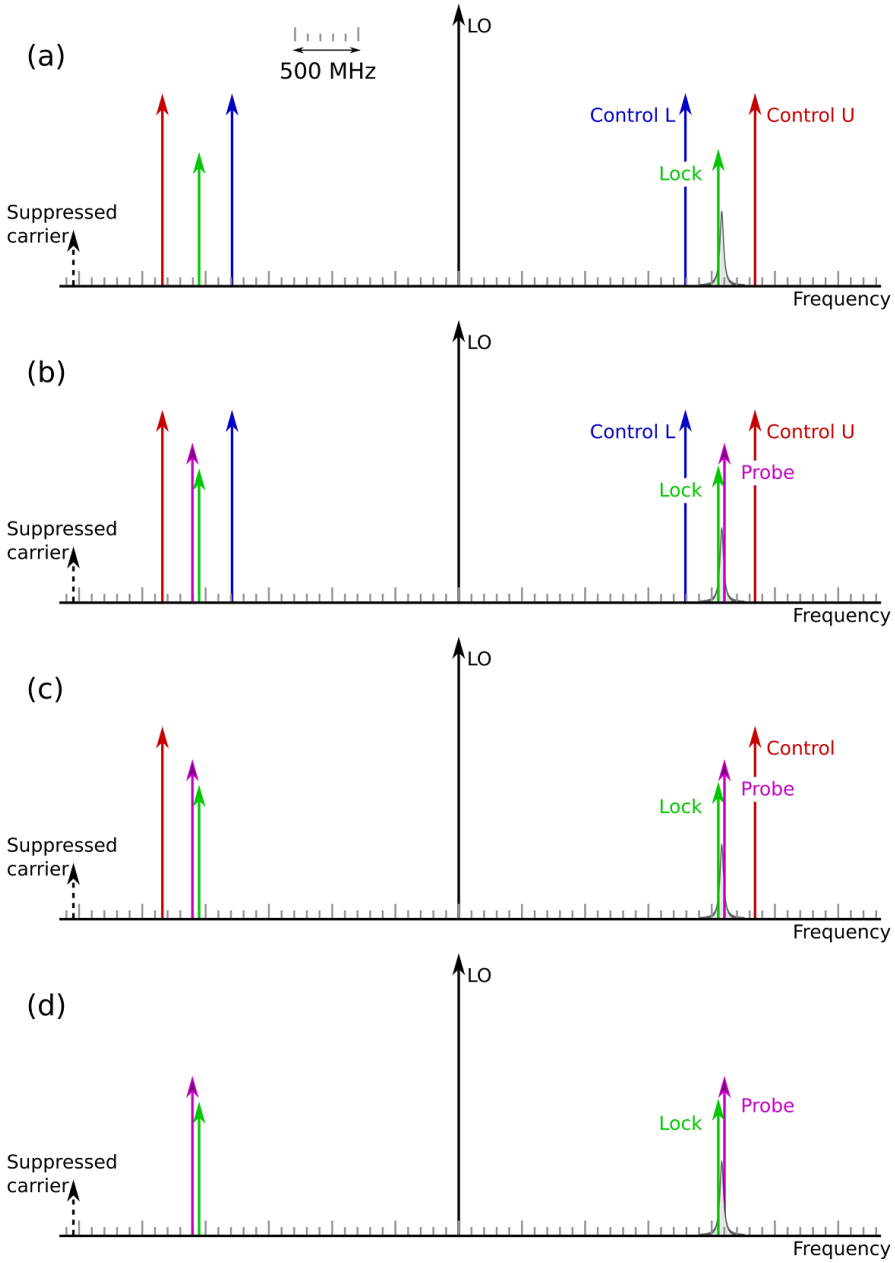

Figure 6.34: Beams incident on the cavity. The horizontal axis is to scale. The suppressed carrier is shown with a dashed line. The phase modulator adds beams on both sides of the LO. The laser is locked to the cavity using one of the lock beams. The cavity lineshape is shown in gray. (a) During the thermal motion measurement. The phase modulator adds 2 control beams and a lock beam. (b) During the OMIT/A measurement done after each thermal motion measurement. The phase modulator adds 2 control beams, a probe beam and a lock beam. The probe beam is first detuned by $+\omega_{\mathrm{m}} \pm \delta$, from the lower control beam and then by $-\omega_{\mathrm{m}} \pm \delta$ from the upper control beam control beam, where $\delta/2\pi = 50$ kHz. (c) During the OMIT/A measurement done to extract optomechanical coupling. The phase modulator adds a control beam, a probe beam and a lock beam. The probe beam is detuned by $\pm\omega_{\mathrm{m}} \pm \delta$ kHz from the control beam and the control beam detuning from the cavity varies between $-\omega_{\mathrm{m}} - 3\kappa$ to $+\omega_{\mathrm{m}} + 3\kappa$. (d) During cavity measurement. The phase modulator adds a probe beam a lock beam. The probe beam detuning varies from $\omega_{\mathrm{Lock}} - 8\kappa$ to $\omega_{\mathrm{Lock}} + 8\kappa$.

half of the desired separation between red and blue sidebands. This tone is mixed with the signal from MWG1 at $\omega_{\mathrm{MWG1}}/2\pi = 1,900$ MHz. The mixed up signal at $\omega_{\mathrm{Control(U)}} = \omega_{\mathrm{Lock}} + \omega_{\mathrm{m}} + \Delta_{\mathrm{Lock,cav}} + \omega_{\epsilon} = 2\pi \times 2,429.343$ MHz is sent to the 4WS.

- The lower Control (L) signal is used to generate the other control beam. It is generated directly by a different microwave generator (MWG2)[57] at $\omega_{\mathrm{Control(L)}} = \omega_{\mathrm{Lock}} - \omega_{\mathrm{m}} + \Delta_{\mathrm{Lock,cav}} - \omega_{\epsilon} = 2\pi \times 1,790.657$ MHz.
- The Probe signal is only on for the OMIT/A measurements. It is generated by the network analyzer (NA)[58] at a frequency $\omega_{\mathrm{Control(U,L)}} \pm \omega_{\mathrm{m}} \pm \delta$, where $\delta/2\pi = 50$ kHz.

The signal out of the 4WS is split and a small portion is sent to a spectrum analyzer (SA)[59], where the spectrum is recorded. This is done to measure the power in all the microwave tones incident on the PM.

For the thermal motion measurements the control beams and the locking beam are on, as shown in figure 6.34(a). The control signals are filtered with high pass filter for the upper control beam and low pass filter for the lower control beam. The filters are used in order to block microwave noise that would produce laser noise near the cavity resonance frequency.

Some OMIT/A measurements are done in the same configurations as thermal motion measurements with the only addition being the probe beam as shown in figure 6.34(b). Those measurements are important for phonon number calibration and are described in section 6.6.4.

For the the other OMIT/A measurements, the lock beam, the probe beam and only one control beam are on, as shown in figure 6.34(c). The frequency of the control beam is changed over a large range. The probe beam frequency is chosen to be $\pm\omega_{\mathrm{m}} \pm \delta$ away from the control beam. Those measurements are done to extract the optomechanical coupling and observe the dynamical back-action effects.

Finally, in order to extract cavity detuning, only the lock beam and the probe beam are on as shown in figure 6.34(d). For these measurements the probe beam is swept over the cavity resonance frequency.

The typical optical powers in the measurements are:

- $P_{\mathrm{Control(U)}} \approx P_{\mathrm{Control(L)}} \approx (0.1 - 0.2)P_{\mathrm{total}}$
- $P_{\mathrm{Lock}} \approx 10^{-6} P_{\mathrm{total}}$
- $P_{\mathrm{Probe}} \approx 10^{-5} P_{\mathrm{total}}$
- $P_{\mathrm{LO}} \approx (0.6 - 0.8)P_{\mathrm{total}}$

The total incident power P_{total} is between 20 μW and 120 μW.

6.5.2.2 Detection

A heterodyne detection scheme is used in all measurements. The signal from the PD is sent through an amplifier, a bias tee (which is used to filter out the DC signal), and a low pass filter with 4 GHz bandwidth, which does not influence the signal but removes some high frequency noise. The remaining signal consists primarily of beating between the LO (which was reflected from the cavity without interacting with it) and the sidebands. These beat notes occur at $\omega_{\mathrm{Lock}}/2\pi = 2,100$ MHz, $\omega_{\mathrm{Control(U)}}/2\pi = 2,429.343$ MHz, $\omega_{\mathrm{Control(L)}}/2\pi = 1,790.657$ MHz, and the motional sidebands of the control beams at $\omega_{\mathrm{Control(U)}} - \omega_{\mathrm{m}} = 2\pi \times 2,110.1$ MHz and $\omega_{\mathrm{Control(L)}} + \omega_{\mathrm{m}} = 2\pi \times 2,109.9$ MHz. If the probe beam is one, there are also a beatnote at $\omega_{\mathrm{Probe}}/2\pi$. The signal is then sent to a three-way splitter (3WS), which splits it into three parts:

[57] Vaunix Lab Brick LMS-232D
[58] Keysight HP 8722D
[59] Rigol DSA1030A

1. The first part is mixed down with the signal from MWG1 (at ω_{MWG1}). During the thermal motion measurements, the mixed-down signal is dominated by 5 frequencies: $\omega_{\mathrm{Lock}} - \omega_{\mathrm{MWG1}} = 2\pi \times 200$ MHz (Lock), $\omega_{\mathrm{Control(U)}} - \omega_{\mathrm{MWG1}} = 2\pi \times 529.343$ MHz (Control (U)), $\left|\omega_{\mathrm{Control(L)}} - \omega_{\mathrm{MWG1}}\right| = 2\pi \times 109.343$ MHz (Control(L)), and $\omega_{\mathrm{Control(L,U)}} \pm \omega_{\mathrm{m}} = 2\pi \times (210 \pm 0.1)$ MHz (motional sidebands of the control beams). It is sent to the LIA, where the spectra at $210 + 0.1$ MHz and $210 - 0.1$ MHz are recorded. The quadratures of the signal at 200 MHz are sent to a field programmable gate array (FPGA)[60], which uses them to generate an error signal, which is then sent to the voltage controlled oscillator (VCO) to vary its output frequency between 3 GHz and 3.5 GHz in order to lock the laser to the experimental cavity. Since the Lock beam is typically detuned by ≈ 10 MHz from the cavity resonance, as indicated in figure 6.34, both motional sidebands are near cavity resonance.

2. The second part is sent to the NA. It gives the amplitude and phase of the beatnote at the probe beam frequency when the probe beam is on (i.e. for OMIT/A measurements and the cavity resonance measurement).

3. The third part is sent to the SA to record the spectrum of the light coming from the experimental cavity.

6.5.3 Calibrations

This section describes the calibration measurements. The power incident on the cavity is found as the geometric mean of the incident and reflected powers measured at the 99:1 splitter. After the filter cavity, the laser light is found to be shot noise limited at 300 MHz for powers less than ≈ 1 mW. To measure the laser phase noise, the technique described in [139, 128] was used. Since the powers in the control beams are at most $10 - 20$ μW, and the LO is 2.1 GHz away, the classical laser noise is expected to be at most a few percent of the shot noise.

6.5.3.1 Power calibrations

During the experiment we measure the voltage output by PD1[61] and PD2[62]. In order to convert those voltages into powers incident on the cavity, we measure powers at the outputs of 99:1 splitter (which has already been calibrated) using a powermeter[63]. We first measure the voltage on both detectors with the laser off (that is V_{dark} – the dark voltage of the detector). Then we turn the laser on and use an attenuator to change the power incident on the cavity. For each laser power we measure the power P at both outputs of the 99:1 splitter as well as the voltages V generated by the PD1 and PD2. The ratio $(V - V_{\mathrm{dark}})/P$ gives the photodetector gain.

6.5.3.2 Calibration of the phase modulator

The relative optical power in the beams after the phase modulator is calibrated using the setup shown in figure 6.35. Light from the TL passes through the PM and a tunable cavity (TC)[64], which acts as an optical spectrum analyzer; the light transmitted through the TC lands on the PD. The PM is driven by a microwave generator (MWG)[65] with varying frequency and power. The SA records the power in the CPL port of the directional coupler (DirC), which is used in the actual experiment. The TC length is swept by applying a triangle wave from the arbitrary wave generator (AWG) to piezoelectric elements within the TC. The TC transmission is fit to a Lorentzian with two sidebands:

$$f(x) = \frac{E_0}{x^2 + (\kappa/2)^2} + \frac{E_1}{(x - d_{\mathrm{sb}})^2 + (\kappa/2)^2} + \frac{E_1}{(x + d_{\mathrm{sb}})^2 + (\kappa/2)^2} \tag{6.38}$$

[60] National Instruments FPGA NI PXI-7854R
[61] Thorlabs PDA10CF
[62] Thorlabs PDA10CF
[63] Thorlabs PM100D
[64] Homebuilt, $\kappa/2\pi = 200$ MHz, $\omega_{\mathrm{FSR}}/2\pi = 1.5$ THz
[65] Agilent N9310A

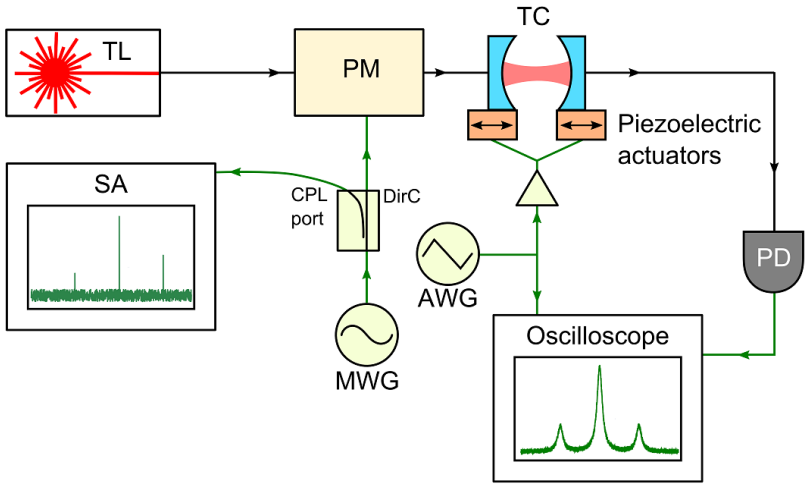

Figure 6.35: Calibration of the phase modulator. SM fiber: black line. Electrical path: green lines. TL: tunable laser. PM: phase modulator. TC: tunable cavity. PD: photodiode. AWG: arbitrary wave generator. MWG: microwave generator. SA: spectrum analyzer. DirC: directional coupler.

The ratio of the sidebands to the carrier is recorded (as a function of microwave drive power and frequency). This ratio is expected to be:

$$\frac{E_1}{E_0} = \frac{J_1(\pi V_{\mathrm{rel}})^2}{J_0(\pi V_{\mathrm{rel}})^2} \tag{6.39}$$

Here J_0 and J_1 are Bessel functions of order 0 and 1. The drive voltage amplitude relative to the half-wave voltage V_π is:

$$V_{\mathrm{rel}} = \frac{V}{V_\pi} = \left(\frac{P}{P_\pi}\right)^{1/2} = 10^{(P_{\mathrm{dBm}} - P_{\pi\mathrm{dBm}})/20} \tag{6.40}$$

Here V is the voltage sent to the phase modulator; the half-wave voltage V_π is the voltage necessary to induce a phase change of π. The values P and P_π are the corresponding powers in Watts and the value P_{dBm} and $P_{\pi\mathrm{dBm}}$ are the corresponding powers in dBm. The value of $P_{\pi\mathrm{dBm}}$ is given relative to the CPL port of the DirC, as that is what is measured during the experiment. This value is independent of microwave power, but varies with microwave frequency. We record its values for frequencies between 1,650 and 2,650 MHz, as that is the range of the microwave tones. For the measurements in this thesis, $P_{\pi\mathrm{dBm}}$ has been found to increase approximately linearly with frequency from 15.7 dBm (for 1.650 MHz) to 17.2 dBm (for 2,650 MHz). The values, of course, will vary if a different coupler is used or if amplifiers and attenuators are added to the measurement path.

During the experiment the optical power in the first order sideband, relative to the total power, is given by $J_1(\pi V_{\mathrm{rel}})^2$, where $P_{\pi\mathrm{dBm}}$ is known from the calibration and P_{dBm} is measured for each microwave tone using the SA.

6.5.3.3 Suppressed carrier calibration

In order to precisely know the powers incident on the cavity, it is important that the system is operated in the single-sideband, suppressed-carrier regime. Therefore, before performing each measurement set we ensure that the carrier is suppressed. The setup for calibration is shown in figure 6.36. Light leaves the TL, goes through the IQM, and beams output by the IQM are measured by sending them through the TC and looking at the resulting signal on the PD. The IQM is driven by 3 DC voltages (-10 V to 10 V, not shown in the main figure). These voltages determine the amplitude and phase of the carrier and the sidebands. During the calibration the voltages are adjusted to suppress the carrier and leave only a single sideband.

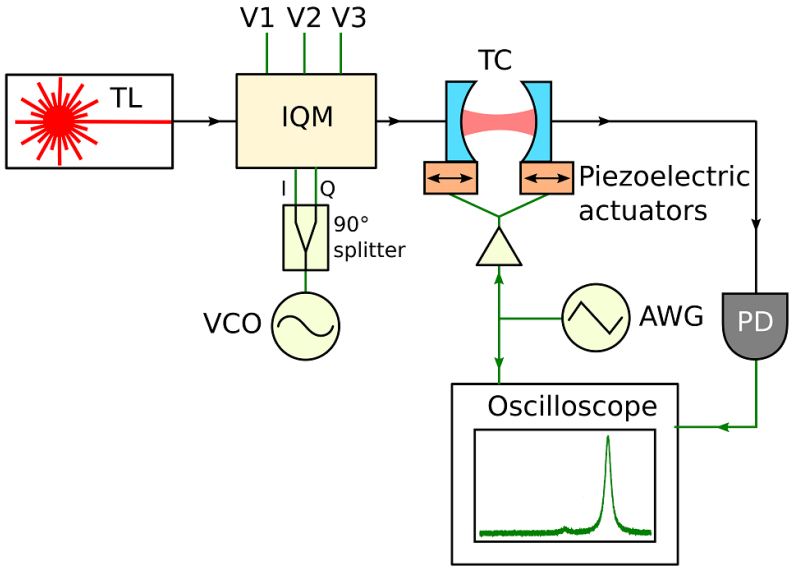

Figure 6.36: Calibration of the phase modulator. SM fiber: black line. Electrical path: green lines. TL: tunable laser. IQM: IQ modulator. TC: tunable cavity. PD: photodiode. AWG: arbitrary wave generator. VCO: Voltage controlled oscillator

6.5.3.4 LIA added noise calibration

The electronic noise added by the detection circuit depends on the input range of the LIA into which the IF output of the mixdown circuit is plugged in. The added noise was measured by changing the input range of the LIA and recording the spectrum background when the EDFA is off. The results are shown in table 6.1.

Range (mV)	**Background** $\times 10^{-15}$**V**^{2}**/Hz**
20	0.0224
50	0.0375
100	0.073
200	1.75
300	2.25
400	2.74

Table 6.1: Background of the LIA for different input ranges.

LIA adds 20 times more noise at 200 mV than at 100 mV, so it is often better to attenuate the signal so that 100 mV input range could be used.

6.5.3.5 EDFA noise figure calibration

The EDFA noise figure is calibrated as shown in figure 6.37.

Light leaving the TL passes through an amplitude modulator (AM)[66], which puts small sidebands ("signal") onto the beam. The amplitude modulator is driven at $\approx$ 30 MHz. At this frequency the laser amplitude noise is lower than shot noise, and the photodiode gain is constant. Light then passes through a variable attenuator and a 90:10 splitter, which

[66] Thorlabs LN81S

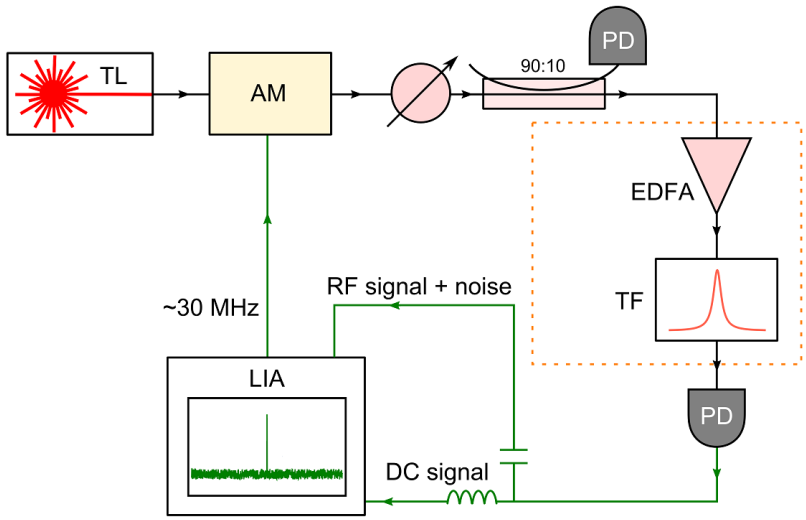

Figure 6.37: Calibration of the EDFA noise. SM fiber: black line. Electrical path: green lines. TL: tunable laser. AM: amplitude modulator. PD: photodiode. EDFA: erbium doped fiber amplifier. TF: tunable filter. LIA: lock-in amplifier.

is used to monitor the incident power. Then it either goes directly onto the PD, or passes through the EDFA and TF first. During the measurement, the power of the AM sidebands and the background power spectral density are recorded as the incident laser power is changed using the attenuator. The ratio of the sideband power to the background gives the signal-to-noise ratio. The DC signal gives the record of laser power.

The gain of the photodiode and the laser noise are calibrated without the EDFA first (i.e., without the components inside the dashed orange square in figure 6.37). We find that background grows linearly with increasing laser power, as expected for shot noise. This data is shown in figure 6.38 (left) with red circles. The solid black line is the best fit to a linear function, the dashed blue line is the best fit to a quadratic function. Clearly, the linear fit captures the data much better. The power of the AM sidebands grows quadratically. This data is shown in figure 6.38 (right) with red circles. The dashed black line is the best fit to a linear function, the solid blue line is the best fit to a quadratic function. In this case the quadratic fit captures the data much better. The radio of the peak power to the background power gives SNR_0, the signal-to-noise ratio without the EDFA.

Then the EDFA and TF are put in, and the signal-to-noise ratio is measured again ($\mathrm{SNR}_{\mathrm{EDFA}}$). The noise figure of the EFDA is calculated as:

$$\mathrm{NF} = 10 \log_{10} \left(\frac{\mathrm{SNR}_0}{\mathrm{SNR}_{\mathrm{EDFA}}} \right) \tag{6.41}$$

NF was found to vary slightly with laser wavelength, so we measured it for a number of different wavelengths. For 1529 nm (the wavelength used for the thermal motion measurements), the EDFA noise figure is plotted in figure 6.39. Note that in this calibration the noise figure of the EDFA is measured after the TF, so it includes the effect of filtering out the ASE.

6.5.3.6 Mixer noise calibration

The noise added by the mixer circuits[67] is calibrated as follows. The laser is turned off. A local oscillator generated by the MWG1 at 1.9 GHz, as well as the signal tone at frequencies between 100 MHz and 600 MHz, generated by the LIA are sent to a mix-up or mix-down circuit. The signal from the circuit is sent to the spectrum analyzer. The power in the mixed-up tone as well as the powers in all the other tones are measured (in dBm). The SNR is given by the difference in the power in the mixed-up tone and power in all other tones. For the IF frequency between 200 and 500 MHz the SNR is

[67] The mixer circuits are image rejection mixers

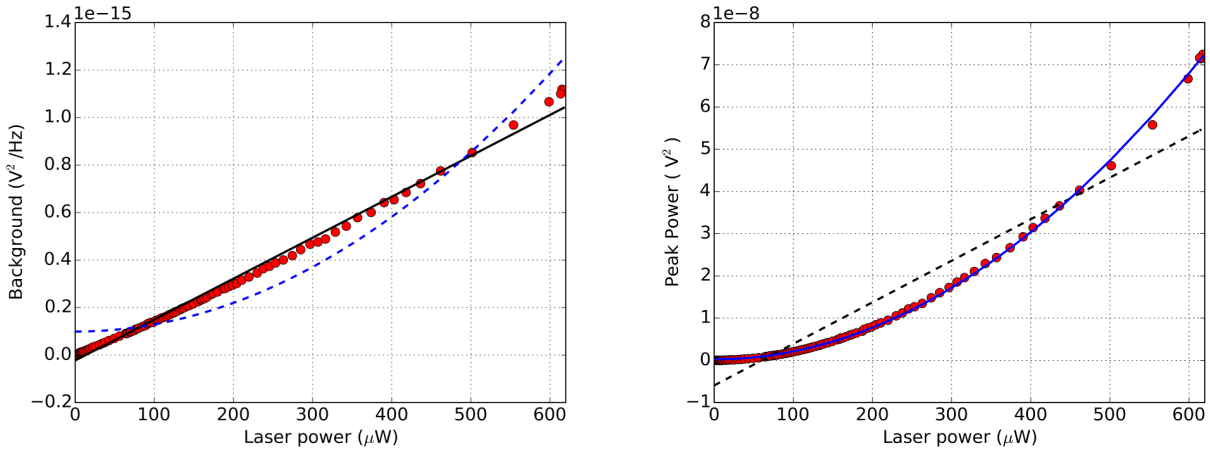

Figure 6.38: Left: the PSD background vs. laser power. The red circles show the data. The solid black line is the best fit to a linear function, the dashed blue line is the best fit to a quadratic function. Right: The AM peak amplitude vs. lase power. The red circles show the data. The dashed black line is the best fit to a linear function, the solid blue line is the best fit to a quadratic function.

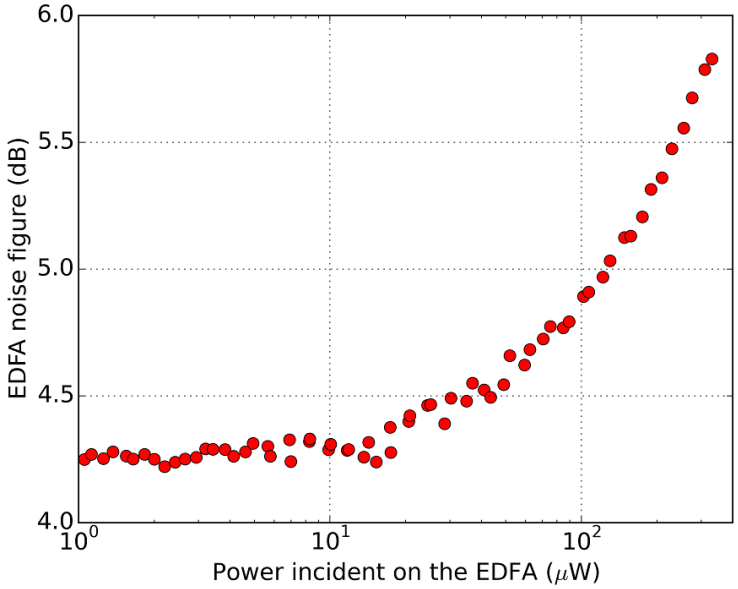

Figure 6.39: The noise figure of the EDFA at 1529 nm vs. power incident on the EDFA.

approximately constant at 25 dB. The corresponding noise figure is 0.01 dB, which is completely negligible compared to the noise figure of the EDFA.

If instead of an image rejection mixer, a single mixer was used, the noise figure would be ≈ 3 dB.

6.6 Data acquisition and analysis

After the device is assembled we measure its parameters. This section described how the data is obtained from the device, how it is fit and what is extracted from the fits.

6.6.1 Cavity length measurement

The first measurement that we perform is the cavity length measurement. We find the cavity length by changing the laser wavelength from ≈ 1500 nm to ≈ 1600 nm, and finding all the TEM_{00} resonances. In order to find the resonances, we step the laser in the steps of 1 pm and sweep the wavelength with finer resolution using an IQM controlled by a VCO. Once we find the resonance we solve the equation:

$$\lambda_{\mathrm{i}-1}(n_{\mathrm{i}}+1) = \lambda_{\mathrm{i}} n_{\mathrm{i}} \tag{6.42}$$

Where $\lambda_{\mathrm{i}-1}$ and λ_{i} are wavelengths of successive $\mathrm{TEM}_0 0$ resonances. $\lambda_{\mathrm{i}} > \lambda_{\mathrm{i}-1}$ and n is a positive integer. Once we find the values of n_{i}, we find the value for cavity length by taking an average of different values of $\lambda_{\mathrm{i}} n_{\mathrm{i}}/2$. We do this measurement for the empty cavity and then again for the filled cavity. We choose the resonance with the best input coupling and the following values are recorded for the cavity and the resonance that is analyzed:

- α – the prompt reflection from the cavity
- $\zeta = \kappa_{\mathrm{ext}}/\kappa$ – the input coupling efficiency, measured as described in section 6.2.2.
- $\sigma_{(\mathrm{top}\rightarrow\mathrm{edfa})}$ – the fraction of power entering the 99:1 splitter on the top of the fridge that reaches EDFA. Calculated by measuring the power at the 1 % output of the 99:1 splitter and measuring the power reaching the EDFA.

6.6.2 Data acquisition

The rest of data acquisition is performed with the laser locked to the experimental cavity, using the locking beam, as described in section 6.5. The detuning between the locking beam and the cavity is kept constant. Multiple data sets are taken. Below I will describe what each data set consists of and how we analyze the data.

The following values are recorded for each data set:

- N_{LIA} – the noise added by the LIA, which is calculated using the input range of the LIA, as described in section 6.5.3.4.
- P_{inc} – the power incident on the cavity at the 99:1 splitter, extracted as described in the calibrations in section 6.5.3.1. The power is monitored continuously and the average power during the time that data set was taken is recorded.
- P_{ref} – the power reflected from the cavity at the 99:1 splitter, extracted as described in the calibrations in section 6.5.3.1. The power is monitored continuously and the average power during the time that data set was taken is recorded.
- λ – the wavelength of the laser. The wavelength is monitored continuously and the average wavelength during the time that data set was taken is recorded.

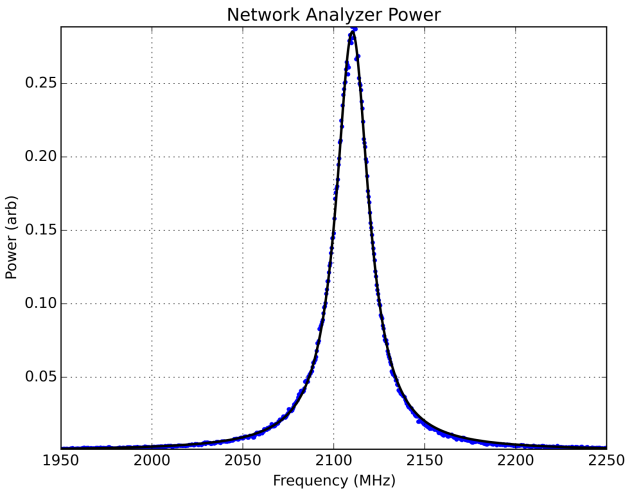

Figure 6.40: Cavity response. The data taken by sweeping the probe beam over the cavity resonance (blue dots) with the Lorentzian fit (black line). The control beams are off.

- T_{MC} – the mixing chamber temperature. The mixing chamber temperature is monitored continuously and the average mixing chamber temperature during the time that data set was taken is recorded.
- $\omega_{\mathrm{Control(U)}}$, $\omega_{\mathrm{Control(L)}}$, ω_{Probe}, ω_{Lock} the frequencies of the microwave signals that are used to generate all the beams.

The following data is fit for each data set:

- **The cavity sweep**.

  Only the probe and the locking beams are on, as shown in figure 6.34(d). The probe beam is swept over the cavity resonance. The response at the probe beam frequency is recorded using the NA. The resulting waveform is fit with a Lorentzian:

$$F_{\mathrm{cav}}(x) = \frac{L^2}{\kappa^2/4 + (x - \Delta_{\mathrm{cav,LO}})^2} \tag{6.43}$$

  Here L, κ and Δ_{LO} are all fit parameters. Figure 6.40 shows the data with a fit. The recorded values are:

  - κ (the cavity linewidth)
  - $\Delta_{\mathrm{cav,LO}}$ (the cavity detuning from the LO)

- **The OMIT/OMIA**.

  The control beams are turned on. If the OMIT/A data is taken together with the thermal motion data, both control beams are on, as shown in figure 6.34(b). If the OMIT/A data is taken on its own to extract the optomechanical coupling and dynamical back-action, only one control beam is on, as shown in figure 6.34(c). The probe beam is first swept from $\omega_{\mathrm{m}} - \delta$ to $\omega_{\mathrm{m}} - \delta$ away from the lower control beam. The probe beam is then swept from $-\omega_{\mathrm{m}} - \delta$ to $-\omega_{\mathrm{m}} + \delta$ away from the upper control beam. The response at the probe beam frequency is recorded using the NA. If only one control beam is on, the probe beam is first swept from $\omega_{\mathrm{m}} - \delta$ to $\omega_{\mathrm{m}} + \delta$ away from the control beam and then from $-\omega_{\mathrm{m}} - \delta$ to $-\omega_{\mathrm{m}} - \delta$ away from the control beam.

  The resulting waveform is fit to a complex Lorentzian on a complex background:

$$F_{\mathrm{OMIT}}(x) = |A_{\mathrm{B}}|e^{i\phi_{\mathrm{B}}} + \frac{|A_{\mathrm{L}}|e^{i\phi_{\mathrm{L}}}}{\gamma_{\mathrm{OMIT}}/2 + i(x - \Delta_{\mathrm{OMIT,LO}})} \tag{6.44}$$

  The real and imaginary parts are fit simultaneously. Here $|A_{\mathrm{B}}|$, ϕ_{B}, $|A_{\mathrm{L}}|$, ϕ_{L} , γ_{OMIT} and $\Delta_{\mathrm{mode,LO}}$ are the fit parameters. Figure 6.41 shows the data and the fits. The recorded values are:

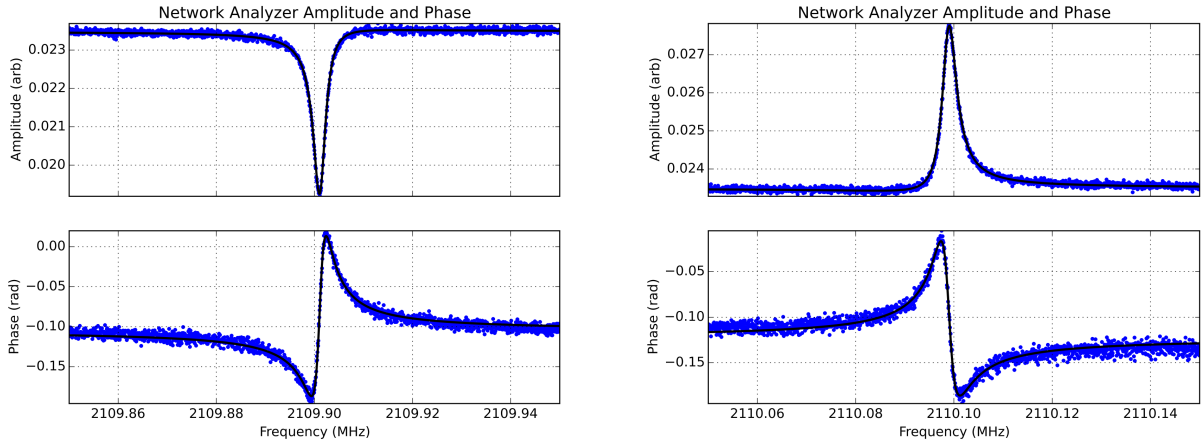

Figure 6.41: OMIT/A data. The data taken by sweeping the probe beam near the cavity resonance (blue dots) with the Lorentzian fit (black line). The control beams are on. Left: probe beam is swept from $+\omega_{\rm m} - \delta$ to $+\omega_{\rm m} + \delta$ away from the lower control beam. Right:probe beam is swept from $-\omega_{\rm m} - \delta$ to $-\omega_{\rm m} + \delta$ away from the upper control beam.

  - $\gamma_{\rm OMIT}$ (effective mechanical linewidth of the mode)
  - $\Delta_{\rm OMIT,LO}$ (the effective detuning of the probe beam response from the LO)
  - $A_{\rm rel} = |2A_{\rm L}/(A_{\rm B}\gamma_{\rm OMIT})|$ (relative to the background amplitude of the Lorentzian)
  - $\phi_{\rm rel} = \phi_{\rm L} - \phi_{\rm B}$ (relative to the background phase of the Lorentzian)

- **Thermal motion**.

  We then measure the thermal motion of the oscillator. This is done in the following manner. The light reflecting from the cavity is sent through the down-mixer to the LIA. The LIA demodulates the signal at frequencies of the motional sidebands of the control beams with ≈ 100 kHz bandwidth, returning two quadratures for each motional sideband. These quadratures are recorded for three minutes. We then apply the Fourier transform to the complex trace composed of the two quadratures, using Python[68]. To find the power spectral density, we square the absolute value of the Fourier transform. The electronic noise $N_{\rm LIA}$ is subtracted from the power spectral density. The frequency axis is scaled so that the frequency is given in radians/second. We fit each power spectral density to a Lorentzian on a constant background:

$$F_{\rm TM}(x) = B + \frac{I\gamma_{\rm TM}}{\gamma_{\rm TM}^2/4 + (x - \Delta_{\rm TM})^2} \tag{6.45}$$

  Here B, I, γ and $\Delta_{\rm trm}$ are the fit parameters. Figure 6.42 shows the data and the fits. The recorded values are:

  - B (the background noise)
  - I (the area under the Lorentzian)
  - $\gamma_{\rm TM}$ (the effective linewidth of the mechanical mode)
  - $\Delta_{\rm TM}$ (the effective detuning of the Lorentzian from the center of the frequency band)

- **Microwave spectrum**

  The spectrum of the microwave signals incident on the phase modulator is recorded. Since the frequencies of the microwave signals are already known, the peaks are found near the frequencies of the signals and the corresponding

[68]The Fast Fourier transform algorithm works much faster, if length of the time trace is equal to a power of 2. Therefore the data is cropped to the nearest power of two.

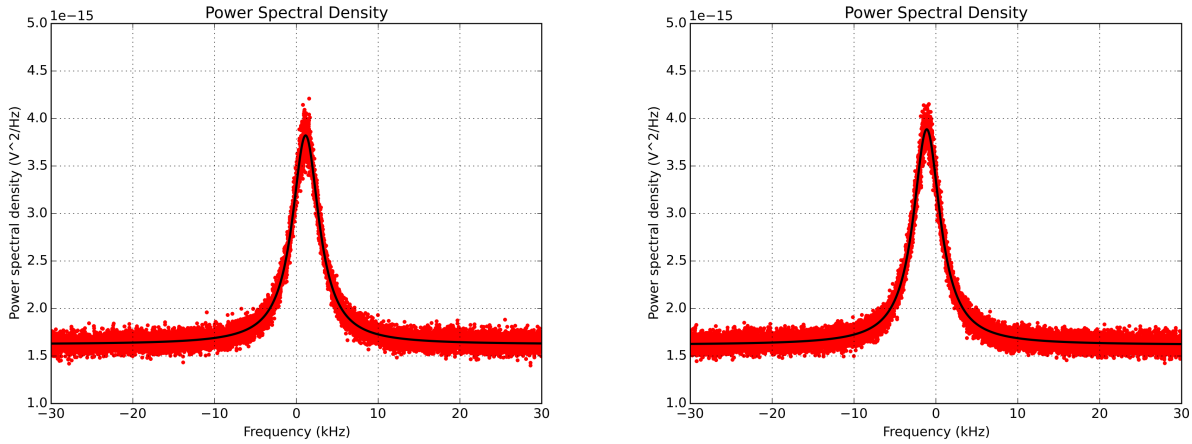

Figure 6.42: The PSD of the thermal motion sidebands (red) with the Lorentzian fit (black line). The control beams are on. Left: the PSD in a band $+\omega_{\mathrm{m}} \pm \delta$ kHz away from the lower control beam. Right: the PSD in a band $-\omega_{\mathrm{m}} \pm \delta$ kHz away from the upper control beam.

power in dBm is recorded. The microwave power is converted into the relative optical power using the calibrations described in section 6.5.3.2:

$$P_{\mathrm{rel}} = J_1(\pi 10^{(P_{\mathrm{dBm}} - P_{\pi\mathrm{dBm}})/20})^2 \tag{6.46}$$

The relative power in the LO is calculated as:

$$P_{\mathrm{rel,LO}} = 1 - 2\sum_{\mathrm{beam}} P_{\mathrm{rel,beam}} \tag{6.47}$$

where "beam" is Control(L), Control(U), Lock, Probe. Figure 6.43 shown the microwave spectrum with the marked peaks. The recorded values are:

- $P_{\mathrm{rel,Control(U)}}$, $P_{\mathrm{rel,Control(L)}}$, $P_{\mathrm{rel,Probe}}$, $P_{\mathrm{rel,Lock}}$, $P_{\mathrm{rel,LO}}$

The following values are extracted from the data:

- The power landing on the cavity is calculated: $P_{\mathrm{total}} = \sqrt{P_{\mathrm{inc}} P_{\mathrm{ref}}/\alpha}$.
- The power in each beam landing on the cavity is calculated: $P_{\mathrm{act,beam}} = P_{\mathrm{rel,beam}} \times P_{\mathrm{total}}$.
- The detuning of each beam from the cavity is calculated as: $\Delta_{\mathrm{beam,cav}} = \omega_{\mathrm{beam}} - \Delta_{\mathrm{cav,LO}}$. The detuning of the LO from the the cavity is $\Delta_{\mathrm{LO,cav}} = -\Delta_{\mathrm{cav,LO}}$
- The input coupling is calculated as $\kappa_{\mathrm{ext}} = \zeta\kappa$
- The circulating photon number due to each beam is calculated as:

$$|\bar{a}|^2_{\mathrm{beam}} = n_{\mathrm{circ,beam}} = \frac{\kappa_{\mathrm{ext}} P_{\mathrm{act,beam}} \frac{\lambda}{2\pi\hbar c}}{\kappa^2/4 + \Delta^2_{\mathrm{beam,cav}}} \tag{6.48}$$

- The total circulating photon number is found as a sum of the circulating photon numbers of all beams: $n_{\mathrm{circ,total}} = n_{\mathrm{circ,LO}} + n_{\mathrm{circ,Control(U)}} + n_{\mathrm{circ,Control(L)}} + n_{\mathrm{circ,Lock}} + n_{\mathrm{circ,Probe}}$. The total circulating photon number is different during the thermal motion measurements and OMIT/A measurement
- The mechanical frequency the oscillator is extracted from the OMIT/A response as $\omega_{\mathrm{m,OMIT}} = |\Delta_{\mathrm{OMIT,LO}} - \omega_{\mathrm{Control(U,L)}}|$

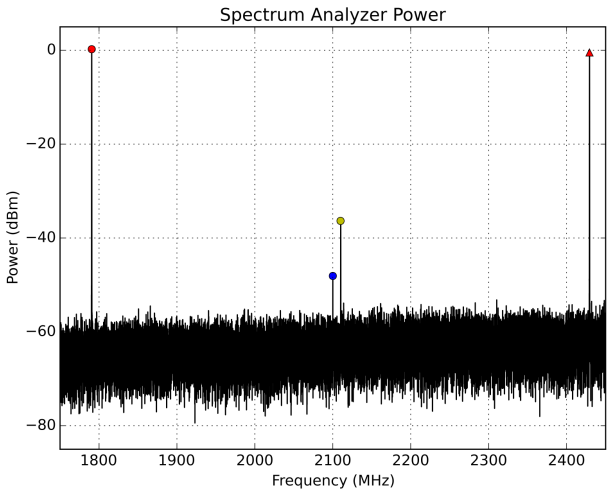

Figure 6.43: The spectrum of the microwave signals incident on the phase modulator. The control beams are marked with red dot and triangle, the probe beam is marked with a yellow dot and the locking beam is marked with a blue dot.

6.6.3 Extracting optomechanical coupling and observing dynamical back-action effects

As described above, in order to extract optomechanical coupling and observe the effects of dynamical back-action, the OMIT/A data is taken with a single control beam. The detuning of the control beam is varied and the incident power is varied as well. The mechanical linewidth γ_{OMIT}, frequency $\omega_{\mathrm{m,OMIT}}$, relative amplitude A_{rel}, phase Φ_{rel}, are extracted from the fit, as described. The values for A_{rel} and Φ_{rel} are fit using equations 5.122, 5.123, 5.124, 5.125, given again here in a slightly different form:

$$A_{\mathrm{rel,red}} = \mathrm{abs}\left[2g_0^2\,|\bar{a}|^2\left(1 - i\frac{g_{0,\mathrm{pt}}}{g_0}\right)\chi_{aa}[\Delta - \omega_{\mathrm{m}}]/\gamma_{\mathrm{eff}}\right] \tag{6.49}$$

$$\Psi_{\mathrm{rel,red}} = \arg\left[2g_0^2\,|\bar{a}|^2\left(1 - i\frac{g_{0,\mathrm{pt}}}{g_0}\right)\chi_{aa}[\Delta - \omega_{\mathrm{m}}]/\gamma_{\mathrm{eff}}\right] \tag{6.50}$$

$$A_{\mathrm{rel,blue}} = \mathrm{abs}\left[-2g_0^2\,|\bar{a}|^2\left(1 + i\frac{g_{0,\mathrm{pt}}}{g_0}\right)\chi_{aa}[\Delta + \omega_{\mathrm{m}}]/\gamma_{\mathrm{eff}}\right] \tag{6.51}$$

$$\Psi_{\mathrm{rel,blue}} = \mathrm{abs}\left[-2g_0^2\,|\bar{a}|^2\left(1 + i\frac{g_{0,\mathrm{pt}}}{g_0}\right)\chi_{aa}[\Delta + \omega_{\mathrm{m}}]/\gamma_{\mathrm{eff}}\right] \tag{6.52}$$

Since the probe can be at $\pm\omega_{\mathrm{m}}$ both red and blue sidebands of the control beam can be measured. Here $|\bar{a}|^2$ is the circulating photon number due to the control beam used for the measurement.

The value for γ_{OMIT} and $\omega_{\mathrm{m,OMIT}}$ are fit simultaneously using equations obtained from 5.119:

$$\gamma_{\mathrm{OMIT}} = \gamma - 2\mathrm{Im}[ig_0^2\,|\bar{a}|^2\left(1 + i\frac{g_{0,\mathrm{pt}}}{g_0}\right)(\chi_{aa}[\omega_{\mathrm{m}} - \Delta] - \chi_{aa}[\omega_{\mathrm{m}} + \Delta])] \tag{6.53}$$

and

$$\omega_{\mathrm{m,OMIT}} = \omega_{\mathrm{m}} + \mathrm{Re}[ig_0^2\,|\bar{a}|^2\left(1 + i\frac{g_{0,\mathrm{pt}}}{g_0}\right)(\chi_{aa}[\omega_{\mathrm{m}} - \Delta] - \chi_{aa}[\omega_{\mathrm{m}} + \Delta])] \tag{6.54}$$

For both of those fits, the only free parameters are the electrostrictive optomechanical coupling g_0 and the photothermal optomechanical coupling $g_{0,\mathrm{pt}}$.

6.6.4 Extracting mechanical phonon number

For the phonon number measurement both upper and lower control beams were on in the second generation device and a single control beam was on in the first generation device. Here we will discuss the measurement when both control beams are on, which can then be extended to a case of a single control beam. The functions describing the photocurrent near the frequencies of the sidebands generated by the thermal motion, assuming no added noise and no losses, are given by equations 5.69, 5.70:

$$S_{ii}^{(rr)}[\delta\omega] \propto \left(\kappa_{\mathrm{ext}}|\chi_{aa}[\Delta_{\mathrm{u}}-\omega_{\mathrm{m}}]|^2 g_0^2|\bar{a}_u|^2\frac{(n_{\mathrm{m}}+1)\gamma_{\mathrm{eff}}}{\gamma_{\mathrm{eff}}^2/4+\delta\omega^2}+1\right) \tag{6.55}$$

$$S_{ii}^{(bb)}[\delta\omega] \propto \left(\kappa_{\mathrm{ext}}|\chi_{aa}[\Delta_{\mathrm{l}}+\omega_{\mathrm{m}}]|^2 g_0^2|\bar{a}_l|^2\frac{n_{\mathrm{m}}\gamma_{\mathrm{eff}}}{\gamma_{\mathrm{eff}}^2/4+\delta\omega^2}+1\right) \tag{6.56}$$

However, as light travels from the cavity to the detector the signal is attenuated due to losses in the fibers (the noise can not be attenuated below the shot noise level).

Additional noise N can be added as well.Therefore the detected photocurrent is:

$$S_{ii}^{(rr)}[\delta\omega] \propto \left(\sigma_{(\mathrm{dev}\to\mathrm{EDFA})}\kappa_{\mathrm{ext}}|\chi_{aa}[\Delta_{\mathrm{u}}-\omega_{\mathrm{m}}]|^2 g_0^2|\bar{a}_u|^2\frac{(n_{\mathrm{m}}+1)\gamma_{\mathrm{eff}}}{\gamma_{\mathrm{eff}}^2/4+\delta\omega^2}+N\right) \tag{6.57}$$

$$S_{ii}^{(bb)}[\delta\omega] \propto \left(\sigma_{(\mathrm{dev}\to\mathrm{EDFA})}\kappa_{\mathrm{ext}}|\chi_{aa}[\Delta_{\mathrm{l}}+\omega_{\mathrm{m}}]|^2 g_0^2|\bar{a}_l|^2\frac{n_{\mathrm{m}}\gamma_{\mathrm{eff}}}{\gamma_{\mathrm{eff}}^2/4+\delta\omega^2}+N\right) \tag{6.58}$$

In the most recent implementation of the measurement setup, the additional noise is composed predominantly of the noise added by the EDFA (N_{EDFA}). It is calculated as:

$$N_{\mathrm{EDFA}} = 10^{(NF[P_{\mathrm{ref}}\sigma_{(\mathrm{top}\to\mathrm{edfa})}]/10)}/P_{\mathrm{rel,LO}} \tag{6.59}$$

Here NF gives the noise figure of the EDFA as a function of power. It was calculated during the EDFA calibration, described in section 6.5.3.5. The value $\sigma_{(\mathrm{top}\to\mathrm{edfa})}$ – the fraction of power leaving the 99:1 splitter at the top of the fridge and reaching the EDFA – is calculated during power calibrations.

The added noise is divided by the relative power in the LO, because we assume that the Lorentzian component arises from beating between the local oscillator and the acoustic sideband, and that the noise floor arises from the beating of the output noise of the EDFA with the local oscillator. However, if other beams are present, the beating of those beams with the output noise of EDFA increases the noise floor.

The fraction of the optical power leaving the device that reaches the EDFA $\sigma_{(\mathrm{dev}\to\mathrm{EDFA})}$ is calculated as:

$$\sigma_{(\mathrm{dev}\to\mathrm{EDFA})} = \sigma_{(\mathrm{dev}\to\mathrm{top})}\sigma_{(\mathrm{top}\to\mathrm{EDFA})} \tag{6.60}$$

Where $\sigma_{(\mathrm{dev}\to\mathrm{top})} = \sqrt{P_{\mathrm{ref}}/(\alpha P_{\mathrm{inc}})}$ is the fraction of power leaving the device and reaching the 99:1 splitter.

The noise from other sources (such as mixer image noise in measurement of the first generation device) increases N as well.

Any microwave amplifiers and attenuators after the EDFA amplify and attenuate the signal and the background by the same factor and do not have any effect on the signal-to-noise ratio (since the background on the output of the EDFA is 20-50 times larger than the shot noise).

Since the thermal motion data was fit with the following expression:

$$F_{\mathrm{TM}}(x) = \frac{I\gamma_{\mathrm{TM}}}{\gamma_{\mathrm{TM}}^2/4+(x-\Delta_{\mathrm{TM}})^2}+B \tag{6.61}$$

it is clear that the following equality must hold for the red sideband of the upper control beam and for the blue sideband of the lower control beam:

$$\frac{I}{B} = \frac{\sigma_{(\mathrm{dev}\rightarrow\mathrm{EDFA})} L_{rr,bb}(n_{\mathrm{r,b}})}{N} \tag{6.62}$$

Where:

$$L_{rr} = \kappa_{\mathrm{ext}} |\chi_{aa}[\Delta_{\mathrm{u}} - \omega_{\mathrm{m}}]|^2 g_0^2 |\bar{a}_u|^2 \tag{6.63}$$

$$L_{bb} = \kappa_{\mathrm{ext}} |\chi_{aa}[\Delta_{\mathrm{l}} + \omega_{\mathrm{m}}]|^2 g_0^2 |\bar{a}_l|^2 \tag{6.64}$$

$$n_{\mathrm{r}} = n_{\mathrm{m}} \qquad n_{\mathrm{b}} = n_{\mathrm{m}} + 1 \tag{6.65}$$

Now the phonon number corresponding to the upper and lower sidebands can be easily calculated, since it depends on the values which are either calculated or extracted from the fit:

$$n_{\mathrm{r,b}} = \frac{IN}{\sigma_{(\mathrm{dev}\rightarrow\mathrm{EDFA})} L_{rr,bb} B} \tag{6.66}$$

However, the precision of determining the phonon number relies on our knowledge of g_0 and circulating photon number.

A way to circumvent this is realizing that the expressions for L_{rr} and L_{bb} can be rewritten in terms of the corresponding OMIT/A amplitudes as:

$$L_{rr} = \mathrm{abs}\left[\frac{A_{\mathrm{rel,red}} \kappa_{\mathrm{ext}} \chi_{aa}[\Delta_{\mathrm{u}} - \omega_{\mathrm{m}}] \gamma_{\mathrm{TM}}}{(1 - i g_{0,\mathrm{pt}}/g_0)}\right] \tag{6.67}$$

and

$$L_{bb} = \mathrm{abs}\left[\frac{A_{\mathrm{rel,blue}} \kappa_{\mathrm{ext}} \chi_{aa}[\Delta_{\mathrm{l}} + \omega_{\mathrm{m}}] \gamma_{\mathrm{TM}}}{(1 + i g_{0,\mathrm{pt}}/g_0)}\right] \tag{6.68}$$

Therefore we can take OMIT/A data with the same parameters as the thermal motion data, fit the OMIT/A data and use its amplitude. In equations 6.67 and 6.68, all the parameters are known and we do not rely on precise knowledge of the circulating photon number and optomechanical coupling. However, we do need to know the ratio of the photothermal coupling to the electrostrictive coupling, which is extracted as described in section 6.6.3.

These two ways of calculating mechanical phonon occupation number are complimentary.

6.6.5 Extracting thermal phonon number

The mechanical phonon occupation number is determined by the temperature of the bath (thermal phonon occupation number n_{th}), laser heating or cooling (which changes γ_{eff}) and driving of the mechanical mode by the beating between the control beam and RPSN (the first term in the equation), as given by equation 5.64:

$$n_{\mathrm{m}} = \frac{1}{\gamma_{\mathrm{eff}}} \left(g_0^2 \kappa \left(|\bar{a}_l|^2 |\chi_{aa}[-\omega_{\mathrm{m,eff}} + \Delta_l]|^2 + |\bar{a}_u|^2 |\chi_{aa}[-\omega_{\mathrm{m,eff}} + \Delta_u]|^2 \right) + \gamma n_{\mathrm{th}} \right) \tag{6.69}$$

Assuming $\Delta_l \approx -\omega_{\mathrm{m}}$ and $\Delta_u \approx \omega_{\mathrm{m}}$ in the resolved sideband regime, $\chi_{aa}[-\omega_{\mathrm{m,eff}} + \Delta_l] \ll \chi_{aa}[-\omega_{\mathrm{m,eff}} + \Delta_u]$, therefore the equation can be simplified to:

$$n_{\mathrm{m}} = \frac{1}{\gamma_{\mathrm{eff}}} \left(g_0^2 \kappa |\bar{a}_u|^2 |\chi_{aa}[-\omega_{\mathrm{m,eff}} + \Delta_u]|^2 + \gamma n_{\mathrm{th}} \right) \tag{6.70}$$

If the mechanical phonon number, and other device parameters are known, the thermal occupation number can be extracted by solving the equation 6.70 for n_{th}, resulting in:

$$n_{\rm th} = \frac{\gamma_{\rm eff} n_{\rm m} - \kappa |\chi_{aa}[\Delta_u - \omega_{\rm m}]|^2 g_0^2 |\bar{a}_u|^2}{\gamma_{\rm eff} - \gamma_{\rm opt}} \tag{6.71}$$

Where we assumed that χ_{aa} is a slowly varying function on the scale of optical frequency shify $\delta\omega_{\rm m,opt}$ and $\chi_{aa}[\Delta_u - \omega_{\rm m,eff}] \approx \chi_{aa}[\Delta_u - \omega_{\rm m}]$. The value $\gamma_{\rm eff}$ is the effective (measured) mechanical linewidth, extracted from the thermal motion measurements. The value $\gamma_{\rm opt}$ is the change in mechanical linewidth due to the drive beams and it is calculated as:

$$\gamma_{\rm opt} = -2{\rm Im}\left[-ig_0^2|\bar{a}_l|^2\chi_{aa}[\omega_{\rm m} + \Delta_l] + ig_0^2|\bar{a}_u|^2\chi_{aa}[\omega_{\rm m} - \Delta_u]\right] \tag{6.72}$$

Here we assumed $\Delta_l \approx -\omega_{\rm m}$ and $\Delta_u \approx \omega_{\rm m}$ and ignored all terms involving $\chi_{aa}[\approx \pm 2\omega_{\rm m}]$, which are small.

With a little algebra we can rewrite everything in terms of OMIT/A amplitudes:

$$n_{\rm th} = \frac{\gamma_{\rm eff} n_{\rm m} - L_{\rm rr}\frac{\kappa}{\kappa_{\rm ext}}}{\gamma_{\rm eff} - \gamma_{\rm opt}} \tag{6.73}$$

$$\gamma_{\rm opt} = -\gamma_{\rm eff}{\rm Re}\left[\frac{A_{\rm rel,blue}e^{i\Psi_{\rm rel,blue}}}{1 + i\frac{g_{0,\rm pt}}{g_0}} + \frac{A_{\rm rel,red}e^{i\Psi_{\rm rel,red}}}{1 - i\frac{g_{0,\rm pt}}{g_0}}\right] \tag{6.74}$$

Again, both ways of calculating $n_{\rm th}$ are complimentary and should give the same result.

6.7 Summary

In this chapter I described how the devices are built and assembled and how the dilution refrigerator is set up. Then I described the measurement setup, calibrations that we performed and the measurements that we did in very general terms. In the next two chapters we will talk about the first generation and the second generation device and apply the data analysis described above to those devices.

Chapter 7

First generation device

In this chapter I will describe the data that we took with the first generation device. I will first talk about the device parameters, that we extracted from the measurements, such as cavity length and optomechanical coupling. Then I will discuss the theoretical predictions for the acoustic quality factor, showing that it depends on the acoustic reflectivity of the mirrors and on the device temperature. I will develop a model describing the device temperature in terms of mixing chamber temperature, circulating and incident powers. I will demonstrate that the data for the quality factor agrees with the predictions. Then I will discuss the measurement of the thermal motion of the mode and the extracted thermal phonon number. Finally I will discuss other (non-paraxial) acoustic modes observed in the system.

The first generation device was cooled down three times. Each time the parameters of the cavities (length and linewidth) were changing, due to slightly different thermal contraction, as was evidenced by the cavity length measurements. For all data described in this section, we did not use the piezoelectric element glued inside the device[1].

7.1 Device parameters

The cavity used in the device consists of two mirrors with radii of curvature $R_1 = 409$ μm and $R_2 = 282$ μm. We first measure the frequency and linewidth of cavity modes when the device is empty. That is done by tuning the TL until it is on resonance with the cavity, locking the laser to the cavity and sweeping the probe beam over a locked cavity using NA, as described in section 6.6.2. We then fill the cavity with helium and perform the measurement again. The results are summarized in table 7.1.

Empty cavity			Filled cavity		
λ (nm)	q_{opt}	$\kappa/2\pi$ (MHz)	λ (nm)	q_{opt}	$\kappa/2\pi$ (MHz)
1504.104	92	100	1497.040	95	60
1520.706	91	50	1512.943	94	50
1537.614	90	46	1529.237	93	46
1554.911	89	47	1545.874	92	54
1572.588	88	52	1562.847	91	48
1590.700	87	64	1580.233	90	54

Table 7.1: The wavelength, longitudinal mode number, and linewidth in both empty and filled cavities

We find the longitudinal mode number and then cavity length, as described in section 6.6.1. The empty cavity length is $L_{\mathrm{empty,opt}} = 69.07 \pm 0.11$ μm. The filled cavity length is $L_{\mathrm{full,opt}} = 71.09 \pm 0.09$ μm. Those values are consistent with

[1] At first we used 1550 nm laser (Koheras Boostik) and changed the cavity length using a piezo. However, the piezo stopped working (we applied voltage that was too high for it), so we acquired a widely tunable laser instead (HP6186F or Pure Photonics PPCL200).

the helium index of refraction: $L_{\mathrm{full,opt}}/L_{\mathrm{empty,opt}} = 1.029 \pm 0.002$. The optical linewidth does not seem to change in any particular manner, which is consistent with the notion that superfluid helium does not absorb light.

During the second cooldown, we observed the paraxial acoustic mode using the OMIT/A technique. We measured the frequencies of the paraxial modes for 8 different optical resonances. We use the wavelengths of the resonances to calculate the filled cavity length for an optical mode $L_{\mathrm{full,opt}} = 73.86 \pm 0.07$ μm, from which we extract the empty cavity length for an optical mode $L_{\mathrm{empty,opt}} = 71.85 \pm 0.07$ μm. We use the frequency spacing of the acoustic modes, to extract the cavity length for the acoustic mode, which we calculate from the equation for the free spectral range

$$\omega_{\mathrm{m,FSR}} = v_{\mathrm{He}}/(2L_{\mathrm{mech}}) \tag{7.1}$$

Since the optical modes couple to every other mechanical mode (from the condition $q_{\mathrm{mech}} = 2q_{\mathrm{opt}}$, where q_{mech} is the number of acoustic half-wavelength between the mirrors), the acoustic cavity length is found as:

$$L_{\mathrm{mech}} = v_{\mathrm{He}}/|\omega_{\mathrm{m,i}} - \omega_{\mathrm{m,i+2}}| \tag{7.2}$$

Calculating the value of L_{mech} for the successive pairs of acoustic mode frequencies we find the average: $L_{\mathrm{mech}} = 70.69 \pm 0.03$ μm (note that since acoustic mode is predominantly confined by the impedance mismatch between the top layer of the optical stack and helium, L_{mech} gives the physical distance between the mirrors). The difference of ≈ 1.1 μm is due to slightly different boundary conditions for optical and mechanical mode, as described in section 4.2.1.1. The acoustic mode is predominantly confined to the helium, while the optical mode penetrates into the stack.

The penetration depth of optical mode into a mirror is given by [134]. It depends on whether the top quarter wavelength layer on the stack has high or low refractive index. If the top layer of the stack has high refractive index, the penetration depth is:

$$L_{\mathrm{p}} = \frac{\lambda}{4\Delta n}\frac{n_{\mathrm{i}}}{\bar{n}_{\mathrm{stack}}} = 0.35\ \mu\mathrm{m} \tag{7.3}$$

If the top layer of the stack has low refractive index, the penetration depth is:

$$L_{\mathrm{p}} = \frac{\lambda}{4\Delta n}\frac{\bar{n}_{\mathrm{stack}}}{n_{\mathrm{i}}} = 1.04\ \mu\mathrm{m} \tag{7.4}$$

Here n_i is the refractive index of the material from which the light is incident, $\bar{n}_{\mathrm{stack}}$ is the average refractive index of the stack and Δn is is difference in the refractive index between different layers of the stack. In the stack that we use, the first layer thickness is unknown[2], it is reasonable to assume that the penetration depth is between these two values, therefore the total increase in cavity length should be between 0.7 μm and 2.08 μm, which is consistent with the measured value of 1.1 μm.

The optical wavelength and the corresponding frequency of the acoustic mode to which optical mode couples are plotted in figure 7.1 with blue circles. Green stars show the expected acoustic frequency, assuming the wavelength of the acoustic mode is half the wavelength of the optical mode: $\omega_{\mathrm{m}} = 2\pi \times 2v_{\mathrm{He}}n_{\mathrm{He}}/\lambda_{\mathrm{opt}}$. These values consistently overestimate the data, due to the difference in the boundary conditions. Red triangles show the acoustic frequencies, calculated from the geometry of the device: $\omega_{\mathrm{m}} = v_{\mathrm{He}}(\pi q_{\mathrm{mech}} + \phi_{\mathrm{G}})/L_{\mathrm{mech}}$, where ϕ_{G} is the Guoy phase shift, defined in B.1. These values agree with the data to within $10 - 20$ kHz, which corresponds to relative error less than 10^{-4}.

[2]The mirror coating companies adjust the thickness of the top layer to achieve the desired transmittivity

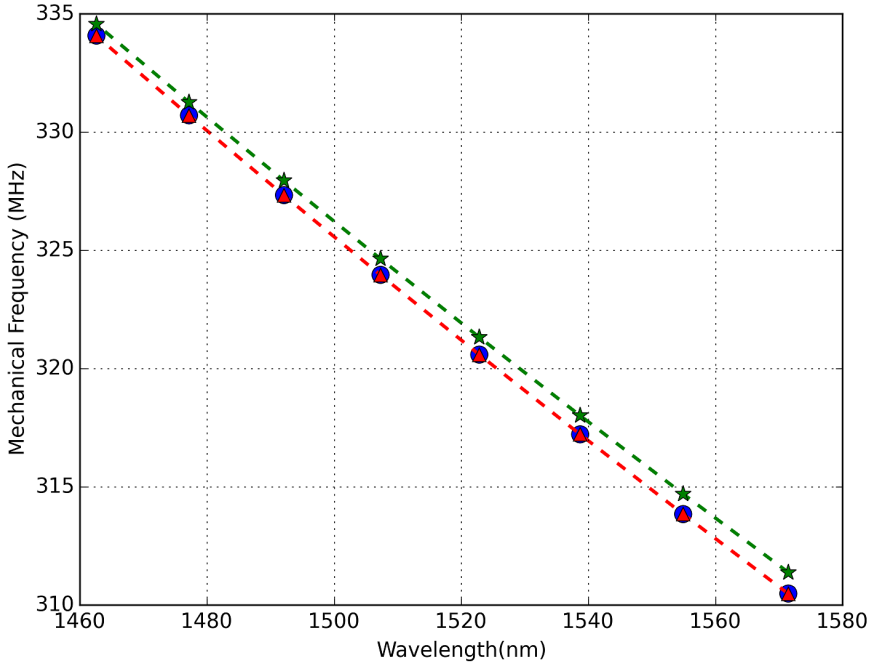

Figure 7.1: Wavelength of the optical modes and frequencies of the acoustic modes in the cavity. Blue circles: the measured frequency of the acoustic mode to a corresponding optical mode couples. Green stars: the calculated mechanical frequency from $\omega_{\rm m} = 2\pi 2 v_{\rm He} n_{\rm He}/\lambda_{\rm opt}$. Red triangles: the calculated mechanical frequency from $\omega_{\rm m} = v_{\rm He}(\pi q_{\rm mech} + \phi_{\rm G})/L_{\rm mech}$

7.2 OMIT/A measurements

During the third cooldown, we performed OMIT/A measurements of the mechanical mode, as described in section 6.5 and 6.6.2. Only one (upper) control beam was present and the probe beam at the frequency of the red sideband is measured. For those measurements $L_{\rm empty,opt} = 85.28 \pm 0.01$ μm, $L_{\rm full,opt} = 87.65 \pm 0.01$ μm, $L_{\rm mech} = 84.19 \pm 0.01$ μm, $\kappa/2\pi = 69 \pm 2$ MHz, $\kappa_{\rm ext}/\kappa = 0.22 \pm 0.01$, $\lambda_{\rm opt} \approx 1538$ nm ($q_{\rm opt} = 112$), $\omega_{\rm m}/2\pi \approx 317.3$ MHz ($q_{\rm mech} = 224$), $T_{\rm MC} \approx 60$ μm,extracted as described in section 6.6.

We performed the OMIT/A measurement for various powers and detunings of the control beam, as described in section 6.6.2. An example data set, normalized so that the background is 1 is shown in figure 7.2 (a). The values of amplitude and phase of the OMIT/A response, extracted from such data sets are shown in figure 7.2 (b).

The data in figure 7.2 (b) was first fit with OMIT/A theory with only electrostrictive coupling. This fit is shown with a dashed line. The extracted value for electrostrictive coupling was $g_0/2\pi = 3.3 \pm 0.2$ kHz. While this fit captures most features of the data, it overestimates Ψ by an amount roughly independent of detuning. The data can be fit more accurately if we include another way the optical field can influence the mechanical mode, namely via a photothermal process that is much slower that $\omega_{\rm m}$. If such a photothermal process is included, then fitting this data with equations given in section 6.6.3 gives $g_0/2\pi = 3.18 \pm 0.2$ kHz and $g_{0,\rm pt}/2\pi = 0.97 \pm 0.05$ kHz. This fit is shown with a solid line. We assumed that the thermal relaxation rate $\kappa_{\rm th}$ is much smaller than the mechanical frequency $\omega_{\rm m}$, so the photothermal force contributes a purely imaginary component of the total optomechanical coupling, as described in section 5.6. The theoretical bounds on g_0 are 3.2 kHz $< g_0/2\pi <$ 3.6 kHz, derived in section 4.2.1.1 in agreement with the experimental results.

From the same measurements we can extract the acoustic frequency and linewidth and therefore the acoustic quality factor. In the next section we will discuss the theoretical expectations for the acoustic quality factor.

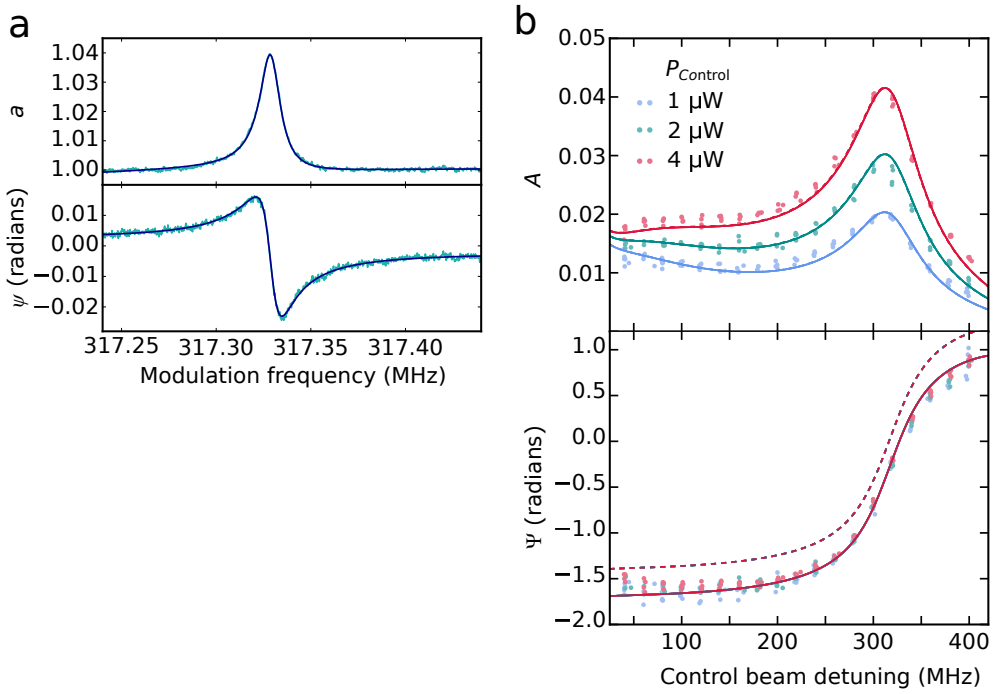

Figure 7.2: OMIT/A measurements. (a) a sample measurement with a fit to a complex lorentzian. We extract linewidth, frequency, amplitude and phase from the fit. (b) Relative amplitude and relative phase plotted vs. detuning of the control beam. The amplitude and phase data was then fit using OMIT theory with only electrostrictive coupling, It is shown with a dashed line. The fit including both electrostrictive and filtered photothermal coupling is shown with solid line

7.3 Theoretical predictions for acoustic quality factor

There are two main mechanisms limiting the acoustic quality factor:

- Boundary loss - due to energy leaking out of the acoustic mode through the mirrors. This is the same as the familiar limitation of optical finesse by the mirror transmission.
- Internal loss - due to attenuation of sound inside helium.

We will consider these limits separately.

7.3.1 Boundary loss

The lifetime and therefore the quality factor of the acoustic mode are limited by losses through the mirrors. The quality factor is related to the mirror transmission as:

$$Q_{\mathrm{ac,ext}} = \frac{2L_{\mathrm{mech}}\omega_{\mathrm{m}}}{v_{\mathrm{He}}(T_{1,\mathrm{ac}} + T_{2,\mathrm{ac}})} = \frac{L_{\mathrm{mech}}\omega_{\mathrm{m}}}{v_{\mathrm{He}}\pi}\mathcal{F}_{\mathrm{ac}} \tag{7.5}$$

Here $T_{1,\mathrm{ac}}$ and $T_{2,\mathrm{ac}}$ are the acoustic transmittivities of the mirrors. A simple estimate of mirror transmittivity can be done using the impedance mismatch between the mirror and helium:

$$T_{\mathrm{ac}} = 1 - R_{\mathrm{ac}} = 1 - \left(\frac{Z_{\mathrm{mirror}} - Z_{\mathrm{He}}}{Z_{\mathrm{mirror}} + Z_{\mathrm{He}}}\right)^2 \tag{7.6}$$

Here $Z = \rho v$ is acoustic impedance of the material. The mirror is composed of alternating layers of SiO_2 and Ta_2O_5. Table 7.2 shows the relevant parameters for each material.

Material	v(m/s)	ρ (kg/m^3)
^{4}He	238[90]	145[90]
SiO_2	5,900 $\pm$ 100[117, 140]	2,200[117]
Ta_2O_5	4,500 $\pm$ 500[117]	7,600 $\pm$ 600[117]

Table 7.2: Material properties of superfluid ^{4}He, SiO_2 and Ta_2O_5

From this simple estimate, we would expect the quality factor for the 317 MHz acoustic mode in a 85 μm long cavity to be between $Q_{\mathrm{ac,ext}} = 66,000$ (if we assume the mirror composed entirely of SiO_2) and $Q_{\mathrm{ac,ext}} = 200,000$ (if we assume the mirror is composed entirely of Ta_2O_5).

To obtain a more precise estimate, we calculate the transmission through the actual DBR stack. This is done in a manner similar to finding DBR transmittivity for a light wave [141, 142], which we did in section 6.1.2 . Assume a sound wave with frequency f and wavelength λ is incident on a DBR. Equating the displacements $(s(x,t))$ and pressures $(p(x,t) = -Kds/dx)$ on both sides of the boundary (K is the bulk modulus) gives:

$$s_j(d,t) = s_{j+1}(d,t) \tag{7.7}$$

$$K_j \frac{ds_j}{dx}(d,t) = K_{j+1}\frac{ds_{j+1}}{dx}(d,t) \tag{7.8}$$

Where s_j and K_j is the displacement and bulk modulus in the j^{th} layer. The fact that acoustic impedance is related to bulk modulus via $Z = K/v = v\rho$, and that the frequency of the mode must be constant throughout the DBR, results in three sets of equations that provide information about the amplitude of the acoustic mode at different interfaces. In these equations Z_j in the acoustic impedance of the j^{th} layer, Z_i and Z_t are the acoustic impedances of the material from which the wave is incident (He II) and into which the wave in transmitted (SiO_2), $s_j^{(f)}$ and $s_j^{(b)}$ are the displacements due the forward and backward propagating waves in the layers, $s^{(r)}$ is the displacement due the wave reflected back into helium from the mirror/helium interface, $s^{(t)}$ is the displacement due to the wave transmitted into the fiber. The amplitude of the wave incident on the mirror surface is set to be 1.

At the first interface:

$$1 + s^{(\mathrm{r})} = s_1^{(\mathrm{f})} + s_1^{(\mathrm{b})} \tag{7.9}$$

$$Z_i(1 - s^{(\mathrm{r})}) = Z_1\left(s_1^{(\mathrm{f})} - s_1^{(\mathrm{b})}\right) \tag{7.10}$$

At the interface between the j^{th} and $(j+1)^{\mathrm{th}}$ layer:

$$s_j^{(\mathrm{f})}e^{ikn_j^{\mathrm{ac}}d_j} + s_j^{(\mathrm{b})}e^{-ikn_j^{\mathrm{ac}}d_j} = s_{j+1}^{(\mathrm{f})} + s_{j+1}^{(\mathrm{b})} \tag{7.11}$$

$$Z_j\left(s_j^{(\mathrm{f})}e^{ikn_j^{\mathrm{ac}}d_j} - s_j^{(\mathrm{b})}e^{-ikn_j^{\mathrm{ac}}d_j}\right) = Z_{j+1}\left(s_{j+1}^{(\mathrm{f})} - s_{j+1}^{(\mathrm{b})}\right) \tag{7.12}$$

Here we defined $k = 2\pi/\lambda$ and $n_j^{\mathrm{ac}} = v_i/v_j$, where v_i and v_j are correspondingly the speed of the sound wave in the medium on the incident side and the speed of sound in the j^{th} layer. At the last interface, assuming a total number of layers p

$$s_p^{(\mathrm{f})}e^{ikn_p^{\mathrm{ac}}d_p} + s_p^{(\mathrm{b})}e^{-ikn_p^{\mathrm{ac}}d_p} = s^{(\mathrm{t})} \tag{7.13}$$

$$Z_p\left(s_p^{(\mathrm{f})}e^{ikn_p^{\mathrm{ac}}d_p} - s_p^{(\mathrm{b})}e^{-ikn_p^{\mathrm{ac}}d_p}\right) = Z_t s^{(\mathrm{t})} \tag{7.14}$$

From equations 7.9-7.14, using the same methods as in section 6.1.2 , a matrix B is obtained:

$$B = \begin{bmatrix} b_{11} & b_{12} \\ b_{21} & b_{22} \end{bmatrix} = \begin{bmatrix} 1 & 1 \\ Z_i & -Z_i \end{bmatrix}^{-1} \prod_{j=1}^{p} M_j^{\mathrm{ac}} \begin{bmatrix} 1 & 0 \\ Z_t & 0 \end{bmatrix} \tag{7.15}$$

where M_j^{ac} is defined as:

$$M_j^{\mathrm{ac}} = \begin{bmatrix} 1 & 1 \\ Z_j & -Z_j \end{bmatrix} \begin{bmatrix} e^{ikn_j^{\mathrm{ac}}d_j} & e^{-ikn_j^{\mathrm{ac}}d_j} \\ Z_j e^{ikn_j^{\mathrm{ac}}d_j} & -Z_j e^{-ikn_j^{\mathrm{ac}}d_j} \end{bmatrix}^{-1} \tag{7.16}$$

Now we have:

$$\begin{bmatrix} 1 \\ s^{(\mathrm{r})} \end{bmatrix} = B \begin{bmatrix} s^{(\mathrm{t})} \\ 0 \end{bmatrix} \tag{7.17}$$

from which we get:

$$r_{\mathrm{ac}} = s^{(\mathrm{r})} = b_{21}/b_{11} \tag{7.18}$$

$$T_{\mathrm{ac}} = 1 - r_{\mathrm{ac}}^2 \tag{7.19}$$

In conclusion, to calculate acoustic reflection/transmission of a DBR the following quantities need to be known:

- d -thickness of each layer
- ρ - density for each layer
- v - sound velocity in each layer

Additionally, it is necessary to know the values of those parameters for the material from which the wave is incident and the material into which the wave is transmitted. For the experiments described in this thesis these are liquid ^{4}He and SiO_2 respectively.

For 1550 nm light, a quarter optical wavelength layer of SiO_2 is 263 nm and a quarter optical wavelength layer of Ta_2O_5 is 189 nm.

The experiment was performed with the mirror surfaces separated by 84 μm. The cavity consisted of a low reflectivity (15 layer pairs) input DBR and high reflectivity (18 layer pairs) back DBR. Both mirrors had an extra quarter wavelength layer of $\mathrm{Ta_2O_5}$ on top of the stack. The laser wavelength was 1538 nm; the frequency of the acoustic mode of interest was $\omega_{\mathrm{ac}} = 2\pi \times 317.3$ MHz.

From equation 7.19 the acoustic transmittivity for the low reflectivity DBR is calculated to be 10,100 $\pm$ 400 ppm ($\mathcal{F}_{\mathrm{ac}} = 310 \pm 10$), while the acoustic transmittivity for the high reflectivity DBR is calculated to be 7,700 $\pm$ 1,300 ppmm ($\mathcal{F}_{\mathrm{ac}} \approx 410 \pm 70$). The uncertainties predominantly come from the material properties of Ta_2O_5 (see Table 7.2). These values of the acoustic transmission lead to the acoustic quality factor for the acoustic mode of interest: $Q_{\mathrm{ac,ext}} = 79,600 \pm 7,000$ ($\mathcal{F}_{\mathrm{ac}} = 360 \pm 40$).

7.3.2 Intrinsic temperature dependent loss

In addition to the boundary loss, sound is attenuated as it propagates through helium. The attenuation of sound in liquid helium was described in section 3.4.1. The intrinsic quality factor of an acoustic mode can be calculated from the attenuation length as:

$$Q_{\mathrm{ac,int}} = \frac{\omega_{\mathrm{ac}}}{2v_{\mathrm{He}}\alpha_{\mathrm{3pp}}} \tag{7.20}$$

For the relevant acoustic mode frequency $\omega_{\mathrm{ac}} = 2\pi \times 317.3$ MHz and temperature $T < 0.5$ K both $\arctan$ arguments in equation 3.10 are $\gg 1$, leading to the simple relationship

$$Q_{\mathrm{ac,int}} = \frac{\chi}{T^4}, \tag{7.21}$$

where $\chi \approx 118$ K^4.

7.4 Device temperature

Since helium does not absorb light, naively one would expect the device temperature to be determined exclusively by the mixing chamber temperature and independent of power in the cavity. In this section we will show that this is not the case. We will describe how and why the device temperature depends on the circulating photon number and incident power. Once we find the expression for the device temperature, we will fit the data using this expression. Finally we will discuss the fit parameters.

In order to understand the device temperature, we need to describe the device geometry and make a few assumptions. A schematic drawing of the device is shown in figure 7.3. A cylindrical volume of helium occupies the space between the faces of two optical fibers (yellow) which are confined within the bore of a glass ferrule (orange). The helium inside the cavity is thermally linked to a larger volume of helium outside the ferrule via two identical sheaths; since these sheaths have the same length, we can represent them as a single sheath with doubled cross-sectional area. We assume that the helium outside the ferrule has a good thermal link to the mixing chamber, so its temperature doesn't depend on the power dissipated inside the cavity and is the same as the mixing chamber temperature.

The temperature of the helium is defined by the mixing chamber temperature, as well as incident power and circulating power. The heating arises because mirrors absorb light both from the inside of the cavity (circulating power) and outside of the cavity (incident power). Since the thermal conductivity of helium is much higher than the thermal conductivity of glass, the heat from the mirrors is predominantly carried away by the helium that they are in contact with. This heats up the helium.

In figure 7.3 red color indicates regions of hotter helium and blue color indicates regions of colder helium.

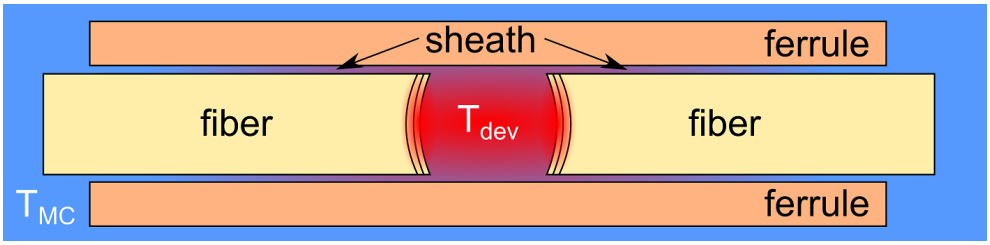

Figure 7.3: Helium temperature inside the first generation device. The fibers are shown in yellow. The ferrule in orange. Red color indicates regions of hotter helium, blue color indicates regions of colder helium.

We assume that since the thermal impedance is outside the cavity, the temperature inside the cavity is uniform. This is not strictly true, as the temperature immediately next to the mirrors is higher, as we will see in the next chapter. However, for this device it is a reasonable assumption, as any influence of those regions on the device temperature or acoustic quality factor, is masked by the overall rise in the device temperature.

Finally, we know that the temperature in the cavity is always < 500 mK, as we have seen that if the MC temperature is increased above 500 mK, the acoustic loss becomes too large for the acoustic mode to be distinguishable on the background.

7.4.1 Heat transport model

Since the temperature in the cavity is always < 500 mK, the heat transport is in the ballistic regime, which was described in section 3.5.1. We have shown that heat conductivity through a tube with diameter D_{tube} in which f_{diff} is the fraction of phonons undergoing diffusive scattering is:

$$k_{\text{He}}(T) = \zeta D_{\text{tube}} \frac{2 - f_{\text{diff}}}{f_{\text{diff}}} T^3 = \xi T^3 \tag{7.22}$$

Where $\zeta = 2.3 \times 10^5$ W/(m$^2\cdot$ K^4). The expression relating heat flow to temperature gradient in ballistic regime is [88]:

$$\frac{\dot{Q}}{A} = -k_{\mathrm{He}}(T)\frac{dT}{dr} \tag{7.23}$$

We assume our device has a heat inflow $\dot{Q}$ and is connected to the mixing chamber (reservoir) at temperature T_{MC} through a thin capillary of length L and diameter D_{tube}, and that A is the cross sectional area of the capillary. Equation 7.23 can be integrated:

$$\dot{Q} = -\frac{A}{L}\int_{T1}^{T2} k_{\mathrm{He}}(T)dT = -\frac{A\xi}{L}\int_{T_{\mathrm{dev}}}^{T_{\mathrm{MC}}} T^3 dT = -\frac{A\xi}{4L}(T_{\mathrm{mc}}^4 - T_{\mathrm{dev}}^4) \tag{7.24}$$

The heat flow into the device is equal to the heat flow out of the device :

$$|\dot{Q}_{\mathrm{circ}}| = \alpha\hbar\omega_{\mathrm{L}}\dot{n}_{\mathrm{circ,int}} = \alpha\hbar\omega_{\mathrm{L}}\kappa_{\mathrm{int}}n_{\mathrm{circ}} \tag{7.25}$$

Where $0 \leq \alpha \leq 1$ is the ratio of photons absorbed by the mirror to all photons lost in the cavity; $\dot{n}_{\mathrm{circ,int}} = \kappa_{\mathrm{int}}n_{\mathrm{circ}}$ is the rate at which circulating photons are lost inside the cavity, and κ_{int} is the internal optical loss.

There is also heat flow due to the laser that reflects off the incident mirror. Some amount of light (determined by $0 \leq \alpha_{\mathrm{inc}} \leq 1$) gets absorbed.

$$|\dot{Q}_{\mathrm{inc}}| = P_{\mathrm{inc}}\alpha_{\mathrm{inc}} \tag{7.26}$$

The total heat inflow into the device is a sum:

$$\dot{Q} = \dot{Q}_{\mathrm{inc}} + \dot{Q}_{\mathrm{circ}} \tag{7.27}$$

Combining equations 7.24 and 7.27 we arrive at the expression for the device temperature:

$$T_{\mathrm{dev}}^4 = T_{\mathrm{MC}}^4 + \frac{4L}{A\xi} \times (\alpha\hbar\omega_{\mathrm{L}}\kappa_{\mathrm{int}}n_{\mathrm{circ}} + \alpha_{\mathrm{inc}}P_{\mathrm{inc}}) \tag{7.28}$$

This means that the device temperature can be written as:

$$T_{\mathrm{dev}}^4 = T_{\mathrm{MC}}^4 + an_{\mathrm{circ}} + bP_{\mathrm{inc}} \tag{7.29}$$

where a and b are constants determined by the device geometry, frequency of the optical mode, the internal losses and the mirror absorption.

7.4.2 OMIT/A measurements of quality factor

As mentioned above, we can extract acoustic quality factor Q_{ac} from the measurements of the OMIT/A spectra , such as ones shown in 7.2. In figure 7.4 we plot Q_{ac} vs. T_{MC} and vs. n_{circ} . From the plot, it is clear that the quality factor is influenced by the mixing chamber temperature, circulating photon number and incident power. The expectation for quality factor, ignoring the heating due to incident and circulating photons is shown with dashed lines. The blue dashed line shows the limit on quality factor due to boundary loss, described in 7.3.1. The red dashed line shows the limit on quality factor due to internal loss, described in 7.3.2. Their combined effect is shown with a black line. While data follows the trend approximately, heating due to circulating photons and incident power is clearly present.

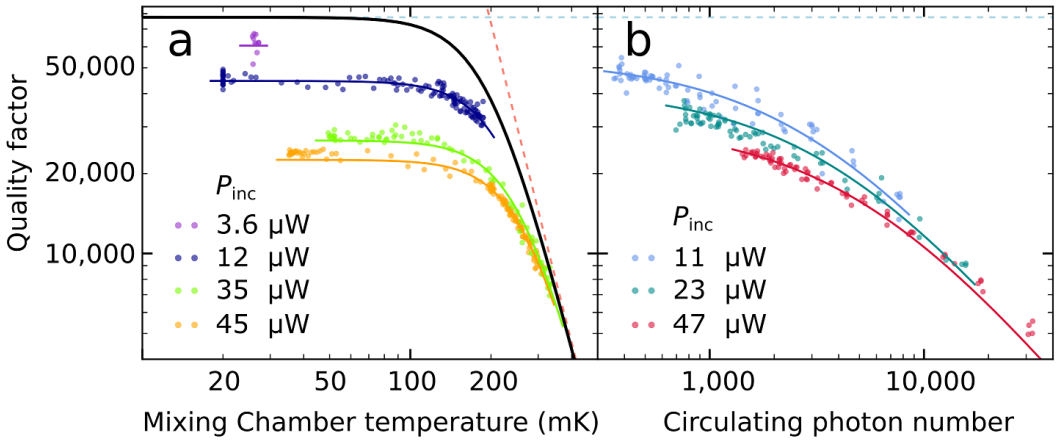

Figure 7.4: Quality factor of the acoustic oscillator. (a) Plotted vs. T_{MC} while keeping n_{circ} constant within each data set. (b) Plotted vs. n_{circ}, while keeping T_{MC} below 100 mK

The expected value for the quality factor is given by:

$$Q_{\mathrm{ac}} = \left(\frac{1}{Q_{\mathrm{ac,ext}}} + \frac{1}{Q_{\mathrm{ac,int}}}\right)^{-1} \tag{7.30}$$

$$= \left(\frac{1}{Q_{\mathrm{ac,ext}}} + \frac{T_{\mathrm{dev}}^4}{\chi}\right)^{-1} \tag{7.31}$$

$$= \left(\frac{1}{Q_{\mathrm{ac,ext}}} + \frac{T_{\mathrm{MC}}^4 + an_{\mathrm{circ}} + bP_{\mathrm{inc}}}{\chi}\right)^{-1} \tag{7.32}$$

This means there is a constant term, and terms depending on T_{MC}, n_{circ} and P_{inc}. We can fit the data in shown in figure 7.4 with this expression. The expression has 4 fit parameters. Their values are found to be: $Q_{\mathrm{ac,int}} = 70600 \pm 2000$, $\chi = 125 \pm 10$ K^4, $a = (7.8 \pm 0.1) \times 10^{-7}$ K^4/photon, $b = 48 \pm 7$ K^4/W. The value of $Q_{\mathrm{ac,int}}$ and χ are close to the theoretically expected values.

The values of a and b are calculated to be:

$$a = \frac{4L}{A\xi}\alpha\hbar\omega_{\mathrm{L}}\kappa_{\mathrm{int}} \tag{7.33}$$

$$b = \frac{4L}{A\xi}\alpha_{\mathrm{inc}} \tag{7.34}$$

We approximate the diameter of the channel by twice the sheath thickness $D_{\mathrm{tube}} = d_{\mathrm{ferrule}} - d_{\mathrm{fiber}} = 3 - 13$ μm. The length of the sheath $L = 3$ mm, and the combined area of the sheaths is: $A = 2\pi/4(d_{\mathrm{ferrule}}^2 - d_{\mathrm{fiber}}^2) = (1.2 - 5.4) \times 10^{-9}$ m^2. The internal loss is $\kappa_{\mathrm{int}}/2\pi \approx 54$ MHz. The laser frequency is $\omega_{\mathrm{L}}/2\pi \approx 195$ THz.

Some *a priori* information about α is provided by room-temperature calorimetry measurements, which give the mirror's absorption coefficient as $a_{\mathrm{abs}} = 3$ ppm (15$\pm$5 ppm) for λ =1,064 nm (532 nm)[116]. To estimate α from this information, we note that the probability for an intracavity photon to be absorbed by a mirror is given by $P_{\mathrm{mir}} = a_{\mathrm{abs}}\frac{\mathcal{F}}{2\pi}\frac{\kappa}{\kappa_{\mathrm{int}}}$, where the cavity finesse is $\mathcal{F} \simeq 50,000$. Assuming $a_{\mathrm{abs}} = 3$ ppm for $\lambda = 1,538$ nm gives $P_{\mathrm{mir}} = 0.03$. Since the cavity is defined by two mirrors, these assumptions would give $\alpha = 2P_{\mathrm{mir}} = 0.06$. This estimate for α is rough, since the absorption coeffecient was measured at room temperature and for a somewhat different wavelength.

With those values and the value of a we got from the fit, we find that $f_{\rm diff}$ is between 4% for the minimum sheath thickness and 60 % for the maximum sheath thickness. Those values appear reasonable for the optically smooth glass surfaces of the ferrule and the fiber and the typical wavelength of thermal phonons $\lambda_{\rm th} = 2\pi\frac{\hbar v_{\rm He}}{3k_B T} \geq 10$ nm for $T < 0.4$ K.

Taking the values that we found for $f_{\rm diff}$, we find the $\alpha_{\rm inc}$ is between 2.8×10^{-4} for maximum sheath thickness and 7.3×10^{-3} for minimum sheath thickness. Those numbers seem high, as we would expect $\alpha_{\rm inc} \approx 3 \times 10^{-6}$ from the values of mirror absorption. However, it is possible there are extra absorbers on the interface between the fiber and DBR (due to the fiber not being perfectly clean before deposition of the DBR), so we condiser those numbers acceptable.

We use the values of a and b from the fit to find $T_{\rm dev}$ using equation 7.29, and then plot the quality factor vs. $T_{\rm dev}$. It is shown in figure 7.5. The data plotted in this figure is the same data, as was plotted in figure 7.4, but now, that it plotted vs. the device temperature, it is clear that it agrees with the theoretical expectations. The color shows the circulating photon number. The data, when plotted vs. device temperature agrees well with the theoretical expectations.

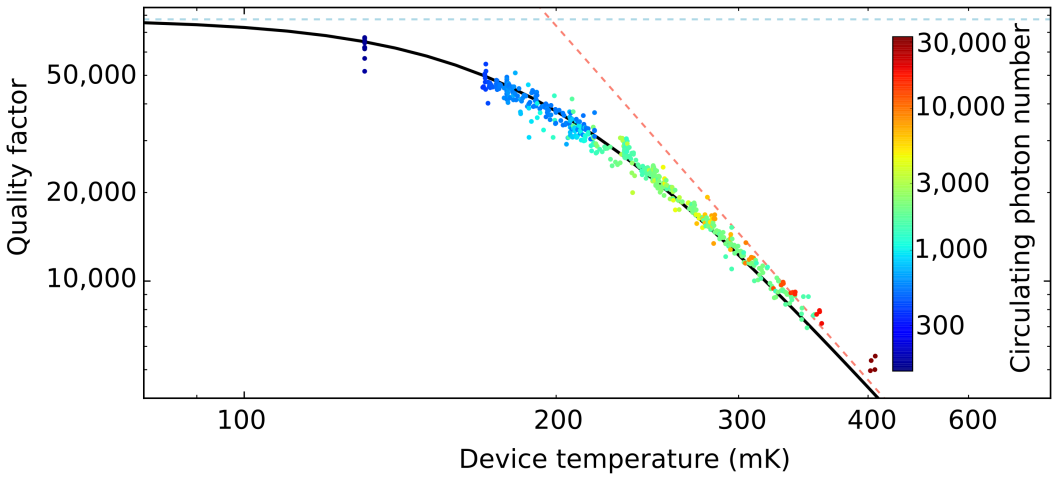

Figure 7.5: Quality factor of the acoustic oscillator vs. $T_{\rm dev}$.

7.5 Thermal motion of the mode

In this section I will describe the results of measuring thermal motion of the mode. I will discuss the attenuation and added noise and show that the measured phonon number agrees with the device temperature extracted using equation 7.29.

We measured the thermal motion of the acoustic mode, as described in section 6.6.2. In this device we only measured the red sideband of the upper control beam. We took data for various device temperatures, obtained by varying the mixing chamber temperature. The data was taken for 2 values of incident power: 12 μW and 46 μW. From this data the phonon number is extracted as described in section 6.6.4.

The attenuation is calculated as follows:

- Only 0.59 of the light leaving the cavity reached the EDFA, so $\sigma_{(\rm dev\rightarrow EDFA)} = 0.59$. This was calculated as described in section 6.6.4.

The added noise is calculated as follows:

- The noise added by EDFA varies with the laser wavelength and power, as described in section 6.5.3.5. With $P_{\rm in} \approx 12\ (46)$ μW, the amount of light that reaches EDFA is 7 (27) μW. The noise figure of the EDFA at 1538 nm was measured to be $NF_{\rm EDFA} = 6.6(5.2)$ dB (this was done without the tunable filter, which was added at a later

time). The relative power in the LO was $P_{\mathrm{rel}} = 0.82$.This means that the total noise added by EDFA is 5.57 (4.04) times the shot noise.

- During the measurement of the first generation device, regular mixers, rather than image-rejection mixers were used. Mixer image noise produces additional noise in the photocurrent power spectral density. Due to the symmetric nature of the mixer, the signal at the IF port at a frequency ω_{IF} will come from the photocurrent both at $\omega_{\mathrm{LO}} + \omega_{\mathrm{IF}}$ and $|\omega_{\mathrm{LO}} - \omega_{\mathrm{IF}}|$. Therefore, assuming a white noise spectrum for the photocurrent signal, the noise at the mixer's IF output is twice the noise at the RF frequency on the mixer's input. To minimize the effect of this added noise, a filter is used to pass the signal band around $\omega_{\mathrm{LO}} + \omega_{\mathrm{IF}}$, and to partially reject the image band at $|\omega_{\mathrm{LO}} - \omega_{\mathrm{IF}}|$. As a result, mixer image noise adds only about (1) 0.25 dB of noise to the photocurrent power spectral density. Hence, $NF_{\mathrm{mix}} = (1)0.25$ dB. (For lower power data, a different filter was used). This increases the noise background by another factor of 1.26 (1.06).

Additionally, since for those measurements the laser was not filtered, classical laser noise was present. A full discussion of the influence of classical laser noise on the thermal motion measurements can be found in [22, 143]. There are two ways in which classical laser noise affects the calibration of the thermal motion data. First, laser phase noise is transformed into amplitude noise through interaction with the optical cavity, and thereby increases the photocurrent noise floor. Second, classical laser noise enters and reflects from the cavity in the same manner as the probe beam used in the OMIA measurements. As a result, the phenomenon of noise (anti-)squashing occurs. Those two effects contribute to SNR degrading by 0.06 (0.3) dB, or equivalently increasing the noise background by a factor of 1.014 (1.07).

The combination of those effects leads to the background increasing by a factor of 7.1 (4.6) above shot noise.

The mechanical and thermal phonon occupation numbers are extracted as described in sections 6.6.4 and 6.6.5 with $N = 7.1$ (4.6) and $\sigma_{(\mathrm{dev}\rightarrow\mathrm{EDFA})} = 0.59$.

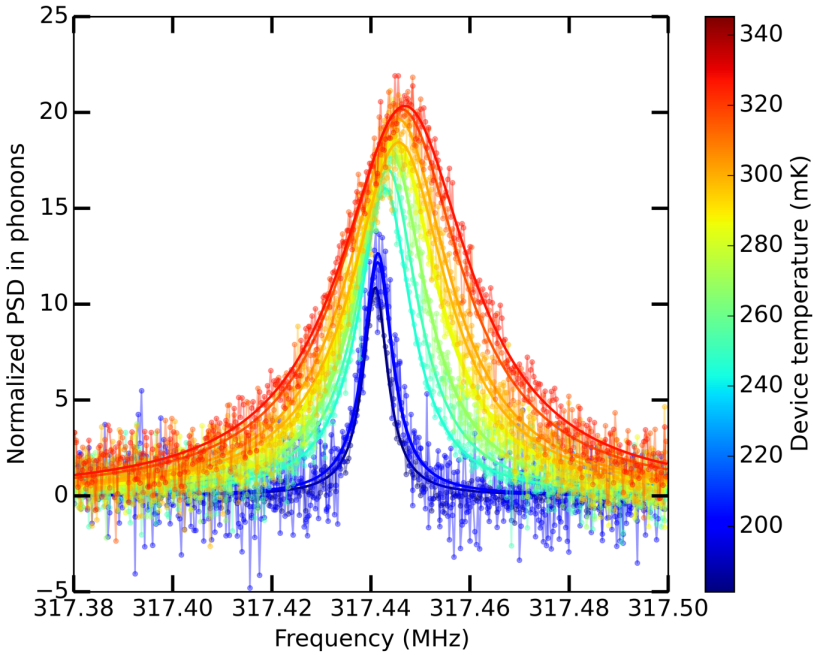

Figure 7.6: The PSDs (with fits) of the lower motional sideband of the control beam for various device temperatures, indicated using color.

Figure 7.6 shown the PSDs of the motional sidebands on the control beam, scaled so that that height of each PSD is in phonons. The frequency axis shows the separation of the PSD from the control beam, giving the frequency of the acoustic oscillator. The color indicates the device temperature. As the temperature increases the resonances broaden and shift

towards higher frequency.

The linewidth of the mechanical oscillator is plotted vs. device temperature calculated using equation 7.29 in figure 7.7 with blue circles. The black line is the expectation for the linewidth $\gamma/2\pi$, extracted from the thermal model:

$$\gamma = \gamma_{\mathrm{ext}} + b_\gamma T^4 \tag{7.35}$$

Here $\gamma_{\mathrm{ext}} = \omega_{\mathrm{m}}/Q_{\mathrm{ac,ext}}$ and $b_\gamma = \omega_{\mathrm{m}}/\chi$. The data agrees with the expectations.

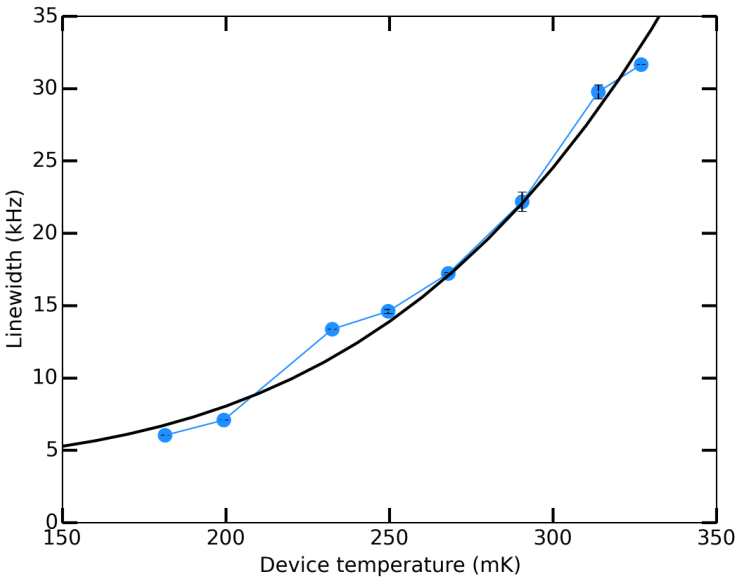

Figure 7.7: The linewidth of the mechanical oscillator vs. device temperature.

The frequency of the oscillator is plotted vs. device temperature in figure 7.8 with blue circles. The black line is a fit to $\omega_{\mathrm{m}}/2\pi$, where

$$\omega_{\mathrm{m}} = \omega_{\mathrm{m,bare}} + b_\omega T^4 \tag{7.36}$$

We find that $b_\omega = 2\pi(0.7 \pm 0.05) \times 10^6$ s^{-1}·K^{-4}. From the expression for the sound velocity, given in 3.4.2, we expect $b_\omega = \frac{\omega_m}{v_{\mathrm{He}}} \approx 2\pi(1 \times 10^6)$ s^{-1}·K^{-4}. The extracted value is close to the expected value.

The thermal phonon number is plotted vs. device temperature in figure 7.9 with pink circles. The black line shows $n_{\mathrm{th}} = k_{\mathrm{B}} T_{\mathrm{dev}}/\hbar\omega_{\mathrm{m}} - 1/2$. The thermal phonon number agrees well with the temperature calculated using our thermal model. The lowest thermal phonon number that was measured was $n_{\mathrm{th}} = 11 \pm 0.3$.

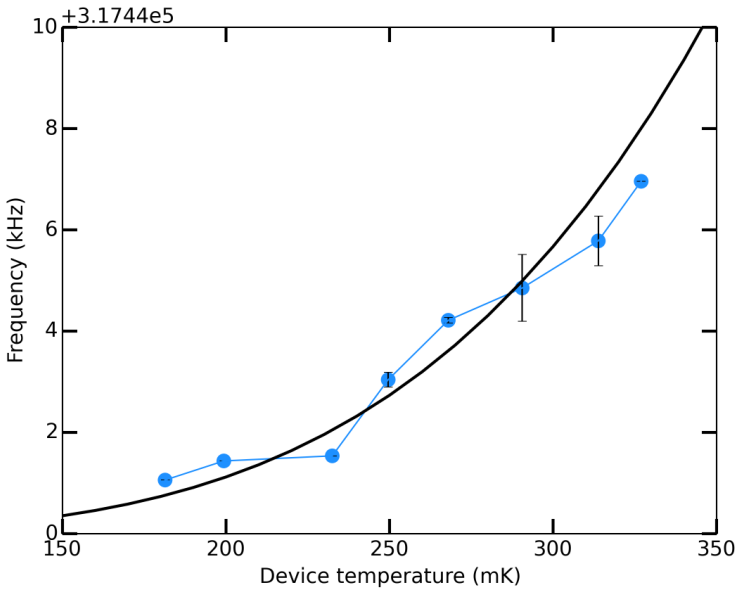

Figure 7.8: The frequency of the mechanical oscillator vs. device temperature.

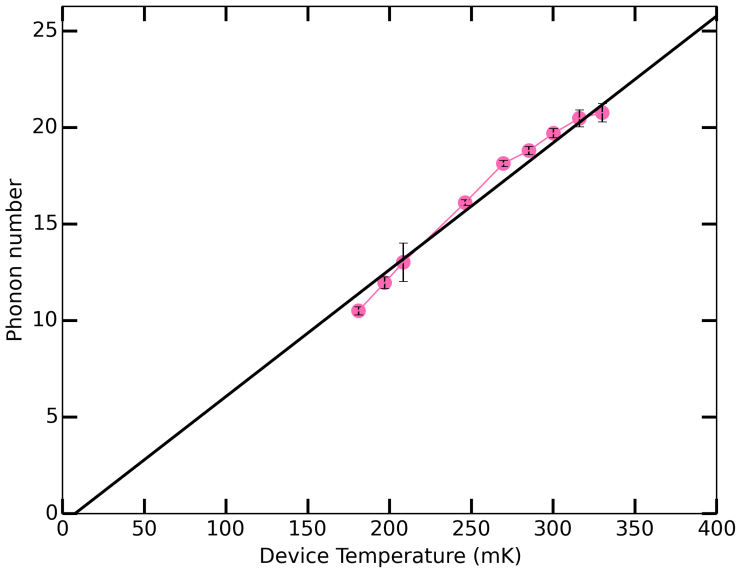

Figure 7.9: The phonon number in the mechanical oscillator vs. device temperature.

7.6 Cooperativity

As described in the introduction, the multiphoton cooperativity and thermal cooperativity are important figures of merit. Here we will calculate the cooperativities for the first generation device.

The single photon cooperativity is $C_0 = 1.3 \times 10^{-4}$ using the following assumptions: $\kappa/2\pi = 69$ MHz, $\gamma_{\text{ext}}/2\pi = 4.5$ kHz (calculated from the fit to Q_{ac}), $g_0/2\pi = 3.18$ kHz. The multiphoton cooperativity is given by:

$$C = \frac{4g_0^2}{\kappa\gamma} n_{\text{cont}} = \frac{4g_0^2}{\kappa(\gamma_{\text{ext}} + \gamma_{\text{int}}(P_{\text{inc}}, n_{\text{total}}))} n_{\text{cont}} \tag{7.37}$$

Here n_{total} gives the total circulating photon number; n_{cont} gives the circulating photon number in the control beam that is used for measurement; $\gamma_{\mathrm{int}}(P_{\mathrm{inc}}, n_{\mathrm{total}})$ was calculated from the thermal model. The circulating photon number is calculated assuming $\Delta_{\mathrm{Control,cav}} = \omega_{\mathrm{m}} \approx 2\pi \times 317$ MHz, and $\Delta_{\mathrm{LO,cav}} = 2\pi \times 1$ GHz; the relative power in the control beam is 9 %; the relative power in the LO is ≈ 82 %; the input coupling is $\kappa_{\mathrm{ext}}/\kappa = 0.22$.

In figure 8.23, the multiphoton cooperativity is plotted vs. power incident on the cavity. The cooperativity increases steadily for powers below 100 μW. After that it stays constant, which represents a balance between increasing n_{cont} and γ_{int}. For the calculations we assume $T_{\mathrm{MC}} = 0$. The black star denotes the maximum cooperativity $C = 4.1 \times 10^{-2}$ achieved in the first generation device.

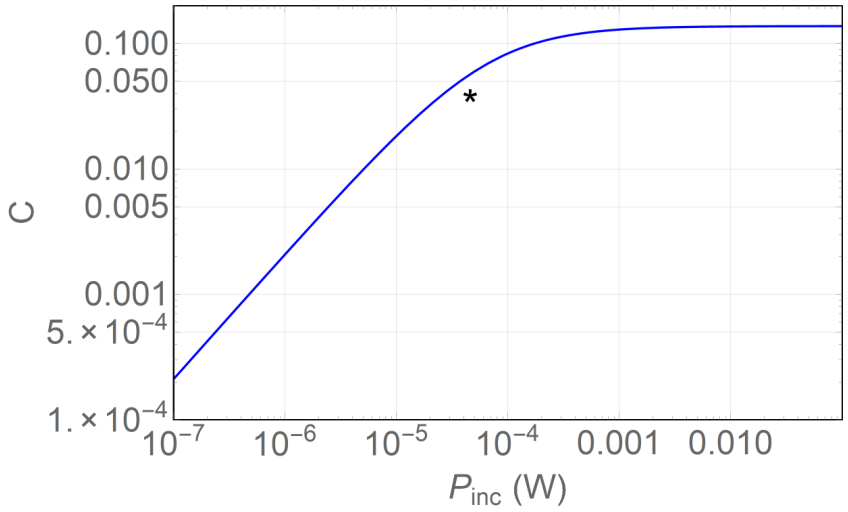

Figure 7.10: The multiphoton cooperativity vs. incident laser power. Blue line - cooperativity in the first generation device. Black star - maximum cooperativity achieved in the first generation device.

Figure 8.24 shows the thermal cooperativity $C_{\mathrm{th}} = C/n_{\mathrm{th}}$. The n_{th} is calculated from T_{dev}. The thermal cooperativity reaches the maximum for about 100 μW incident power. Above that incident power, the multiphoton cooperativity stays constant, while n_{th} is increasing, which leads to a decrease in the thermal cooperativity. The black star denotes the maximum thermal cooperativity $C_{\mathrm{th}} = 2.5 \times 10^{-3}$ achieved in the first generation device.

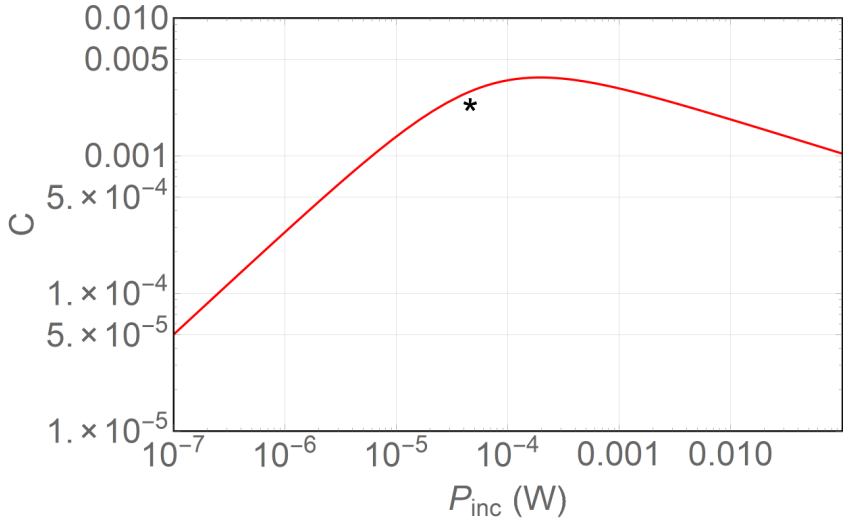

Figure 7.11: The thermal cooperativity in the first generation device vs. incident laser power. Red line - thermal cooperativity in the first generation device. Black star - maximum thermal cooperativity achieved in the first generation device.

7.7 Summary

In conclusion, the first generation device was a success. For the first time, optomechanical coupling was observed between the optical and acoustic modes of a cavity with with superfluid helium. We observed the effects of optomechanically induced amplification and measured the thermal motion of an acoustic mode.

This system achieved dimensionless figures of merit comparable to state-of-the-art, solid-based optomechanical systems ($\omega_{\rm m}/\kappa = 4.6$, $g_0/\kappa = 4.6 \times 10^{-5}$, $n_{\rm th} = 11$), and without the need for *in situ* alignment. The acoustic loss in this system agreed well with a simple model. The maximum thermal cooperativity was 0.0025, which could be improved with a few simple changes to the device geometry to provide a better thermal link to the mixing chamber. These changes will be described in the next chapter. The single photon cooperativity can be improved by making mirrors more reflective to the acoustic waves. I will describe our attempts to do that in the next chapter as well.

In this device, it was only possible to have a positive (blue) detuning of the control beam from the cavity. Detuning the control beam to the red side, resulted in parametric instability, in which the low frequency modes ($\omega_{\rm m} \approx 20 - 100$ kHz) would oscillate and prevent us from being able to lock the laser to the cavity.

Next section will describe some of these low frequency modes, that we observed in the device. I will discuss their origin, frequency and the optomechanical coupling to these modes.

7.8 Low frequency modes

In addition to the 317 MHz paraxial modes, two other distinct families of acoustic modes are observed: low frequency modes ($20 - 300$ KHz) and high frequency modes ($2 - 20$ MHz). Some of the low frequency modes show strong dependence on the helium level, so we concluded that the mode profiles extend beyond the cavity volume into the helium sheath between the fiber and the ferrule, and into the funnel. Those modes are referred to as "ferrule modes". In contrast, the high frequency modes are independent of the helium level and have frequencies consistent with the radial acoustic modes of a cylinder of helium. Those modes are referred to as "radial modes", described briefly in section 4.1.3.2. This section will be an exploration of those modes. Since the frequencies of the ferrule modes depend on helium level in the device, we need to understand how the device gets filled.

7.8.1 Helium level in the device

As described in section 6.4.1, helium is added to the device cell using the experimental gas handling system (expGHS). Helium is added to the cell in discrete doses. Each dose ("large volume") at room temperature contains $\simeq 13.4$ cm^3 helium gas at a pressure of $\simeq 1100$ mbar. The doses are added at a rate of approximately one every three minutes. Due to the geometry of the system (shown in Figure 7.12), helium first condenses inside the volume containing the sintered silver heat exchanger (which is a local gravitational minimum), and then "creeps" as a Rollin film, described in section 3.2 along the walls of a connecting capillary to fill the cell.

Before helium starts to condense in the cell, all parts of the system (the sintered silver heat exchanger, the cell, the capillary connecting the sintered silver heat exchanger to the cell) are covered by the superfluid Rollin film. The surface area of the sintered silver heat exchanger is specified to be $\simeq 10$ m^2 [144] which is at least two orders of magnitude larger than the combined surface area of other parts of the system. The volume of liquid helium necessary to cover the sintered silver heat exchanger with Rollin film is estimated to be 0.16 cm^3 $< V_{\rm film} < 0.38$ cm^3. Both bounds are found by assuming constant film thickness throughout the sinter. The lower bound results from assuming the bulk helium level to be located in the device (6 cm below the top of the sinter), while the upper bound results from assuming the bulk helium level to be located in the volume containing the sinter (0.5 cm below the bottom of the sinter).

As soon as the amount of helium in the system exceeds $V_{\rm film}$, helium starts condensing at the bottom of the volume containing the sintered silver heat exchanger and starts flowing into the cell at a rate $\dot{V}$, given by equation 3.2. The

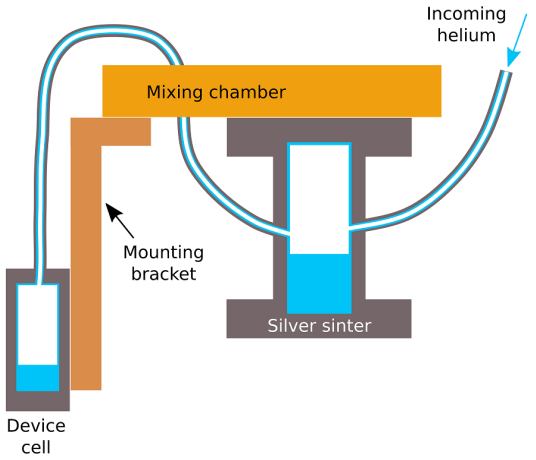

Figure 7.12: A schematic drawing of the helium delivery system at the mixing chamber (MC) of the dilution refrigerator. The helium (blue) enters through a capillary (shown on the right). It first condenses in a silver sinter (gray), and then flows via Rollin film into the cell. The cell is attached to a gold-plated OFHC copper mounting bracket, which is attached to the MC.

highest point of the capillary is located $\simeq$ 20 cm above the minimum liquid level in the sinter, resulting in the minimum film thickness $\simeq$ 14 nm. Therefore the rate of filling the device is $\dot{V} = 4 \times 10^{-4}$ cm^3/min. If, at any point, there is no helium accumulated at the bottom of the sintered silver heat exchanger volume, helium stops flowing into the device.

Using this model, we can describe the volume of liquid helium accumulated in the device as a function of time, as shown in figures 7.13 and 7.14. As we record the time and volume of each "dose" of helium (blue dots), we can calculate the total amount of helium added (blue line), where we assume that it takes about a minute for helium to condense in the system (from monitoring the temperature of the mixing chamber). The helium starts to accumulate in the silver sinter (purple line) covering it with the Rollin film. When the volume of helium in the sinter reaches V_{film} the helium starts flowing into the device cell at a rate $\dot{V}$. The red line shows the helium level in the device. We noted after which dose the device gets filled, but we did not note the exact time. Therefore we can only be sure that device got filled in some time after that dose, but before the next one. That time interval is indicated by the grey shading. From the CAD model of the device we calculated that the volume necessary to fill the cavity is 0.103 cm^3 - shown with the horizontal black line. Ideally, we expect the red line to cross the horizontal black line within the gray area. When we fit the data, as described later, we find the optimal values for $V_{\mathrm{film}} = 0.22$ cm^3 (within the range) and $\dot{V} = 6.5 \times 10^{-4}$ cm^3/s (larger that original estimate, which could be due to increased inner area of the capillaries, for example if the inner surface of the capillaries is not smooth but rough).

Using a CAD model of the cell, the helium level in the cell can be modeled as a function of the volume of helium accumulated in the device. This is shown with a blue line on Figure 7.15.

7.8.2 Helium level inside the ferrule

Since the cavity is located inside the ferrule, the helium level in the ferrule is of interest. The helium level in the ferrule is higher than the helium level in the cell due to capillary action [145]. Here we calculate the helium level in the ferrule as a function of the helium level in the cell.

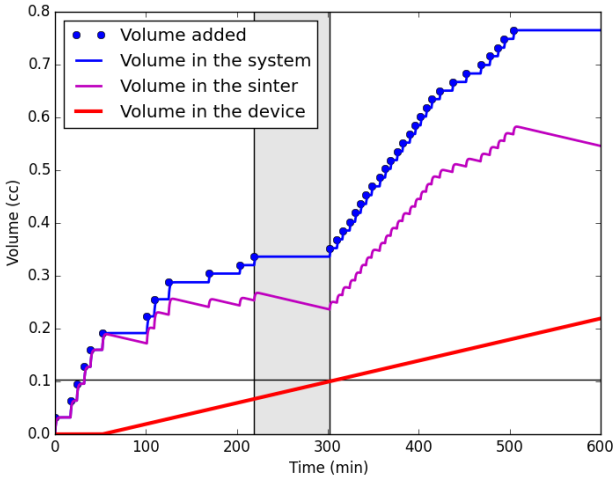

Figure 7.13: Volume of helium accumulated in the various parts of the system. Here we take $V_{\text{film}} = 0.16$ cm^3 and $\dot{V} = 4 \times 10^{-4}$ cm^3/s

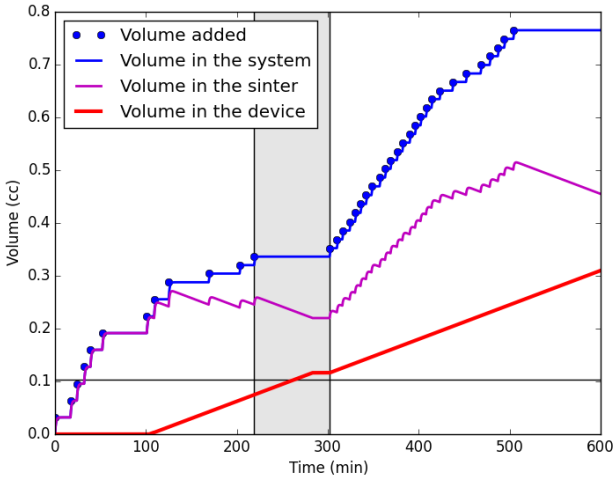

Figure 7.14: Volume of helium accumulated in the various parts of the system. Here we take $V_{\text{film}} = 0.22$ cm^3 and $\dot{V} = 6.5 \times 10^{-4}$ cm^3/s

7.8.2.1 Hollow tube of constant radius

To understand capillary action in the ferrule, consider first a simple model: a thin tube of radius r submerged in a fluid bath. Assume that the pressure above the bath is zero. The surface tension is σ and the contact angle is θ_c, as shown in the inset of figure 3.5 (b).

The height h^* to which the fluid rises can be determined by balancing gravitational potential energy and interfacial energy, which is done done by minimizing the free energy. The free energy of the system is given by:

$$F(h) = \int_V \rho g z dV - \int_A \sigma \cos\theta_c dA \tag{7.38}$$

Here V is the volume of the fluid in the capillary above the bath level, and A is the area over which helium is in contact with glass above the bath level. The values ρ and g are the density of the fluid and the gravitational constant. In the case

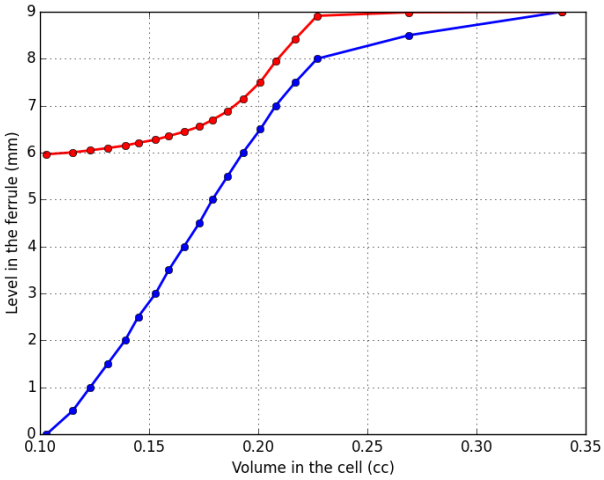

Figure 7.15: Blue: Helium level in the cell as a function of the volume of helium accumulated in the device. Zero on the vertical axis corresponds to the bottom of the ferrule. As more helium is added to the cell, the helium level in the cell changes non-linearly, due to cell geometry. A CAD model of the cell geometry was used to calculate helium level inside the cell, given the volume of added helium. Red: helium level in the ferrule calculated in section 7.8.2.

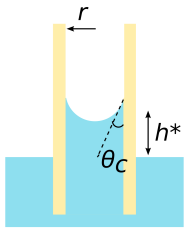

Figure 7.16: A schematic drawing of a cylindrical capillary of radius r, submerged in liquid. The contact angle is θ. Due to capillary action the liquid rises to height h^*

above, ignoring the meniscus, we arrive at equation:

$$F(h) = \rho g \pi r^2 \int_0^h z dz - \sigma \cos\theta_c 2\pi r h = \rho g \pi r^2 \frac{h^2}{2} - \sigma \cos\theta_c 2\pi r h \tag{7.39}$$

The height of the fluid in the capillary is found by setting the derivative of the free energy to zero:

$$h^* = \frac{2\sigma \cos\theta_c}{\rho g r} \tag{7.40}$$

The ferrule diameter is 133 μm. For the capillary of this diameter submerged in superfluid helium ($\rho_{\mathrm{He}} = 145$ kg/m^3 [90], $\theta_{\mathrm{c,He}} = 0°$ [146] and $\sigma_{\mathrm{He}} = 3.78 \times 10^{-4}$ J/m^2 [146], the fluid rises by $h^* = 8$ mm.

7.8.2.2 Hollow axissymmetric tube of arbitrary shape

The ferrule is a hollow axissymmetric tube of arbitrary shape: $r = r(z)$. Here r is the distance from the axis of the ferrule and z is the distance from the bottom of the ferrule. The free energy is:

$$F(h) = \rho g \pi \int_0^h r(z)^2 z dz - \sigma \cos\theta_c 2\pi \int_0^h r(z) \sqrt{1 + \left(\left. \frac{dr}{dz} \right|_z \right)^2} dz \tag{7.41}$$

In addition, there is a fiber in the center of the ferrule, which is modeled as a solid tube of constant radius r_{fib}. The free energy then is:

$$F(h) = \rho g \pi \int_0^h \left[r(z)^2 z - r_{\text{fib}}^2 h \right] dz - \sigma \cos\theta_c 2\pi \int_0^h \left[r(z) \sqrt{1 + \left(\left. \frac{dr}{dz} \right|_z \right)^2} + r_{\text{fib}} \right] dz \tag{7.42}$$

The derivative of the free energy with respect to h, evaluated at h^* is:

$$\left. \frac{dF}{dh} \right|_{h^*} = \rho g \pi \left[r(h^*)^2 - r_{\text{fib}}^2 \right] h^* - \sigma \cos\theta_c 2\pi \left[r(h^*) \sqrt{1 + \left(\left. \frac{dr}{dz} \right|_{h^*} \right)^2} + r_{\text{fib}} \right] = 0 \tag{7.43}$$

Equation 7.43 can be used to find the height of the capillary rise for the ferrule with a fiber, provided the ferrule profile is known.

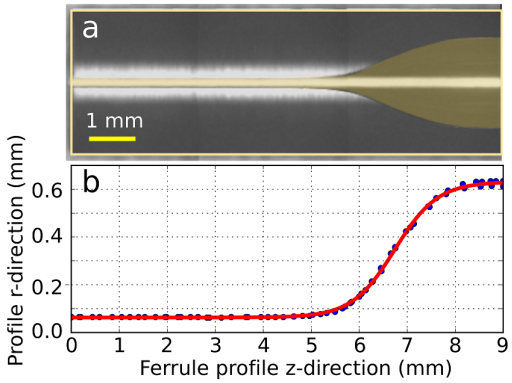

Figure 7.17: (a) A photograph of the ferrule. Yellow shading indicates the funnel and the bore. The ferrule profile extracted from the photograph (a) is shown using blue dots. The red line is a fit of equation 7.44 to the profile.

A photo of the ferrule is shown in the Figure 7.17(a). The ferrule is made of borosilicate glass with index of refraction $n = 1.52$. The length and diameter of the ferrule are 9 mm and 3 mm respectively. This information can be used to correct the image and extract the profile of the ferrule bore. The extracted profile is shown in Figure 7.17(b) with blue circles. In order to evaluate equation 7.43 analytically, the profile is fit to the function:

$$r(z) = C \tanh\left(\frac{x - A}{B} \right) + C + D \tag{7.44}$$

The following values are found for the fit parameters: $A = 6739.5$ μm, $B = 890.41$ μm, $C = 293.7$ μm, $D = 65.2$ μm. The fit is shown in Figure 7.17(b) with a red line.

7.8.2.3 Young-Laplace equation

Young-Laplace equation describes the shape of an interface between two fluids. It is given by the following:

$$\sigma \left(\frac{1}{R_1} + \frac{1}{R_2} \right) = \delta p \tag{7.45}$$

Here R_1 and R_2 are the two principal radii of curvature and δp is the difference in pressure at the interface.

Consider a capillary of radius r_c submerged into fluid. Assume we choose a horizontal plane and take the difference in pressure in this plane to be δp_0. As we go up along the z-axis from the plane the difference in pressure will change linearly according to:

$$\delta p = \delta p_0 - \rho g z \tag{7.46}$$

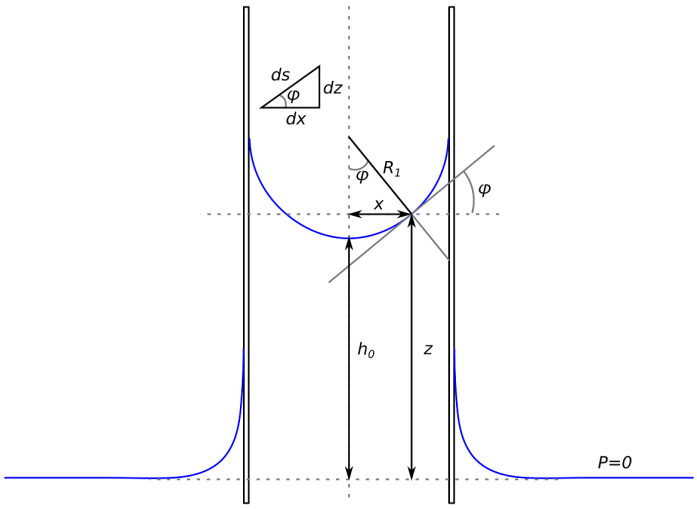

Figure 7.18: A capillary submerged into fluid.

In this equation ρ is density of the fluid, g is the gravitational constant and z is the distance along z-axis. The two radii of curvature for any point are defined as follows:

$$\frac{1}{R_1} = -\frac{\sin\phi}{x} \qquad \frac{1}{R_2} = -\frac{d\phi}{ds} \tag{7.47}$$

Here s is the arclength along the interface and everything else is defined in figure 7.18. The negative sign is due to the surface being concave for both R_1 and R_2. Far away from the capillary, the surface of the liquid is flat, therefore the pressure difference $\delta p_0 = 0$. Combining all together we arrive at equation:

$$\sigma\left(\frac{\sin\phi}{x} + \frac{d\phi}{ds}\right) = \rho g z \tag{7.48}$$

This equation can be rearranged as:

$$\frac{d\phi}{ds} = \frac{z}{l^2} - \frac{\sin\phi}{x} \tag{7.49}$$

Where $l = \sqrt{\frac{\rho g}{\sigma}}$ is the capillary length.

Now consider a point anywhere on the surface. Immediately in the vicinity of that point, we can say (see fig 7.18 inset):

$$\cos\phi = \frac{dx}{ds} \qquad \sin\phi = \frac{dz}{ds} \tag{7.50}$$

The coupled differential equations 7.49 and 7.50 can be solved with appropriate boundary conditions, however it it sometimes useful to have the equations in terms of the angle, rather than arclength. To do that, we define:

$$\frac{d\phi}{ds} = \frac{z(\phi)}{l^2} - \frac{\sin\phi}{x(\phi)} \equiv Q(\phi) \tag{7.51}$$

From equation 7.50, we can then write:

$$\frac{dx}{d\phi} = \frac{\cos\phi}{Q(\phi)} \qquad \frac{dz}{d\phi} = \frac{\sin\phi}{Q(\phi)} \tag{7.52}$$

Now, we only have two coupled differential equations. The boundary conditions are $x(0) = 0$, $x(\pi/2) = r_c$. In practice, we first solve equations 7.52 numerically for ϕ varying from 0 to $\pi/2$ with $x(0) = 0$ and $z(0) = h_0$, where h_0 is a free

parameter. Afterwards, we find the value of h_0 for which $x(\pi/2) = r_c$. We take the value for h_0 obtained using equation 7.40 as the initial guess.

For a hollow tube of arbitrary shape $r(z)$ with a fiber of radius R_f in the center, equations are exactly the same, except we first solve equations 7.52 numerically for angle varying from $-\pi/2$ to $\pi/2$ with $x(-\pi/2) = R_f$ $z(-\pi/2) = h_0$, where h_0 is a free parameter. We then numerically find the value of h_0 for which:

$$\arctan(r'(z(\pi/2-\theta))) = \theta \qquad x(\pi/2-\theta) = r(z(\pi/2-\theta)) \tag{7.53}$$

We take an initial guess for h_0 using equation 7.43. The initial guess for θ is $\arctan(r'(h_0))$. Figure 7.19 shows a solution for a ferrule submerged into helium by 6.5 mm.

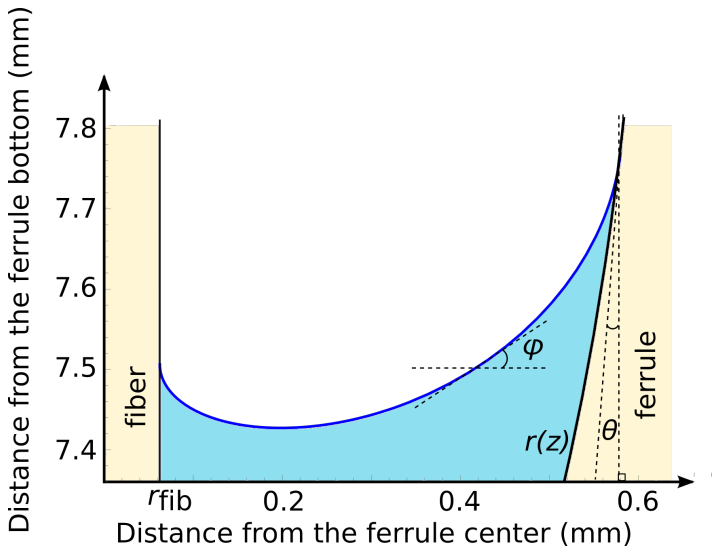

Figure 7.19: A solution for the ferrule in question submerged into fluid. Here the helium level is 6.5 mm above the bottom of the ferrule.

Now that we know the helium level in the ferrule as a function of helium level in the device, we find the helium level in the ferrule as a function of helium volume in the device. It is shown in figure 7.15 using a red line.

7.8.3 Comsol simulations and experimental results

The frequencies of the radial modes do not change appreciably with the change of helium level. We can find the expected frequencies for the radial modes using COMSOL to solve the wave equation for a cylinder of helium with length $L = 84$ μm and radius $R = 67$ μm with the 1.5 μm deep indentations for the mirrors with appropriate radii of curvature. The wave equation is solved for both $m = 0$ and $m = 1$ cases. The boundary condition is "zero flux" on all the boundaries. In figure 7.20 the thick black line shows a typical measurement of the OMIT/OMIA response for the intracavity beatnote frequency in the range 1-20 MHz. The sharp features are the radial modes. The dashed lines are the predicted frequencies for the radial indices $m = 0$ (red) and $m = 1$ (blue), obtained using COMSOL simulations. The frequencies obtained from COMSOL show good agreement with the frequencies obtained experimentally. The features associated with the $m = 0$ modes are dominant, but there is also clearly coupling to the $m = 1$ modes, which confirms that the optical mode is not perfectly aligned with the axis of the cylinder.

The frequencies of the ferrule modes are found by implementing the whole geometry of the ferrule, fibers and meniscus in COMSOL and solving the wave equation for this geometry. All of the helium-glass boundaries are "zero flux" boundaries. The bottom end of the ferrule is open, so it requires zero-pressure boundary condition ("Dirichlet boundary condition") and the top surface of the helium (helium-vacuum boundary), which has the meniscus shape, is described by a "free surface" boundary condition. Since it was experimentally observed that the frequencies of some of the ferrule modes

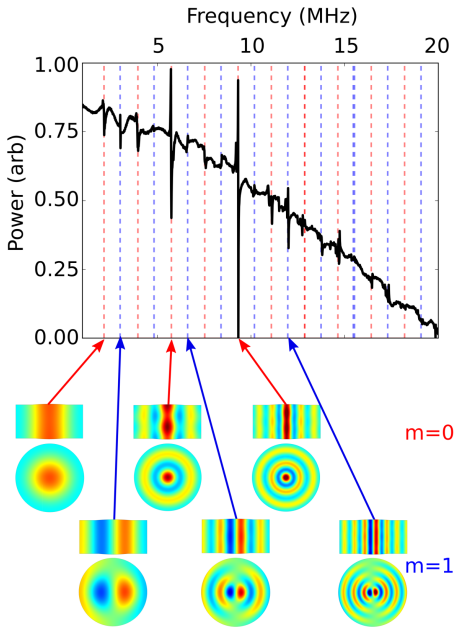

Figure 7.20: The frequencies of the radial modes. Red: $m = 0$ modes, blue: $m = 1$ modes. The OMIT/A signal for the intracavity beatnote frequency in range 1-20 MHz is shown with a thick black line. The overall downward slope is due to the cavity filtering. The measured mode frequencies match well with the predicted frequencies for $m = 0$ and $m = 1$ modes. The profiles of some of the modes are shown in the bottom part of the figure.

change with the level of helium, we simulate the mode frequencies vs. the helium level in the ferrule. Figure 7.21 (a) shows the profiles of the modes when the helium level in the ferrule is 6.8 mm. The solid lines in figure 7.21 (b) show the mode frequencies obtained via COMSOL simulations for different volumes of helium accumulated in the device. The color of each line indicates the relative amount of energy stored in the sheath to the energy stored in the funnel. The modes with a large fraction of energy stored in the funnel show dependence on the helium level, decreasing in frequency as the helium level increases.

Figure 7.21 (b) and (c) shows a density plot of the OMIT/A response for intracavity beatnote frequencies in the range 20-300 kHz (the frequency range of the ferrule modes). The vertical axis is the amount of helium accumulated in the device. Figure 7.21(b) additionally shows the overlaid COMSOL simulation of the frequencies of the modes. In order for the data to agree with the COMSOL simulations, we need to take the volume of the helium film to be $V_{\text{film}} = 0.22$ cm^3, which is within the predicted bounds. The rate at which helium accumulates in the device is found to be $\dot{V} = 6.5 \times 10^{-4}$ cm^3/min, which is larger than the original prediction of 4×10^{-4} cm^3/min, obtained using equation 3.2.

7.8.4 Optomechanical coupling

In order to understand the optomechanical coupling to the modes, we measured the OMIT/A feature for the 7.5 MHz radial mode and the 23 kHz ferrule mode. One of the sweeps for each mode is shown in figure 7.22.

These modes clearly showed the familiar optical spring and optical damping [3], however the sign and relative magnitude of these effects were inconsistent with coupling via electrostriction. Figure 7.23 shows the linewidth, frequency, amplitude, and phase of the OMIT feature relative to the background as a function of the control beam detuning for the 7.5 MHz mode. The data is fit with the OMIT/OMIA theory described in section 5.6, using the theoretical value of electrostrictive coupling $g_0/2\pi \approx 300$ (calculated in section 4.2.2) and assuming the acoustic mode profile $p(r, \theta) = J_0(\alpha_{05} r/R)$ (described in section 4.1.3.2). From this fit, we extract the intrinsic linewidth of the mode to be 11.7 kHz (corresponding to

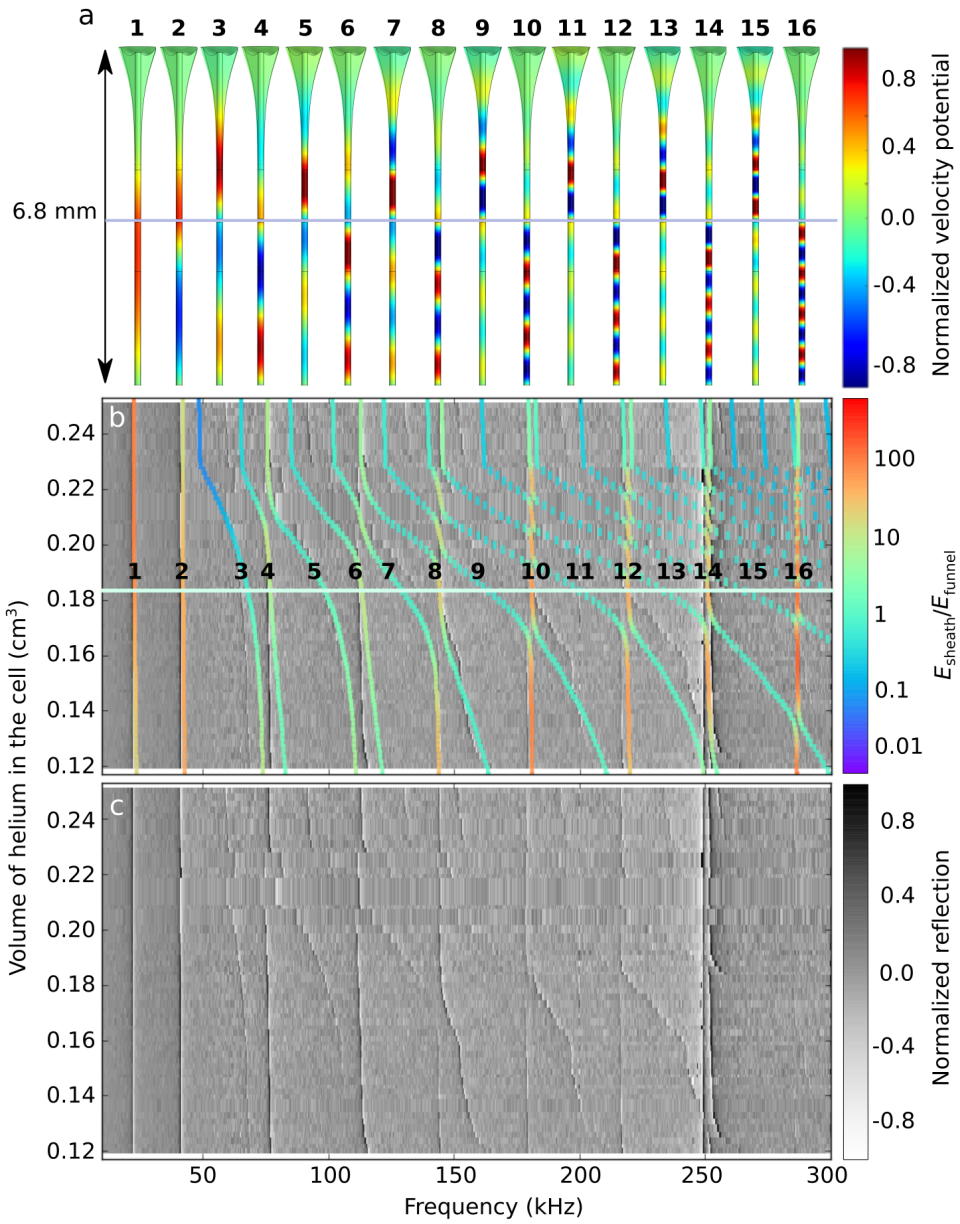

Figure 7.21: a) Several mode profiles of the helium in the ferrule when the helium level is 6.8 mm,calculated using COMSOL. The color indicates the normalized velocity potential. Some of the modes (e.g. 10,12,14,16) are mostly localized in the sheath of helium surrounding the fibers in the bore below the cavity. Some other modes (e.g. 9,11,13,15) are mostly localized in the helium above the cavity. The gray line shows the position of the cavity. b) Solid lines: the frequencies of the modes as a function of the volume of helium accumulated in the device. The color indicates the ratio of energy stored in the sheath to the energy stored in the funnel. The modes that are mostly confined in the sheath do not change in frequency as the more helium accumulates in the cell. The modes that extend into the funnel show a decrease in frequency as the helium level rises. The light blue line is at 0.182 cm^3 (which corresponds to 6.8 mm of helium in the ferrule and hence the simulations is panel (a)). The black numbers are located at the intersections of the light blue line with the colored lines correspond to the numbers in panel (a). Density plot: the measurements also shown in (c). c) Density Plot of the OMIT/OMIA signal for intracavity beatnote frequencies in range 10-300 kHz as a function of the volume of helium condensed in the device.

a quality factor Q = 642), and $\kappa_{\rm th}/2\pi = 1.1 \pm 0.2$ MHz

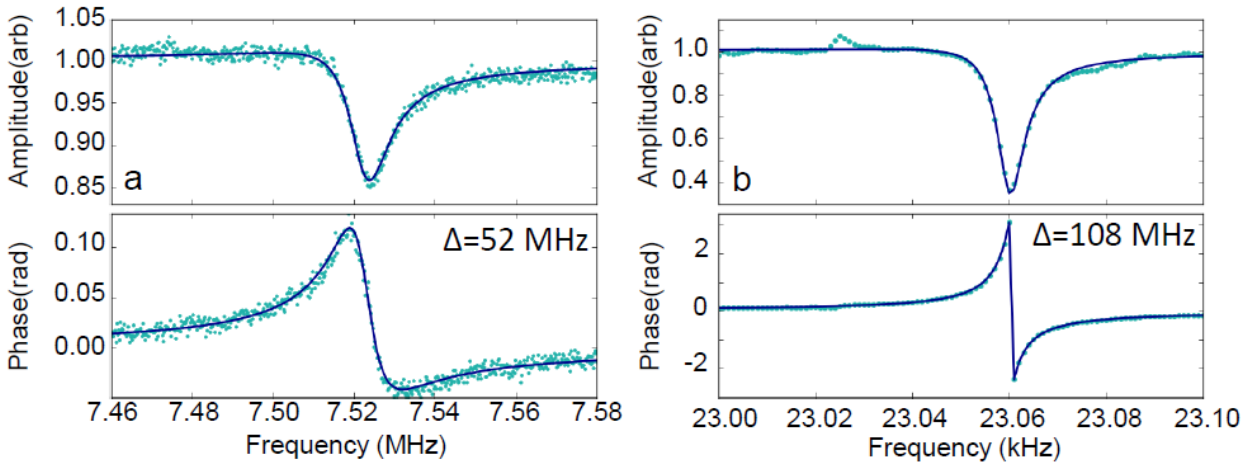

Figure 7.22: OMIT/A measurements. The teal points are the normalized amplitude (a) and phase (ψ) of the OMIT signal as a function of the intracavity beat note frequency $|\omega_{\rm control} - \omega_{\rm probe}|/2\pi$. The data is taken by sweeping the frequency difference between the control and probe beams. Shown are the sweeps of the probe beam, which is blue-detuned from the control beam. The data is normalized so that far from the resonance $a = 1$ and $\psi = 0$. The solid blue line is fit to a complex Lorentzian. The fit parameters are A_+ and Ψ_+ (the overall amplitude and phase of the OMIT effect), $\omega_{\rm m}$ (the acoustic frequency), and γ_m (the acoustic damping rate). **a)** The sweep over one of the radial modes. The intracavity beat note frequency is varied between 7.46 and 7.58 MHz. The control beam is detuned from the cavity resonance by 52 MHz. **b)** The sweep over one of the ferrule modes. The intracavity beat note frequency is varied between 23.0 and 23.1 kHz. The control beam is detuned from the cavity resonance by 108 MHz.

Figure 7.24 shows the corresponding measurements for the 23 kHz ferrule mode. The intrinsic linewidth of this mode is 19 Hz, corresponding to a quality factor $Q = 1,200$. The value of electrostrictive coupling to the ferrule modes is not known *a priori*, so the fits are underconstrained. However large values of $\kappa_{\rm th}$ result in almost perfect cancellation of g_1 and g_0. For example, for $\kappa_{\rm th}/2\pi > 30$ kHz, the ratio $|g_1/g_0 + 1| < 0.05$. Since there is no physical mechanism that would cause the coupling rates to almost cancel, we limit $\kappa_{\rm th} < 2\pi \times 30$ kHz. This allows us to put bounds on $g_0/2\pi$ to be between 230 Hz and 600 Hz.

The findings are summarized in Table 7.3, where the real and imaginary parts of $g_{1,\rm filt}$ are calculated as well to ease the comparison with the paraxial mode described earlier in the chapter and in [37].

Mode	$\omega_{\rm m}/(2\pi)$	$g_0/(2\pi)$	$\kappa_{\rm th}/(2\pi)$	${\rm Re}[g_{1,\rm filt}]/(2\pi)$	${\rm Im}[g_{1,\rm filt}]/(2\pi)$
Ferrule	23 kHz	$0.23 \sim 0.6$ kHz	< 30 kHz	$0 \sim -0.5$ kHz	$-0.5 \sim -0.16$ kHz
Radial	7.5 MHz	0.3 kHz	1.1 ± 0.2 MHz	-1.1 ± 0.4 kHz	-7.5 ± 1.7 kHz
Paraxial	317 MHz	3.18 ± 0.2 kHz	$\ll 317$ MHz	set to 0 Hz	0.97 ± 0.05 kHz

Table 7.3: Properties of the two types of mode (ferrule and radial) studied, as well as the corresponding properties of the paraxial mode.

We note that for the paraxial mode, we used the assumption that the photothermal bandwidth is much smaller than the driving frequency, which allowed us to set the real part of $g_{1,\rm filt}$ to zero. This assumption was justified because of the large frequency $\omega_{\rm m} \simeq 317$ MHz. We are not making the same assumption for the modes studied here, which allows us to extract the value of $\kappa_{\rm th}$. We note that $\kappa_{\rm th}$ differs greatly between ferrule and radial modes, from which we can infer that there are at least two different photothermal coupling mechanisms, described in section 5.6.

The photothermal coupling to the 23 kHz ferrule mode (and other ferrule modes) could result from helium counterflow. The bandwidth for this effect is set by the thermal equilibration time inside the cavity, which was measured in [37] to be $\tau \approx 350$ μs, corresponding to bandwidth of 0.5 kHz, which is consistent with the range of $\kappa_{\rm th}$ found for this mode

($< 2\pi \times 30$ kHz).

The photothermal coupling to the 7.5 MHz radial mode can be explained in terms of the thermal expansion of the fiber mirrors due to laser heating. The value of $\kappa_{\rm th}$ found for this mode ($2\pi \times 1.1 \pm 0.2$ MHz) is consistent with the results of [147], where the bandwidth for the expansion of similar mirrors was measured at room temperature. The rough agreement between our results (for which $T < 1$ K) and the room temperature results of [147] may reflect an approximate cancellation of the temperature dependence of thermal conductivities and heat capacities for the relevant materials.

While both mechanisms are always present in the system, our analysis assumes that one of them dominates for each mode family. This makes sense intuitively: the counterflow mechanism results in larger helium density in the region between the fibers but with little variation within that region, and so should not couple efficiently to the radial modes. Additionally, the bandwidth of the counterflow mechanism is low, so the coupling of this mechanism to the radial modes is strongly filtered. In contrast, the expansion mechanism couples efficiently to modes whose wavelength is on the order of the hot spot (≈ 10 μm), resulting in stronger coupling to radial modes.

In this section, we have studied two families of acoustic modes that exist in a superfluid-filled optical cavity. These families are associated with the overall geometry of the device and its surroundings, rather than the with the cavity's paraxial modes. The frequencies of the modes and their dependence on the amount of helium added to the cell were understood. Additionally, the modes' optical spring and optical damping were measured, and these results were analyzed using a model that includes an instantaneous electrostricitve coupling as well as a non-instantaneous photothermal coupling. Both types of modes show a significant photothermal coupling. However they show widely divergent time scales for this coupling. We attribute this to the presence of two different microscopic mechanisms for photothermal coupling in this system. The first is the thermal expansion of the materials confining the superfluid. The second is the different rate of mass transport via superfluid flow and thermal excitations. These two mechanisms are associated with different time scales and also with different spatial profiles, which tends to ensure that each one couples to only one type of acoustic mode. These results highlight the wide range of microscopic mechanisms that can give rise to optomechanical coupling [3, 148, 149] and provide insight into the behavior of superfluid-filled optical cavities.

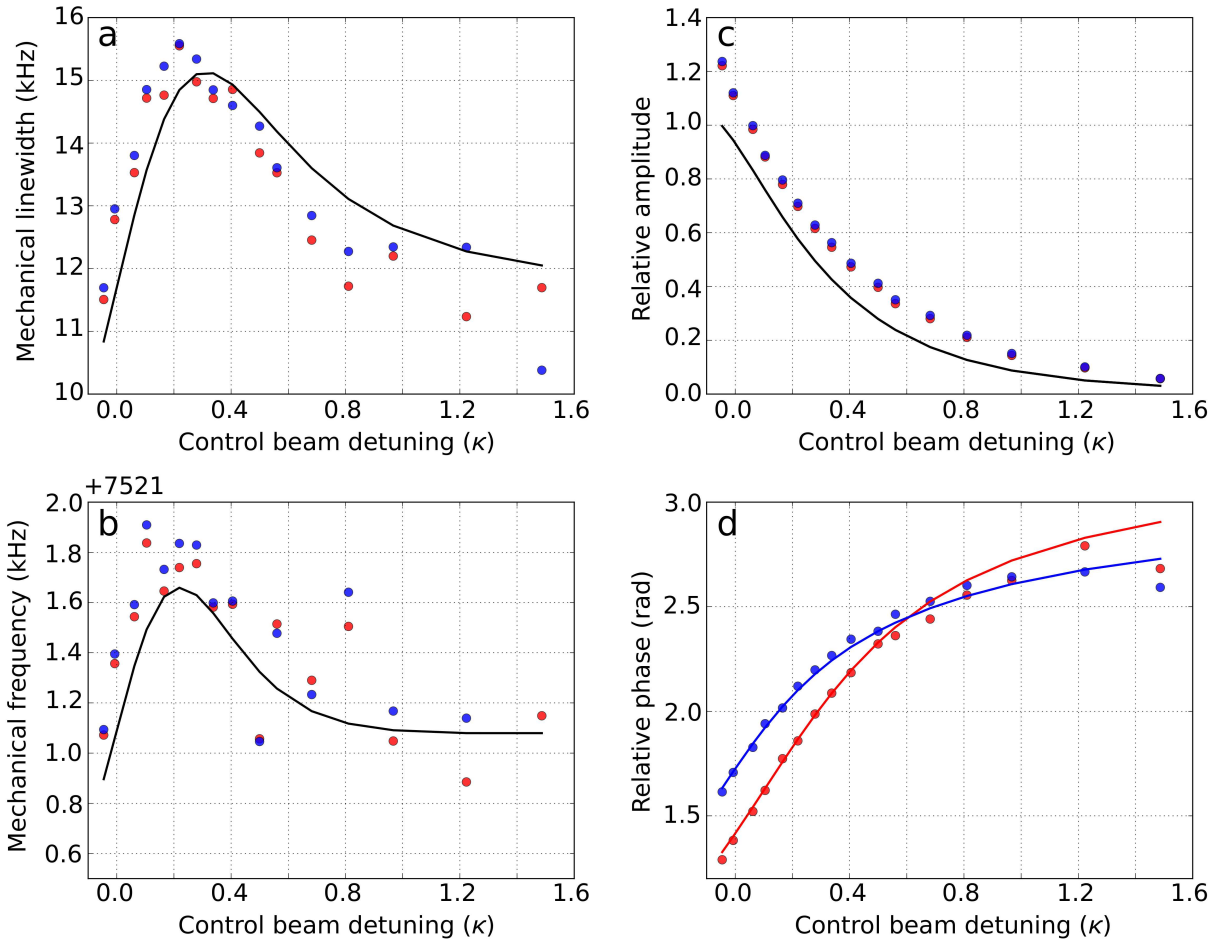

Figure 7.23: Optomechanical effects for the 7.5 MHz radial mode. Plotted with blue (red) points are the values of the fit parameters for the OMIT/A response at upper (lower) probe beam frequencies extracted from data sweeps such as shown in Figure 7.22 (a) for various detunings of the control beam.The power in the control beam is 0.6 μm. The horizontal axis is the detuning of the control beam from the cavity in units of κ. The solid lines are the fits discussed in the text, using the measured values of κ, $\kappa_{\rm ext}$, $a_{\rm i}$ and $\bar{\Delta}$. The fits to the acoustic linewidth, acoustic frequency, amplitude and phase of the OMIT/OMIT response relative to the background are all done simultaneously, assuming the theoretical value of electrostrictive coupling $g_0 = 2\pi \times 300$ Hz. The values of $\kappa_{\rm th} = 2\pi \times 1.1 \pm 0.2$ MHz, as well as the the intrinsic linewidth $\gamma = 2\pi \times 11.7$ kHz and the intrinsic frequency $\omega_{\rm m} = 2\pi \times 7.52$ MHz are the fit parameters extracted from the fit. **a)** The acoustic linewidth. The solid line is the fit to: $(\gamma + \gamma_{\rm opt})/2\pi$. **b)** The acoustic frequency. The solid line is the fit to: $(\omega_{\rm m} + \Delta\omega_{\rm m,opt})/2\pi$. **c)** The amplitude of the OMIT/A response relative to the background. The solid line is the fit to A_+ and A_- which are the same in the case of amplitude modulation. **d)** The phase of the OMIT/A response relative to the background. The solid blue (red) line is the fit to Ψ_+ (Ψ_-).

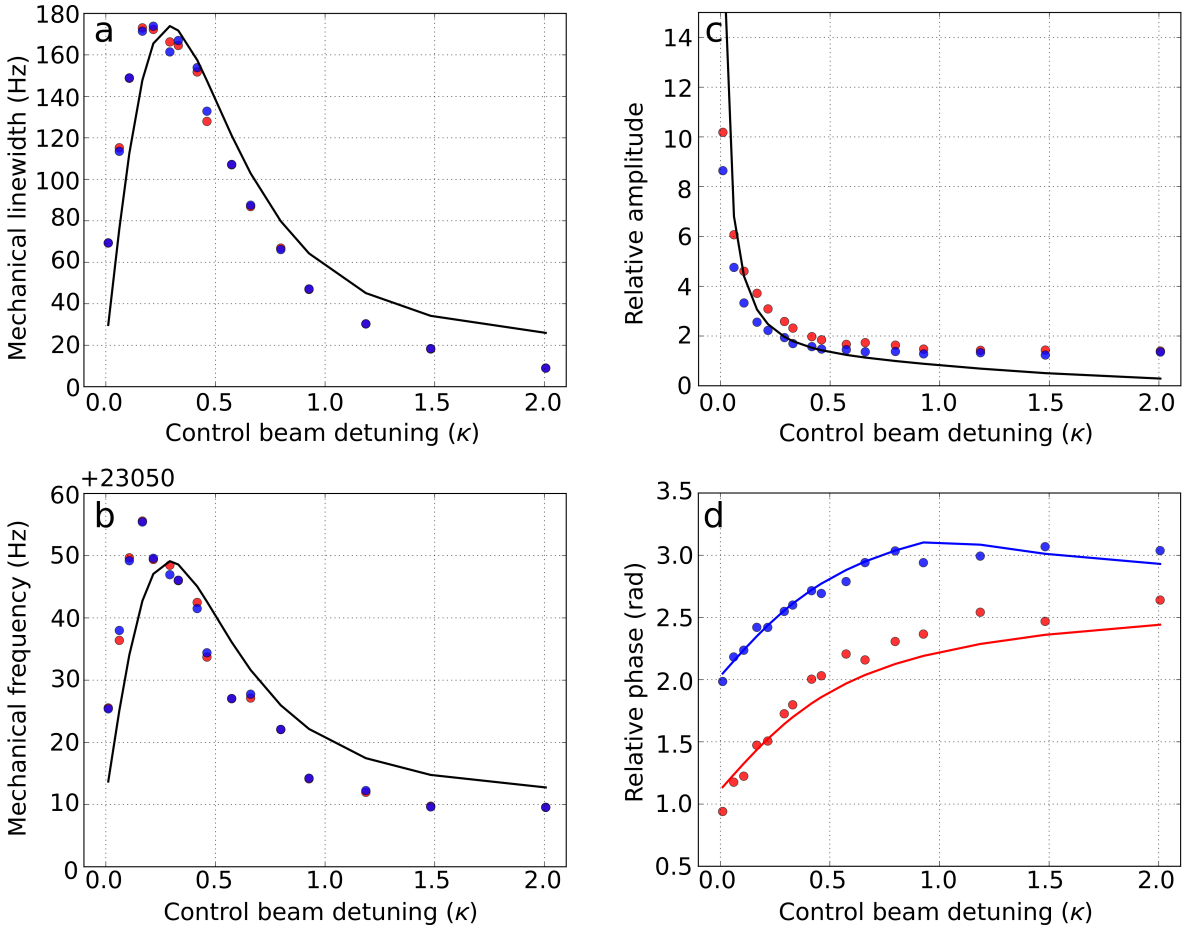

Figure 7.24: Optomechanical effects for the 23 kHz ferrule mode. Plotted with blue (red) points are the values of the fit parameters for the OMIT/A response at upper (lower) probe beam frequencies extracted from data sweeps such as shown in Figure 7.22 (b) for various detunings of the control beam. The power in the control beam is 0.6 μm. The detuning of the control beam is plotted on the x-axis in units of κ. The solid lines are the theory fits, using the measured values of κ, $\kappa_{\rm ext}$, $a_{\rm i}$ and $\bar{\Delta}$. The fits to the acoustic linewidth, acoustic frequency, amplitude and phase of the OMIT/A response relative to the background are all done simultaneously. The intrinsic linewidth $\gamma = 2\pi \times 19$ Hz and the intrinsic frequency $\omega_{\rm m} = 2\pi \times 23.061$ kHz are the fit parameters extracted from the fit. Additionally the value of $\kappa_{\rm th}$ is less than $2\pi \times 30$ kHz and the electrostrictive coupling rate g_0 is between $2\pi \times 230$ Hz and $2\pi \times 600$ Hz as described in the text **a)** The acoustic linewidth. The solid line is the fit to: $(\gamma + \gamma_{\rm opt})/2\pi$. **b)** The acoustic frequency. The solid line is the fit to: $(\omega_{\rm m} + \Delta\omega_{\rm m,opt})/2\pi$. **c)** The amplitude of the OMIT/A response relative to the background. The solid line is the fit to A_+ and A_- which are the same in the case of amplitude modulation. **d)** The phase of the OMIT/A response relative to the background. The solid blue (red) line is the fit to Ψ_+ (Ψ_-).

Chapter 8

Second generation device

The second generation device was built to improve on the parameters achieved in the first device. The main goal was to improve cooperativity. We improved it in two ways. First, we used a more open geometry which allowed a better thermal link to the mixing chamber, as described in section 6.3.2. Second, we developed acoustic DBR structures to increase the mirrors' reflectivity for acoustic waves. As we will see in the end of the chapter, we increased the maximum multiphoton cooperativity by a factor of 28 and the maximum thermal cooperativity by a factor of 37. This increase allowed us to observe optomechanical dynamical back-action, as well as asymmetry between the Stokes and anti-Stokes sidebands.

One qualitative difference between the first and second generation device is that the open geometry in the second generation device causes the temperature in the cavity to be non-uniform. In section 8.4 we will explain how the temperature varies using known properties of superfluid helium.

This device was also cooled down twice. Most of the data presented here was taken during the second cooldown.

8.1 Device parameters

The cavity used in the device consists of two mirrors with radii of curvature $R_1 = 497$ μm and $R_2 = 325$ μm. During the second cooldown $L_{\mathrm{empty,opt}} = 69.21 \pm 0.01$ μm, $L_{\mathrm{full,opt}} = 71.12 \pm 0.01$ μm, and $L_{\mathrm{mech}} = 68.0 \pm 0.01$ μm, all extracted in the same manner as for the first generation device. The optical mode with $\lambda = 1529.7$ nm ($q_{\mathrm{opt}} = 91$) was used. It coupled to the acoustic mode with $\omega_{\mathrm{m}}/2\pi = 319.24$ MHz ($q_{\mathrm{mech}} = 182$). The cavity linewidth was $\kappa/2\pi = 21 \pm 1$ MHz. The input coupling was $\kappa_{\mathrm{ext}}/\kappa = 0.44 \pm 0.03$. All these values were extracted as described in section 6.6.2.

8.2 OMIT/A measurements

We took OMIT/A data with a single control beam detuned far from the cavity resonance ($12\kappa < |\Delta| < 17\kappa$) on both red and blue sides. From the data we extracted the amplitude and phase of the OMIT/A signal relative to background, as well as acoustic mode's frequency and linewidth. The plots showing relative amplitude and phase, frequency and linewidth for different control beam powers and detunings, along with the theory fits are shown in figure 8.1. Due to the increased cooperativity, it was possible to observe optical spring and damping.

From the fits, shown in figure 8.1 we extracted the optomechanical and photothermal coupling. The optomechanical coupling was $g_0/2\pi = 3.6 \pm 0.1$ kHz. The photothermal coupling was $g_{0,\mathrm{pt}}/2\pi = 0.83 \pm 0.1$ kHz. The theoretical bounds on g_0 are 3.7 kHz$< g_0/2\pi < 4.1$ kHz.

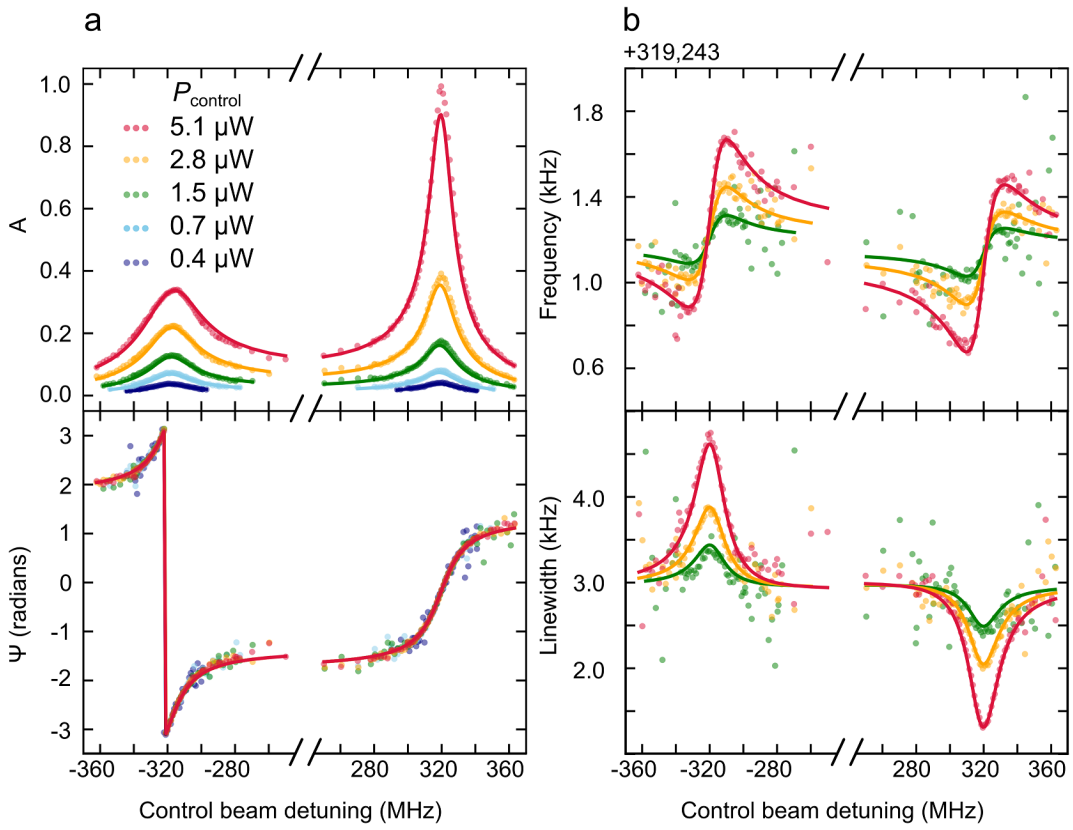

Figure 8.1: OMIT/A measurements and observations of optical spring and damping.**(a)** Amplitude A (top) and phase Ψ (bottom) of the OMIT feature relative to the background for five different control beam powers. The data is normalized so that far away from the mechanical resonance the signal is 1. The solid lines are fit to OMIT/A theory. **(b)**: acoustic frequency $\omega_{\rm m}/2\pi$ (top) and linewidth $\gamma/2\pi$ (bottom) as a function of control beam detuning for three different control beam powers. The solid lines show fits to the optomechanical back-action theory with photothermal coupling.

The bare (external) mechanical linewidth extracted from the fits is $\gamma_{\rm ext}/2\pi \approx 3.1 \pm 0.3$ kHz, which corresponds to mechanical quality factor $Q \approx 100,000$, which is an improvement over the previous device, and, as we will see in section 8.3.1, consistent with our calculation of the acoustic transmittivity of the DBR.

In the data sets shown in figure 8.1, the effects of the control beam on helium temperature inside the cavity are unnoticeable (otherwise the optical spring and damping would not be anti-symmetric). However, when data is taken with the control beam closer to the cavity resonances, it is clear that heating is present.

The linewidth and frequency extracted from the data sets taken with a wider range of the control beam detunings are shown in the top panel of figure 8.2. This data was taken during the first cooldown and the laser wavelength was $\lambda = 1538.9$ nm. We separate the data into the odd and even part. The middle panel shows the even part. The bottom panel shows the odd part. The odd part shows the familiar optical spring and damping effects. The even part shows that when the control beam is near the cavity resonance, then the linewidth increases and the frequency decreases. This is a result of the heating of the cavity by the circulating photons. I will explain in section 8.4 how this heating arises.

During the same cooldown, we decided to check if the optical mode with longitudinal mode number $q_{\rm opt}$ couples to any acoustic modes besides the one with longitudinal mode number $2q_{\rm opt}$. We took OMIA measurements, keeping the probe beam near cavity resonance and shifting the control beam to change the frequency difference $|\omega_{\rm Control} - \omega_{\rm Probe}|$. Two data traces are plotted on top of each other with red and blue lines in figure 8.3. The background was subtracted. In the range $310 - 325$ MHz only one peak (at 317.271 MHz) is clearly visible. The amplitude of the noise is at most 10% of the

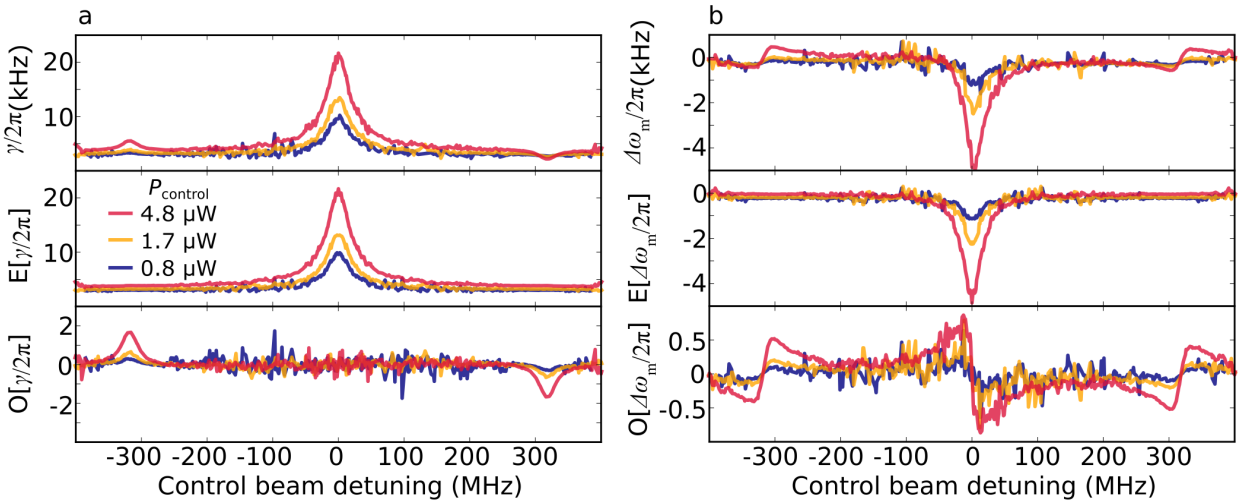

Figure 8.2: Linewidth and frequency of the acoustic mode for a wide range of control beam detunings. **(a)** Linewidth $\gamma/2\pi$ (top), even part of linewidth E$[\gamma/2\pi]$ (middle) and odd part of linewidth O$[\gamma/2\pi]$ (bottom) as a function of control beam detuning for three different control beam powers. **(b)**: Change in frequency $\Delta\omega_{\rm m}/2\pi = \omega_{\rm m}/2\pi - 317.271$ MHz (top), even part of change in frequency E$[\Delta\omega_{\rm m}/2\pi]$ (middle) and odd part of change in frequency O$[\Delta\omega_{\rm m}/2\pi]$ (bottom) as a function of control beam detuning for three different control beam powers

peak, therefore any feature with amplitude larger that 10 % of the peak would be clearly observable. Since the amplitude of the OMIA feature is proportional to g_0^2, we estimate that we would be able to observe the mode with optomechanical coupling greater than 30 % of the optomechanical coupling to the mode with longitudinal mode number $2q_{\rm opt}$. This is the data that we used to put a lower limit on the optomechanical coupling in section 4.2.1.

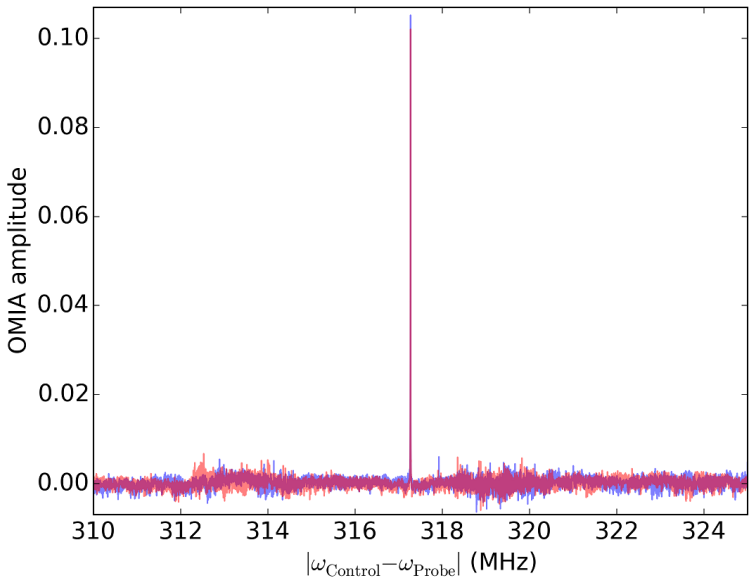

Figure 8.3: OMIA sweep over a large frequency range. Two data traces are plotted with red and blue lines.

8.3 Theoretical predictions for acoustic quality factor

As in the previous device, there are two mechanisms limiting the acoustic quality factor: boundary loss and internal loss. Here I will consider these two mechanisms separately.

8.3.1 Boundary loss

As described in the introduction to the chapter, we developed a DBR structure that is reflective for the paraxial acoustic mode. In this section I will explain how we developed the structure. I will calculate the acoustic transmittivity of this structure and the acoustic finesse of a cavity made from two such structures, assuming infinitely large mirrors with an infinitely large acoustic mode incident on them (equivalent to assuming 1-Dimension). I will then show how the finite size of the mirrors and the acoustic mode limit the acoustic finesse (3-Dimensions).

8.3.1.1 Calculations in one dimension

The formalism for finding acoustic transmission through a DBR is derived in section 7.3.1. In this section we consider the possibility of improving the acoustic finesse by adding an acoustic DBR between the substrate and the optical DBR.

We consider a cavity in which optical confinement is provided by optical DBRs with 15 and 18 layers pairs, optimized for maximum reflectivity at 1550 nm, and acoustic confinement is enhanced by additional layers forming an acoustic DBR. There are a few complications:

- The thickness of an optical layer is determined as:

$$d_{\mathrm{opt,layer}} = \frac{\lambda_{\mathrm{opt,layer}}}{4} = \frac{\lambda_{\mathrm{opt}}}{4}\frac{c_{\mathrm{layer}}}{c} \tag{8.1}$$

  Therefore for light with vacuum wavelength $\lambda_{\mathrm{opt}} = 1550$ nm, the thickness of $\mathrm{Ta_2O_5}$ layer is $187\ \mathrm{nm}$ and $\mathrm{SiO_2}$ layer: $264\ \mathrm{nm}$. The deposition of layers with this thickness is a well known and developed technique.

  The thickness of acoustic layer is determined as:

$$d_{\mathrm{ac,layer}} = \frac{\lambda_{\mathrm{ac,layer}}}{4} = \frac{\lambda_{\mathrm{ac,He}}}{4}\frac{v_{\mathrm{layer}}}{v_{\mathrm{He}}} \tag{8.2}$$

  However, the sound velocities in $\mathrm{SiO_2}$ and $\mathrm{Ta_2O_5}$ are a factor of ≈ 20 higher than the sound velocities in helium. Therefore for sound wave with wavelength $\lambda_{\mathrm{ac}} = 754$ nm (corresponding to $\omega_{\mathrm{m}}/2\pi = 316$ MHz), the thickness of a quarter wavelength $\mathrm{Ta_2O_5}$ layer is $3.6 \pm 0.4\ \mu\mathrm{m}$ and the thickness of a quarter wavelength $\mathrm{SiO_2}$ layer is $4.7 \pm 0.1\ \mu\mathrm{m}$, where the uncertainty is due to the uncertainty in the sound velocity in these materials. The deposition of layers with this thickness is not very well developed.

- Technical aspects of the coating process impose the requirement that the total stack thickness $d_{\mathrm{total}} < 25\ \mu$m [116], putting a limit on the total number of acoustic layers.

- Technical aspects of the coating process impose the requirement that the thickness of each acoustic layer is an integer multiple of the corresponding optical layer thickness [116].

The proposed structure is shown in figure 8.4. However, since the acoustic wave acquires some phase shift as it travels through the optical coating, the first two acoustic layers do not necessarily have to be quarter-wavelength thick. To find how thick they should be, we calculate the acoustic finesse for different thicknesses of the layers. The results are summarized in figures 8.5 and 8.6. In all figures the x (y) axis the thickness of the top acoustic layer of $\mathrm{SiO_2}$ ($\mathrm{Ta_2O_5}$). The color scale in figure 8.5 shows the acoustic finesse, assuming a stack consisting of one acoustic layer pair. The color scale in figure 8.6 shows the acoustic finesse assuming a stack consisting of two acoustic layer pairs, where the layer pair deposited immediately on the fiber is a quarter-wavelength layer pair (thickness of $\mathrm{SiO_2}$ layer is 4.76 μm and the

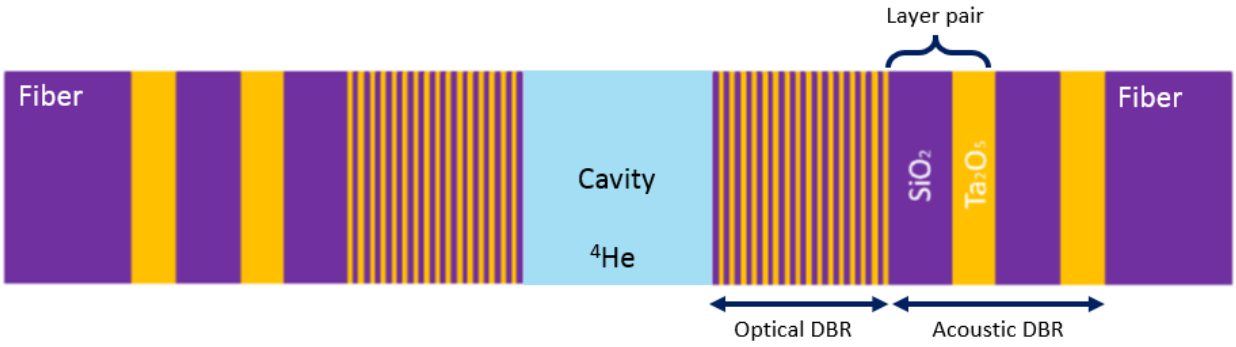

Figure 8.4: An example of a DBR structure that would be reflective for both optical and acoustic waves

thickness of Ta_2O_5 layer is 3.56 μm). All plots on the left assume 15 optical layer pairs and all plots on the right assume 18 optical layer pairs. The color indicates the acoustic finesse. Below the white line the thickness of the stack satisfies the condition $d_{\text{total}} < 25$ μm.

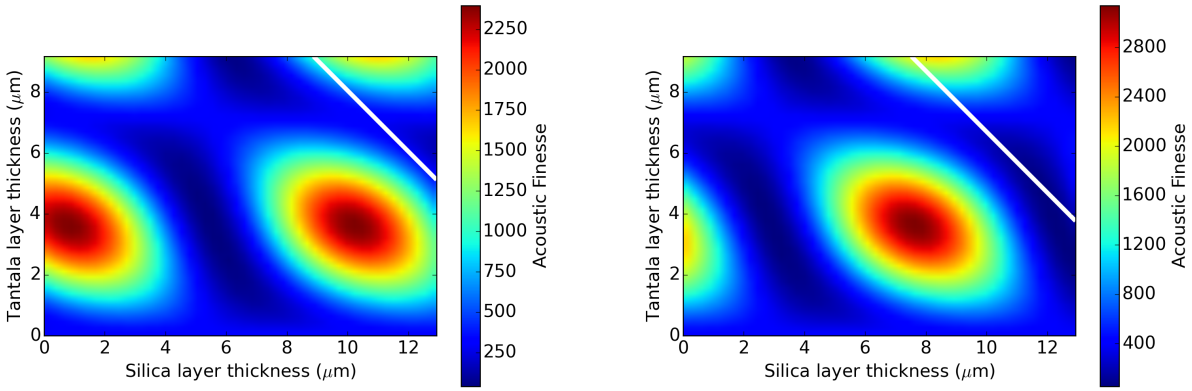

Figure 8.5: The acoustic finesse for a DBR structure with one acoustic layer pair. Above the white line, the total length of the stack becomes larger than 25 μm. Left: low optical finesse (15 optical layer pairs). Right: high optical finesse (18 optical layer pairs).

For these calculations we assumed $v_{SiO_2} = 6,000$ m/s and $\rho_{SiO_2} = 2,200$ kg/m^3, and $v_{Ta_2O_5} = 4,500$ m/s and $\rho_{Ta_2O_5} = 8,200$ kg/m^3. As it is possible to stay within the total thickness limit and achieve higher acoustic finesse using two layer pairs, that is what we decided to do.

We then optimized for minimal transmission, allowing the thicknesses of all layers to vary. Table 8.1 shows stack parameters for the mirrors used in the first generation device (that we already had) as well as the stack parameters for the new mirrors, that were used in the second generation device.

We use equations 6.19 and 7.19 to calculate the optical and acoustic transmission for the DBRs presented in table 8.1 and use these values to calculate the optical and acoustic finesse. The results are shown in table 8.2. The optical finesse doesn't change appreciably as more acoustic layers are added, as the acoustic layers are outside of the optical mode. At the same time, the acoustic layers increase the acoustic finesse by more than an order of magnitude. The acoustic finesse for the cavity constructed from Stack #3 and Stack #4 in Tables 8.1 and 8.2 is predicted to be $\mathcal{F}_{\text{ac}} = 15,500 \pm 9,500$, where the uncertainly is primarily due to the acoustic parameters of Ta_2O_5. The corresponding quality factor for a 100 μm long cavity is $Q_{\text{ac,ext}} = (4.1 \pm 2.5) \times 10^6$.

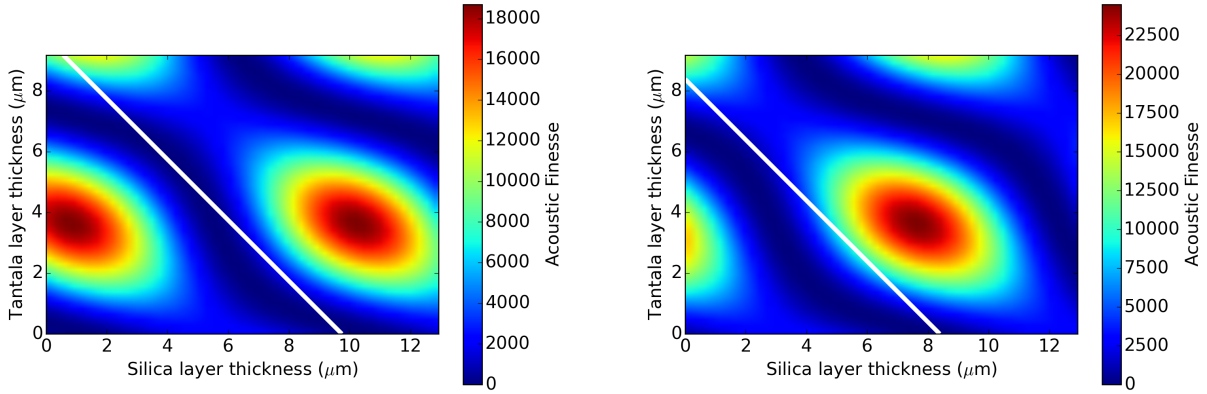

Figure 8.6: The acoustic finesse for a DBR structure with two acoustic layer pairs. Above the white line, the total length of the stack becomes larger than 25 μm. Left: low optical finesse (15 optical layer pairs). Right: high optical finesse (18 optical layer pairs).

Number	Design
1 (1st gen)	Substrate$\times$(189 nm $Ta_2O_5\times$253 nm SiO_2)$^{15}\times$189 nm Ta_2O_5
2 (1st gen)	Substrate$\times$(189 nm $Ta_2O_5\times$253 nm SiO_2)$^{18}\times$189 nm Ta_2O_5
3 (2nd gen)	Substrate$\times$3591 nm $Ta_2O_5\times$4554 nm $SiO_2\times$3591 nm $Ta_2O_5\times$759 nm $SiO_2\times$ (189 nm $Ta_2O_5\times$253 nm SiO_2)$^{15}\times$189 nm Ta_2O_5
4 (2nd gen)	Substrate$\times$3780 nm $Ta_2O_5\times$4554 nm $SiO_2\times$3213 nm $Ta_2O_5\times$ (253 nm $SiO_2\times$189 nm Ta_2O_5)^{18}

Table 8.1: The stack designs used in the first generation device and the stack designs used in the second generation device

Number	$\mathcal{F}_{\mathrm{opt}}$	$\mathcal{F}_{\mathrm{ac}}$	d_{total} (μm)
1	43,000	320 ± 30	6.6
2	300,000	400 ± 70	8.3
3	43,000	$16,000 \pm 10,000$	19.68
4	300,000	$15,000 \pm 9,000$	19.87

Table 8.2: The calculated parameters for different stacks. The optical finesse ($\mathcal{F}_{\mathrm{opt}}$), acoustic finesse ($\mathcal{F}_{\mathrm{ac}}$) and thickness ($d_{\mathrm{total}}$).

Acoustic loss inside the DBR layers. In addition to being limited by the transmission of the acoustic mode into the fiber, the acoustic Q factor can also be limited by dissipation in the DBR. To estimate the Q factor associated with this loss, the following expression is used

$$\frac{1}{Q_{\mathrm{ac,loss}}} = \frac{U^{\mathrm{SiO_2}}\phi_{\mathrm{SiO_2}} + U^{\mathrm{Ta_2O_5}}\phi_{\mathrm{Ta_2O_5}}}{U^{\mathrm{He}}} \tag{8.3}$$

Here U is the energy stored in the material; ϕ is the acoustic loss angle for the material.

To find the stored energy, we find the displacement field in each layer from calculations described in section 7.3.1. The

stored energy can then be expressed as

$$\begin{aligned} U_j^{\text{stored}} &\propto \int_0^{d_j} \omega_{\text{ac}}^2 \rho_j |s_j^{(\text{f})} e^{ikn_j^{\text{ac}}x} + s_j^{(\text{b})} e^{-ikn_j^{\text{ac}}x}|^2 dx \\ &= \omega_{\text{ac}}^2 \rho_j \left[\left(|s_j^{(\text{f})}|^2 + |s_j^{(\text{b})}|^2 \right) d_j - \frac{1}{kn_j^{\text{ac}}} \text{Im}\left(s_j^{(\text{f})*} s_j^{(\text{b})} (e^{-2ikn_j^{\text{ac}} d_j} - 1) \right) \right] \end{aligned} \tag{8.4}$$

The calculated ratios of energy stored in SiO_2 and Ta_2O_5 are shown in table 8.3. For convenience we calculate all values assuming 100 μm long cavity. The ratio of energy stored in the material to the energy stored in helium can be calculated for any other cavity length as: $U^{\text{mat}}/U^{\text{He}} \times 100\ \mu\text{m}/L_{\text{cav}}$. Both ϕ_{SiO_2} and $\phi_{\text{Ta}_2\text{O}_5}$ have been measured over a range of temperatures and for frequencies mostly much lower than 300 MHz [150, 151, 152, 153, 154, 155, 156, 157]. All of these measurements show $\phi_{\text{SiO}_2}; \phi_{\text{Ta}_2\text{O}_5} < 10^{-3}$. The values of the quality factor due to absorption in the DBR ($Q_{\text{ac,loss}}$), assuming $\phi_{\text{SiO}_2} = \phi_{\text{Ta}_2\text{O}_5} = 10^{-3}$ and $L_{\text{cav}} = 100\ \mu$m, are shown in Table 8.2. For all designs $\mathcal{F}_{\text{ac,loss}}$ is much larger than $\mathcal{F}_{\text{ac}}$. As a result, the acoustic finesse should not be limited by the acoustic absorption in the DBR.

Number	$\frac{U^{\text{SiO}_2}}{U^{\text{He}}}$ **(ppm)**	$\frac{U^{\text{Ta}_2\text{O}_5}}{U^{\text{He}}}$ **(ppm)**	$Q_{\text{ac,loss}}$	$\mathcal{F}_{\text{ac,loss}}$
1	5.5 ± 0.5	17.1 ± 2.1	5.0×10^7	190,000
2	5.4 ± 0.8	16.8 ± 1.5	5.1×10^7	190,000
3	3.2 ± 0.8	9.5 ± 2.0	8.9×10^7	330,000
4	2.6 ± 0.8	7.8 ± 1.4	10.9×10^7	410,000

Table 8.3: The calculated parameters for different stacks. The ratios of the energy stored in SiO_2 ($U^{\text{SiO}_2}/U^{\text{He}}$) and Ta_2O_5 ($U^{\text{Ta}_2\text{O}_5}/U^{\text{He}}$) to the energy stored in Helium and the resulting limit on the quality factor in a 100 μm long cavity, and acoustic finesse.

8.3.1.2 Calculations in three dimensions

The approach described above gives the correct results if the wave incident on a mirror is a plane wave with infinite lateral extent, and the mirror is infinite as well. In reality, the acoustic wave that is incident on a mirror has a Gaussian transverse profile. The size of the mirrors are fixed by the size of the fibers to 125 or 200 μm diameter, so we can study how the radius of the incident Gaussian mode influences the acoustic transmission of the mirror.

We model the full geometry in COMSOL and vary the mode field radius. The fiber diameter is taken to be 200 μm. The acoustic properties of silica and tantala are assumed to be $v_{\text{SiO}_2} = 6,000$ m/s and $\rho_{\text{SiO}_2} = 2,200$ kg/m^3, and $v_{\text{Ta}_2\text{O}_5} = 4,500$ m/s and $\rho_{\text{Ta}_2\text{O}_5} = 8,200$ kg/m^3.

Figure 8.7 shows the acoustic finesse calculated for the two cases: the solid green (red) line shows the acoustic finesse calculated from 3D simulations of Stack #3 (#4); the dashed green (red) line shows the acoustic finesse calculated from 1D simulations of Stack #3 (#4). It is clear that the acoustic finesse increases with the mode field radius until $\approx 150\ \mu$m, which is when the walls of the fiber start to play a larger role and reflections from the walls limit the finesse.

The reason for the acoustic finesse increasing with increasing mode size is the difference in wavelength of sound inside helium and inside SiO_2 and Ta_2O_5. If the transverse size of the mode is smaller than the wavelength of the mode, the wave will diverge rapidly. This is clearly seen for the simple case of an acoustic wave with mode field diameter $w = 14\ \mu$m incident on a silica fiber without any coating shown in figure 8.8. If the acoustic wavelength in helium is $\lambda_{\text{ac,He}} = 754$ nm, then the acoustic wavelength in helium is $\lambda_{\text{ac,SiO}_2} = 19\ \mu$m. For such wavelength and mode field diameter the divergence angle is $\theta = \frac{\lambda_{\text{ac,SiO}_2}}{\pi w} = 0.43$ rad, shown with white lines in figure 8.8. For such large beam divergence the mode is not paraxial anymore and, if the DBR layers are present, they do not match the wave fronts, so the proposed design would not constitute a good mirror for this acoustic mode, as seen from figure 8.9. However, if we

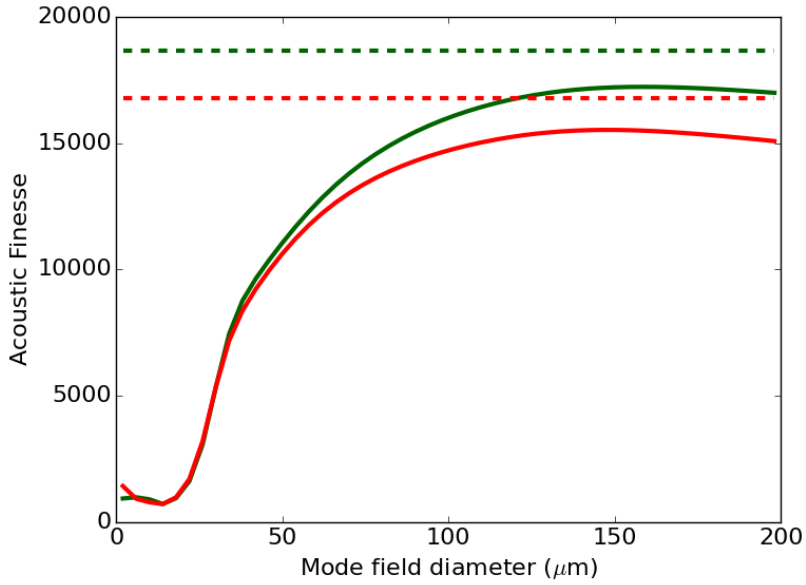

Figure 8.7: Acoustic finesse. Solid lines: acoustic finesse calculated from 3D simulations. Dashed line: acoustic finesse calculated from 1D simulations.

consider a larger incident mode for example $w = 50$ μm, the divergence angle is smaller ($\theta = 0.12$ rad) and the design serves as a reasonable acoustic mirror, as seen form figure 8.10.

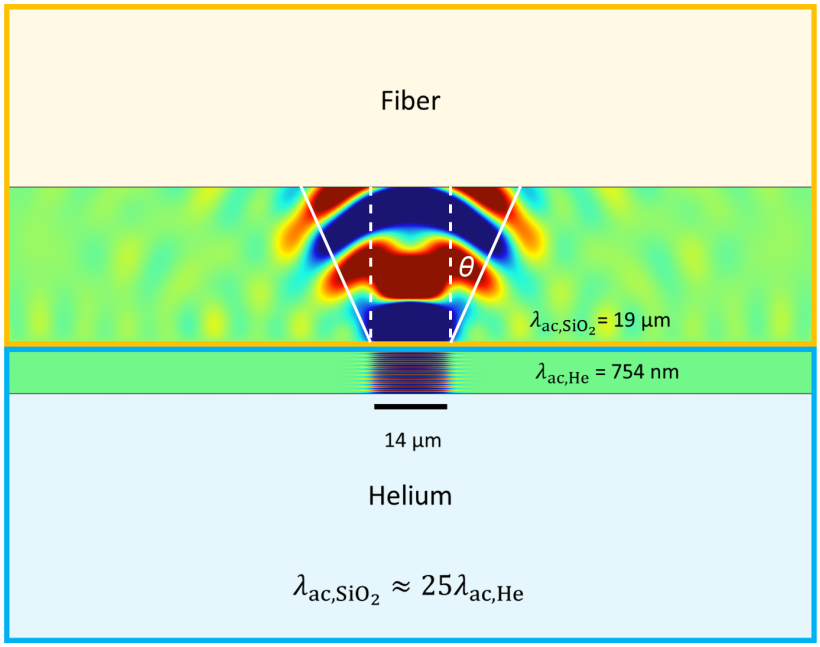

Figure 8.8: Acoustic pressure profile inside of a fiber for the mode field diameter $w = 14$ μm. The blue rectangle indicates helium, the orange rectangle indicates fiber. The acoustic mode spreads out in the fiber due to transverse size of the mode being smaller than the wavelength in the fiber.

The mode field diameter depends on the cavity length and the ratio of ROC to the cavity length R/L_{cav}, for the constant R/L_{cav} it is proportional to $\sqrt{L_{\text{cav}}}$. Therefore longer cavities would allow for a larger mode and would let us take full advantage of the acoustic DBR. Fiber cavities up to 1 mm long have been built [133]. A 1 mm long cavity can result in mode field diameter of 40 μm and noticeably higher theoretical acoustic quality factor. Another option would be to build

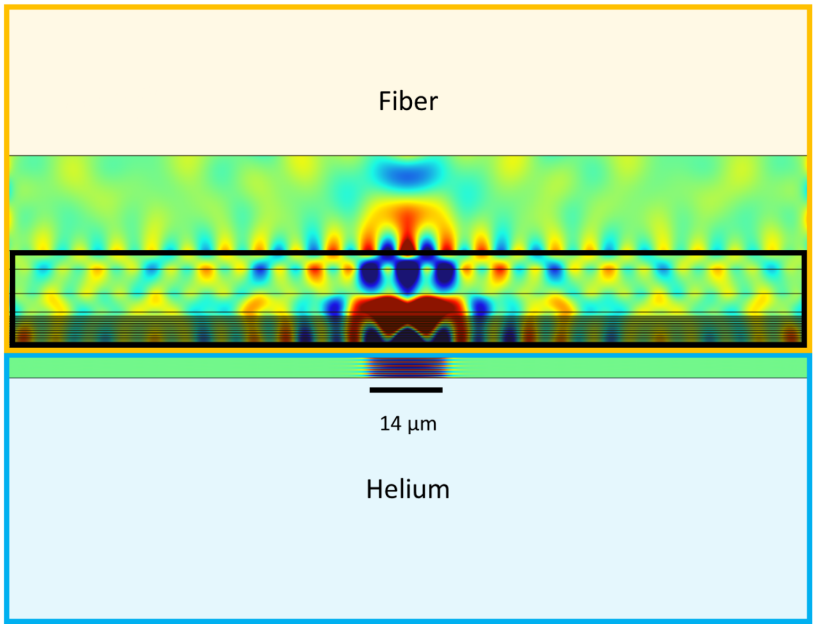

Figure 8.9: Acoustic pressure profile inside of a fiber mirror (optical and acoustic stack) for the mode field diameter $w = 14$ μm. The blue rectangle indicates helium, the orange rectangle indicated fiber. The black rectangle indicates the optical and acoustic stack.

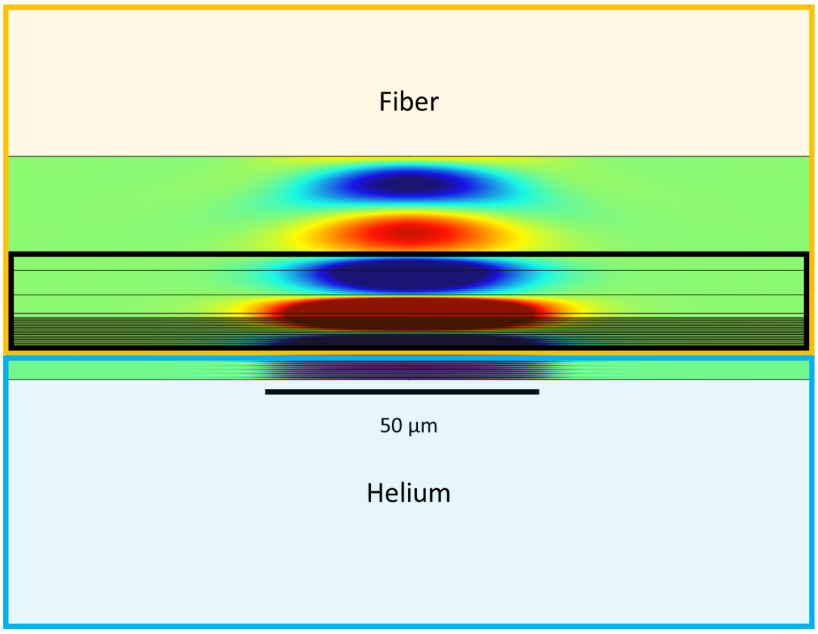

Figure 8.10: Acoustic pressure profile inside of a fiber mirror (optical and acoustic stack) for the mode field diameter $w = 50$ μm. The blue rectangle indicates helium, the orange rectangle indicated fiber. The black rectangle indicates the optical and acoustic stack.

cavities out of macroscopic mirrors ($d_{\mathrm{mirror}} = 1/2 - 1$ in), as they could easily have large mode field diameter.

For the cavity used in this experiment the acoustic mode field diameter at the fiber surfaces is $w \approx 11$ μm. The expected finesse is $\mathcal{F}_{\mathrm{ac}} \approx 700$. For the 70 μm long cavity used in the experiment, it corresponds to the quality factor $Q_{\mathrm{ac,ext}} \approx 130,000$ and the corresponding linewidth $\gamma_{\mathrm{ext}}/2\pi \approx 2.5$ kHz. Note that we have found that in the 1-D calculations the theoretical quality factor varies by 60 % (due to uncertainty in the acoustic properties of SiO_2 and Ta_2O_5). Therefore we

assume that the quality factor calculated from 3D simulations is from $Q_{\mathrm{ac,ext}} = 130,000 \pm 70,000$ and the corresponding linewidth is $\gamma_{\mathrm{ext}}/2\pi = 4.0 \pm 2.4$ kHz to $\gamma_{\mathrm{ext}}/2\pi = 6.4$ kHz.

8.3.2 Intrinsic temperature-dependent loss

The intrinsic temperature dependent loss is proportional to the attenuation of sound in helium, as described in section 3.4.1. In the previous device we assumed that the helium temperature inside the cavity was uniform. Here, we can not assume that, as described in section 8.2. In order to understand the quality factor due to intrinsic loss we first need to understand the temperature of the helium in the device. I will describe this in the next section.

8.4 Device temperature

The temperature dependence of the speed of sound and acoustic damping in liquid helium are described in section 3.4. It is straightforward to calculate the temperature dependence of the acoustic mode's frequency ω_{m}, damping γ, and mean thermal phonon number n_{th}, provided that the temperature is uniform throughout the cavity, as in the previous device. However in the present device the temperature is not uniform. Here we calculate the expected temperature profile within the cavity using well-known thermal properties of liquid helium (in section 8.4.1). We then use this result to calculate ω_{m}, γ, and n_{th} (in section 8.4.2).

8.4.1 Temperature distribution inside the cavity

As found in our analysis of the first generation device, in a superfluid-filled optical cavity the helium's temperature is set by the balance between heating (caused by optical absorption in the cavity mirrors) and the transport of this heat through the helium to the mixing chamber (MC). In the first generation device this transport was limited by the thermal impedance of a narrow "sheath" of helium that connected the cavity to the MC. The sheath's large impedance ensured that the temperature drop between the cavity and the MC occurred primarily in the sheath, leaving the cavity at an approximately uniform temperature. The second generation device's more open geometry results in an improved thermal link to the MC and allows the cavity to reach lower temperatures, but the absence of a bottleneck means that the temperature within the cavity is less uniform.

We model the temperature distribution in the present device by assuming that the heating originates in sub-μm absorbers (located in the DBR coatings) that overlap with the cavity's optical mode, and that the resulting heat propagates outward through the helium. We find that in the overwhelming majority of the cavity the temperature and heat flux density are low enough that heat is transported by ballistic phonons. However within ≈ 1 μm of each absorber the heat flux density is high enough to produce turbulence, with the result that thermal transport within this small region is described by the Gorter-Mellinck model. Despite the smallness of the turbulent region, we find that it plays an important role in the device's performance.

8.4.1.1 Optical absorption

A schematic illustration of the device is shown in figure 8.11. The cavity is formed between the end faces of two optical fibers, each having a radius of $r_{\mathrm{out}} = 100$ μm. The separation between the fibers is $d = 70$ μm. We assume that laser light is absorbed where the cavity's optical mode overlaps with the mirrors. This corresponds to a disk-shaped region on the fiber surfaces with radius $r_{\mathrm{opt}} \approx 7$ μm. The total heat flux from this absorption is:

$$\dot{Q} = \hbar \omega_{\mathrm{L}} n_{\mathrm{circ}} \kappa_{\mathrm{int}} \alpha \tag{8.5}$$

Here $\hbar$ is the reduced Planck's constant, $\omega_{\mathrm{L}}/2\pi = 196.21$ THz is the frequency of the optical mode, n_{circ} is the circulating photon number, $\kappa_{\mathrm{int}}/2\pi \approx 10$ MHz is the internal cavity loss rate, and α is the fraction of the internal loss that leads to

heating (as distinguished from the internal due to photons being elastically scattered out of the cavity mode and absorbed in some distant part of the apparatus). As in section 7.4.2, we can estimate α, from the cavity finesse $\mathcal{F} \approx 100,000$, the total and internal linewidths and $a_{\mathrm{abs}} = 3$ ppm: $\alpha = 2a_{\mathrm{abs}} \frac{\mathcal{F}}{2\pi} \frac{\kappa}{\kappa_{\mathrm{int}}} = 0.2$.

We assume that the absorption occurs in small (sub-μm) absorbers distributed throughout the DBR layers (as illustrated by the small red circles in figure 8.11). Each absorber will produce an average heat flux

$$\dot{Q}_1 = \dot{Q}/N \tag{8.6}$$

where N is the number of absorbers within the optical mode. The heat from each absorber is assumed to spread isotropically into the helium, since the optical fibers' thermal conductivity is extremely low at the relevant temperatures.

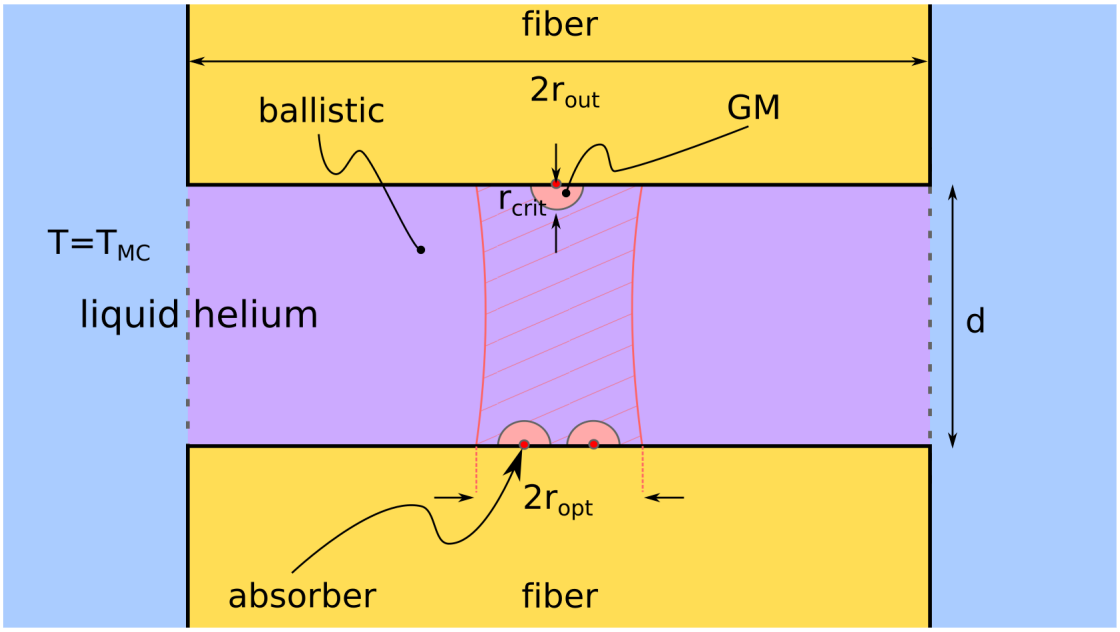

Figure 8.11: The model of the device.

8.4.1.2 Relevant regimes of thermal transport in liquid helium

The character of thermal transport in Helium II depends strongly on the size of the helium channel, its temperature, and the heat flux density, as described in section 3.5. As described below, we find that thermal transport is in the ballistic regime throughout nearly all of the cavity. The only exception is a small region around each absorber, in which thermal transport is in the Gorter-Mellinck regime.

To calculate the temperature profile, we assume that helium in the region outside of the cavity (i.e., the blue region in figure 8.11) is at the temperature of the mixing chamber T_{MC}. For all T_{MC} used in this work the phonon mean free path λ_{MFP} [158] is much larger than any of the device's dimensions. As a result, wherever $T \approx T_{MC}$ thermal transport is via ballistic phonons. Thus, at the boundary of the blue region in Fig. 8.11 and for some distance inwards (i.e., towards the absorbers) thermal transport is in the ballistic regime.

However the ballistic regime does not extend all the way to the absorbers. This is because the heat flux density $\dot{q} = \dot{Q}_1/2\pi r^2$ increases as the distance r from the absorber decreases. At some distance r_{crit} from the absorber, $\dot{q}$ exceeds the critical value $\dot{q}_{\mathrm{crit}}$ for generating turbulence (two values of $\dot{q}_{\mathrm{crit}}$ were calculated in section 3.5.2.3 as a function of temperature). Within the turbulent region (i.e., for $r < r_{\mathrm{crit}}$), thermal transport is in the Gorter-Mellinck (GM) regime.

We calculate the temperature profile $T(r)$ throughout the entire cavity by concatenating these two regimes. Specifically, we start with the boundary condition $T(r_{\rm out}) = T_{\rm MC}$, and integrate the expressions describing ballistic transport towards decreasing r, stopping when $\dot{q} = \dot{q}_{\rm crit}$ (or equivalently, when $r = r_{\rm crit}$). We then use the calculated $T(r_{\rm crit})$ as a new boundary condition for integrating the GM expressions for $r < r_{\rm crit}$.

Since heat propagates uniformly from the absorbers into the helium, the heat flux per unit area is:

$$\dot{q} = \frac{\dot{Q}_1}{2\pi r^2} \tag{8.7}$$

Therefore:

$$r_{\rm crit} = \sqrt{\frac{\dot{Q}_1}{2\pi \dot{q}_{\rm crit}}} = \eta\sqrt{n_{\rm eff}} \tag{8.8}$$

Here we have defined $n_{\rm eff} = n_{\rm circ}\alpha/N$ (the number of photons absorbed by an individual absorber per cavity lifetime) and η is the value of $r_{\rm crit}$ for $n_{\rm eff} = 1$.

Figure 8.12 shows $\eta(T)$. From the figure it is apparent that $5 \times 10^{-9} \leq \eta \leq 7 \times 10^{-8}$ m. In the following analysis, we assume η is constant and use it as a fit parameter. For estimations performed prior to the final analysis, we will assume $\eta = 1.0 \times 10^{-8}$ m.

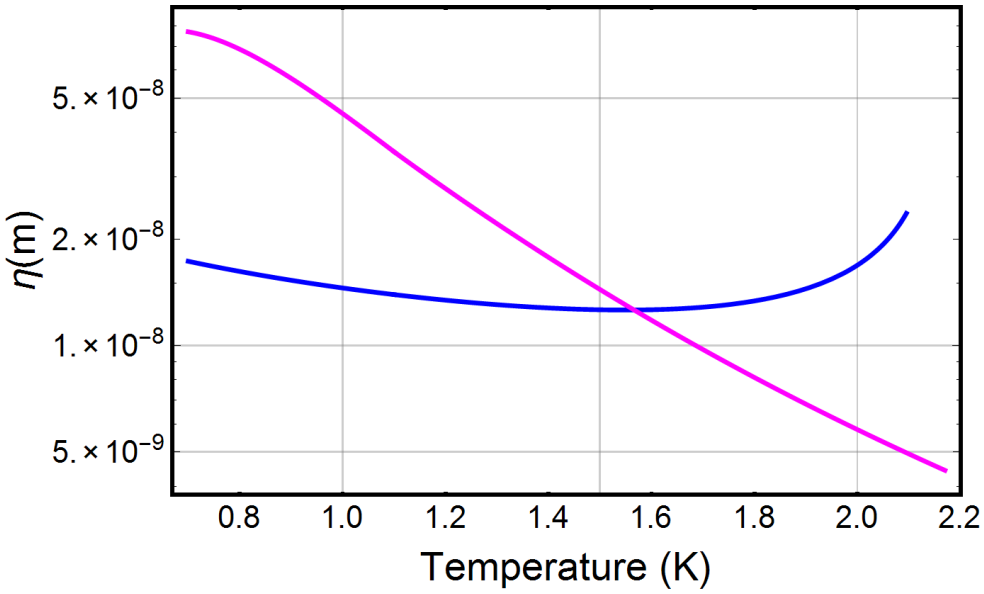

Figure 8.12: The value of η as a function of temperature. Blue line shows η set by the superfluid turbulence and magenta line shows η set by normal fluid turbulence.

For this approach to be valid, one necessary condition is that the spacing between the absorbers be larger than $r_{\rm crit}$:

$$N < \frac{r_{\rm opt}^2}{r_{\rm crit}^2} \tag{8.9}$$

In the present device, this is equivalent to the condition

$$n_{\rm circ}\alpha < 3 \times 10^5 \tag{8.10}$$

which is satisfied for all the measurements described.

8.4.1.3 Heat propagation in the ballistic regime

As stated before, for $r > r_{\rm crit}$, the heat propagation is in the ballistic regime described in section 3.5.1.

We find $f_{\rm diff} \approx 0.01$ as described in section 3.5.1, from the rms surface roughness σ , which for similarly prepared fibers was measured to be 0.24 nm [130] and from the most likely wavelength $\lambda_{\rm th}$, which in our experiments varies from from 20 nm (for $T_{\rm MC} = 500$ mK) to 500 nm (for $T_{\rm MC} = 20$ mK). If we take $D_{\rm tube} = 70$ μm (the separation between the fibers) we can then rewrite expression 3.15 as:

$$k_{\rm He}(T) = \xi T^3 \tag{8.11}$$

where the constant $\xi = 3200\ {\rm W}\cdot{\rm m}^{-1}\cdot{\rm K}^{-4}$. The expression relating heat flow to temperature gradient is [88]:

$$\frac{1}{2}\frac{\dot{Q}}{A} = -k_{\rm He}(T)\frac{dT}{dr} \tag{8.12}$$

Here $A = 2\pi r^2$ is the area over which the heat is distributed. The factor of $1/2$ is there to account for the presence of two mirrors. Equation 8.12 can be rewritten as

$$\frac{\dot{Q}}{4\pi r^2}dr = -\xi T^3 dT \tag{8.13}$$

Assuming that $T(r_{\rm out}) = T_{\rm MC}$, the temperature at r can be found by integrating equation 8.13:

$$\frac{\dot{Q}}{4\pi}\int_{r_{\rm out}}^{r}\frac{1}{r^2}dr = -\xi\int_{T_{\rm MC}}^{T} T'^3 dT' \tag{8.14}$$

$$\frac{\dot{Q}}{4\pi}\left(\frac{1}{r_{\rm out}} - \frac{1}{r}\right) = -\frac{\xi}{4}(T^4 - T_{\rm MC}^4) \tag{8.15}$$

$$T(r) = \left(T_{\rm MC}^4 + \frac{\dot{Q}}{\pi\xi}\left(\frac{1}{r} - \frac{1}{r_{\rm out}}\right)\right)^{1/4} \tag{8.16}$$

Figure 8.13 shows the temperature profile between $r_{\rm crit}$ and $r_{\rm out}$ for three different circulating photon numbers and for $T_{\rm MC} = 50$ mK. Note that the red line shows the most extreme case for which we have done measurements ($T_{\rm MC} = 50$ and $n_{\rm circ} = 100,000$). Higher $T_{\rm MC}$ or lower $n_{\rm circ}$ leads to more uniform temperature throughout the cavity, as evidenced by figure 8.14. We define $T_{\rm crit} = T(r_{\rm crit})$. The color scale in figure 8.14 shows the ratio $T_{\rm crit}/T_{\rm MC}$ for different values of $T_{\rm MC}$ and the circulating photon number. The white dots in the figure show the conditions under which data were taken with this device. For all data, it is a reasonable approximation that the temperature throughout the cavity is constant and equal to $T_{\rm MC}$.

8.4.1.4 Heat propagation in the Gorter-Mellink regime

When the heat flux is above the critical value (i.e., for $r < r_{\rm crit}$), thermal conductance is described by the Gorter-Mellink model. This regime is characterized by the following equation [83]:

$$\left(\frac{\dot{Q}_1}{A}\right)^3 = -g(T)\frac{dT}{dr} \tag{8.17}$$

Note that the heat flux from a single absorber $\dot{Q}_1$ is used. The function $g(T)$ is given by:

$$g(T) = \frac{s^4\rho_s^3 T^3}{A_{\rm GM}\rho_n} \tag{8.18}$$

To find the temperature profile inside the critical radius, we integrate the temperature from the critical radius inward:

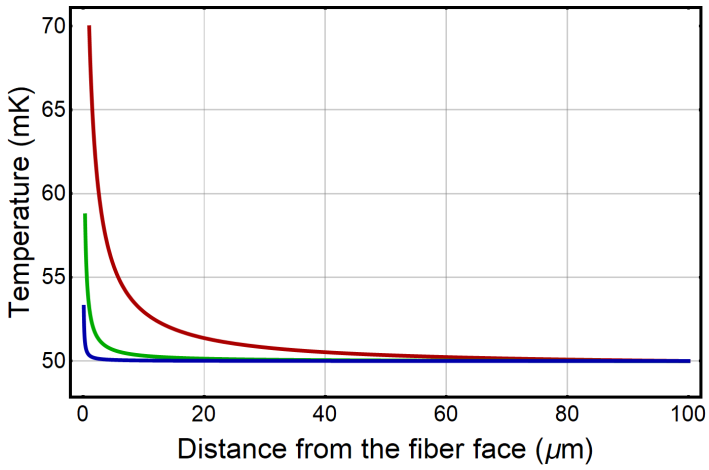

Figure 8.13: The temperature profile between r_{crit} and r_{out} in three cases. Blue: $n_{\text{circ}} = 1,000$. Green: $n_{\text{circ}} = 10,000$. Red: $n_{\text{circ}} = 100,000$. In all three cases $T_{\text{MC}} = 50$ mK, $\alpha = 0.2$ and each fiber mirror absorbs the same amount of light.

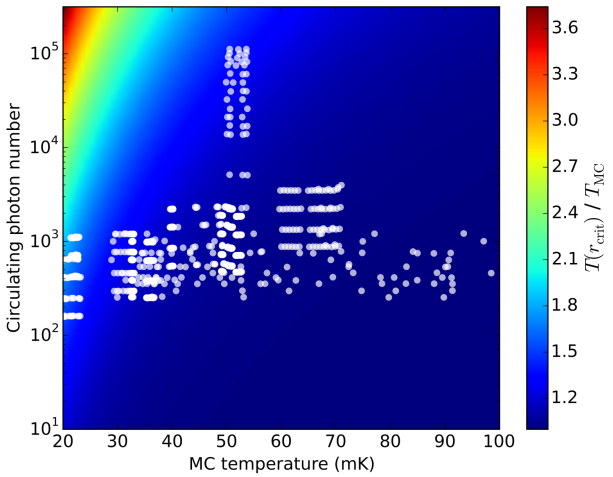

Figure 8.14: The ratio $T_{\text{crit}}/T_{\text{MC}}$ for different values of mixing chamber temperature and circulating photon number.

$$\left(\frac{\dot{Q}_1}{2\pi}\right)^3 \int_{r_{\text{crit}}}^{r} \frac{1}{r'^6} dr' = -\int_{T_{\text{crit}}}^{T} g(T')dT' \tag{8.19}$$

$$\left(\frac{\dot{Q}_1}{2\pi}\right)^3 \frac{1}{5}\left(\frac{1}{r^5} - \frac{1}{r_{\text{crit}}^5}\right) = f(T) - f(T_{\text{crit}}) \tag{8.20}$$

The function $f(T)$ is defined as the indefinite integral of $g(T)$. It can be written analytically; however, the expression is cumbersome, so instead we make use of the fact that it can be approximated (to within a factor of 5) by

$$f_{\text{app}}(T) = \beta T^{18} \tag{8.21}$$

where $\beta = 0.5 \times 10^8$ W^3/(m$^5 \cdot$ K^{18}) for 0.7 K < T < 2 K (Figure 8.15).

So:

$$T^{18} = T_{\text{crit}}^{18} + \left(\frac{\dot{Q}_1}{2\pi}\right)^3 \frac{1}{5\beta}\left(\frac{1}{r^5} - \frac{1}{r_{\text{crit}}^5}\right) \tag{8.22}$$

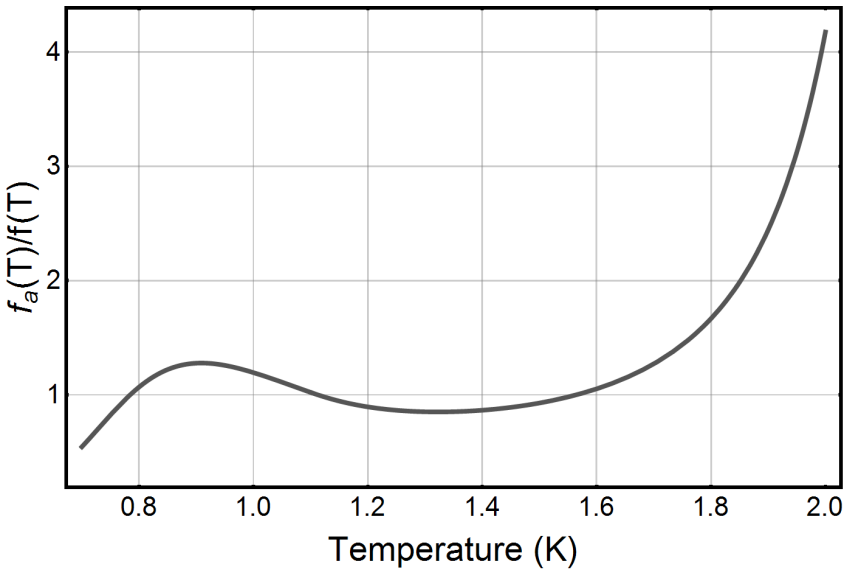

Figure 8.15: The ratio $f_{\mathrm{a}}(T)/f((T)$

There is one further simplification that can be made: T_{crit} is very close to the T_{MC}, as shown above, which is always smaller than 300 mK. Even for $T_{\mathrm{crit}} = 300$ mK and the photon number $n = 100$ photons (the lowest measurable), the second term on the right-hand-side of equation 8.22 dominates in the the region ($0 \leq r \leq 0.99 r_{\mathrm{crit}}$), so the temperature inside the critical radius depends only the on the circulating photon number and not on T_{MC}:

$$T(r) = \left(\left(\frac{\dot{Q}_1}{2\pi} \right)^3 \frac{1}{5\beta} \left(\frac{1}{r^5} - \frac{1}{r_{\mathrm{crit}}^5} \right) \right)^{1/18} \tag{8.23}$$

An important condition is that the critical radius is larger than the thermal phonon wavelength – so that it is possible to define local temperature inside the critical radius. From equation 8.23, we find that the helium temperature for $r \leq 0.99 r_{\mathrm{crit}}$ is larger than:

$$T(0.99 r_{\mathrm{crit}}) = \epsilon \frac{n_{\mathrm{eff}}^{1/36}}{\eta^{5/18}} \tag{8.24}$$

where $\epsilon = 3.1 \times 10^{-3}\ \mathrm{K} \cdot \mathrm{m}^{5/18}$. The corresponding average thermal wavelength is smaller than:

$$\lambda_{\mathrm{th}} = 2\pi \frac{\hbar v_{\mathrm{He}}}{3 k_{\mathrm{B}} T(0.99 r_{\mathrm{crit}})} = \frac{\sigma \eta^{5/18}}{\epsilon n_{\mathrm{eff}}^{1/36}} \tag{8.25}$$

where $\sigma = 3.8 \times 10^{-9}\ \mathrm{m} \cdot \mathrm{K}$. We would like to compare this value to the critical radius $r_{\mathrm{crit}} = \eta \sqrt{n_{\mathrm{eff}}}$. We arrive at the following condition that needs to be satisfied:

$$\eta^{13/18} n_{\mathrm{eff}}^{19/36} > \tau \tag{8.26}$$

where $\tau = 1.2 \times 10^{-6}\ \mathrm{m}^{13/18}$. This condition is satisfied for $5 \times 10^{-9} \leq \eta \leq 7 \times 10^{-8}$, assuming $n_{\mathrm{circ}} = 100$ (the lowest measurable), $\alpha \geq 0.2$ and $N \leq 10$. For the extracted fit parameters, described later in section 8.4.3.2 ($\eta = 1 \times 10^{-8}$, $\alpha = 0.7$ and $N = 2$), the left hand side of the inequality 8.26 is at least 9 times larger (for $n_{\mathrm{circ}} = 100$) than the right hand side of the inequality 8.26.

8.4.1.5 Temperature profile summary

To summarize, the temperature profile within the cavity is calculated via the following steps:

- The temperature of helium outside of the cylinder defined by the fibers is at the mixing chamber temperature $T(r \geq r_{\text{out}}) = T_{\text{MC}}$.
- The total heat radiating into the helium is $\dot{Q} = \hbar\omega_{\text{L}} n_{\text{circ}} \kappa_{\text{int}} \alpha$.
- The heat is radiated isotropically into the helium from point-like absorbers. The amount of heat radiated from each absorber is $\dot{Q}_1 = \dot{Q}/N$.
- The heat flux density drops off with distance from the absorber as $\dot{q} = \frac{\dot{Q}_1}{2\pi r^2}$. For $r < r_{\text{crit}}$ thermal transport is in the Gorter-Mellink regime. For $r > r_{\text{crit}}$ the propagation is in ballistic regime.
- For $r > r_{\text{crit}}$ the temperature is very close to T_{MC}.
- For $r < r_{\text{crit}}$ the temperature is roughly independent of T_{MC}

Using equations 8.16 and 8.23, the temperature profile $T(r)$ can be calculated. Figure 8.16 shows $T(r)$ for $n_{\text{circ}} = 10^5$, $T_{\text{MC}} = 100$ mK, $\alpha = 0.2$, $f = 0.01$, and $N = 2$.

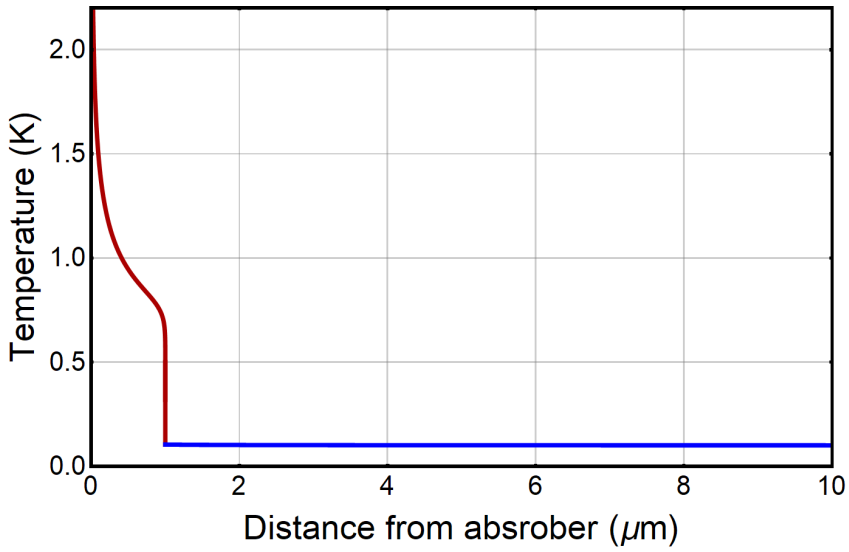

Figure 8.16: The temperature profile inside the critical radius (red), and outside the critical radius (blue)

8.4.2 Linewidth, frequency and occupation number the mode in the inhomogeneous medium

Since the temperature varies throughout the cavity, the local values of the speed of sound, density and linewidth will vary as well. Figures 8.17, 8.18, and 8.19 show the profiles for the local change in the speed of sound, local change in density and local linewidth correspondingly.

Now we know the profiles of temperature, speed of sound, density and local linewidth inside the cavity. From this information we need to extract frequency, linewidth and temperature of the acoustic mode. We can do this by solving a wave equation in an inhomogeneous fluid given in [115]:

$$\rho(\vec{r})\nabla \cdot \left(\frac{1}{\rho(\vec{r})}\nabla p(\vec{r},t)\right) - \frac{1}{v(\vec{r})^2}\frac{\partial^2 p(\vec{r},t)}{\partial t^2} = 0 \tag{8.27}$$

The same reference shows how attenuation is included in the wave equation in a homogeneous fluid:

$$\nabla^2 p(\vec{r},t) - \frac{1}{v^2}\frac{\partial^2 p(\vec{r},t)}{\partial t^2} + b\frac{\partial^3 p(\vec{r},t)}{\partial t^3} = 0 \tag{8.28}$$

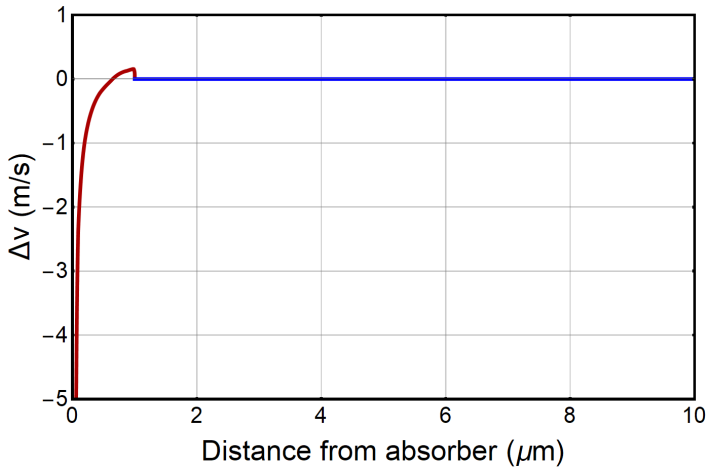

Figure 8.17: The change in speed of sound from the 232.3 m/s inside the critical radius (red), and outside the critical radius (blue)

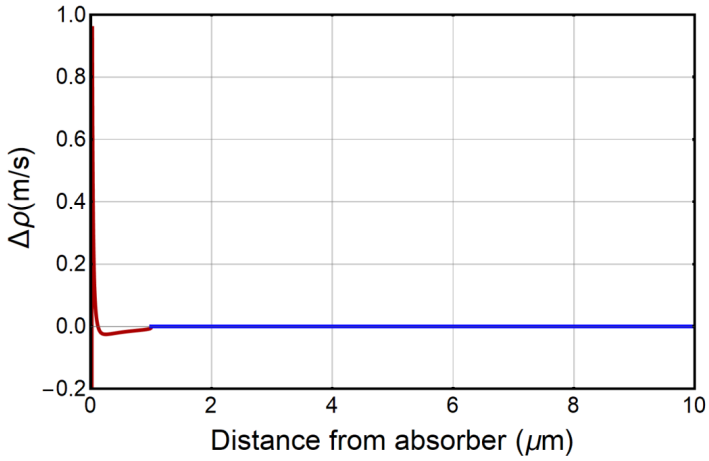

Figure 8.18: The change in density from the 145.14 kg/m^3 inside the critical radius (red), and outside the critical radius (blue)

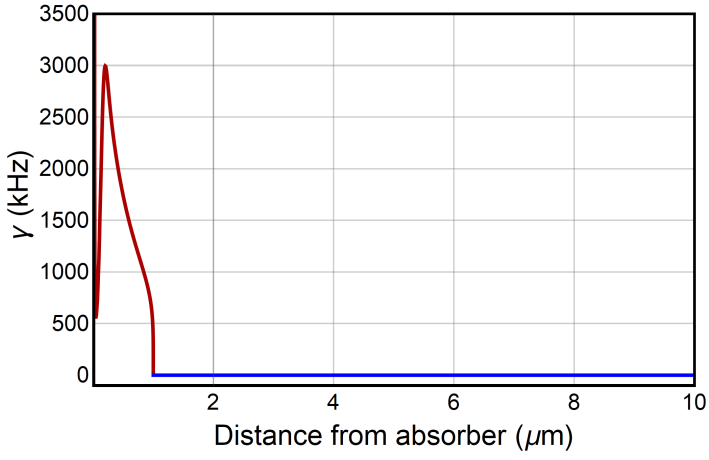

Figure 8.19: The linewidth inside the critical radius (red), and outside the critical radius (blue)

where b is a function of viscosity, sound velocity and thermal conductivity. The exact functional form of b is not important for our calculation. We will assume that attenuation can be included in a similar manner in an inhomogeneous fluid, giving

the following wave equation:

$$\rho(\vec{r})\nabla\cdot\left(\frac{1}{\rho(\vec{r})}\nabla p(\vec{r},t)\right)-\frac{1}{v(\vec{r})^2}\frac{\partial^2 p(\vec{r},t)}{\partial t^2}+b(\vec{r})\frac{\partial^3 p(\vec{r},t)}{\partial t^3}=0 \tag{8.29}$$

Using the vector identity

$$\nabla\cdot(\phi\nabla\psi)=\phi\nabla^2\psi+\nabla\phi\cdot\nabla\psi \tag{8.30}$$

to rewrite equation 8.29 as:

$$\nabla^2 p(\vec{r},t)+\rho(\vec{r})\nabla\left(\frac{1}{\rho(\vec{r})}\right)\cdot\nabla p(\vec{r},t)-\frac{1}{v(\vec{r})^2}\frac{\partial^2 p(\vec{r},t)}{\partial t^2}+b(\vec{r})\frac{\partial^3 p(\vec{r},t)}{\partial t^3}=0 \tag{8.31}$$

We will first use equation 8.28 to find an expression for b in terms of other parameters, such as γ, v and ω. We will then apply perturbation theory to equation 8.31 to find how the small changes in $\gamma(\vec{r})$, $v(\vec{r})$ and $\rho(\vec{r})$ change the frequency and linewidth of a mode.

The value of b in terms of known parameters Assume that the solution to the wave equation in the homegeneous medium (including attenuation) is: $p(\vec{r},t)=U(\vec{r})e^{i\tilde{\omega}t}$. Here $\tilde{\omega}$ is complex and is given by:

$$\tilde{\omega}=\omega+i\frac{\gamma}{2} \tag{8.32}$$

Here ω is the frequency of the wave and $\gamma/2$ shows how the amplitude of the wave decays in time. Plugging this solution into equation 8.28 we find:

$$\nabla^2 U(\vec{r})=-\left(\frac{\tilde{\omega}^2}{v^2}-i\tilde{\omega}^3 b\right)U \tag{8.33}$$

The left side of equation 8.33 is real, which means that the right side must be real as well. That leads to the following condition:

$$b=\frac{\gamma}{v^2\omega^2} \tag{8.34}$$

Therefore equation 8.31 becomes:

$$\nabla^2 p(\vec{r},t)+\rho(\vec{r})\nabla\left(\frac{1}{\rho(\vec{r})}\right)\cdot\nabla p(\vec{r},t)-\frac{1}{v(\vec{r})^2}\frac{\partial^2 p(\vec{r},t)}{\partial t^2}+\frac{\gamma(\vec{r})}{v(\vec{r})^2\omega^2}\frac{\partial^3 p(\vec{r},t)}{\partial t^3}=0 \tag{8.35}$$

Assuming the solution $p=p(\vec{r},t)=U(\vec{r})e^{i\tilde{\omega}t}$, we can rewrite equation 8.35 as:

$$\nabla^2 U(\vec{r})+\rho(\vec{r})\nabla\left(\frac{1}{\rho(\vec{r})}\right)\cdot\nabla U(\vec{r})+\frac{\tilde{\omega}^2}{v(\vec{r})^2}U(\vec{r})-i\tilde{\omega}\frac{\gamma(\vec{r})}{v(\vec{r})^2}U(\vec{r})=0 \tag{8.36}$$

Where U solves the unperturbed equation:

$$\nabla^2 U(\vec{r})+\frac{\omega^2}{v^2}U(\vec{r})=0 \tag{8.37}$$

Perturbation theory To find the change in acoustic frequency due to small changes in the sound velocity, density and local linewidth, the use similar approach to the one we used in section 4.2 to derive optomechanical coupling (the change in optical frequency due to small changes in the refractive index of helium). We apply perturbation theory to equation 8.35. We will assume the following perturbations:

$$v(\vec{r})=\bar{v}+\delta v(\vec{r}) \tag{8.38}$$
$$\rho(\vec{r})=\bar{\rho}+\delta\rho(\vec{r}) \tag{8.39}$$
$$\gamma(\vec{r})=\bar{\gamma}+\delta\gamma(\vec{r}) \tag{8.40}$$
$$U(\vec{r})=\bar{U}(\vec{r})+\delta U(\vec{r}) \tag{8.41}$$
$$\tilde{\omega}=\bar{\omega}+\delta\tilde{\omega} \tag{8.42}$$

The perturbations on various powers of the perturbed quantities in equation 8.36 are:

$$\frac{1}{\rho(\vec{r})} = \frac{1}{\bar{\rho}}\left(1 - \frac{\delta\rho(\vec{r})}{\bar{\rho}}\right) \tag{8.43}$$

$$\frac{1}{v(\vec{r})^2} = \frac{1}{\bar{v}^2}\left(1 - \frac{2\delta v(\vec{r})}{\bar{v}}\right) \tag{8.44}$$

$$\tilde{\omega}(\vec{r})^2 = \bar{\omega}^2 + 2\bar{\omega}\delta\tilde{\omega} \tag{8.45}$$

Where we take the values of $\bar{v} = 238.2$ m/s, $\bar{\rho} = 145.14$ kg/m^3 and $\bar{\gamma} = 0$ Hz (all values are taken at $T = 0$ K). It is convenient to apply the perturbations to v, ρ and γ separately. Additionally, we assume that the boundary conditions are such that either both $U(\vec{r})$ and $\delta U(\vec{r})$ or both $\nabla U(\vec{r})$ and $\nabla\delta U(\vec{r})$ vanish at the boundaries.

- **Keeping ρ, γ constant, perturbing v**

  In this situation, equation 8.36 takes the following form:

  $$\nabla^2(\bar{U}(\vec{r}) + \delta U(\vec{r})) + \frac{1}{\bar{v}^2}\left(1 - \frac{2\delta v(\vec{r})}{\bar{v}}\right)(\bar{\omega}^2 + 2\bar{\omega}\delta\tilde{\omega})(\bar{U}(\vec{r}) + \delta U(\vec{r})) = 0 \tag{8.46}$$

  Simplifying, removing all the non-linear terms, and taking advantage of the fact that $\bar{U}$ solves the unperturbed equation, we arrive at the following:

  $$\nabla^2\delta U(\vec{r}) + \frac{\bar{\omega}^2\delta U(\vec{r})}{\bar{v}^2} - \frac{2\bar{\omega}^2\delta v(\vec{r})\bar{U}(\vec{r})}{\bar{v}^3} + \frac{2\bar{\omega}\delta\tilde{\omega}\bar{U}(\vec{r})}{\bar{v}^2} = 0 \tag{8.47}$$

  We now multiply this equation by $\bar{U}(\vec{r})$ and integrate over the cavity volume:

  $$\int_V (\nabla^2\delta U(\vec{r}))\bar{U}(\vec{r})d^3\vec{r} + \frac{\bar{\omega}^2}{\bar{v}^2}\int_V \delta U(\vec{r})\bar{U}(\vec{r})d^3\vec{r} \tag{8.48}$$

  $$- \frac{2\bar{\omega}^2}{\bar{v}^3}\int_V \delta v(\vec{r})\bar{U}(\vec{r})^2 d^3\vec{r} + \frac{2\bar{\omega}\delta\tilde{\omega}}{\bar{v}^2}\int_V \bar{U}(\vec{r})^2 d^3\vec{r} = 0 \tag{8.49}$$

  The first integral can be integrated by parts twice giving:

  $$\int_V (\nabla^2\delta U(\vec{r}))\bar{U}(\vec{r})d^3\vec{r} = \int_V \delta U(\vec{r})\nabla^2\bar{U}(\vec{r})d^3\vec{r} \tag{8.50}$$

  The first two integrals in equation 8.49 cancel because $\bar{U}(\vec{r})$ solves the unperturbed wave equation, so we are left with:

  $$\delta\tilde{\omega} = \bar{\omega}\frac{\int_V \delta v(\vec{r})\bar{U}(\vec{r})^2 d^3\vec{r}}{\int_V \bar{v}\bar{U}(\vec{r})^2 d^3\vec{r}} \tag{8.51}$$

  This equation describes the real shift in frequency due to variations in sound velocity.

- **Keeping v, γ constant, perturbing ρ**

  In this situation, after we use the fact that $U(\vec{r})$ solves the unperturbed wave equation, equation 8.36 takes the following form :

  $$\nabla^2\delta U(\vec{r}) - \left(1 + \frac{\delta\rho(\vec{r})}{\bar{\rho}}\right)\frac{\nabla\delta\rho(\vec{r})}{\bar{\rho}}\nabla(\bar{U}(\vec{r}) + \delta U(\vec{r})) + \frac{\bar{\omega}^2}{\bar{v}^2}\delta U(\vec{r}) + \frac{2\bar{\omega}\delta\tilde{\omega}}{\bar{v}^2}\bar{U}(\vec{r}) = 0 \tag{8.52}$$

  Simplifying and removing non-linear terms, we arrive at:

  $$\nabla^2\delta U(\vec{r}) - \frac{\nabla\delta\rho(\vec{r})}{\bar{\rho}}\nabla\bar{U}(\vec{r}) + \frac{\bar{\omega}^2}{\bar{v}^2}\delta U(\vec{r}) + \frac{2\bar{\omega}\delta\tilde{\omega}}{\bar{v}^2}\bar{U}(\vec{r}) = 0 \tag{8.53}$$

We multiply both sides by $\bar{U}(\vec{r})$ and integrate over the cavity volume. The first and the third integral cancel for the same reason as before: $\bar{U}(\vec{r})$ solves the unperturbed equation. The other two integrals can be rearranged to give:

$$\delta\tilde{\omega} = \frac{1}{2}\frac{\bar{v}^2}{\bar{\omega}}\frac{\int_V(\nabla\delta\rho(\vec{r}))\bar{U}(\vec{r})(\nabla\bar{U}(\vec{r}))d^3\vec{r}}{\int_V \bar{\rho}\bar{U}(\vec{r})^2 d^3\vec{r}} \tag{8.54}$$

The integral in the numerator can be integrated by parts by taking $u = \bar{U}(\vec{r})\nabla\bar{U}(\vec{r})$ and $\nabla v = \nabla\delta\rho(\vec{r})$:

$$\int_V(\nabla\delta\rho(\vec{r}))\bar{U}(\vec{r})(\nabla\bar{U}(\vec{r}))d^3\vec{r} = -\int_V \delta\rho(\vec{r})\bar{U}(\vec{r})\nabla^2\bar{U}(\vec{r})d^3\vec{r} - \int_V \delta\rho(\vec{r})(\nabla\bar{U}(\vec{r}))^2 d^3\vec{r} \tag{8.55}$$

Since $\nabla^2\bar{U}(\vec{r}) = -\bar{\omega}^2/\bar{v}^2\bar{U}(\vec{r})$, we can rewrite the integral as:

$$\int_V(\nabla\delta\rho(\vec{r}))\bar{U}(\vec{r})(\nabla\bar{U}(\vec{r}))d^3\vec{r} = \int_V \delta\rho(\vec{r})\frac{\bar{\omega}^2}{\bar{v}^2}\bar{U}(\vec{r})^2 d^3\vec{r} - \int_V \delta\rho(\vec{r})(\nabla\bar{U}(\vec{r}))^2 d^3\vec{r} \tag{8.56}$$

Plugging this back into equation 8.54, we get:

$$\delta\tilde{\omega} = \frac{1}{2}\frac{\int_V \delta\rho(\vec{r})\bar{U}(\vec{r})^2 d^3\vec{r}}{\int_V \bar{\rho}\bar{U}(\vec{r})^2 d^3\vec{r}}\bar{\omega} - \frac{1}{2}\frac{\bar{v}^2}{\bar{\omega}}\frac{\int_V \delta\rho(\vec{r})(\nabla\bar{U}(\vec{r}))^2 d^3\vec{r}}{\int_V \bar{\rho}\bar{U}(\vec{r})^2 d^3\vec{r}} \tag{8.57}$$

The integral in the denominator in the second term in equation 8.57, can be expanded as:

$$\int_V \bar{\rho}\bar{U}(\vec{r})^2 d^3\vec{r} = \int_V \bar{\rho}\bar{U}(\vec{r})\bar{U}(\vec{r})d^3\vec{r} = -\int_V \bar{\rho}\bar{U}(\vec{r})\frac{\bar{v}^2}{\bar{\omega}^2}\nabla^2\bar{U}(\vec{r})d^3\vec{r} \tag{8.58}$$

This integral can now be integrated by parts by taking $u = \bar{U}(\vec{r})$ and $\nabla v = \nabla^2\bar{U}(\vec{r})$, which gives:

$$-\frac{\bar{v}^2}{\bar{\omega}^2}\int_V \bar{\rho}\bar{U}(\vec{r})\nabla^2\bar{U}(\vec{r})d^3\vec{r} = \frac{\bar{v}^2}{\bar{\omega}^2}\int_V \bar{\rho}(\nabla\bar{U}(\vec{r}))^2 d^3\vec{r} \tag{8.59}$$

Finally plugging this into equation 8.57 gives:

$$\delta\tilde{\omega} = \left(\frac{1}{2}\frac{\int_V \delta\rho(\vec{r})\bar{U}(\vec{r})^2 d^3\vec{r}}{\int_V \bar{\rho}\bar{U}(\vec{r})^2 d^3\vec{r}} - \frac{1}{2}\frac{\int_V \delta\rho(\vec{r})(\nabla\bar{U}(\vec{r}))^2 d^3\vec{r}}{\int_V \bar{\rho}(\nabla\bar{U}(\vec{r}))^2 d^3\vec{r}}\right)\bar{\omega} \tag{8.60}$$

This equation describes the real shift in frequency due to variations in density.

- **Keeping v, ρ constant, perturbing γ**

  In this situation, after we use the fact that $U(\vec{r})$ solves the unperturbed wave equation, equation 8.36 takes the following form :

$$\nabla^2\delta U(\vec{r}) + \frac{\bar{\omega}^2}{\bar{v}^2}\delta U(\vec{r}) + \frac{2\bar{\omega}\delta\tilde{\omega}}{\bar{v}^2}\bar{U}(\vec{r}) \tag{8.61}$$

$$- i\frac{1}{\bar{v}^2}(\bar{\omega} + \delta\tilde{\omega})\delta\gamma(\vec{r})(\bar{U}(\vec{r}) + \delta U(\vec{r})) = 0 \tag{8.62}$$

  Simplifying and removing non-linear terms we have:

$$\nabla^2\delta U(\vec{r}) + \frac{\bar{\omega}^2}{\bar{v}^2}\delta U(\vec{r}) + \frac{2\bar{\omega}\delta\tilde{\omega}}{\bar{v}^2}\bar{U}(\vec{r}) - \frac{i}{\bar{v}^2}\bar{\omega}\delta\gamma(\vec{r})\bar{U}(\vec{r}) = 0 \tag{8.63}$$

  We multiply everything by $\bar{U}(\vec{r})$ and integrate over the cavity volume. That allows us to get rid of the first two terms as in previous derivations and the rest can be rearranged as:

$$\delta\tilde{\omega} = \frac{i}{2}\frac{\int_V \delta\gamma(\vec{r})\bar{U}(\vec{r})^2 d^3\vec{r}}{\int_V \bar{U}(\vec{r})^2 d^3\vec{r}} \tag{8.64}$$

  This equation describes the imaginary shift in frequency due to variations in linewidth.

To summarize, the shifts in frequency are as follows:

$$\mathrm{Re}[\delta\tilde{\omega}] = \left(\frac{\int_V \delta v(\vec{r})\bar{U}(\vec{r})^2 d^3\vec{r}}{\int_V \bar{v}\bar{U}(\vec{r})^2 d^3\vec{r}} + \frac{1}{2}\frac{\int_V \delta\rho(\vec{r})\bar{U}(\vec{r})^2 d^3\vec{r}}{\int_V \bar{\rho}\bar{U}(\vec{r})^2 d^3\vec{r}} - \frac{1}{2}\frac{\int_V \delta\rho(\vec{r})(\nabla\bar{U}(\vec{r}))^2 d^3\vec{r}}{\int_V \bar{\rho}(\nabla\bar{U}(\vec{r}))^2 d^3\vec{r}} \right) \bar{\omega} \tag{8.65}$$

$$\mathrm{Im}[\delta\tilde{\omega}] = \frac{1}{2}\frac{\int_V \delta\gamma(\vec{r})\bar{U}(\vec{r})^2 d^3\vec{r}}{\int_V \bar{U}(\vec{r})^2 d^3\vec{r}} \tag{8.66}$$

As we showed before, $\mathrm{Re}[\delta\tilde{\omega}] = \delta\omega$ and $\mathrm{Im}[\delta\tilde{\omega}] = \gamma/2$, where $\delta\omega$ is the change in frequency of the mode and $\gamma/2$ is the mode linewidth. We can now consider a particular situation of an acoustic mode confined between two mirrors. We will assume that the mode is described by $U \propto \cos(2\pi z/\lambda_{\mathrm{ac}})$ (pressure has antinodes at the mirror/helium boundary), where λ_{ac} is the wavelength of the acoustic mode. We also assume that the mode has uniform area throughout the cavity, calculated as $A = \pi w_0^2$ where $w_0 \approx 5.7$ μm is the mode field radius (this assumption is acceptable for the given cavity length and mirror ROCs).

8.4.2.1 The acoustic mode frequency

The acoustic mode frequency is calculated as:

$$\delta\omega_{\mathrm{mode}} = \left(\frac{\int_V \delta v(\vec{r})\bar{U}(\vec{r})^2 d^3\vec{r}}{\int_V \bar{v}\bar{U}(\vec{r})^2 d^3\vec{r}} + \frac{1}{2}\frac{\int_V \delta\rho(\vec{r})\bar{U}(\vec{r})^2 d^3\vec{r}}{\int_V \bar{\rho}\bar{U}(\vec{r})^2 d^3\vec{r}} - \frac{1}{2}\frac{\int_V \delta\rho(\vec{r})(\nabla\bar{U}(\vec{r}))^2 d^3\vec{r}}{\int_V \bar{\rho}(\nabla\bar{U}(\vec{r}))^2 d^3\vec{r}} \right) \bar{\omega} \tag{8.67}$$

It is also convenient to split the integrals in the numerators into 2 parts ($r < r_{\mathrm{crit}}$ and $r > r_{\mathrm{crit}}$) , giving us two contributions for the change in frequency. Inside the critical radius (in the GM region) the temperature is determined only by n_{circ} so we will define $\delta\omega_{\mathrm{GM}}(n_{\mathrm{circ}})$:

$$\delta\omega_{\mathrm{GM}}(n_{\mathrm{circ}}) \equiv \delta\omega_{\mathrm{mode}}(r < r_{\mathrm{crit}}) = N \left(\frac{2\int_0^{r_{\mathrm{crit}}}\int_0^{\pi/2} \delta v(T(r,\theta))\cos(2\pi r\cos\theta/\lambda_{\mathrm{ac}})^2 2\pi r^2 \sin\theta d\theta dr}{\bar{v}AL_{\mathrm{cav}}} \right. \tag{8.68}$$

$$+ \left(\frac{\int_0^{r_{\mathrm{crit}}}\int_0^{\pi/2} \delta\rho(T(r,\theta))\cos(2\pi r\cos\theta/\lambda_{\mathrm{ac}})^2 2\pi r^2 \sin\theta d\theta dr}{\bar{\rho}AL_{\mathrm{cav}}} \right. \tag{8.69}$$

$$\left. \left. - \left(\frac{\int_0^{r_{\mathrm{crit}}}\int_0^{\pi/2} \delta\rho(T(r,\theta))\sin(2\pi r\cos\theta/\lambda_{\mathrm{ac}})^2 2\pi r^2 \sin\theta d\theta dr}{\bar{\rho}AL_{\mathrm{cav}}} \right) \bar{\omega} \right. \right. \tag{8.70}$$

Note that δv and $\delta\rho$ are now described as functions of temperature, which is a function of position. Here N is the total number of absorbers on *both* mirrors. As long as $\lambda_{\mathrm{ac}} < r_{\mathrm{crit}}$, the second and third term will nearly cancel. We also calculated that even if they don't cancel, they contribute at most 1 % of the first term, since the relative change in the density is much smaller than the relative change in the sound velocity.

Outside the critical radius (in the ballistic region), the temperature is constant: $T \approx T_{\mathrm{MC}}$ and independent of n_{circ}. Assuming $r_{\mathrm{crit}} \ll L_{\mathrm{cav}}$, equation 8.67 will simplify. We will define $\delta\omega_{\mathrm{ball}}(T_{\mathrm{MC}})$:

$$\delta\omega_{\mathrm{ball}}(T_{\mathrm{MC}}) \equiv \delta\omega_{\mathrm{mode}}(r > r_{\mathrm{crit}}) \approx \frac{\delta v(T_{\mathrm{MC}})}{\bar{v}}\bar{\omega} \propto T_{\mathrm{MC}}^4 \tag{8.71}$$

Here we have used the fact that for $T < 600$ mK the change in speed of the sound is proportional to T^4, as stated in section 3.4.2.

The measured frequency of the mode is then written as:

$$\omega_{\mathrm{mode}}(n_{\mathrm{circ}}, T_{\mathrm{MC}}) = \omega_{\mathrm{bare}} + \delta\omega_{\mathrm{GM}}(n_{\mathrm{circ}}) + b_\omega T_{\mathrm{MC}}^4 \tag{8.72}$$

Here ω_{bare} is the frequency of the mode for $T_{\mathrm{MC}} = 0$ K and $n_{\mathrm{circ}} = 0$; b_ω is a fit parameter. From the fit to the change in sound velocity performed in section 3.4.2, we expect $b_\omega/2\pi \approx 1 \times 10^6$ Hz/K^4.

8.4.2.2 The acoustic mode linewidth

The mode linewidth is calculated similarly:

$$\gamma_{\mathrm{mode,int}} = \frac{\int_V \delta\gamma(T(\vec{r}))\bar{U}(\vec{r})^2 d^3\vec{r}}{\int_V \bar{U}(\vec{r})^2 d^3\vec{r}} \tag{8.73}$$

As before separate the integral in the numerator into two parts. For $r < r_{\mathrm{crit}}$, we define $\gamma_{\mathrm{GM}}(n_{\mathrm{circ}})$:

$$\gamma_{\mathrm{GM}}(n_{\mathrm{circ}}) \equiv \gamma_{\mathrm{mode,int}}(r < r_{\mathrm{crit}}) = \frac{2N\int_0^{r_{\mathrm{crit}}}\int_0^{\pi/2}\delta\gamma(T(r,\theta))\cos(2\pi r\cos\theta/\lambda_{\mathrm{ac}})^2 2\pi r^2\sin\theta d\theta dr}{AL_{\mathrm{cav}}} \tag{8.74}$$

And for $r > r_{\mathrm{crit}}$, we define γ_{ball}:

$$\gamma_{\mathrm{ball}} \equiv \gamma_{\mathrm{mode,int}}(r > r_{\mathrm{crit}}) \approx \delta\gamma(T_{\mathrm{MC}}) \propto T_{\mathrm{MC}}^4 \tag{8.75}$$

as we have shown in section 3.4.1

The linewidth of the mode is then written as:

$$\gamma_{\mathrm{mode}}(n_{\mathrm{circ}}, T_{\mathrm{MC}}) = \gamma_{\mathrm{ext}} + \gamma_{\mathrm{GM}}(n_{\mathrm{circ}}) + b_\gamma T_{\mathrm{MC}}^4 \tag{8.76}$$

The value γ_{ext} is the linewidth due to leaking of the acoustic mode into the fiber calculated in 8.3.1.2, and b_γ is a fit parameter, which, from the theory described in section 3.4.1 is expected to be $b_\gamma/2\pi = 2.70 \times 10^6$ Hz/K^4 .

8.4.2.3 The acoustic mode thermal phonon number

For an acoustic mode coupled to multiple baths, each described by the thermal number n_{i} and coupling strength γ_{i}, the acoustic mode thermal phonon number can be calculated as:

$$n_{\mathrm{mode}}\gamma_{\mathrm{mode}} = \sum_i n_i\gamma_i \tag{8.77}$$

The local thermal phonon number is determined as:

$$n(\vec{r}) \approx \frac{k_{\mathrm{B}}T(\vec{r})}{\hbar\omega_{\mathrm{m}}} - \frac{1}{2} \tag{8.78}$$

Where $\hbar$ is Planck's constant, ω_{m} is the frequency of the mechanical mode, k_{B} is Boltzmann's constant and $T(\vec{r})$ is the helium temperature at position $\vec{r}$.

In the case described here, it is convenient to consider the acoustic mode as coupled to three baths:

1. The fiber at temperature T_{fiber}, which can be calculated assuming thermal conductivity of the mirror is proportional to T^k:

   $$T_{\mathrm{fiber}} = (T_{\mathrm{MC}}^{k+1} + \sigma^{k+1}n_{\mathrm{circ}})^{1/(k+1)} \tag{8.79}$$

   Here σ describes by how many degrees one circulating photon heats up the fiber. The coupling rate to the fiber is γ_{ext}. The constants σ and k will be used as fit parameters.

2. The helium in the cavity outside of r_{crit}. The temperature of that helium is T_{MC} and the coupling rate is $b_\gamma T_{\mathrm{MC}}^4$.

3. The helium in the cavity inside $r_{\rm crit}$. This bath is not at a uniform temperature and the phonon number in this bath is calculated as:

$$n_{\rm GM} \equiv n_{\rm mode}(r < r_{\rm crit}) = \frac{\int_0^{r_{\rm crit}} \int_0^{\pi/2} n(T(r))\gamma(T(r)) \cos(2\pi r \cos\theta/\lambda_{\rm ac})^2 2\pi r^2 \sin\theta d\theta dr}{\int_0^{r_{\rm crit}} \int_0^{\pi/2} \gamma(T(r)) \cos(2\pi r \cos\theta/\lambda_{\rm ac})^2 2\pi r^2 \sin\theta d\theta dr} \tag{8.80}$$

   The coupling rate to that bath is $\gamma_{\rm GM}(n_{\rm circ})$.

Therefore the mode thermal phonon number is:

$$n_{\rm mode}(n_{\rm circ}, T_{\rm MC})\gamma = \left(\frac{k_{\rm B}}{\hbar\omega_{\rm m}}(T_{\rm MC}^{k+1} + \sigma^{k+1} n_{\rm circ})^{1/(k+1)} - \frac{1}{2}\right)\gamma_{\rm ext} \tag{8.81}$$

$$+ n_{\rm GM}(n_{\rm circ}) \times \gamma_{\rm GM}(n_{\rm circ}) + \left(\frac{k_{\rm B}}{\hbar\omega_{\rm m}} T_{\rm MC} - \frac{1}{2}\right) b_\gamma T_{\rm MC}^4 \tag{8.82}$$

If the fiber did not have the DBR stack on it, we would expect $k = 1.91$ (based on thermal conductivity of amorphous silica at low temperature) [88].

8.4.3 Fit of the data to the model

We have developed a model that can be used to fit the data for the mode γ, $\omega_{\rm m}$ and $n_{\rm th}$. The values of γ and $\omega_{\rm m}$ are extracted from the OMIT/A data described in section 8.2. The value of $n_{\rm th}$ is extracted from the thermal motion measurements. The general procedure is described in section 6.6.2. Here I will briefly discuss extracting the thermal phonon number in this particular device.

8.4.3.1 Thermal motion

In this device we measured both the red sideband of the upper control beam and the blue sideband of the lower control beam. Both beams were on simultaneously. We took data for various device temperatures, obtained by varying the mixing chamber temperature. From this data the mechanical phonon number is extracted as described in section 6.6.4 and from that the thermal phonon number is extracted as described in section 6.6.5. The relevant attenuation and background noise are described below:

The attenuation is calculated as follows:

- Only 66.5 % of the light leaving the cavity was reaching EDFA, so $\sigma_{(\rm dev\to EDFA)} = 0.665$. This was calculated as described in section 6.6.4.

In this device we eliminated classical laser noise (by introducing a filter cavity), and mixer image noise (by using an image-rejection mixer), so the only noise source was the EDFA.

- Data was taken for a variety of incident laser powers. The laser wavelength was $\lambda = 1529$ nm. The EDFA noise for various powers was measured at 1529 nm (this is shown in figure 6.39). Since can calculate the power reaching the EDFA for each individual data set, we can figure out the noise added by the EDFA as well. Additionally we record the relative power in the LO for each data set. The noise figure of EDFA for the data was measured to be $4.27 < NF_{\rm EDFA} < 4.64$ dB. The relative power in the LO was $0.54 < P_{\rm rel} < 0.93$. This means that the total noise added by EDFA is between 2.87 and 5.38 times the shot noise.

Now that we know the thermal phonon number for various temperatures and powers, we can fit the data.

8.4.3.2 Fits of the linewidth, frequency and thermal phonon number to the model

For the first step, we considered measurements of γ and $\omega_{\rm m}$ for which $n_{\rm circ} < 500$. As shown in figure 8.20, these measurements are approximately independent of $n_{\rm circ}$. From this observation we conclude that when $n_{\rm circ} < 500$ no appreciable heating occurs from optical absorption, so we fit this data to the expressions derived above with $n_{\rm circ}$ set to zero:

$$\omega(0, T_{\rm MC}) = \omega_{\rm bare} + b_\omega T_{\rm MC}^4 \tag{8.83}$$

$$\gamma(0, T_{\rm MC}) = \gamma_{\rm ext} + b_\gamma T_{\rm MC}^4 \tag{8.84}$$

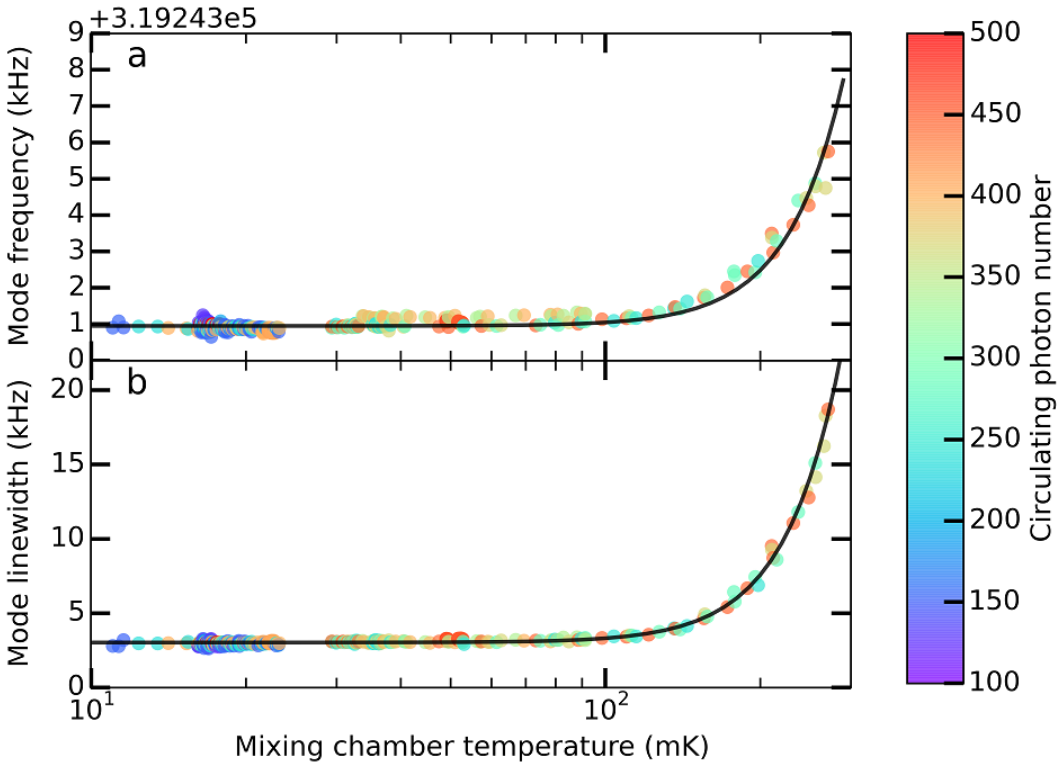

Figure 8.20: (a) Frequency and (b) linewidth vs $T_{\rm MC}$ for $n_{\rm circ} < 500$. The dots represent data, with the color corresponding to $n_{\rm circ}$. The solid lines are the fits described in the text

The advantage of this approach is that it employs only four fitting parameters: $\omega_{\rm bare}$, b_ω, $\gamma_{\rm ext}$ and $+b_\gamma$. The resulting fits are shown in figure 8.20. The best-fit values of $\omega_{\rm bare}$, b_ω, $\gamma_{\rm ext}$ and $+b_\gamma$ are listed in table 8.4, along with their *a priori* expected values.

The second step involves fitting the complete set of measurements of γ, $\omega_{\rm m}$ and $n_{\rm th}$ to the expressions derived in the previous section:

$$\omega_{\rm mode}(n_{\rm circ}, T_{\rm MC}) = \omega_{\rm bare} + \delta\omega_{\rm GM}(n_{\rm circ}) + b_\omega T_{\rm MC}^4 \tag{8.85}$$

$$\gamma_{\rm mode}(n_{\rm circ}, T_{\rm MC}) = \gamma_{\rm ext} + \gamma_{\rm GM}(n_{\rm circ}) + b_\gamma T_{\rm MC}^4 \tag{8.86}$$

$$n_{\rm mode}(n_{\rm circ}, T_{\rm MC})\gamma = \left(\frac{k_{\rm B}}{\hbar\omega_{\rm m}}(T_{\rm MC}^{k+1} + \sigma^{k+1} n_{\rm circ})^{1/(k+1)} - \frac{1}{2}\right)\gamma_{\rm ext} \tag{8.87}$$

$$+ n_{\rm GM}(n_{\rm circ}) \times \gamma_{\rm GM}(n_{\rm circ}) + \left(\frac{k_{\rm B}\hbar\omega_{\rm m}}{T}_{\rm MC} - \frac{1}{2}\right) b_\gamma T_{\rm MC}^4$$

Parameter [units]	Value from fit	Expected value
$\omega_{\rm bare}/2\pi$ [Hz]	$319.24 \times 10^6 \pm 4$	319.24×10^6
$\gamma_{\rm bare}/2\pi$ [Hz]	3026 ± 3	4000 ± 2400
$b_\omega/2\pi$ [Hz/K^3]	$(0.93 \pm 0.01) \times 10^6$	1×10^6
$b_\gamma/2\pi$ [Hz/K^4]	$(2.79 \pm 0.01) \times 10^6$	2.70×10^6
σ [K]	$(1.4 \pm 0.2) \times 10^{-2}$	-
k	2.2 ± 0.1	1.91
α	0.7 ± 0.1	0.2
N	$1 - 2$	> 1
η [m]	$(1.0 \pm 0.1) \times 10^{-8}$	$5 \times 10^{-9} < \eta < 7 \times 10^{-8}$

Table 8.4: Fit parameters and the expected values

The values $\omega_{\rm bare}$,$\gamma_{\rm ext}$, b_ω and b_γ obtained from the first step are used as the initial conditions in the next fit, in which frequency, linewidth and phonon number are fit simultaneously, using the following expressions: This leaves five fitting parameters: N, α, η, k, and d. The result of this fit is shown as the solid curves in fig. 8.21 . The best-fit values are listed in Table 8.4, along with their *a priori* expected values. For the fits, the value of α was constrained to be less than 1 and the value of N was constrained to be greater than 1. The values extracted from the fit are reasonably close to expected theoretical values. The largest discrepancy is in the value of α, however as we said before, the theoretical estimate on α is necessarily rough.

Equations 8.85, 8.86 and 8.87 can now be used to calculate the expected frequency, linewidth, and thermal occupation number given the $n_{\rm circ}$ and $T_{\rm MC}$.

The effective mode temperature can be calculated from the phonon number as:

$$T_{\rm eff} = \left(n_{\rm mode} + \frac{1}{2} \right) \frac{\hbar \omega_{\rm m}}{k_{\rm B}} \tag{8.88}$$

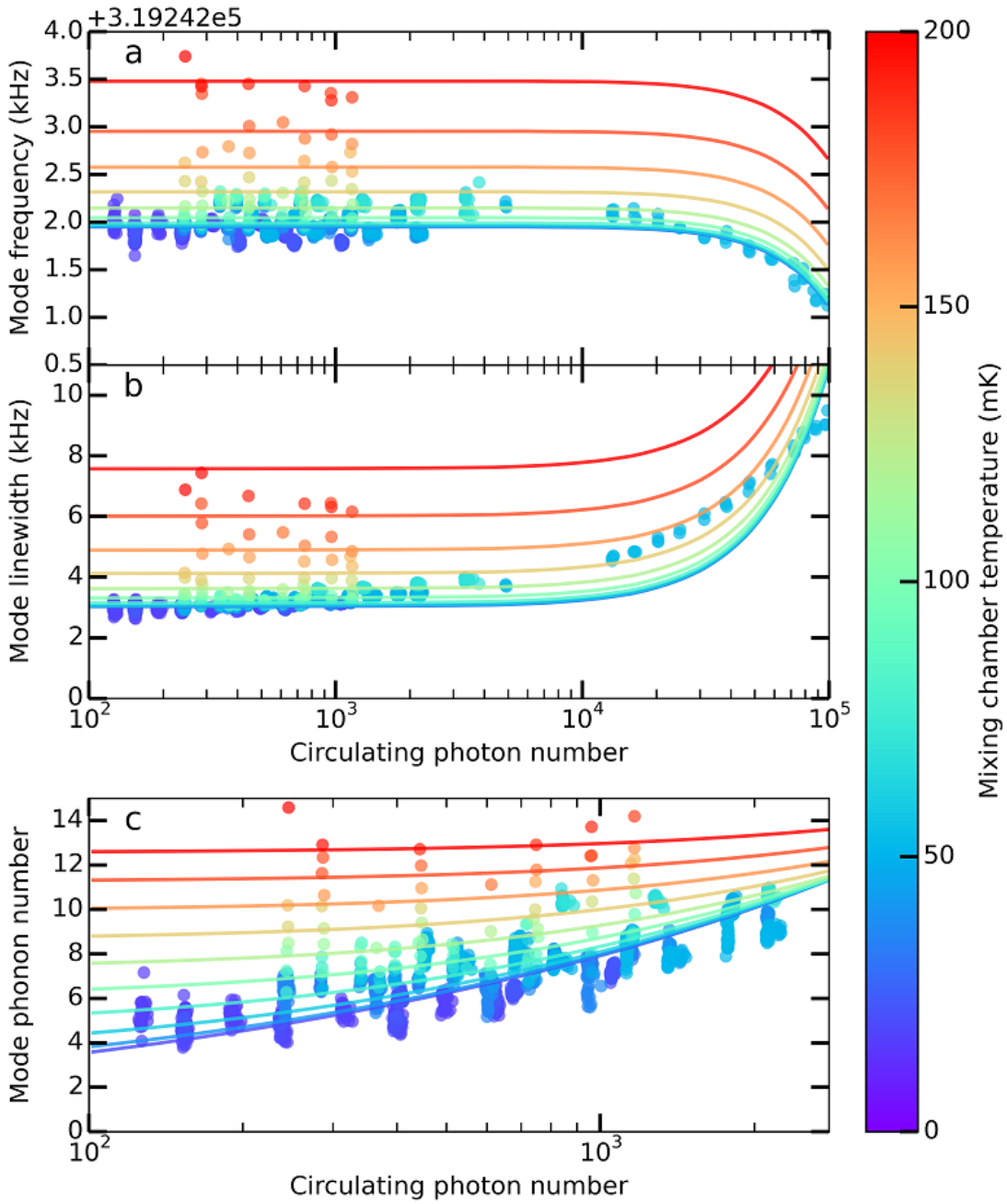

Figure 8.21: (a)Frequency, (b) linewidth and (c) mode phonon number vs n_{circ} for $T_{\mathrm{MC}} < 200$ mK. The dots represent data, with the color corresponding to T_{MC}. The solid lines are the fits described in the text, with the color corresponding to T_{MC} as well

8.5 Sideband asymmetry measurements

In this device we also measured the asymmetry between the Stokes and anti-Stokes sidebands. For these measurements two control beams (detuned by $\pm\omega_{\mathrm{m}}$) were used, as described in section 6.5. The data was recorded and analyzed in the same way as described in section 8.4.3.1. The data was taken for a few different mixing chamber temperatures and circulating photon numbers. The resulting thermal phonon number is plotted in figure 8.22 (top). Since the mode

temperature is not the same as the mixing chamber temperature, we also plot the thermal phonon number vs. the mode temperature, calculated in section 8.4.3.2 in the middle plot. Finally the bottom plot shows the mechanical phonon number difference between red and blue sidebands. It is near 1 for a range of temperatures. The deviations at higher temperatures are due to less data having been taken at those temperatures.

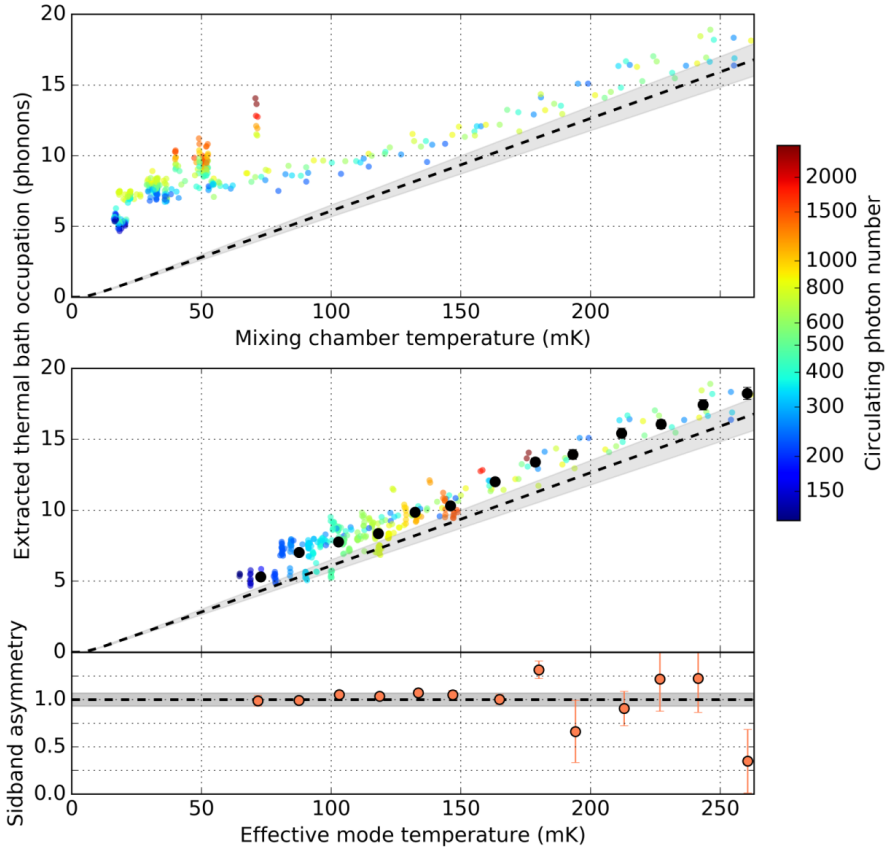

Figure 8.22: **(a)** The phonon number $n_{\rm th}$ plotted vs. the mixing chamber temperature. **(b)**: The phonon number $n_{\rm th}$ plotted vs. the effective mode temperature. **(c)** The difference $n_{\rm m}^{rr} - n_{\rm m}^{bb}$ plotted vs. the effective mode temperature.

The difference of one phonon between n_m^{rr} and n_m^{bb} is a signature of quantum behavior of the device, as the energy difference between two sidebands is proportional to the single quanta of energy $\hbar\omega_{\rm m}$. This confirms that optomechanical coupling is predominantly unitary. Additionally, it provides a way to confirm the measurement calibrations, which does not rely on the knowledge of $n_{\rm th}$.

8.6 Cooperativity

In this section we calculate the cooperativities for the second-generation device and compare them to the cooperativities achieved in the first-generation device.

The single photon cooperativity is $C_0 = 8 \times 10^{-4}$ using the following assumptions: $\kappa/2\pi = 21$ MHz, $\gamma_{\rm ext}/2\pi = 3.0$ kHz (calculated from the fit to linewidth), $g_0/2\pi = 3.6$ kHz. It is 6 times larger than the single photon cooperativity in the first-generation device.

The multiphoton cooperativity is given by:

$$C = \frac{4g_0^2}{\kappa\gamma} n_{\rm cont} = \frac{4g_0^2}{\kappa(\gamma_{\rm ext} + \gamma_{\rm int}(n_{\rm Total}))} n_{\rm Control(U/L)} \tag{8.89}$$

Here n_{total} gives the total circulating photon number; $n_{\mathrm{Control(U/L)}}$ gives the circulating photon number in the control beam that is used for measurement; $\gamma_{\mathrm{int}}(n_{\mathrm{total}})$ was calculated from the thermal model. The circulating photon number is calculated assuming $\Delta_{\mathrm{Control}} = \omega_{\mathrm{m}} \approx 2\pi \times 319$ MHz and $\Delta_{\mathrm{LO}} = 2\pi \times 2.1$ GHz; the relative power in the control beam is up to 12 %; the relative power in the LO can be as small as ≈ 54 %; the input coupling is $\kappa_{\mathrm{ext}}/\kappa = 0.44$. Now that two control beams are present, $n_{\mathrm{Total}} = n_{\mathrm{LO}} + n_{\mathrm{Control(U)}} + n_{\mathrm{Control(L)}}$.

In figure 8.23, the multiphoton cooperativity achievable in the second-generation device is plotted vs. power incident on the cavity with a solid green line. For the calculations we assume $T_{\mathrm{MC}} = 0$. The cooperativity increases steadily for powers below 2 mW. For powers above that, it stays constant. The black cross denotes the maximum cooperativity $C = 1.14$ achieved in the second-generation device. For comparison the multiphoton cooperativity achievable (solid blue line) and achieved (black star) in the first-generation device are also shown (this was described in section 7.6).

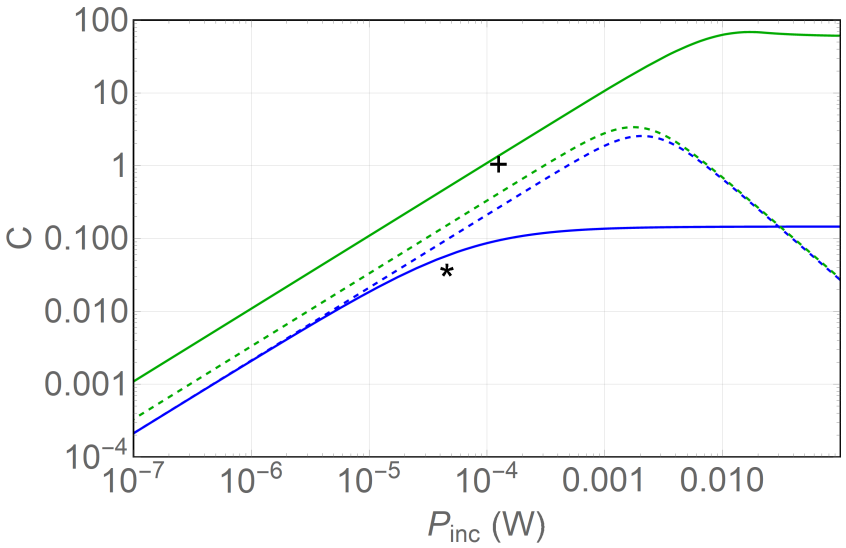

Figure 8.23: The multiphoton cooperativity vs. incident laser power. Solid green line - cooperativity in the second-generation device. Black cross - maximum cooperativity achieved in the first-generation device. Solid blue line - cooperativity in the first-generation device. Black star - maximum cooperativity achieved in the first-generation device. Dashed green and blue lines - limit on cooperativity due to the heating of the mixing chamber.

Figure 8.24 shows the thermal cooperativity $C_{\mathrm{th}} = C/n_{\mathrm{th}}$ with a solid purple line. The value of n_{th} is calculated from the thermal model. The thermal cooperativity reaches a maximum for 2 mW incident power. Above that incident power, the multiphoton cooperativity stays constant while the n_{th} is increasing, which leads to decrease in thermal cooperativity. The black cross denotes the maximum thermal cooperativity $C_{\mathrm{th}} = 9.2 \times 10^{-2}$ achieved in the second-generation device. For comparison the thermal cooperativity achievable (solid red line) and achieved (black star) in the first-generation device are also shown (this was described in section 7.6).

From these plots it looks like it would be possible to achieve much higher cooperativity and thermal cooperativity in the second-generation device, that was demonstrated. However, there is one more effect that was not accounted for. All of the calculation above assume $T_{\mathrm{MC}} = 0$. However, the mixing chamber temperature increases as the incident power increases, which puts a limit on cooperativity as well.

We can estimate the dependence of T_{MC} on the incident power from the values of the T_{MC} that we observed during our measurements, when the mixing chamber heater was off. The plot of that is given in figure 8.25. The circles represent data. Blue circles - data taken with the first-generation device, when the laser is far off-resonance. Red circles - data taken with the second-generation device when the LO is 2.1 GHz away from resonance and the control beams are $\pm\omega_{\mathrm{m}}$ detuned from the cavity resonance. The lines are the fits to a power law: $T_{\mathrm{MC}} = \zeta_P P_{\mathrm{inc}}^n$, where ζ_P and n are fit parameters. For the first-generation device, the values of these parameters are: $\zeta_P = 7.7\ \mathrm{K} \cdot \mathrm{W}^{-0.6}$ and $n = 0.6$. For the second-generation device, the values of these parameters are: $\zeta_P = 43.3\ \mathrm{K} \cdot \mathrm{W}^{-0.7}$ and $n = 0.7$. The discrepancy is most likely attributed to different regimes of operating the dilution refrigerator - that is it is possible to decrease T_{MC} by increasing the rate of

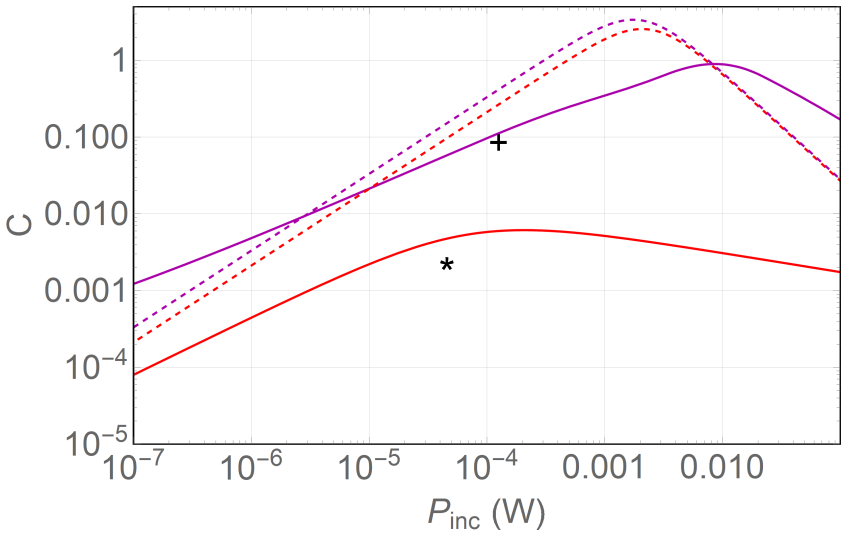

Figure 8.24: The thermal cooperativity vs. incident laser power. Solid purple line - thermal cooperativity in the second-generation device. Black star - maximum thermal cooperativity achieved in the second-generation device. Solid red line - thermal cooperativity in the first-generation device. Black star - maximum thermal cooperativity achieved in the first-generation device. Dashed purple and red lines - limit on thermal cooperativity due to the heating of the mixing chamber.

mix circulation. It is also likely that neither of these plots demonstrate the most optimal scenario and it is in principle possible to lower T_{MC} even further. However, it is very clear that T_{MC} depends on the incident laser power.

We will calculate the limits on cooperativity and thermal cooperativity assuming the lower plot for the dependence of mixing chamber temperature on the incident power in figure 8.25. For these calculations we assume $n_{\mathrm{Total}} = n_{\mathrm{Control(U/L)}} = 0$. These limits are shown in figures 8.23 and 8.24. These limits are pretty flexible. They can be changed by increasing the rate of mix circulation in the dilution refrigerator or decreasing the duty cycle (keeping laser on for 10% of the time).

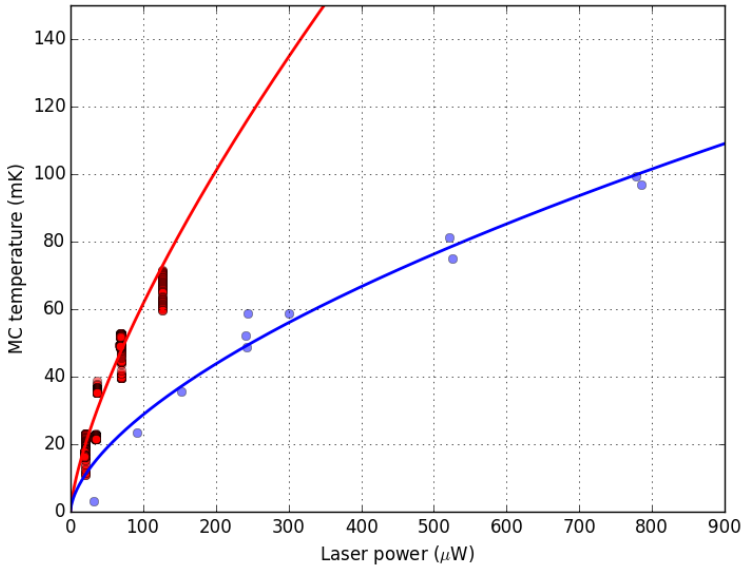

Figure 8.25: Mixing chamber temperature vs. incident laser power. The blue circles represent the data taken with the first-generation device. The laser is off-resonant. The red circle represent the data taken with the second-generation device. The laser is on resonance with the cavity.

8.7 Summary

In conclusion, the second-generation device was an improvement over the first-generation device. The increased mirror reflectivity and thermal conductivity lead to increase in maximum multiphoton cooperativity by a factor of 28 and increase in maximum thermal cooperativity by a factor of 37.

The more open geometry led to an increase in thermal conductivity. However, it also resulted in the temperature in helium inside the cavity not being uniform. We had to develop a more complicated thermal model to account for that.

Finally, we were able to send control beams detuned by both $+\omega_{\mathrm{m}}$ and $-\omega_{\mathrm{m}}$. That allowed us to observe sideband asymmetry (by observing simultaneously the red slideband of the upper control beam and the blue sideband of the lower control beam).

Chapter 9

Outlook and conclusion

The previous chapters described the devices that we built and what we have done with them. This chapter is a look into the future and what we can still do with the system.

- **Non-Gaussian quantum optomechanics**. It is desirable to interface single optical photons with single phonons in the quantum regime. However, it is difficult to do this using traditional methods, such as the ones described in this thesis, because in order to overcome the effects of optical and mechanical decoherence in the system, strong single photon cooperativity is necessary ($C_0 > 1$). A way to circumvent this was implemented in [14]. That scheme uses photon counting to project a mechanical resonator into a non-Gaussian state. The cavity is illuminated with a very weak pulse detuned by $\approx \pm\omega_{\rm m}$. The sideband photons at the cavity resonance frequency are detected, using single photon detectors (SPDs). If the oscillator is originally in the ground state $n_{\rm th} \approx 0$, then the detection of a single photon when the pulse is blue-detuned from the cavity projects the mechanical resonator into a Fock state. The state of the resonator is read out by sending a red-detuned pulse. It is necessary to filter the photons at the cavity resonance from the photons in the incident pulse. The relatively large frequency of the acoustic mode in our device would allow us to filter the sideband photons efficiently. Additionally, the superfluid helium density mode at 315 MHz has occupation number $n_{\rm th} \approx 0.5$ at the base temperature of the dilution refrigerator. This makes our system a good candidate for this approach. This experiment is currently underway in out lab.
- **Optomechanics with macroscopic cavities**. As demonstrated in section 4.3, the optomechanical cooperativity in a superfluid helium filled cavity is independent of cavity length, meaning that macroscopic cavities can be used in place of fiber cavities. However, using macroscopic cavities would lead to larger acoustic mode size on the mirrors and therefore will enable us to take full advantage of the acoustic DBR design, described in section 8.3.1. That could improve the optomechanical cooperativity by a factor of 20-80 (with the spread due to th uncertainty in the material properties of $\rm Ta_2O_5$. An issue with using macroscopic cavity is that, since $\kappa \propto 1/L_{\rm cav}$, the cavity linewidth becomes narrow. That means that, in order to achieve the same circulating photon number, larger incident powers are required. Large incident powers would heat up the mixing chamber, as we have found that the mixing chamber temperature is $T_{\rm MC} \propto P_{\rm inc}^{2/3}$. This, however, can be circumvented by decreasing the duty cycle of the measurement (turn the control beam on only 10 % of the time). The setup to perform this experiment is being built as well.
- **Optomechanics with ripplons**. If the cavity is only partially filled, it should be possible to couple optically to the helium/vacuum interface. This is the topic I will explain in more detail.

9.1 Optomechanics with ripplons in a partially filled cavity

In order to couple to a surface wave, the cavity needs to be partially filled with helium. I will first discuss how we partially fill the fiber cavity (which is non-trivial due to capillary effects). Then I will discuss the shape of the surface modes and

calculate the optomechanical coupling to them. It is also possible to observe optomechanical effects with ripplons in a cavity made using macroscopic mirrors. I will calculate the single photon optomechanical coupling in a 2 mm long cavity formed in a 1 mm diameter tube.

9.1.1 Partially filled cavity

It is difficult to partially fill a fiber cavity located inside of a *single* solid ferrule with inner radius $R_{\text{fer,in}} \approx 100\ \mu m$. When a ferrule of this inner radius is submerged into helium, the level in the tube is $h^*_{\text{empty}} = 5$ mm above the bulk level (calculated using equation 7.40). If there is a fiber of radius $R_{\text{fiber}} \approx 100\ \mu$m in the ferrule, the capillary rise can be on the order of $h^*_{\text{fiber}} = 0.3 \pm 0.2$ m (depending on the difference $R_{\text{fer,in}} - R_{\text{fiber}}$). Therefore in order to stably partially-fill the cavity, the cavity length needs to be at least $h^*_{\text{fiber}} - h^*_{\text{empty}} \approx 0.3 \pm 0.2$ m, which is impossible. It is possible however, to build a partially-filled cavity using two ferrules. Alternatively, we can use a single ferrule with holes drilled through it, as described in section 6.3.4. In this section, for simplicity, I will use the two-ferrule design for calculations, through the situation should be fairly similar if a single ferrule with holes is used instead, although computationally more difficult. There are two different ways to partially fill a cavity, both described below.

9.1.1.1 Partially filled cavity outside the ferrules

First let's consider the case, of a partially filled cavity formed outside the ferrules, as shown in figure 9.1 (a). Here the surface mode is bounded by the outside wall located a distance R_{bound} away from the cavity axis (in our device, it is the wall of the indentation in which the ferrules are glued). If the cavity is short, a configuration shown in figure 9.1(b) is possible for the same volume of helium as the configuration shown in figure 9.1(a). However, if the separation between the fibers is large enough, the situation arises where only the solution shown in figure 9.1(a) exists.

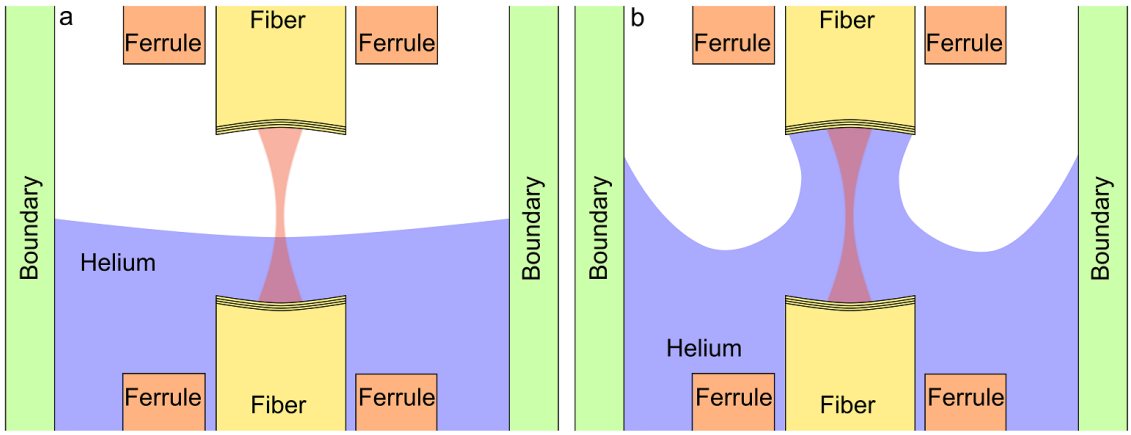

Figure 9.1: The cavity formed between two ferrules. Not to scale. a) Helium level between the fibers. b) A meniscus is formed connecting the top fiber to the wall.

To figure out how long should a cavity be, in order for only the solution shown in figure 9.1(a) to exist, we solve the Young-Laplace equation for two cases outlined above. In the first case, shown in figure 9.1 (a) we solve equations derived in section 7.8.2.3:

$$\frac{dx(s)}{ds} = \cos(\phi(s)) \tag{9.1}$$
$$\frac{dz(s)}{ds} = \sin(\phi(s)) \tag{9.2}$$
$$\frac{d\phi(s)}{ds} = \frac{z(s)}{l^2} - \frac{\sin(\phi(s))}{x(s)} \tag{9.3}$$

Here $l = \sqrt{\sigma_{\mathrm{He}}/(\rho_{\mathrm{He}} g)} = 515$ μm is the capillary length, x is the radial coordinate measured from the axis, z is measured upwards, ϕ is the angle between the surface and horizontal and s is the arc-length.

For the first case, the boundary conditions are: $x(0) = 0$, $\phi(0) = 0$, $x(s_{\mathrm{c}}) = R_{\mathrm{bound}}$, $\phi(s_{\mathrm{c}}) = \pi/2$, where s_{c} is the total arc length. The solution is shown in figure 9.2 with a blue line. We calculate the volume of helium under this curve, using the method of cylinders.

For the second case, the initial conditions are: $x(0) = R_{\mathrm{fiber}} = 100$ μm, $\phi(0) = \phi_{\mathrm{init}}$, $x(s_{\mathrm{c}}) = R_{\mathrm{bound}}$, $\phi(s_{\mathrm{c}}) = \pi/2$, where $-\pi < \phi_{\mathrm{init}} < -\pi/2$. The variation in the angle is due to the fact that helium is attached to the *edge* of the top fiber, as shown in figure 9.1 (b). The contact angle of the helium with surfaces is $\theta_{\mathrm{c,He}} = 0$, however helium can be in contact with any part of the fiber, as shown in the inset of figure 9.2. One of the possible solutions for the second case is shown in figure 9.2 with a red line. The volume of helium is calculated in this case as well (using the method of cylinders and adding the helium located under the fiber).

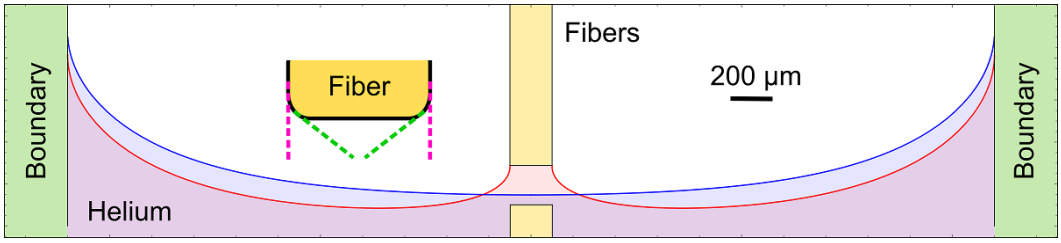

Figure 9.2: The solutions for the cases 1 (blue line) and 2(red line). The black line is the scale bar. Inset: The helium is in contact with the top fiber. Both green and purple line represent the situation in which the contact angle is zero.

It is clear from figure 9.2 that the volume of helium required to have an interface between the fibers (blue line) is larger than the volume of helium when helium is attached to the top fiber (red line). That means that as the cavity is being filled with helium, any vibration can cause helium to attach to the top fiber.

We calculate the volumes for different ϕ_{init}, and find that the minimum cavity length for which there exists a solution corresponding to helium interface between the fibers, which requires less helium than the solution corresponding to helium attached to the top fiber is $L_{\mathrm{cav}} \approx 260$ μm. (Note that this corresponds to helium interface exactly at the level of the bottom fiber. In order for the helium interface be x μm above the bottom fiber, the cavity length needs to be $L_{\mathrm{cav}} = (260 + x)$ μm).

We can also calculate the minimum cavity length for different R_{bound}, which we can in principle alter by changing the device geometry. Figure 9.3 shows the two limits on the minimum cavity length. The green line is calculated, as described above, by comparing the volumes corresponding to the solutions with helium interface between the fibers and helium attached to the top fiber. The purple line is calculated as $L_{\mathrm{cav,min}} = h^*_{\mathrm{fiber}} - h^*_{\mathrm{empty}}$, as described in section 9.1.1. The minimum cavity length is found as a maximum of these two lines for a given R_{bound}. The shortest cavity can be built for $R_{\mathrm{bound}} \approx 0.6$ mm and has the length 200 μm.

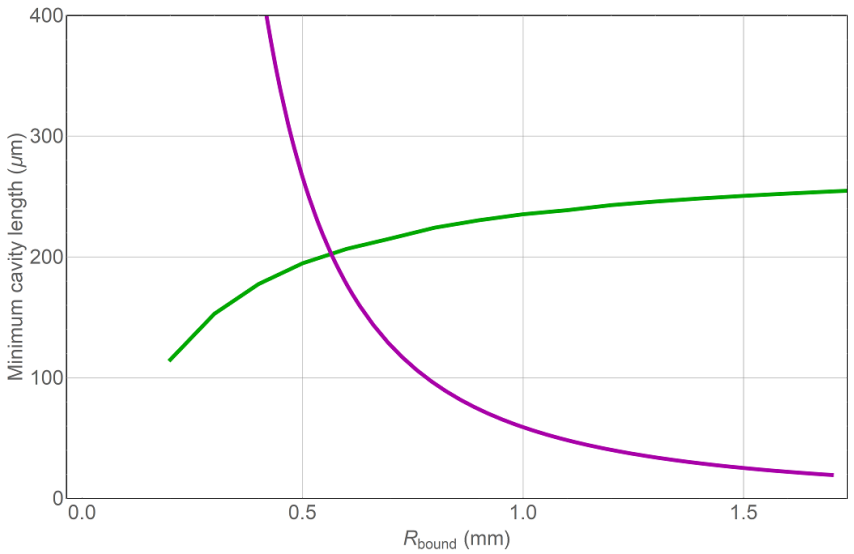

Figure 9.3: Minimal cavity length, calculated for different values of R_{bound}. Green line: the minimum cavity length for which the configuration shown in figure 9.1 (a) requires less helium volume than the configuration shown in figure 9.1. Purple line: $L_{\mathrm{cav,min}} = h^*_{\mathrm{fiber}} - h^*_{\mathrm{empty}}$.

9.1.1.2 Partially filled cavity with one fiber inside the ferrule

Alternatively, we can retract the bottom fiber into the ferrule, as shown in figure 9.4 (a). The helium level can be adjusted to be at the top of bottom the ferrule by setting the helium bulk level $h_{\mathrm{bulk}} = h^*_{\mathrm{empty}}$. As more helium is added, $h_{\mathrm{bulk}} < h^*_{\mathrm{empty}}$ and the surface of helium will become more flat (the helium can be in contact with any part of the inner edge of the ferrule).

Therefore there will be a helium surface bounded by the ferrule inner radius with adjustable curvature. However, it is still possible for helium to attach to the top fiber, as shown in figure 9.4 (right), therefore we need the separation between the top fiber and the ferrule to be large enough for such solutions to not exist. To find that separation, we solve equations above, subject to the following boundary conditions: $x(0) = R_{\mathrm{fiber}}$, $z(0) = h_{\mathrm{bulk}}$, $\phi(0) = \phi_{\mathrm{init}}$ and either $x(s_{\mathrm{f}}) = R_{\mathrm{fer,out}} = 900$ μm (corresponding to helium attaching to the edge of the ferrule, as shown in figure 9.5 (a)), or $\phi(s_{\mathrm{f}}) = 0$ (corresponding to zero contact angle on the ferrule face, as shown in figure 9.5(b)). Here h_{bulk} is the height above bulk helium level, which can be at most 5 mm (the capillary rise inside the ferrule).

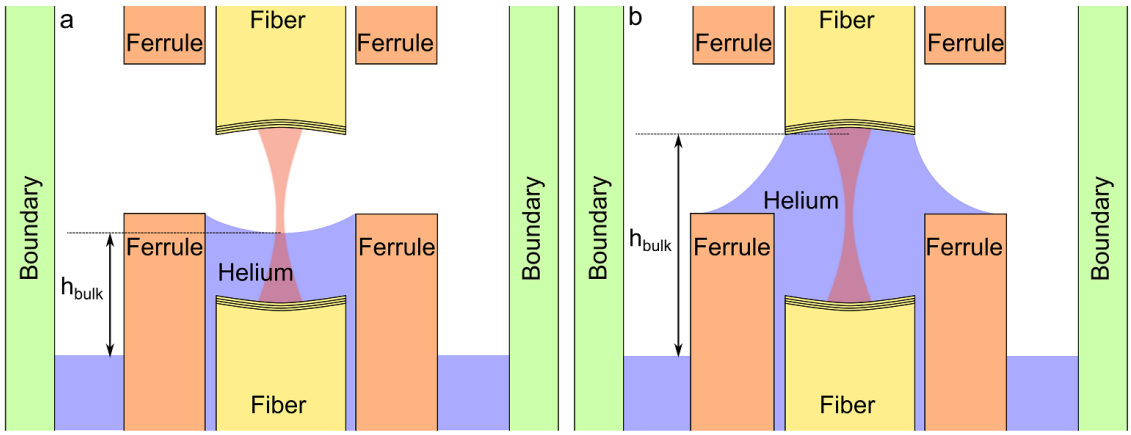

Figure 9.4: The cavity formed between two ferrules with one fiber retracted. Not to scale. Left: Helium level between the fibers. Right: A bridge is formed connecting two the top fiber and a ferrule.

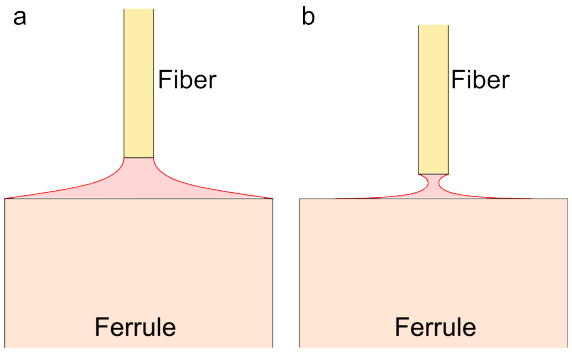

Figure 9.5: Two possible solutions for the bridge connecting the top fiber and the ferrule. (a) $x(s_\mathrm{f}) = R_\mathrm{fer,out}$, corresponding to helium attaching to the edge of the ferrule. (b) $\phi(s_\mathrm{f}) = 0$, corresponding to zero contact angle on the ferrule face.

The maximum distance from the ferrule to the top fiber for which there is a solution is plotted vs. the distance from bulk level of helium to the top of the ferrule in figure 9.6. There are never solutions if the fiber is separated by more than 260 μm from the ferrule. However, as the distance to the bulk helium level increases the fiber can be brought closer. That means that it could be possible to build short partially filled cavities.

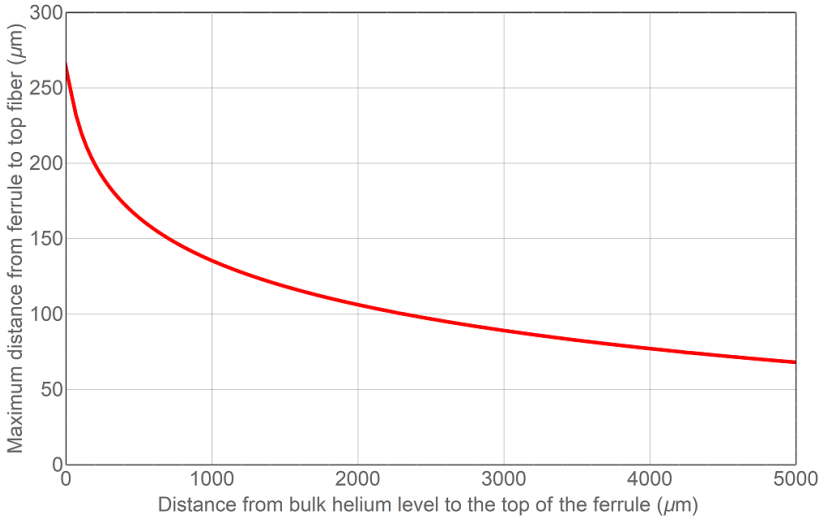

Figure 9.6: Minimum cavity length for which no solutions shown in figure 9.4(b) exist.

If the ferrules with smaller $R_\mathrm{fer,out}$ are used, the minimum cavity length can be as small as 200 μm for $R_\mathrm{fer,out} = 600$ μm.

9.1.2 Optomechanical coupling to ripplon modes

In this section I will calculate the optomechanical coupling to ripplon modes. I will first derive the shape of the modes and the mode frequencies. Then I will calculate the zero point motion of the modes and finally, I will calculate the single photon optomechanical coupling g_0.

9.1.2.1 Deriving the dispersion relation

I will start by deriving the dispersion relation to calculate the frequency of the modes. This derivation is based on [159], but with different boundary conditions. Assume we have a container of radius R filled with superfluid helium up to level d. We are working in cylindrical coordinates with the origin at the surface of the liquid on the axis of the cylinder. Take $\vec{u}$ to be the fluid velocity. We assume liquid helium to be non-viscous, irrotational ($\vec{\nabla} \times \vec{u} = \vec{0}$), incompressible -since we are interested in the surface modes, ($\nabla \cdot \vec{u} = 0$) and described by the Euler equation:

$$\rho_{\mathrm{He}} \left(\frac{\partial \vec{u}}{\partial t} + (\vec{u} \cdot \nabla)\vec{u} \right) = -\nabla p + \rho_{\mathrm{He}} \vec{g} \tag{9.4}$$

Here $\vec{g} = -9.8$ m/s$^2 \hat{z}$ and p is the pressure in the fluid. Using the following vector identity:

$$\nabla(\vec{A} \cdot \vec{B}) = \vec{A} \times (\nabla \times \vec{B}) + \vec{B} \times (\nabla \times \vec{A}) + (\vec{A} \cdot \nabla)\vec{B} + (\vec{B} \cdot \nabla)\vec{A} \tag{9.5}$$

which in our case is:

$$\nabla(\vec{u} \cdot \vec{u}) = 2\vec{u} \times (\nabla \times \vec{u}) + 2(\vec{u} \cdot \nabla)\vec{u} \tag{9.6}$$

we can express:

$$(\vec{u} \cdot \nabla)\vec{u} = \frac{1}{2}\nabla u^2 - \vec{u} \times (\nabla \times \vec{u}) = \frac{1}{2}\nabla u^2 \tag{9.7}$$

So the Euler equation for the irrotational fluid is:

$$\rho_{\mathrm{He}} \left(\frac{\partial \vec{u}}{\partial t} + \frac{1}{2}\nabla u^2 \right) = -\nabla p + \rho_{\mathrm{He}} \vec{g} \tag{9.8}$$

Now we can introduce the velocity potential, such that $\vec{u} = \nabla\phi$. With some rearranging equation 9.8 becomes:

$$\nabla \left(\frac{\partial \phi}{\partial t} + \frac{1}{2}u^2 + \frac{p}{\rho_{\mathrm{He}}} \right) = \vec{g} \tag{9.9}$$

The acceleration due to gravity can be expressed as a gradient of the scalar:

$$\vec{g} = \nabla(g_x x + g_y y + g_z z) \tag{9.10}$$

Only g_z is non-zero, so we can rewrite equation as:

$$\frac{\partial \phi}{\partial t} + \frac{1}{2}u^2 + \frac{p}{\rho_{\mathrm{He}}} + gz = \mathrm{const} \tag{9.11}$$

Now let's assume that the liquid surface profile is given by $z = \zeta(r, \theta, t)$. The pressure right under the surface is proportional to the curvature of the surface: $P = -\sigma_{\mathrm{He}} \frac{\partial^2 \zeta(r,\theta,t)}{\partial \vec{r}^2}$. Plugging this back in, we find that this equation is satisfied for flat liquid when the constant on the RHS of the equation 9.11 is zero, so we can set this constant to zero. Additionally we drop the higher order terms, giving:

$$\rho_{\mathrm{He}} \frac{\partial \phi}{\partial t} - \sigma_{\mathrm{He}} \frac{\partial^2 \zeta(r,\theta,t)}{\partial \vec{r}^2} + \rho_{\mathrm{He}} g \zeta(r,\theta,t) = 0 \tag{9.12}$$

For the free surface of the liquid we have:

$$u_z = \frac{\partial \zeta(r,\theta,t)}{\partial t} = \left. \frac{\partial \phi(r,\theta,z,t)}{\partial z} \right|_{z=0} \tag{9.13}$$

Taking a time derivative of equation 9.12 and using equation 9.13 we get:

$$\rho_{\mathrm{He}} \frac{\partial^2 \phi}{\partial t^2} - \sigma_{\mathrm{He}} \frac{\partial}{\partial z} \frac{\partial^2 \phi}{\partial \vec{r}^2} + \rho_{\mathrm{He}} g \left. \frac{\partial \phi}{\partial z} \right|_{z=0} = 0 \tag{9.14}$$

Since $\vec{r}$ is the vector defining the position in r and θ, I will rewrite equation 9.14 using the Laplacian in cylindrical coordinates without the z-term:

$$\rho_{\mathrm{He}}\frac{\partial^2\phi}{\partial t^2} - \sigma_{\mathrm{He}}\frac{\partial}{\partial z}\left[\frac{1}{r}\frac{\partial}{\partial r}\left(r\frac{\partial\phi}{\partial s}\right) + \frac{1}{r^2}\frac{\partial^2\phi}{\partial\theta^2}\right] + \rho_{\mathrm{He}}g\frac{\partial\phi}{\partial z}\bigg|_{z=0} = 0 \tag{9.15}$$

This equation is one of our boundary conditions.

The fluid everywhere in the vessel must satisfy the Laplace equation:

$$\nabla^2\phi = 0 \tag{9.16}$$

or:

$$\frac{1}{r}\frac{\partial}{\partial r}\left(r\frac{\partial\phi}{\partial s}\right) + \frac{1}{r^2}\frac{\partial^2\phi}{\partial\theta^2} + \frac{\partial^2\phi}{\partial z^2} = 0 \tag{9.17}$$

along with the boundary conditions that the normal velocity component is zero at all the boundaries:

$$\frac{\partial\phi}{\partial z}(r,\theta,-d) = 0 \tag{9.18}$$

$$\frac{\partial\phi}{\partial r}(R,\theta,z) = 0 \tag{9.19}$$

The solution to the Laplace equation in cylindrical coordinates is found by separation of variables to be:

$$\phi_m(r,\theta,z,t) = [A_m J_m(kr) + B_m N_m(kr)][C_m\sin(m\theta) + D_m\cos(m\theta)][E_m\sinh(kz) + F_m\cosh(kz)]\psi_m(t) \tag{9.20}$$

In order to keep the solution from diverging at $r = 0$, B_m must be zero. In order to satisfy the boundary condition at the bottom of the cylinder ($z = -d$) :

$$[E_m\sinh(kz) + F_m\cosh(kz)] = G_m\cosh(k(d+z)) \tag{9.21}$$

In order to satisfy the boundary conditions at the sides of the cylinder ($r = R$) we want:

$$\frac{dJ_m(kr)}{dr}\bigg|_{r=R} = 0 \tag{9.22}$$

This equation is satisfied when $kR = \beta_n^{(m)}$, where $\beta_n^{(m)}$ is the n-th positive root of the derivative of the m-th Bessel function. Taking all of those things into account, we can rewrite:

$$\phi_m(r,\theta,z,t) = J_m(\beta_n^{(m)}r/R)[A_m\sin(m\theta) + B_m\cos(m\theta)]\cosh(\beta_n^{(m)}(d+z)/R)\psi_m(t) \tag{9.23}$$

where A_m and B_m are redefined. Plugging this equation into equation 9.15, we get:

$$J_m(kr)[A_m\sin(m\theta) + B_m\cos(m\theta)](\rho_{\mathrm{He}}gk + \sigma_{\mathrm{He}}k^3)\psi_m(t)\sinh(kd) + \rho_{\mathrm{He}}\cosh(kd)\psi_m''(t)) = 0 \tag{9.24}$$

Rearranging:

$$\psi_m''(t) + \left(gk + \frac{\sigma_{\mathrm{He}}}{\rho_{\mathrm{He}}}k^3\right)\tanh(kd)\psi_m(t) = 0 \tag{9.25}$$

Or we can write it as equation for the simple harmonic oscillator:

$$\psi_m''(t) + \omega_{\mathrm{m}}^2\psi_m(t) = 0 \tag{9.26}$$

where:

$$\omega_{\mathrm{m}}^2 = \left(gk + \frac{\sigma_{\mathrm{He}}}{\rho_{\mathrm{He}}}k^3\right)\tanh(kd) \tag{9.27}$$

Rewriting k in terms of zeros of the Bessel function:

$$\omega_{\mathrm{m}}^2 = \left(\frac{\beta_n^{(m)}g}{R} + \frac{\sigma_{\mathrm{He}}}{\rho_{\mathrm{He}}}\left(\frac{\beta_n^{(m)}}{R}\right)^3\right)\tanh\left(\frac{\beta_n^{(m)}d}{R}\right) \tag{9.28}$$

Thus we have derived the dispersion relation.

9.1.2.2 Mode frequencies

We are interested in modes with $m = 0$, because for $m > 0$ the average increase of the helium height near cavity axis is zero (technically coupling to $m = 1$ modes is possible, if the optical mode is offset from the cavity axis, however, we will not consider this situation here). From equation 9.13 we see that the mode shape $\zeta(r, \theta, t)$ is the same as the velocity potential $\phi(r, \theta, z, t)$ evaluated at $z = 0$ up to some multiplicative constant.

$$\zeta_0(r, \theta, z) \propto J_0(\beta_n^{(0)} r/R) \tag{9.29}$$

Here $\beta_n^{(0)}$ is the n-th positive root of J_0'. Conveniently, the zeros of the derivative of the zeroth order Bessel function are the same as the zeros of the first order Bessel function, which we will now write as $\alpha_n^{(1)}$, so :

$$\omega_{\mathrm{m}} = \sqrt{\left(\frac{\alpha_n^{(1)} g}{R} + \frac{\sigma_{\mathrm{He}}}{\rho_{\mathrm{He}}}\left(\frac{\alpha_n^{(1)}}{R}\right)^3\right) \tanh\left(\frac{\alpha_n^{(1)} d}{R}\right)} \tag{9.30}$$

A few things to consider:

- The surface waves can be capillary (the dynamics is determined by the effects of surface tension) or gravitational (the dynamics is determined by the force of gravity) We can find the radius for which the waves are gravitational and capillary by considering this quantity:

$$\frac{\sigma_{\mathrm{He}}}{\rho_{\mathrm{He}} g}\left(\frac{\alpha_n^{(1)}}{R}\right)^2 \tag{9.31}$$

  Figure 9.7 shows this quantity as a function of the container radius R for different values of n. The blue region is the region where waves are predominantly capillary, the red region where waves are predominantly gravitational. We see that the waves in the ferrule ($R \simeq 100$ μm) are always capillary.

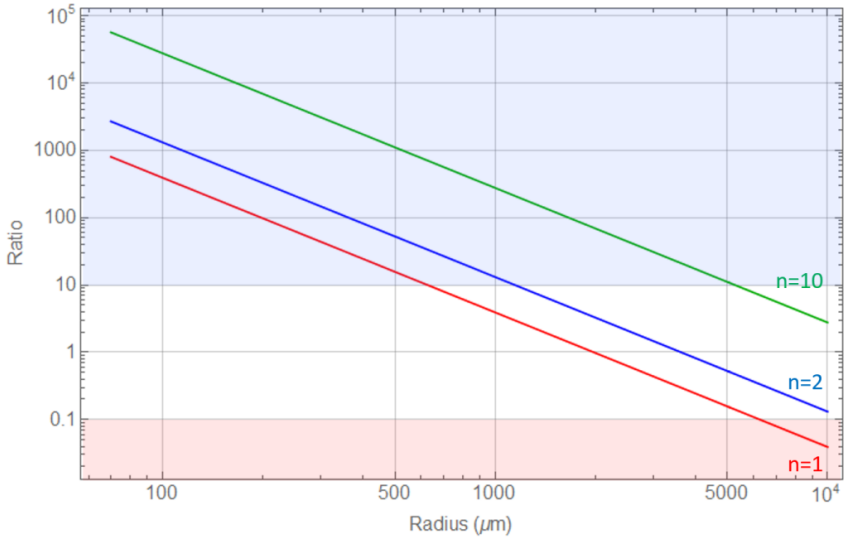

Figure 9.7: The quantity $\frac{\sigma_{\mathrm{He}}}{\rho_{\mathrm{He}} g}\left(\frac{\alpha_n^{(1)}}{R}\right)^2$ plotted vs. radius of the mode for modes with $n = 1$ (red), $n = 2$ (blue) and $n = 10$ green.

- To understand whether the depth has an effect on the mode frequency, we consider the quantity $\tanh\left(\frac{\alpha_n^{(1)} d}{R}\right)$. This is the only quantity in the expression for the mode frequency which depends on d. As long as this quantity is close to 1, the frequency is independent of helium depth. For the lowest order mode $\tanh\left(\frac{\alpha_1^{(1)} d}{R}\right) > 0.96$ for $d > 0.5R$, therefore the depth does not play a role as long as the container is filled to a depth equal to half of its radius.

9.1.2.3 Zero-point motion

In this section I will calculate the amplitude of the zero-point fluctuations of the ripplon mode. The ripplon mode is written as:

$$\zeta(r) = AJ_0(kr) \tag{9.32}$$

Where A is the amplitude. Its derivative is:

$$\zeta'(r) = -AkJ_1(kr) \tag{9.33}$$

To find the surface area, we use the standard formula:

$$A_{\rm s} = \int_0^a 2\pi r \sqrt{1 + \left(\frac{d\zeta}{dr}\right)^2} dr \tag{9.34}$$

$$A_{\rm s} = \int_0^a 2\pi r \sqrt{1 + A^2k^2J_1(kr)^2} dr \tag{9.35}$$

Since $Ak \ll 1$, we can Taylor expand:

$$\sqrt{1 + A^2k^2J_1(kr)^2} \simeq 1 + \frac{A^2k^2}{2}J_1(kr)^2 \tag{9.36}$$

We are only interested in the change of the surface area, so:

$$\Delta A_{\rm s} = A^2 \int_0^a \pi r k^2 J_1(kr)^2 dr \tag{9.37}$$

We know the surface tension per unit area, so the energy stored in this oscillation will be:

$$\Delta E = \sigma_{\rm He} A^2 \int_0^a \pi r k^2 J_1(kr)^2 dr \tag{9.38}$$

We can now set it equal to $\hbar\omega_{\rm m}/4$ and solve for A, which is the amplitude of motion:

$$\sigma_{\rm He} A^2 \int_0^a \pi r k^2 J_1(kr)^2 dr = \frac{\hbar\omega_{\rm m}}{4} \tag{9.39}$$

$$A = \sqrt{\frac{\hbar\omega_{\rm m}}{4\sigma_{\rm He}\int_0^a \pi r k^2 J_1(kr)^2 dr}} = \sqrt{\frac{\hbar\omega_{\rm m}}{4\sigma_{\rm He}\int_0^a \pi r (\alpha_n^{(1)}/a)^2 J_1(\alpha_n^{(1)} r/a)^2 dr}} \tag{9.40}$$

Below is the plot of the amplitude of zero point fluctuations vs. the frequency of the mode for 2 different geometries of half-filled cavities:

If we assume the waves are capillary, we can simplify the expression for A by rewriting $J_1(x) = \sin(x)/\sqrt{x}$. We get:

$$A = \sqrt{\frac{\hbar\omega_{\rm m}}{4\sigma_{\rm He}\int_0^R \pi k \sin(kr)^2 dr}} = \sqrt{\frac{\hbar\omega_{\rm m}}{\pi\sigma_{\rm He}(2Rk - \sin(2Rk))}} \simeq \sqrt{\frac{\hbar\omega_{\rm m}}{2\pi\sigma_{\rm He}Rk}} \propto \sqrt{\frac{\omega_{\rm m}}{k}} \propto \sqrt{\frac{\omega_{\rm m}}{\omega_{\rm m}^{2/3}}} \propto \omega_{\rm m}^{1/6} \tag{9.41}$$

Therefore the amplitude of the zero point fluctuations is proportional to $\omega_{\rm m}^{1/6}$.

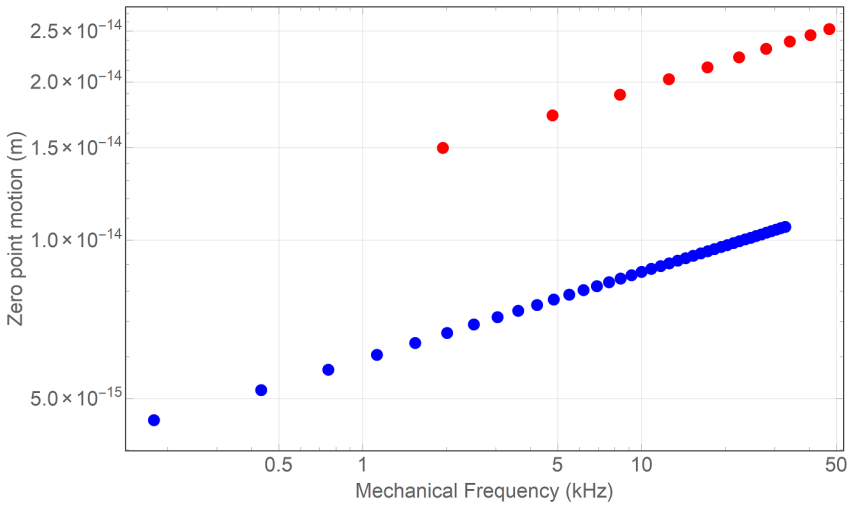

Figure 9.8: The zero point fluctuation amplitude vs. mechanical frequency for a cavity of length $l = 300$ μm formed in a 200 μm diameter ferrule (red), and a cavity of length $l = 2$ mm formed in 1 mm diameter tube(blue).

9.1.2.4 Optomechnanical coupling

The optomechanical coupling was derived in section 4.2 as:

$$g_0 = \omega_{\rm cav} \frac{\int_V I(r,z) dn(r) d^3\vec{r}}{\int_V I(r,z) d^3\vec{r}} \tag{9.42}$$

The index of refraction changes abruptly at the surface of helium ($z = 0$) by $n_{\rm He} - 1$. So we can rewrite the coupling as:

$$g_0 = \omega_{\rm cav}(n_{\rm He} - 1) \frac{\int_V I(r,z)\zeta(r,\theta)\delta(z) d^3\vec{r}}{\int_V I(r,z) d^3\vec{r}} \tag{9.43}$$

Assume the optical intensity is maximum at $z = 0$, we can write the expression for the optical intensity as:

$$I = \cos^2(2\pi z/\lambda_{\rm opt}) e^{\frac{-2r^2}{w^2}} \tag{9.44}$$

We can rewrite the expression for g_0 as:

$$g_0 = \omega_{\rm cav}(n_{\rm He} - 1) \frac{\int_0^{2\pi}\int_0^R e^{\frac{-2r^2}{w^2}} A J_0(kr) r dr d\theta}{\int_{-d}^{d}\int_0^{2\pi}\int_0^a \cos^2(2\pi z/\lambda_{\rm opt}) e^{\frac{-2r^2}{w^2}} r dr d\theta dz} \tag{9.45}$$

and evaluate the integrals over the angle θ to get:

$$g_0 = \omega_{\rm cav}(n_{\rm He} - 1) \frac{\int_0^R e^{\frac{-2r^2}{w^2}} A J_0(kr) r dr}{\int_{-d}^{d}\int_0^a \cos^2(2\pi z/\lambda_{\rm opt}) e^{\frac{-2r^2}{w^2}} r dr dz} \tag{9.46}$$

In the limit of $w \ll R$ the integral in the denominator evaluates to :

$$\int_{-d}^{d}\int_0^R \cos^2(2\pi z/\lambda_{\rm opt}) e^{\frac{-2r^2}{w^2}} r dr dz \simeq \frac{dw^2}{4} \tag{9.47}$$

The single photon coupling is:

$$g_0 = 4\omega_{\rm cav}(n_{\rm He} - 1) A \frac{\int_0^a e^{\frac{-2r^2}{w^2}} J_0(\alpha_n^{(1)} r/R) r dr}{dw^2} \tag{9.48}$$

Figure 9.9 is a plot of the single photon coupling vs. the frequency of the mode for 2 different geometries of half-filled cavities: a cavity of length $l = 300$ μm formed in a 200 μm diameter ferrule (red), and a cavity of length $l = 2$ mm formed in 1 mm diameter tube (blue). The highest optomechanical coupling that can be achieved in a fiber cavity is 500 Hz.

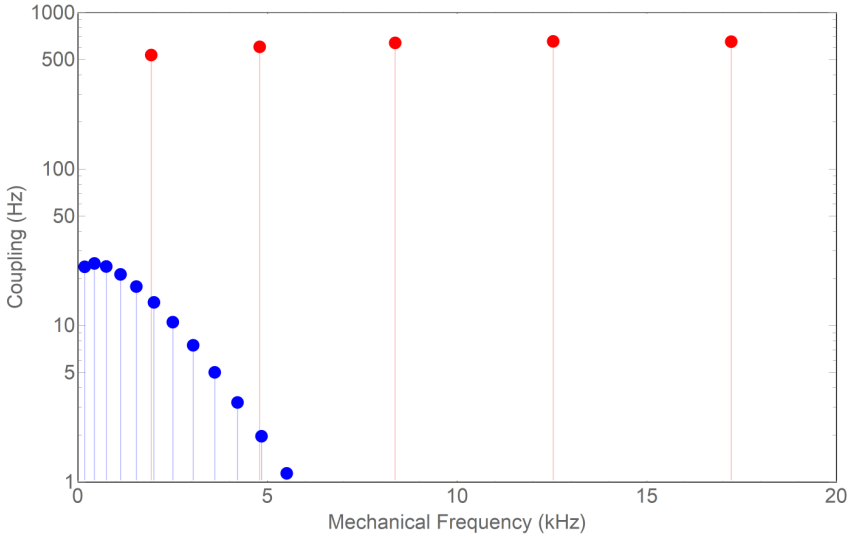

Figure 9.9: The single photon coupling vs. mechanical frequency for a cavity of length $l = 300$ μm formed in a 200 μm diameter ferrule (red), and a cavity of length $l = 2$ mm formed in 1 mm diameter tube (blue).

The optomechanical coupling is smaller when the helium/vacuum interface does not overlap with the region of high optical intensity. However, it is possible to achieve that overlap by changing the helium level, or by addressing a different optical mode.

9.1.3 Summary

The purpose of this chapter was to develop some ideas that we have for future devices. There are three main directions in which we are heading right now: non-Gaussian optomechanics (using single photon detectors), optomechanics with macroscopic cavities, and optomechanics with ripplons. I focused mostly on the optomechanics with ripplons, as that was something I have been working towards. I described how can we achieve a partially filled cavity. Then I discussed the optomechanical coupling to ripplons and showed that it can be as large as 500 Hz. We still do not know what are the mechanical quality factors of the ripplon modes and they will hopefully be found experimentally.

9.2 Conclusion

The next year will mark 150 years since the discovery of helium and 80 years since the discovery of superfluidity. The fascinating properties of superfluid helium were studied extensively in the middle of 20th century, however, despite its unique properties, superfluid helium was not considered for applications in non-linear or quantum optics until the 21st century. In my opinion, there are a few reasons for that:

- Low polarizability of superfluid helium implies very weak interactions with light, so large optical powers are necessary to observe significant effects. On the other hand, superfluid helium also has very low optical absorption, so it could be interfaced with large optical powers. In order to achieve large optical powers a cavity could be employed. Recent advances in dielectric coating technology allowed us to build very high finesse optical cavities, which was impossible before.

- Commercial availability of dilution refrigerators made it possible to achieve temperatures at which superfluid helium has low acoustic loss.
- The development of the field of optomechanics gave us the framework to describe the interaction between the light and the superfluid helium.

Our motivation for using superfluid helium in an optomechanical system was to achieve high optomechanical and thermal cooperativites (C and $C_{\rm th}$), which, as was shown in chapter 2, are probably the most important figures of merit in Gaussian optomechanics.

I described the experiments that we performed with the superfluid helium filled Fabry-Perot cavity. With the first device we achieved $C = 4.1 \times 10^{-2}$ and $C_{\rm th} = 2.5 \times 10^{-3}$. The modifications that we made for the second device (improving thermal link between the mode and the mixing chamber, improving optical finesse, and slightly improving acoustic finesse of the mirrors) allowed us to achieve higher values of cooperativity $C = 1.14$ and $C_{\rm th} = 9.2 \times 10^{-2}$. These values, while relatively small ($C = 146,000$ was achieved in [160]) are still larger than the cooperativites demonstrated in other superfluid helium optomechanical devices [32, 34]. We also have a fairly straightforward way to improve C and $C_{\rm th}$ by another factor of 20-80 by using macroscopic cavities. However, it still seems that optical heating (due to heating of the mirrors) would put a limit on the cooperativity that we can achieve. The large effect that optical heating has on the acoustic mode was unexpected, especially in the second generation device – we did not anticipate that the heat flux from the absorbers on the mirrors would be high enough to make helium turbulent and thus decrease its thermal conductivity.

Despite this challenge, we were able to observe multiple optomechanical effects in our system. We observed optomechanically induced transparency and amplification and the thermal motion of the acoustic mode. The relatively large value of the cooperativity enabled us to observe dynamical back-action. We were the first to observe dynamical back-action arising from a unitary interaction in a superfluid. We also were the first to observe quantum optomechanical effects in a fluid. Additionally, we gained a deep understanding of both devices: the measured optomechanical coupling agreed with theoretical predictions; we understood the frequencies of all modes that we observed in both first and second generation devices; and we developed models which accurately describe the temperature of helium in the devices and the resulting linewidth and frequency of the paraxial acoustic modes.

The optomechanical effects observed in our system are not novel in themselves [69, 22, 21]. However, the observations of these effects (especially the asymmetry between the Stokes and anti-Stokes sidebands) were possible due to our carefully designed and well-calibrated measurement setup. I hope that the descriptions of the measurement setup and the calibrations would be useful to the readers, as the measurement setup can be easily applied to any system.

The work described in this thesis paved the way to more studies of optomechanics with superfluid helium in the Harris lab. The second generation device that we built is going to be used in the experiments on non-Gaussian optomechanics with SPDs. Another device is currently being built whose design is described in this thesis (the "fifth generation device", section 6.3.5), and which will be used to study optomechanics with ripplons. The macroscopic mirrors with the acoustic DBR coatings are being used to build a macroscopic helium-filled cavity. Lastly, a new experiment in which a whispering gallery mode of light couples to the motion of superfluid helium in a magnetically levitated superfluid helium droplet is underway in our lab as well. In this system, it should be possible to take advantage of the unique properties of superfluid helium without the detrimental effects of optical heating or contact with solid objects.

In conclusion, I hope that I have succeeded in presenting the history of optomechanics and superfluid helium, as well as the state of the art of superfluid optomechanics. The interest in superfluid helium optomechanics is growing with multiple exciting experiments and theoretical proposals every year [33, 31, 34, 35, 36, 32, 37, 38, 39, 40, 41, 42, 43, 44]. There are definitely more discoveries underway in this field and I hope that my work is useful to people working in this field.

Appendices

Appendix A

Fabry-Perot cavity in 1D

A.1 Derivation of the reflected, transmitted and intracavity fields of a 1D Fabry-Perot cavity

In this section I will derive the reflected, transmitted and intracavity fields of 1D Fabry-Perot cavity. Assume the cavity is composed of the following: two infinite dielectric slabs with refractive indexes n_1 and n_2 , separated by distance L, with vacuum ($n = 1$) between them. This is conceptually similar to our setup of a fiber cavity, bounded by the highly reflective dielectric coating, as changing the refractive indexes, changes the reflectivity of the dielectric/vacuum interface, so the power reflection and transmission coefficients are given by:

$$R_{\text{opt}} = \left|\frac{n_i - n_t}{n_i + n_t}\right|^2 \qquad T_{\text{opt}} = 1 - R_{\text{opt}} = \frac{4n_i n_t}{(n_i + n_t)^2} \tag{A.1}$$

In our system, the mirror reflectivities are $R_{\text{opt},1} = 0.9999$ and $R_{\text{opt},2} = 0.99999$. Since the refractive index of vacuum is 1, the effective refractive indexes of dielectrics are $n_1 \approx 40,000$ and $n_2 \approx 400,000$. Throughout the derivation we will work in the limit $R_{\text{opt},1} \approx R_{\text{opt},2} \approx 1$.

A plane wave with amplitude $E^{(\text{i})}$ approaches the vaccum gap from one of the slabs at normal incidence, as shown in figure A.1.

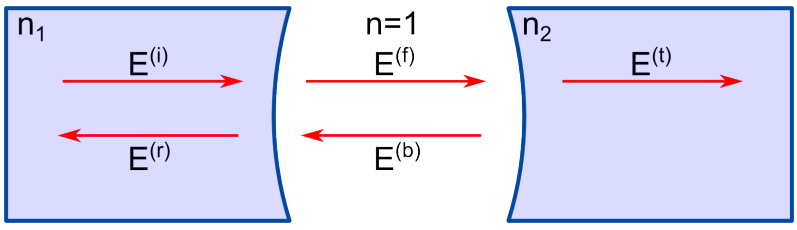

Figure A.1: Field amplitudes inside the slabs and in the vacuum gap between them.

The parallel components of electric and magnetic fields must be continuous at each interface, which results in the following boundary conditions for amplitudes:

$$E_j(x,t) = E_{j+1}(x,t) \tag{A.2}$$

$$\frac{dE_j(x,t)}{dx} = \frac{dE_{j+1}(x,t)}{dx} \tag{A.3}$$

Where E_j is the amplitude of the electric field on the right on the interface between two layers and E_{j+1} is the amplitude of the electric field on the left on the interface between two layers. At the front interface:

$$E^{(\mathrm{i})} + E^{(\mathrm{r})} = E^{(\mathrm{f})} + E^{(\mathrm{b})} \tag{A.4}$$

$$n_1\left(E^{(\mathrm{i})} - E^{(\mathrm{r})}\right) = E^{(\mathrm{f})} - E^{(\mathrm{b})} \tag{A.5}$$

Here $E^{(\mathrm{r})}$ is the amplitude reflected field, $E^{(\mathrm{f})}$ and $E^{(\mathrm{b})}$ are the amplitudes of the forward and backward propagating fields in the vacuum gap. At the back interface:

$$E^{(\mathrm{f})}e^{ikL} + E^{(\mathrm{b})}e^{-ikL} = E^{(\mathrm{t})} \tag{A.6}$$

$$E^{(\mathrm{f})}e^{ikL} - E^{(\mathrm{b})}e^{-ikL} = n_2 E^{(\mathrm{t})} \tag{A.7}$$

Here $E^{(\mathrm{t})}$ is the amplitude of the transmitted field, and $k = 2\pi/\lambda$ is the wavenumber. This is a system of 4 linear equations with 4 unknowns. The solution is:

$$E^{(\mathrm{f})} = \frac{2E^{(\mathrm{i})}\frac{n_1}{n_1+1}}{1 - e^{2ikL}\frac{n_1-1}{n_1+1}\frac{n_2-1}{n_2+1}} \tag{A.8}$$

$$E^{(\mathrm{b})} = \frac{-2E^{(\mathrm{i})}\frac{n_1}{n_1+1}\frac{n_2-1}{n_2+1}e^{2ikL}}{1 - e^{2ikL}\frac{n_1-1}{n_1+1}\frac{n_2-1}{n_2+1}} \tag{A.9}$$

$$E^{(\mathrm{r})} = \frac{E^{(\mathrm{i})}\left(\frac{n_1-1}{n_1+1} - e^{2ikL}\frac{n_2-1}{n_2+1}\right)}{1 - e^{2ikL}\frac{n_1-1}{n_1+1}\frac{n_2-1}{n_2+1}} \tag{A.10}$$

$$E^{(\mathrm{t})} = \frac{E^{(\mathrm{i})}\frac{4n_1}{(n_1+1)(n_2+1)}}{1 - e^{2ikL}\frac{n_1-1}{n_1+1}\frac{n_2-1}{n_2+1}} \tag{A.11}$$

Using equations A.1, to express the refractive indexes in terms of reflectivities we arrive at the following expressions for the field amplitudes:

$$E^{(\mathrm{f})} = \frac{E^{(\mathrm{i})}(1 + \sqrt{R_{\mathrm{opt},1}})}{1 - e^{2ikL}\sqrt{R_{\mathrm{opt},1}R_{\mathrm{opt},2}}} \tag{A.12}$$

$$E^{(\mathrm{b})} = -\frac{E^{(\mathrm{i})}(1 + \sqrt{R_{\mathrm{opt},1}})\sqrt{R_{\mathrm{opt},2}}e^{2ikL}}{1 - e^{2ikL}\sqrt{R_{\mathrm{opt},1}R_{\mathrm{opt},2}}} \tag{A.13}$$

$$E^{(\mathrm{r})} = \frac{E^{(\mathrm{i})}\sqrt{R_{\mathrm{opt},1}} - E^{(\mathrm{i})}\sqrt{R_{\mathrm{opt},2}}e^{2ikL}}{1 - e^{2ikL}\sqrt{R_{\mathrm{opt},1}R_{\mathrm{opt},2}}} \tag{A.14}$$

$$E^{(\mathrm{t})} = \frac{E^{(\mathrm{i})}(1 + \sqrt{R_{\mathrm{opt},1}})(1 - \sqrt{R_{\mathrm{opt},2}})e^{ikL}}{1 - e^{2ikL}\sqrt{R_{\mathrm{opt},1}R_{\mathrm{opt},2}}} \tag{A.15}$$

We can make a few simplifications by realizing that $1 - T_{\mathrm{opt}} = R_{\mathrm{opt}}$. Taking square root of both sides and Taylor expanding we get:

$$\sqrt{R_{\mathrm{opt}}} \approx 1 - \frac{T_{\mathrm{opt}}}{2} \tag{A.16}$$

And similarly:

$$\sqrt{R_{\mathrm{opt},1}R_{\mathrm{opt},2}} \approx 1 - \frac{T_{\mathrm{opt},1}}{2} - \frac{T_{\mathrm{opt},2}}{2} \tag{A.17}$$

With this assumption after canceling higher order terms equations A.12, A.13, A.14 and A.15 become:

$$E^{(\mathrm{f})} = 2\frac{E^{(\mathrm{i})}\left(2-\frac{T_{\mathrm{opt},1}}{2}\right)}{2-e^{2ikL}(2-T_{\mathrm{opt},1}-T_{\mathrm{opt},2})} \tag{A.18}$$

$$E^{(\mathrm{b})} = -2\frac{E^{(\mathrm{i})}(2-\frac{T_{\mathrm{opt},1}}{2}-T_{\mathrm{opt},2})e^{2ikL}}{2-e^{2ikL}(2-T_{\mathrm{opt},1}-T_{\mathrm{opt},2})} \tag{A.19}$$

$$E^{(\mathrm{r})} = 2\frac{E^{(\mathrm{i})}\left(1-\frac{T_{\mathrm{opt},1}}{2}\right)-E^{(\mathrm{i})}\left(1-\frac{T_{\mathrm{opt},2}}{2}\right)e^{2ikL}}{2-e^{2ikL}(2-T_{\mathrm{opt},1}-T_{\mathrm{opt},2})} \tag{A.20}$$

$$E^{(\mathrm{t})} = 2\frac{E^{(\mathrm{i})}T_{\mathrm{opt},2}e^{ikL}}{2-e^{2ikL}(2-T_{\mathrm{opt},1}-T_{\mathrm{opt},2})} \tag{A.21}$$

Now assume that light is on resonance with the cavity of the length L, meaning that there are integer number (q_{opt}) of half-wavelengths inside the gap:

$$\lambda_0 = \frac{2L}{q_{\mathrm{opt}}} \qquad \text{or} \qquad k_0 = \frac{2\pi}{\lambda_0} = \frac{\pi q_{\mathrm{opt}}}{L} \tag{A.22}$$

This means: $e^{2ik_0L} = 1$. For a perturbation: $k = k_0 + \delta k$, $e^{2ikL} = e^{2i\delta kL}$. But $\delta k = \frac{\delta\omega}{c}$, and we can write $\delta\omega$ as detuning Δ. Taylor expanding to the first order, we get: $e^{2i\delta kL} \approx 1 + \frac{2iL\Delta}{c} = 1 + \frac{2\pi i\Delta}{\omega_{\mathrm{FSR}}}$.

This allows us to simplify equations A.18, A.19, A.20 and A.21 further. Additionally we can neglect all values of $T_{\mathrm{opt},1}$, $T_{\mathrm{opt},2}$ and $4\pi i\Delta/\omega_{\mathrm{FSR}}$, which appear in a sum with a number on the order of 1:

$$E^{(\mathrm{f})} = 4\frac{E^{(\mathrm{i})}}{T_{\mathrm{opt},1}+T_{\mathrm{opt},2}-\frac{4\pi i\Delta}{\omega_{\mathrm{FSR}}}} \tag{A.23}$$

$$E^{(\mathrm{b})} = -4\frac{E^{(\mathrm{i})}}{T_{\mathrm{opt},1}+T_{\mathrm{opt},2}-\frac{4\pi i\Delta}{\omega_{\mathrm{FSR}}}} \tag{A.24}$$

$$E^{(\mathrm{r})} = 2\frac{E^{(\mathrm{i})}\left(\frac{T_{\mathrm{opt},2}}{2}-\frac{T_{\mathrm{opt},1}}{2}-\frac{2\pi i\Delta}{\omega_{\mathrm{FSR}}}\right)}{T_{\mathrm{opt},1}+T_{\mathrm{opt},2}-\frac{4\pi i\Delta}{\omega_{\mathrm{FSR}}}} \tag{A.25}$$

$$E^{(\mathrm{t})} = 2\frac{E^{(\mathrm{i})}(-1)^{q_{\mathrm{opt}}}T_{\mathrm{opt},2}}{T_{\mathrm{opt},1}+T_{\mathrm{opt},2}-\frac{4\pi i\Delta}{\omega_{\mathrm{FSR}}}} \tag{A.26}$$

We can rewrite T_1 and T_2 if we consider the two definitions of finesse:

$$\mathcal{F}_{\mathrm{opt}} = \frac{\pi(R_{\mathrm{opt},1}R_{\mathrm{opt},2})^{1/4}}{1-\sqrt{R_{\mathrm{opt},1}R_{\mathrm{opt},2}}} \approx \frac{\pi}{1-\sqrt{R_{\mathrm{opt},1}R_{\mathrm{opt},2}}} \approx \frac{2\pi}{T_{1,\mathrm{opt}}+T_{2,\mathrm{opt}}} \tag{A.27}$$

and

$$\mathcal{F}_{\mathrm{opt}} = \frac{\omega_{\mathrm{FSR}}}{\kappa} \tag{A.28}$$

where κ is the total loss in the cavity.

From here we can write:

$$T_{\mathrm{opt},1(2)} = \frac{2\pi}{\omega_{\mathrm{FSR}}}\kappa_{1,(2)} \tag{A.29}$$

Where $\kappa_{1,(2)}$ is the loss through the first (second) mirror. We can now rewrite the equations A.23, A.24, A.25 and A.26 in terms of κ, κ_1 and κ_2.

$$E^{(\mathrm{f})} = \frac{E^{(\mathrm{i})}\frac{\omega_{\mathrm{FSR}}}{\pi}}{\frac{\kappa}{2} - i\Delta} \tag{A.30}$$

$$E^{(\mathrm{b})} = -\frac{E^{(\mathrm{i})}\frac{\omega_{\mathrm{FSR}}}{\pi}}{\frac{\kappa}{2} - i\Delta} \tag{A.31}$$

$$E^{(\mathrm{r})} = E^{(\mathrm{i})} - \frac{E^{(\mathrm{i})}\kappa_1}{\frac{\kappa}{2} - i\Delta} \tag{A.32}$$

$$E^{(\mathrm{t})} = (-1)^{q_{\mathrm{opt}}}\frac{E^{(\mathrm{i})}\kappa_2}{\frac{\kappa}{2} - i\Delta} \tag{A.33}$$

Let's now consider these fields separately:

- **Forward and backward propagating fields.** The forward propagating and backward propagating fields have the same amplitudes, as expected.

  The circulating power is often the quantity of interest, and therefore the field which is the square root of this circulating power. The amplitude of this field is given by:

  $$E^{(\mathrm{circ})} = \sqrt{\frac{1}{n_1}}E^{(\mathrm{f})} = \frac{E^{(\mathrm{i})}\sqrt{T_{\mathrm{opt},1}}\frac{\omega_{\mathrm{FSR}}}{2\pi}}{\frac{\kappa}{2} - i\Delta} = \frac{E^{(\mathrm{i})}\sqrt{\kappa_1}\sqrt{\frac{\omega_{\mathrm{FSR}}}{2\pi}}}{\frac{\kappa}{2} - i\Delta} \tag{A.34}$$

  Here we used the fact that transmission between a material with high n and $n = 1$ can be simplified to $T_{\mathrm{opt}} = \frac{4}{n_i}$.

  The energy stored in the cavity is the product of circulating power and the cavity round-trip time which is $\frac{2L}{c} = \frac{2\pi}{\omega_{\mathrm{FSR}}}$. The field amplitude, corresponding to the energy stored in the cavity, is then:

  $$E^{(\mathrm{circ,energy})} = \frac{E^{(\mathrm{i})}\sqrt{\kappa_1}}{\frac{\kappa}{2} - i\Delta} \tag{A.35}$$

- **Reflected field** The reflected field given above is already the square root of reflected power.

  $$E^{(\mathrm{meas,r})} = E^{(\mathrm{i})} - \frac{E^{(\mathrm{i})}\kappa_1}{\frac{\kappa}{2} - i\Delta} \tag{A.36}$$

- **Transmitted field** Since the transmitted power is measured, we scale the field so that it is the square root of that power. That field is given by:

  $$E^{(\mathrm{meas,t})} = \sqrt{\frac{n_2}{n_1}}E^{(\mathrm{t})} = \sqrt{\frac{T_{\mathrm{opt},1}}{T_{\mathrm{opt},2}}}E^{(\mathrm{t})} = (-1)^{q_{\mathrm{opt}}}\frac{E^{(\mathrm{i})}\sqrt{\kappa_1\kappa_2}}{\frac{\kappa}{2} - i\Delta} \tag{A.37}$$

It is useful to write the field amplitudes in terms of photons per second. The power carried by the incident field is given by:

$$P = \frac{1}{2}\epsilon_0 c|E^{(\mathrm{i})}|^2 \tag{A.38}$$

But the power can also be expressed in terms of photons per second $|a_{\mathrm{i}}|^2$:

$$P = \hbar\omega_{\mathrm{L}}|a_{\mathrm{i}}|^2 \tag{A.39}$$

Equating those two expressions, we see that:

$$a_{\mathrm{i}} = \sqrt{\frac{\epsilon_0 c}{2\hbar\omega_{\mathrm{L}}}}E^{(\mathrm{i})} \tag{A.40}$$

Since all the fields (transmitted, intracavity and reflected) are proportional to the incident field, we can rewrite all fields in terms of photons per second:

$$a = \frac{a_{\rm i}\sqrt{\kappa_1}}{\frac{\kappa}{2} - i\Delta} \tag{A.41}$$

$$a_{\rm r} = a_{\rm i} - \frac{a_{\rm i}\kappa_1}{\frac{\kappa}{2} - i\Delta} \tag{A.42}$$

$$a_{\rm t} = (-1)^q \frac{a_{\rm i}\sqrt{\kappa_1\kappa_2}}{\frac{\kappa}{2} - i\Delta} \tag{A.43}$$

Note that $|a|^2$ is measured in photons, while $|a_{\rm i}|^2$, $|a_{\rm r}|^2$ and $|a_{\rm t}|^2$ are measured in photons/sec.

Appendix B

Hermite-Gaussian modes of a Fabry-Perot cavity

B.1 General solution of a paraxial wave equation

In this section we will solve the paraxial wave equation, given by:

$$\nabla_T^2 u(\vec{r}) - 2ik\frac{\partial u(\vec{r})}{\partial z} = 0 \tag{B.1}$$

Where ∇_T^2 is a Laplacian operating on either (x, y) or (r, ϕ) coordinates, k is the wavenumber and u is defined so that:

$$\psi(\vec{r}) = u(\vec{r})e^{-ikz} \tag{B.2}$$

where ψ is the solution of the full wave equation. We assume a trial solution of the form:

$$u(\vec{r}) = A(z) \times \exp\left(-ik\frac{x^2+y^2}{2p(z)}\right) \tag{B.3}$$

Where $A(z)$ and $p(z)$ are unknown complex functions of z. Plugging this back into equation B.1 and working in Cartesian coordinates, we get, after some algebra:

$$-2i\left(1 + \frac{p(z)}{A(z)}\frac{dA(z)}{dz}\right) + \frac{k(x^2+y^2)}{p(z)}\left(\frac{dp(z)}{dz} - 1\right) = 0 \tag{B.4}$$

This expression is satisfied for all values of x and y only if both expressions in parenthesis are zero, which gives us two differential equations:

$$\frac{dp(z)}{dz} = 1 \qquad \text{and} \qquad \frac{dA(z)}{dz} = -\frac{A(z)}{p(z)} \tag{B.5}$$

The solutions to these equations are:

$$p(z) = p_0 + z - z_0 \qquad \text{and} \qquad A(z) = \frac{A_0 p_0}{p(z)} \tag{B.6}$$

Since p is complex, we can write it as a combination of real and imaginary parts, which we will choose to write as:

$$\frac{1}{p(z)} = \frac{1}{R(z)} - i\frac{\lambda}{\pi w(z)^2} \tag{B.7}$$

Here the "–" sign is necessary to prevent the solution from diverging at large distances from the beam axis. Plugging the expressions into equation B.3:

$$u(\vec{r}) = \frac{A_0 p_0}{p(z)} \times \exp\left(-ik\frac{x^2+y^2}{2R(z)} - \frac{x^2+y^2}{w(z)^2}\right) \tag{B.8}$$

From this expression it is clear that $w(z)$ is the transverse size of the beam (mode field radius) and $R(z)$ is the radius of curvature of the field. Any beam will have a focal point (the point where $w(z)$ is minimized). It is conventional to set $z = z_0 = 0$ at that point, that allows us to define the beam waist ($w_0 = w(0)$). The radius of curvature at that point is infinite. That allows us to define $p_0 = i\pi w_0^2/\lambda = iz_R$ (where we define the Rayleigh length $z_R = \pi w_0^2/\lambda$) and consequentially $p(z) = z + iz_R$. Plugging this back into equation B.7:

$$\frac{1}{z+iz_R} = \frac{1}{R(z)} - i\frac{\lambda}{\pi w(z)^2} \tag{B.9}$$

$$\frac{z-iz_R}{z^2+z_R^2} = \frac{1}{R(z)} - i\frac{\lambda}{\pi w(z)^2} \tag{B.10}$$

Matching real and imaginary parts, we get:

$$R(z) = \frac{z^2+z_R^2}{z} = \frac{z^2(1+(z_R/z)^2)}{z} = z\left(1+\left(\frac{z_R}{z}\right)^2\right) \tag{B.11}$$

and

$$w(z) = w_0\sqrt{1+\left(\frac{z}{z_R}\right)^2} \tag{B.12}$$

Putting everything back together, we get:

$$u(\vec{r}) = A_0\left(\frac{w_0^2}{w(z)^2} + i\frac{\pi w_0^2}{R(z)\lambda}\right) \times \exp\left(-ik\frac{x^2+y^2}{2R(z)} - \frac{x^2+y^2}{w(z)^2}\right) \tag{B.13}$$

If we rewrite the complex quantity as $Ae^{i\phi}$ we get:

$$u(\vec{r}) = A_0\frac{w_0}{w(z)} \times \exp\left(i\arctan\left(\frac{z\lambda}{\pi w_0^2}\right)\right) \times \exp\left(-ik\frac{x^2+y^2}{2R(z)} - \frac{x^2+y^2}{w(z)^2}\right) \tag{B.14}$$

The term $\arctan\left(\frac{z\lambda}{\pi w_0^2}\right)$ represents the additional phase the beam accumulates due to being Gaussian, as opposed to a plane wave. It is called Guoy phase shift.

A more general solution to the paraxial wave equation is:

$$u_{m,n}(\vec{r}) = A_0\frac{w_0}{w(z)}H_n\left(\frac{\sqrt{2}x}{w(z)}\right)H_m\left(\frac{\sqrt{2}y}{w(z)}\right) \times \exp\left(-\frac{r^2}{w(z)^2}\right)\exp\left(-i\left[\frac{kr^2}{2R(z)} - \phi_{\mathrm{G}}(z)\right]\right) \tag{B.15}$$

Where H_n and H_m are the Hermite polynomials, $\phi_{\mathrm{G}}^{(n,m)}(z) = (1+n+m)\arctan\left(\frac{z\lambda}{\pi w_0^2}\right)$ is the Guoy phase shift for higher order modes, and the $r^2 = x^2+y^2$ is the distance from the axis of propagation.

B.2 Gaussian mode in a Fabry-Perot cavity

Now consider a Fabry-Perot cavity. It consists of two mirrors with radius of curvature R_1 and R_2 separated by the distance L. We would like to find a Gaussian beam that will fit between those two mirrors. An important boundary condition is

that the mirror radius of curvature must match the radius of curvature of the Gaussian beam at each mirror. If we call the distance from the waist to one of the mirrors z_1 and the distance to the other mirror z_2, we can write:

$$R(z_1) = z_1\left(1+\left(\frac{z_R}{z_1}\right)^2\right) = -R_1 \tag{B.16}$$

$$R(z_2) = z_2\left(1+\left(\frac{z_R}{z_2}\right)^2\right) = R_2 \tag{B.17}$$

The "-" sign is there to account for the fact that mirrors are facing each other and that z_1 is negative. The cavity length is given by

$$L = z_2 - z_1 \tag{B.18}$$

It is convenient to define resonator g-parameters:

$$g_1 = 1 - \frac{L}{R_1} \qquad g_2 = 1 - \frac{L}{R_2} \tag{B.19}$$

The Rayleigh range can then be calculated from equations B.16, B.17 and B.18 as:

$$z_R^2 = \frac{g_1 g_2(1-g_1 g_2)}{(g_1+g_2-2g_1g_2)^2}L^2 \tag{B.20}$$

The locations of the two mirrors relative to the beam waist is then given by:

$$z_1 = -\frac{g_2(1-g_1)}{g_1+g_2-2g_1g_2}L \qquad z_2 = \frac{g_1(1-g_2)}{g_1+g_2-2g_1g_2}L \tag{B.21}$$

Assuming the mirrors are the perfect quarter wave stacks, the phase accumulated by a beam during the round trip should be an integer multiple of 2π, that is: $2(\phi(z_2)-\phi(z_1)) = 2\pi q$, where q is an integer. From here we write:

$$k^{(q,n,m)}(z_2-z_1) - (\phi_G^{(n,m)}(z_2) - \phi_G^{(n,m)}(z_1)) = \pi q \tag{B.22}$$

$$k^{(q,n,m)}L - (n+m+1)\arccos(\pm\sqrt{g_1 g_2}) = \pi q \tag{B.23}$$

Here the "+" sign corresponds to the situation when $R_1, R_2 > L$ and the "-" sign corresponds to the situation $R_1, R_2 < L$. We can solve this equation for k:

$$k^{(q,n,m)} = \pi q/L + (n+m+1)\arccos(\pm\sqrt{g_1 g_2})/L \tag{B.24}$$

We define the total Guoy phase accumulated as the wave travels through the cavity as:

$$\phi_{\mathrm{G}} = (n+m+1)\arccos(\pm\sqrt{g_1 g_2})/L \tag{B.25}$$

The mode inside the cavity can be written as:

$$\psi_{q,m,n}(\vec{r}) = A_0\frac{w_0}{w(z)}H_n\left(\frac{\sqrt{2}x}{w(z)}\right)H_m\left(\frac{\sqrt{2}y}{w(z)}\right) \tag{B.26}$$

$$\times \exp\left(-\frac{r^2}{w(z)^2}\right)\sin\left(k^{(q,n,m)}z + \frac{k^{(q,n,m)}r^2}{2R(z)} - \phi_{\mathrm{G}}^{(n,m)}(z) + \theta^{(q,n,m)}\right) \tag{B.27}$$

Where $\theta^{(q,n,m)}$ is defined to ensure the wave has the right phase at the boundaries. If the boundary conditions require the wave to have a node at the boundaries, then:

$$\theta^{(q,n,m)} = -k^{(q,n,m)}z_1 + \phi_{\mathrm{G}}^{(n,m)}(z_1) \tag{B.28}$$

If on the other hand, there should be an antinode at the boundary, then:

$$\theta^{(q,n,m)} = -k^{(q,n,m)} z_1 + \phi_{\mathrm{G}}^{(n,m)}(z_1) + \pi/2 \tag{B.29}$$

Note that this is equivalent to replacing $\sin$ with $\cos$ in equation B.27.

Finally it is convenient to define the waist size w_0:

$$w_0 = \sqrt{\frac{2L}{k^{(q,n,m)}}} \left(\frac{g_1 g_2 (1 - g_1 g_2)}{(g_1 + g_2 - 2 g_1 g_2)^2} \right)^{1/4} \tag{B.30}$$

Since we are usually working with TEM_{00} mode ($m = 0$, $n = 0$), we will write the electric field as:

$$\psi_{q,0,0}(\vec{r}) = E_0 \frac{w_0}{w(z)} e^{-\frac{r^2}{w(z)^2}} \sin\left(k^{(q,0,0)} z + \frac{k^{(q,0,0)} r^2}{2R(z)} - \phi_{\mathrm{G}}^{(0,0)}(z) + \theta^{(q,0,0)} \right) \tag{B.31}$$

We will also be making use of equations describing the mode waist at the mirrors, which are given by:

$$w_1 = \sqrt{\frac{2L}{k^{(q,n,m)}}} \left(\frac{g_2}{g_1 (1 - g_1 g_2)} \right)^{1/4} \tag{B.32}$$

$$w_2 = \sqrt{\frac{2L}{k^{(q,n,m)}}} \left(\frac{g_1}{g_2 (1 - g_1 g_2)} \right)^{1/4} \tag{B.33}$$

Appendix C

Machine drawings

This appendix provides the machine drawings used to build the devices, described in this thesis.

C.1 First generation device

In this section I provide the machine drawings that were used to machine the first generation device. All parts were machined out of brass. Figure C.1 shows the cell bottom of the first generation device. In this design we attempted to minimize the amount of helium necessary to fill the device. We later found that matching the size of the pocket into which the ferrules are epoxied to the size of the ferrules was not ideal, since the differential thermal contraction of the brass and glass led to cracking of one of the ferrules. The cell top for the first generation device, shown in figure C.2, was machined to fit exactly into the cell bottom, after the ferrules and piezo were glued. That also served to minimize the total volume of helium. Figure C.3 shows the brass plate that was epoxied to the piezo and to which the fibers were epoxied. Finally figure C.4 shows the stress reliefs used in the device. The length of the stress reliefs was chosen after all the cavities were glued to exactly accommodate all the fibers, therefore the stress reliefs are rather short.

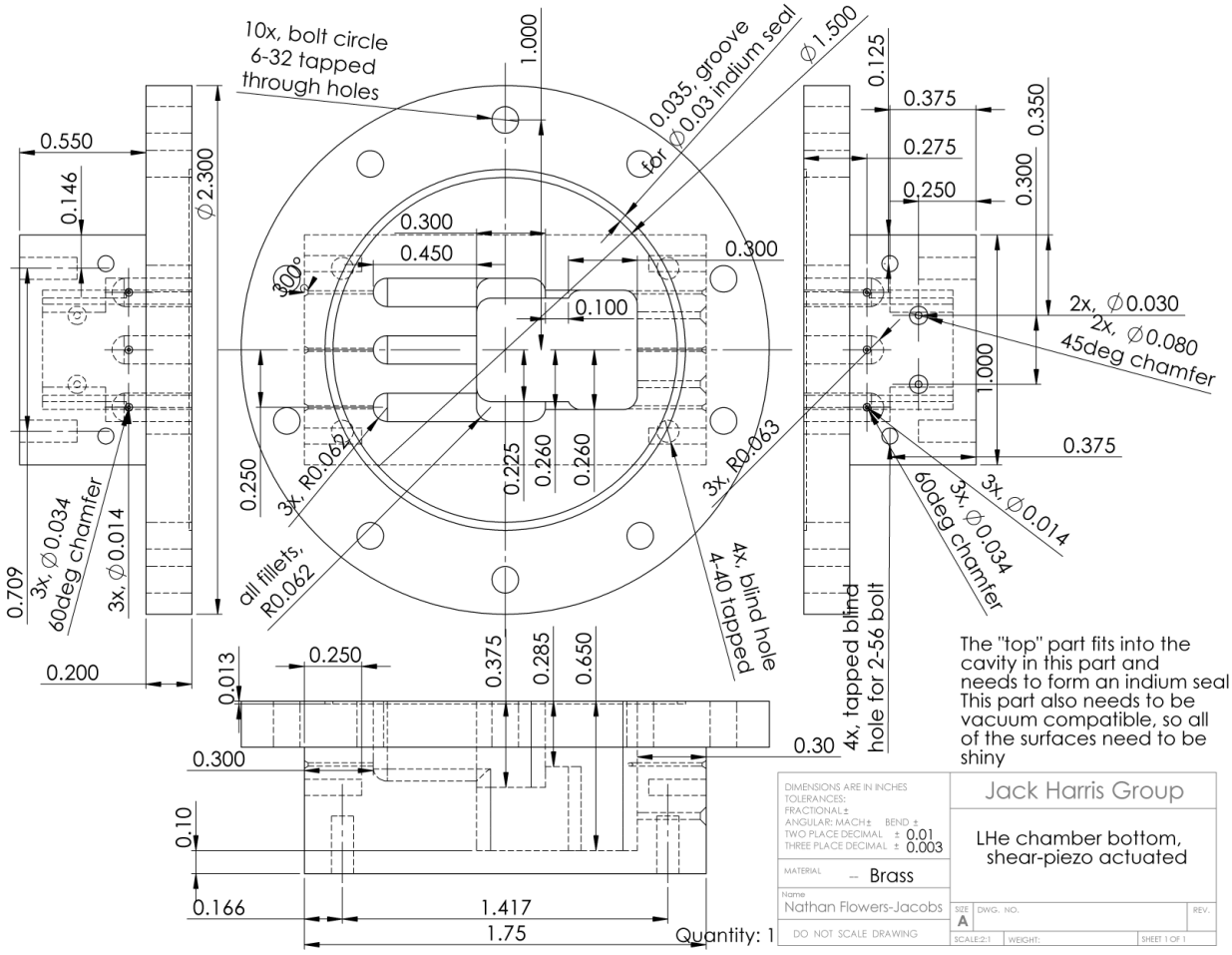

Figure C.1: First generation device cell bottom. This part was machined out of brass.

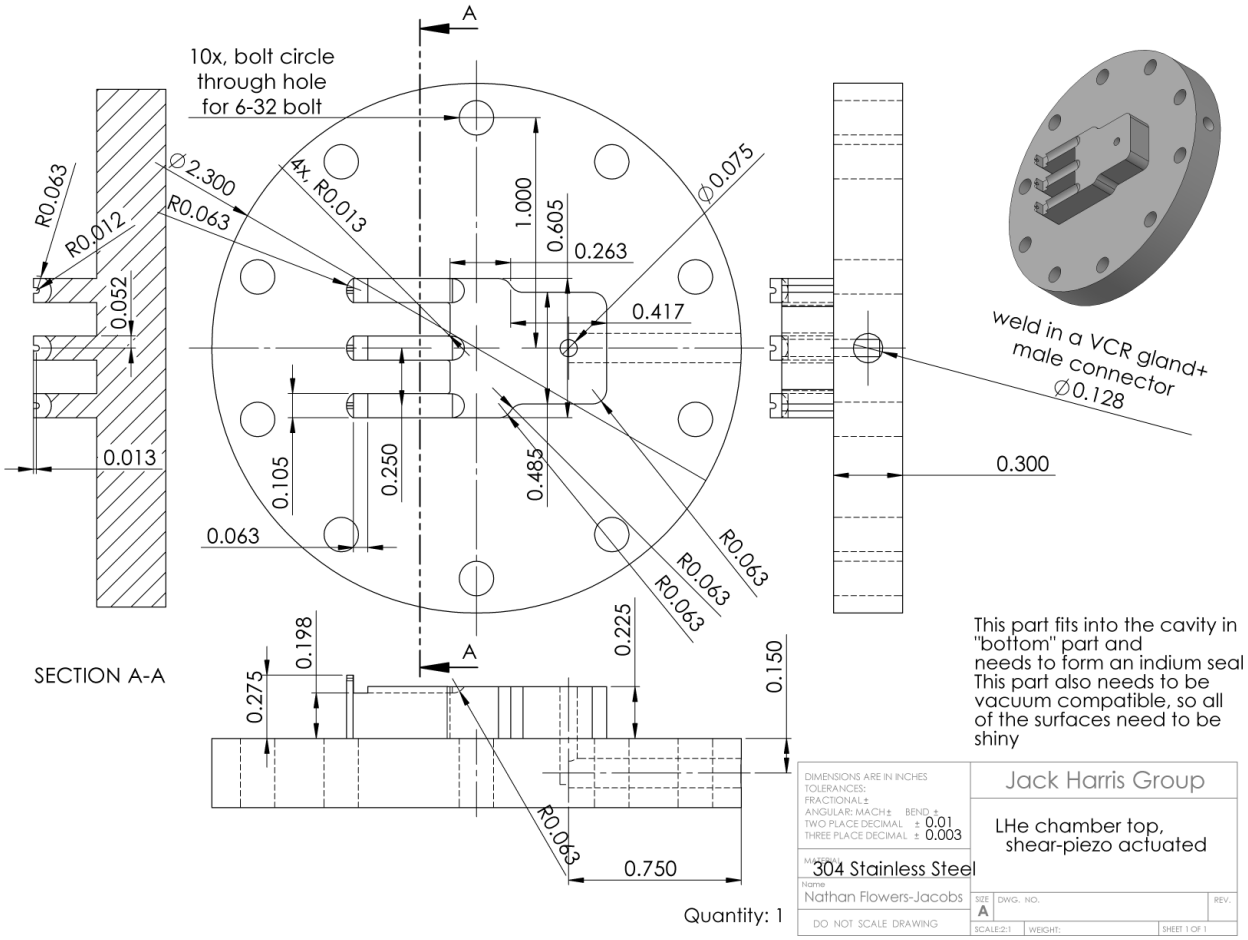

Figure C.2: First generation device cell top. This part was machined out of brass. Afterwards a 1/8" VCR®fitting was silver soldered into the opening.

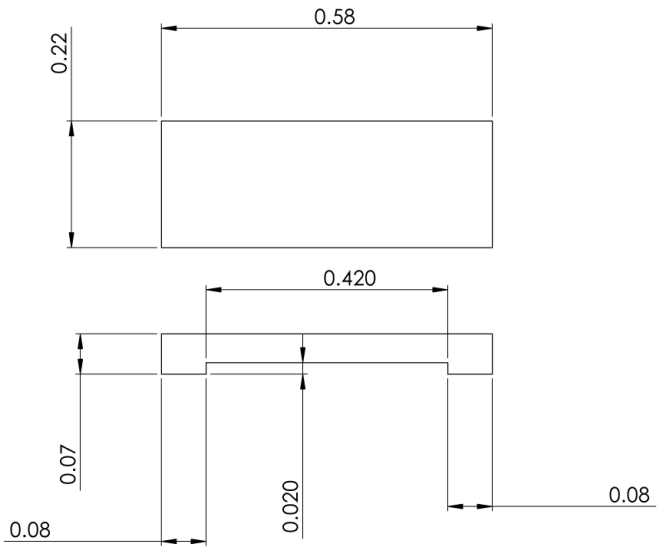

This part also needs to be vacuum compatible, so all of the surfaces need to be shiny

DIMENSIONS ARE IN INCHES TOLERANCES: FRACTIONAL ± ANGULAR: MACH ± BEND ± TWO PLACE DECIMAL ±0.01 THREE PLACE DECIMAL ±0.003	Jack Harris Group
MATERIAL brass --	LHe chamber piezo plate, shear-piezo actuated
Name Nathan Flowers-Jacobs	SIZE A / DWG. NO. / REV.
DO NOT SCALE DRAWING	SCALE:5:1 / WEIGHT: / SHEET 1 OF 1

Quantity: 1

Figure C.3: First generation device brass plate, that was glued to the piezo. This part was machined out of brass.

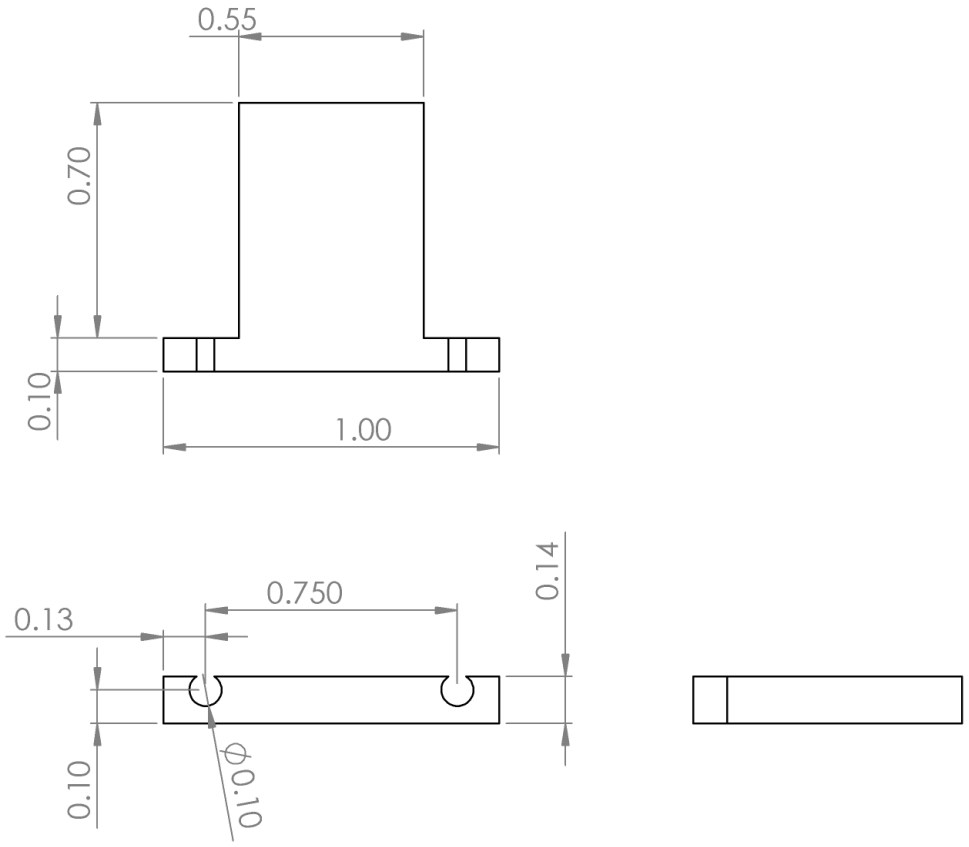

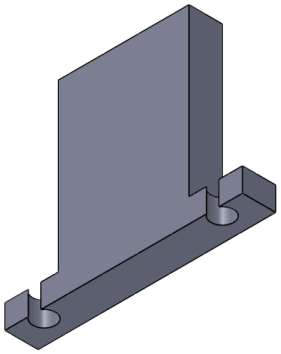

Name	Stress relief
Quantity	2
Generation	1
Material	Brass
Units	Inches
Tolerances	x.x ±0.05 x.xx ±0.005 x.xxx ±0.001
Designed by	Anna Kashkanova
Group	Jack Harris

Figure C.4: First generation device stress relief. Two of those parts were machined out of brass.

C.2 Second generation device

In this section I provide the machine drawings that were used to machine the second generation device. In order to improve thermal conductivity we machined both cell bottom (shown in figure C.5) and cell top (shown in figure C.6) out of OFHC copper and then had them gold-plated. In this design we decided that we do not need to minimize the total amount of helium, as long as we are careful about pumping out all helium from the device before warming up the fridge. Since we were not attempting to minimize the amount of helium anymore, the design for the cell bottom and cell top was simpler. The cell bottom had three indentations into which glass slides with ferrules were epoxied. There was just one flat protrusion on the cell top to occupy some of the empty space in the cell bottom. The stress reliefs (shown in figure C.7) were longer, as we had them machined before assembling the cavities. Finally we machined a mount (shown in figure C.8) and an adapter (shown in figure C.9) to attach the device to the fridge. Both parts are machined from OFHC copper and gold-plated. The drawings of the mount and the adapter are provided so that future designs for the devices could reuse this mount.

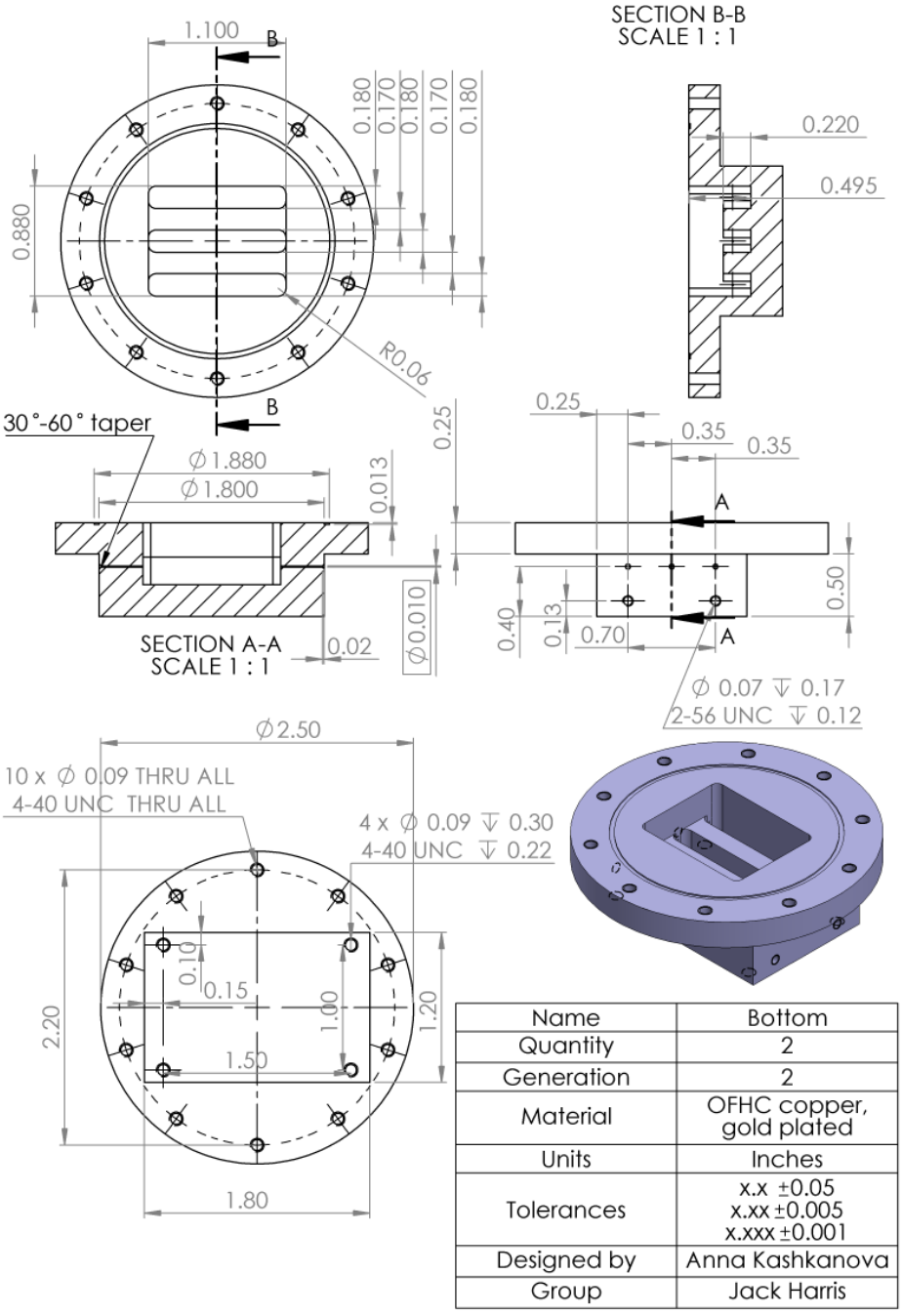

Name	Bottom
Quantity	2
Generation	2
Material	OFHC copper, gold plated
Units	Inches
Tolerances	x.x ±0.05 x.xx ±0.005 x.xxx ±0.001
Designed by	Anna Kashkanova
Group	Jack Harris

Figure C.5: Second generation device cell bottom. This part was machined out of OFHC copper, then gold plated.

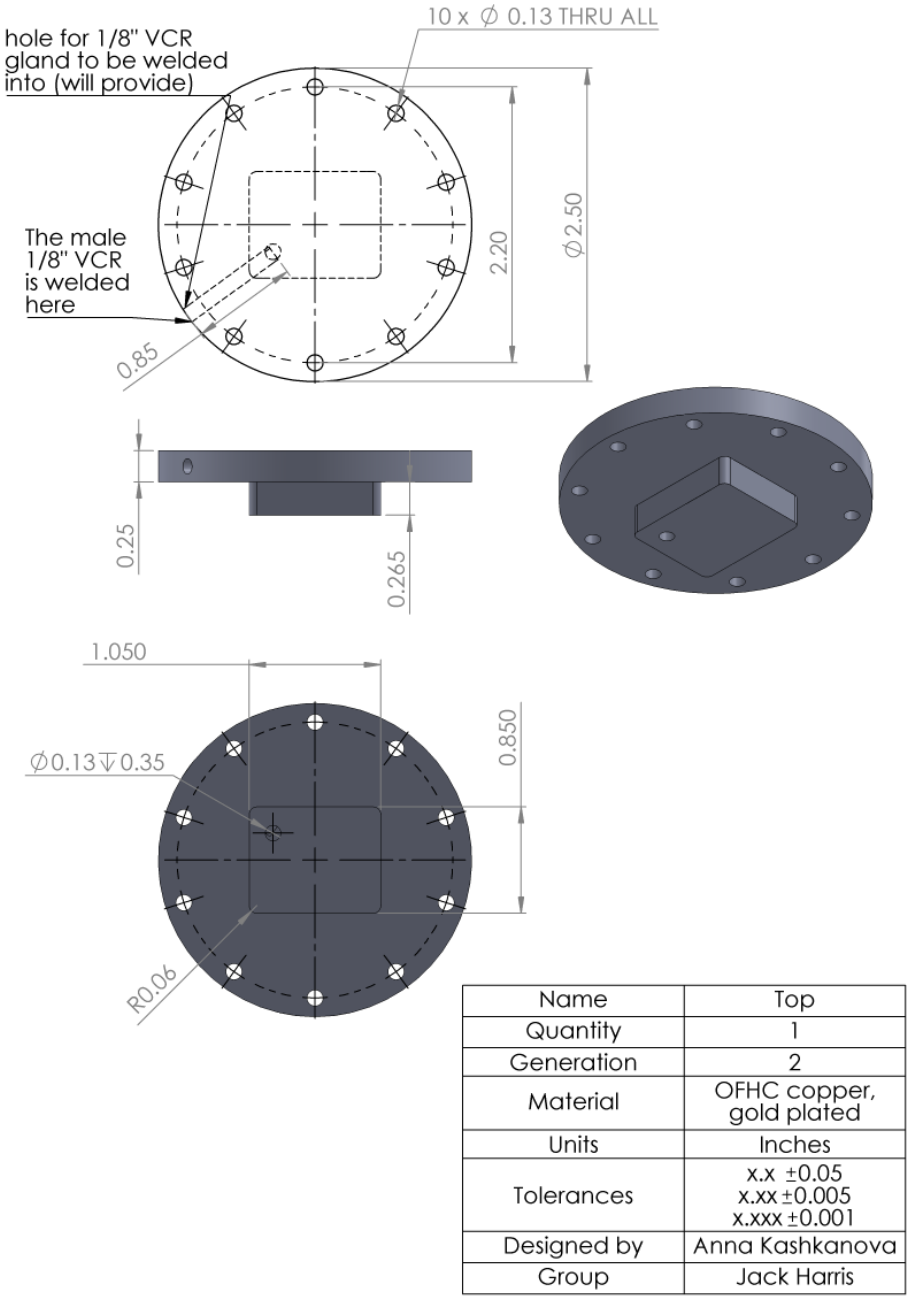

Name	Top
Quantity	1
Generation	2
Material	OFHC copper, gold plated
Units	Inches
Tolerances	x.x ±0.05 x.xx ±0.005 x.xxx ±0.001
Designed by	Anna Kashkanova
Group	Jack Harris

Figure C.6: Second generation device cell top. This part was machined out of OFHC copper. The gold plated. Afterwards a 1/8" VCR was silver soldered into the opening.

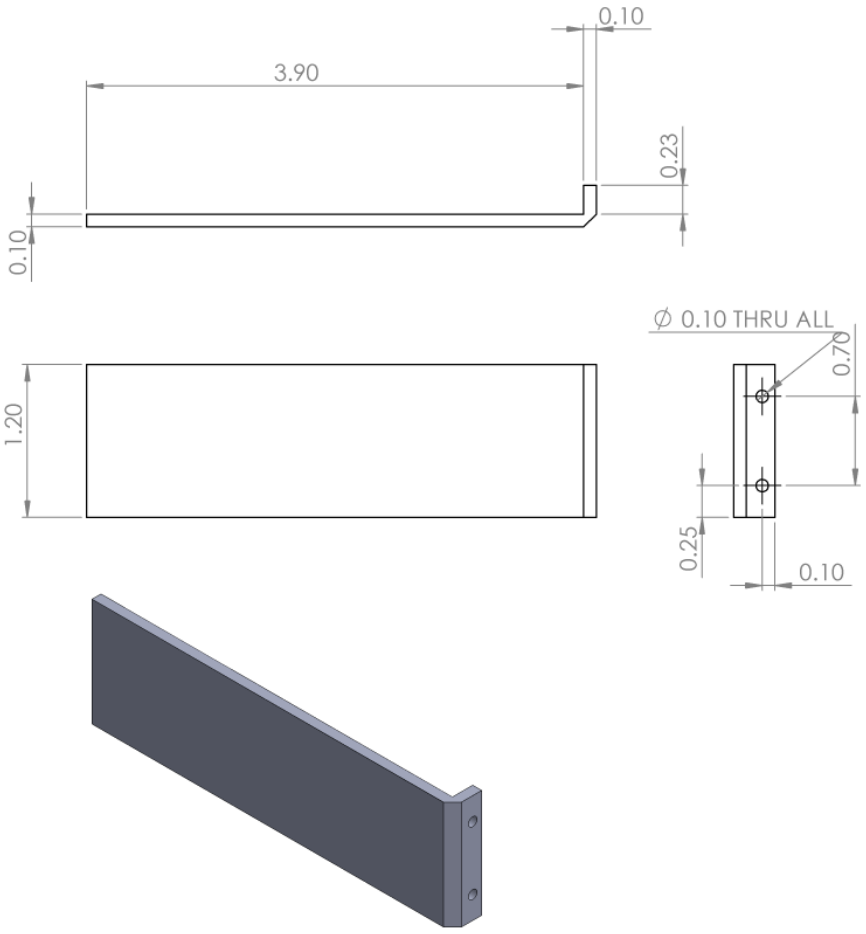

Name	Stress relief
Quantity	2
Generation	2,3
Material	Brass
Units	Inches
Tolerances	x.x ±0.05 x.xx ±0.005 x.xxx ±0.001
Designed by	Anna Kashkanova
Group	Jack Harris

Figure C.7: Second generation device stress relief. Two of those parts were machined out of brass.

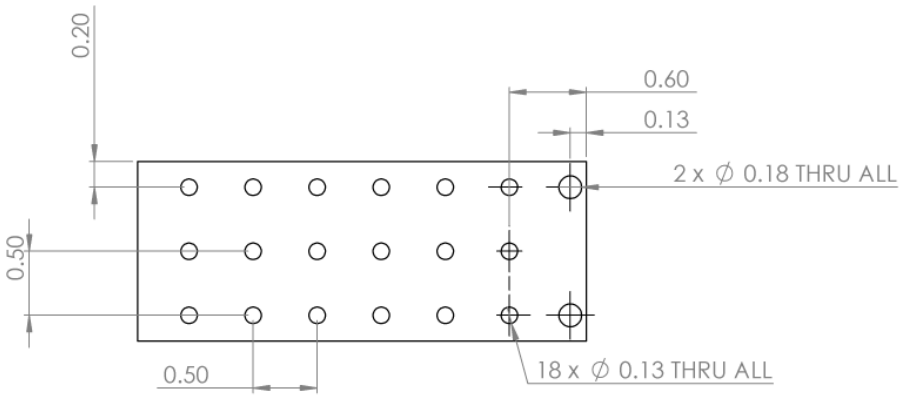

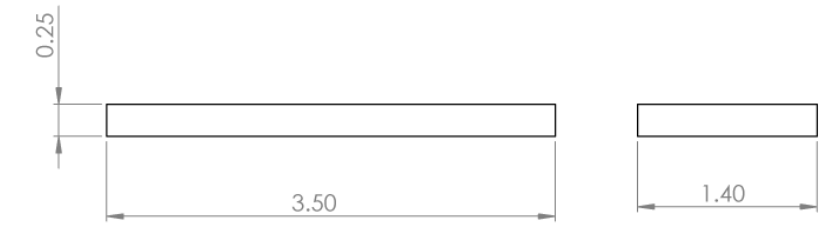

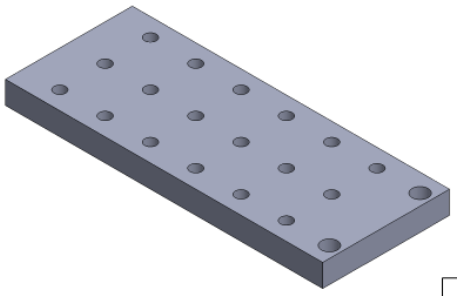

Name	Device mount
Quantity	1
Generation	2,3,4,5
Material	OFHC copper, gold plated
Units	Inches
Tolerances	x.x ±0.05 x.xx ±0.005 x.xxx ±0.001
Designed by	Anna Kashkanova
Group	Jack Harris

Figure C.8: Second generation device mount. Machined out of OFHC copper, then gold plated.

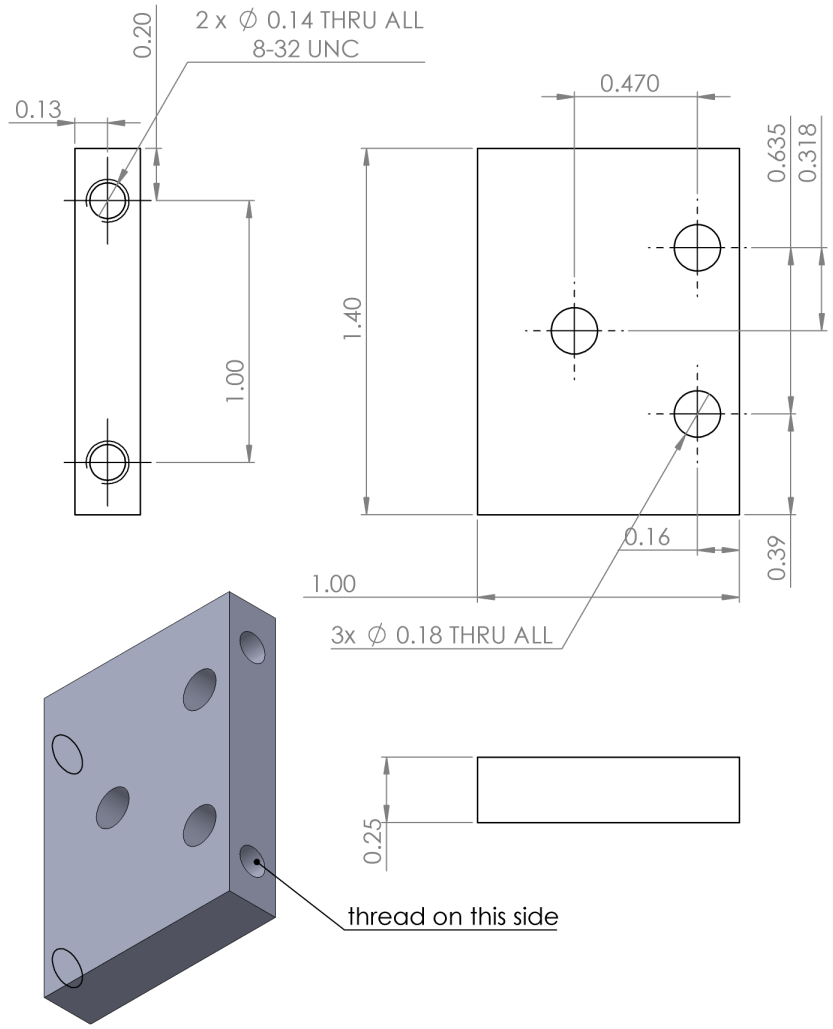

Name	Fridge adaptor
Quantity	1
Generation	2,3,4,5
Material	OFHC copper, gold plated
Units	Inches
Tolerances	x.x ±0.05 x.xx ±0.005 x.xxx ±0.001
Designed by	Anna Kashkanova
Group	Jack Harris

Figure C.9: Second generation device fridge adapter. Machined out of OFHC copper, then gold plated.

C.3 Third generation device

For the third generation device we machined the cell bottom out of brass, using the same design as for the second generation device (shown in figure C.5). In order to provide thermal link to the mixing chamber, we machined a new cell top out of copper. In addition, we made the protrusion on the cell top smaller (so that it only filled half of the volume in the cell bottom). This was done so that if a rapid boil-off of helium was to occur, there would be a pocket that gaseous helium could fill before it flows through the capillaries to the relief volume. The stress reliefs, mount and adapter were machined according to the design in figures C.7, C.8 and C.9.

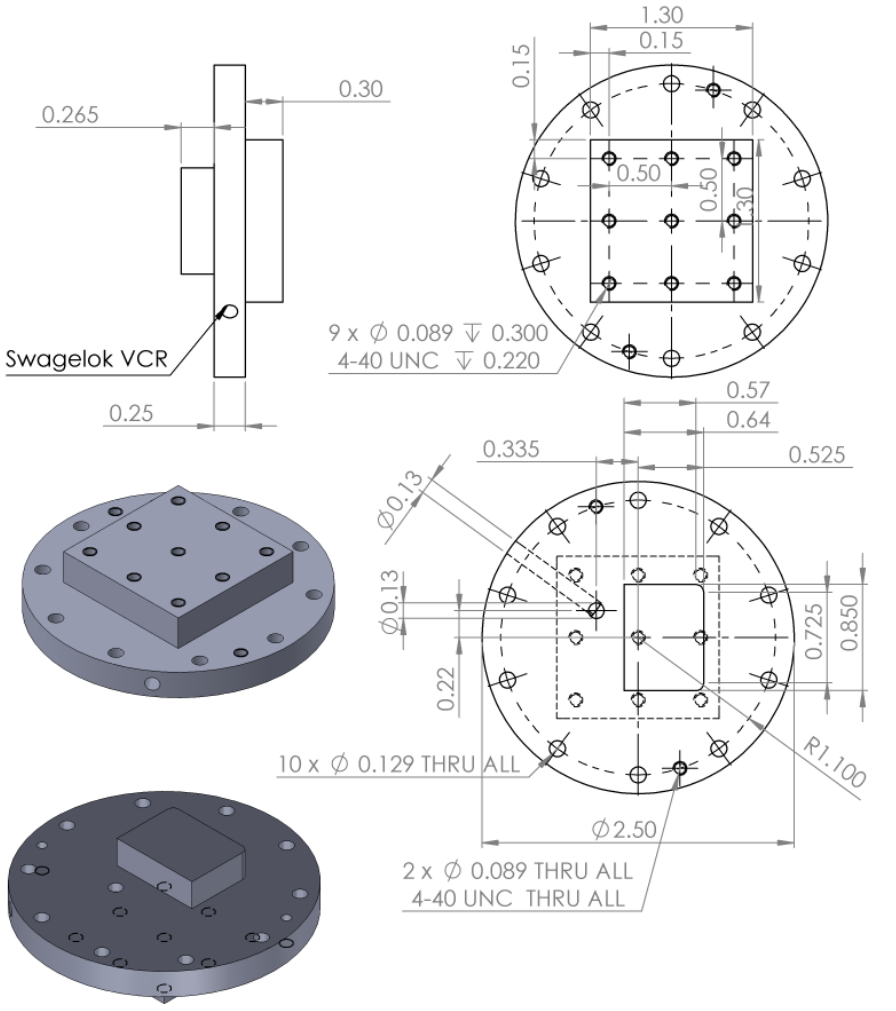

Name	Top
Quantity	1
Generation	3,4,5
Material	OFHC copper, gold plated
Units	Inches
Tolerances	x.x ±0.05 x.xx ±0.005 x.xxx ±0.001
Designed by	Anna Kashkanova
Group	Jack Harris

Figure C.10: Third generation device cell top. This part was machined out of OFHC copper. The gold plated. Afterwards a 1/8" VCR was silver soldered into the opening.

C.4 Fourth generation device

For the fourth generation device, we machined the cell bottom (shown in figure C.13) out of Invar to reduce thermal contraction. We reused the cell top, machined for the third generation device, according to figure C.10. We machined new stress reliefs, which are more easily mounted on the cell bottom. We reused the mount and adapter, machined for the second generation device and shown in figures C.8 and C.9.

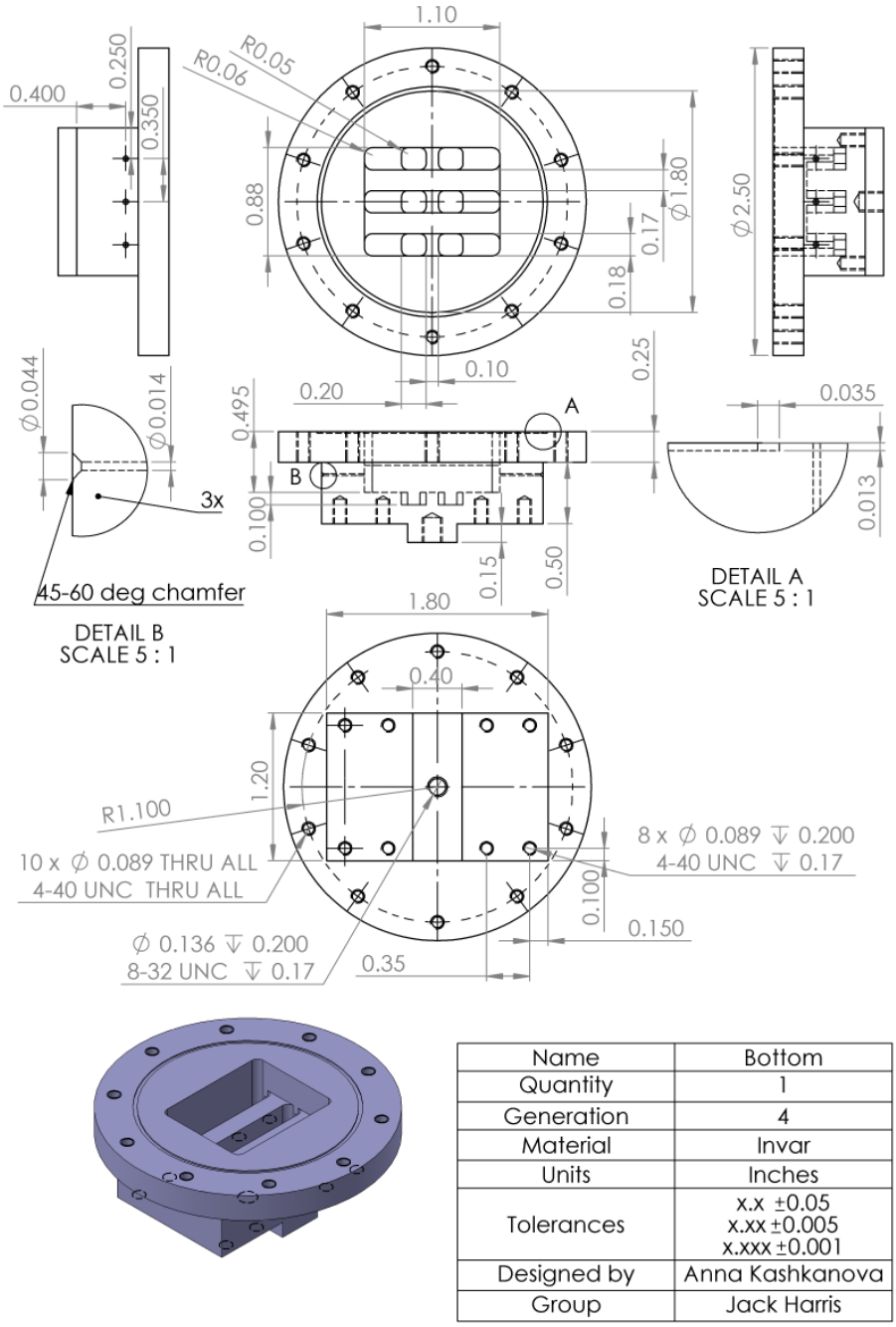

Name	Bottom
Quantity	1
Generation	4
Material	Invar
Units	Inches
Tolerances	x.x ±0.05 x.xx ±0.005 x.xxx ±0.001
Designed by	Anna Kashkanova
Group	Jack Harris

Figure C.11: Fourth generation device cell bottom. This part was machined out of invar.

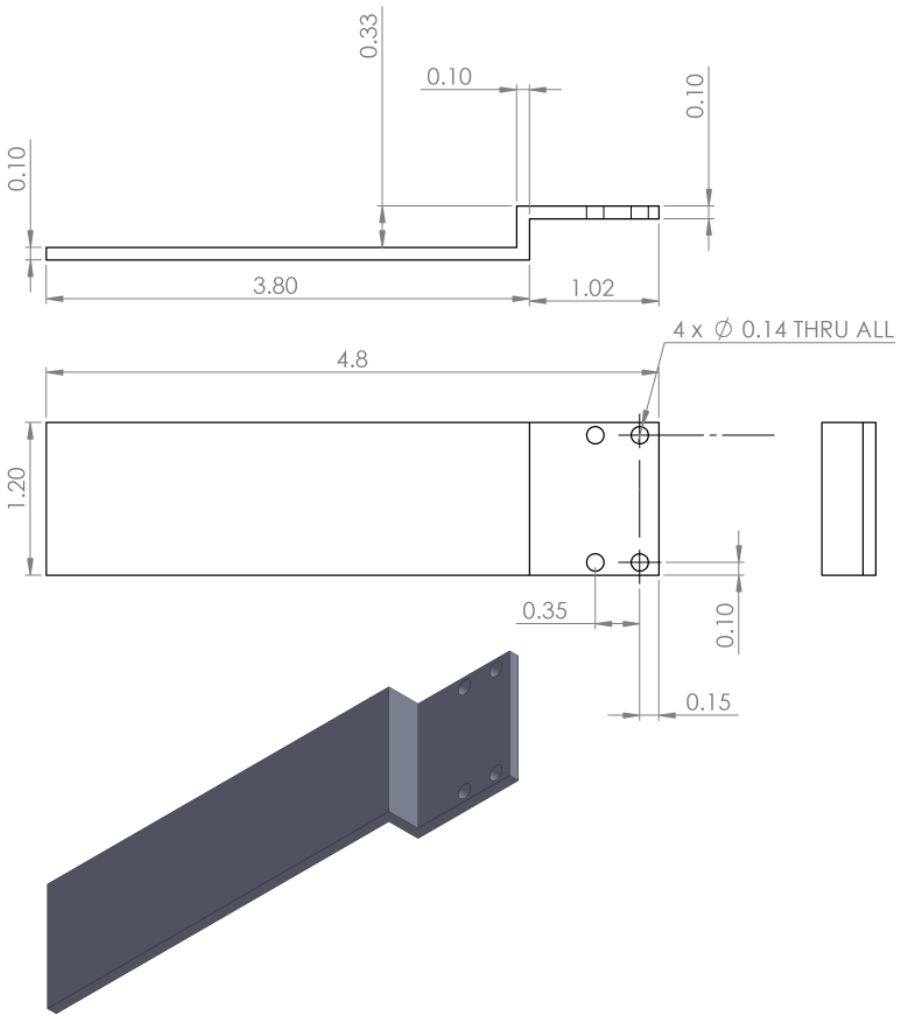

Name	Stress Relief
Quantity	2
Generation	4,5
Material	Brass
Units	Inches
Tolerances	x.x ±0.05 x.xx ±0.005 x.xxx ±0.001
Designed by	Anna Kashkanova
Group	Jack Harris

Figure C.12: Fourth generation device stress relief. Two of those parts were machined out of invar.

C.5 Fifth generation device

For the fifth generation device we machined the cell bottom (shown in figure C.13) out of Invar. To the cell bottom we attached tubes into which the fibers would be glued, as described in section 6.3.5. Additionally we made the stress reliefs wider to accommodate for the tubes, as described in section 6.3.5. We reused the mount and adapter, machined for the second generation device and shown in figures C.8 and C.9.

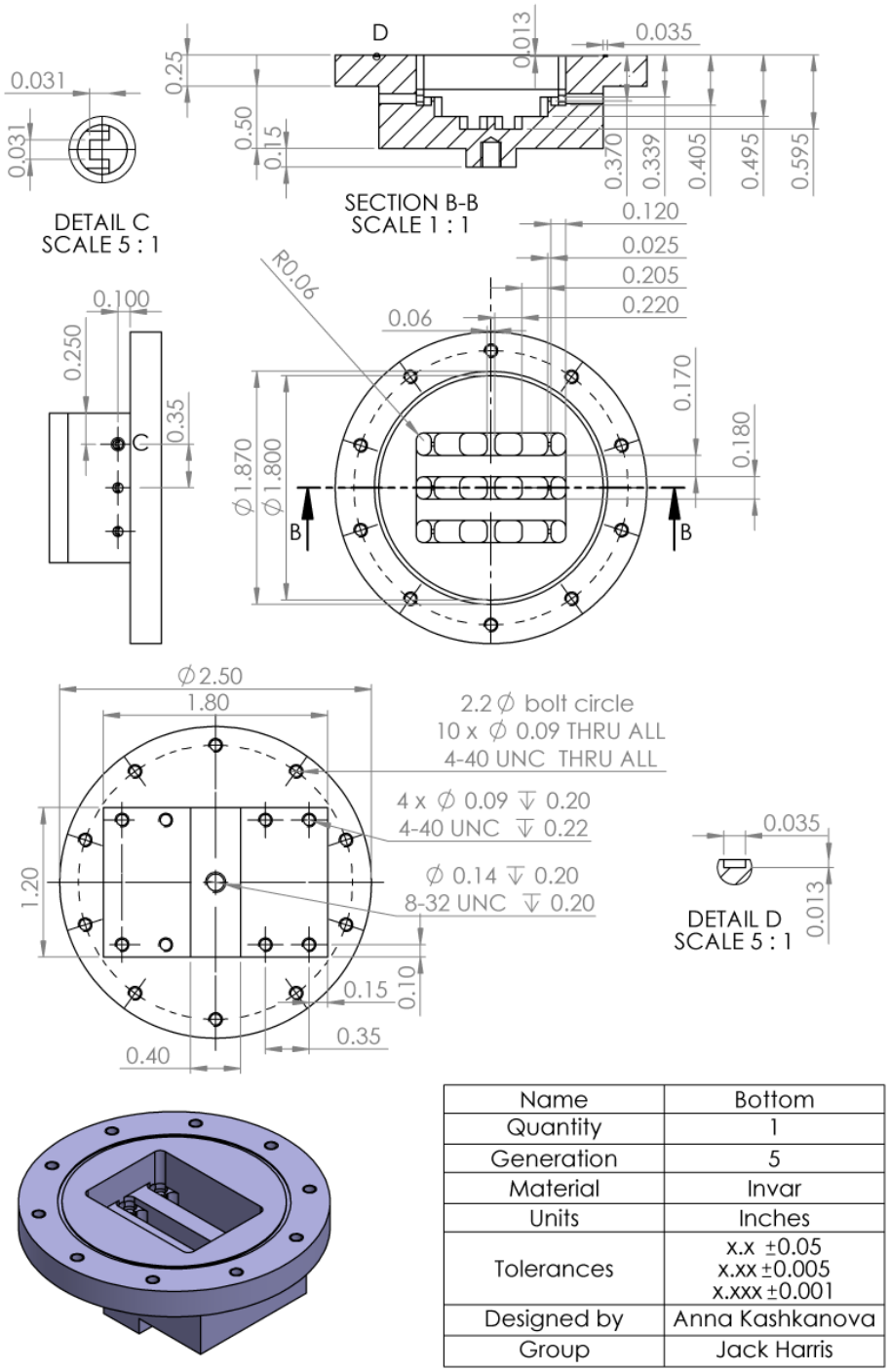

Name	Bottom
Quantity	1
Generation	5
Material	Invar
Units	Inches
Tolerances	x.x ±0.05 x.xx ±0.005 x.xxx ±0.001
Designed by	Anna Kashkanova
Group	Jack Harris

Figure C.13: Fifth generation device cell bottom. This part was machined out of Invar.

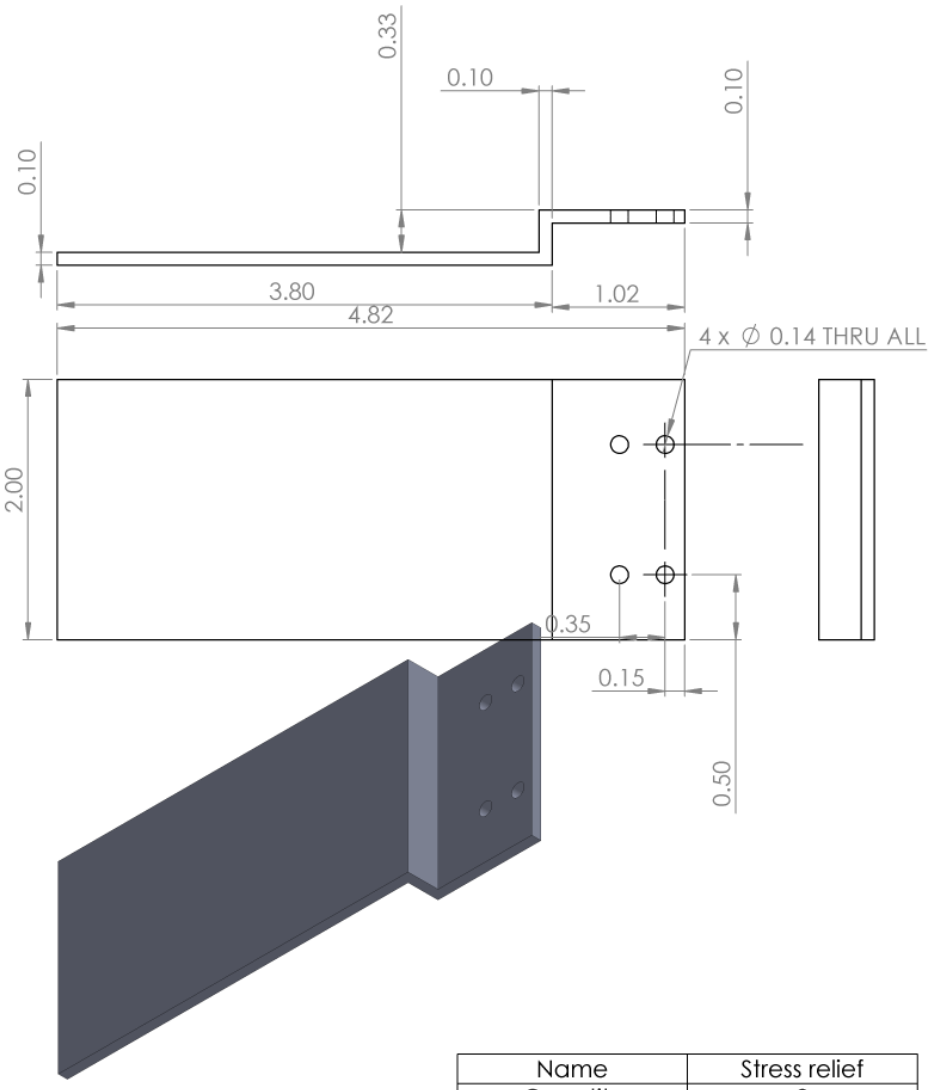

Name	Stress relief
Quantity	2
Generation	5
Material	Invar
Units	Inches
Tolerances	x.x ±0.05 x.xx ±0.005 x.xxx ±0.001
Designed by	Anna Kashkanova
Group	Jack Harris

Figure C.14: Fifth generation device stress relief. Two of those parts were machined out of invar.

C.6 Sintered silver heat exchanger box

We machined a box to house the sintered silver heat exchanger. The drawings for the box are shown in figures C.15, C.16. We machined the part that would be in contact with the mixing chamber and the sinter, out of copper. The rest of the box is made of stainless steel. The copper and stainless steel are silver soldered together, as shown in figure C.16 The reason to use copper was to improve thermal contact between the mixing chamber and the sinter. The reason to use stainless steel was to be able to weld VCR's to the box. The hole pattern on the top of the box was complicated by the fact that we wanted to attach the box to the mixing chamber with at least 2 screws. The hole pattern is shown in figure C.17.

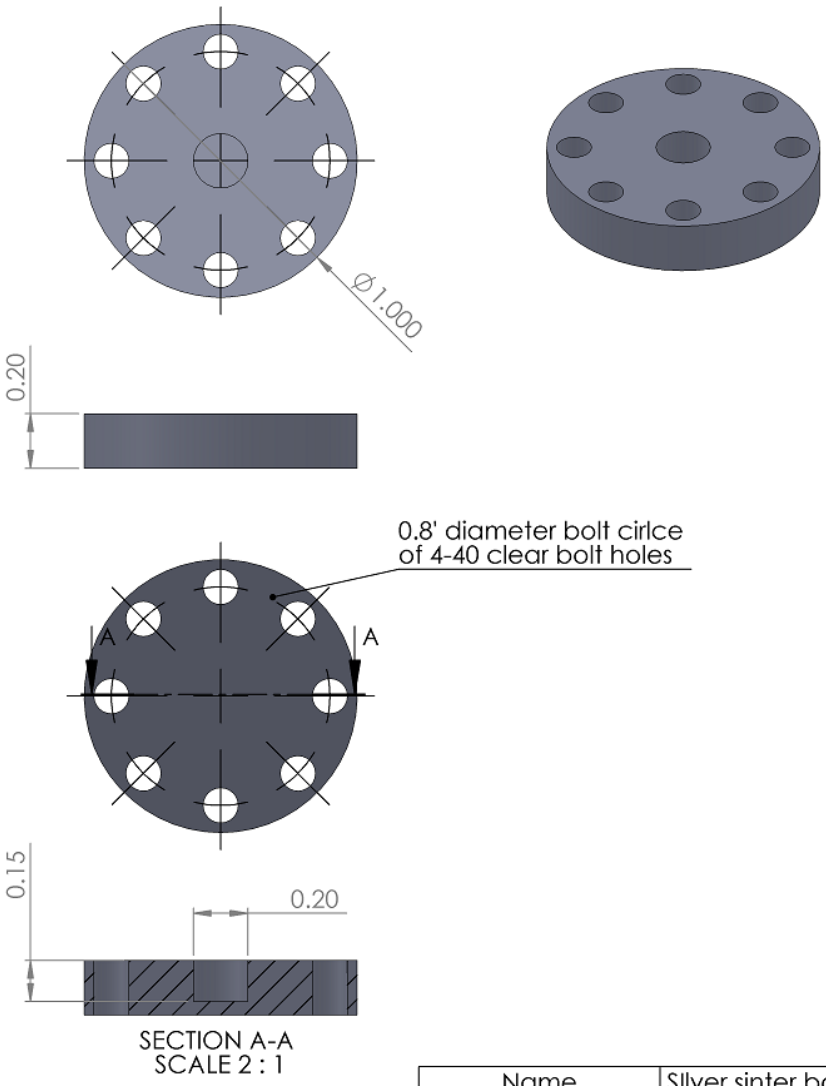

Name	SIlver sinter bottom
Quantity	1
Generation	1,2,3,4,5
Material	Stainless steel
Units	Inches
Tolerances	x.x ±0.05 x.xx ±0.005 x.xxx ±0.001
Designed by	Anna Kashkanova
Group	Jack Harris

Figure C.15: Sintered silver heat exchanger box bottom piece machined out of stainless steel

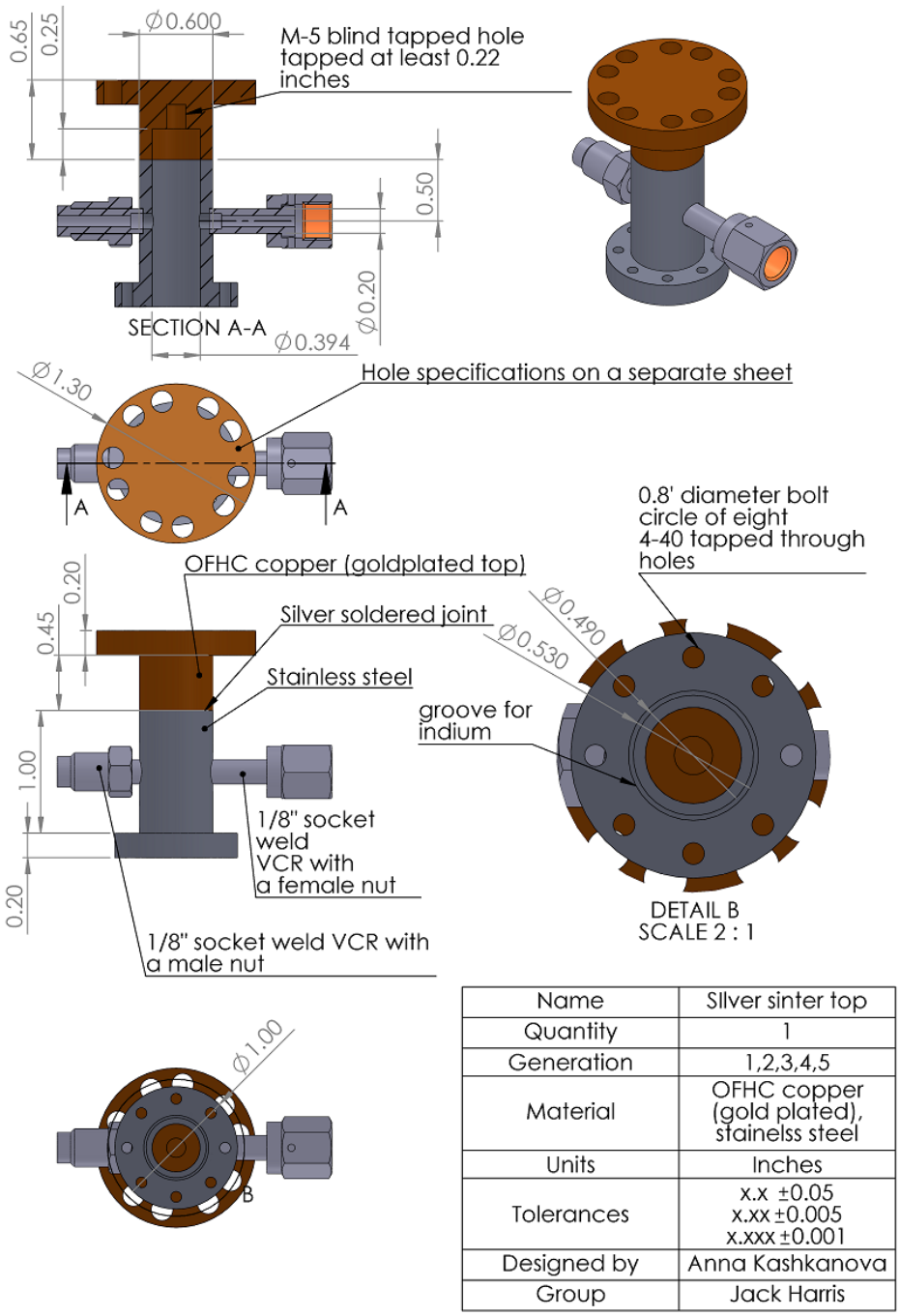

Name	SIlver sinter top
Quantity	1
Generation	1,2,3,4,5
Material	OFHC copper (gold plated), stainelss steel
Units	Inches
Tolerances	x.x ±0.05 x.xx ±0.005 x.xxx ±0.001
Designed by	Anna Kashkanova
Group	Jack Harris

Figure C.16: Sintered silver heat exchanger box top piece machined out of stainless steel and copper

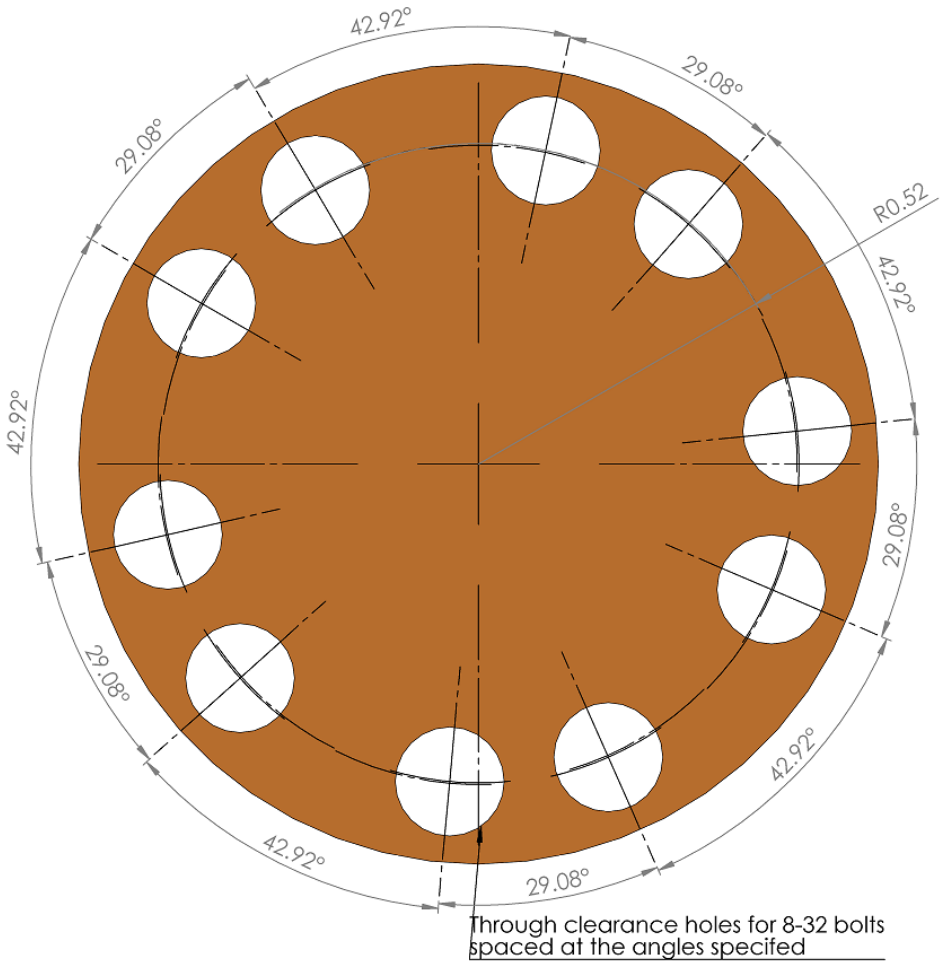

Name	Silver sinter top
Quantity	1
Generation	1,2,3,4,5
Material	OFHC copper, gold plated
Units	Inches
Tolerances	x.x ±0.05 x.xx ±0.005 x.xxx ±0.001
Designed by	Anna Kashkanova
Group	Jack Harris

Figure C.17: Sintered silver heat exchanger box top piece hole pattern

C.7 Room temperature fiber feedthrough

In figure C.18 I provide the drawing for the room temperature fiber feedthrough. It is a simple feedthrough for 12 fibers that will eventually need to be replaced (after we will have spliced to the fibers and broken the splices multiple times and the fibers become too short to use).

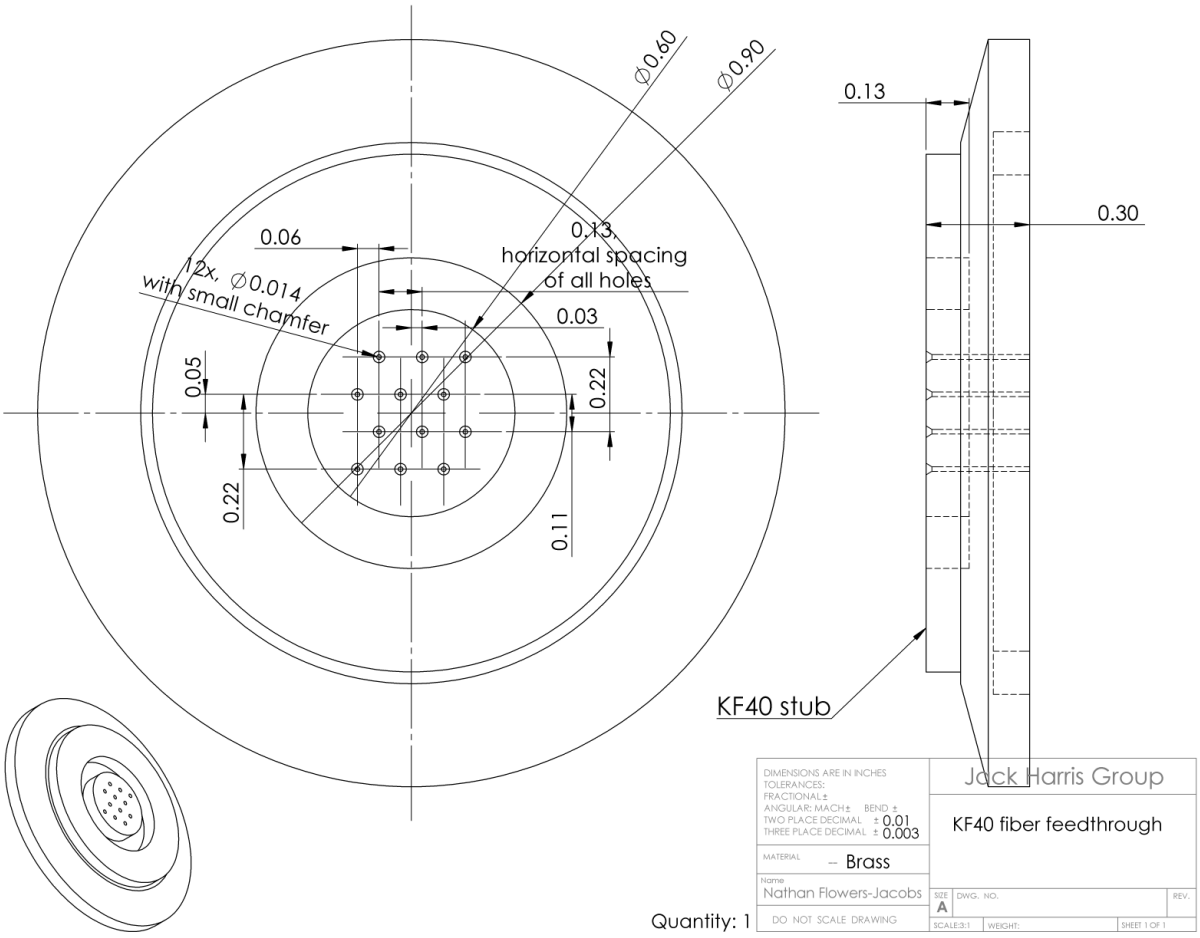

Figure C.18: Room temperature fiber feedthrough, machined out of a brass KF40 stub.

C.8 4K fiber heat sink

In figure C.19 I provide the drawing for the 4K fiber heat sink. This heat sink will eventually need to be replaced as well for the same reason as the room temperature fiber feedthrough.

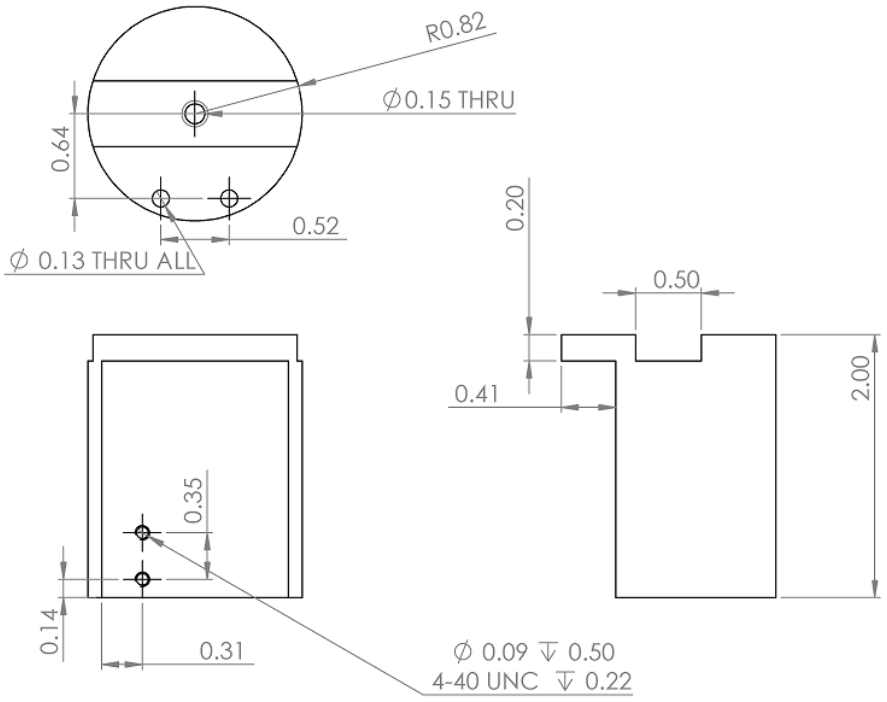

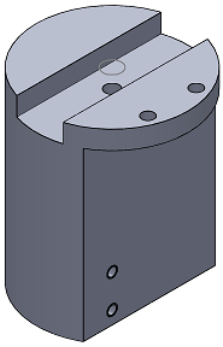

Name	Fiber heat sink
Quantity	1
Generation	1,2,3,4,5
Material	Brass
Units	Inches
Tolerances	x.x ±0.05 x.xx ±0.005 x.xxx ±0.001
Designed by	Anna Kashkanova
Group	Jack Harris

Figure C.19: 4K fiber heat sink machined out of brass.

Bibliography

[1] T. J. Kippenberg and K. J. Vahala. Cavity optomechanics: back-action at the mesoscale. *Science*, 321(5893):1172–6, 2008.

[2] P. Meystre. A short walk through quantum optomechanics. *Ann. Phys.*, 525(3):215–233, 2013.

[3] M. Aspelmeyer, T. J. Kippenberg, and F. Marquardt. Cavity optomechanics. *Rev. Mod. Phys.*, 86, 2014.

[4] M. Aspelmeyer, T. J. Kippenberg, and F. Marquardt. *Cavity optomechanics: nano- and micromechanical resonators interacting with light*. Quantum Science and Technology. Springer Berlin Heidelberg, 2014.

[5] W.P. Bowen and G.J. Milburn. *Quantum optomechanics*. Taylor & Francis, 2015.

[6] C. Caves. Quantum-mechanical radiation-pressure fluctuations in an interferometer. *Phys. Rev. Lett.*, 45(2):75–79, 1980.

[7] D. O'Connell et al. Quantum ground state and single-phonon control of a mechanical resonator. *Nature*, 464(7289):697–703, 2010.

[8] J. Chan et al. Laser cooling of a nanomechanical oscillator into its quantum ground state. *Nature*, 478(7367):89–92, 2011.

[9] M. Underwood et al. Measurement of the motional sidebands of a nanogram-scale oscillator in the quantum regime. *Phys. Rev. A - At. Mol. Opt. Phys.*, 92(6):1–5, 2015.

[10] T. P. Purdy, R. W. Peterson, and C. A. Regal. Observation of radiation pressure shot noise on a macroscopic object. *Science*, 339(6121):801–805, 2013.

[11] T. P. Purdy, K. E. Grutter, K. Srinivasan, and J. M. Taylor. Observation of optomechanical quantum correlations at room temperature. *Pre-print*, 2016.

[12] A. B. Shkarin. Quantum Optomechanics with superfluid helium. In preparation. 2017.

[13] R. W. Andrews et al. Bidirectional and efficient conversion between microwave and optical light. *Nat. Phys.*, 10(4):321–326, 2014.

[14] R. Riedinger et al. Nonclassical correlations between single photons and phonons from a mechanical oscillator. *Nature*, 530(7590):1–12, 2016.

[15] A. Safavi-Naeini et al. Squeezed light from a silicon micromechanical resonator. *Nature*, 500(7461):185–9, 2013.

[16] D. A. Golter et al. Optomechanical quantum control of a nitrogen-vacancy center in diamond. *Phys. Rev. Lett.*, 116(14):1–6, 2016.

[17] A. Cleland and M. Geller. Superconducting qubit storage and entanglement with nanomechanical resonators. *Phys. Rev. Lett.*, 93(7):070501, 2004.

[18] D. Kleckner et al. High finesse opto-mechanical cavity with a movable thirty-micron-size mirror. *Phys. Rev. Lett.*, 96(17):1–4, 2006.

[19] M. J. Weaver et al. Nested trampoline resonators for optomechanics. *Appl. Phys. Lett.*, 108(3), 2016.

[20] J D Thompson et al. Strong dispersive coupling of a high-finesse cavity to a micromechanical membrane. *Nature*, 452(7183):72–5, 2008.

[21] N. E. Flowers-Jacobs et al. Fiber-cavity-based optomechanical device. *Appl. Phys. Lett.*, 101(22):221109, 2012.

[22] A. M. Jayich et al. Cryogenic optomechanics with a Si_3N_4 membrane and classical laser noise. *New J. Phys.*, 14(11):115018, 2012.

[23] A.B. Shkarin et al. Optically Mediated Hybridization between Two Mechanical Modes. *Phys. Rev. Lett.*, 112(1):013602, 2014.

[24] D. Lee et al. Multimode optomechanical dynamics in a cavity with avoided crossings. *Nat. Commun.*, 6:6232, 2015.

[25] R. W. Peterson et al. Laser Cooling of a micromechanical membrane to the quantum backaction limit. *Phys. Rev. Lett.*, 116(6):1–6, 2016.

[26] M. Eichenfield, J. Chan, R. M. Camacho, K. J. Vahala, and O. Painter. Optomechanical crystals. *Nature*, 462(7269):78–82, 2009.

[27] M. Hossein-Zadeh, H. Rokhsari, A. Hajimiri, and K. Vahala. Characterization of a radiation-pressure-driven micromechanical oscillator. *Phys. Rev. A*, 74(2):023813, 2006.

[28] G. Anetsberger et al. Near-field cavity optomechanics with nanomechanical oscillators. *Nat. Phys.*, 5(12):909–914, 2009.

[29] J. D. Teufel et al. Sideband cooling micromechanical motion to the quantum ground state. *Nature*, 475(7356):359–363, 2011.

[30] C. Grebenkemper and J. Hagen. The dielectric constant of liquid helium. *Phys. Rev.*, 80:89–89, 1950.

[31] L. A. DeLorenzo and K. C. Schwab. Superfluid optomechanics: coupling of a superfluid to a superconducting condensate. *New J. Phys.*, 16:113020, 2014.

[32] L. A. DeLorenzo and K. C. Schwab. Ultra-high Q acoustic resonance in superfluid 4He. *J. Low Temp. Phys.*, 186(3-4):1–5, 2016.

[33] G. S. Agarwal and S. S. Jha. Theory of optomechanical interactions in superfluid He. *Phys. Rev. A*, 90(2):023812, 2014.

[34] G. I. Harris et al. Laser cooling and control of excitations in superfluid helium. *Nat. Phys.*, 12:788–793, 2016.

[35] X. Rojas and J. P. Davis. Superfluid nanomechanical resonator for quantum nanofluidics. *Phys. Rev. B*, 91(2):1–10, 2015.

[36] G. Koolstra, D. McKay, G. Yang, D. Czaplewski, and D. Schuster. Optomechanics with ripplons on superfluid helium. *Bulletin of the American Physical Society*, 60, 2015.

[37] A.D. Kashkanova et al. Superfluid Brillouin optomechanics. *Nat. Phys.*, 1(October):449–450, 2016.

[38] D. L. Mcauslan et al. Microphotonic forces From superfluid flow. *Phys. Rev. X*, 6(2):021012, 2016.

[39] S. Singh, L. A. De Lorenzo, I. Pikovski, and K. C. Schwab. Detecting continuous gravitational waves with superfluid ^{4} he. *arXiv preprint arXiv:1606.04980*, 2016.

[40] F. Souris, X. Rojas, P. H. Kim, and J. P. Davis. Ultralow-dissipation superfluid micromechanical resonator. *Phys. Rev. Appl.*, 7(4):1–15, 2017.

[41] A.D. Kashkanova et al. Optomechanics in superfluid helium coupled to a fiber-based cavity. *Journal of Optics*, 19(3):034001, 2017.

[42] A. D. Kashkanova et al. Observation of thermal fluctuations in a superfluid optomechanical system. In *Proc. of SPIE Vol*, volume 10116, pages 101160Q–1, 2017.

[43] A. B. Shkarin et al. Quantum optomechanics with superfluid helium density waves. *Bulletin of the American Physical Society*, 62, 2017.

[44] C. Brown, G. Harris, and J. G. E. Harris. Optomechanics in a levitated droplet of superfluid helium. *Bulletin of the American Physical Society*, 62, 2017.

[45] X. Sun, X. Zhang, C. Schuck, and H. X. Tang. Nonlinear optical effects of ultrahigh-Q silicon photonic nanocavities immersed in superfluid helium. *Sci. Rep.*, 3:1436, 2013.

[46] D.J. Griffiths. *Introduction to electrodynamics; 4th ed.* Pearson, Boston, MA, 2013.

[47] C.E. Mungan. Repairing an elementary explanation of radiation pressure. *Am. J. Phys.*, 77(November):965, 2009.

[48] W. Crookes. On attraction and repulsion resulting from radiation. *Philos. Trans. R. Soc. London*, 1(1874):501–527, 1874.

[49] O. Reynolds. On certain dimensional properties of matter in the gaseous state. *Philos. Trans. R. Soc. London*, 170(January):pp. 727–845, 1879.

[50] P.N. Lebedev. Experimental examination of light pressure. *Ann. der Physik*, 6(433):1–26, 1901.

[51] E. F. Nichols and G. F. Hull. A preliminary communication on the pressure of heat and light radiation. *Phys. Rev. (Series I)*, 13(5):307–320, 1901.

[52] E.F. Nichols and G.F. Hull. The pressure due to radiation. *Astrophysical journal*, 17(5):315–351, 1903.

[53] A. Ashkin. Acceleration and trapping of particles by radiation pressure. *Phys. Rev. Lett.*, 24(4):156–159, 1969.

[54] A. Ashkin, J. M. Dziedzic, J. E. Bjorkholm, and S. Chu. Observation of a single-beam gradient force optical trap for dielectric particles. *Opt. Lett.*, 11(5):288–290, 1986.

[55] L. Jauffred et al. Optical trapping of gold nanoparticles in air. *Nano Lett.*, 15(7):4713–4719, 2015.

[56] A. Ashkin, J. M. Dziedzic, and T. Yamane. Optical trapping and manipulation of single cells using infrared laser beams. *Nature*, 330(6150):769–771, 1987.

[57] P. M. Bendix and L. B. Oddershede. Expanding the optical trapping range of lipid vesicles to the nanoscale. *Nano Lett.*, 11(12):5431–5437, 2011.

[58] J.-D. Wen et al. Force unfolding kinetics of RNA using optical tweezers. . *Biophys. J.*, 92(9):2996–3009, 2007.

[59] M.D. Wang, H. Yin, R. Landick, J. Gelles, and S.M. Block. Stretching DNA with optical tweezers. *Biophys. J.*, 72(3):1335–1346, 1997.

[60] M Planck. On the law of the energy distribution in the normal spectrum. *Ann. Phys*, 4:1–11, 1901.

[61] A. Einstein. Concerning an heuristic point of view toward the emission and transformation of light. *Am. J. Phys.*, 33(5):367, 1965.

[62] A. Einstein. On the present status of radiation problem. *Phys. Zeitschrift*, 10(6):323, 1909.

[63] W. A. Edelstein, J. Hough, J. R. Pugh, and W. Martin. Limits to the measurement of displacement in an interferometric gravitational radiation detector. *J. Phys. E.*, 11(7):710, 1978.

[64] P. L. Bender et al. The Lunar laser ranging experiment. *Science*, 182(4109):229–38, 1973.

[65] B. Schwarz. Lidar: mapping the world in 3D. *Nat. Photonics*, 4(7):429–430, 2010.

[66] A. A. Michelson and E. W. Morley. On the relative motion of the Earth and the Luminiferous Ether. *Science (80-.).*, 34(203):333–345, 1887.

[67] B. P. Abbott et al. Observation of gravitational waves from a binary black hole merger. *Phys. Rev. Lett.*, 116(6):1–16, 2016.

[68] V. B. Braginskiy, A. B. Manukin, and M. Yu. Tikhonov. Investigation of dissipative ponderomotive effects of electromagnetic radiation. *Sov. J. Exp. Theor. Phys.*, 31(5):829–830, 1970.

[69] S. Weis et al. Optomechanically induced transparency. *Science*, 330(6010):1520–1523, 2010.

[70] H. Rokhsari, T. J. Kippenberg, T. Carmon, and K. J. Vahala. Radiation-pressure-driven micro-mechanical oscillator. *Opt. Express*, 13(14):5293, 2005.

[71] O. Arcizet, P.-F. Cohadon, T. Briant, M. Pinard, and A. Heidmann. Radiation-pressure cooling and optomechanical instability of a micromirror. *Nature*, 444(7115):71–4, 2006.

[72] F. Lecocq, J. B. Clark, R. W. Simmonds, J. Aumentado, and J. D. Teufel. Mechanically mediated microwave frequency conversion in the quantum regime. *Phys. Rev. Lett.*, 116(4):1–5, 2016.

[73] T. A. Palomaki, J. W. Harlow, J. D. Teufel, R. W. Simmonds, and K. W. Lehnert. Coherent state transfer between itinerant microwave fields and a mechanical oscillator. *Nature*, 495(7440):210–214, 2013.

[74] T. A. Palomaki, J. D. Teufel, R. W. Simmonds, and K. W. Lehnert. Entangling mechanical motion with microwave fields. *Science (80-.).*, 342(November):710–714, 2013.

[75] W. W. Campbell. Sir Joseph Normal Lockyer—1836-1920. *Publications of the Astronomical Society of the Pacific*, pages 265–268, 1920.

[76] D. Van Delft. Heike Kamerlingh Onnes and the road to liquid helium. *100 Years of Superconductivity*, 2011.

[77] P. Kapitza, J. F. Allen, and A.D. Misener. Viscosity of liquid helium below the λ-point. *Nature*, 141(3558):74–74, 1938.

[78] J. F. Allen and A. D. Misener. Flow of liquid helium II. *Nature*, 141(2):75–75, 1938.

[79] F. London. The λ-phenomenon of liquid helium and the Bose-Einstein degeneracy. *Nature*, 141:643–644, 1938.

[80] H. London. Thermodynamics of the thermomechanical effect of liquid He II. *Proc. R. Soc. London. Ser. A, ...*, pages 484–496, 1939.

[81] L. Landau. Theory of the superfluidity of helium II. *Phys. Rev.*, 60(4):356–358, 1941.

[82] L. Landau. On the theory of superfludity. *Phys. Rev. Lett.*, 75(5):88–885, 1949.

[83] Arp, V. Heat transport through helium II. *Cryogenics (Guildf).*, 10:96–105, 1970.

[84] A. D. B. Woods and R. A. Cowley. Structure and excitations of liquid helium. *Reports Prog. Phys.*, 36(9):1135–1231, 1973.

[85] H. Jackson. Foundations of a comprehensive theory of liquid ^{4}He. *Phys. Rev. B*, 20(11):4762–4762, 1979.

[86] H. A. Fairbank and C. T. Lane. Rollin film rates in liquid helium. *Phys. Rev.*, 76(8):1209–1211, 1949.

[87] B.V. Rollin and F. Simon. On the "film" phenomenon of liquid helium II. *Physica*, 6(2):219 – 230, 1939.

[88] F. Pobell. *Matter and methods at low temperatures*. Springer, Berlin, 2007.

[89] M. Wolfke and W. H. Keesom. On the change of the dielectric constant of liquid helium with the temperature . *Proceedings of the Koninklijke Akademie van Wetenschappen te Amsterdam*, 31(1/5):81–89, 1928.

[90] R. J. Donnelly and C. F. Barenghi. The observed properties of liquid helium at the saturated vapour pressure. *J. Phys. Chem. Ref. Data*, 27(6), 1998.

[91] T. J. Greytak and J. Yan. Light scattering from rotons in liquid helium. *Phys. Rev. Lett.*, 22(19):987–990, 1969.

[92] L. D. Landau and E. M. Lifshitz. *Electrodynamics of continuous media*. 1960.

[93] G. M. Seidel, R. E. Lanou, and W. Yao. Rayleigh scattering in rare-gas liquids. *Nucl. Instruments Methods Phys. Res. Sect. A Accel. Spectrometers, Detect. Assoc. Equip.*, 489(February):189–194, 2002.

[94] H. Z. Cummins and R. W. Gammon. Rayleigh and Brillouin scattering in liquids: The Landau—Placzek ratio. *J. Chem. Phys.*, 44(7):2785–2796, 1966.

[95] I. M. Khalatnikov and D. M. Chernikova. Relaxation phenomena in superfluid helium. *Sov. Phys. JETP*, 22(6):1336–1346, 1966.

[96] H. J. Maris and W. E. Massey. Phonon dispersion and the propagation of sound in liquid helium-4 below 0.6° K. *Phys. Rev. Lett.*, 25(4):25–27, 1970.

[97] H. J. Maris. Attenuation and velocity of sound in superfluid helium. *Phys. Rev. Lett.*, 28(5):277–280, 1972.

[98] H. J. Maris. Hydrodynamics of superfluid helium below 0.6 K. II. Velocity and attenuation of ultrasonic waves. *Phys. Rev. A*, 8(5), 1973.

[99] H. J. Maris. Phonon-phonon interactions in liquid helium. *Rev. Mod. Phys.*, 49(2), 1977.

[100] C. J. Pethick and D. T. Haar. On the attenuation of sound in liquid helium. *Physica*, 1966.

[101] W. Whitney and C.E. Chase. Ultrasonic velocity and dispersion in liquid helium II from 0.15 to 1.8 K. *Phys. Rev.*, 158(1):200–214, 1967.

[102] M. Barmatz and I. Rudnick. Velocity and attenuation of first sound near the λ point of helium. *Phys. Rev.*, 170(1967):224–238, 1968.

[103] J. S. Imai and I. Rudnick. Ultrasonic attenuation in liquid helium at 1 GHz. *Phys. Rev. Lett.*, 22(14), 1969.

[104] B. M. Abraham, Y. Eckstein, J. B. Ketterson, M. Kuchnir, and J. Vignos. Sound propagation in liquid ^{4}He. *Phys. Rev.*, 181(1):347–373, 1969.

[105] J. Jäckle. Calculation of the sound absorption in superfluid helium below 0.6 K. *Zeitschrift für Phys.*, 376:362–376, 1970.

[106] B. M. Abraham, Y. Eckstein, J. B. Ketterson, M. Kuchnir, and P. R. Roach. Velocity of sound, density, and Gruneisen constant in liquid ^{4}He. *Phys. Rev. A*, 1(2):250–257, 1970.

[107] R. K. Wehner and R. Klein. Sound absorption in liquid helium below 0.6 K. *Phys. Rev. Lett.*, 23(1):23–25, 1969.

[108] J. Jäckle and K. W. Kehr. Note on phonon lifetimes in He II. *Phys. Lett. A*, 37(3):205–206, 1971.

[109] R. L. St. Peters, T. J. Greytak, and G. B. Benedek. Brillouin scattering measurements of the velocity and attenuation of high frequency sound waves in superfluid helium. *Opt. Commun.*, 1:412–416, 1970.

[110] M. Sciacca, A. Sellitto, and D. Jou. Transition to ballistic regime for heat transport in helium II. *Phys. Lett. A*, 378(34):2471–2477, 2014.

[111] B. Bertman and T. A. Kitchens. Heat transport in superfluid filled capillaries. *Cryogenics (Guildf).*, 8(1):36–41, 1968.

[112] H. E. Bennett and J. O. Porteus. Relation between surface roughness and spectral reflectance at normal incidence. *J. Opt. Soc. Am.*, 51(2):123–129, 1961.

[113] C J Gorter and J H Mellink. On the irreversible processes in liquid helium II. *Physica*, 15(3-4):285–304, 1949.

[114] S. W. Van Sciver. *Helium cryogenics*. Springer New York, New York, NY, 2012.

[115] A. D. Pierce. *Acoustics*. McGraw-Hill Book Companyu, New York, NY, USA, 1982.

[116] Correspondence with LaserOptik mirror coating company, 2014.

[117] J. Capilla et al. Characterization of amorphous tantalum oxide for insulating acoustic mirrors. *2011 Jt. Conf. IEEE Int. Freq. Control Eur. Freq. Time Forum Proc.*, pages 1–6, 2011.

[118] M. J. Dodge. Refractive properties of magnesium fluoride. *Appl. Opt.*, 23(12):1980, 1984.

[119] W. M. Chu Wang, M. Jirmanus, N. Jirmanus, K. A. McCarthy, and H. H. Sample. Acoustic properties of hot-pressed cadmium sulfide and hot-pressed magnesium fluoride. In *Electro-Optics*, pages 59–62. International Society for Optics and Photonics, 1973.

[120] A. Duncanson and R. W. H. Stevenson. Some properties of magnesium fluoride crystallized from the melt. *Proceedings of the Physical Society*, 72(6):1001, 1958.

[121] H. R. Phillip and E. A. Taft. Kramers-Kronig Analysis of Reflectance Data for Diamond. *Phys. Rev.*, 136(5A), 1964.

[122] S. F. Wang et al. Determination of acoustic wave velocities and elastic properties for diamond and other hard materials. *Mater. Chem. Phys.*, 85(2-3):432–437, 2004.

[123] W. H. Renninger, P. Kharel, R. O. Behunin, and P. T. Rakich. Bulk crystalline optomechanics. *arXiv preprint arXiv:1703.08231*, 2017.

[124] Glen Harris, personal communication, 2017.

[125] R. Riviere, O. Arcizet, A. Schliesser, and T. J. Kippenberg. Optical response of silica microcavities in gaseous and superfluid Helium-4. *Lasers Electro-Optics Quantum Electron. Laser Sci. Conf. (QELS), 2010 Conf.*, 2010.

[126] X. Rojas, B. D. Hauer, A. J R Macdonald, P. Saberi, Y. Yang, and J. P. Davis. Ultrasonic interferometer for first-sound measurements of confined liquid He 4. *Phys. Rev. B - Condens. Matter Mater. Phys.*, 89(17):1–9, 2014.

[127] H. J. Carmichael. Spectrum of squeezing and photocurrent shot noise: a normally ordered treatment. *J. Opt. Soc. Am. B*, 4(10):1588, 1987.

[128] A. Shkarin. *Alexey Shkarin Thesis*. PhD thesis, Yale University, 2017.

[129] P. H. Roberts and R. J. Donnelly. Superfluid Mechanics. *Annu. Rev. Fluid Mech.*, 6:179–225, 1974.

[130] D. Hunger, C. Deutsch, R. J. Barbour, R. J. Warburton, and J. Reichel. Laser micro-fabrication of concave, low-roughness features in silica. *AIP Adv.*, 2:012119, 2012.

[131] D. Hunger et al. A fiber Fabry Perot cavity with high finesse. *New J. Phys.*, 12:065038, 2010.

[132] N. Thau. Optical fiber cavities. Master's thesis, Bonn University, 2012.

[133] K. Ott et al. Millimeter-long Fiber Fabry-Perot cavities. *Optics express*, 24:9839–9853, 2016.

[134] L. R. Brovelli and U. Keller. Simple analytical expressions for the reflectivity and the penetration depth of a Bragg mirror between arbitrary media. *Opt. Commun.*, 116(4-6):343–350, 1995.

[135] I. H. Malitson. Interspecimen comparison of the refractive index of fused silica. *JOSA*, 55(10), 1965.

[136] L. Gao, F. Lemarchand, and M. Lequime. Exploitation of multiple incidences spectrometric measurements for thin film reverse engineering. *Opt. Express*, 20(14):15734–15751, 2012.

[137] Nichrome 80 and Other Resistance Alloys - Technical Data and Properties. `http://www.wiretron.com/nicrdat.html`.

[138] A. M. Putnam and D. M. Lee. Repairing a small leak in a dilution refrigerator. *Journal of Low Temperature Physics*, 101(3-4):587–591, 1995.

[139] D. Lee et al. Observation of quantum motion in a nanogram-scale object. *arXiv Prepr. arXiv ...*, 2014.

[140] J. T. Krause. Anomalous temperature-frequency dependence of acoustic properties of vitreous silica at low temperatures. *Phys. Lett. A*, 43(4):325–326, 1973.

[141] A. Soukiassian et al. Acoustic Bragg mirrors and cavities made using piezoelectric oxides. *Appl. Phys. Lett.*, 90(4):042909, 2007.

[142] I. Koné et al. Guided acoustic wave resonators using an acoustic Bragg mirror. *Appl. Phys. Lett.*, 96(22):223504, 2010.

[143] Underwood M. *Cryogenic Optomechanics with a Silicon Nitride Membrane*. PhD thesis, Yale University, 2016.

[144] H. Franco, J. Bossy, and H. Godfrin. Properties of sintered silver powders and their application in heat exchangers at millikelvin temperatures. *Cryogenics*, 24(9):477 – 483, 1984.

[145] Z. Wang et al. Capillary rise in a microchannel of arbitrary shape and wettability: Hysteresis loop. *Langmuir*, 28(49):16917–16926, 2012.

[146] J. R. Eckardt, D. O. Edwards, S. Y. Shen, and F. M. Gasparini. Surface tension and surface entropy of superfluid ^{4}He. *Phys. Rev. B*, 16(5):1944–1953, 1977.

[147] J. F. S. Brachmann, H. Haupp, T. W. Hansch, and D. Hunger. Photothermal effects in ultra-precisely stabilized tunable microcavities. *Optics express*, 24(18):12813–12820, 2016.

[148] O. Florez et al. Brillouin scattering self-cancellation. *Nat. Commun.*, 7:11759, 2016.

[149] A. Butsch, J. R. Koehler, R. E. Noskov, and P. St. J. Russell. CW-pumped single-pass frequency comb generation by resonant optomechanical nonlinearity in dual-nanoweb fiber. *Optica*, 1(3):158–164, 2014.

[150] S. D. Penn et al. Mechanical loss in tantala/silica dielectric mirror coatings. *Class. Quantum Gravity*, 20(13):2917–2928, 2003.

[151] D. R. M. Crooks et al. Experimental measurements of mechanical dissipation associated with dielectric coatings formed using sio_2, ta_2o_5 and al_2o_3. *Class. Quantum Gravity*, 23(15):4953–4965, 2006.

[152] K. Numata et al. Systematic measurement of the intrinsic losses in various kinds of bulk fused silica. *Phys. Lett. Sect. A Gen. At. Solid State Phys.*, 327:263–271, 2004.

[153] I. Martin et al. Comparison of the temperature dependence of the mechanical dissipation in thin films of Ta_2O_5 and Ta_2O_5 doped with TiO_2. *Class. Quantum Gravity*, 26(15):155012, 2009.

[154] E. Hirose et al. Mechanical loss of a multilayer tantala/silica coating on a sapphire disk at cryogenic temperatures: Toward the KAGRA gravitational wave detector. *Phys. Rev. D*, 90:2–7, 2014.

[155] K. Yamamoto and S. Miyoki. Mechanical Loss of Reflective Coating at Low Temperature. In *Int. Cosm. Ray Conf.*, pages 3111–3114, 2003.

[156] M. Principe et al. Material loss angles from direct measurements of broadband thermal noise. *Phys. Rev. D*, 91:1–10, 2015.

[157] R. O. Pohl, X. Liu, and E. Thompson. Low-temperature thermal conductivity and acoustic attenuation in amorphous solids. *Rev. Mod. Phys.*, 74(October):991–1013, 2002.

[158] R. W. Whitworth. Experiments on the flow of heat in liquid helium below 0.7 degrees K. *Proc. R. Soc. A Math. Phys. Eng. Sci.*, 246(1246):390–405, 1958.

[159] I. Skachko. *Phase Diagram of a 2-Dimensional Electron System on the Surface of Liquid Helium*. PhD thesis, Rutgers University, 2006.

[160] M. Yuan, V. Singh, Y. M. Blanter, and G. A. Steele. Large cooperativity and microkelvin cooling with a three-dimensional optomechanical cavity. *Nat. Commun.*, 6, 2015.